Special Paper 472

THE GEOLOGICAL SOCIETY OF AMERICA®

Sixth Hutton Symposium

The Origin of Granites and Related Rocks

Edited by John D. Clemens, Colin Donaldson, Carol D. Frost, Alexander F.M. Kisters, Jean-François Moyen, Tracy Rushmer, and Gary Stevens

Sixth Hutton Symposium on The Origin of Granites and Related Rocks

Proceedings of a Symposium held in Stellenbosch, South Africa 2–6 July 2007

Guest Editor-in-Chief:
John D. Clemens
Department of Earth Sciences
University of Stellenbosch
Private Bag X1
7602 Matieland
South Africa

EESTRSE Editor:
Colin Donaldson

Guest Editors:
Carol D. Frost
Alexander F.M. Kisters
Jean-François Moyen
Tracy Rushmer
Gary Stevens

Copublished in volume format by arrangement with, and with permission of, The Royal Society of Edinburgh

THE GEOLOGICAL SOCIETY OF AMERICA®

Special Paper 472

3300 Penrose Place, P.O. Box 9140 ▪ Boulder, Colorado 80301-9140 USA

2010

© 2010 The Royal Society of Edinburgh

COPYRIGHT: It is the policy of The Royal Society of Edinburgh not to charge any royalty for the production of a single copy of any one article made for private study or research. Specific permission will not be required for photocopying multiple copies of copyrighted material to be used for bone fide educational purposes, provided this is done by a member of the staff of the university, school, or other comparable institution, for distribution without profit to student members of that institution and provided the copies are made from the original publication. Requests for copying or reprinting of any article for any other purpose should be sent to the Royal Society of Edinburgh.

The papers in this volume were originally published together as Earth and Environmental Science Transactions of the Royal Society of Edinburgh, Volume 100, parts 1 and 2 (ISBN 978 0 902198 31 9). Copies of that issue are available from the Royal Society of London's distribution agents.

Copyright is not claimed on any material prepared wholly by government employees within the scope of their employment.

Copublished as a limited edition in volume format in the United States by The Geological Society of America, Inc., 3300 Penrose Place, P.O. Box 9140, Boulder, Colorado 80301-9140, USA.

www.geosociety.org

Printed in USA

Library of Congress Cataloging-in-Publication Data

Hutton Symposium on the Origin of Granites and Related Rocks (6th : 2007 : Stellenbosch, South Africa)
Sixth Hutton Symposium on the Origin of Granites and Related Rocks : proceedings of a symposium held in Stellenbosch, South Africa, 2-6 July 2007 / guest editor-in-chief, John D. Clemens.
p. cm. -- (Special paper ; 472)
Includes bibliographical references.
ISBN 978-0-8137-2472-0 (pbk.)
1. Granite--Congresses. I. Clemens, John D. II. Title.

QE462.G7H88 2007
552'.3--dc22

2010027738

Cover: Photomicrograph of a Tasmanian dolerite containing residual silicic interstitial glass with a major element composition very similar to associated granophyric sills. Crossed polars; width = 4 mm. (From paper by S. Turner and T. Rushmer, "Similarities between mantle-derived A-type granites and voluminous rhyolites in continental flood basalt provinces.")

10 9 8 7 6 5 4 3 2 1

CONTENTS

J. D. CLEMENS
Preface v

Sharad MASTER
Plutonism versus Neptunism at the southern tip of Africa: the debate on the origin of granites at the Cape, 1776–1844 1

Hervé MARTIN, Jean-François MOYEN and Robert RAPP
The sanukitoid series: magmatism at the Archaean–Proterozoic transition 15

J.-F. MOYEN, D. CHAMPION and R. H. SMITHIES
The geochemistry of Archaean plagioclase-rich granites as a marker of source enrichment and depth of melting 35

Simon TURNER and Tracy RUSHMER
Similarities between mantle-derived A-type granites and voluminous rhyolites in continental flood basalt provinces 51

Luke LONGRIDGE, Roger L. GIBSON and Paul A. M. NEX
Structural controls on melt segregation and migration related to the formation of the diapiric Schwerin Fold in the contact aureole of the Bushveld Complex, South Africa 61

Jean H. BEDARD
Parental magmas of Grenville Province massif-type anorthosites, and conjectures about why massif anorthosites are restricted to the Proterozoic 77

Paul D. BONS, Jens K. BECKER, Marlina A. ELBURG and Kristjan URTSON
Granite formation: Stepwise accumulation of melt or connected networks? 105

Eric HORSMAN, Sven MORGAN, Michel de SAINT-BLANQUAT, Guillaume HABERT, Andrew NUGENT, Robert A. HUNTER and Basil TIKOFF
Emplacement and assembly of shallow intrusions from multiple magma pulses, Henry Mountains, Utah 117

M. O. M. RAZANATSEHENO, A. NEDELEC, M. RAKOTONDRAZAFY, J. G. MEERT and B. RALISON
Four-stage building of the Cambrian Carion pluton (Madagascar) 133

Keith BENN
Anisotropy of magnetic susceptibility fabrics in syntectonic plutons as tectonic strain markers: the example of the Canso pluton, Meguma Terrane, Nova Scotia 147

J. D. CLEMENS, P. A. HELPS and G. STEVENS
Chemical structure in granitic magmas – a signal from the source? 159

R. C. ECONOMOS, V. MEMETI, S. R. PATERSON, J. S. MILLER, S. ERDMANN and J. ŽÁK
Causes of compositional diversity in a lobe of the Half Dome granodiorite, Tuolumne Batholith, Central Sierra Nevada, California 173

Axel MÜLLER, Alfons M. van den KERKHOF, Hans-Jürgen BEHR, Andreas KRONZ and Monika KOCH-MÜLLER
The evolution of late-Hercynian granites and rhyolites documented by quartz – a review 185

C. JUNG, S. JUNG, E. HELLEBRAND and E. HOFFER
Trace element constraints on mid-crustal partial melting processes – A garnet ionprobe study from polyphase migmatites (Damara orogen, Namibia) 205

M. P. SEARLE, J. M. COTTLE, M. J. STREULE and D. J. WATERS
Crustal melt granites and migmatites along the Himalaya: melt source, segregation, transport and granite emplacement mechanisms 219

Takashi HOSHIDE and Masaaki OBATA
Zoning and resorption of plagioclase in a layered gabbro, as a petrographic indicator of magmatic differentiation 235

AUTHOR INDEX 251

Preface

J. D. Clemens

Department of Earth Sciences, University of Stellenbosch, Private Bag X1, 7602 Matieland, South Africa

The Sixth Hutton Symposium on the Origin of Granites and Related Rocks was held on July 2–6, 2007 at the University of Stellenbosch, South Africa, founded on granite, nestled at the feet of towering mountains and fringed by the rolling wine-lands of the Western Cape. This Special Issue opens with Master's historical account of how the Cape granites influenced 18th and early 19th century thinking on the origins of these rocks. The fascinating fact is that the granites of the Western Cape were apparently the first intrusive granites recognised outside Britain. The balance of the volume contains a collection of research papers derived from the meeting and illustrates some of the important directions in which granite research may be evolving. One of the characteristics of the papers and talks presented at the meeting was that there seemed to be some shift in interest, away from the crust as a source of granitic magmas and towards mantle rocks that have been metasomatised by subduction-zone fluids or melts. Nevertheless, the crust still holds pride of place as the cradle of granite genesis.

The next 15 papers fall into four groups. Those concerning the origins of the magmas themselves include Martin *et al*., Moyen *et al*., Turner & Rushmer, Longridge *et al*. and Bédard. Martin and his co-workers deal with sanukitoids and Closepet-type magmatism. Both these kinds of magmas are effectively unique to the period of time that marks the transition between the Archaean and the Proterozoic, and both are believed to be produced by partial melting of enriched mantle, rather than the crust. Martin *et al*. present their ideas on how the Archaean mantle was enriched, and they correlate the production of these distinctive magmas with the temporal evolution of heat production in the planet. The enrichment theme is continued in the paper by Moyen *et al*., who describe geochemical differences among Archaean TTG rocks (tonalites, trondhjemites and granodiorites) that lead them to recognise three subgroups whose chemistry they interpret as reflecting the degree of source enrichment and the depth of melting. Turner & Rushmer draw a parallel between the continental flood basalts and some A-type granites that they interpret as being mantle-derived. They note the geochemical similarities between rhyolitic rocks that cap flood basalt sequences and some kinds of A-type granites. They suggest that these A-type granitic rocks were produced by fractionation of basaltic parent magmas. Staying with the theme of mafic magmas, Longridge *et al*. examine the thermal effects of the Bushveld Complex on underlying metapelites. They show how partial melt from the metapelites was segregated, and they describe structures that indicate slow, buoyant diapiric ascent of the felsic magma, attended by ductility enhancement that allowed the formation of marginal shear zones. Bédard presents a model for the production of different types of anorthositic magmas by partial melting either of basaltic arc crust or of mantle enriched by subduction-derived fluids. He goes on to speculate as to why anorthositic magmas may or may not be present in a terrane, depending on temporal changes in lithospheric heat-production.

The papers dealing with the construction of plutons and emplacement include Bons *et al*., Horsman *et al*., Razanatseheno *et al*. and Benn. Considering the mechanisms of melt transfer from partially molten source to pluton, Bons *et al*. challenge the idea of a continuum model, with small veins progressively feeding ever-larger veins and dykes. Instead, they outline the features of, and evidence for, a model involving stepwise accumulation of melt volumes, arguing that the full range of vein/dyke sizes never coexists in nature. Horsman *et al*. describe evidence for the multi-pulse assembly of some shallow-level plutons in a tectonically-quiescent regime. They describe a progression from sill to laccolith to piston-type emplacement as the magma systems increase in volume. Focusing on a crudely-zoned pluton in Madagascar, Razanatseheno *et al*. provide structural and AMS (anisotropy of magnetic susceptibility) evidence of steeply-inclined magmatic foliations and lineations reflecting upward flow of the magmas, to fill the pluton in pulses of different composition. Benn continues the theme of AMS as a tool to study the structural evolution of plutons during and after their magmatic histories. He demonstrates that fabrics formed during the emplacement of syn-tectonic plutons can be distinguished from the effects of post-emplacement deformation, and that the post-emplacement fabrics can be used to shed light on regional bulk kinematics.

Several of the papers are concerned with the mechanisms by which granitic plutons acquired their internal compositional diversity. Clemens *et al*. review the evidence from a broad range of granitic bodies and find a common lack of evidence for significant degrees of differentiation. Departing from conventional wisdom, they conclude that the heterogeneities in most granitic bodies were not brought about through crystal fractionation, magma mixing, restite unmixing or any other differentiation mechanism, but were inherited from the magma sources and only slightly modified thereafter. In contrast, Economos *et al*. examine the causes of compositional diversity in the Tuolumne batholith, taking the Half Dome granodiorite as their example, and conclude that fractionation was the dominant process. Taking a less conventional approach to these kinds of problems, Müller *et al*. review the evolution of Late Hercynian felsic magmas through the study of quartz crystals in the rocks. They use cathodoluminescence imaging, Fourier-transform infrared spectroscopy and electron probe microanalysis to reveal the growth and alteration features that reflect the changes in magma compositions (including dissolved H_2O content) and crystallisation conditions. Features such as adiabatic and non-adiabatic magma ascent, temporary storage of magma and mixing with more mafic magma can all be discerned, illustrating the utility of this technique for tracing a magma's history.

The balance of the volume consists of three papers presenting specific case studies that range from work on prospective protoliths for granitic magmas and the processes of melting and magma migration to a study of the genesis of some anorthositic magmas. Jung *et al*. use garnet REE zoning patterns to reveal the intricacies of chemical equilibrium and disequilibrium during partial melting of metasedimentary rocks in the Damara orogen of Namibia. The results have importance for the understanding of REE patterns in

© 2009 The Royal Society of Edinburgh. doi:10.1017/S175569100901620X

crustally-derived granitic magmas. In the context of granitic magmatism in continental collision zones, Searle *et al*. investigate the formation of Himalayan granites. They find that, here, fluid-absent, mid-crustal melting of the Proterozoic protolith was due to a combination of thermal relaxation and high rates of internal heat production. Both mantle heat sources and the oft-cited shear-heating mechanism are ruled out. Finally, in a return to the mantle whence, it has been claimed, all good things come, Hoshide & Obata describe the fractionation mechanisms, in the Murotomisaki gabbro (Japan), that led to the production of layers of felsic magma. Surprisingly, it seems that flushing by aqueous fluids led to preferential remelting of plagioclase, and the formation of anorthositic layers that spawned diapiric upwellings within the magma body.

From the above it will be apparent that there is a great degree of variety here, and something for nearly every taste. If these papers represent the present thrust of granite-related research, it would seem that we can expect future progress particularly in understanding (1) the melting processes that lead to the formation of granitic magmas; (2) the physical, chemical and kinetic controls on the compositions of granitic magma; and (3) the relationships between the production of magma pulses and the mechanisms and time-scales of pluton construction and magma flow within plutons. As with most predictions, this is probably incorrect. In any case, it will be fascinating to see what themes dominate in the next Hutton Symposium.

Plutonism versus Neptunism at the southern tip of Africa: the debate on the origin of granites at the Cape, 1776–1844

Sharad Master

Economic Geology Research Institute, School of Geosciences, University of the Witwatersrand, P. Bag 3, WITS 2050, Johannesburg, South Africa
Email: sharad.master@wits.ac.za

ABSTRACT: The Cape Granites are a granitic suite intruded into Neoproterozoic greywackes and slates, and unconformably overlain by early Palaeozoic Table Mountain Group orthoquartzites. They were first recognised at Paarl in 1776 by Francis Masson, and by William Anderson and William Hamilton in 1778. Studies of the Cape Granites were central to some of the early debates between the Wernerian Neptunists (Robert Jameson and his former pupils) and the Huttonian Plutonists (John Playfair, Basil Hall, Charles Darwin), in the first decades of the 19th Century, since it is at the foot of Table Mountain that the first intrusive granites outside of Scotland were described by Hall in 1812. The Neptunists believed that all rocks, including granite and basalt, were precipitated from the primordial oceans, whereas the Plutonists believed in the intrusive origin of some igneous rocks, such as granite. In this paper, some of the early descriptions and debates concerning the Cape Granites are reviewed, and the history of the development of ideas on granites (as well as on contact metamorphism and sea level changes) at the Cape in the late 18th Century and early to mid 19th Century, during the emerging years of the discipline of geology, is presented for the first time.

KEY WORDS: Abel, Anderson, Barrow, Darwin, Degrandpré, Hall, Hamilton, Hausmann, Itier, Jameson, Krauss, Masson, Paarl, South Africa, Table Mountain

The Cape Granites, situated in the Western Cape Province of South Africa, at the southern tip of the African continent, are a granitic suite dated at c. 550–510 Ma, intruded into Malmesbury Group greywackes and slates of the Neoproterozoic Saldanian Belt (Armstrong *et al*. 1998; Da Silva *et al*. 2000). These Neoproterozoic rocks are unconformably overlain by the early Palaeozoic Cape Supergroup, of which the lowermost Table Mountain Group, comprising mainly orthoquartzites, constitutes the top two-thirds of Table Mountain in Cape Town (Moore 1994; Compton 2004).

Whilst aspects of the geology of Table Mountain and the Cape Granites have been studied for more than two centuries, it is not generally known that the Cape Granites have played a not insignificant role in the history of granite research. Actually, studies of the Cape Granites were central to some of the early debates between the Neptunists and the Plutonists, at the end of the 18th and in the first decades of the 19th Century, yet they seem to have escaped the attention of standard histories of the subject. The Neptunists, led by the ideas of Abraham Gottlob Werner (1749–1817) (Fig. 1a) believed that all rocks, including granite and basalt, were precipitated from the primordial oceans (Werner 1787, 1791; see discussions in Adams 1938; Hallam 1983). The Plutonists, who followed the ideas of James Hutton (1726–1797) (Fig. 1b), believed in the intrusive origin of some igneous rocks, such as granite, which were believed to have been injected, in a molten state, into previously existing rocks (Hutton 1795; Adams 1938; Hallam 1983). In this paper, some of the early descriptions and debates concerning the Cape Granites are reviewed, and the history of the development of the ideas on granites at the Cape in the late 18th Century and early to mid 19th Century is presented for the first time. Extensive quotes are given from the original literature, much of which is in extremely rare books and obscure journals (which may explain why this chapter in the history of granite studies has not been better known).

1. Geology of Table Mountain and the Cape Granites – early accounts

Ever since the discovery of the sea route to India via the Cape of Good Hope by Portuguese navigators in the late 15th Century, Table Bay has been a favoured stopping place for ships travelling between Europe and Asia. The first known ascent of Table Mountain was by the Portuguese explorer Antonio de Saldanha in 1503 (Raven-Hart 1967). There are many detailed descriptions of the topography of Table Mountain by travellers and explorers in the 17th and 18th Centuries, e.g., by Sir Thomas Herbert (1634); Guy Tachard (1686); Peter Kolb (1719); François Valentyn (1726); the Abbé Nicolas Louis de la Caille (1763), who even named a constellation (Mensa) after the mountain; Carl Frederick Brink (1778); and Otto Mentzel (1785).

The Cape Granites were first recognised (as a variety of 'saxum' or granite), not in Cape Town, where they outcrop prominently, but at Paarl (Fig. 2), some 50 km to the NE, by the Scottish botanist Francis Masson (1741–1805) (Fig. 3). In 1772 Masson accompanied the distinguished Swedish botanist Carl Peter Thunberg on a journey to the interior of South Africa (Masson 1776, 1994; Thunberg 1788). Masson (1994) noted in his journal for 17th December 1772:

> "17th, I went up to the top of the Perel Berg, where I spent a whole day in search of plants, and hunting a sort

© 2009 The Royal Society of Edinburgh. doi:10.1017/S1755691009016193

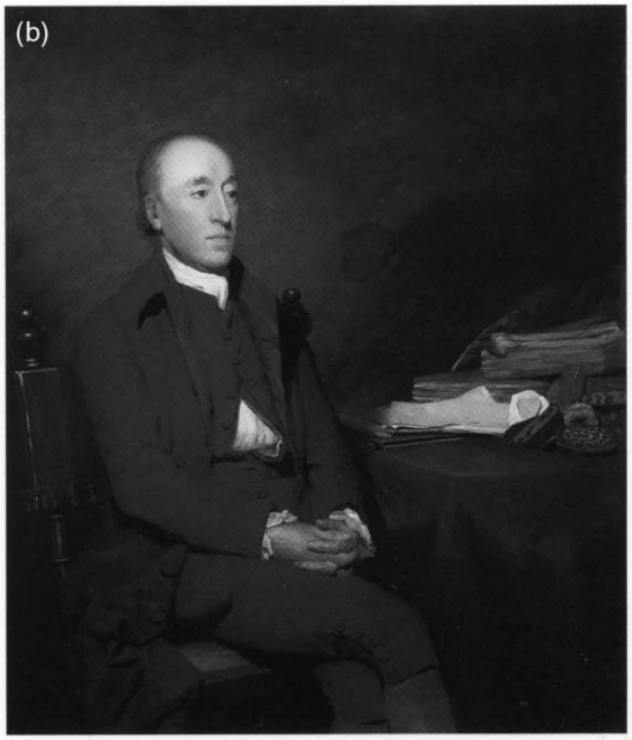

Figure 1 (a) Abraham Gottlob Werner (1749–1817), founder of the Neptunist School. Engraving by Ambroise Tardieu after an original portrait by Vogel. Source: Wikimedia Commons (b) James Hutton (1726–1797), founder of the Plutonist School. Image courtesy of the Scottish National Portrait Gallery: *Sir Henry Raeburn, James Hutton, Scottish National Portrait Gallery; Purchased with the aid of The Art Fund and the National Heritage Memorial Fund 1986*.

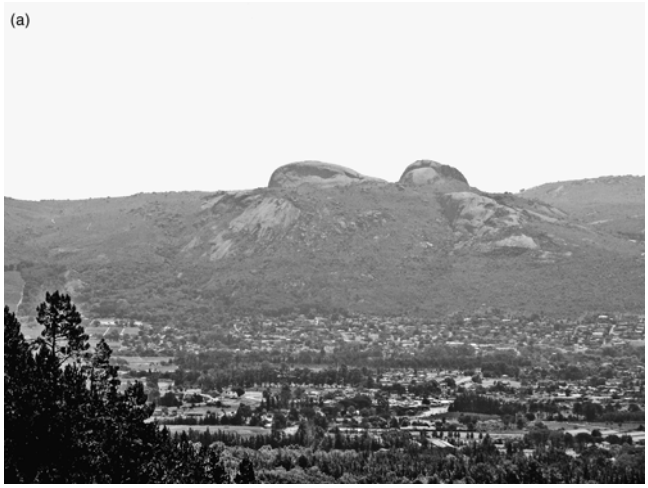

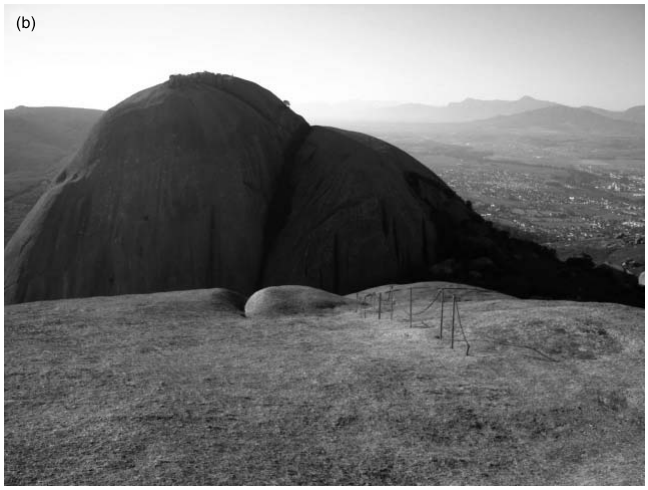

Figure 2 (a) View of Paarlberg ('Pearl Mountain'), above the town of Paarl, showing the two granite domes referred to today as the Suider Paarl ('Southern Pearl', left) and Noorder Paarl ('Northern Pearl', right). (b) View of bald granite monoliths making up the Paarl Mountain. Note the vertical crevasses described by Pierre Sonnerat (1782) and by Dugald Carmichael in 1806. (c) Aplite dykes cutting the Paarl Granite, described by Anderson (1778), and water-filled weathering basins, described by Sonnerat (1782).

> of antelope called Ree Bock; but had no success. I saw nothing here so worthy of observation as two large solid rocks, of a roundish figure; each of which, I may positively say, is more than a mile about the base, and upward of two hundred feet high above the ground. Their surfaces are nearly smooth, without chink or fissures, and they are found to be a species of saxum or

Figure 3 Francis Masson (1741–1805), Scottish botanist who first discovered granite at Paarl Mountain. Detail from a painting by George Garrard. From Masson (1994).

> granite, different from that which compose the neighbouring mountains.''

Masson did not have time to examine the 'Perel Berg' or Paarl (Pearl) mountain in more detail. However, he persuaded William Anderson, who had been surgeon's mate and naturalist on Captain James Cook's voyages, to make a more detailed study (Forbes 1965). Anderson visited the Paarl Mountain sometime in 1776, and made an attempt to determine its size and shape, and its geological constitution. In a letter dated 24th November, 1776, sent from Cape of Good Hope, Anderson communicated his findings to Sir John Pringle (then President of the Royal Society), who had been involved with Cook's expedition. Pringle published the letter (which was read on 15th January, 1777) in the *Philosophical Transactions* of the Royal Society in 1778; meanwhile Anderson went on to join Cook's third voyage to the Pacific Ocean, where he perished. Anderson (1778) described the Paarl Mountain as:

> ''a stone of extraordinary size ... The Stone is so remarkable that it is called by the people here the Tower of Babel, and by some the Pearl Diamond. ... It is of an oblong shape, and lies North and South. The South end is highest; the East and West sides are steep and high; but the top is rounded, and slopes away gradually to the North end, so that you can ascend it by that way, and enjoy a most extensive prospect of the whole country.''

He estimated its circumference as ''exceeding half a mile'', and as for its height, he ventured to say ''it equalled the dome of St Paul's Church''. As to its monolithic nature, Anderson (1778) observed that

> ''it would certainly impress every beholder, at first sight, with the idea of its being one stone, not only from its figure, but because it is really one solid uniform mass from top to bottom, without any interruption; which is contrary to the general character of the high hills of this country, they being commonly divided, or composed of different strata ...''

Anderson observed, however, a second variety of rock cutting across the main mass:

> ''near its North end a stratum of a more compact stone runs across, which is not above twelve or fourteen inches thick, with its surface divided into little squares, or oblongs, disposed obliquely. This stratum is perpendicular; but whether it cuts the other to its base, or is superficial, I cannot determine ... I have sent a specimen of the rock and of the stratum, which are both what the mineralogists call *saxa conglutinata* or *aggregata*, and consequently are different from the more solid stones which constitute the greatest part of the mountains here; and is likewise another proof of its being a single stone.''

Note that the second, 'more compact' stratum is an aplite dyke, but was not recognised as such by Anderson (1778), since it was only some 17 years later that Hutton (1795) first described intrusive dykes. The volcanologist Sir William Hamilton (1730–1803), famous for his descriptions of Vesuvius and the Eifel District of Germany, studied Anderson's samples of the Paarl granites sent to him by Sir John Pringle. In a brief letter written at Grosvenor Place on 25th July 1777, and published as an appendix to Anderson's article, Hamilton (1778) stated:

> ''I return you many thanks for the sight of the stones from the Cape of Good Hope. I have not time to examine them very minutely; but they seem to be both of the same nature, granites, the smaller piece being only of a finer texture. The highest points of the Alps are composed of granite of the same nature, and seem to have been lifted up by exhalations, volcanic explosions, or some such causes. This singular immense fragment of granite most probably has been raised in the same manner. Most of the mountains which are called primitive (which I believe is only a term) are of this texture.''

The famous Paarl Mountain was also described by many subsequent travellers to the Cape. The French botanist Pierre Sonnerat (1748–1814), who journeyed to Asia between 1774 and 1781, and stopped at the Cape, called it the 'Montagne de la Perle', and described it as follows (Sonnerat 1782, II, 91; translated by SM):

> ''The Paarl Mountain, which lies several leagues within the country, merits a description, being one of the highest in the vicinity of the Cape. It is composed of a single block of granite crevassed in many places. Nature has fashioned near the summit various caves and depressions, where one finds crystals of white and yellow rocks.''

John Barrow (1801) mentioned the observations of the Paarl Mountain by Masson, Anderson and Hamilton in the *Philosophical Transactions*, and noted that from their descriptions, ''it would appear that these two masses of stone rested upon their own bases, and were detached from the mountain; whereas they grow out, and form a part, of it.'' He regarded the Paarl granite as being identical to the granite he had found at the foot of Table Mountain, and described it as being made of ''aggregates of quartz and mica; the first in large irregular masses, and the latter in black clumps resembling shorl [*sic*]: they contain also cubic pieces of feltspar [*sic*], and seem to be bound together by plates of a clayey iron stone.'' Playfair

(1802, pp. 399, 410) in his popular explication of Hutton's *Theory of the Earth*, concurred with the view that the Paarl Rocks were part of the mountain whose summit they form; however, he erred in attributing to Barrow the statement that the Paarl Rocks lie upon sandstone strata (Forbes 1965, p. 139). Barrow's (1801) descriptions of the Paarl granites were further commented on by Louis O'Hier Degrandpré (1801b), who had translated Barrow's work into French, and by the German naturalist Hinrich Lichtenstein (1811–1812). Captain Dugald Carmichael (1772–1827) was a Hebridean soldier, surgeon and naturalist knowledgeable in botany, geology and ichthyology (Smith 1831). He participated in the British occupation of the Cape in 1805–1806, but managed some geological observations during his military duties, noting in his journal for the 17th January 1806 (Smith 1831, p. 15):

> ''Notwithstanding the fatigue of a nocturnal march, curiosity prompted me to walk up to the top of this hill, to which the colonists, struck by some peculiarity in its appearance, have given the name of Paarlberg. The summit is of granite, worn into a hemispherical form, and furrowed here and there by deep fissures, through which the atmospherical moisture, condensed from the clouds, gushes down in perpetual rills. . . . On top of this granitic cupola, a number of detached masses of the same material lie scattered about, some of them apparently so nicely poised, that a slight push might roll them down upon the village.''

The botanist Carl Peter Thunberg, who had accompanied Masson, published in 1788 a detailed account of his travels at the Cape. He had climbed Table Mountain no less than fifteen times, and gave a basic description of its geological structure, as follows: ''The uppermost strata are quite horizontal, but the lower ones lie in an oblique position. At the top, the rock appears to be a kind of sandstone, or volcanic ash; the middle stratum trapp, and the lowermost slate'' (Thunberg 1986). The uppermost strata are made of quartzitic Table Mountain sandstone (no volcanics are present); the 'trapp' that makes up the middle stratum is most likely the Cape Granite; and the 'slate' (originally 'skiffer', Thunberg 1788, I, p. 251) of the lowermost strata refers to the greywackes and shales of the Malmesbury Group.

Another Swedish botanist, Anders Sparrman, who was a friend of Thunberg and, like him, a protégé of Carolus Linnaeus, also visited the Cape in the late 18th Century, in 1772, and 1775–1776 (Forbes 1965), and wrote a valuable account of his travels, first published in Swedish in 1783. Sparrman (1783) believed that the sandy wastes of the Cape Flats (which separated Table Bay from False Bay, and connected the Cape Peninsula with the Hottentots Holland Mountains near Stellenbosch) had formerly been covered by the sea. However, he appeared to believe that the exposure of these tracts was brought about not by a drop in sea level, but that they had been formed ''particularly with sand, sea-shells, trunks of trees and such like rubbish'' driven by the ''violence of the south-east wind in False Bay'' (Sparrman 1785; Forbes 1965, 1977).

The French adventurer and ornithologist Francois le Vaillant (1795), believed, like Sparrman, that a fall in sea level at the Cape of Good Hope was evidenced by the sand dunes, sea shells and low elevations of the Cape Flats, which showed that they must have been recently submerged. He extended his hypothesis to include the interior mountains, far from the sea, which he believed had also been partly covered by the sea, and the retreat of this universal ocean was as postulated under the Neptunian hypothesis (Forbes 1965, pp. 126–127, 1977). Le Vaillant (1795, I, p. 143) also remarked that the chain of mountains making up the Cape Peninsula, extending from Table Mountain to the Cape of Good Hope, was made up of granite.

The geological structure of Table Mountain was first described in detail by Louis Degrandpré (1801a) and Barrow (1801). Degrandpré had visited the Cape in 1793 (Kennedy 1954). He made observations concerning the geological constitution of Table Mountain (he thought that the summit of Table Mountain was made of granite), and he argued that the sea level had been much higher in the past, isolating the Cape Peninsula as an island. Degrandpré's (1801a) notions of the receding of the sea and the emergence of the Cape Flats, similar to those of Le Vaillant (1795) and Barrow (1801), were derived from the ideas of Delisle de Sales (1779). Delisle de Sales, *nom de plume* of Jean-Baptiste Claude Izouard, was the author of a 52-volume work, *La Nouvelle Histoire des Hommes*, which dealt with numerous subjects, including subterranean geography, the foundations of a new cosmogeny, volcanoes and earthquakes, famous discoveries of the primitive earth, etc., in which a three-volume subsection, *Histoire du Monde Primitif*, formed the main source of Degrandpré's (1801a) geological speculations concerning the Cape. Delisle de Sales (1779) was in turn, like the Neptunists, probably influenced by the speculative cosmogenies of Burnet (1691) and Buffon (1774).

Barrow (1801), who had visited the Cape in 1797 and 1798, observed that the shore of Table Bay and the substratum on which Cape Town is built, is composed of ''a bed of a blue, compact schistus''. Upon the schistus, Barrow noted, ''lies a body of strong pale yellow to deep red clay abounding with mica, which seems to have been formed from the decomposition of granite, immense blocks of which are embedded in the clay''. Barrow further observed that ''resting on the granite and clay is the first horizontal stratum of the Table Mountain, commencing at about five hundred feet above the level of the sea''. Barrow (1801) noted the presence of beds of sea shells, buried under vegetable earth and clay at a height of no less than three hundred feet ($\sim$100 m) above sea level. He commented that ''the human mind can form no idea as to the measure of time required for the sea to have progressively retreated from such elevations''.

The geological observations of Barrow and Degrandpré were noted by the French traveller Jacques Gérard Milbert (1766–1840), who published an account of his travels to the Cape in 1812 (Milbert 1812; translated into German as Milbert 1825). Milbert (1812, 1825, p. 558) posed the question of what Table Mountain was made of, and simply gave, without taking sides, the answers of Barrow (1801), who thought that the summit was made of sandstone, and of his translator Degrandpré, who had reiterated his original opinion that it was made of granite (Degrandpré 1801a) in his notes accompanying his translation of Barrow (Degrandpré 1801b). Milbert (1812) included a view of Table Mountain among the illustrations accompanying his account (Fig. 4a).

2. Plutonism versus Neptunism at the Cape

Sir James Hall (1761–1832) was a chemist and geologist, and is regarded by some as the founder of experimental geology (e.g., Hall 1798; Craig & Jones 1985, pp. 162–163). Hall and John Playfair (1748–1819), both professors at the University of Edinburgh, had been friends and disciples of Dr James Hutton. Captain Basil Hall (1788–1844) was the second son of Sir James, and was educated at the High School of Edinburgh. He had a successful naval career, and wrote many articles and

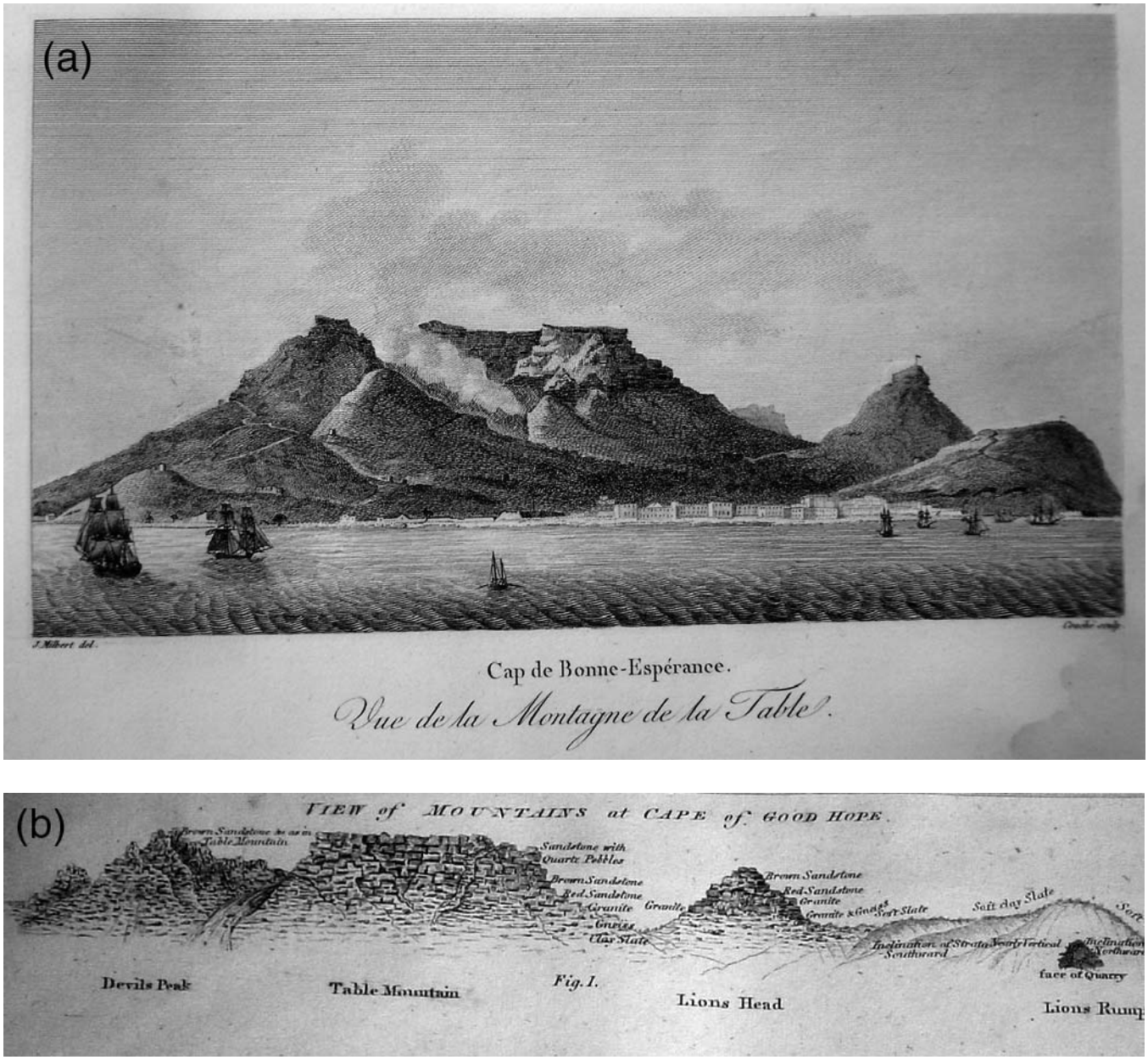

Figure 4 (a) Sketch entitled: 'Cape of Good Hope. View of Table Mountain', from Milbert (1812). (b) Sketch showing the topography and geology of Table Mountain and surroundings, after information supplied by Dr Adam of Calcutta, from Jameson (1819).

multi-volume works about his naval life, first for "young persons" (Hall 1831), reprinted later as a set of autobiographical sketches (Hall 1861). A biographical account of Basil Hall is given by Anonymous (2006).

Basil Hall (1831, pp. 22–23) described how, as a youth, he met Professor Playfair at a house in the country, and how Playfair patiently explained to him the use of a sextant. He went on to say (Hall 1831, p. 179):

> "About this period I began to dabble a little in geology, for which science I had acquired a taste by inheritance, and, in some degree, from companionship with more than one of the Scottish school, who, at the beginning of this century, were considered more than half-cracked, merely for supporting the igneous theory of Dr. Hutton, which, with certain limitations and extensions, and after thirty years of controversy, experiment, and observation, appears now pretty generally adopted. Sailors, indeed, have excellent opportunities of making geological observations, for they have the advantage of seeing Nature, as it were, with her face washed, more frequently than most other observers; and can seldom visit any coast, new or old, without having it in their power to bring off something interesting to inquirers in this branch of knowledge. That is, supposing they have eyes to see, and capacity to describe, what meets their observation."

In July 1812, Captain Basil Hall visited the Cape of Good Hope, putting into False Bay, and made an excursion to Table Mountain (Fig. 5), where he described the contact between the Cape granite and the Malmesbury greywacke, which he called 'killas', in letters to his father, Playfair and others. Playfair (Fig. 6a) published these observations (Playfair & Hall 1813) as a crucial example of the intrusive origin of granite, in support of Huttonian Plutonism, and in direct opposition to Wernerian Neptunism, represented at that time by his colleague at Edinburgh University, Robert Jameson (Fig. 6b), the arch-disciple of Werner in Scotland.

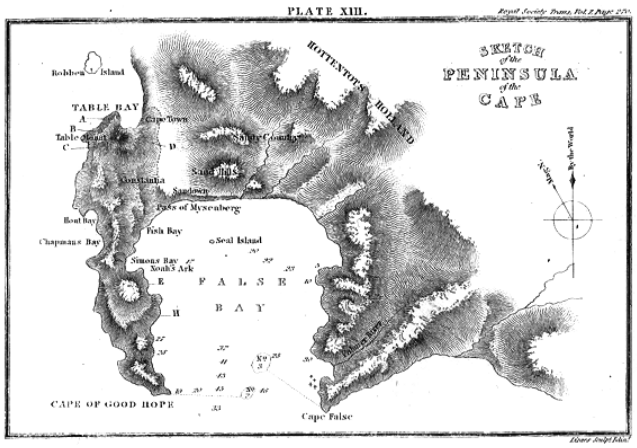

Figure 5 Map of the Cape Peninsula and False Bay, from Playfair & Hall (1813).

Captain Hall, in a letter to his father Sir James, recounted his visit to Table Mountain, along a ravine now known as Platteklip Gorge – the most popular and steepest route to the top (Playfair & Hall 1813):

> ''I came after a short ascent, to a space where many yards of rock were laid perfectly bare, and I found myself walking on vertical Schistus, or on what might be called *Killas*. This rock was in beds highly inclined and stretching from east to west, which is nearly the direction of the mountain...On looking forward a little higher up, I saw another portion of rock that was also laid bare, and which appeared to be Granite. I had now no doubt of reaching in a few minutes the precise junction of the two rocks, and I ventured to predict to my companion, who was not a little surprised at the pleasure I seemed to feel on this occasion, that we should immediately see veins from the main body of the granite, penetrating into the rock on which we were now standing. In this I was not deceived; the contact was the finest thing of the kind I ever saw; the *Windy Shoulder* itself not excepted. The number of veins that we could distinctly trace to the main body of the granite was truly astonishing; and the ramifications, which extended on every side, were of all sizes, from the breadth of two yards to the hundredth of an inch. Masses of killas, cut off entirely from the main body of that rock, floated in the granite, without numbers, especially near the line of contact, and the strata appeared there broken, disordered, and twisted in a most remarkable degree.
>
> From this point, following up the course of the stream for about 300 yards, I found the whole a solid mass of granite. The granite is characterised by large crystals of feldspar, which, indeed, is true of all the granite which I met with at the Cape. Besides quartz and mica, large masses of hornblend *[sic]* enter occasionally into the composition of this rock.
>
> After ascending about 300 yards farther, I came to a line where the granite ceased, and was succeeded by strata of superincumbent Sandstone. These strata were horizontal, and without any symptom of disturbance or violence whatsoever. There was not a shift nor a vein; and this junction formed a most marked contrast with that which we had left below.
>
> Looking round from the point where I now stood, to all the parts of the amphitheatre, in the centre of which I was placed, I could trace the same line of junction, extending horizontally on every side.

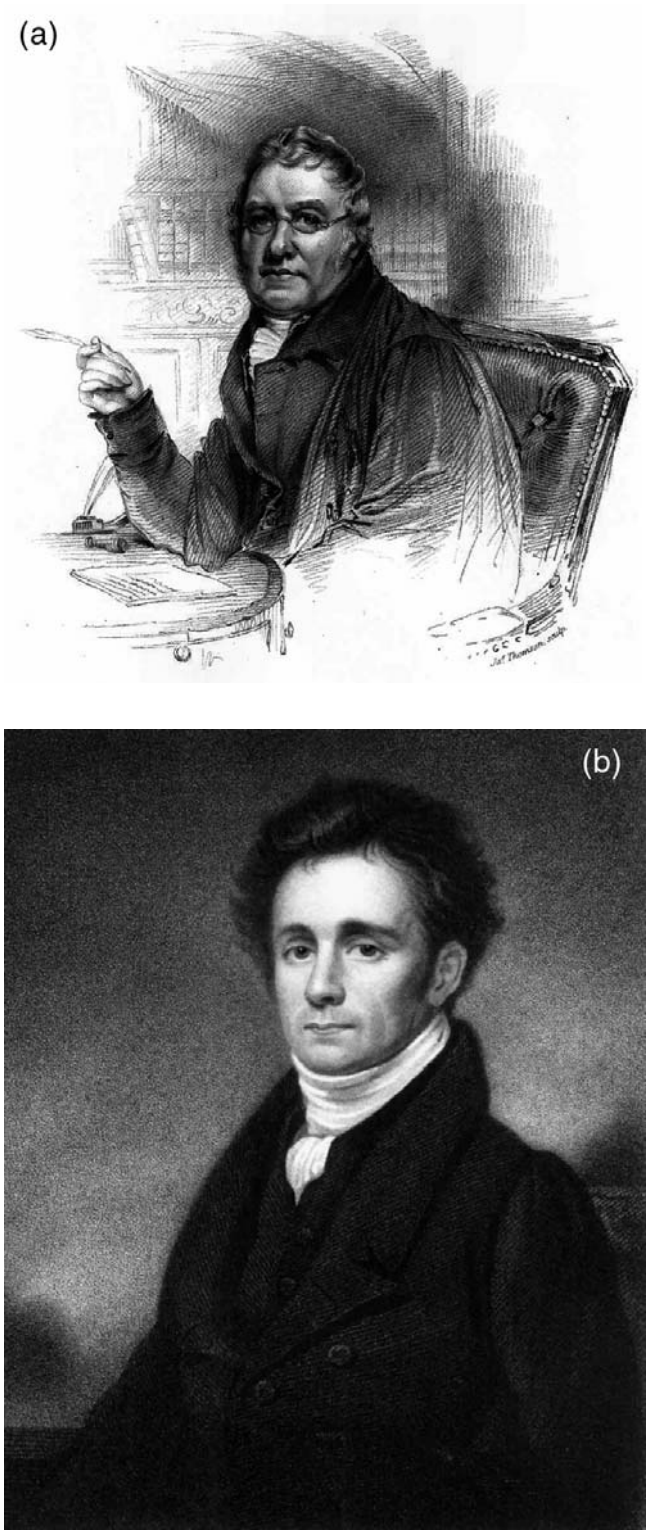

Figure 6 (a) Professor John Playfair (1748–1819), the principal advocate of Huttonian Plutonism. Source: Wikimedia Commons (b) Professor Robert Jameson (1774–1854), principal advocate of Wernerian Neptunism. Source: Wikimedia Commons.

> From this point, where the sandstone was first discovered, for about 150 or 200 feet perpendicular, the rock continued of the same kind, viz. a red sandstone, in horizontal beds of no great thickness. From thence all the way to the summit the sandstone was of a much more indurated kind, quite white, and having pieces of water-worn quartz imbedded in it, from the size of a pea to that of a potatoe. The top is a plane of about ten acres, somewhat uneven, though, on the whole, nearly level.''

Playfair, in a footnote, stated that the *Windy Shoulder* referred to by Hall "is on the side of Loch Ken in Kirkcudbrightshire, and is remarkable for veins of Granite, of the same kind with those here described" (Playfair & Hall 1813, p. 273). Commenting on Hall's observations, Playfair remarked that

> "the phenomena here described point out two separate epochas [*sic*], distinguished by very different conditions of the substances which now compose the peninsula of the Cape. That peninsula, it now appears, is a wall of granite, highest at the northern extremity, and lowering gradually to the south; faced, at its base, with grauwacky [*sic*], and covered, at its top, with a platform of horizontal sandstone. The penetration of the killas or grauwacky, by veins from the mass of granite which it surrounds, proves that the killas, though the superior rock, is of older formation than the granite. The granite, therefore, is a mineral that has come up from below into the situation it now occupies, and is not one of which the materials have been deposited by the sea in any shape, either mechanical or chemical. It is a species, therefore, of subterraneous lava, and the progeny of that active and powerful element, which we know, from the history both of the present and the past, has always existed in the bowels of the earth.
>
> The introduction of the granite into the situation it now occupies, must have taken place while the whole was deep under the level of the sea; this is evident from the covering of sandstone which lies on the granite, to the thickness of 1500 feet; for there can be no doubt whatever that this last was deposited by water. After this deposition, the whole must have been lifted up, as Captain Hall supposes, with such quietness and regularity, and in so great a body, as not to disturb or alter the relative position of the parts. Thus the granite is shewn, I think with great probability, to be newer than one of the rocks incumbent on it, and older than the other. I know not that we have ever before had an example of a fact which so directly ascertains the place which granite really occupies, in respect of the other parts of the mineral kingdom; it is one that from analogy might be expected to take place, and it is highly favourable to the opinion, that granite does not derive its origin from aqueous deposition. It seems, indeed, to be an *instantia crucis*, with respect to the two theories concerning the formation of rocks" (Playfair & Hall 1813, pp. 277–278).

The intrusive nature of the granite on the lower slopes of Table Mountain, as depicted by Playfair & Hall (1813) (Fig. 7) was the first published example of intrusive granite outside of Scotland, where Hutton (1795) had originally described intrusive granites.

Clarke Abel (1818) had made geological observations at the Cape in 1816 and 1817, on his way to and from China. He was the first to record the granite–schist contact along the coast near Green Point and Sea Point in Cape Town, and he illustrated the complex relationships in the contact zone in a series of very accurate drawings (Figs 8, 9, 10). He reached similar conclusions to Hall and Playfair concerning the intrusive origin of the granite and its injection into the greywackes, which he called 'schistus', and he cited contradictions with the Neptunian view put forward by Jameson (1808). However, he then regarded the overlying sandstones of Table Mountain as having been precipitated from the ocean in the manner advocated by the Neptunians. Abel thus concluded that "the mountains at the Cape of Good Hope exhibit phenomena illustrative and confirmative of certain positions of both the Huttonian and Wernerian theories." The anonymous reviewer of Abel's book in the *Quarterly Review* suggested that he could have omitted the "the geological discussion on the appearances of the peninsula of the Cape, especially as they have been described more fully and more scientifically by Captain Hall in the Philosophical Transactions of Edinburgh" (Anonymous 1819).

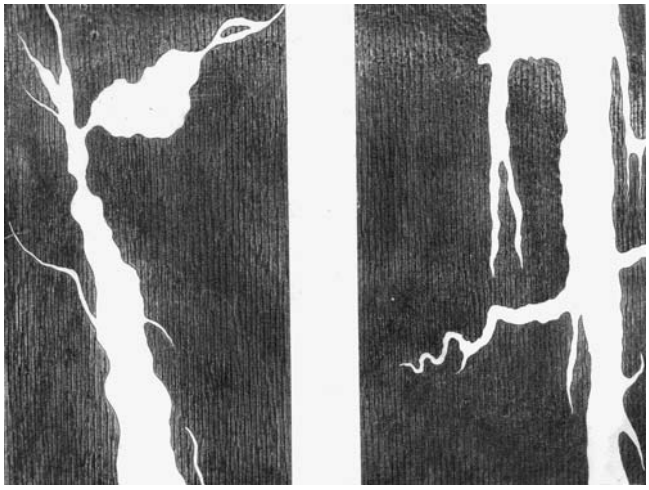

Figure 7 Sketch showing granite veins (white) intruding 'killas' or schists at Platteklip Gorge, from Playfair & Hall (1813).

Robert Jameson (1774–1854), Regius Professor of Natural Philosophy at Edinburgh, had studied for two years under Werner in Freiberg, and was the principal proponent of the Neptunist school in Scotland, having been a founder of the Wernerian Natural History Society in 1808 (Geikie 1897). Although Jameson was elected president of this latter society on the 14th November, 1810 (Anonymous 1811), not everybody had a high opinion of him. Thomas Carlyle, writing to Robert Mitchell on 27th November, 1818, made the following remarks about him (Craig & Jones 1985, pp. 160–161):

> "I have heard Professor Jameson deliver two lectures. I am doubtful whether I ought to attend his class after all. He is one of those persons whose understanding is overburthened by their memory. Destitute of accurate science, without comprehension of mind, – he details a chaos of facts, which he accounts for in a manner as slovenly as he selects and arranges them."

Jameson countered the views on the intrusive origin of granite proposed by Playfair, Hall and Abel, in an article published in 1819 in the *Edinburgh Philosophical Journal*, which he had also founded. He reproduced, at length, their observations (Jameson 1819), and obtained further information, including a sketch, from one of his former pupils, Dr Adam of Calcutta (Fig. 4b). He summarised the positions of the Plutonists, as advocating that two of the formations, namely the slate and the sandstone, were of aqueous origin, while the third, granite, was of intrusive origin. He then continued:

> "We consider this explanation as unsatisfactory, and are inclined to view these rocks as of Neptunian and simultaneous formation; because they alternate with, and pass into each other, thus exhibiting the same general geognostical relations as occur in formations composed of sandstone and limestone, or of sandstone and gypsum. The junctions of the granite and gneiss, and of the sandstone and slate, do not present any species of veins,

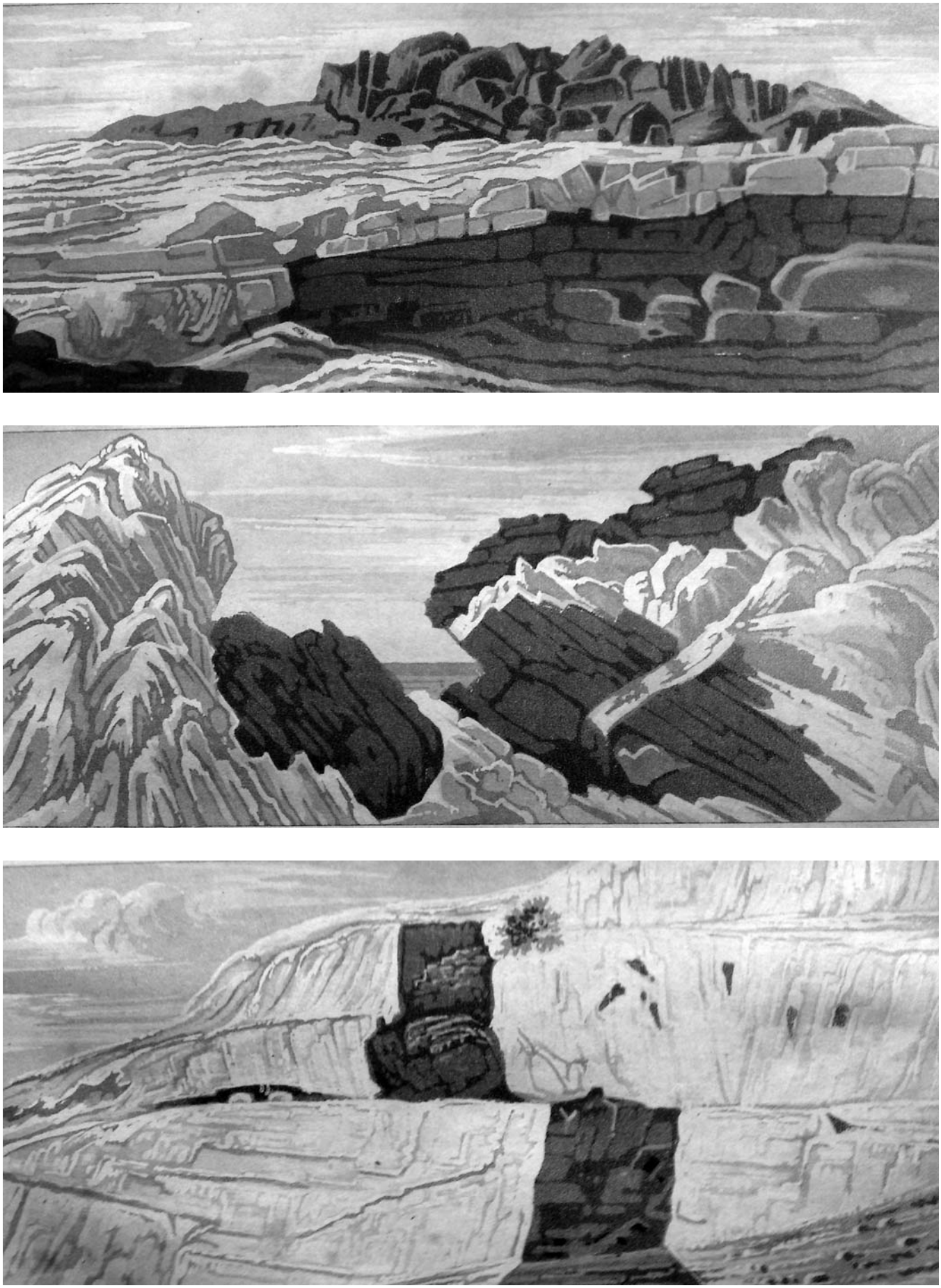

Figure 8 Three views of granite dykes (light) intruding into 'clay-slate' (dark) at Sea Point, from Abel (1818). The engravings are by T. Fielding, after drawings by H. Raper, Esq.

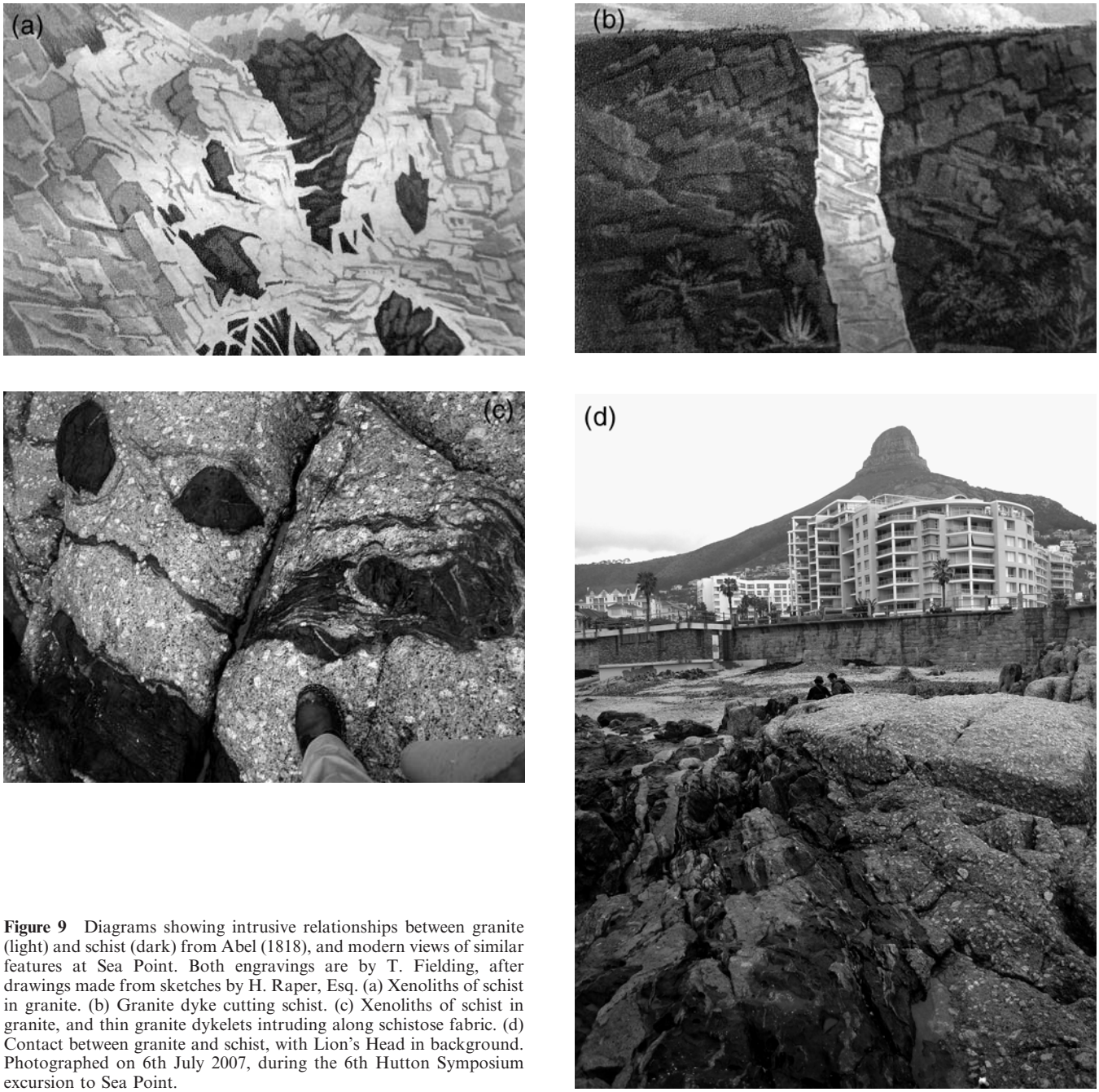

Figure 9 Diagrams showing intrusive relationships between granite (light) and schist (dark) from Abel (1818), and modern views of similar features at Sea Point. Both engravings are by T. Fielding, after drawings made from sketches by H. Raper, Esq. (a) Xenoliths of schist in granite. (b) Granite dyke cutting schist. (c) Xenoliths of schist in granite, and thin granite dykelets intruding along schistose fabric. (d) Contact between granite and schist, with Lion's Head in background. Photographed on 6th July 2007, during the 6th Hutton Symposium excursion to Sea Point.

> or varieties of intermixtures, or of imbedded portions (fragments of the Huttonians), or convolutions, that do not occur at the junctions of universally admitted Neptunian rocks, such as limestone, claystone, gypsum, and sandstone.
>
> In short, the mountains and hills of the peninsula of the Cape of Good Hope, are to be considered as variously aggregated compounds of quartz, feldspar, and mica, and the whole as the result of one nearly simultaneous process of crystallisation.''

There was no immediate rejoinder to Jameson's views (Playfair had died in 1819). The Rev. Friedrich Hesse, who translated Latrobe's journal into German, made cursory geological observations in Cape Town, including on the 'schistus' and the granite, without addressing the controversy (Latrobe & Hesse 1820). Dugald Carmichael (1821) made further observations on the geological structure of the Cape, which confirmed some of the earlier results of Hall and Abel. Jameson *et al*. (1830) repeated the observations of Hall and Abel, and added those of Carmichael, but reproduced, unchanged, Jameson's earlier (1819) arguments about the Neptunian origin of the strata in the Cape Peninsula. Jameson *et al*. (1830) did, however, give two rival Plutonist positions, and admitted that the second of these may be regarded as ''most in accordance with prevailing geological hypotheses'':

> ''At what period did the Cape rocks rise above the level of the sea? This question has been variously answered, according to the geological creed of those who have considered the subject. The Neptunians maintain, on plausible grounds, that all these rocks are crystallisations and deposites [*sic*] from the ancient waters of the globe, which have taken place in succession, – the granite being the first formed, the slate and greywacke the next, and last of all, the principal portion of the sandstone; that, during the deposition of these different rocks, the level of the ocean gradually sank; and that thus the mountains rose above its surface. The

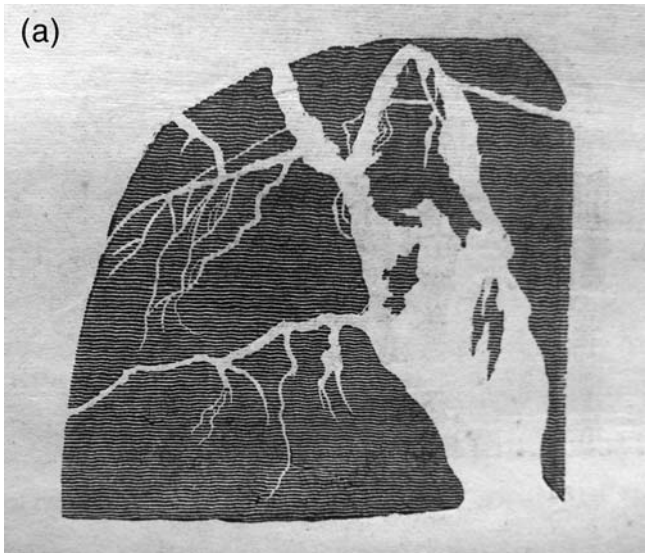

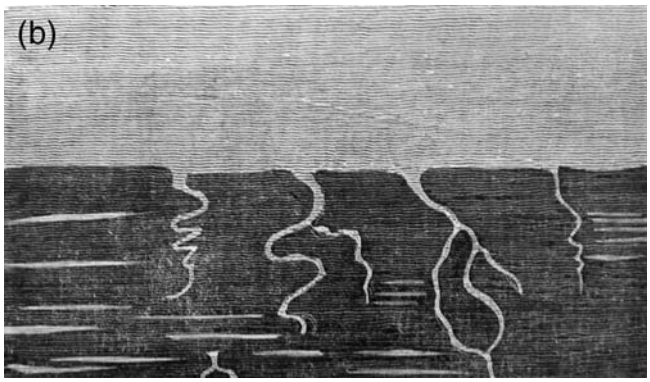

Figure 10 (a) and (b) Drawings illustrating thin granite veins (light) intruding into schist (dark) at Sea Point, from Abel (1818). (c) Photograph showing thin granite veins (light) intruding schist (dark), at Sea Point.

> Plutonians, or the supporters of the igneous origin of the granular crystallised rocks, view the formation in a different manner. Some of the advocates of the igneous system maintain that the slate was first deposited in horizontal strata, at the bottom of the sea, – that these strata were afterwards softened by heat, and raised from their original horizontal to their present highly inclined position, by the action of fluid granite rising from the interior of the earth; and that in this way the granite and slate mountains were elevated above the sea: that the sea again invaded the land, and covered it to a great depth; and that from this ocean was deposited the sandstone strata; that the sea again retired, and left exposed mountains, and chains of mountains of sandstone. Other Plutonists are of opinion that the slate, greywacke, and sandstone, were deposited, in uninterrupted succession, at the bottom of the sea; and that the whole mass of stratified matter was raised gradually or suddenly above the level of the ocean, forming mountains, chains of mountains, and table-lands, by that igneous agency which sent up the granite, and probably also the augit-greenstone rocks. This, of the two Plutonian views, is the most plausible, and indeed is that explanation which may be viewed as most in accordance with prevailing geological hypotheses.''

It was revealed by Jameson *et al*. (1830) that Clarke Abel, together with his local guide, Captain Wauchope of the Royal Navy, as well as Dr Adam of Calcutta, and the recently deceased Dugald Carmichael, had all been former pupils of Dr Jameson in Edinburgh. George Champion (1836) further introduced Cape geology and topography to an American audience, following on American editions of the work by Jameson *et al*. (1830).

In 1837, the German mineralogist Johann Friedrich Ludwig Hausmann (1782–1859) published a ''contribution to the knowledge of the geognostical constitution of South Africa'', in which he discussed the geological observations of his compatriot Hesse (Latrobe & Hesse 1820), and Hall (Playfair & Hall 1813) concerning the schists and greywackes at the foot of Table Mountain, and compared them to his observations of similar schists in the Harz mountains. Being clearly in the Neptunian camp, Hausmann (1837) attempted a correlation with the Wernerian global stratigraphy and tentatively tried to assign the schists to the 'Übergangsgebirge' or 'Transitional beds', and the overlying sandstones of Table Mountain to the 'Flötzgebirge' (mechanical sediments, but partly of chemical origin) (Adams 1938; Hallam 1983). In 1839, the German geologist and palaeontologist Ferdinand Krauss published an accurate account of the geology of Table Mountain and the Cape Peninsula, in which he noted, in addition to the rock types described by previous workers, the presence of several dolerite dykes which cut across both the Cape Granites and the schists and greywackes that they intruded (Krauss 1839).

The Rev. William Branthwaite Clarke (1798–1878), who was a prolific researcher regarded as the 'Father of Australian Geology' (Grainger 1982), passed through the Cape in March and April 1839, and studied its geology. In spite of the many excellent descriptions that preceded him, Clarke (1841) commenced his paper on the geological phenomena in the vicinity of Cape Town by stating that ''having derived no advantage from the labours of previous geologists, his remarks must be regarded as independent of any prior description.'' While admitting that the granite was intrusive into the schists, Clarke (1841) even suggested that the granite had intruded into the overlying sandstones. ''These phænomena'', he stated, ''clearly establish the induction, that though the periods may have been distant, the schistose rocks owe their elevation to the up-burst of the granite before the deposition of the sandstone; and that subsequently the granite has been re-heated and further elevated, carrying with it the whole area described to a higher level.'' Despite his initially dismissive attitude towards the work of his predecessors, Clarke (1841) did later acknowledge that Clarke Abel had previously identified an intrusive dyke at Kloof.

Charles Darwin had visited the Cape in 1836 on the last leg of his famous voyage on the *Beagle* (Compton & Singer 1958). Darwin had been a former pupil of Robert Jameson at

Edinburgh in 1826–1827, but had found his lectures on geology and zoology 'incredibly dull'. Darwin added that "the sole effect they produced on me was the determination never as long as I lived to read a book on Geology, or in any way to study the science" (Darwin 1887, p. 41). It was only under the influence of Lyell (1833), whose *Principles* Darwin had taken with him on board the *Beagle*, that Darwin re-ignited his interest in geology that had been so thoroughly snuffed out by Jameson (see Adams 1938, p. 226). Darwin arrived at the Cape (in 'Simon's Bay') on 31st May 1836, and on the 4th June he visited the famous Paarl Mountain, which he described as "a singular group of rounded granite hills" (Keynes 2001, p. 425). From the 8th to 15th June 1836, Darwin examined the outcrops of the Green Point granite–schist contact (which had been described by Abel (1818)), in the course of several 'long geological rambles' in the company of Dr Andrew Smith, with whom he remained on friendly terms for many years afterwards (Kirby 1965). Darwin (1844) referred to the previous accounts of the geology of the Cape of Good Hope by Barrow, Carmichael, Hall and Clarke. He described in meticulous detail the junction of the granite and the clay-slate, and the presence of rafts or xenoliths of clay-slate within the granite, which preserved their uniform NW–SE cleavage. He alluded to similar observations from other areas having been advanced, e.g. by Keilhau (1843), as a "great difficulty on the ordinary theory of granite having been injected whilst liquefied". Darwin (1844) continued, however:

> ". . . but if we reflect on the probable state of the lower surface of a laminated mass, like clay-slate, after having been violently arched by a body of molten granite, we may conclude that it would be full of fissures parallel to the planes of cleavage; and that these would be filled with granite, so that wherever the fissures were close to each other, mere parting layers or wedges of the slate would depend into the granite. Should, therefore, the whole body of rock afterwards become worn down and denuded, the lower ends of these dependent masses or wedges of slate would be left quite isolated in the granite; yet they would retain their proper lines of cleavage, from having been united, whilst the granite was fluid, with a continuous covering of clay-slate."

It was only after Charles Darwin had published his 1836 observations on the Green Point granite–schist contact (Darwin 1844), that the Plutonist position became firmly entrenched. The ageing Professor Jameson was eventually persuaded to change his own views on the origin of granite, as he admitted at a meeting of the Geological Society of Edinburgh (Adams 1938).

Also in 1844 appeared a detailed account of the geology of the Cape of Good Hope by Jules Itier, who described the basal part of Table Mountain as follows (Itier 1844, p. 961; translated by SM):

> "The base of Table Mountain, on the side facing Cape Town, is a very distinctive porphyritic granite which is emplaced forcibly among schistose psammites, whose beds it has dislocated during penetration by injection, and whose sedimentary texture it has more or less profoundly modified."

Itier (1844) further observed that the contact metamorphism in the sediments adjacent to the granite, which had transformed them into fine-grained garnetiferous schists, was very similar to that he had observed in schists modified by porphyritic granites at various places in the eastern Pyrenees, notably in the valleys of Carol and Railleu.

Itier (1848 pp. 343–349) later expanded his account of Cape geology to include the first published colour geological map of the Cape of Good Hope. By the time Andrew Geddes Bain published his pioneering paper on the geology of South Africa (Bain 1856), the geological history of the Cape Peninsula and Table Mountain had become pretty much fixed according to the following view, obtaining from the labours of Hall, Abel, Krauss, Darwin and Itier: the schist/greywacke was first deposited, then was folded and intruded by the Cape Granite; following erosion and peneplanation, the Table Mountain sandstones were deposited unconformably on the granite and schist/greywacke; the whole edifice was then uplifted, and intruded by dolerite dykes. The standard version was further entrenched by the paper on the geology of the region around the Cape of Good Hope by the French consul in Cape Town, Francois de Castelnau (1858). However, a discordant note was struck by Henry Piers (1870), who regarded the Cape granite as having intruded laterally along the contact between the schists/greywackes at the base of Table Mountain, and the subhorizontal sandstones that overlie them. In a footnote following Piers' (1870) article, the editor of the *Cape Monthly Magazine*, Professor Roderick Noble, inserted the following comments, which may be taken to satisfactorily sum up the consensus view on the geology of Table Mountain, and of the origin of the Cape Granite, a view that persists, more or less unchanged, to the present day (Noble 1870):

> "We insert the above communication with pleasure, partly from the careful minuteness of its observation, and partly from a desire to provoke intelligent discussion on the subject. At the same time, however, we must state that our own opinion differs from that of Mr. Piers, on both of the questions which he raises . . . We think that Mr. Bain's geology of Table Mountain is substantially accurate. It is quite true that the granite is a more recent formation (or intrusion rather) than the clay-slate; but still, in the ordinary sense of the term, it is the 'fundamental' rock. About a hundred yards below Platte Klip, there is a spot which Capt. Basil Hall has in a sense rendered classic. Some forty years ago, when the Neptunian and Plutonic theories were still contending for victory, the celebrated navigator 'spotted' this particular locality where the igneous granite thrust up two great veins vertically through the superincumbent clay-slate, or as it was then called, grauwacke. This seems to us to prove conclusively that the flow of the granite was not lateral, but vertical. And we have further indications to the same effect on the Wynberg side and out at Joostenberg, and still more conspicuously at Paarl. . . . As to the chronology of Table Mountain, we are satisfied that the clay-slate is the most ancient; that in course of ages it was upheaved and tilted to its present angle, and thereafter penetrated by the vertically intrusive granite; following which, the sandstone horizontal strata were deposited in a primeval Devonian sea."

Note that when Noble (1870) wrote the above paragraph, the controversy between the 'Neptunian and Plutonic theories' had long subsided, but some forty years previously, they had been 'contending for victory'. Such a stark typically Victorian view of the debate, in terms of winners and losers, is nowadays (see Rupke 1994, and references therein) given a more nuanced treatment, which acknowledges the beneficial influence of Wernerian Neptunism in the development of stratigraphy, and some of the errors and self-promoting mythologising of the Huttonian Plutonists, and their later champions such as Lyell (1833) and Geikie (1897). In the debate on the origin of the

Cape Granites, it can be seen that Wernerian Neptunists like Clarke Abel were in agreement with Plutonists like Basil Hall, concerning the intrusive nature of the granites, whilst still regarding the overlying sandstones as being the products of marine precipitation. On the other hand, we also see how Plutonists such as William Clarke and Henry Piers, whilst believing in the intrusive nature of the granite, could also have erroneously believed these granites to be intrusive into the Table Mountain sandstones. The Table Mountain Sandstone is Ordovician in age (Theron 1984), and not Devonian, as Noble (1870) had stated.

Subsequent descriptions of the Green Point/Sea Point granite–schist contact have added vast amounts of additional petrographic details (von Hochstetter 1866; Cohen 1874, 1897; Prosser 1878; Shaw 1878; Mennell 1903a, b; Rogers 1905; Hatch & Costorphine 1905; Cole 1906; Schwartz 1913; du Toit 1929; Walker 1929; Haughton 1933; Walker & Mathias 1946; Theron 1984), and, more recently, geochronological information (Armstrong *et al*. 1998). Despite this, our understanding of the basic geological situation in these celebrated exposures near Table Mountain (arrived at after much wrangling between the disciples of Werner and Hutton) has not changed much since the detailed descriptions of Darwin and Itier in 1844. The classic geology of the Cape Peninsula has played an important part in our emerging understanding of granite intrusions, contact metamorphism and sea level changes, during the emerging years of the discipline of geology, when Neptunists and Plutonists contested at the southern tip of Africa.

3. Acknowledgements

I thank the librarians Margaret Northey and Peter Duncan at the Africana Library, University of the Witwatersrand, for their considerable help in tracking down obscure references. I am grateful to Vicki Hammond for her editorial input. Several portraits were obtained from Wikimedia Commons*. The names of original artists have been given, where traceable. All modern photographs are by the author.

*Editor's note: reproduction permission for these has been sought where possible. The RSE apologies for any omissions, and will acknowledge these if further information is received.

4. References

Abel, C. 1818. *Narrative of a Journey into the Interior of China, and of a Voyage to and from that Country in the years 1816 and 1817*. London: Longman, Hurst, Rees, Orme and Brown.

Adams, F. D. 1938. *The Birth and Development of the Geological Sciences*. Baltimore, Maryland: Williams and Wilkins.

Anderson, W. 1778. An account of a large Stone near Cape Town. In a letter from Mr. Anderson to Sir John Pringle, Bart. PRS; with a Letter from Sir William Hamilton, KB, FRS to Sir John Pringle, on having seen pieces of the said Stone. *Philosophical Transactions of the Royal Society, London* **68**, 102–6.

Anonymous 1811. Proceedings of the Wernerian Natural History Society. *Scots Magazine and Edinburgh Literary Miscellany* **73**, 886.

Anonymous 1819. Narrative of a Journey into the Interior of China, and of a Voyage to and from that Country in the years 1816 and 1817; containing an account of the most interesting transactions of Lord Amherst's embassy to the court of Pekin, and observations on the countries which it visited. By Clarke Abel, FLS. London. 1818. *Quarterly Review, New York* **21**, January & April 1819, 67–91.

Anonymous 2006. Significant Scots: Captain Basil Hall. http://www.electricscotland. com/history/other/hall_basil.htm

Armstrong, R., de Wit, M. J., Reid, D., York, D. & Zartman, R. 1998. Cape Town's Table Mountain reveals rapid Pan-African uplift of its basement rocks. *Journal of African Earth Sciences* **27** (1A), 10.

Bain, A. G. 1856. On the Geology of South Africa. *Transactions of the Geological Society, London* **7** (4), 175–92.

Barrow, J. 1801. *An account of travels into the interior of Southern Africa in the years 1797 and 1798*. London: T. Cadell Jun. and W. Davies.

Brink, C. F. 1778. *Nieuwste en beknopte beschryving van de Kaap de Goede Hoop; nevens een dag-verhaal van eenen landtogt, naar het binnenste van Afrika, door het Land der kleine en groote Namacquas*. Amsterdam: H. J. Schneider.

Buffon, C^{te} de 1774. *Oeuvres complètes, Tome Premier. Théorie de la Terre*. Paris: Panckoucke.

Burnet, T. 1691. *Sacred Theory of the Earth*. London: R. Norton.

Carmichael, D. 1819–1821. On the geological structure of part of the Cape of Good Hope. *Transactions of the Geological Society, London* **1** (5), 614–16.

Castelnau, F. de 1858. Lettre sur la constitution géologique de quelques cantons voisins du Cap de Bonne Espérance. *Comptes Rendus de l'Académie des Sciences, Paris* **46**, 56–7.

Champion, G. 1836. Remarks on the topography, scenery, geology, &c., of the vicinity of the Cape of Good Hope. *American Journal of Science* **29**, 230–6.

Clarke, Rev. W. B. 1841. On the Geological Phenomena in the vicinity of Cape Town, South Africa. *Proceedings of the Geological Society, London* **3** (2), 418–23.

Cohen, E. 1874. Geognostisch-petrographische Skizzen aus Südafrika. *Neues Jahrbuch für Mineralogie, Geologie und Palaeontologie, Stuttgart* **1874**, 460–505.

Cohen, E. 1897. Turmalinhornfels aus der Umgebung von Capstadt. *Tschermaks mineralogisches und petrographisches Mittheilungen, Wien* **17**, 287–8.

Cole, G. A. V. 1906. On the marginal phenomena of granite domes. *Geological Magazine* **3**, 80.

Compton, A. W. & Singer, R. 1958. Darwin's visit to the Cape. *Quarterly Bulletin of the South African Library* **13** (1), 9–11.

Compton, J. S. 2004. *The rocks and mountains of Cape Town*. Cape Town: Double Storey Books.

Craig, G. Y. & Jones, E. J. (eds) 1985. *A Geological Miscellany*. Princeton: Princeton University Press.

Da Silva, L. C., Gresse, P. G., Scheepers, R., McNaughton, N. J., Hartmann, L. A. & Fletcher, I. 2000. U–Pb and Sm–Nd age constraints on the timing and sources of the Pan-African Cape Granite Suite, South Africa. *Journal of African Earth Sciences* **30**, 795–815.

Darwin, C. 1844. *Geological observations on the Volcanic Islands visited during the voyage of H.M.S. Beagle, together with some brief notes on the geology of Australia and the Cape of Good Hope*. London: Smith Elder.

Darwin, F. (ed.) 1887. *The Life and Letters of Charles Darwin*, Vol. 1. London: John Murray.

Degrandpré, L. M. J. O'H. 1801a. *Voyage a la Côte Occidentale d'Afrique, fait dans les années 1786 et 1787; Suivi d'un Voyage fait au cap de Bonne-Espérance, contenant la description militaire de cette colonie*, 2 volumes. Paris: Dentu.

Degrandpré, L. 1801b. Notes du Chapitre Premier, pp. 91–103. Notes du Chapitre Deux, pp. 194–199. *In* Barrow, J. (1801) *Voyage dans la partie méridionale de l'Afrique; fait dans les années 1797 et 1798. Tome Premier*. Traduit de l'anglais par L. Degrandpré. Paris: Dentu.

Delisle de Sales 1779. *Histoire du Monde Primitif ou des Atlantes*, 3 volumes. Paris: (no name, Gay et Gide?).

du Toit, A. L. 1929. *The Geology of South Africa*. Edinburgh: Oliver & Boyd.

Forbes, V. S. 1965. *Pioneer Travellers of South Africa. A geographical commentary upon notes, records, observations and opinions of travellers at the Cape 1750–1800*. Cape Town: A. A. Balkema.

Forbes, V. S. 1977. Some scientific matters in early writings on the Cape. *In* Brown, A. C. (ed.) *A History of Scientific Endeavour in South Africa*. Cape Town: Royal Society of South Africa.

Geikie, A. 1897. *The Founders of Geology*. London: Macmillan.

Grainger, E. 1982. *The Remarkable Reverend Clarke – the life and times of the Father of Australian Geology*. Melbourne: Oxford University Press.

Hall, Capt. B. 1831. *Fragments of Voyages and Travels, including Anecdotes of a Naval Life: Chiefly for the Use of Young Persons*, Volume 1. Edinburgh: Robert Cadell.

Hall, Capt. B. 1861. *Lieutenant and Commander: being autobiographical sketches from his own career, from Fragments of Voyages and Travels*. London: Bell & Daldy; Sampson, Low, Son & Co.

Hall, J. 1798. Experiments on whinstone and lava. *Transactions of the Royal Society of Edinburgh* **5**, 43–66.

Hallam, A. 1983. *Great Geological Controversies*. Oxford: Oxford University Press.
Hamilton, W. 1778. Letter from Sir William Hamilton, K. B. F. R. S. to Sir John Pringle. *Philosophical Transactions of the Royal Society, London* **68**, Part I, 106.
Hatch, F. H. & Costorphine, G. S. 1905. *The Geology of South Africa*. London: Macmillan and Co.
Hausmann, J. F. L. 1837. Beiträge zur Kunde der geognostischen Constitution von Südafrika. *Göttinger Geologischer Anzeige, Göttingen* **1837**, 1449–62; *Neues Jahrbuch für Mineralogie, Geognosie, Geologie und Petrefaktenkunde, Stuttgart* **1838**, 181–7.
Haughton, S. H. 1933. *The Geology of Capetown and adjoining country. Explanation of Sheet No. 247 (Capetown)*. Pretoria: Geological Survey of South Africa.
Herbert, T. 1634. *Some Years Travels into Divers Parts of Africa and Asia the Great*. London: R. Everingham, R. Scot, T. Beard, J. Wright & R. Chiswell.
Hochstetter, F. von 1866. Beiträge zur Geologie des Caplandes. Novara Expedition, geologischer Theil. II. Band, I. Abth., Wien, 19–38. *Neues Jahrbuch für Mineralogie, Geologie und Palaeontologie, Stuttgart* **1866**, 474–5.
Hutton, J. 1795. *Theory of the Earth with Proofs and Illustrations*. Edinburgh: Creech.
Itier, J. 1844. Notice sur la constitution géologique du Cap de Bonne-Espérance. *Comptes Rendus de l'Académie des Sciences, Paris* **19**, 960–70.
Itier, Jules 1848. *Journal d'un voyage en Chine en 1843, 1844, 1845, 1846*, Vol. 1. Paris: Dauvin et Fontaine.
Jameson, R. 1808. *System of Mineralogy, comprehending oryctognosy, geognosy, mineralogical chemistry, mineralogical geography, and economical mineralogy*, Vol. 3. Edinburgh: William Blackwood.
Jameson, R. 1819. On the geognosy of the Cape of Good Hope. *Edinburgh Philosophical Journal* **1** (2), October 1819, 283–9.
Jameson, R., Wilson, J. & Murray, H. 1830. *Narrative of Discovery and Adventure in Africa, from the earliest ages to the present time: with illustrations of Geology, Mineralogy and Zoology*. Edinburgh: Oliver & Boyd.
Keilhau, M. 1843. Theory on Granite. *Edinburgh New Philosophical Journal* **24**, 402.
Kennedy, R. F. 1954. An American hero in Table Bay. *Africana Notes and News* **11** (3), 66–8.
Keynes, R. D. (ed.) 2001. *Charles Darwin's* Beagle *Diary*. Cambridge: Cambridge University Press.
Kirby, P. R. 1965. *Sir Andrew Smith, M.D., K.C.B. His Life, Letters and Works*. Cape Town: A.A. Balkema.
Kolb, P. 1719. *Caput Bonae Spei hodiernum: das ist vollständige Beschreibung des afrikanische Vorgebürges der Guten Hofnung*. Nürnberg: P. C. Monath.
Krauss, F. 1839. Briefwechsel. Mittheilungen an den Geheimenrath v. Leonhard gerichtet. Capstadt, 21. Juli 1838. *Neues Jahrbuch für Mineralogie, Geognosie, Geologie und Petrefaktenkunde, Stuttgart* **1839**, 61–3.
La Caille, l'Abbé de 1763. *Journal Historique du Voyage fait au Cap de Bonne-Espérance*. Paris: Guillyn.
Latrobe, C. J. & Hesse, F. 1820. *Des Evangelischen Predigers C. J. Latrobe Tagebuch einer Besuch-Reise nach Süd-Afrika in den Jahren 1815 und 1816*. Halle und Berlin: Buchhandlung des Hallischen Waisenhauses.
Le Vaillant, F. 1795. *Second Voyage dans l'Interior de l'Afrique par le Cap de Bonne-Espérance; dans les années 1783, 84 et 85, Tome I*. Paris: H. J. Jansen et Cie.
Lichtenstein, H. 1811–12. *Reisen im Südlichen Afrika in den Jahren 1803, 1804, 1805 und 1806*, 2 vols. Berlin: C. Salfeld.
Lyell, C. 1833. *The Principles of Geology*. London: J. Murray.
Masson, F. 1776. Mr Masson's Botanical Travels. An account of three journeys from the Cape into the interior parts of Africa. *Philosophical Transactions of the Royal Society, London* **66** (1), 268–317.
Masson, F. 1994. *Francis Masson's account of Three Journeys at the Cape of Good Hope 1772–1775*. With an Introduction and annotations by Frank R. Bradlow. Cape Town: Tablecloth Press.
Mennell, F. P. 1903a. Minerals of some South African granites. *Report of the South African Association for the Advancement of Science, First Meeting, Cape Town*, 282–5.
Mennell, F. P. 1903b. The minerals of some South African granites. *Geological Magazine, New Series*, Decade IV **10**, 345–7.
Mentzel, O. 1785–1787. *Vollständige und zuverlässige geographische und topographische Beschreibung des beruhmten und aller Betrachtung so merkwurdigen afrikanischen Vorgebirges der Guten Hofnung*, 2 volumes. Glogau: Christian Friedrich Günther.
Milbert, J. 1812. *Voyage pittoresque à L'île de France, au Cap de Bonne-Esperance*, 2 volumes. Paris: A. Napveu.
Milbert, J. 1825. *Milbert's Reise nach Isle-de-France, dem Vorgebirge der Guten hofnung und der Insel Teneriffa*. Edited and translated by Joh. Georg Rudolph Blumhof. Frankfurt am Main: Verlag von Franz Barrentrapp.
Moore, J. 1994. Geology and climate of Table Mountain. *In* Hey, D. (ed.) *The Mountain: An Authoritative Guide to the Table Mountain Chain*, 31–42. Cape Town: Tafelberg.
Noble, R. 1870. Editorial Footnote. *Cape Monthly Magazine, Cape Town* **2**(1), 255.
Piers, H. W. 1870. The Geology of Table Mountain. *Cape Monthly Magazine, Cape Town* **2** (1), 253–5.
Playfair, J. 1802. *Illustrations of the Huttonian Theory of the Earth*. Edinburgh: Creech.
Playfair, J. & Hall, B. 1813. Account of the structure of Table Mountain and other parts of the peninsula of the Cape; drawn up by Prof. Playfair, from the observations made by Capt. Basil Hall, RN, FRS Edin. *Transactions of the Royal Society of Edinburgh* **7**, 269–78.
Prosser, W. 1878. The Granites and Gneiss of the Colony. *Transactions of the South African Philosophical Society, Cape Town* **1** (9), 93–100.
Raven-Hart, Maj. R. 1967. *Before Van Riebeeck. Callers at South Africa from 1488 to 1652*. Cape Town: C. Struik.
Rogers, A. W. 1905. *An Introduction to the Geology of Cape Colony*. London: Longmans, Green & Co.
Rupke, N. A. 1994. A second look: C. C. Gillespie's Genesis and Geology. *Isis* **85** (9), 261–70.
Schwartz, E. H. L. 1913. The Sea Point granite-slate contact. *Transactions of the Geological Society of South Africa* **16**, 33–8.
Shaw, J. 1878. The Petrography of Table Mountain Valley. *Transactions of the South African Philosophical Society, Cape Town* **1** (6), 55–65.
Smith, Rev. C. 1831. Biographical notice of the late Captain Dugald Carmichael. *In* Hooker, W. J. (ed.) *Botanical Miscellany* **2**, 1–59; 258–89. London: John Murray.
Sonnerat, P. 1782. *Voyage aux Indes orientales et à la Chine, fait par ordre du roi depuis 1774 jusqu'en 1781*, 2 volumes. Paris: Sonnerat, Froullé, Nyon, Barrois.
Sparrman, A. 1783. *Resa till Goda Hopps-Udden, Södra Pol-kretsen och omkring Jordklotet samt till Hottentott och Caffer-Landen, åre 1772–76*. Stockholm: Anders J. Nordstrom.
Sparrman, A. 1785. *A Voyage to the Cape of Good Hope, towards the Antarctic Polar Circle, and round the world; but chiefly into the country of the Hottentots and Caffres, from the year 1772 to 1776*, 2 volumes. Dublin: White, Cash & Byrne.
Tachard, G. 1686. *Voyage de Siam des Pères Jésuites, enyoyez par le Roy aux Indes & à la Chine, avec leurs Observations Astronomiques, et leurs Remarques de Phisique, de Géographie, d'Hydrographie, & d'Histoire*. Paris: Seneuze et Horthemels.
Theron, N. J. 1984. *The Geology of Cape Town and environs. Explanation of Sheets 3318 CD and DC, and 3418 AB, AD and BA*. Pretoria: Geological Survey of South Africa.
Thunberg, C. P. 1788. *Resa uti Europa, Africa, Asia förrättad åren 1770–1779, vol. 1, 1788; vol. 2, 1789; vol. 3, 1791; vol. 4, 1793*. Uppsala: Joh. Edman (vols. 1–3) & Joh. Edmans Enka (vol. 4).
Thunberg, C. P. 1986. *Carl Peter Thunberg: Travels at the Cape of Good Hope 1772–1775*. Edited by V.S. Forbes. Cape Town: Van Riebeeck Society.
Valentyn, F. 1726. *Beschryving van 't Nederlandsch Comptoir op de Kust van Malabar, en van onzen Handel in Japan, mitsgaders een Beschryving van Kaap der Goede Hoope en 't Eyland Mauritius, met de zaaken tot de voornoemde Ryken en Landen behoorden*. Dordrecht: Johannes van Braam.
Walker, A. R. E. 1929. The Sea Point granite-slate contact. *15th International Geological Congress, South Africa, Guidebook* **A3**.
Walker, F. & Mathias, M. 1946. The petrology of two granite-slate contacts at Cape Town, South Africa. *Quarterly Journal of the Geological Society, London* **102** (4), 499–518.
Werner, A. G. 1787. *Kurze Klassifikation und Beschreibung der verschiedenen Gebirgsarten*. Dresden: Waltherischen Hofbuchhandlung.
Werner, A. G. 1791. *Neue Theorie von der Entstehung der Gänge, mit Anwendung auf den Bergbau besonders den freibergischen*. Freiberg: Gerlach.

MS received 4 December 2008. Accepted for publication 5 December 2008 (Stellenbosch); 15 January 2009 (RSE).

The sanukitoid series: magmatism at the Archaean–Proterozoic transition

Hervé Martin[1a,b,c], Jean-François Moyen[2] and Robert Rapp[3]

[1a] Clermont Université, Université Blaise Pascal, Laboratoire Magmas et Volcans, BP 10448, F-63000 Clermont-Ferrand, France

[1b] CNRS, UMR 6524, LMV, F-63038 Clermont-Ferrand, France

[1c] IRD, R 163, LMV, F-63038 Clermont-Ferrand, France
Email: h.martin@opgc.univ-bpclermont.fr

[2] Department of Geology, University of Stellenbosch, Private Bag X 01, 7602 Matieland, South Africa

[3] Research School of Earth Sciences, The Australian National University, Canberra, ACT, 0200 Australia

ABSTRACT: A specific type of granitoid, referred to as sanukitoid (Shirey & Hanson 1984), was emplaced mainly across the Archaean–Proterozoic transition. The major and trace element composition of sanukitoids is intermediate between typical Archaean TTG and modern arc granitoids. However, among sanukitoids, two groups can be distinguished on the basis of the Ti content of the less differentiated rocks of the suite: high- and low-Ti sanukitoids. Melting experiments and petrogenetic modelling show that they may have formed by either (1) melting of mantle peridotite previously metasomatised by felsic melts of TTG composition, or (2) by reaction between TTG melts and mantle peridotite (assimilation). Rocks of the sanukitoid suite were emplaced at the Archaean–Proterozoic boundary, possibly marking the time when TTG-dominated granitoid magmatism changed to a more modern-style, arc-dominated magmatism. Consequently, the intermediate character of sanukitoids is not only compositional but chronological. The succession of granitoid magmatism with time is integrated in a plate tectonic model where it is linked to the thermal evolution of subduction zones, reflecting the progressive cooling of Earth: (1) the Archaean Earth's heat production was high enough to allow the production of large amounts of TTG granitoids formed by partial melting of recycled basaltic crust ('slab melting'); (2) at the end of the Archaean, due to the progressive cooling of the Earth, the extent of slab melting was reduced, resulting in lower melt:rock ratios. In such conditions the slab melts can be strongly contaminated by assimilation of mantle peridotite, thus giving rise to low-Ti sanukitoids. It is also possible that the slab melts were totally consumed in reactions with mantle peridotite, subsequent melting of this 'melt-metasomatised mantle' producing the high-Ti sanukitoid magmas; (3) after 2·5 Ga, Earth heat production was too low to allow slab melting, except in relatively rare geodynamic circumstances, and most modern arc magmas are produced by melting of the mantle wedge peridotite metasomatised by fluids from dehydration of the subducted slab. Of course, such changes did not take place exactly at the same time all over the world. The Archaean mechanisms coexisted with new processes over a relatively long time period, even if they were subordinate to the more modern processes.

KEY WORDS: geochemistry, granitoid, magma/melt interactions, petrogenesis, slab melting, temporal change in magma production

The genesis of the continental crust started very early in Earth's history: indeed, detrital zircons from Jack Hills, in Western Australia record the existence of 4·40 Ga granitic (*s.l.*) crust (Wilde *et al.* 2001). Whilst the first half of Earth history mainly corresponds to the extraction of juvenile crust from the mantle, recycling mechanisms existed before 4·0 Ga ago (Cavosie *et al.* 2004, 2005, 2006; Watson & Harrison 2005; Harrison & Schmitt 2007; Blichert-Toft & Albarède 2008), but were highly subordinated processes. Due to the greater Earth heat production (Brown 1985), the petrogenetic processes that operated were different from modern ones, resulting in the genesis of unique lithologies such as komatiites and massive volumes of tonalite trondhjemite and granodiorite (TTG) magmas (Viljoen & Viljoen 1969; Glikson 1971; Windley & Bridgwater 1971; Arth & Hanson 1972; Barker & Arth 1976; McGregor 1979; Condie 1981; Jahn *et al.* 1981; Martin *et al.* 1983). Based on petrological and experimental studies, as well as on geochemical modelling, the genesis of Archaean TTG has been explained by partial melting of hydrous basalt metamorphosed into garnet-bearing amphibolite or eclogite (Barker & Arth 1976; Martin 1986, 1987, 1993, 1994; Rapp *et al.* 1991, 2003; Rapp & Watson 1995; Martin *et al.* 1997, 2005; Foley *et al.* 2002; Martin & Moyen 2002). In contrast, it is more seldom proposed that TTG are generated by the extensive fractional crystallisation of water-rich basalt in a subduction environment (Kamber *et al.* 2002; Kleinhanns *et al.* 2003). If most researchers consider that TTG were generated by the melting of hydrated basalt, they disagree about the exact site where this melting took place. The two end-member possibilities are: (1) partial melting of basalt which underplated

© 2009 The Royal Society of Edinburgh. doi:10.1017/S1755691009016120

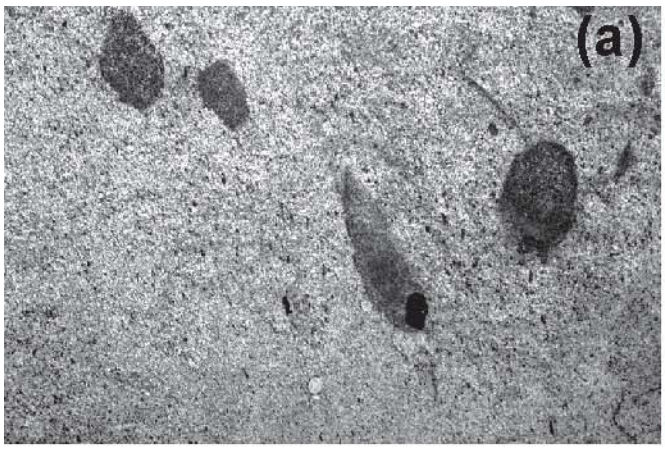
(a)

(b)

(c)

(d)

(e)

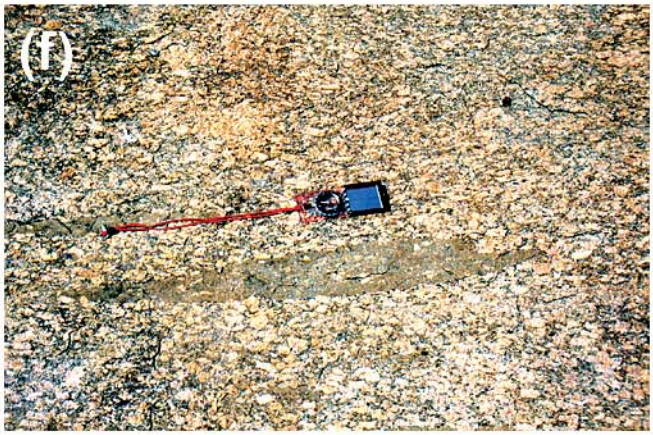
(f)

(g)

(h)

a thickened crust (Atherton & Petford 1993; Rudnick 1995; Albarède 1998; de Wit 1998; Smithies 2000; Smithies *et al*. 2005; Bédard 2006); (2) a subducted hot oceanic slab that melted rather than dehydrating (Martin 1986; Condie 1989; Rollinson 1997; Barth *et al*. 2002; Foley *et al*. 2002; Kamber *et al*. 2002; Martin & Moyen 2002; Rapp *et al*. 2003; Condie 2005; Nair & Chacko 2005; Martin *et al*. 2008). After the end of the Archaean (2·5 Ga), and until today, most of the juvenile continental crust is formed by melting of a fluid metasomatised peridotite followed by different degrees of differentiation, generating the BADR (Basalt Andesite Dacite Rhyolite) suites typical of subduction environments. There, the source of the magmas is considered as being the mantle wedge peridotite metasomatised by fluids resulting from the dehydration of the subducted slab (Tatsumi 1989; Pawley & Holloway 1993; Liu *et al*. 1996; Schmidt & Poli 1998; Forneris & Holloway 2003).

The transition between TTGs and BADRs roughly took place at the Archaean–Proterozoic transition, about 2·5 Ga ago. At the same period, high-Mg dioritic, tonalitic and granodioritic magmatic rocks were generated and emplaced into all Archaean cratons. These plutons, commonly called late granodioritic or granitic plutons, were first identified by Shirey & Hanson (1984), who referred to them as Archaean sanukitoids. These rocks are now found in most Late Archaean terranes (2·9–2·5 Ga) (Shirey & Hanson 1984; Stern 1989; Stern & Hanson 1991; Smithies & Champion 1999; Moyen *et al*. 2001b, 2003); they possess both modern (classical calc-alkaline differentiation, similar to BADR association, high transition element contents) and Archaean (low HREE contents, strongly fractionated REE patterns, etc. . . .) geochemical characteristics. The transitional character of sanukitoids is not only compositional but also chronologic, being emplaced during the 'hinge' period between two epochs dominated by TTG (Archaean) and BADR (Proterozoic/Phanerozoic) juvenile crustal magmatism. Consequently, their study could provide not only new insights into the change in petrogenetic mechanisms during this period, but also into the changing geodynamics on Earth across the ~2·5 Ga boundary.

The purpose of this paper is: (1) to review the geochemical and petrologic characteristics of sanukitoids; (2) to address their petrogenesis; (3) to discuss possible geodynamic environments for their generation; and (4) to consider their temporal distribution over the whole of Earth's crustal evolution.

1. Sanukitoids

1.1. Definition

Shirey & Hanson (1984) first recognised a suite of Late Archaean felsic intrusive and volcanic rocks in the Superior Province that had both mineralogical and chemical characteristics clearly different from TTG, which had up until then been viewed as, volumetrically, the overwhelmingly dominant granitoid throughout the Archaean. Because the major element geochemistry of these rocks resembled that of Miocene high-Mg Andesite (Sanukite) from the Setouchi volcanic belt of Japan (e.g. Tatsumi & Ishizaka 1982), Shirey & Hanson (1984) referred to them as 'Archaean sanukitoids'. Since this pioneering work, sanukitoids have been described in most Archaean terranes: the Superior Province (Shirey & Hanson 1984, 1986; Stern & Hanson 1991; Bédard 1996; Stevenson *et al*. 1999), Wyoming (Frost *et al*. 1998), the Baltic shield (Querré 1985; Lobach-Zhuchenko *et al*. 2000, 2005, 2008; Halla 2005; Kovalenko *et al*. 2005; Samsonov *et al*. 2005; Käpyaho 2006), South India (Balakrishnan & Rajamani 1987; Jayananda *et al*. 1995; Krogstad *et al*. 1995; Moyen *et al*. 2001b, 2003; Sarvothaman 2001), China (Jahn *et al*. 1998), Limpopo (Barton *et al*. 1992; Millonig *et al*. 2008), the Central Pilbara craton (Smithies & Champion 1999) and the Amazonian craton (Medeiros & Dall'Agnol 1988; Althoff 1996; Leite *et al*. 2004). Compared with TTG, sanukitoids still represent a volumetrically subordinate component of the Archaean crust; however, they are a common component of most Late Archaean cratons.

1.2. Composition

Based on field observations, sanukitoids define a complete magmatic series, from diorites to granites (the 'sanukitoid suite' of Stern & Hanson 1991). The two most common rock types are: (1) medium-grained, equigranular monzodiorites to granodiorites, containing small (5–10 mm) clusters of biotite, hornblende and rare relicts of hornblende-rimmed clinopyroxene, which give the rock a very distinctive, black and white 'spotted' aspect; (Fig. 1a–b); (2) porphyritic monzogranite (Fig. 1d–e), with large (2–5 cm) to very large (~10 cm) phenocrysts of K-feldspar in a coarse-grained matrix.

In both case, the paragenesis consists of quartz, plagioclase ($An_{20–30}$), perthitic microcline, hornblende and biotite. Accessory phases are magnetite, ilmenite, epidote, sphene, apatite, zircon and allanite. Microgranular, mafic dioritic to monzodioritic enclaves are common (Fig. 1c, f–h); they are fine grained (0·1–1 mm), with occasional K-feldspar phenocrysts with rapakivi texture. They also typically contain small mafic clusters of biotite with 'spots' of dull black amphibole. In some places, relict diopside has been observed within amphibole grains.

Sanukitoid can occur as plutons of all sizes, with a broad range of crustal emplacement levels and degrees of heterogeneity. For example, sanukitoids in the Central Pilbara Craton (Smithies & Champion 1999) form small (<1 km), homogeneous stocks of shallowly emplaced magmas, whereas sanukitoids of South India (the 'Closepet granite', Jayananda *et al*. 1995; Moyen *et al*. 1997, 2001a), form a huge intrusive body that is about 400 km long and 20 km wide and is rooted in the lower granulitic crust. The porphyritic monzogranite of the Closepet batholith is associated with migmatites and anatectic granites derived from melting of the surrounding TTG basement.

Sanukitoid compositions range between mafic (SiO_2 ~ 50% and MgO ~ 8%) and felsic (SiO_2 ~ 75% and MgO ~ 0·1%) end-members (Fig. 2). This could result either from differentiation of a primitive parental magma (e.g. Reddy 1991; Stern & Hanson 1991) or from contamination by older crustal

Figure 1 Field appearance of sanukitoids: (a)–(c) medium-grained, equigranular monzodiorite (Low-Ti sanukitoid); (d)–(h), porphyritic monzogranite (High-Ti sanukitoid). (a) Typical sanukitoid amphibole granodiorite; 2·55 Ga 'Dod gneisses', Kolar belt, India (Krogstad *et al*. 1991; Chardon *et al*. 2002). (b) Biotite ± amphibole bearing granodiorite in the 2·67 Ga Matok Pluton, Limpopo Belt, South Africa (Kreissig *et al*. 2001). (c) Mafic microgranular enclave-bearing sanukitoid of the Rio Maria terrane, Amazonian Craton, Brazil (courtesy R. Dall'Agnol) (Medeiros & Dall'Agnol, 1988). (d) Porphyritic monzogranite from the Closepet batholith, South India. (e) Porphyritic monzogranite in the 2·57 Ga Bulai Pluton, Limpopo Belt, South Africa (Barton *et al*. 1992). (f). Stretched microgranular mafic enclave in the Closepet batholith. (g) Pillowed (monzo-) dioritic enclave, Closepet. (h) Mingling relationships between a porphyritic monzogranite and monzodiorites, Matok.

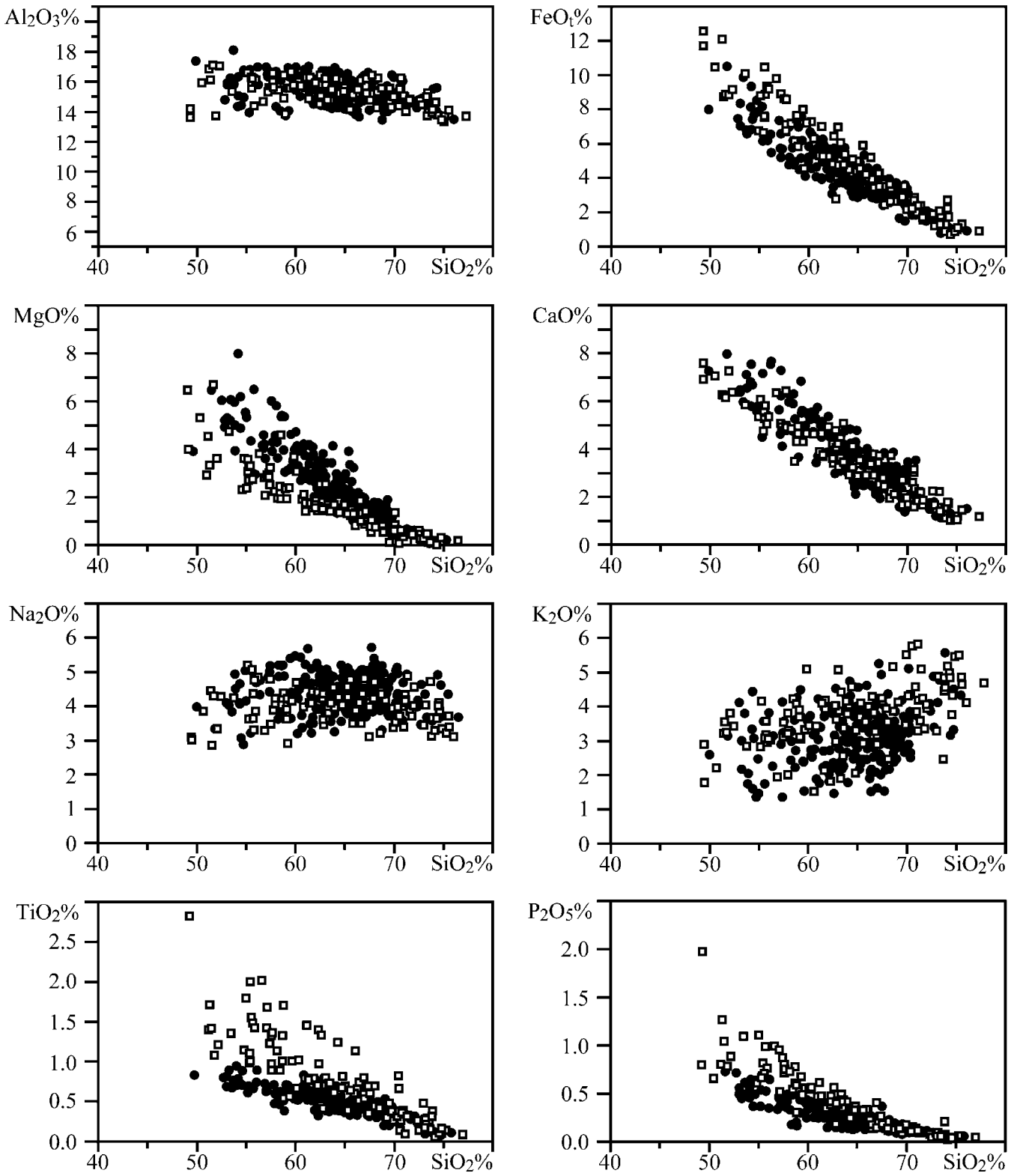

Figure 2 Harker diagrams for both low-Ti (filled circles) and high-Ti (open squares) sanukitoids.

components during emplacement (Moyen *et al*. 2001a). For the Closepet batholith for example, it has been demonstrated (Jayananda *et al*. 1995; Moyen *et al*. 1997, 2001a; among others) that the linear trends for both major and trace elements, over a wide variation of SiO_2 contents (from ~50% up to 75%) are the result of crustal contamination. In this case, mantle-derived magmas interacted with the crust in which they intruded. Their mantle characters were obliterated and altered by a superimposed crustal signature, such that they were often considered to have a mixed origin.

The details of this 'late' evolution are not the focus of this paper, which deals with the origin of the juvenile component, regardless of its subsequent evolution. Consequently, this paper will only refer to the less differentiated component of the sanukitoid suites, thus excluding all samples with SiO_2>62%, that are assumed to be strongly modified by either interaction with a felsic crustal component, or by differentiation of these primary magmas.

The differences between the two main petrologic types identified above (medium-grained, equigranular monzodiorites

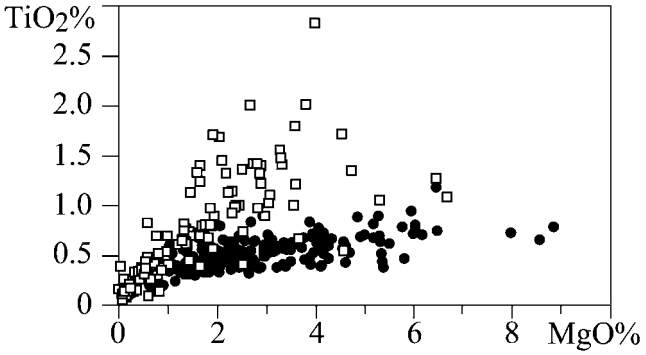

Figure 3 TiO_2 *vs.* MgO plot showing that for the same degree of differentiation (anti-correlated with MgO), TiO_2 content is significantly higher in porphyritic monzogranite (open squares) than in medium-grained, equigranular monzodiorites (filled circles), thus supporting the discrimination between two groups of sanukitoids (Low-Ti and high Ti).

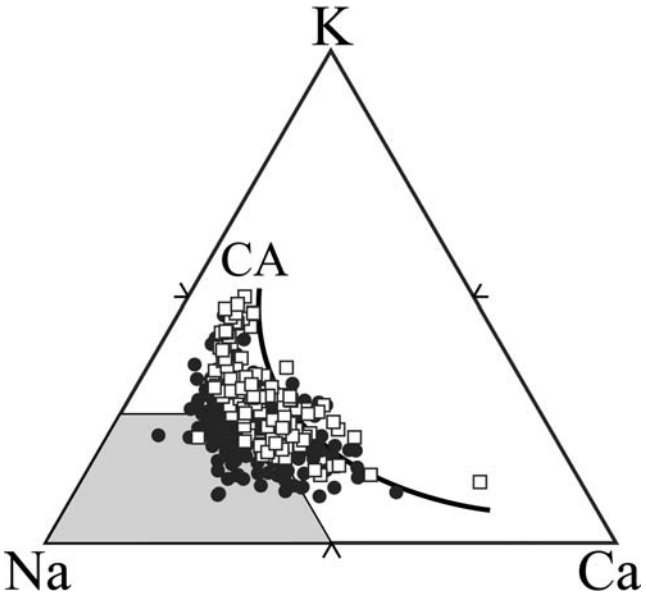

Figure 4 Cationic Ca–Na–K diagram showing that both the low-Ti (filled circles) and high-Ti (open squares) sanukitoids are different of Archaean TTG (grey field, Martin *et al.* 2005). They show a K-enrichment, thus occupying a position intermediate between TTG and the classical calc-alkaline trend (CA) as defined by Barker & Arth (1976). It must also be noted that the high-Ti sanukitoids are slightly K-richer than the low-Ti ones.

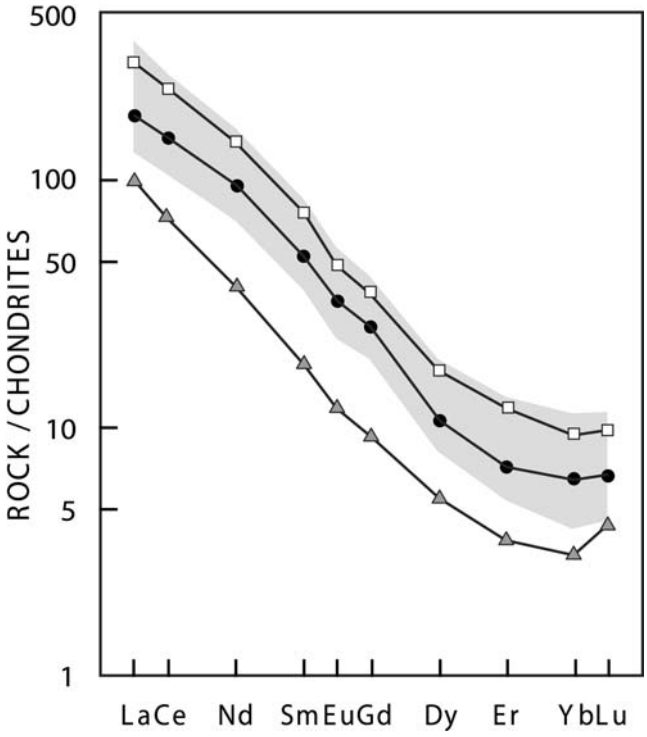

Figure 5 Chondrite normalised REE patterns for average Archaean TTG (grey triangles), low-Ti (filled circles) and high-Ti (open squares) sanukitoids with SiO_2<62%. The grey field represents the compositional field for sanukitoids. Normalisation values are from Masuda *et al.* (1973) divided by 1·2.

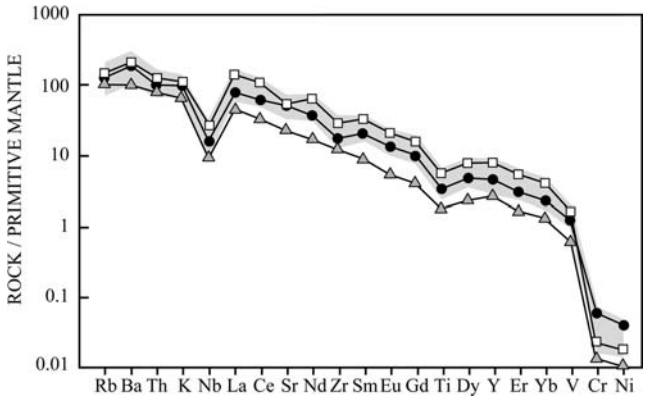

Figure 6 Primitive mantle (Sun & McDonough 1989) normalised multi element diagram for average Archaean TTG (grey triangles), both low-Ti (filled circles) and high-Ti (open squares) sanukitoids with SiO_2<62%. The grey field represents the compositional field for sanukitoids.

and porphyritic monzogranite), are not only textural, but also correspond to geochemical differences. Figure 2 shows that for some elements (e.g., Al_2O_3, Na_2O and K_2O), chemical trends are exactly the same in the two groups, but for other elements the geochemical evolution differs, particularly for the less differentiated rocks. This is well exemplified by the TiO_2 *vs.* SiO_2 (Fig. 2) or TiO_2 *vs.* MgO (Fig. 3) plots, where for the same degree of differentiation, TiO_2 content is significantly higher in porphyritic monzogranite than in medium-grained, equigranular monzodiorites. Consequently, it is proposed to discriminate these two sanukitoid types on the basis of their TiO_2 content: in this paper, the medium-grained, equigranular monzodiorites will subsequently be referred to as low-Ti sanukitoids, whereas the porphyritic monzogranites will be referred as high-Ti sanukitoids.

In a K–Na–Ca cationic triangle (Fig. 4), sanukitoids do not show any affinity with Archaean TTG (Martin *et al.* 2005) and rather show an evolution trend similar to the classical calc-alkaline differentiation trend of Barker & Arth (1976). It must be noted that the low-Ti sanukitoids are slightly poorer in K and richer in Na than their high-Ti equivalents.

Table 1 reports the average composition of 104 sanukitoids from the literature. Out of the published data, only samples with SiO_2 lower than 62% were kept, as they are considered to be representative of the mafic pole of the differentiation suites – regardless of the differentiation mechanism involved. These 104 analyses were classified into 57 low-Ti- and 47 high-Ti sanukitoids, whose average composition is also given. The sanukitoids are meta-aluminous (A/CNK=0·79) and moderately potassic (K_2O/Na_2O=0·72). Mg# (molecular Fe/(Fe+Mg)) is quite high (0·53), as are Ni and Cr contents (54 and 104 ppm, respectively). Sr and Ba are typically greater than 1000 ppm (1108 and 1471 ppm respectively); Na_2O (4·31%) and K_2O (3·11%), (as well as most LILE) contents are also high. Similarly, LREE (e.g. La_N=234) contents are high

Table 1 Average composition and standard deviation for 104 sanukitoids from the literature. Only samples with SiO_2 lower than 62% were taken into consideration, as they are considered as representative of the mafic pole of the differentiation suites, regardless of the differentiation mechanism that operated. These 104 analyses fall into two groups: 57 are low-Ti- and 47 are high-Ti sanukitoids. The average compositions of 250 modern arc granitoids (Martin 1994) and 1094 TTGs (Martin *et al.* 2005) are also given for comparison. Fe_2O_3*=Total iron expressed as Fe_2O_3; Mg#=molecular ratio Mg/(Mg+Fe); A/CNK=molecular ratio Al/(Ca+Na+K).

	TTG (*n=1094*)		Sanukitoid <62% SiO_2 (*n=104*)		Low-Ti Sanukitoid <62% SiO_2 (*n=57*)		High-Ti Sanukitoid <62% SiO_2 (*n=47*)		Modern Arc Granitoids (*n=250*)	
	Average	*Std. dev.*	Average	*Std. dev.*	Average	*Std. dev.*	Average	*Std. dev.*	Average	*Std. dev*
wt.%										
SiO_2	69·51	*3·64*	58·65	*3·56*	59·18	*3·31*	58·00	*3·47*	68·1	*6·2*
Al_2O_3	15·59	*1·14*	16·14	*1·10*	16·08	*1·07*	16·22	*1·39*	15·07	*1·6*
Fe_2O_3*	3·24	*1·56*	6·75	*1·94*	6·14	*1·49*	7·50	*1·71*	4·36	*2*
MnO	0·05	*0·05*	0·12	*0·07*	0·10	*0·03*	0·13	*0·07*	0·09	*0·1*
MgO	1·25	*0·77*	3·90	*1·41*	4·33	*1·27*	3·39	*1·83*	1·55	*1*
CaO	3·16	*1·11*	5·53	*1·24*	5·52	*1·33*	5·55	*1·39*	3·06	*0·64*
Na_2O	4·72	*0·77*	4·31	*0·73*	4·49	*0·75*	4·09	*0·82*	3·68	*0·49*
K_2O	1·95	*0·77*	3·11	*0·82*	3·04	*0·85*	3·20	*0·88*	3·4	*1·1*
TiO_2	0·38	*0·21*	0·93	*0·42*	0·69	*0·18*	1·21	*0·46*	0·54	*0·32*
P_2O_5	0·15	*0·10*	0·56	*0·27*	0·42	*0·12*	0·72	*0·31*	0·15	*0·08*
ppm										
Rb	66	*43*	87	*43*	83	*37*	92	*38*	110	*50*
Ba	713	*465*	1471	*601*	1493	*575*	1445	*699*	715	*205*
Nb	7	*5*	13	*7*	10	*3*	17	*7*	12·1	*5*
Sr	490	*217*	1108	*512*	1202	*563*	994	*366*	316	*150*
Zr	135	*108*	237	*112*	172	*55*	316	*104*	171	*53*
Y	12	*16*	27	*14*	20	*7*	35	*13*	26	*5*
Th	7	*0·6*	9	*7*	9	*5*	10	*9*	11·8	*6·5*
Ni	18	*17*	54	*33*	69	*28*	36	*41*	10·5	*8*
Cr	40	*75*	104	*73*	143	*60*	58	*55*	23	*15*
V	48	*29*	118	*43*	110	*34*	127	*42*	76	*45*
La	31·4	*23·8*	73·9	*42·2*	57·0	*17·4*	94·4	*51·6*	31	*9*
Ce	57·8	*257·0*	152·4	*66·7*	120·5	*34·0*	191·1	*90·7*	67	*17*
Nd	22·4	*17·0*	69·7	*28·1*	56·5	*16·0*	85·8	*37·4*	27	*7*
Sm	4	*2·3*	11·7	*4·7*	9·5	*2·8*	14·3	*5·9*	5·3	*14*
Eu	0·9	*0·4*	2·8	*1·1*	2·4	*0·7*	3·3	*1·2*	1	*0·5*
Gd	2·4	*1·4*	7·8	*2·9*	6·7	*2·0*	9·2	*2·4*	5·5	*1*
Dy	1·7	*0·9*	4·4	*1·8*	3·5	*1·2*	5·5	*1·2*	5·2	*0·1*
Er	0·76	*0·49*	1·97	*0·88*	1·49	*0·55*	2·56	*0·68*	3	*1*
Yb	0·64	*0·40*	1·60	*0·78*	1·29	*0·50*	1·98	*0·76*	3·2	*0·5*
Lu	0·13	*0·50*	0·26	*0·12*	0·21	*0·07*	0·32	*0·11*	0·5	*0·1*
K_2O/Na_2O	0·41		0·72		0·68		0·78		0·92	
Mg#	0·43		0·53		0·58		0·47		0·41	
A/CNK	1·00		0·79		0·78		0·80		0·98	
$(La/Yb)_N$	32·4		30·5		29·2		31·5		6·4	

and HREE (e.g. Yb_N=7·7) moderately low, resulting in strongly fractionated patterns ($(La/Yb)_N$=30·5); which do not show any significant Eu anomaly (Fig. 5). In addition, high-Ti sanukitoids are enriched in REE relative to their low-Ti counterparts. On a primitive mantle-normalised multi-element diagram (Fig. 6), sanukitoids (both types) do not show significant negative anomalies in Zr or Y and only a small negative one for Ti.

On Harker plots, (Fig. 2), both low and high-Ti sanukitoids plot on a single trend for most elements (Al_2O_3, CaO, Na_2O, K_2O and partly FeO_t), pointing to the fact that the two groups formed from a similar source by similar mechanisms. Only MgO and TiO_2 depict slightly different trends that converge towards a common silica-rich pole. This confirms that the differences between the two groups do not reflect differentiation mechanisms, but rather correspond to distinct mafic end-members. Figures 5 and 6 also show that both REE and multi-element patterns are parallel, except for a slight negative Sr anomaly in high-Ti sanukitoids that does not exist in the low-Ti group. This parallelism strongly militates in favour of a similar source for the two facies. In addition, the trace element patterns are also essentially parallel to those of average Archaean TTG, leading us to conclude that TTG are genetically related to sanukitoids in some way.

1.3. Petrogenesis

The average Mg# in sanukitoids is 0·53, but can reach values >0·65 in the more mafic samples. These very high Mg#s and correspondingly high Cr and Ni concentrations (>100 ppm and >300 ppm respectively) in the most primitive members of the sanukitoid suites preclude a crustal (including basaltic) source; for reference, the Mg# of experimental TTG liquids

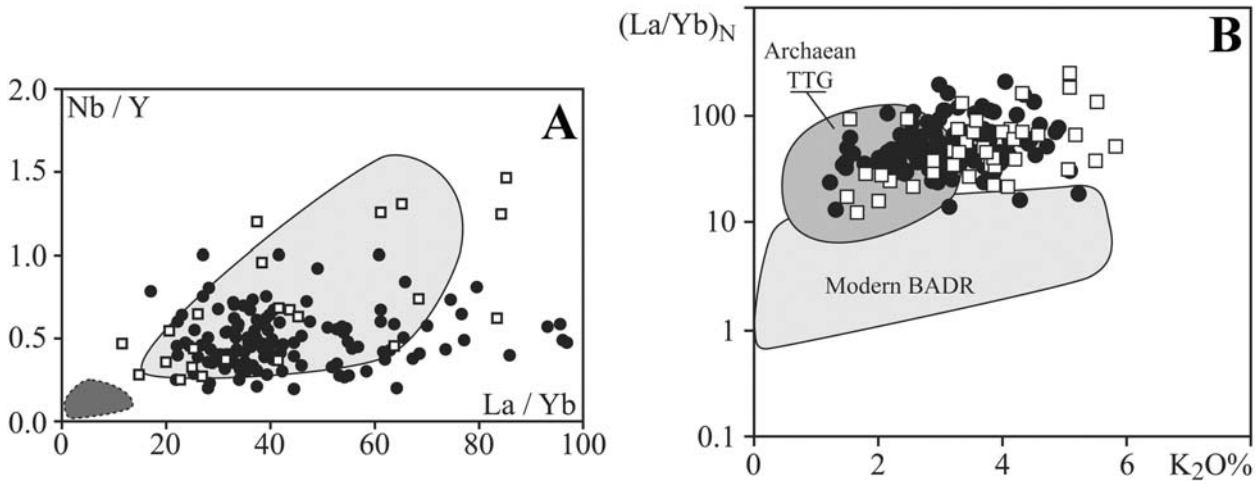

Figure 7 (A) (Nb/Y) *vs.* (La/Yb) plot for low-Ti (filled circles) and high-Ti (open squares) sanukitoids with SiO_2<62%. The dark grey field is that of arc magmas generated by melting of a peridotite metasomatised by fluids. Data are from Fiji (Rogers & Setterfield, 1994) and the New Hebrides (Monzier *et al*. 1997). The light grey field is that of modern high-Mg andesites considered to be generated by the melting of a mantle peridotite enriched by felsic melts. Data are from Baja California (Calmus *et al*. 2003) and Ecuador (Bourdon *et al*. 2003; Hoffer 2008). See text for more detailed explanation. Sanukitoids point to a mantle source metasomatised by felsic melts. (B) $(La/Yb)_N$ *vs.* K_2O plot that compares the composition of sanukitoids with that of typical arc BADR suites (Martin 1994). Sanukitoids, draw a trend parallel to that of BADR field, thus pointing to similar petrogenetic mechanisms and source. However, the fact that the field of Archaean TTG perfectly plots on one extremity of the sanukitoid trend indicates the possible role of a metasomatic agent played by TTG magma.

generated by partial melting of basalts never exceeds 0·45 (Rapp & Watson 1995; Zamora 2000). Similarly the SiO_2 content of the less differentiated TTG is of about 60% (Martin 1994), whereas it is of about 50% in sanukitoids. Therefore, the source of sanukitoids must be ultramafic. On the other hand, the same rocks are very rich in LILE; which because of the high Mg#, Cr and Ni, precludes any interpretation in terms of enrichment through fractional crystallisation, as this process would efficiently deplete compatible elements from the magmas (Martin & Sigmarsson 2007). Contamination of an LILE-rich felsic continental crust by komatiitic or basaltic magmas could also generate sanukitoid magmas. However, Stern (1989), and more recently Smithies & Champion (1999) modelled the interaction between mafic (or ultramafic) melts and the felsic crust, and demonstrated that this process cannot reproduce both characteristics of primitive sanukitoids (high Mg#, Ni and Cr together with high SiO_2 and LILE contents). Therefore, the present authors interpret the LILE enrichment as a primary characteristic, reflecting the nature of the source; that source must at least in part be ultramafic (because of the high Mg#s, Cr and Ni), and LILE enriched; the only reliable and realistic possibility is that sanukitoids derive from a source formed by the interaction of a felsic (TTG) melt and ultramafic rock (mantle peridotite). The sanukitoid melt itself may come about from a single stage process of melt infiltration, hybridisation, and assimilation (e.g., Rapp *et al*. 1999), or in a two-stage process in which melt metasomatism is followed by partial melting of the metasomatised peridotitic source.

In a modern subduction zone, where a metasomatised and geochemically enriched mantle wedge is the main source of arc magmatism, two metasomatic agents, (both derived from crustal components of the subducting oceanic lithosphere) are generally invoked: hydrous, solute-rich, possibly supercritical fluids, and hydrous, SiO_2-rich (i.e., felsic) melts. These two metasomatic agents have very contrasted behaviour with respect to some chemical elements like HFSE; for instance $Kd_{Nb}^{solid/fluid}$ >10, whereas $Kd_{Nb}^{solid/melt}$ <1. In other words, hydrous fluids are unable to transfer Nb from the slab into the mantle wedge, whereas a felsic melt can. In addition, felsic melts generated within the garnet stability field will have an 'adakitic' signature characterised by very low Y and Yb contents (Martin *et al*. 2005; Macpherson *et al*. 2006; Moyen 2009). Consequently, the nature of the metasomatic agent can be discussed in the (Nb/Y) *vs.* (La/Yb) diagram (Fig. 7A), where the composition of sanukitoids is compared with that of modern arc magmas. The dark grey field is that of modern magmas from New Hebrides (Monzier *et al*. 1997) and Fiji (Rogers & Setterfield 1994) where the magmatic signature is free of any continental contamination and where the metasomatic agent is considered to be exclusively fluids produced by sub-solidus dehydration of the subducted slab. The light grey field is that of modern high-Mg andesites and low-silica adakites (Bourdon *et al*. 2003; Hoffer 2008), which are also considered to be the result of partial melting of melt-metasomatised mantle peridotite. Since Late Archaean sanukitoids have higher Nb/Y and La/Yb than typical modern arc magmas, a fluid-metasomatised mantle source can be ruled out. On the other hand, sanukitoids overlap the field for high-Mg andesites or low-silica adakites, magmas that are considered as generated either through partial of a mantle peridotite metasomatised by adakitic melts (Martin *et al*. 2005, for review), or by direct reaction (assimilation) of mantle peridotite with TTG melts (e.g., Rapp *et al*. 1999). In addition, Figures 5 and 6 shows that except for transition elements, the REE and multi-element patterns of sanukitoids are strictly parallel to TTG patterns, thus pointing to a strong genetic link between them. This conclusion is reinforced by the $(La/Yb)_N$ *vs.* K_2O plot (Fig. 7B), comparing the composition of sanukitoids with typical arc BADR suites and Archaean TTGs (Martin 1994). Sanukitoids follow a trend parallel to the BADR field, with the same range of K_2O contents, $(La/Yb)_N$ being closely correlated with K_2O. This reflects the similarity of the petrogenetic processes: possibly melting of a metasomatised mantle. However, the BADR and sanukitoid trends are parallel but not superimposed, the later having higher $(La/Yb)_N$, indicating different metasomatic agents; the overlap between the TTG field and the end of the sanukitoid trend points to TTGs being a possible metasomatic agent.

Collectively, these evidences show that the most likely metasomatic agent responsible for the peridotitic source enrichment is a TTG-like felsic melt.

2. Experimental petrology

The only way to obtain appreciable volumes of LILE-enriched magmas from a peridotitic source is by enrichment of the mantle source prior to melting. This would imply a two-stage petrogenetic process for sanukitoid magmas in which melting is preceded by metasomatism, i.e., the reaction between an LILE-enriched fluid or melt and mantle peridotite. As discussed above (Fig. 7), this metasomatic agent is considered as being an SiO_2-rich melt. In a modern subduction zone setting, these felsic melts are presumed to be produced by partial melting of subducted basaltic oceanic crust, referred to as 'adakites', a term more or less synonymous with the 'slab melt' (henceforth referred to as 'pristine' adakites, to denote a slab melt that has yet to experience modification by reaction with mantle peridotite). As Archaean TTG, the chemistry of adakites shows that they are derived by partial melting of garnet-bearing mafic (metabasaltic) crust, followed by variable degrees of subsequent 'interaction' with mantle peridotite, presumably in the overlying mantle wedge (see Martin *et al.* 2005, for review). Given the geochemical evidence presented above for a genetic link between TTG granitoids and sanukitoids, a number of experimental studies looking at various aspects of chemical interaction between TTG liquids and peridotite have been undertaken in recent years (e.g. Sen & Dunn 1994; Yaxley & Green 1998; Rapp *et al.* 1999, 2006; Prouteau *et al.* 2001; Hoffer 2008). These studies focused on the equilibrium between the 'hybridised slab melt' (Rapp *et al.* 1999) and the modified peridotite assemblage. They implicitly assume a 'one-stage' process, in which the adakitic (or TTG) melt is transformed into a sanukitoid on its way up to the surface; sanukitoid forms contemporaneously with the geological event that generated the felsic melt (Fig. 8).

Earlier experimental studies in the 1970s and 1980s examined processes of 'melt hybridisation in subduction zones' (Nicholls & Ringwood 1973; Sekine & Wyllie 1982; Johnson & Wyllie 1989), where 'assimilation of mantle peridotite by an ascending slab-derived melt' led to the formation of 'zones of hybrid olivine pyroxenite which, in turn, could be remelted to generate a spectrum of island arc magmas' (Nicholls & Ringwood 1973; Johnson & Wyllie 1989). This scenario immediately calls to mind a 'two-stage' process, in which the metasomatic event is separated in time from the melting (or remelting) event, which yields sanukitoids (Fig. 8).

Deciding between a 'one-stage' and a 'two-stage' process is difficult, if not impossible, on experimental grounds alone. Indeed, the only conclusions that can be drawn from experiments is that a sanukitoid melt can be formed in equilibrium with a mafic to ultramafic mineral assemblage, which provides no constrains on the path that was followed in the P–T–X space to reach these conditions, let alone the duration of this path.

A critical factor in the reaction between slab-derived, pristine melts and peridotite in the mantle wedge is the so-called 'effective melt-to-rock ratio' (Rapp *et al.* 1999), which refers to the relative proportions of adakite melt and peridotite 'rock' involved in the 'melt-rock reaction' (Kelemen *et al.* 1993, 1998). This parameter is obviously easily controlled in laboratory experiments, but in nature, it depends upon the scale at which the interaction between slab-derived melts and the mantle wedge are considered, as well as the physical mechanism for melt infiltration (e.g., porous flow? fracture propagation?). The melt:rock ratio can be high; this does not mean that the mantle as a whole was soaked with melts, but rather that the scale of the interactions was such that only limited portions of the mantle were allowed to react with the melt. In other words, low melt:rock ratios correspond to interactions involving large amounts of the mantle – maybe corresponding to narrow magma pathways, or magma percolating through the mantle on a grain-scale, with a correspondingly high interface surface between melt and mantle. In contrast, high melt:rock ratios can be obtained where large magma conduits restrict the contact surface between the melt and the peridotite, and/or high magma flow in large conduits reduces the time range available for interaction, and/or armouring of the edges of the conduit makes further reactions difficult or impossible. Consequently, in natural geological systems, the melt:rock ratio can vary between zero and infinity, as a function of the magma flow rate, overall supply, and of the size and geometry of the magma pathways, and the mechanism involved in melt infiltration and transport.

Regardless of these issues, melt–rock reactions in the overlying mantle wedge above a subducting slab can generally be assumed to be dominated by processes of assimilation when the effective melt:rock ratio is high (one-stage process; Fig. 8), and by cryptic and modal metasomatic processes when the effective melt:rock ratio is low. In the former case, mantle-hybridised adakitic melts will be produced, and in the latter case a melt-metasomatised peridotite (*sensu lato*) mantle wedge is formed, which itself can then become the source for magmas by subsequent partial melting events (i.e., the 'two-stage' process; Fig. 8).

The composition of 'mantle-hybridised slab melts' and the metasomatic mineral assemblages that form as a result of such melt–rock reactions in the mantle wedge, will clearly depend upon such factors as the 'effective melt:rock ratio', pressure, temperature, and water content (all strictly controlled in laboratory experiments), and comprehensive and systematic experimental studies are lacking. Nevertheless, certain general observations can be made regarding the processes of peridotite assimilation, melt hybridisation, and mantle metasomatic reactions from the laboratory experiments that have been carried out. First, olivine is consumed in these reactions (i.e., reactant phases are olivine and pristine adakite melt), and the primary metasomatic phases are orthopyroxene and amphibole or phlogopite (i.e., products). Secondly, at high melt:rock ratios and/or relatively high temperatures, most, if not all, of the original olivine in the peridotite is consumed, and one is left with a hybridised adakitic melt in equilibrium with a pyroxenite reaction residue (Rapp *et al.* 1999; Prouteau *et al.* 2001). At low melt:rock ratios and/or lower temperatures, the metasomatic phase assemblage is dominated by amphibole/phlogopite and orthopyroxene, and although generally some of the original olivine is also present, it is often not clear from the experiments whether or not 'armouring' of the original olivine by orthopyroxene has taken place (Sen & Dunn 1994; Rapp *et al.* 1999; Prouteau *et al.* 2001), In this case the trace element signature of the slab melt is effectively transferred to the mantle wedge, and this adakite-metasomatised pyroxenite then becomes a potential source for 'mantle-derived' melts in the future. Martin *et al.* (2005) have classified the melts that are associated with these two different outcomes of slab melt-peridotite reactions in the mantle wedge as 'high-SiO_2 adakites' (HSA; mantle-hybridised adakites), and 'low-SiO_2 adakites' (LSA; partial melts of adakite-metasomatised peridotite). It is important to note that, although the experimental analogues of 'HSAs' have been produced in the laboratory (e.g., Rapp *et al.* 1999), experimental 'LSAs' have not. The

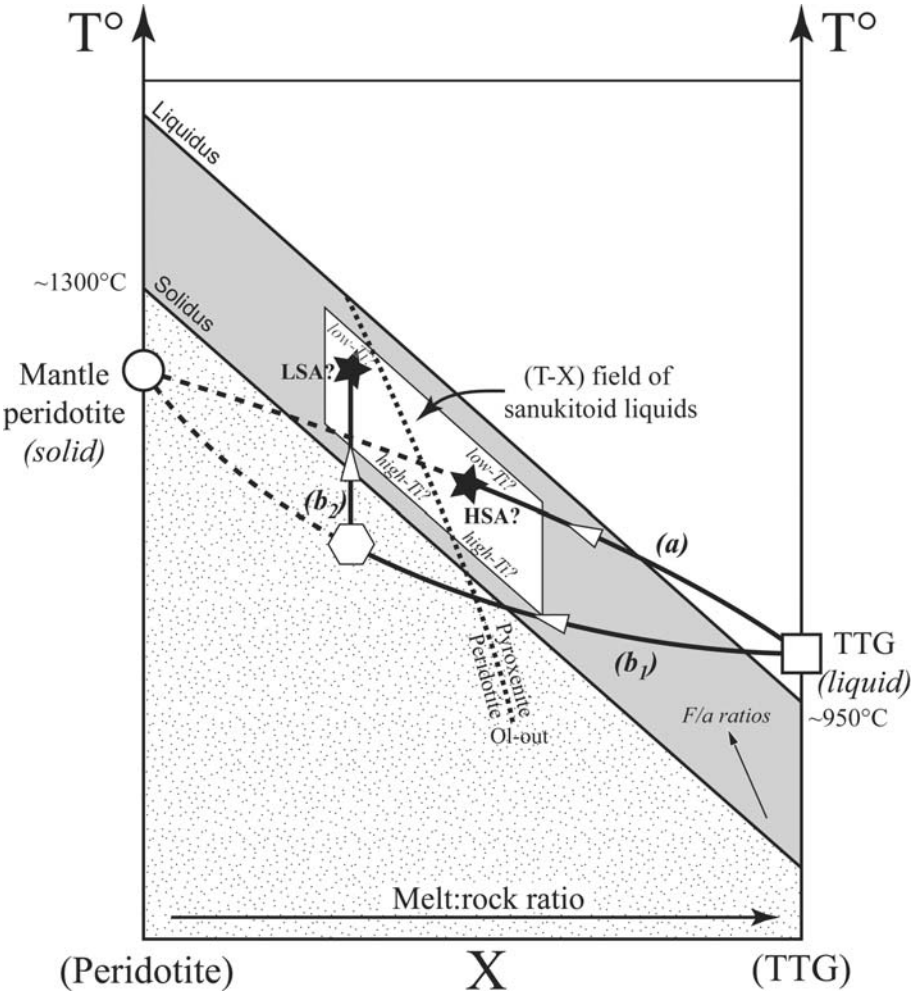

Figure 8 Schematic diagram summarising the possible modes of interactions between TTG liquids and mantle wedge peridotites. This diagram reports the temperature (T°) *vs.* the bulk composition of the system (X). X ranges between a pure peridotite and a pure TTG liquid. In a 'true' pseudosection, both the liquidus and solidus curves would probably be stepped; however for purpose of simplification, they are drawn as lines. The dotted line represents the (conceptual) limit of stability for olivine, i.e. the limit between peridotitic and pyroxenitic solids (residuum if in equilibrium with the melt, 'metasomatised mantle' otherwise). Sanukitoid liquids exist for bulk compositions that are mixtures of TTG and peridotite, and for melt fractions ranging between the solidus and the liquidus (white parallelogram field). This field can be reached along different paths. Path (*a*) is the 'one-stage' process mentioned in the text. In this case the TTG liquid reacts with peridotites to give a sanukitoid liquid in equilibrium with a mafic or ultramafic solid. HSA liquids probably form along this trend (for high melt:rock ratios); lower TTG proportions would rather result in LSA or sanukitoids. Path (*b*) is the 'two-stage' process, (b_1) is the complete assimilation of TTG liquids via metasomatic reactions with the peridotite, and (b_2) corresponds to subsequent melting of this modified composition. The black *F/a* arrow shows how the *F/a* ratio (discussed in section 3) increases, inside the inter solidus–liquidus domain.

present authors expect that in fact a petrogenetic and compositional continuum probably exists between HSA and LSA magmas, and where a given magma falls along that continuum is probably highly dependent upon the mechanism and dynamics of melt infiltration and propagation.

The distinction between the two groups (HSAs and LSAs) may in fact lie in the nature of the mineral assemblage with which they may have equilibrated: experimental results have shown that HSA melts are in equilibrium with a pyroxenite residue ($\pm$ garnet $\pm$ amphibole/phlogopite), whereas LSA melts are likely to be in equilibrium with an olivine-bearing (i.e., peridotite or garnet peridotite) phase assemblage, with the melting reaction being controlled by the breakdown of metasomatic amphibole and/or phlogopite. Hirose (1997) does report partial melts of hydrous lherzolite at 1·0 GPa that have the appropriate major-element composition of LSAs (e.g., SiO_2 = 54–60 wt.%), and are in equilibrium with a spinel peridotite residue (ol + opx $\pm$ cpx + spl). Unfortunately, in this paper no trace element data was available. In the present interpretation of LSA and sanukitoid petrogenesis, the peridotitic source in these experiments would have experienced a metasomatism event prior to melting, in order for the TTG or 'slab melt' signature to be transferred to the mantle. The Late-Archaean sanukitoids are equated (Fig. 9) with LSA melts, possibly in equilibrium with an olivine-bearing pyroxenitic residue.

3. Discussion

3.1. Numerical modelling of sanukitoid genesis and diversity

The chemical composition of sanukitoid liquids obtained by experimental fusion can be reproduced using numerical modelling, which provides important clues in understanding the details of petrogenetic mechanisms. For instance, it allows the processes that lead to the difference between low- and high-Ti

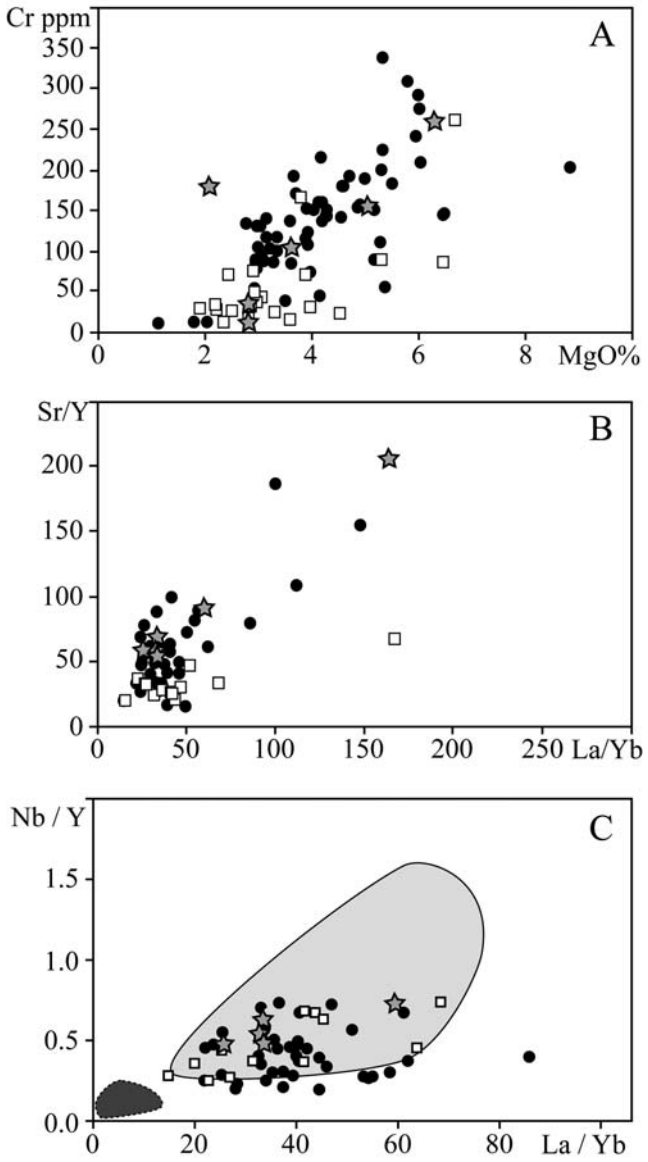

Figure 9 Diagrams comparing the composition of low-Ti (filled circles) and high-Ti (open squares) sanukitoids with SiO_2<62%, with liquids experimentally produced by interaction between a mantle peridotite and an Archaean TTG melt (grey stars) (Rapp *et al.* 2006): (A) Cr *vs.* MgO; (B) Sr/Y *vs.* La/Yb; (C) Nb/Y *vs.* La/Yb. Experimental melts display compositions identical with sanukitoids; in addition, inset (C) also shows that all experimental liquids plot in the light grey field, which is the field of modern high-Mg andesites considered as generated by melting of a mantle peridotite enriched by felsic melts (see Fig. 7 and text for more details).

sanukitoids to be addressed. Both types share many characteristics (Figs 2–6). However, systematic differences are observed for a few key geochemical parameters (mostly compatible elements ratios), as summarised in section 1.2, where it has been demonstrated that they reflect different, albeit related, primitive magmas. These differences could be accounted for by two distinct processes: (1) different degree of melting of a same source; and (2) different degrees of metasomatism of a mantle peridotite by TTG melts. A simple model has been built (Moyen 2009) in order to take into account the co-variations of these two parameters; it mimics the experimental procedure and is simply based on the batch melting of a mantle peridotite, which composition has been modified by mixing with TTG melt. If the concentration of an element in the mantle before metasomatism is C_m, it becomes C_{mm} after metasomatism by a mass fraction a of TTG melt; C_{TTG} being the concentration of the element in the TTG melt. C_{mm} is given by the mixing equation (1)

$$C_{mm}=a.C_{TTG}+(1-a).C_m \text{ (Equation 1)}$$

The melt:rock ratio in the sense of Rapp *et al.* (1999, 2006), i.e. the relative melt and rock proportions actually involved in the interactions, is represented by $a/1-a$.

The composition of the melt (C_l) is given by the equilibrium melting equation (Shaw 1970) where F is the degree of melting and D the general distribution coefficient:

$$C_l = \frac{C_{mm}}{F + D(1-F)} \text{ (Equation 2)}$$

Partition coefficients are from Rollinson (1993). For Fe and Mg, 'pseudo' partition coefficients were calculated from minerals phases found in adakite-metasomatised peridotite nodules (Kepezhinskas *et al.* 1996; Grégoire *et al.* 2008). Equilibrium melting is used to ensure consistency with experimental results, which are by construction at (or near) equilibrium. While simple, this model nevertheless allows for melt consumption ($a>F$) or, conversely, additions to the melt ($F>a$) during the interactions; the parameter F/a indicates the amount of melt gained or lost during the interactions. The difficulty consists in assigning realistic values for a and F, thus leading to a poorly constrained model. However, it appears that the only relevant parameter controlling the composition of the melt after the interaction with peridotite is the F/a ratio (Moyen 2009), i.e. the net gain or loss of melt during the process (Fig. 10). With increasing F/a values (i.e., towards a net melt gain – the interactions result in more addition to the melt than formation of new minerals by reactions between the melt and the peridotite), the resulting melt evolves to higher Mg#, but also lower incompatible element contents (REE, Sr, Y), and lower La/Yb and Sr/Y ratios. In contrast, low F/a values (i.e., the interactions result mostly in the formation of new minerals out of the melt, reducing its net volume) concentrate the incompatible elements, increase the La/Yb and Sr/Y ratios, and generate lower Mg# melts – although still with values higher than in the non-reacted TTG. In the same way as experimental petrology, this model is based on equilibrium between liquid and mineral phases for a given bulk composition X (P and T are implicit in the choice of mineral phases used for the calculation of D); consequently, the model cannot *per se* provide constrains on the P–T path (i.e., a one- or two-stage process) followed to reach the final P–T–X state.

The FeO, MgO and TiO_2 behaviour is adequately accounted for by this model (Fig. 11). Indeed, decreasing F/a ratios result in a diminution of MgO correlated with a slight increase in FeO and a significant augmentation of TiO_2, thus adequately providing an explanation for the difference between low- and high-Ti sanukitoids. However, some of the high-Ti sanukitoids display TiO_2 contents that are too high to be accounted by the present model. This can be explained by the choice of some parameters in the calculation: average TTG compositions (TiO_2=0·38%) were used as a 'starting material', but TTG compositions are actually more diverse, and TiO_2 contents of 0·7–0·8% are not rare. Such a TiO_2-richer TTG melt would easily account for the high-Ti sanukitoid characteristics. An alternative possibility is that the basic hypothesis of this model – equilibrium melting – is not true. Indeed, in the case of selective melting of only the Ti-rich portion of the metasomatised mantle (i.e., the amphibole-rich portion), without allowing bulk equilibrium with the residuum, the resulting liquid can be Ti-enriched well over that predicted by equilibrium models.

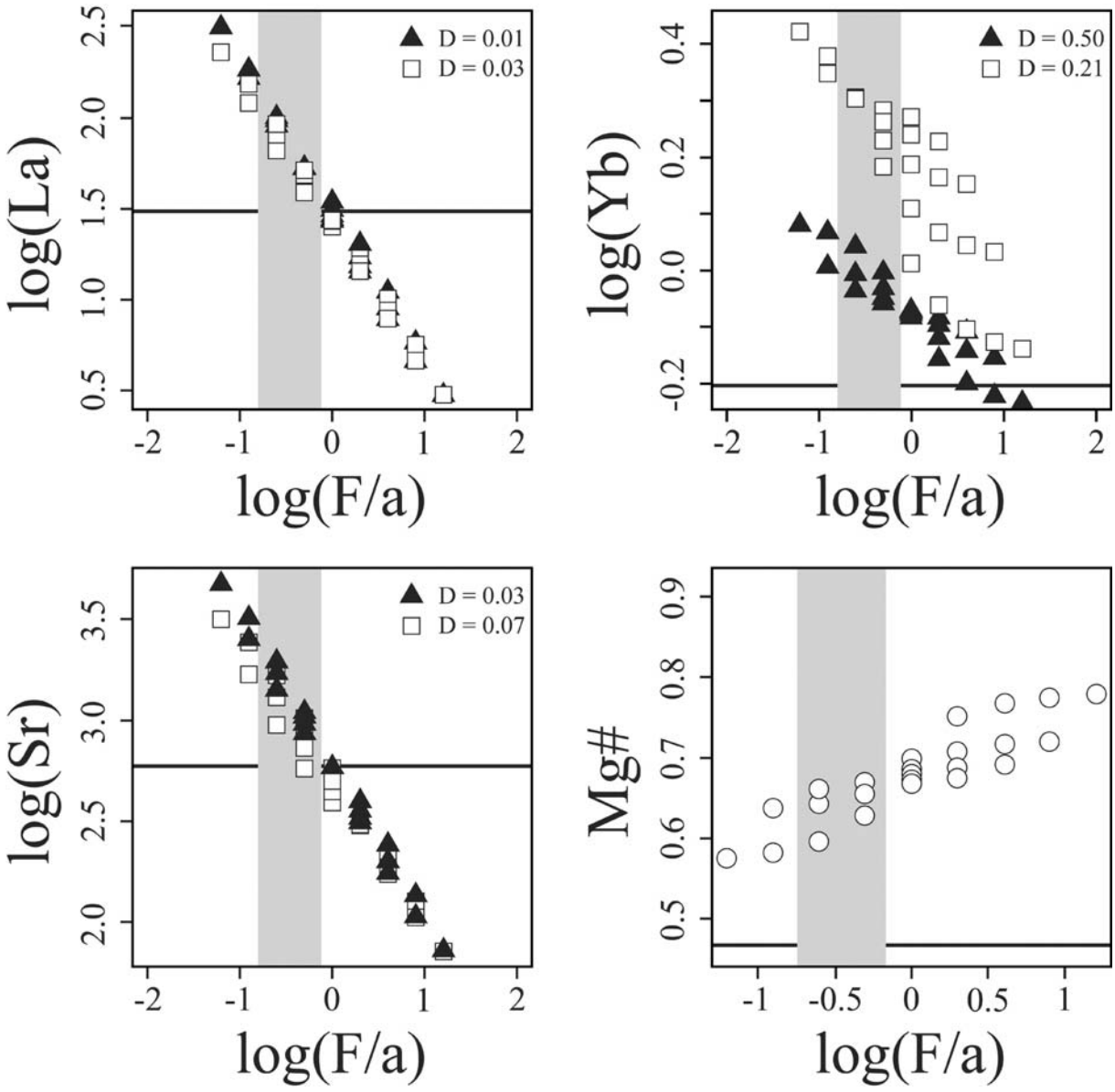

Figure 10 Log(La), log(Yb), log(Sr) and Mg# *vs.* Log(F/a). *F* represents the proportion of liquid (degree of melting) and *a* the degree of metasomatism of a peridotitic source by TTG melts. The light grey domain corresponds to the *F/a* ratios that yield values closer to those measured in sanukitoids. Triangles and squares respectively represent the presence and absence of garnet during melting of the mantle peridotite. The thick black horizontal line corresponds to the average TTG composition used in the model. The D values used in computation are also given (see text and Moyen 2009 for more details).

Therefore, it is proposed that the difference between the high- and the low-Ti series essentially reflects differences in the *F/a* ratio (Fig. 8): the high-Ti group formed by low F/a (low degree of melting and/or more enriched source), and melting was probably far from equilibrium, allowing amphibole breakdown to control the melt's composition without re-equilibrating with the rest of the rock. In contrast, the low-Ti group could correspond to higher (*F/a*) (high degree of melting and/or lower source enrichment), in conditions close to equilibrium melting. These two situations may reflect different geological/geodynamical scenarios; indeed, whereas the low-Ti situation can arise in one single event, in which the mantle contamination and the generation of the sanukitoid melt are concomitant, the disequilibrium scenario envisioned for the high-Ti group requires a two-step process, in which amphibole is allowed to physically form, before being destroyed by a subsequent selective melting event. This requires a more complex geological history. However, Figure 10 shows that for all elements, the composition of both low- and high-Ti sanukitoids is achieved only for F/a<1, which means that the reaction between TTG melt and mantle is mostly TTG melt consuming leading to the formation of new minerals, in the mantle peridotite. This is consistent with the observed consumption of melt in assimilation experiments between depleted peridotite and 'slab-derived' TTG melts (Rapp *et al*. 1999). Moreover, in the case of a two-stage process, the amount of melt formed is lower than the melt consumed by the initial interactions.

3.2. Residual garnet and conditions of melting

Sanukitoids have an average Yb content of 1·60 ppm, with a correlated high La/Yb=46·2. These values are intermediate between average TTG (Yb=0·64 ppm and La/Yb=59) and typical arc dacites and granodiorites (Yb=4·4 ppm and La/Yb=9·7). Both experimental work (Rapp *et al*. 1999, 2006) and geochemical modelling done on sanukitoids as well as on low-silica adakites (LSA) (Moyen 2009) show that residual garnet is not absolutely necessary to account for the geochemical characteristics of most sanukitoids. The general shape of

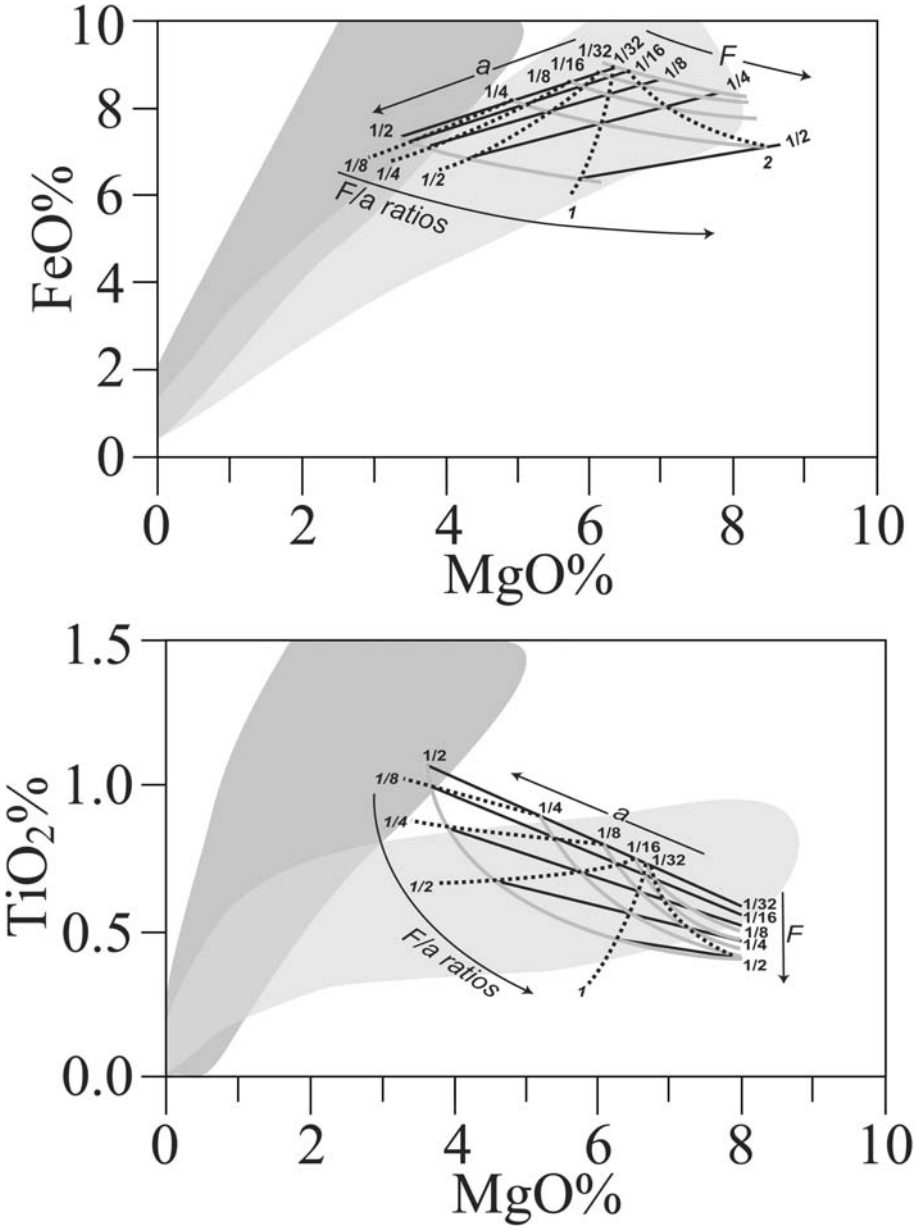

Figure 11 FeO *vs*. MgO and TiO_2 *vs*. MgO diagrams comparing the results of geochemical modelling with the composition of sanukitoids. The dark grey field is that of high-Ti sanukitoids whereas the light grey field represents the low-Ti sanukitoids. In both models, the black and grey lines correspond to the evolution of liquid controlled by *a* and *F* parameters respectively. Dotted lines represent a constant *F/a* ratio. These diagrams show a change in the *F/a* ratio that accounts for the observed diversity of sanukitoids. (More details are given in the text).

the REE patterns of TTG seems to be transferred to sanukitoids, after a shift to higher values (Yb=0·64 ppm in TTG and 1·6 ppm in sanukitoids). However, experiments and modelling show that the presence of small amounts of residual garnet would make the acquisition of sanukitoid melt characteristics easier. Indeed, Figure 12 is a La *vs*. Yb plot for all sanukitoids; it points to diversity among sanukitoids. The range of La/Yb ratios observed is consistent with the presence of variable proportions of residual garnet during melting. As proposed by Francis & Ludden (1995) and Dalpé & Baker (2000), this garnet could be the result of peritectic reactions associated with the breakdown of amphibole.

The variability in residual garnet could indicate that the TTG melt/mantle peridotite interactions were able to take place over a wide range of pressure, whatever the real mechanism is: direct hybridisation of the TTG melt or remelting of a peridotite metasomatised by TTG melts. It must also be noted that the La/Yb systematic does not coincide with the low/high-Ti classification, thus indicating that the two parameters are independent (both low and high F/a can be realised at shallow as well as at great depths). Garnet stability does not only depend on pressure, but is also controlled by rock composition. In a peridotite, garnet is stable only for pressure higher than 2·5 to 3·0 GPa; whereas for an amphibolitic (basaltic) composition it is stable at pressure as low as 1·0 to 1·2 GPa. Consequently, metasomatism of mantle peridotite by felsic melts will modify the peridotite composition: high TTG input resulting in garnet stable at lower pressure.

Since the density of TTG melts is lower than that of mantle peridotite, they can only ascend through the mantle. This implies that the source for TTG is located below the mantle peridotite. In the case where garnet is stable in the mantle peridotite, this means that TTG melts are necessarily generated at depth greater than 40–60 km, depending on the amount of TTG melt having reacted with mantle peridotite. During melting of amphibolites, the garnet proportion increases with

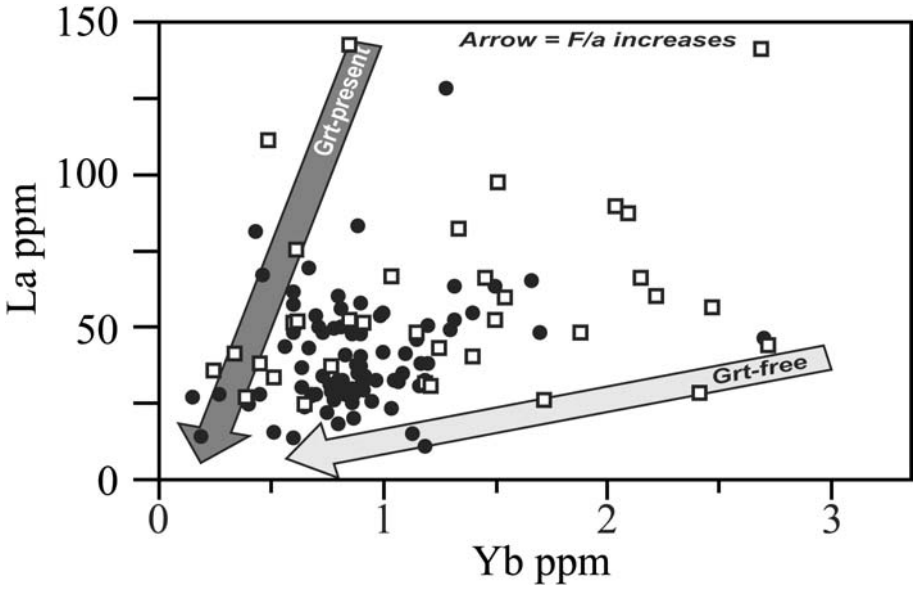

Figure 12 La *vs.* Yb diagram showing the diversity of La/Yb ratios in sanukitoids. La/Yb variations are not correlated with the two-fold low-Ti (filled circles) and high-Ti (open squares) sanukitoid classification. The variability of La/Yb is accounted by different proportions of residual garnet.

depth; in order to have enough garnet to produce a proper TTG composition, the depth of melting must be at least greater than 45–50 km (1·5 GPa) (Moyen & Stevens 2006; Nair & Chacko 2008): which is consistent with the depth of 40–60 km deduced from sanukitoids. This requires a generally efficient geodynamic process able to carry hydrated basalts to depths greater than 40–60km. The only mechanism able to straightforwardly and systematically realise such geometry with hydrous basalts under a mantle slice, at depths of >40–60 km, is subduction. Therefore, sanukitoids can be regarded as markers of at least some kind of subduction, with burial into the mantle of significant portions of surface mafic hydrated material.

3.3. Geodynamic implications and Archaean–Proterozoic boundary

The sanukitoids mainly emplaced at the Archaean–Proterozoic boundary, during a period where the dominant mechanism of genesis of the juvenile continental crust changed from melting of hydrous basalt (Archaean) to fusion of the fluid metasomatised mantle peridotite (post-Archaean). As discussed earlier, evidence supports the genesis of most TTG and sanukitoids in a subduction environment; following this logic, the present authors can propose a general model for the generation of juvenile continental crust across the Archaean–Proterozoic boundary.

Today, the subducted oceanic crust is old (60 Ma on average) and cold; it contributes to the cooling of the mantle wedge, such that geothermal gradient along the Benioff plane is low (Fig. 13) and dehydration reactions in subducted basalt occur before it reaches its hydrous solidus. Consequently, the oceanic slab loses its water and is unable to melt at low temperature. Fluids liberated by dehydration reactions rise up towards the surface through the mantle wedge and induce its partial melting. The rising fluids also transfer soluble elements such as LILE and LREE from the subducted lithosphere into the mantle wedge. In other words, most of the present-day juvenile continental crust is generated in subduction geodynamic environments, by the melting of a mantle wedge, whose composition has been modified by fluids liberated by dehydration of the crustal portions of subducted slabs of oceanic lithosphere. During the Archaean, Earth heat production was greater, resulting in higher geothermal gradients in subduction zones. Along such high geothermal gradients, the order in which the dehydration reaction and hydrous solidus curves are crossed is inverted (Fig. 13): the subducted oceanic slab reaches its hydrous solidus temperature before dehydration begins and is able to melt at relatively low temperature and shallow depth, but deep enough for garnet to be stable in the residue, giving rise to TTG magmas. Consequently, TTG is the result of relatively shallow depth melting of subducted oceanic crust metamorphosed into garnet amphibolite or eclogite. Today, in some exceptional cases, in subduction zones, where an abnormally young oceanic crust is subducted (active ridge subduction such as Patagonia), adakitic magmas are generated; which are very similar to Archaean TTG. This shows that hot geothermal gradients in subduction zones are able to result in slab melting and TTG-like magma genesis (see Martin 1999; Smithies 2000; Martin *et al.* 2005, for discussion and overviews).

Recently, Smithies (2000), Smithies & Champion (2000) and Martin & Moyen (2002), showed that the chemical composition of the parental magma of TTG has changed through Archaean times. These authors consider that change as progressive, whereas Condie (2005) sees it as an abrupt event at about 2·7 Ga. According to Martin & Moyen (2002), the Mg# of the more primitive TTG magmas increased from maximum values of 0·45 at 4·0 Ga to 0·65 at 2·5 Ga. In the same period, the maximum concentrations of Ni and Cr increased, as Sr did, from ~550 ppm at 3·8 Ga to ~1200 ppm at 2·5 Ga (Fig. 14). On the other hand, the high Mg# (0·65) of the younger TTG (<3·0 Ga), is higher than values determined by experimental high-pressure melting of basaltic material, which requires that a mantle component played a role in the genesis of these magmas. Consequently, this time-related change is interpreted in terms of a secular increase of the interactions between the TTG parental and the mantle wedge peridotites (e.g. Maury *et al.* 1996; Rapp *et al.* 1999; Smithies 2000; Martin & Moyen 2002). Similarly, these authors interpret the Sr content in TTG parental magmas in terms of plagioclase stability; indeed, not only Sr content increases in course of time, but also $(CaO+Na_2O)$ and Al_2O_3. As plagioclase stability is pressure dependent; they conclude that, from 4·0 Ga to 2·5 Ga the depth of melting of the subducted slab progressively increased.

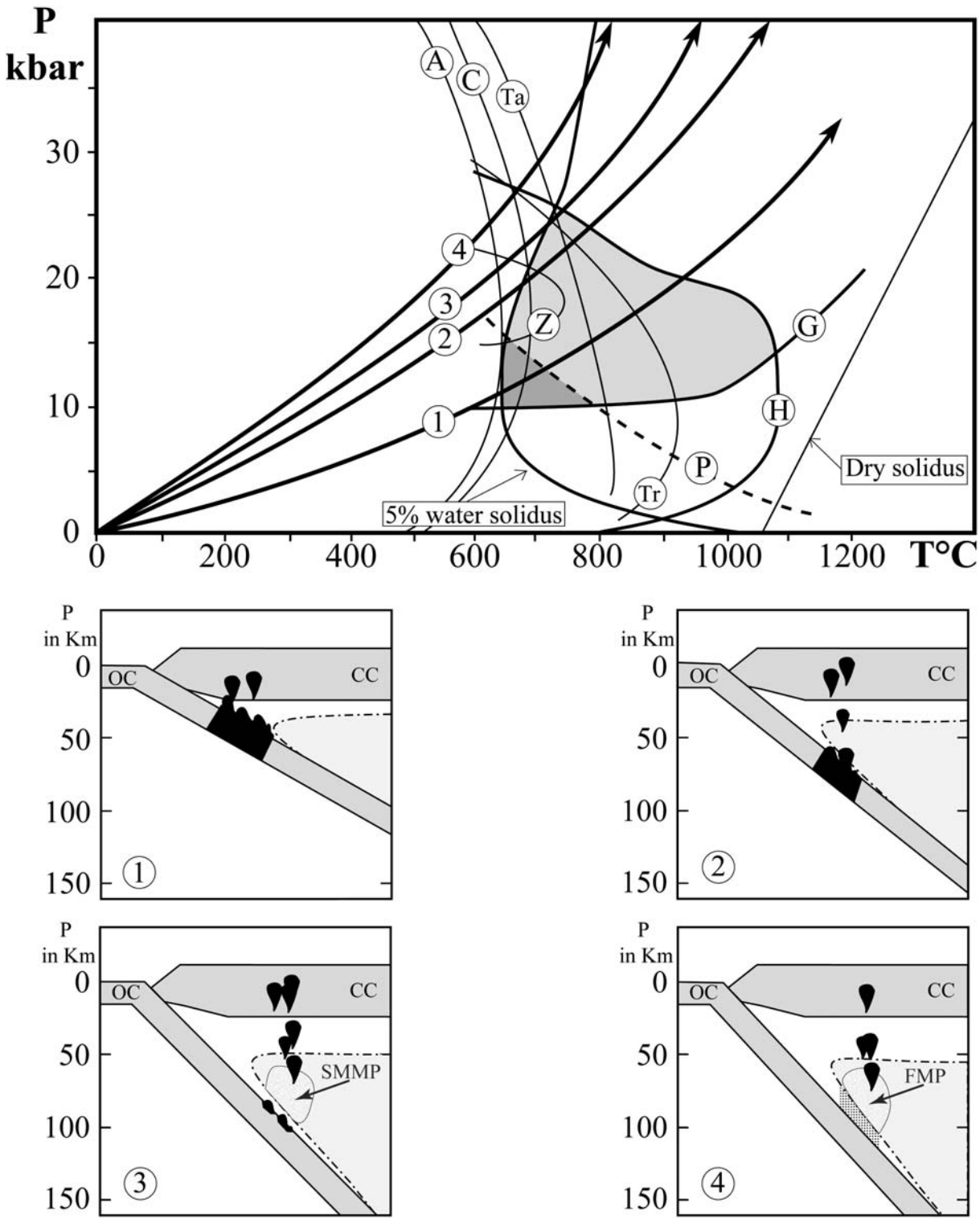

Figure 13 P–T diagram and synthetic cross-sections of subduction zones (after Martin & Moyen 2002). (1) In the Early Archaean (4·0 Ga) the geothermal gradient along the Benioff plane was very high, thus the subducted slab melts at shallow depth. Due to the thinness of the wedge and the low temperature, mantle and melt interactions are limited or absent; (2) After 3·0 Ga, the Earth was cooler, the geothermal gradient was lower and slab melting occurred at greater depth. The overlying mantle wedge is thick and hot, and interactions can occur between mantle and slab melts; (3) At the Archaean–Proterozoic transition, geothermal gradients are too low to allow a high degree of slab melting. Slab melts are almost totally consumed in a reaction with the mantle. Low-Ti sanukitoid are assumed to be the result of a single event of contamination of slab melts by peridotite, whereas low-Ti sanukitoids formed through a two-step process where the mantle metasomatised by slab melts is subsequently molten; (4) After 2·5 Ga, geothermal gradients are so low that slab melting is precluded. The oceanic crust dehydrates and the liberated fluids metasomatise the mantle wedge, whose melting produces modern arc magmatism. Dehydration reactions: H=hornblende out; A=antigorite out; C=chlorite out; Ta=talc out; Tr=tremolite out; Z=zoisite out. G and P lines represent stability fields of garnet and plagioclase respectively. Grey field is P–T TTG window. OC=oceanic crust; CC=continental crust; dotted line=solidus of hydrous mantle; black areas=magma; dotted area=fluids; SMMP=slab melt metasomatised peridotite; FMP=fluid metasomatised peridotite.

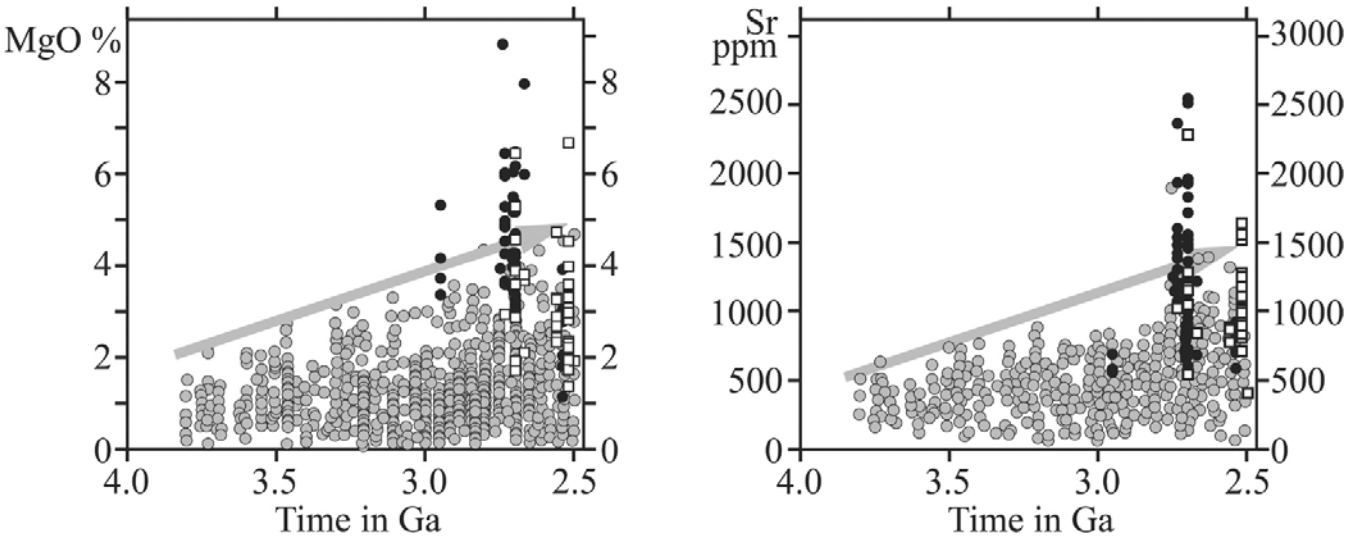

Figure 14 Diagrams showing the time-evolution of MgO and Sr content of the primitive TTG parental magmas (grey circles) from 4·0 Ga to 2·5 Ga (after Martin & Moyen 2002). The less different low-Ti (black circles) and high-Ti (open squares) sanukitoids have both MgO and Sr content far greater than in TTG, thus pointing to the fact that they were generated from a different source or/and a different mechanism.

However, most basalt melting experiments show that the amount of plagioclase stable together with garnet remains relatively low. Consequently, another possibility would be that in absence of significant amounts of residual plagioclase, Sr has an incompatible behaviour, its content in the magmatic liquid becoming only dependent on the degree of melting. In this case, the augmentation of Sr content in TTG magmas in the course of time would only reflect a decrease in the degree of melting of the basaltic source of TTG; which would also be consistent with the progressive cooling of the Earth. However, lower degrees of melting should result in lower Mg# and Ni and Cr contents in TTG magma, thus leading to an anti-correlation between Sr and Mg# (and Ni and Cr), whereas the opposite is observed. Whatever the cause of the time-dependent variation of Sr may be, it can be interpreted in terms of progressive cooling of the Earth, resulting in lower geothermal gradients in subduction systems (Fig. 13), thus leading to deeper slab melting. It must be noted that sanukitoids do not plot on this 'trend' but display significantly higher values for MgO and Sr (Fig. 14) as well as for Ni and Cr.

The present authors propose that throughout the Archaean, the Earth's heat production was high enough (curves 1 and 2, Fig. 13) to allow a high degree of melting of the subducted slab, consequently the 'effective melt:rock ratio' (as discussed above) was high and all slab melt was not consumed by mantle interaction, and was consequently emplaced largely as TTG. However, with time, Earth's geothermal gradient decreased and slab melting took place at progressively greater depths, such that some degree of interaction with peridotitic lithologies of the mantle wedge became increasingly likely. At about 2·7–2·5 Ga ago, further reduction in geothermal gradients resulted in smaller degrees of melting of the subducted slab, such that most of the TTG melts coming off the slab would be consumed in metasomatic reactions with peridotite. In these conditions, the mantle imprint would be stronger and could be achieved in two different ways: (1) in a single event where the mantle contamination and the generation of the sanukitoid melt are concomitant; this mechanism could result in low-Ti sanukitoid genesis; or (2) in a two-step process in which metasomatic minerals must crystallise in the mantle peridotite, before being destroyed by a subsequent melting event, thus giving rise to high-Ti sanukitoids (curve 3, Fig. 13). After Archaean times geothermal gradients were too low to allow slab melting and modern continental crust was generated by fluid metasomatised mantle wedge melting (curve 4, Fig. 13). This model accounts for the 'transitory' character of sanukitoids, as well as for their location at the Archaean–Proterozoic boundary.

4. Summary and conclusion

The temporal evolution of magmas at the Archaean–Proterozoic boundary can be synthesised as follows (Fig. 15):

1. In the Early Archaean (T>3·5 Ga), the terrestrial heat production was important, such that the subducted basalts underwent high degree of melting at shallow depth. The 'effective melt:rock ratio' in the mantle above the source of TTGs was high and the TTG magmas emplaced after minor or no interaction with the peridotite.
2. In the Middle to Late Archaean, the heat production was lower and the degree of melting of the subducted slab was slightly lower and took place at greater depth. However, the efficiency of slab-melting was high enough to maintain high slab-melt/mantle peridotite ratios. Thus, the slab-melt was not totally consumed in reaction with peridotite (Rapp *et al.* 1999, 2006), and consequently TTG magma was emplaced into the crust.
3. During the Late Archaean, and particularly at the Archaean–Proterozoic boundary, the Earth heat production and the efficiency of slab-melting had both declined. Slab-melt/mantle peridotite ratios had correspondingly declined such that slab-melts were almost totally consumed in reaction with mantle peridotite, thus producing Archaean sanukitoids. These later could result from either a single event where the mantle contamination and the generation of the sanukitoid melt are concomitant, (low-Ti sanukitoids) or from a two-step process where the mantle metasomatised by slab melts is subsequently molten (high-Ti sanukitoids).
4. Since the Lower Proterozoic, Earth's heat production was too low to allow subducted slab-melting under 'normal' conditions. Consequently, a slab dehydrates and classic BADR calc-alkaline magmatism results from melting of a peridotite that has been metasomatised by slab dehydration fluids.

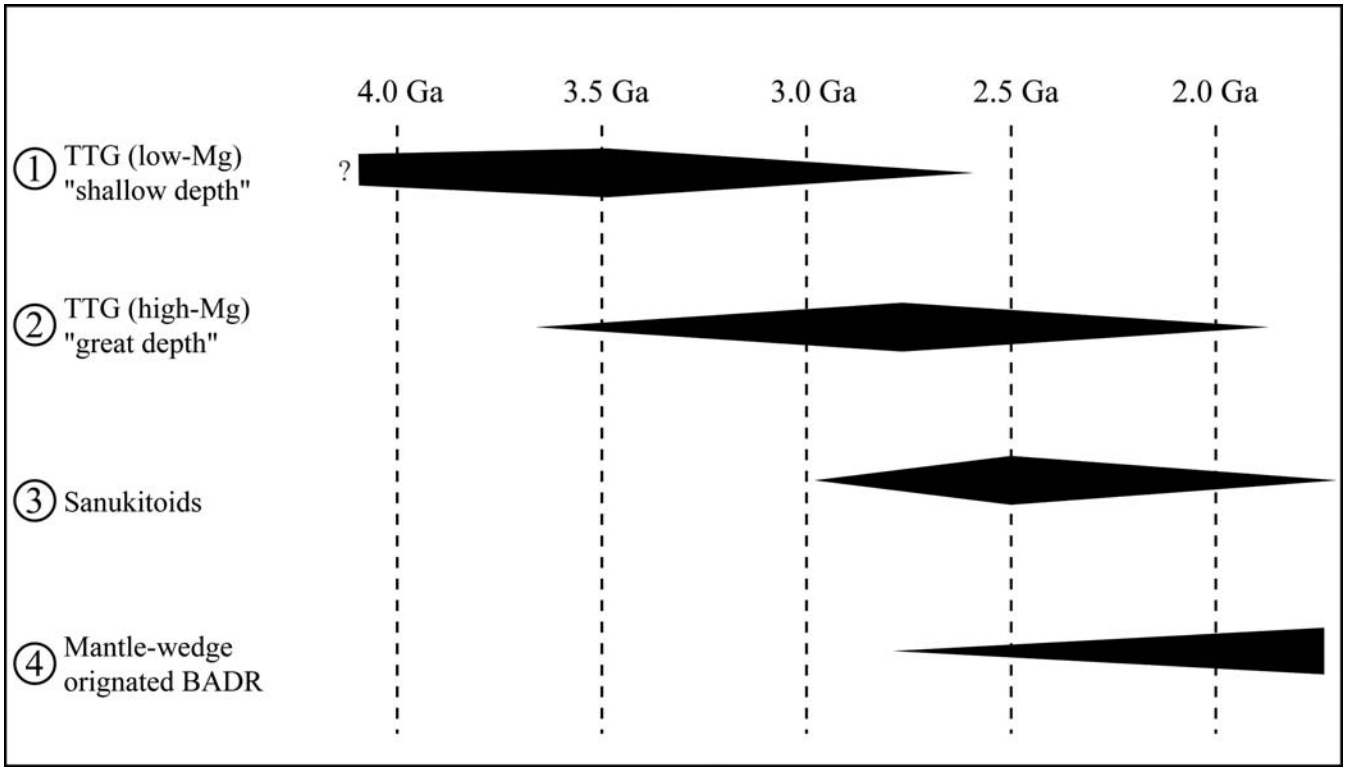

Figure 15 Schematic diagram illustrating the evolution of the juvenile crustal magmatism in course of the Earth's history. The thickness of the dark domain is qualitatively indicative of the volumetric importance of the magmatism. It clearly points to a large domain of overlapping at the Archaean–Proterozoic transition (2·5 Ga).

In other words, with regards to continental crust genesis, it appears that the Archaean–Proterozoic transition corresponds to a major change from a crustal (oceanic basalts) to a mantle source. The sanukitoid magmatism that shows both crustal and mantle imprint appears to be a good marker of these changes. Of course, this presentation of the timing of juvenile continental crust genesis over the course of Earth history is very simplistic and schematic. If today, in subduction environments, BADR magmatism is the more widespread, slab melting can also locally take place, leading to adakite genesis. Whenever, Archaean-like thermal regimes are established in the modern Earth, TTG-like (adakite) magmas are produced. However, this mechanism remains very minor on a global scale, but was once dominant. During Earth cooling, new thermodynamic conditions appeared, but not everywhere at the same time, because local conditions play an important role in controlling these thermodynamic regimes. This results in an overlap of petrogenetic mechanisms during time (Fig. 15), leading, for instance, to simultaneous TTG and sanukitoid magmatism: the apparently progressive character of petrogenetic changes near the Archaean–Proterozoic boundary is a statistic effect that reflects the progressive onset and development of some petrogenetic processes, and the diminishing importance of others. The dominant process of the Early Archaean was shallow slab melting that generated low-Mg TTG; this process became progressively less important during the later periods, and was all but replaced during Late Archaean times by deeper slab melting, which allowed for more significant interactions with mantle peridotite, and resulted in increased production of high-Mg TTG. Low-Mg TTG persisted late into the Archaean, even if not as important as they once were. In turn, the importance of high-Mg TTG decreased during the Proterozoic, and became a very rare process in the Phanerozoic; it was progressively replaced by BADR magmatic activity, which first appears in the Early Proterozoic and which became progressively dominant. Sanukitoids represent the 'missing link' between the (high-Mg) TTGs and the BADR; indeed, their transitional character is not only compositional but also chronologic, since they were emplaced about 2·5 Ga ago, during the transitional period between two epochs respectively dominated by TTG and BADR juvenile crustal magmatism.

5. References

Albarède, F. 1998. The growth of continental crust. *Tectonophysics* **296**, 1–14.

Althoff, F. J. 1996. *Etude pétrologique et structurale des granitoïdes de Marajoara (Pará, Brésil): leur rôle dans l'évolution archéenne du craton amazonien (2·7–3·2 Ga)*. Nancy: Henri Poincarré. 296 pp.

Arth, J. G. & Hanson, G. N. 1972. Quartz diorites derived by partial melting of eclogite or amphibolite at mantle depth. *Contributions to Mineralogy and Petrology* **37**, 164–74.

Atherton, M. P. & Petford, N. 1993. Generation of sodium-rich magmas from newly underplated basaltic crust. *Nature* **362**, 144–6.

Balakrishnan, S. & Rajamani, V. 1987. Geochemistry and petrogenesis of granitoids around Kolar schist belt: constraints for crustal evolution in Kolar area. *Journal of Geology* **95**, 219–40.

Barker, F. & Arth, J. G. 1976. Generation of trondhjemitic–tonalitic liquids and Archaean bimodal trondhjemite–basalt suites. *Geology* **4**, 596–600.

Barth, M. G., Foley, S. F. & Horn, I. 2002. Partial melting in Archaean subduction zones: constraints from experimentally determined trace element partition coefficients between eclogitic minerals and tonalitic melts under upper mantle conditions. *Precambrian Research* **113**, 323–40.

Barton, J. J. M., Doig, R., Smith, C. B., Bohlender, F. & van Reenen, D. D. 1992. Isotopic and REE characteristics of the intrusive charnoenderbite and enderbite geographically associated with the Matok Pluton, Limpopo Belt, southern Africa. *Precambrian Research* **55** (1–4), 451–67.

Bédard, J. 2006. A catalytic delamination-driven model for coupled genesis of Archaean crust and subcontinental lithospheric mantle. *Geochimica et Cosmochimica Acta* **70**, 747–71.

Bédard, P. 1996. Archean High-Mg monzodiorite plutonic suite: A reevaluation of the parental magma and differentiation. *Journal of Geology* **104**, 713–28.

Blichert-Toft, J. & Albarède, F. 2008. Hafnium isotopes in Jack Hills zircons and the formation of the Hadean crust. *Earth and Planetary Science Letters* **265** (3–4), 686–702.

Bourdon, E., Eissen, J.-P., Gutscher, M.-A., Monzier, M., Hall, M. L. & Cotten, J. 2003. Magmatic response to early aseismic ridge subduction: the Ecuadorian margin case (South America). *Earth and Planetary Science Letters* **205** (3–4), 123–38.

Brown, G. C. 1985. Processes and problems in the continental lithosphère: geological history and physical implications. *In* Snelling, N. (ed.) *The chronology of the geological record. Geological Society, London, Memoir* **10**, 326–34. Bath, UK: The Geological Society Publishing House.

Calmus, T., Aguillon-Robles, A., Maury, R. C., Bellon, H., Benoit, M., Cotten, J., Bourgois, J. & Michaud, F. 2003. Spatial and temporal evolution of basalts and magnesian andesites ('bajaites') from Baja California, Mexico: the role of slab melts. *Lithos* **66** (1–2), 77–105.

Cavosie, A. J., Wilde, S. A., Liu, D., Weiblen, P. W. & Valley, J. W. 2004. Internal zoning and U–Th–Pb chemistry of Jack Hills detrital zircons: a mineral record of early Archean to Mesoproterozoic (4348–1576 Ma) magmatism. *Precambrian Research* **135** (4), 251–79.

Cavosie, A. J., Valley, J. W., Wilde, S. A. & E.I.M.F. 2005. Magmatic [delta]^{18}O in 4400–3900 Ma detrital zircons: A record of the alteration and recycling of crust in the Early Archean. *Earth and Planetary Science Letters* **235** (3–4), 663–81.

Cavosie, A. J., Valley, J. W. & Wilde, S. A. 2006. Correlated microanalysis of zircon: Trace element, [delta]^{18}O, and U–Th–Pb isotopic constraints on the igneous origin of complex >3900 Ma detrital grains. *Geochimica et Cosmochimica Acta* **70** (22), 5601–16.

Chardon, D., Peucat, J.-J., Jayananda, M., Choukroune, P. & Fanning, M. C. 2002. Archean granite-greenstone tectonics at Kolar (South India): Interplay of diapirism and bulk inhomogeneous contraction during juvenile magmatic accretion. *Tectonics* **21** (3), 7.1–7.17.

Condie, K. C. 1981. *Archaean greenstone belts.* Amsterdam: Elsevier. 434 pp.

Condie, K. C. 1989. *Plate tectonics and crustal evolution.* Oxford: Pergamon. 476 pp.

Condie, K. C. 2005. TTGs and adakites: are they both slab melts? *Lithos* **80**, 33–44.

Dalpé, C. & Baker, D. R. 2000. Experimental investigation of large-ion-lithophile-element-, high-field-strength-element- and rare-earth-element-partitioning between calcic amphibole and basaltic melt: the effects of pressure and oxygen fugacity. *Contributions to Mineralogy and Petrology* **140**, 233–50.

de Wit, M. J. 1998. On Archean granites, greenstones, cratons and tectonics: does the evidence demand a verdict? *Precambrian Research* **91** (1–2), 181–226.

Foley, S. F., Tiepolo, M. & Vannucci, R. 2002. Growth of early continental crust controlled by melting of amphibolite in subduction zones. *Nature* **417**, 637–40.

Forneris, J. F. & Holloway, J. R. 2003. Phase equilibria in subducting basaltic crust: implications for H_2O release from the slab. *Earth and Planetary Science Letters* **214**, 187–201.

Francis, D. & Ludden, J. 1995. The signature of amphibole in mafic alkaline lavas, a study in the Northern Canadian Cordillera. *Journal of Petrology* **36**, 1171–91.

Frost, C. D., Frost, B. R., Chamberlain, K. R. & Hulsebosch, T. P. 1998. The late Archaean history of the Wyoming province as recorded by granitic magmatism in the Wind River Range, Wyoming. *Precambrian Research* **89**, 145–73.

Glikson, A. Y. 1971. Primitive Archaean element distribution patterns: chemical evidence and geotectonic significance. *Earth and Planetary Science Letters* **12**, 309–20.

Grégoire, M., Jégo, S., Maury, R. C., Polvé, M., Payot, B., Tamayo, R. A. Jr. & Yumel, G. P. Jr. 2008. Metasomatic interactions between slab-derived melts and depleted mantle: Insights from xenoliths within Monglo adakite (Luzon arc, Philippines). *Lithos* **103** (3–4), 415–30.

Halla, J. 2005. Late Archean high-Mg granitoids (sanukitoids) in the southern Karelian domain, eastern Finland: Pb and Nd isotopic constraints on crust-mantle interactions. *Lithos* **79** (1–2), 161–78.

Harrison, T. M. & Schmitt, A. K. 2007. High sensitivity mapping of Ti distributions in Hadean zircons. *Earth and Planetary Science Letters* **261**(1–2), 9–19.

Hirose, K. 1997. Melting experiments on lherzolite KLB-1 under hydrous conditions and the generation of high-magnesian andesitic melts. *Geology* **25**, 42–4.

Hoffer, G. 2008. *Fusion partielle d'un manteau métasomatisé par un liquide adakitique: approches géochimique et expérimentale de la genèse et de l'évolution de l'arrière arc équatorien*. PhD Thesis, Université Blaise Pascal, Clermont Ferrand, France. 320 pp.

Jahn, B. M., Glikson, A. Y., Peucat, J.-J. & Hickman, A. H. 1981. REE geochemistry and isotopic data of Archaean silicic volcanics and granitoids from the Pilbara Block, western Australia: implications for the early crustal evolution. *Geochimica et Cosmochimica Acta* **45**, 1633–52.

Jahn, B.-M., Gruau, G., Capdevila, R., Cornichet, J., Nemchin, A., Pidgeon, R. & Rudnik, V. A. 1998. Archaean crustal evolution of the Aldan shield, Siberia: geochemical and isotopic constraints. *Precambrian Research* **91**, 333–63.

Jayananda, M., Martin, H., Peucat, J.-J. & Mahabaleswar, B. 1995. Late Archaean crust-mantle interactions in the Closepet granite, Southern India: evidence from Sr–Nd isotopes, major and trace element geochemistry. *Contributions to Mineralogy and Petrology* **119**, 314–29.

Johnson, A. D. & Wyllie, P. J. 1989. The system tonalite-peridotite-H_2O at 30 kbar, with applications to hybridization in subduction zone magmatism. *Contributions to Mineralogy and Petrology* **102**, 257–64.

Kamber, B. S., Ewart, A., Collerson, K. D., Bruce, M. C. & McDonald, G. A. 2002. Fluid-mobile trace element constraints on the role of slab melting and implications for Archaean crustal growth models. *Contributions to Mineralogy and Petrology* **144**, 38–56.

Käpyaho, A. 2006. Whole-rock geochemistry of some tonalite and high Mg/Fe gabbro, diorite, and granodiorite plutons (sanukitoid suites) in the Kuhmo district, eastern Finland. *Bulletin of the Geological Society of Finland* **78**, 121–41.

Kelemen, P. B., Shimizu, H. & Dunn, T. 1993. Relative depletion of niobium in some arc magmas and the continental crust: partitioning of K, Nb, La and Ce during melt/rock reaction in the upper mantle. *Earth and Planetary Science Letters* **120**, 111–34.

Kelemen, P. B., Hart, S. R. & Bernstein, S. 1998. Silica enrichment in the continental upper mantle via melt/rock reaction. *Earth and Planetary Science Letters* **164**, 387–406.

Kepezhinskas, P. K., Defant, M. J. & Drummond, M. S. 1996. Progressive enrichment of island arc mantle by melt-peridotite interaction inferred from Kamchatka xenoliths. *Geochimica et Cosmochimica Acta* **60**, 1217–29.

Kleinhanns, I. C., Kramers, J. D. & Kamber, B. S. 2003. Importance of water for Archaean granitoid petrology: a comparative study of TTG and potassic granitoids from Barberton Mountain and, South Africa. *Contributions to Mineralogy and Petrology* **145**, 377–89.

Kovalenko, A., Clemens, J. D. & Savatenkov, V. 2005. Petrogenetic constraints for the genesis of Archaean sanukitoid suites: geochemistry and isotopic evidence from Karelia, Baltic Shield. *Lithos* **79** (1–2), 147–60.

Kreissig, K., Holzer, L., Frei, R., Villa, I. M., Kramers, J. D., Kroner, A., Smit, C. A. & van Reemen, D. D. 2001. Geochronology of the Hout River Shear Zone and the metamorphism in the Southern Marginal Zone of the Limpopo belt, Southern Africa. *Precambrian Research* **109**, 145–73.

Krogstad, E. J., Hanson, G. N. & Rajamani, V. 1991. U–Pb ages of zircon and sphene for two gneiss terranes adjacent to the Kolar schist belt, South India: evidence for separate crustal evolution histories. *Journal of Geology* **99**, 801–16.

Krogstad, E. J., Hanson, G. N. & Rajamani, V. 1995. Sources of continental magmatism adjacent to late Archaean Kolar suture zone, south India: distinct isotopic and elemental signatures of two late Archaean magmatic series. *Contributions to Mineralogy and Petrology* **122**, 159–73.

Leite, A. A. S., Dall'Agnol, R., Macambira, M. J. B. & Althoff, F. J. 2004. Geologia e geocronologia dos granitóides arqueanos da região de Xinguara e suas implicações na evolução do Terreno Granito–Greenstone de Rio Maria, Cráton Amazônico. *Revista Brasileira de Geociencias* **34** (4), 447–58.

Liu, J., Bohlen, S. R. & Ernst, W. G. 1996. Stability of hydrous phases in subducting oceanic crust. *Earth and Planetary Science Letters* **143**, 167–71.

Lobach-Zhuchenko, S. B., Kovalenko, A. V., Krylov, I. N., Levskii, L. K. & Bogomolov, E. S. 2000. Geochemistry and petrology of the ancient Vygozero granitoids, Southern Karelia. *Geochemistry International* **38**, 584–99.

Lobach-Zhuchenko, S. B., Rollinson, H. R., Chekulaev, V. P., Arestovaa, N. A., Kovalenko, A. V., Ivanikov, V. V., Guseva, N. S., Sergeev, S. A., Matukov, D. I. & Jarvis, K. E. 2005. The Archaean sanukitoid series of the Baltic Shield: geological setting,

geochemical characteristics and implications for their origin. *Lithos* **79** (1–2), 107–28.

Lobach-Zhuchenko, S. B., Rollinson, H., Chekulaev, V. P., Savatenkov, V. M., Kovalenko, H., Martin, A. V., Guseva, N. S. & Arestova, N. A. 2008. Petrology of a Late Archaean, Highly Potassic, Sanukitoid Pluton from the Baltic Shield: Insights into Late Archaean Mantle Metasomatism. *Journal of Petrology* **49** (3), 393–420.

Macpherson, C. G., Dreher, S. T. & Thirlwall, M. F. 2006. Adakites without slab melting: High pressure differentiation of island arc magma, Mindanao, the Philippines. *Earth and Planetary Science Letters* **243** (3–4), 581–93.

Martin, E., Martin, H. & Sigmarsson, O. 2008. Could Iceland be a modern analogue for the Earth's early continental crust? *Terra Nova* **20**, 463–68.

Martin, E. & Sigmarsson, O. 2007. Low-pressure differentiation of tholeiitic lavas as recorded in segregation veins from Reykjanes (Iceland), Lanzarote (Canary Islands) and Masaya (Nicaragua). *Contributions to Mineralogy and Petrology* **154**, 559–73.

Martin, H. 1986. Effect of steeper Archean geothermal gradient on geochemistry of subduction-zone magmas. *Geology* **14,** 753–6.

Martin, H. 1987. Petrogenesis of Archaean trondhjemites, tonalites and granodiorites from eastern Finland: major and trace element geochemistry. *Journal of Petrology* **28**(5), 921–53.

Martin, H. 1993. The mechanisms of petrogenesis of the Archaean continental crust – comparison with modern processes. *Lithos* **30**, 373–88.

Martin, H. 1994. The Archean grey gneisses and the genesis of the continental crust. *In* Condie, K. C. (ed.) *The Archean crustal evolution. Developments in Precambrian Geology*, 205–59 Amsterdam: Elsevier.

Martin, H. 1999. The adakitic magmas: modern analogues of Archaean granitoids. *Lithos* **46**(3), 411–29.

Martin, H., Chauvel, C. & Jahn, B. M. 1983. Major and trace element geochemistry and crustal evolution of granodioritic Archaean rocks from eastern Finland. *Precambrian Research* **21**, 159–80.

Martin, H., Sabaté, P., Peucat, J.-J. and Cunha, J. C. 1997. Crustal evolution in the early Archaean of South America: example of the Sete Voltas Massif (Bahia State, Brazil). *Precambrian Research* **82**, 35–62.

Martin, H., Smithies, R. H., Rapp, R., Moyen, J.-F. & Champion, D. 2005. An overview of adakite, tonalite–trondhjemite–granodiorite (TTG), and sanukitoid: relationships and some implications for crustal evolution. *Lithos* **79** (1–2), 1–24.

Martin, H. & Moyen, J.-F. 2002. Secular changes in TTG composition as markers of the progressive cooling of the Earth. *Geology* **30**(4), 319–22.

Masuda, A., Nakamura, N. & Tanaka, T. 1973. Fine structures of mutually normalized rare-earth patterns of chondrites. *Geochimica et Cosmochimica Acta* **37**, 239–44.

Maury, R. C., Sajona, F. G., Pubellier, M., Bellon, H. & Defant, M. J. 1996. Fusion de la croûte océanique dans les zones de subduction/collision récentes: l'exemple de Mindanao (Philippines). *Bulletin de la Société Géologique de France* **167** (5), 579–95.

McGregor, V. R. 1979. Archaean grey gneisses and the origin of the continental crust: evidence the Godthaab region, west Greenland. *In* Barker, F. (ed.) *Trondhjemites, dacites and related rocks*, 169–204. Amsterdam: Elsevier.

Medeiros, H. & Dall'Agnol, R. 1988. Petrologia da porção leste do Batólito Granodiorítico Rio Maria, sudeste do Pará. *In Anais do 35 Congresso Brasileiro de Geologia*, 1488–99. Belém: Sociedade Brasileira de Geologia.

Millonig, L., Zeh, A., Gerdes, A. & Klemd, R. 2008. Neoarchaean high-grade metamorphism in the Central Zone of the Limpopo Belt (South Africa): Combined petrological and geochronological evidence from the Bulai pluton. *Lithos* **103** (3–4), 333–51.

Monzier, M., Robin, C., Hall, M. L., Cotton, J., Mothes, P., Eissen, J.-P. & Samaniego, P. 1997. Les adakites d'Equateur: modèle préliminaire. *Compte Rendus de l'Académie des Sciences de Paris* **324**, 545–52.

Moyen, J.-F. 2009. High Sr/Y and La/Yb ratios: the meaning of the 'adakitic signature'. *Lithos* **112**(3–4) 556–74.

Moyen, J.-F., Martin, H. & Jayananda, M. 1997. Origine du granite fini-Archéen de Closepet (Inde du Sud): apports de la modélisation géochimique du comportement des éléments en traces. *Compte Rendus de l'Académie des Sciences de Paris* **325**, 659–64.

Moyen, J.-F., Martin, H. & Jayananda, M. 2001a. Multi-element geochemical modelling of crust-mantle interactions during late-Archaean crustal growth: the Closepet granite (South India). *Precambrian Research* **112**, 87–105.

Moyen, J.-F., Nédélec, A., Martin, H. & Jayananda, M. 2001b. Contrasted granite emplacement modes within an oblique crustal section: the Closepet Granite, South India. *Physics and Chemistry of the Earth (A)* **26** (4–5), 295–301.

Moyen, J.-F., Martin, H., Jayananda, M. & Auvray, B. 2003. Late Archaean granites: a typology based on the Dharwar Craton (India). *Precambrian Research* **127** (1–3), 103–23.

Moyen, J.-F. & Stevens, G. 2006. Experimental constraints on TTG petrogenesis: implications for Archaean geodynamics. *In* Benn, K. Condie, K. C. & Mareschal, J. C. (eds) *Archaean geodynamics and environments. AGU Monograph* **164**, 149–75. Washington, DC: American Geophysical Union.

Nair, R. & Chacko, T. 2008. Role of oceanic plateaus in the initiation of subduction and origin of continental crust. *Geology* **36** (7), 583–6.

Nair, R. K. & Chacko, T. 2005. Oceanic plateaus: nuclei for Archean cratons. *Geological Society of America Annual Meeting, Salt Lake City*, 494. Boulder, Colorado and Lawrence, Kansas: The Geological Society of America and University of Kansas Press.

Nicholls, I. A. & Ringwood, A. E. 1973. Production of silica saturated tholeiitic magmas in island arcs. *Earth and Planetary Science Letters* **16**, 243–6.

Pawley, A. R. & Holloway, J. R. 1993. Water source for subduction zone volcanism: new experimental constrains. *Science* **121**, 664–7.

Prouteau, G., Scaillet, B., Pichavant, M. & Maury, R. C. 2001. Evidence for mantle metasomatism by hydrous silicic melts derived from subducted oceanic crust. *Nature* **410**, 197–200.

Querré, G. 1985. Palingenèse de la croûte continentale à l'Archéen: les graniteïdes tardifs (2·5–2·4 Ga) de Finlande orientale; pétrologie et géochimie. *Mémoires et Documents du Centre Armoricain d'Etude Structurale des Socles* **2.** Rennes: Université de Rennes.

Rapp, R. P., Watson, E. B. & Miller, C. F. 1991. Partial melting of amphibolite/eclogite and the origin of Archaean trondhjemites and tonalites. *Precambrian Research* **51**, 1–25.

Rapp, R. P., Shimizu, N., Norman, M. D. & Applegate, G. S. 1999. Reaction between slab-derived melts and peridotite in the mantle wedge: experimental constraints at 3·8 GPa. *Chemical Geology* **160**, 335–56.

Rapp, R. P., Shimizu, N. & Norman, M. D. 2003. Growth of early continental crust by partial melting of eclogite. *Nature* **425**, 605–9.

Rapp, R. P., Laporte, D., Martin, H. & Shimizu, N. 2006. Experimental insights into slab-mantle interactions in subduction zones: Melting of adakite-metasomatized peridotite and the origin of the 'arc signature'. *Geochimica et Cosmochimica Acta* **70** (18, Supplement 1), A517.

Rapp, R. P. & Watson, E. B. 1995. Dehydration melting of metabasalt at 8–32 kbar: implications for continental growth and crust-mantle recycling. *Journal of Petrology* **36** (4), 891–931.

Reddy, G. S. 1991. *Geochemistry and petrogenesis of granitic rocks around Sakarsanahalli (Kolar) South India.* PhD Thesis, Bangalore University, Bangalore. 147 pp.

Rogers, N. W. & Setterfield, T. N. 1994. Potassium and incompatible-element enrichment in shoshonitic lavas from the Tavua volcano. Fiji. *Chemical Geology* **118**, 43–62.

Rollinson, H. 1993. *Using geochemical data: evaluation, presentation, interpretation.* London: Longman. 352 pp.

Rollinson, H. 1997. Eclogite xenoliths in west African kimberlites as residues from Archaean granitoid crust formation. *Nature* **389**, 173–6.

Rudnick, R. L. 1995. Making continental crust. *Nature* **378**, 571–7.

Samsonov, A. V., Bogina, M. M., Bibikova, E. V., Petrova, A. Y. & Shchipansky, A. A. 2005. The relationship between adakitic, calc-alkaline volcanic rocks and TTGs: implications for the tectonic setting of the Karelian greenstone belts, Baltic Shield. *Lithos* **79** (1–2), 83–106.

Sarvothaman, H. 2001. Archaean High-Mg granitoids of mantle origin in the Eastern Dharwar craton of Andhra Pradesh. *Journal of the Geological Society of India* **58**, 261–8.

Schmidt, M. W. & Poli, S. 1998. Experimentally based water budgets for dehydrating slabs and consequences for arc magma generation. *Earth and Planetary Science Letters* **163** (1–4), 361–79.

Sekine, T. & Wyllie, P. J. 1982. The system granite-peridotite-H2O at 30 kbar, with applications to subduction zone magmatism. *Contributions to Mineralogy and Petrology* **81**, 190–202.

Sen, C. & Dunn, T. 1994. Experimental modal metasomatism of a spinel lherzolite and the production of amphibole-bearing peridotite. *Contributions to Mineralogy and Petrology* **119**, 422–32.

Shaw, D. M. 1970. Trace element fractionation during anatexis. *Geochimica et Cosmochimica Acta* **34**, 237–43.

Shirey, S. B. & Hanson, G. N. 1984. Mantle derived Archaean monzodiorites and trachyandesites. *Nature* **310**, 222–4.

Shirey, S. B. & Hanson, G. N. 1986. Mantle heterogeneity and crustal recycling in Archaean granite-greenstone belts: evidence from Nd isotopes and trace elements in the Rainy Lake province, Ontario, Canada. *Geochimica et Cosmochimica Acta* **50**, 2631–51.

Smithies, R. H. 2000. The Archaean tonalite–trondhjemite–granodiorite (TTG) series is not an analogue of Cenozoic adakite. *Earth and Planetary Science Letters* **182**, 115–25.

Smithies, R. H., Van Kranendonk, M. J. & Champion, D. C. 2005. It started with a plume – early Archaean basaltic proto-continental crust. *Earth and Planetary Science Letters* **238** (3–4), 284–97.

Smithies, R. H. & Champion, D. C. 1999. High-Mg diorite from the Archaean Pilbara Craton; anorogenic magmas derived from a subduction-modified mantle. *Geological Survey of Western Australia, Annual Review* **1998–99**, 45–59.

Smithies, R. H. & Champion, D. C. 2000. The Archaean high-Mg diorite suite: Links to Tonalite–Trondhjemite–Granodiorite magmatism and implications for early Archaean crustal growth. *Journal of Petrology* **41** (12), 1653–71.

Stern, R. 1989. *Petrogenesis of the Archaean sanukitoid suite*. New York: State University at Stony Brook. 275 pp.

Stern, R. A. & Hanson, G. N. 1991. Archaean high-Mg granodiorite: a derivative of Light Rare Earth enriched monzodiorite of mantle origin. *Journal of Petrology* **32**, 201–38.

Stevenson, R., Henry, P. & Gariépy, C. 1999. Assimilation-fractional crystallization origin of Archaean sanukitoid suites: Western Superior Province, Canada. *Precambrian Research* **96**, 83–99.

Sun, S. S. & McDonough, W. F. 1989. Chemical and isotopic systematics of oceanic basalts: implications for mantle composition and processes. *In* Saunders, S. D. & Norry, M. J. (eds) *Magmatism in the ocean basins. Geological Society, London, Special Publication* **42**, 313–45. Bath, UK: The Geological Society Publishing House.

Tatsumi, Y. 1989. Migration of fluid phase and genesis of basalt magma in subduction zones. *Journal of Geophysical Research* **94**, 4697–707.

Tatsumi, Y. & Ishizaka, K. 1982. Origin of high-magnesian andesites in the Setouchi volcanic belt, southwest Japan, I. Petrographical and chemical characteristics. *Earth and Planetary Science Letters* **60** (2), 293–304.

Viljoen, M. J. & Viljoen, R. P. 1969. The chemical evolution of the granitic rocks of the Barberton region. *Geological Society of South Africa Special Publication* **2**, 189–220.

Watson, E. B. & Harrison, T. M. 2005. Zircon thermometer reveals minimum melting conditions on earliest Earth. *Science* **308**, 841–4.

Wilde, S. A., Valley, J. W., Peck, W. H. & Graham, C. M. 2001. Evidence from detrital zircons for the existence of continental crust and oceans on the Earth 4·4 Ga ago. *Nature* **409**, 175–78.

Windley, B. F. & Bridgwater, D. 1971. The evolution of Archaean low- and high-grade terrains. *Geological Society of Australia Special Publication* **3**, 33–46.

Yaxley, G. M. & Green, D. H. 1998. Reactions between eclogite and peridotite: mantle refertilisation by subduction of oceanic crust. *Schweizeriche Mineralogische und Petrographische Mitteilungen* **78**, 243–55.

Zamora, D. 2000. *Fusion de la croûte océanique subductée: approche expérimentale et géochimique.* PhD Thesis, Université Blaise Pascal, Clermont-Ferrand, France. 314 pp.

MS received 1 February 2008. Accepted for publication 19 November 2008 (Stellenbosch); 15 January 2009 (RSE).

Earth and Environmental Science Transactions of the Royal Society of Edinburgh, **100**, 35–50, 2010 (for 2009)

The geochemistry of Archaean plagioclase-rich granites as a marker of source enrichment and depth of melting

J.-F. Moyen[1], D. Champion[2] and R. H. Smithies[3]

[1] Department of Geology, Geography and Environmental Studies, University of Stellenbosch, PVT Bag X1, 7602 Matieland, South Africa
Email: moyen@sun.ac.za
Current address: Département de Géologie, Université Jean-Monnet & CNRS 23, rue du Docteur Michelon, 42023 Saint-Etienne cedex, France
Email: jean.francois.moyen@univ-st-etienne.fr

[2] Geoscience Australia, Canberra, Australia
Email: David.Champion@ga.gov.au

[3] GSWA, Perth, W. Australia
Email: hugh.smithies@dmp.wa.gov.au

ABSTRACT: In geochemical diagrams, granitoids define 'trends' that reflect increasing differentiation or melting degree. The position of an individual sample in such a trend, whilst linked to the temperature of equilibration, is difficult to interpret. On the other hand, the positions of the trends within the geochemical space (and not the position of a sample within a trend) carry important genetic information, as they reflect the nature of the source (degree of enrichment) and the depth of melting. This paper discusses the interpretation of geochemical trends, to extract information relating to the sources of granitoid magmas and the depth of melting.

Applying this approach to mid-Archaean granitoids from both the Barberton granite–greenstone terrane (South Africa) and the Pilbara Craton (Australia) reveals two features. The first is the diversity of the group generally referred to as 'TTGs' (tonalites, trondhjemites and granodiorites). These appear to be composed of at least three distinct sub-series, one resulting from deep melting of relatively depleted sources, the second from shallower melting of depleted sources, and the third from shallow melting of enriched sources. The second feature is the contrast between the (spatial as well as temporal) distributions and associations of the granites in both cratons.

KEY WORDS: Geochemistry, geochemical diagrams, granitoids, trace elements

The bulk of the Archaean continental crust is made of granite or granitoids (e.g. Windley 1995), occurring either as well-defined plutons, or as polyphase, deformed, commonly formerly partially melted 'grey gneiss complexes' (Martin 1994). Understanding their origin and petrogenesis is therefore critical to our understanding of the formation and differentiation of the Earth's crust. Also, because they represent a strongly dominant rock type in the Archaean crust, granitoids can be useful geodynamic indicators, providing information can be extracted pertaining to the P–T regimes, the geometry of the crust, or the tectonic conditions in the crust during melting of their parental rocks, or the intrusion of granitic magmas. Classical thermobarometry, such as is used on metamorphic assemblages, is of limited use in granitoids, because such rocks typically lack 'good' metamorphic minerals such as garnet or aluminium silicates. However, it is increasingly recognised that the geochemistry of granites records at least some information not only on the source, but also of the condition of melting of this source (Moyen & Stevens 2006; Champion & Smithies 2007a; Collins 2007).

This signal is obscured by the fact that even simple granitoid plutons typically display a range of composition, forming geochemical 'trends' from lower to higher silica compositions. Whilst this evolution is customary referred to as a range of rocks, from 'less differentiated' to 'more differentiated', the trends can reflect either melt fractions (during melting), or latter differentiation (during cooling and emplacement). This paper discusses the role of petrogenetic effects such as the degree and depth of melting, the nature of the source, and the amount of fractionation, on the shape and position of the trends in the composition space. It is shown that depth of melting and source composition exert a major control on the trends, and that the degree of melting or fractionation mostly results in composition changes within one given trend. Consequently, it is concluded that rather than individual analyses, the discussion on granites geochemistry should be based on trends affecting whole rock units, as these carry the most valuable geodynamic information, and a graphical technique is proposed that simultaneously depicts information relating to source enrichment and to pressures of melting of the source. This analysis is then applied to the dominant type of Archaean granites – here referred to as 'plagioclase-rich granitoids' or 'TTGM' (defined below). Since granitoids represent a large portion of the exposed Archean crust, and in some areas are the only remaining evidence for whole portions of the accretion history of some

© 2009 The Royal Society of Edinburgh. doi:10.1017/S1755691009016132

Archaean blocks, this approach provides a very valuable tool in interpreting Archaean geodynamics.

1. Archaean granitoids

1.1. Different types of granites

Archaean granitoids belong to one of four broad groups (Champion & Smithies 1999, 2007a; Moyen *et al.* 2003b). These groups are (1) either muscovite or (less commonly) cordierite bearing peraluminous S-type granites; (2) alkaline to peralkaline granites and associated syenites; (3) magnesio-potassic granitoids, including sanukitoids (Shirey & Hanson 1984; Stern *et al.* 1989; Stern & Hanson 1991; Smithies & Champion 2000; Moyen *et al.* 2003b; Martin & Moyen 2005, 2007; Martin *et al.* 2005); and (4) plagioclase-rich granitoids, or tonalite–trondhjemite–granodiorite–monzogranite (TTGM) group (Feng & Kerrich 1992). In the first three groups, alkali feldspar is at least as abundant as plagioclase – these are granites s.s. (i.e. monzogranites and syenogranites) and granodiorites. By contrast, K-feldspar is a subordinate mineral in the last group (plagioclase-rich granitoids), which includes the tonalite–trondhjemite–granodiorite (TTG) series, as well as a large number of 'post-tectonic potassic granites' (typically, granodiorites to monzogranites). These plagioclase-rich granitoids are by far the dominant component of Archaean plutonic rocks, and indeed of the preserved Archaean crust in general, perhaps corresponding to as much as 80% or 90% of the preserved Archaean continents.

Plagioclase-rich granitoids define a continuum, between true TTG to more K-rich granites with K_2O/Na_2O up to ~1·5. It is common practice to separate the TTG (sodic granitoids) from the potassic granites (e.g. Windley 1995); indeed in many Archaean provinces, the TTG mostly occur as part of the 'background' orthogneisses, whereas the potassic terms of the TTGM group form late, well-identified plutons, and some proposed Archaean granite classifications emphasise this difference (TTG *vs.* biotite-bearing granites in Moyen *et al.* 2003b). However, this two-fold classification is an oversimplification. Closer examination of some 'late potassic granites', such as the GMS (granodorite–monzogranite–syenite) suite of the Barberton granite–greenstone terrane, reveals that the supposedly potassic batholiths actually contain a significant proportion of sodic (tonalitic and trondhjemitic) rocks, and that they define a continuum, from these sodic compositions to potassic granites and syenites (Anhaeusser & Robb 1983b; Robb 1983; Westraat *et al.* 2004; Belcher & Kisters 2006). Symmetrically, many of the 'grey gneiss complexes', supposedly dominated by the sodic TTGs, do actually contain a significant potassic component, e.g. the granitoid 'domes' of the Pilbara terrain, the gneiss complex in the Eastern Dharwar Craton in India, etc. (Moyen *et al.* 2003a; Champion & Smithies 2007b). Consequently, other attempts at classifying Archean granites have rather emphasised the similarities between rocks in the plagioclase-rich granitoids group, e.g. by referring to the potassic members as LILE-enriched TTGs (Champion & Smithies 2007b).

Furthermore, from an experimental perspective, all rocks of the plagioclase-rich granitoids group (and, in fact, all granitoids without a clear mantle connection) probably share a common origin, by melting of a source made of feldspars and hydrous mafic silicates (Clemens & Vielzeuf 1987; Vielzeuf & Montel 1994; Patiño-Douce & Beard 1995; Montel & Vielzeuf 1997; Stevens *et al.* 1997; Vielzeuf & Schmidt 2001; Moyen & Stevens 2006). Typical melting reactions correspond to incongruent breakdown of the hydrous minerals: amphibole in the more mafic sources (yielding sodic melts), biotite in the more felsic, enriched sources (giving potassic melts). At higher pressures (>20–25 kbar), where amphibole becomes unstable (Schmidt & Poli 1998), epidote breakdown can play a role, although melting reactions in this part of the P–T space are poorly understood (Skjerlie & Patiño-Douce 2002; Patiño-Douce 2005). For instance, the amphibole breakdown reaction (Rapp *et al.* 1991; Rapp & Watson 1995; Moyen & Stevens 2006) has the general form plagioclase+amphibole=melt+clinopyroxene+(orthopyroxene or garnet), where garnet is typically stable at pressures higher than 15 kbar (Fig. 1). This melting behaviour is broadly similar to biotite breakdown reactions (biotite+plagioclase+quartz=melt+(orthopyroxene+garnet). This reaction (or group of reactions) are relevant to melting over a large range of sources compositions – from relatively primitive tholeiitic amphibolites (amphibole+calcic plagioclase), to more evolved rocks such as tonalites ($An_{30–40}$ plagioclase, quartz, amphibole and occasional biotite) or even trondhjemites (quartz, An_{30}, biotite). In fact, many aspects of the geochemical discussion that follows are also applicable to the melting of greywacke sources (plagioclase+quartz+biotite) that generate Phanerozoic S-type granites (Clemens & Vielzeuf 1987; Vielzeuf & Montel 1994; Stevens *et al.* 1997; Vielzeuf & Schmidt 2001).

Therefore, all of the Archaean plagioclase-rich granitoids, either sodic or potassic (and actually, all the crustally-derived granitoids, including the S-type granites), form through similar petrogenetic processes, by comparable melting reactions and, importantly, with the same sort of residual minerals; this implies that the resulting melts will have the same geochemical behaviour, and that the same interpretation applies to all of them – from the sodic TTG proper, to the more potassic members of this group.

1.2. Melting reactions and composition of the residuum

Whilst dominated by plagioclase, the crustal sources for plagioclase-rich granitoids (and for most granitoids in general) include a hydrous mafic mineral. As a result, melting is controlled by very similar reactions tied to the breakdown of either amphibole or biotite. This releases (i) water, which triggers the melting of whatever feldspar is available, and of quartz if present; and (ii) an anhydrous silicate, such as cordierite, garnet or orthopyroxene, or various combinations of these minerals (Stevens *et al.* 1997). The sodic component of plagioclase preferentially enters the melt (at lower temperatures than the calcic component), so any residual plagioclase will be more calcic than the original feldspar (Rapp *et al.* 1991; Vielzeuf & Montel 1994; Patiño-Douce & Beard 1995; Rapp & Watson 1995; Stevens *et al.* 1997; Patiño-Douce 2005; Moyen & Stevens 2006).

As a result, granitoid melts typically coexist with a solid residuum that comprises relatively calcic plagioclase and mafic minerals such as cordierite, garnet or pyroxene. At temperatures greater than 1000–1100°C, these minerals are also incorporated into the melt and disappear, although such temperatures are probably uncommon in the crust (Fig. 1).

The nature of the residual assemblage is also strongly influenced by the pressure (depth) of melting. Garnet is stable at pressures greater than 6 to 15 kbar, depending on the composition of the source assemblage, with rocks containing excess aluminium producing garnet much more easily, and at lower depths, compared to Al-poor compositions (Stevens *et al.* 1997; Moyen *et al.* 2006). Plagioclase also disappears from the residuum at high pressure; the pattern is more complicated, as in the absence of melt, the plagioclase-out line is positively sloped in the P–T space and its position depends on the anorthite content of the plagioclase. Therefore, sodic plagioclase is intrinsically stable at higher pressures, but is also

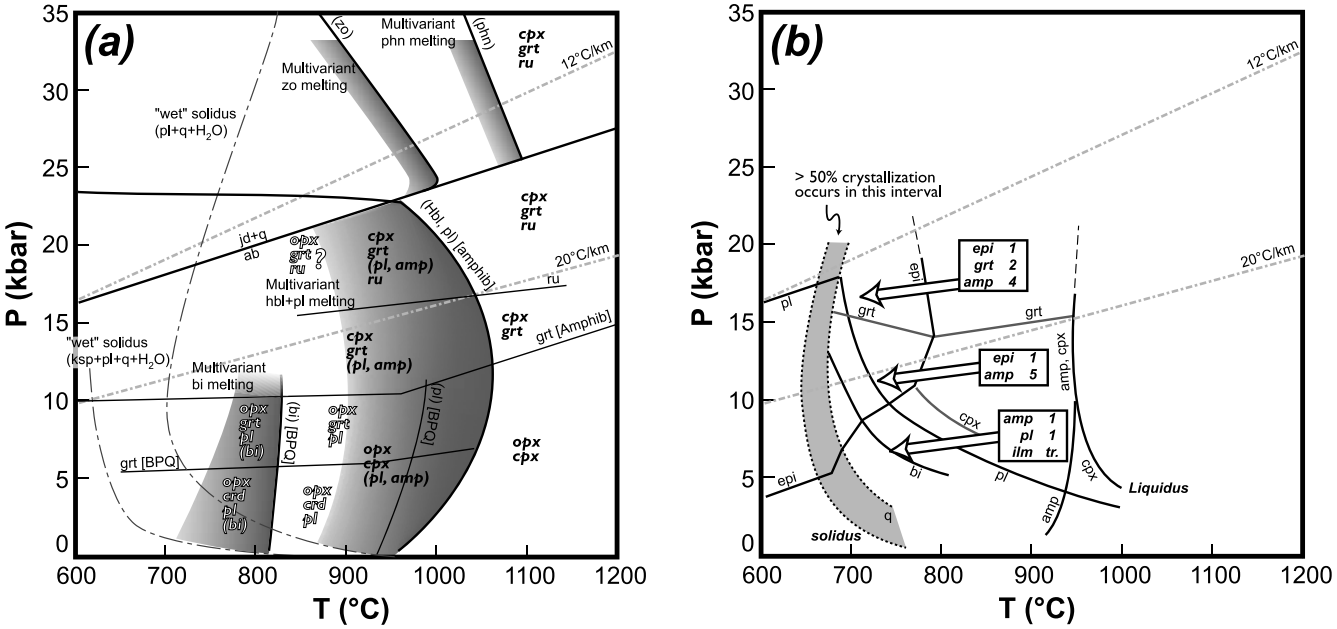

Figure 1 Simplified phase relations applicable to (a) melting of plagioclase-amphibole ± biotite sources (compiled after Moyen & Stevens (2006), with modifications based on Skjerlie & Patiño-Douce (2002) and Patiño-Douce (2005) at high pressure) and (b) fractionation of water-saturated tonalitic liquids (Schmidt & Thompson 1996). Geotherms indicated for reference (grey, dashed-dotted) in both figures. Mineral abbreviations: (amp) amphibole; (bi) biotite; (cpx) clinopyroxene; (epi) epidote; (grt) garnet; (ilm) ilmenite; (opx) orthopyroxene; (phn) phengite; (pl) plagioclase; (q) quartz; (ru) rutile; (zo) zoisite. In (a), the grey field represent the 'band' in which the multivariant melting reactions occur; solid lines correspond either to mineral stability boundaries (mineral appear on the side of the line which is labelled) or to upper limit of mineral stabilities (in the case of multivariant melting reactions; the mineral are unstable on the side where the mineral abbreviation is parenthesised). [Amphib] and [BPQ] labels denote lines applicable only to either amphibolite or biotite–plagioclase–quartz sources, respectively. Mineral associations coexisting with melt are indicated in italic, black for amphibolite sources and white for BPQ. In (b), the lines correspond to mineral appearance (mineral stable on the side its name is written); the grey field denotes the near-solidus region where most of the crystallisation occurs. The arrows correspond to the three possible crystallisation paths discussed in section 3.2, and the mineral proportions used in each model are indicated in the boxes.

consumed by melting at lower temperatures, compared to more calcic plagioclase. The result is a negatively-sloped plagioclase-out line in the P–T space, the position of which depends on the calcic or sodic nature of the rock (more calcic lithologies tend to have an expanded plagioclase stability field: Moyen & Stevens 2006).

Investigating the nature of the residuum in terms of phase relationships, however, obscures the fact that the residuum continuously changes with changing P–T conditions. Mapping of the phase proportions in the P–T space (Moyen & Stevens 2006) has revealed that (a) above the garnet-in line, the amount of garnet increases with increasing pressures and with decreasing temperatures and, (b) below the plagioclase-out line, the amount of plagioclase decreases with increasing temperatures and pressures.

2. Controls on the composition of Archaean plagioclase-rich granitoids (TTGM): composition of primary melts

2.1. The chemistry of primary melts

For trace elements, the link between the composition of the source and of the melt is expressed in the batch melting equation:

$$C_l = \frac{C_0}{F + D.(1 - F)}$$

where C_l is the concentration of an element in the liquid and C_0 the concentration of that element in the source (Shaw 1970). The melt fraction (F) is largely a function of the conditions of melting – i.e. of temperature, H_2O content and, to a lesser degree, pressure. D is the bulk partition coefficient, and is expressed as

$$D = \sum_i K_D^i X_i$$

where X_i is proportion of mineral i in the residue and K_D^i is the partition coefficient of an element between melt and that mineral. While the K_D values are not strictly constant over the P–T-melt composition space, their variations are sufficiently minor to be 'masked' by the overall uncertainties of the model (see the discussion in Bédard 2010), especially with a broad approach as used in the present paper, and so constant values are used (Table 1). The mineral proportions in the residuum are a function of the conditions of melting (pressure, temperature and water activity) as well as the nature of the source. Therefore, Shaw's equation as written above expresses the fact that the composition of a (granitoid) melt is a function of the source's composition, and of the P–T–H_2O conditions of melting.

Most crustal rocks will produce very similar residuum assemblages when they melt (plagioclase, orthopyroxene and garnet being the dominant minerals) (Fig. 1) This means that, for the elements with a high K_D in the restite-making minerals, the nature of the protolith actually exerts a much smaller effect on the composition of a granitoid melt than the P–T conditions of melting. In most cases, crustal melting will occur under fluid-absent conditions associated with the breakdown of hydrous phases like biotite or amphibole, such that the

variation of the water content is relatively minor. In any case, higher water contents would usually lead to higher melt fractions without substantially altering the nature of the residual phases, and so the effect that higher water contents would have on the composition of a granitoid melt would be indistinguishable from that of higher temperatures.

This implies that the trace element composition of primary granitic melts is primarily controlled by only three parameters:

1. The temperature of melting, or more precisely the degree of melting (as higher pressures tend to decrease the melt fraction, whereas higher water contents increase it). High melt fraction liquids are more mafic – i.e., have lower concentrations of SiO_2 and higher MgO and FeO. Most elements are strongly correlated with SiO_2, resulting in narrow, linear trends in Harker diagrams. Accordingly, the effect of SiO_2-correlated geochemical variation to a granitoid (or granitic suites) 'geochemical signal' should ideally be filtered out before any discussion on the geochemical differences or similarities between granitic melts.
2. The composition of the source, especially with regard to its concentration of incompatible elements. In the case of a strongly incompatible element ($D \approx 0$), the batch melting equation approaches $C_l = C_0/F$: i.e., the concentration of that element in the melt is only a function of the melt fraction and the concentration of that element in the source. In Harker diagrams, melts from different source compositions therefore define stacked parallel trends, with melts from richer sources plotting towards higher compositions. LILE (Rb, Ba, Th), LREE and some of the HFSE (Th, Zr, Nb) behave in this way.

   Significantly, K also behaves as an incompatible trace element in alkali feldspar-free and biotite-free assemblages, such as the source of the plagioclase-rich granites considered here, and its concentration in these melts is likewise affectively only a function of source composition and the degree of melting. However, K-enriched sources will yield liquids in which K behaves as a major element, defining K-rich trends that do lead to alkali feldspar bearing rocks that extend from tonalites to granodiorites and to monzogranites. Therefore, depending on the degree of K-enrichment, 'plagioclase-rich' granitoids will define either 'tonalite–trondhjemite' or 'tonalite–granodiorite' series.
3. The depth of melting. Recent work focused on the critical examination of experimental data on partial melting of amphibolites (Moyen & Stevens 2006) showed that two minerals, whose stability and abundance is strongly pressure-dependant, play a key role in controlling the concentration of important trace elements during melting of plagioclase-amphibole dominated assemblages. Plagioclase disappears at pressures in excess of 10–20 kbar, depending on temperature and source composition (etc.), and controls the concentration of Sr and Eu (or more interestingly, the magnitude of the Eu anomaly) in the melt. Melts coexisting with plagioclase are relatively Sr- and Eu-poor, owing to the large K_D of plagioclase for this element. To some extent, Al (and to a lesser degree Na) will also be preferentially partitioned into plagioclase during melting. Garnet appears at ca. 12 kbar and becomes increasingly abundant with increasing pressure (towards eclogitic assemblages) and controls the concentration of HREE and Y in the melt, such that melts in equilibrium with garnet are Y and HREE poor. The combined effect of these two minerals during melting at progressively higher pressures is an evolution from HREE- and Y-rich melts that are Sr-poor and have a negative Eu anomaly, to relatively HREE- and Y-poor melts with higher Sr contents and no Eu anomaly. The effect that source enrichment has on the concentration of these trace elements in a melt is secondary compared to the control exerted by the absence or presence of these mineral phases. Again, melts formed at different pressures define stacked trends in Harker diagrams; the degree of melting primarily controls the absolute concentrations and the position within a trend.

The expected result is that melts will define 'trends' in Harker-type diagrams (Fig. 2), where the SiO_2 and compatible elements contents will be tightly correlated and reflect the degree of melting; melts from different depths will yield 'stacked' trends in diagrams using pressure-sensitive elements such as Sr, Y or Nb (but will be superposed on diagrams using either very incompatible elements, or purely compatible elements); melts from different sources will define stacked trends in diagrams using incompatible elements (but will be superposed when looking at pressure-sensitive or compatible elements).

2.2. A test based on experimental data

In order to demonstrate the reliability of this approach, it was tested on granitic melts from known sources generated under known conditions of melting. Such a situation does not occur naturally, but can be produced in controlled experiments. One difficulty here is that trace elements are rarely analysed in experimental melts, such that a real, direct comparison is not feasible. Nevertheless, experimental charges are probably the one situation in which the conditions of equilibrium and of closed systems are realised, and therefore perhaps correspond to the only situation where Shaw's (1970) batch melting equation can reliably be applied to calculate the melt composition. Therefore, data on modal compositions from >350 experiments (compiled by Moyen & Stevens 2006) and published partition coefficients (Table 1) were used to calculate the trace element compositions of the corresponding melts. Three different source compositions were used; one corresponds to a normal, to slightly enriched MORB (mid-ocean ridge basalt), such as the one proposed for Archaean MORBs (Jahn *et al.* 1980; Condie 1981; Jahn 1994); another, more enriched source, has a composition close to that of an arc basalt; whilst the third source corresponds to a tonalitic composition. Obviously, melting of a tonalite would not give exactly the same melting reactions, melt fractions, etc., and using this composition is not strictly rigorous. The point here, however, is merely to test the influence of contrasting sources compositions.

This simple model confirms the qualitative conclusions outlined above. Two main classes of elements are evident. Elements such as Rb, Th, etc. are primarily controlled by the nature of the source, and pressure exerts little or no influence on their concentration within the melt. On the other hand, for Sr, Y and Nb, pressure appears as the dominant parameter, and the source-related variations, while playing a role, remain second-order.

Clearly, the two parameters (pressure and enrichment) are not completely independent (Fig. 3). For example, at pressures where plagioclase is not stable, Sr-enriched sources will yield Sr-richer melts compared to Sr-depleted sources. In contrast, at low pressures, plagioclase is stable and high Sr contents in a melt are impossible to achieve regardless of the Sr concentration of the source. On the other hand, while Y is clearly pressure-controlled, high Y concentrations can be achieved only at low pressures (no garnet in the residuum); but low Y concentrations can exist both at high pressure (given a garnet-bearing residuum) or at low pressures (for a Y poor source).

Diagrams employing elements that are controlled by source enrichment alone (or nearly so – e.g. Rb, Th or K_2O/

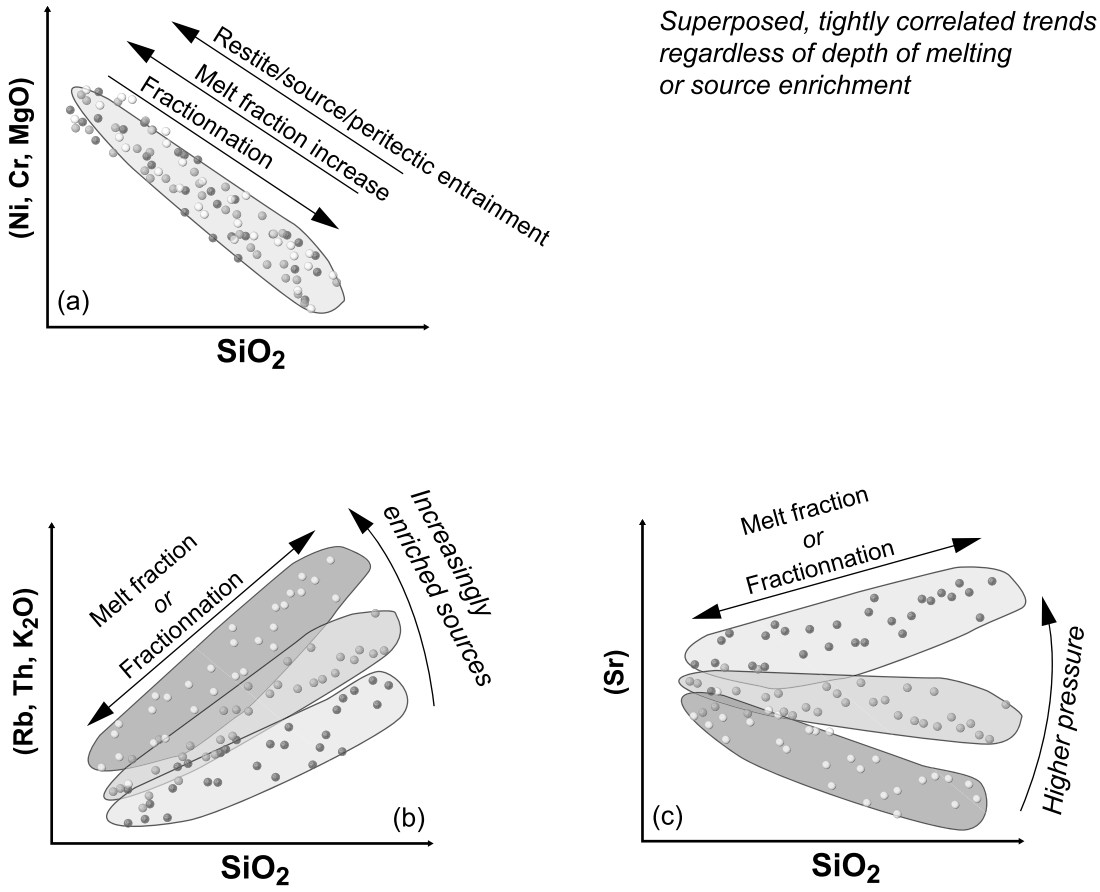

Figure 2 Expected positions of trends generated by partial melting in Harker type diagrams. (a) Diagrams using compatible elements (Mg, Ni, Cr) will yield tightly correlated trends that reflect the melt amount, and do not give information regarding the depth of melting or the nature of the source. Fractionation will move the composition to the right, whereas melting and solids entrainment (section 3.1) will displace the composition to the left, keeping it in the same, narrow trend; (b) Diagrams using incompatible elements (Th, Rb, K) show stacked trends, which position reflects the source enrichment; (c) Diagrams using pressure-sensitive elements (Sr, Nb, Y) produce stacked trends, and their position gives information on the depth of melting.

Table 1 Partition coefficients and source concentrations used in the model. Partition coefficients from (Foley *et al*. 2000; Foley *et al*. 2002; Schmidt *et al*. 2004; Bédard 2006), using values applicable for intermediate to felsic liquids in equilibrium with amphibole ± plagioclase ± garnet.

	Partition coefficients								Source compositions (ppm)		
	Amphibole	*Clinopyroxene*	*Garnet*	*Ilmenite*	*Orthopyroxene*	*Plagioclase*	*Rutile*	*Olivine*	*MORB-like*	*Arc basalt*	*Tonalitic*
Ba	0·046	0·006	0·0004	0·018	0·047	1·016	0·0043	0·0205	10	50	690
Rb	0·055	0·01	0·0007	0·025	0·047	0·068	0·0076	0·0231	1	10	55
Th	0·055	0·104	0·0075	0·09	0·13	0·095	0·2	0·0542	0·015	0·5	6·9
Nb	0·274	0·007	0·04	3	0·01	0·239	n.a.	0·0103	3·5	3·507	10
Ta	0·477	0·028	0·08	2·7	0·126	0·053	n.a.	0·1260	0·2	0·2	0·5
La	0·319	0·028	0·028	0·015	0·0003	0·358	0·0057	0·0216	3	5	32
Ce	0·56	0·059	0·08	0·012	0·0007	0·339	0·0065	0·0185	8	12	56
Sr	0·389	0·032	0·019	0·0022	0·047	6·65	0·036	0·0306	100	300	454
Nd	1·32	0·115	0·222	0·01	0·0028	0·289	0·0082	0·0123	8	11·2	21·4
P	0·225	0·162	0·184	0·002	0·05	0·079	0·03	0·0357	520	570	—
Sm	2·09	0·259	1·43	0·009	0·0085	0·237	0·0954	0·0091	3·5	3·75	3·3
Zr	0·417	0·125	0·537	2·3	0·031	0·078	3·7	0·0365	80	104·24	152
Hf	0·781	0·208	0·431	2·4	0·246	0·069	4·97	0·0195	2·4	2·974	3·9
Y	2·47	0·603	14·1	0·037	0·054	0·138	0·0118	0·0301	28	35·82	7·5
Yb	1·79	0·635	23·2	0·13	0·125	0·094	0·0126	0·0581	3·3	3·9	0·55

Na_2O) – can yield unambiguous information (Fig. 2). Likewise, diagrams using elements whose concentration is strongly pressure-dependant (Sr, Y, HREE) give slightly more ambiguous, but still useful, results. However, most other elements do not exhibit such specific behaviour. (Either there are no phases with high enough K_D values to allow for spectacular pressure-related changes, or these elements are not incompatible enough to be used as good source tracers.) Diagrams using these elements are typically harder to interpret, but are, in any case, of no relevance in the present paper since the aim is to establish

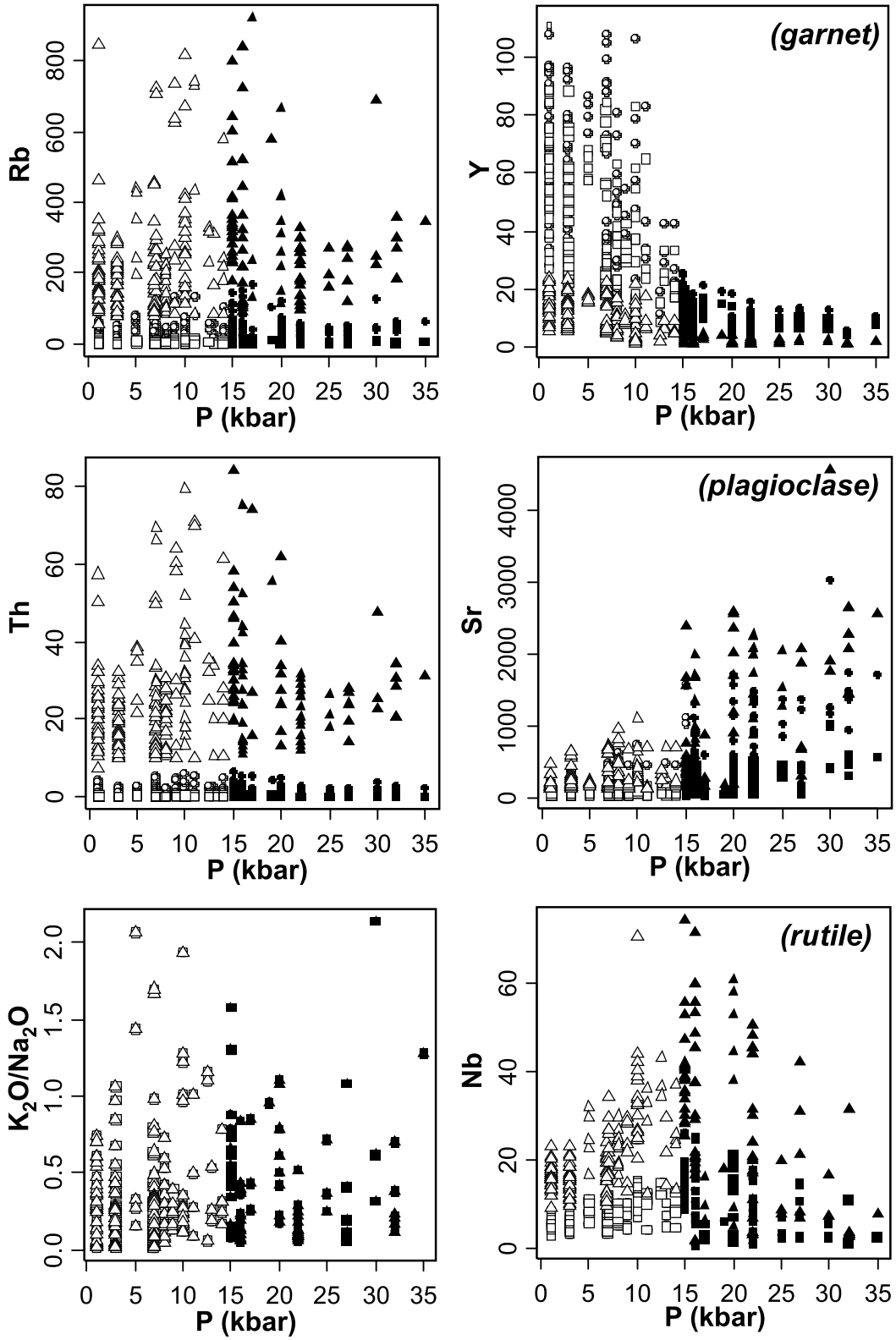

Figure 3 Pressure *vs.* composition diagrams for experimental melts. All panels show pressure *vs.* element diagrams, recalculated from experimental data. Black symbols correspond to pressures >15 kbar, open symbols <15 kbar; triangles are tonalitic sources, circles are 'arc-like' and squares 'MORB-like' (Table 1). The left three panels show typical source-controlled elements, whereas the right hand side panels show typical depth-controlled elements, with the key mineral indicated on the panel. Trace elements in ppm and majors in wt.%, in this figure and all the following.

a tool to derive information on the pressure of melting and the enrichment of the source.

Another way to show the pressure effects on melt compositions is the use of multi-element diagrams (spidergrams, Fig. 4). With increasing pressures of melting, the depth of the Nb–Ta anomaly increases, the negative Sr anomaly is progressively reduced, and the Y–Yb segment on the right-hand side is progressively depressed. These effects respectively correspond to the increasing role of rutile, the decreasing plagioclase contents, and the increasing proportion of residual garnet, and in this case are directly correlated to changes in the abundance of these minerals. In contrast, variations in source composition

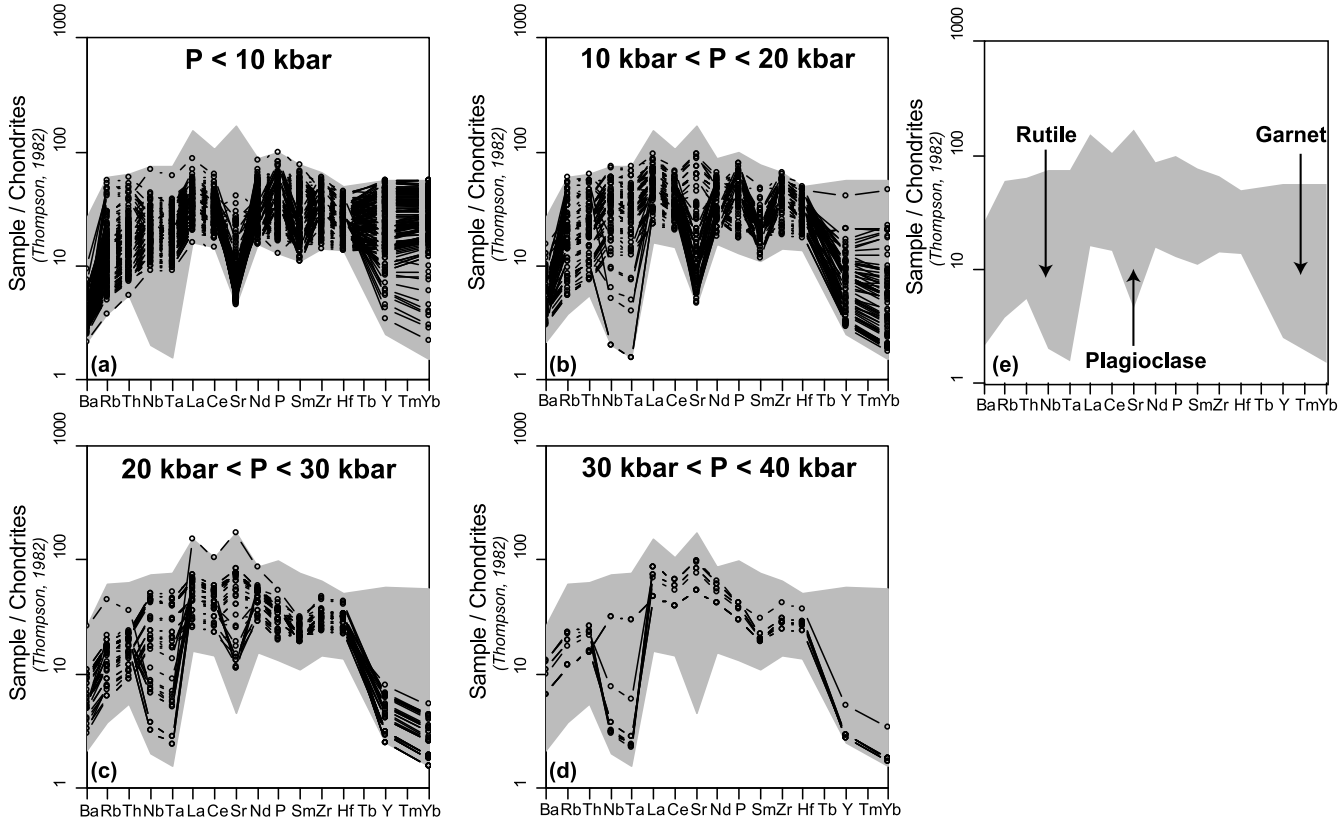

Figure 4 Multi-elements diagrams (Thompson 1982) for calculated experimental melts in different pressure bands. The source used is the MORB-like composition (Table 2). Panels (a)–(d) show different pressure bands (panel (e)). in each case the grey background field indicate the whole spread of data. Panel (e) summarises which mineral controls different sections of the spectrum: rutile for the Nb–Ta, through plagioclase for the Sr anomaly and garnet for the Tb–Yb section.

result in stacked but parallel patterns in spidergrams, especially in the left-hand part (more incompatible elements) of the diagrams.

In Harker diagrams (Fig. 5), the behaviour described here is also evident, and stacked trends are produced as predicted. Each pair (source composition, depth band) yields a specific 'trend'. Diagrams using a 'depth-controlled' element produce stacked trends, separated according to pressure (different source compositions giving superposed trends). In contrast, diagrams using an 'enrichment-controlled' element give trends separated by the degree of enrichment. As stated above, the separation is actually much better in the case of the source control, than in the depth control. In either case, moving along the trend gives information on the degree of melting (F), with more mafic compositions corresponding to higher degree of melting.

3. From primary melts to granites

The previous discussion focused solely on the composition of primary granitoid melts. It is likely, however, that granitoids (the rocks themselves) do not represent pure liquid composition, and certainly do not reflect primary melt compositions. Several processes can combine to modify the composition of primary melts. These include entrainment of solid phases (restite as well as entrained crystals that formed from the melt itself), mixing with other (mantle-derived?) magmas, assimilation of country rock, and fractional crystallisation. Therefore, it may be difficult to directly link the granite's composition with source conditions.

3.1. Entrainment of solids

In granitoids in general, and in the Archaean crustal (plagioclase-rich) granitoids studied in the present paper, solids entrained from the source with the magma can affect the bulk rock geochemistry of granitoids (effectively, solid-liquid mixtures). This can be either easy to identify in the field, when the granitoids studied are actually diatexites (Sawyer 1998; Moyen *et al.* 2003a; Bédard 2006); or more cryptic, through processes such as restite unmixing (Chappell *et al.* 1987) or entrainment of peritectic minerals (Stevens *et al.* 2007). In all cases however, the net, geochemical effect of these processes is to add part of the source to the melt; the resulting compositions are therefore intermediate between the pure melt and the source. In other words, the net result is to extend the geochemical trend towards the source (the apparent temperature or F, as observed from the trends, will be higher); on the other hand, distinct trends will remain clearly separated (Fig. 2).

3.2. Fractional crystallisation

Fractional crystallisation has the potential to affect the composition of any magmatic rock, and its influence must be assessed. Indeed, on pure geochemical (trace elements) grounds it is possible to dramatically increase e.g. the Sr/Y and La/Yb ratios of melts, therefore moving magmas from one trend to another one (e.g. Bédard 2006).

However, it seems extremely unlikely that fractionation plays a significant role in shaping the geochemical features of TTGM – and in particular, in explaining the differences between different trends: (1) In granites in general, there is now a growing consensus that fractionation plays only a limited role (Clemens *et al.* 2010), and indeed there is no well-documented example for which geochemical trends in granitoids can be ascribed to fractional crystallisation. One does not see why Archaean granitoids would be an exception to this; (2) When well identified, mappable TTG plutons are studied (e.g. the 3·45 Ga Stolzburg pluton of Barberton (Moyen *et al.* 2007)),

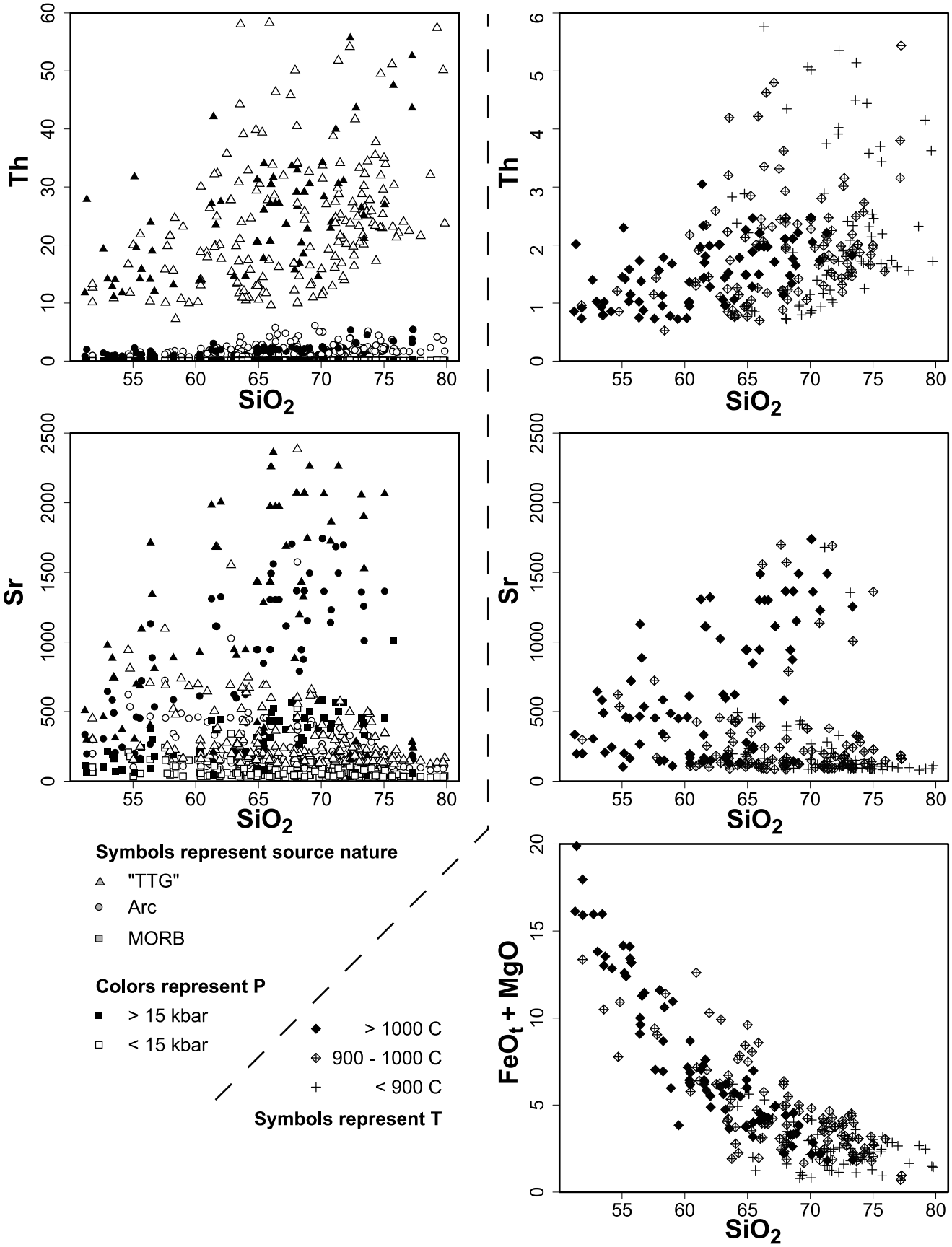

Figure 5 Harker diagrams for one pressure-dependant (Th) and one source-dependant (Sr) element. Compositions recalculated from experimental data. On the left (same caption as for Fig. 3), colours indicate the depth and symbols the nature of the source. Stacked trends as described in the text are obvious, reflecting clearly the different sources for Th, less clearly the depth of melting for Sr (note that there are actually two low-Th trends, that appear superposed due to the low overall abundances, but are nevertheless one order of magnitude different, with typical values <0·1 for the depleted MORB source and ca. 1 ppm for the arc source). On the right, the same diagrams, plus SiO_2 *vs.* FeO+MgO, are drawn using symbols corresponding to different temperatures; the temperature is broadly correlated to the position in the trend (scatter is due to differences related to the water content, the depth of melting, the nature of the source, etc.)

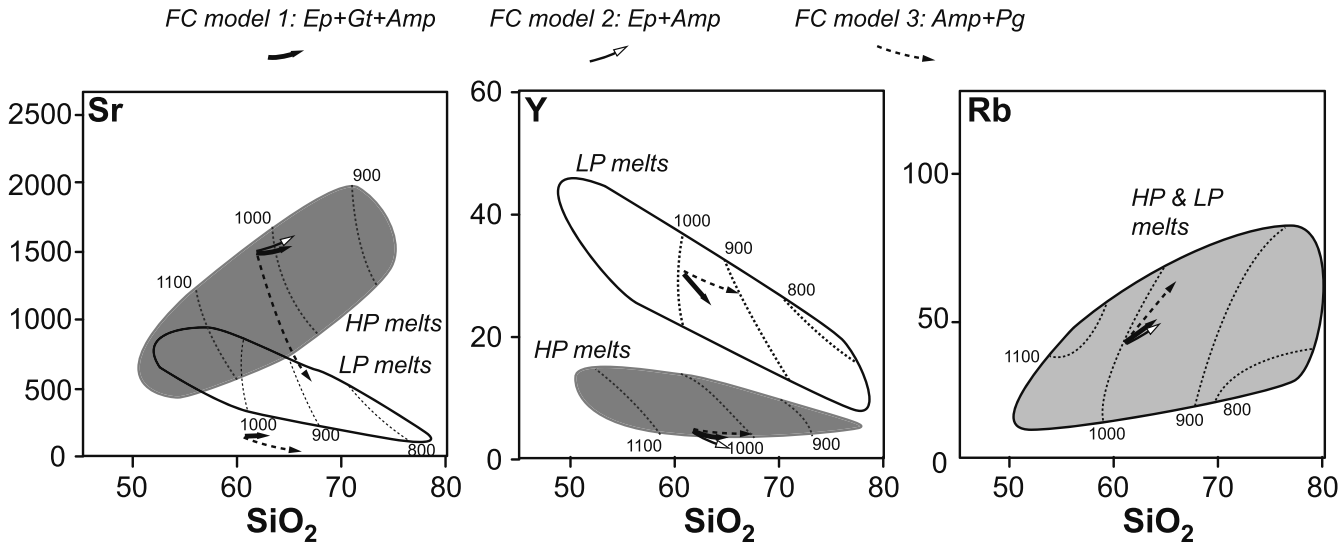

Figure 6 Effects of fractional crystallisation. The low pressure (LP) and high pressure (HP) domains correspond to experimental compositions, compiled from the literature or recalculated as described in the text (section 2.2); HP is >15 kbar and LP<15 kbar, 'isotherms' are schematically depicted, from generalisation of the data from Figure 5. The arrows correspond to the three fractionation models ('FC model') discussed in the text (section 3.2; see also Fig. 1).

the range of compositions – that could possibly be ascribed to fractionation – is actually restricted. Likewise, whenever fractional crystallisation was studied and modelled for major and traces together (Martin 1987), it turned out that it produced only small, short trends (a few SiO_2 percent points, from 67% to 72%). This probably puts an empirical upper limit on the effect of fractionation; (3) While fractional crystallisation can indeed change significantly the trace elements compositions of the melts (especially if phases such as amphibole or garnet do fractionate), the degree of fractionation (especially of mafic minerals) is strongly limited by the available Fe and Mg; even the most primitive TTGs rarely exceed 6–7% of FeO+MgO, meaning that no more than ±30% of a typical, 15–25% FeO+MgO, cumulate (Moyen *et al.* 2007) can fractionate – this does strongly limit the potential of fractionation; (4) Finally, in order to strongly affect the Sr, Y or Yb contents, the cumulate would need to be garnet-rich and therefore to correspond to high pressure fractionation: in other words, an high pressure evolution is required to arrive to compositions similar to the high Sr series, be it from high pressure melting or high pressure fractionation.

To illustrate the last two points above, models of fractionation were calculated at different pressures. Based on phase diagram for water-saturated tonalitic melts and experimental results (Schmidt & Thompson 1996; Fig. 1), three possible cooling and fractionation paths were identified: (1) a high pressure (>15 kbar) evolution, in which clinopyroxene, the liquidus phase, is replaced by epidote and amphibole through peritectic reactions; this results in the fractionation of epidote, garnet and amphibole in proportions of approximately 1:2:4. (2) A medium pressure (ca. 10 kbar) evolution, where a similar peritectic reaction occurs, below the garnet stability field; epidote and amphibole crystallise in proportions close to 1:5. (3) A low pressure (<10 kbar) evolution, corresponding to crystallisation during emplacement within the crust, where the fractionating phases are amphibole and plagioclase in approximately equal proportions, with traces of ilmenite; this is similar to the case modelled by Martin (1987).

In each case, the amount of crystallisation that can be achieved before running out of Fe and Mg is actually small, in the range of 20–30%. This is consistent with the geochemical models of Martin (1987) and does also match the experimental results of Schmidt and Thompson (1996): most of the crystallisation occurs close to the solidus, in the field where quartz and feldspars form. The resulting vectors are plotted on Figure 6, together with the fields obtained for experimental melts as described above. The longest possible trends are the one produced by low-pressure (syn-emplacement?) evolution and fractionation of amphibole + plagioclase; even these are actually short, compared to the range that can be generated by melting trends.

Furthermore, the fractionation vectors are largely superposed to the melting trends. This actually underlines the fact that melting and fractionation are effectively symmetrical processes, and thermodynamically reversible reactions: for given P–T conditions, the melting reaction, say Amp+Pl= Melt+Opx at low pressure, is effectively the same as the fractionation reaction (that consumes the early formed Opx in peritectic reactions) (Stevens *et al.* 1997). In theory both processes are different – crystallisation is generally regarded as 'fractional' and therefore as a disequilibrium process, with instantaneous removal of crystals formed, whereas melting is supposed to be mostly an equilibrium process. Geochemical common wisdom therefore leads to treating both processes in different ways (and with different equations). However, given the increasing recognition that granitic melts have viscosities too high to permit significant solid/melt separation (Giordano *et al.* 2008), and the field and petrological evidence that granites are poorly separated mushes (solid+crystals) (Weinberg 2006; Stevens *et al.* 2007), one may seriously question the 'fractional' nature of crystallisation in granites. If both melting and fractionation are mostly equilibrium processes (or processes with the same 'amount of disequilibrium', so to say), they are therefore perfectly symmetrical and undistinguishable on geochemical grounds. The trends observed for a given unit (one magma batch) can therefore be a combination of melting, or crystallisation, or both. As long as both occur at the same or similar depths, the melting and crystallisation trends will be superposed.

It is therefore concluded (1) that the role of fractionation is actually a second order effect, compared to the role of melting; and that the trends defined by Archaean TTGM are, at least in first approximation, essentially melting trends; and (2) that even when fractionation plays a role, it will affect the 'within

trend' variability, but not the 'inter-trend' diversity. Once generated, granitic melts remain confined to their trend, regardless of subsequent modifications.

3.3. Mixing with mantle-derived melts

Mixing with melts from different origins (typically, mantle derived melts, such as sanukitoids) has the greatest potential to move the compositions away from the main, melting-related trends. Therefore, all the interpretation proposed in the present paper (and in particular, the Δ diagrams discussed below (see section 4)) holds if, and only if, it can be demonstrated that the melts are purely crustal melts, with no mantle component. In other words, the interpretation proposed must not be used indistinctly, but rather at the end of a comprehensive petrological study.

Some indications that mantle melts (or interactions with the mantle) did play a role, and therefore that the present analyses do not hold, are: (1) field evidences such as microgranular mafic enclaves (Didier *et al.* 1982; Didier & Barbarin 1991); and (2) geochemical evidence, as particularly well expressed in sanukitoids (Shirey & Hanson 1984; Stern *et al.* 1989; Stern & Hanson 1991; Smithies & Champion 2000; Moyen *et al.* 2003b; Martin *et al.* 2005, 2010; Martin & Moyen 2005, 2007). Coupled enrichment in LILE and compatible elements, i.e. high K_2O values for low SiO_2 and high MgO (as an empirical criteria) K_2O contents >2%, for MgO>2%, is a reasonably strong indication of a mantle component (Miller *et al.* 2008), high contents in Rb, Th, Ni, Cr and Sr at the same time, etc.

3.4. The meaning of geochemical trends

The discussion above shows that some care must be exercised in using the geochemistry of granitic rocks to discuss source processes, and that the approach outlined here should not replace a careful petrological and geochemical interpretation. However, if the composition of individual samples from a suite can vary considerably, the 'trend' (be it a melting, or a differentiation, controlled trend) that the suite as a whole forms provides the best reflection of the nature of the source and of the melting conditions.

The shapes and positions of the trends (here, in Harker type diagrams) are primarily controlled by the nature of the source and the depth of melting, provided some assumptions (e.g., no mantle influence, etc.) can be demonstrated to be true. The differences between granites of different origins is typically larger than the differences induced by post-melting processes: i.e. the petrogenetic processes that form the primary melt typically have a compositional signature that survives the petrogenetic processes that subsequently modify primary melt compositions. On the other hand, the very nature of the 'trend' approach erases any information on the degree of melting (and/or of fractionation, and/or of solid entrainment); these processes are not resolved by this approach, as they essentially result in moving compositions along the trends, but not from one to another.

4. Interpreting the geochemical signal in terms of depth and enrichment

As demonstrated, granitoid series from different origins (in terms of source or pressure of melting) should define 'stacked' trends in Harker diagrams. Diagrams using incompatible elements (LILE, K_2O, LREE, HFSE such as Th, Zr or Nb) will reflect the degree of source enrichment, whereas diagrams using Sr, Na, Al or Eu will give an indication of plagioclase stability or instability, and diagrams using HREE or Y will reflect the absence or presence of garnet – the latter two being proxies for the pressure of melting.

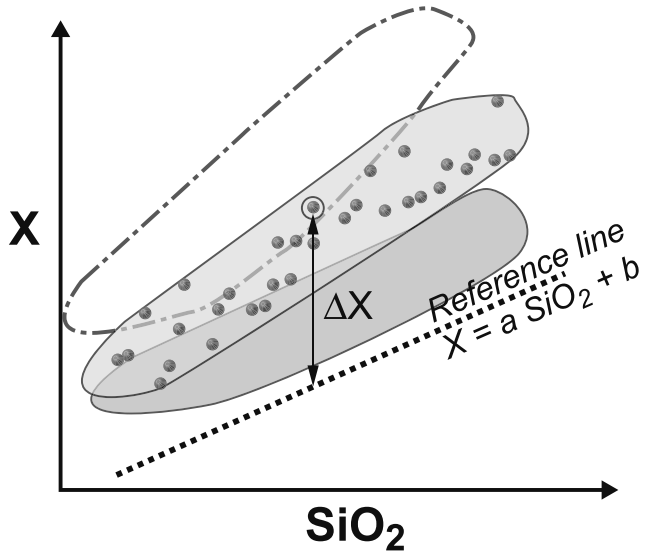

Figure 7 Building delta-diagrams. Rocks from different granite suites will typically depict stacked trends in Harker-type diagrams (X *vs.* SiO_2), such that the absolute value of the concentration in an element X is ambiguous. On the other hand, the trends are distinctive, and reflect different degrees of enrichment or depth of melting. By calculating, for each sample, the distance between the analysis and a reference line, the delta parameters mostly reflects the trend to which a sample belong – more than its absolute concentration.

Devising diagrams showing both characteristics at the same time is problematic. For example, diagrams that simply plot one 'source-enrichment tracer' against one 'depth tracer' (e.g., plotting La *vs.* Yb or Rb *vs.* Sr) will be complicated by the fact that each series evolves along its own trend (in Harker diagrams), and that all elements vary as a function of SiO_2 – resulting in large overlaps for granites from different origins. Trace element ratios are commonly used in geochemistry to avoid this problem, and this is why diagrams such as Sr/Y *vs.* Y or La/Yb *vs.* Yb largely behave as pressure indicators.

In the present paper a new set of diagrams is developed that can simultaneously reveal information relating both to source enrichment (composition) and to pressure of melting. These diagrams explicitly remove the contribution of SiO_2-related evolution, and use as an indicator a new parameter ΔX, where X is any given element. For each element, ΔX is taken as the distance between the analysed value, and a reference line, in a SiO_2–X (Harker) diagram (Fig. 7). The choice of the reference line is not critical, but because these diagrams were developed initially to assist the interpretation of Archaean plagioclase-rich granites, the divide between the Pilbara high- and low-Sr series (Champion & Smithies 2007b) was chosen as a reference (Fig. 8). Using another line with the same slope would just uniformly move the values up or down, without changing their relative position; using another line with a different slope will have greater effects. On the other hand, as long as the reference line chosen is one that fits the global evolution and shape of the geochemical trends, the differences will be relatively small. Problems would arise only if the reference line was at a large angle with the trend's slope; in this case, the delta parameter would vary with SiO_2, therefore negating the expected gains. Plotting SiO_2 against delta (not shown) does help in testing whether the reference line used is correct (the resulting diagram should yield flat or nearly flat trends), and the parameters of the reference line were tested and adjusted by trial and error.

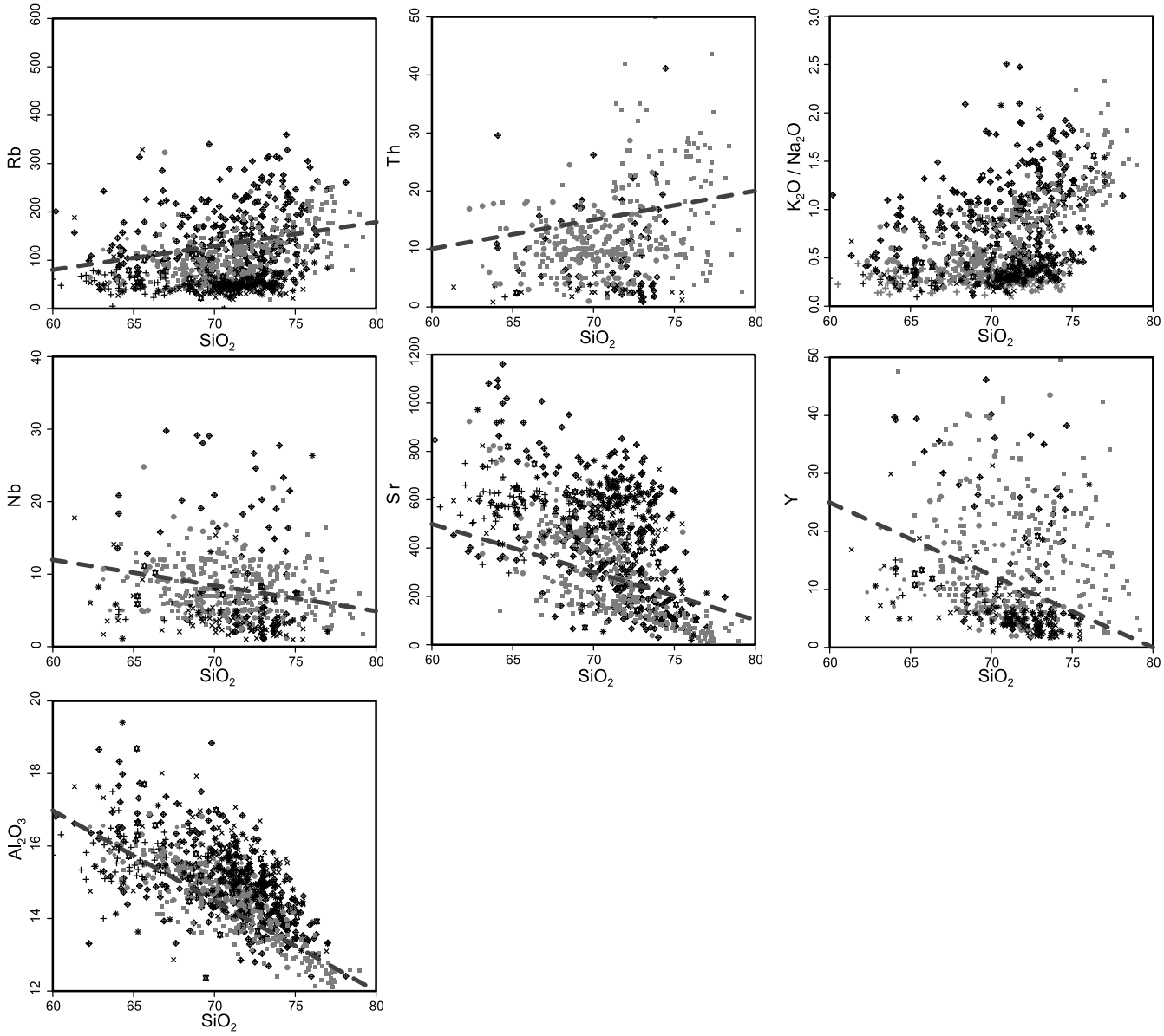

Figure 8 Harker diagrams for Pilbara and Barberton rocks. The dashed grey line is the reference line used for calculating the delta parameter. Stacked trends, reflecting either different sources (Rb, Th, K_2O/Na_2O) or the depth of melting (Sr, Y, Al_2O_3, Nb to some degree) are evident. Pilbara data (Champion & Smithies 2007b) are in grey and Barberton data (Moyen *et al.* 2007) in black. Different symbols correspond to different plutons as in Figure 10.

Table 2 Constants used in the calculation of delta parameters. For each element, $\Delta X = X - (a\ SiO_2 + b)$. a and b are empirically estimated, by using a reference line (plotted in Fig. 8) that separates Pilbara's different sub-series (Champion *et al.* 2007b).

	a	*b*
Sr	− 20	1700
Y	− 1·25	100
Nb	− 0·35	33
Th	0·5	− 20
Rb	5	− 220
A_2O_3	− 0·25	32

If the equation of the reference line is written as $X = a\ SiO_2 + b$, we define $\Delta X = X - (a\ SiO_2 + b)$ (Table 2). In theory, for very incompatible elements (D=0), the evolution line related to melting (or fractionation) should rather be a hyperbolic or exponential curve (as their concentration is $C_1 = C_0/F$, with F being a function of SiO_2), and it would be more rigorous to use such a curve as a reference line. In practice, however, this does not result in a significant improvement over 'linear' fits. It was also found that ΔK could be readily substituted by the simpler K_2O/Na_2O parameter, since Na concentrations are not strongly affected by the degree of source enrichment; they are affected by the depth of melting, but this effect is small compared to the effect source enrichment has on the K_2O/Na_2O ratio.

Most of the variance in the geochemical signal is related to differentiation, with SiO_2 contributing most of it. The diagrams presented aim at eliminating the variance related to the differentiation component, to focus on the smaller components of the variance. In essence, this approach is fairly similar to the 'sliding normalisation' of Liégeois *et al.* (1998), or the 'oxide*' parameters of Bonin (1986).

Diagrams plotting ΔA *vs.* ΔB – where A is a depth-controlled element (Sr, Y, HREE) and B is an enrichment-controlled element (LILE, LREE, some HFSE) – can therefore be interpreted as a 'depth of melting *vs.* source enrichment

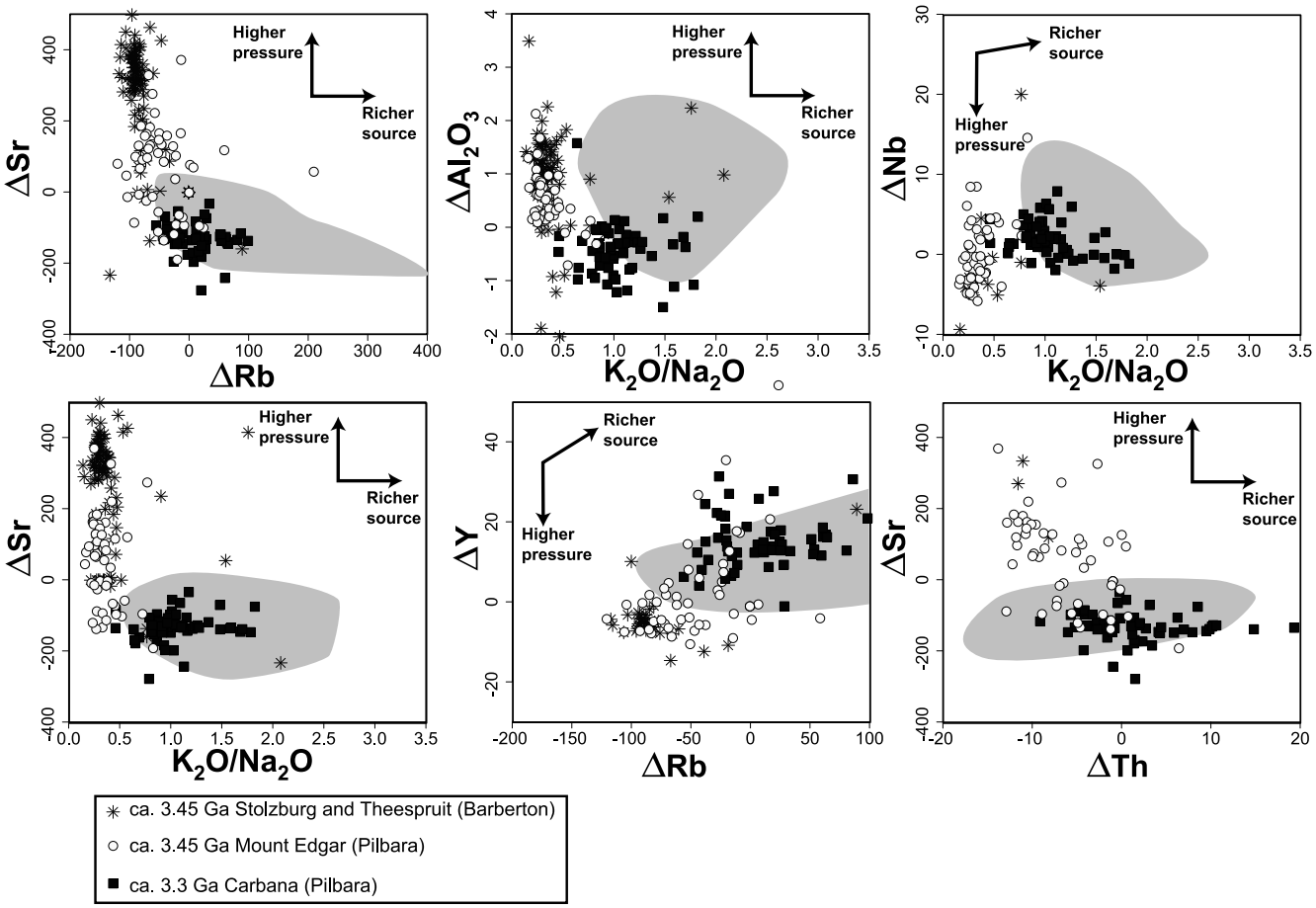

Figure 9 Identification of granitoid groups with different geochemical signatures, using three units as an example. The three examples used are the ca. 3·45 Ga plutons in Barberton (Moyen *et al.* 2007); the ca. 3·45 Ga Mount Edgar suite of the Pilbara craton (Champion & Smithies 2007b), and the ca. 3·3 Ga Carbaa suite of the Pilbara. The grey field corresponds to the field of post-Archaean S-type granites (compilation from the literature, >350 analyses). Diagrams use either the delta parameter as explained in the text, or K_2O/Na_2O. On each diagram, the arrows show qualitatively the effects of pressure and source enrichment. In all diagrams, there is a clear split between two angled trends, one going towards deep sources (relatively depleted) and one towards shallower, but richer, sources. S-type granites typically plot along the shallow/rich trend.

diagram'. As discussed above, effects relating to the melt fraction, or indeed to further differentiation, essentially result in moving the compositions along one trend and therefore have been mostly removed from the geochemical signal.

However, such diagrams should not be used indiscriminately and do not replace a comprehensive petrological analyses; one must be especially aware of potential problems such as (1) the role of mantle components, that will falsify many of the assumptions these diagrams are based on; or (2) a-typical sources or processes, resulting in an ambiguous (or misleading) geochemical signal. A telltale sign would be the de-correlation between geochemical indicators supposedly carrying the same information (i.e., Sr and Y, or Rb and K); such decorrelations should always be treated as a sign of potential 'problems' and evidence that some of the basic assumptions of the method do not hold.

5. Application to meso-Archaean granites from Barberton and the Pilbara

Delta diagrams were applied to granites from the two reasonably well-known meso-Archaean (3·5–3·1 Ga) provinces, the Barberton granite–greenstone terrane of South Africa (BGGT) (Moyen *et al.* 2007) and the Eastern Pilbara Craton of Australia (Champion & Smithies 2007b). These provinces are dominated by seemingly similar granitoids.

5.1. Different types of TTGM associations

Using the delta diagrams devised as explained above provides a convenient way to compare the geochemistry of different granitoids; compared to Harker-type diagrams, the interpretation is easier, as most of the differentiation component (i.e., SiO_2-related scatter) is removed; compared to classical spidergrams, the resulting diagrams are less cluttered. Delta diagrams using a range of enrichment-related (K_2O/Na_2O, Rb, Th) and pressure-related (Sr, Nb, Y, Al_2O_3) elements were first used to illustrate the fact that different series have very distinctive geochemical signatures.

Figure 9 shows the delta diagram for three plutonic units in Barberton and the Pilbara craton; they were chosen because they show fairly extreme geochemical characteristics, and are effectively representative end-members that illustrate the validity of this approach. For comparison, the field for Phanerozoic S-type granites was also plotted on these diagrams. These rocks derive from potassic metasediment-dominated sources, where K-feldspar and possibly muscovite or aluminium silicates play a significant role during melting. Predictably, they plot in the 'low-pressure, enriched sources' region of the diagrams, consistent with their origin by intracrustal melting.

The ca. 3·45 Ga-old plutons from Barberton (Theespruit, Stolzburg) are characterised by their position in the 'deep, depleted' quarter of the diagrams; this reflects deep melting of

a fairly depleted (or not enriched) source (Clemens *et al*. 2006; Moyen *et al*. 2007). The ca. 3·3 Ga Carbana suite in the Pilbara Craton (Champion & Smithies 2007b) shows an opposite behaviour (shallow melting of enriched sources), in fact largely overlapping with the field of S-type granites. Between the two, the 3·45 Ga Mont Edgar granitoids (Pilbara: Champion & Smithies 2007b) reflect the shallower melting of a source maybe marginally more enriched than the source of Barberton examples.

5.2. Regional histories of granitoid plutonism

Delta diagrams provide a simple tool to discuss and compare the geochemistry of plutonic suites, and more importantly, to understand their geodynamical signification. As an illustration, the evolution of granitoid compositions between ca. 3·5 Ga and 3·2 Ga is now compared, in both Barberton and the Pilbara.

In Barberton, three successive, well-defined plutonic cycles are known before 3·2 Ga (Anhaeusser & Robb 1980, 1983a; Anhaeusser *et al*. 1983; Clemens *et al*. 2006; Moyen *et al*. 2007):

- At 3·55–3·51 Ga, a small composite pluton (the Steynsdorp pluton) made of tonalites and granodiorites is formed south-east of the main greenstone belt;
- At 3·45 Ga, the trondhjemitic plutons of the 'Stolzburg domain' are formed (mainly the Stolzburg and Theespruit pluton, but also some smaller occurrences).
- At 3·27–3·21 Ga, large trondhjemitic to tonalitic plutons are formed west and north of the greenstone belt (the Badplaas, Nelshoogte and Kaap Valley plutons).

A more complicated pattern emerges for the Eastern Pilbara Craton. There are four successive 'supersuites' older than 3·1 Ga, but these do not show systematic relative geographic distribution – i.e. rocks from all suites occur throughout the terrain (Champion & Smithies 2007b). These suites are the Callina supersuite (3·45–3·5 Ga), the Tambina supersuite (3·45–3·4 Ga, broadly synchronous with the Stolzburg and associated plutons in Barberton), the Emu Pool supersuite (ca. 3·3 Ga) and the Cleland supersuite (3·3–3·2 Ga, synchronous with the Badplaas, Nelshoogte and Kaap Valley plutons). Within each of the supersuites, both 'high Al' and 'low Al' types have been identified and both 'LILE-enriched' and 'normal' types are present.

Champion & Smithies (2007b) and Moyen *et al*. (2007) provide a detailed petrogenetic interpretation of the Pilbara and Barberton granites. Harker diagrams for all the meso-Archaean rocks (Fig. 8) show clear 'stacked' trends. Very high Sr concentrations distinguish the Barberton 3·45 Ga group, whilst the low-Al, low-Sr 3·3 Ga Emu Pool suite of the Pilbara Craton is also clearly identified. Likewise, the high K/Na, and corresponding high Rb, of part of Pilbara's Emu Pool suite, and of Barberton's GMS, is clearly illustrated.

'Delta' diagrams illustrate very clear differences between the supersuites (Fig. 10), but allow these differences to be more readily interpreted in terms of petrogenesis. Collectively, the data define 'angled' trends separating two end-member processes: deep melting of depleted sources (melting along a subducted slab?) and shallow melting of richer sources (intracrustal melting?). Rocks with compositions that can be interpreted as reflecting either deep melting of rich sources or shallow melting of depleted sources appear to be less common. Three main types of granitoids are represented in the two provinces, as described previously:

- The majority of the samples belong to a group evolving by shallow or medium-pressure melting of depleted to poorly enriched sources. The 3·45 Ga Mt Edgar and Shaw suites in the Pilbara belong to this type, as do most of the suites from the 3·3 Ga Emu Pool supersuite, and in Barberton, most of the Steynsdorp pluton and of the ca. 3·2 Ga intrusive rocks.
- The second type, commonly associated, is represented by shallow melts of enriched sources. They form a minority component in the Steynsdorp and 3·2 Ga plutons of Barberton (Badplaas in particular); and are abundant in the Emu Pool (3·3 Ga) and Cleland (3·25 Ga) supersuites of the Pilbara. Champion & Smithies (2007b) proposed that this 'high-LILE granite group' from the Pilbara Craton suite are a result of recycling an enriched, felsic crustal source, likely over a range of pressures lower than those required to stabilise abundant garnet and destabilise plagioclase.
- The ca. 3·45 Ga granite group from Barberton is distinctive in typically having a combination of higher Sr and lower Y and Yb than other granites. This was interpreted to reflect high-pressure melting of a depleted (metabasaltic) source – the most commonly invoked model for Archean granites of variably TTG-like composition.

The crustal recycling component (melting of an enriched, felsic source) that is proposed for some of the Pilbara rocks (high-LILE), and the Barberton GMS suite, is well reflected by high K_2O/Na_2O, high ΔRb values, corresponding to horizontal extensions along the X-axes in the diagrams. It also correlates with low-pressure signatures. A high-pressure origin for the ca. 3·45 Ga group in Barberton is also clearly established, as is the depleted nature of their source, as they plot along the Y-axes. As outlined above, the 'depth-related' signal tends to be less clear than the 'source related' signal in delta diagrams. This is obvious in diagrams using ΔSr or ΔY as a depth-related parameter, in which the 'enrichment' trend is slightly oblique to, rather than parallel with, the X-axes (in other words, there is a positive correlation between Rb or K/Na, and Sr or Y).

In geodynamic terms, it is noticeable that the granitoids geochemistry gives a fairly different picture for both cratons, even though they form in a broadly synchronous way (Zegers *et al*. 1998). The Steynsdorp event (3·55–3·51 Ga) has no documented equivalent in the Pilbara. The ca. 3·45 Ga event is represented in Barberton by a short-lived burst of high-pressure granitoids (Stolzburg, Theespruit), but corresponds in the Pilbara to a much longer-lived (80 Ma, Callina and Tambina Supersuites) period of melts generated from possibly similar sources, but at shallower depths. The massive ca. 3·3 Ga event (the Emu Pool supersuite in the Pilbara), that is proposed to be concomitant with the main some-forming event (Van Kranendonk *et al*. 2007), consists in mostly shallow melting of mixed sources; it has no match in Barberton, except the small (and poorly documented) Stentor Pluton (Kamo & Davis 1994). Finally, both cratons do show some plutonic activity at 3·25–3·2 Ga; whereas it is the major event in Barberton, where a range of compositions reflect time and space shifts in melting regions (Moyen *et al*. 2007), it is only a minor component (the Cleland Supersuite) of the evolution of the East Pilbara, in which only enriched shallow sources are involved.

6. Conclusion

The first order source of variance in the composition of Archaean crustal (plagioclase-rich, or TTGM) granitoids is related to the position of individual samples on 'differentiation trends' – regardless of the origin of such trends. However, this

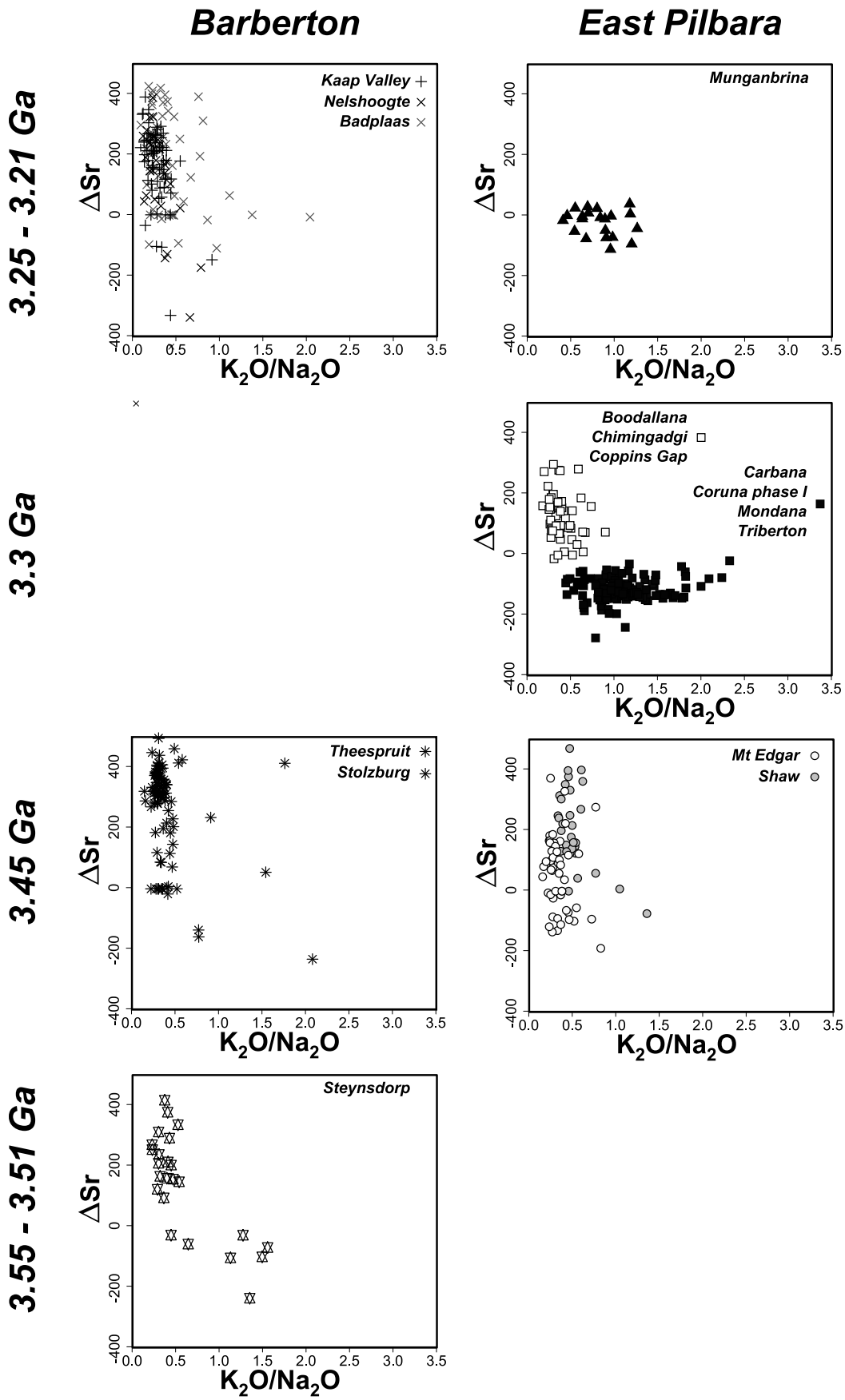

Figure 10 Delta diagrams for Barberton and Pilbara rocks. Due to space constraint, only one diagram (K_2O/Na_2O *vs.* ΔSr) was plotted for each suite; this diagram is chosen as being one of the most informative (compare Fig. 9), and also because these three elements are analysed in all the datasets, even for samples from the literature whose composition was obtained before the advent of cheap trace elements analyses. Barberton samples on the left, Pilbara on the right; samples are grouped by chronological order, bottom to top. Discussion in text.

range of composition carries little information on petrogenetic processes that are 'hidden' in second-order variations. The relevant petrogenetic information (source enrichment and depth of melting) is 'hidden' behind the differentiation history, and is reflected by the position of the trend to which a sample belongs, rather than the composition of that individual sample.

Constructing diagrams that allow the geochemistry of granitic rocks to be described as belonging to a specific trend, rather than in terms of absolute composition, directly facilitates interpretations about source composition as well the depth of melting. This in turn places constrains on the geometry, and to some degree the P–T condition, of a crustal segment during granite formation.

Applying that approach to the mid-Archaean Barberton and Pilbara granites reveals unexpected petrogenetic diversity for magmas typically referred to as 'TTGs'. Melting depths as well as source compositions vary widely, such that generalisations about the compositions and origins of 'TTGs' become rather meaningless. These revelations, when considered in conjunction with the contrasting way particular compositional groups of granites are spatially and temporally distributed within each of these contemporaneous cratons, should lead to more robust interpretations regarding the distinct geodynamic environments that may have prevailed.

7. Acknowledgements

JFM's work in Barberton was funded through a NRF grant awarded to A. Kisters, University of Stellenbosch (grant no. NRF 2053186), and a 'starting grant' by the University of Stellenbosch.

8. References

Anhaeusser, C. R. & Robb, L. J. 1980. Regional and detailed field and geochemical studies of archean trondhjemitic gneisses, migmatites and greenstone xenoliths in the southern part of the Barberton mountain land, South Africa. *Precambrian Research* **11**, 373–97.

Anhaeusser, C. R., Robb, L. J. & Viljoen, M. J. 1983. Notes on the Provisional geological map of the Barberton greenstone belt and surrounding granitic terrane, eastern Transvaal and Swaziland (1:250 000 colour map). *In* Anhaeusser, C. R. (ed.) *Contributions to the geology of the Barberton Mountain Land. National Geodynamic Programme, Barberton Project. Geological Society of South Africa Special Publication* **9**, 221–3.

Anhaeusser, C. R. & Robb, L. J. 1983a. Chemical analyses of granitoid rocks from the Barbeton Mountain Land. *In* Anhaeusser, C. R. (ed.) *Contributions to the geology of the Barberton Mountain Land. National Geodynamic Programme, Barberton Project. Geological Society of South Africa Special Publication* **9**, 189–219.

Anhaeusser, C. R. & Robb, L. J. 1983b. Geological and geochemical characteristics of the Heeenveen and Mpuluzi batholiths south of the Barberton greenstone belt, and preliminary thoughts on their petrogenesis. *In* Anhaeusser, C. R. (ed.) *Contributions to the geology of the Barberton Mountain Land. National Geodynamic Programme, Barberton Project. Geological Society of South Africa Special Publication* **9**, 131–51.

Bédard, J. 2006. A catalytic delamination-driven model for coupled genesis of Archaean crust and sub-continental lithospheric mantle. *Geochimica et Cosmochimica Acta* **70**, 1188–214.

Bédard, J. 2010. Parental magmas of Grenville Province massif-type anorthosites, and conjectures about why massif anorthosites are restricted to the Proterozoic. *Earth and Environmental Science Transactions of the Royal Society of Edinburgh* **100** (for 2009), 77–103.

Belcher, R. W. & Kisters, A. F. M. 2006. Progressive adjustments of ascent and emplacement controls during incremental construction of the 3·1 Ga Heerenveen batholith, South Africa. *Journal of Structural Geology* **28**, 1406–21.

Bonin, B. 1986. *Ring complexes and anorogenic magmatism*. Amsterdam: Elsevier.

Champion, D. C. & Smithies, R. H. 1999. Archaean granites of the Yilgarn and Pilbara cratons: secular changes. *In* Barbarin, B. (ed.) *The Origin of Granites and Related Rocks, Fourth Hutton Symposium Abstracts*, 137. Clermont-Ferrand, France: BRGM.

Champion, D. C. & Smithies, R. H. 2007a. Three billion years of granite magmatism: Paleoarchaean to Permian granites of Australia. *In* Miller, J. A. & Kisters, A. F. M. (eds) *6th International Hutton Symposium Abstract Volume & Program Guide*, 63–64. Stellenbosch, South Africa: Department of Geology, Geography & Environmental Sciences, University of Stellenbosch. 236 pp.

Champion, D. C. & Smithies, R. H. 2007b. Geochemistry of Paleoarchean granites of the East Pilbara terrane, Pilbara Craton, Western Australia: implications for early Archean crustal growth. *In* Van Kranendonk, M. J., Smithies, R. H. & Bennet, V. (eds) *Earth's Oldest Rocks. Developments in Precambrian Geology* **15**, 369–410. Amsterdam: Elsevier.

Chappell, B. W., White, A. J. R. & Wyborn, D. 1987. The Importance of Residual Source Material (Restite) in Granite Petrogenesis. *Journal of Petrology* **28** (6), 1111–38.

Clemens, J. D., Yearron, L. M. & Stevens, G. 2006. Barberton (South Africa) TTG magmas: geochemical and experimental constraints on source-rock petrology, pressure of formation and tectonic setting. *Precambrian Research* **151**, 53–78.

Clemens, J. D., Helps, P. A. & Stevens, G. 2010. Chemical structure in granitic magmas – a signal from the source? *Earth and Environmental Science Transactions of the Royal Society of Edinburgh* **100** (for 2009), 159–72.

Clemens, J. C. & Vielzeuf, D. 1987. Constraints on melting and magma production in the crust. *Earth and Planetary Science Letters* **86**, 287–306.

Collins, W. J. 2007. Using the mantle to unravel granite geodynamics. *In* Miller, J. A. & Kisters, A. F. M. (eds) *6th International Hutton Symposium Abstract Volume & Program Guide*, 72–73. Stellenbosch, South Africa: Department of Geology, Geography & Environmental Sciences, University of Stellenbosch, 236 pp.

Condie, K. C. 1981. *Archean greenstone belts*. Amsterdam: Elsevier.

Didier, J. & Barbarin, B. 1991. *Enclaves and Granite Petrology*. Amsterdam: Elsevier.

Didier, J., Duthou, J. L. & Lameyre, J. 1982. Mantle and crustal granites: genetic classification of orogenic granites and the nature of their enclaves. *Journal of Volcanology and Geothermal Research* **14**, 125–32.

Feng, R. & Kerrich, R. 1992. Geochemical evolution of granitoids from the Archean Abitibi southern volcanic zone and the Pontiac subprovince, Superior Province, Canada: implications for tectonic history and source regions. *Chemical Geology* **98**, 23–70.

Foley, S. F., Barth, M. G. & Jenner, G. A. 2000. Rutile/melt partition coefficients for trace elements and an assessment of the influence of rutile on the trace element characteristics of subduction zone magmas. *Geochimica et Cosmochimica Acta* **64**, 933–8.

Foley, S. F., Tiepolo, M. & Vannucci, R. 2002. Growth of early continental crust controlled by melting of amphibolite in subduction zones. *Nature* **417**, 637–40.

Giordano, G., Russel, J. & Dingwell, D. B. 2008. Viscosity of magmatic liquids: a model. *Earth and Planetary Science Letters* **271**, 123–34.

Jahn, B. 1994. Géochimie des granitoïdes archéens et de la croûte primitive. *In* Hagemann, R., Jouzel, J., Treuil, M. & Turpin, L. (eds) *La géochimie de la Terre*. CEA-Masson.

Jahn, B., Auvray, B., Blais, S., Capdevila, R., Cornichet, J., Vidal, F. & Hammeurt, J. 1980. Trace elements geochemistry and petrogenesis of Finnish greenstone belts. *Journal of Petrology* **21**, 201–44.

Kamo, S. L. & Davis, D. W. 1994. Reassessment of Archean Crustal Development in the Barberton Mountain Land, South-Africa, Based on U–Pb Dating. *Tectonics* **13** (1), 167–92.

Liégeois, J. P., Navez, J., Hertogen, J. & Black, R. 1998. Contrasting origin of post-collisional high-K calc-alkaline and shoshonitic versus alkaline and peralkaline granitoids. The use of sliding normalization. *Lithos* **45**(1–4), 1–28.

Martin, H. 1987. Petrogenesis of Archaean trondhjemites, tonalites and granodiorites from eastern Finland; major and trace element geochemistry. *Journal of Petrology* **28** (5), 921–53.

Martin, H. 1994. The Archean grey gneisses and the genesis of the continental crust. *In* Condie, K. C. (ed.) *Archean crustal evolution. Developments in Precambrian Geology* **11**, 205–59. Amsterdam: Elsevier.

Martin, H., Smithies, R. H., Rapp, R. P., Moyen, J.-F. & Champion, D. C. 2005. An overview of adakite, tonalite–trondhjemite–granodiorite (TTG) and sanukitoid: relationships and some implications for crustal evolution. *Lithos* **79** (1–2), 1–24.

Martin, H., Moyen, J.-F. & Rapp, R. 2010. The sanukitoids series: magmatism at the Archaean–Proterozoic transition. *Earth and Environmental Science Transactions of the Royal Society of Edinburgh* **100** (for 2009), 15–33.

Martin, H. & Moyen, J.-F. 2005. The Archaean–Proterozoic transition: sanukitoid and Closepet-type magmatism. *Mineralogocial Society of Poland Special Papers* **26**, 57–68.

Martin, H. & Moyen, J.-F. 2007. Sanukitoid and Closepet-type magmatism: the Archaean–Proterozoic transition. *In* Miller, J. A. & Kisters, A. F. M. (eds) *6th International Hutton Symposium Abstract Volume & Program Guide*, 129–30. Stellenbosch, South Africa: Department of Geology, Geography & Environmental Sicences, University of Stellenbosch. 236 pp.

Miller, J. A., Moyen, J.-F. & Benn, K. 2008. The 2·74–2·66 Ga Kenogamissi complex (Abitibi): evolving sources of plutons mirroring geodynamics. *Geochimica et Cosmochimica Acta* **72** (12S), A629.

Montel, J. M. & Vielzeuf, D. 1997. Partial melting of metagreywackes, part II. Compositions of minerals and melts. *Contributions to Mineralogy and Petrology* **128**, 176–96.

Moyen, J.-F., Martin, H., Jayananda, M. & Peucat, J.-J. 2003a. *Magmatism during the accretion of the late Archaean Dharwar Craton (South India): sanukitoids and related rocks in their geological context*. Abstracts from EGS–AGU–EUG Joint Assembly, Nice, France, 6–11 April 2003, Abstract EAE03-A-00516.

Moyen, J.-F., Martin, H., Jayananda, M. & Auvray, B. 2003b. Late Archaean granites: a typology based on the Dharwar Craton (India). *Precambrian Research* **127** (1–3), 103–23.

Moyen, J.-F., Stevens, G. & Kisters, A. F. M. 2006. 3·2 Ga high-pressure, low-temperature metamorphism in the Barberton greenstone belt: the evidence for Archaean mountain belts and subduction zones. *In* Condie, K. C., Kröner, A. & Stein, R. J. (eds) *When did plate tectonics begin on Earth? Theoretical and empirical constraints*. GSA Penrose Conference, Lander, Wyoming, 13–18 June 2006. Boulder, Colorado: Geological Society of America.

Moyen, J.-F., Stevens, G., Kisters, A. F. M. & Belcher, R. W. 2007. TTG plutons of the Barberton granitoid–greenstone terrain, South Africa. *In* Van Kranendonk, M. J., Smithies, R. H. & Bennet, V. (eds) *Earth's Oldest rocks. Developments in Precambrian geology*, 606–68. Amsterdam: Elsevier.

Moyen, J.-F. & Stevens, G. 2006. Experimental constraints on TTG petrogenesis: implications for Archean geodynamics. *In* Benn, K., Mareschal, J.-C. & Condie, K. C. (eds) *Archean geodynamics and environments. AGU Geophysical Monograph* **164**, 149–78. Washington, DC: American Geophysical Union.

Patiño-Douce, A. E. & Beard, J. S. 1995. Dehydration-melting of Bt gneiss and Qtz amphibolite from 3 to 15 kB. *Journal of Petrology* **36**, 707–38.

Patiño-Douce, A. E. 2005. Vapor-absent melting of tonalite at 15–32 kbar. *Journal of Petrology* **46** (2), 275–90.

Rapp, R. P., Watson, E. B. & Miller, C. F. 1991. Partial melting of amphibolite/eclogite and the origin of Archaean trondhjemites and tonalites. *Precambrian Research* **51**, 1–25.

Rapp, R. P. & Watson, E. B. 1995. Dehydration melting of metabasalt at 8–32 kbar: implications for continental growth and crust-mantle recycling. *Journal of Petrology* **36** (4), 891–931.

Robb, L. J. 1983. Geological and geochemical characteristics of late granite plutons in the Barberton region and Swaziland, with an emphasis on the Dalmein pluton – a review. *In* Anhaeusser, C. R. (ed.) *Contributions to the geology of the Barberton Mountain Land. National Geodynamic Programme, Barberton Project. Geological Society of South Africa Special Publication* **9**, 153–67.

Sawyer, E. W. 1998. Formation and evolution of granite magmas during crustal reworking; the significance of diatexites. *Journal of Petrology* **39** (6), 1147–67.

Schmidt, M. W., Dardon, A., Chazot, G. & Vannucci, R. 2004. The dependence of Nb and Ta rutile-melt partitioning on melt composition and Nb/Ta fractionation during subduction processes. *Earth and Planetary Science Letters* **226**, 415–32.

Schmidt, M. W. & Poli, S. 1998. Experimentally based water budgets for dehydrating slabs and consequences for arc magma generation. *Earth and Planetary Science Letters* **163**, 361–79.

Schmidt, M. W. & Thompson, A. B. 1996. Epidote in calc-alkaline magmas: an experimental study of stability, phase relationships and the role of epidote in magmatic evolution. *American Mineralogist* **81**, 462–74.

Shaw, D. M. 1970. Trace Element Fractionation During Anatexis. *Geochimica et Cosmochimica Acta* **34** (2), 237–43.

Shirey, S. B. & Hanson, G. N. 1984. Mantle-derived Archaean monzodiorites and trachyandesites. *Nature* **310**, 222–4.

Skjerlie, K. & Patiño-Douce, A. E. 2002. The fluid-absent partial melting of a zoisite bearing quartz eclogite from 1·0 to 3·2 GPA: implications for melting of a thickened continental crust and for subduction-zone processes. *Journal of Petrology* **43**, 291–314.

Smithies, R. H. & Champion, D. C. 2000. The Archaean high-Mg diorite suite: Links to Tonalite–Trondhjemite–Granodiorite magmatism and implications for early Archaean crustal growth. *Journal of Petrology* **41** (12), 1653–71.

Stern, R. A., Hanson, G. N. & Shirey, S. B. 1989. Petrogenesis of mantle-derived, LILE- enriched Archean monzodiorites and trachyandesites (sanukitoids) in Southwestern Superior Province. *Canadian Journal of Earth Sciences* **26**, 1688–712.

Stern, R. A. & Hanson, G. N. 1991. Archaean high-Mg granodiorites: a derivative of light rare earth enriched monzodiorite of mantle origin. *Journal of Petrology* **32**, 201–38.

Stevens, G., Clemens, J. D. & Droop, G. T. R. 1997. Melt production during granulite-facies anatexis: experimental data from 'primitive' metasedimentary protoliths. *Contributions to Mineralogy and Petrology* **128**, 352–70.

Stevens, G., Villaros, A. & Moyen, J.-F. 2007. Selective peritectic garnet entrainment as the origin of geochemical diversity in S-type granites. *Geology* **35** (1), 9–12.

Thompson, R. N. 1982. British tertiary volcanic province. *Scottish Journal of Geology* **18**, 49–107.

Van Kranendonk, M. J., Hickman, A. H., Smithies, R. H. & Champion, D. C. 2007. Paleoarchean development of a continental nucleus: the East Pilbara terrane of the Pilbara craton, Western Australia. *In* Van Kranendonk, M. J., Smithies, R. H. & Bennet, V. (eds) *Earth's Oldest rocks. Developments in Precambrian Geology* **15**, 307–37. Amsterdam: Elsevier.

Vielzeuf, D. & Montel, J. M. 1994. Partial melting of metagreyackes. Part I. Fluid-absent experiments and phase relationships. *Contributions to Mineralogy and Petrology* **117**, 375–93.

Vielzeuf, D. & Schmidt, M. W. 2001. Melting reactions in hydrous systems revisited: application to metapelites, metagreywackes and metabasalts. *Contributions to Mineralogy and Petrology* **141**, 251–67.

Weinberg, R. 2006. Melt segregation structures in granitic plutons. *Geology* **34**, 305–8.

Westraat, J. D., Kisters, A. F. M., Poujol, M. & Stevens, G. 2004. Transcurrent shearing, granite sheeting and the incremental construction of the tabular 3·1 Ga Mpuluzi batholith, Barberton granite–greenstone terrane, South Africa. *Journal of the Geological Society, London* **161**, 1–16.

Windley, B. F. 1995. *The Evolving Continents*. Chichester: John Wiley & Sons.

Zegers, T. E., de Wit, M. J., Dann, J. & White, S. H. 1998. Vaalbara, Earth's oldest assembled continent? A combined structural, geochronological, and palaeomagnetic test. *Terra Nova* **10** (5), 250–9.

MS received 12 March 2007. Accepted for publication 23 September 2008 (Stellenbosch); 15 January 2009 (RSE).

Similarities between mantle-derived A-type granites and voluminous rhyolites in continental flood basalt provinces

Simon Turner and Tracy Rushmer

[1] GEMOC, Department of Earth and Planetary Sciences, Macquarie University, Sydney NSW 2109, Australia
Email: sturner@els.mq.edu.au; trushmer@els.mq.edu.au

ABSTRACT: Many continental flood basalt provinces contain rhyolites with 'A-type' compositions and many studies have concluded that these higher silica rocks are crustal melts from metapelitic or tonalitic country rock. However, although many of the low-Ti continental flood basalt sequences exhibit a marked a silica gap from ~55–65 wt.% SiO_2, many incompatible element ratios, and the calculated eruption temperatures (950–1100°C) are strikingly similar between the rhyolites and associated basalts. Using experimental evidence, derivation of the low-Ti rhyolites from a basaltic parent is shown to be a viable alternative to local crustal melting. Comparison of liquid compositions from experimental melting of both crustal and mantle-derived (basaltic) source materials allows the two to be distinguished on the basis of Al_2O_3 and FeO content. The basalt experiments are reversible, such that the same melts can be produced by melting or crystallisation. The effect of increased water content in the source is also detectable in the liquid composition. The majority of rhyolites from continental flood basalt provinces fall along the experimental trend for basalt melting/ crystallisation at relatively low water content. The onset of the silica gap in the rhyolites is accompanied by an abrupt decrease in TiO_2 and FeO*, marking the start of Fe–Ti oxide crystallisation. Differentiation from 55–65 wt.% SiO_2 requires ~30% fractional crystallisation in which magnetite is an important phase, sometimes accompanied by limited crustal contamination. The rapid increase in silica occurs over a small temperature interval and for relatively small changes in the amount of fractional crystallisation, thus intermediate compositions are less likely to be sampled. It is argued that the presence of a silica gap is not diagnostic of a crustal melting origin for either A-type granites or rhyolites in continental flood basalt provinces. The volume of these rhyolites erupted over the Phanerozoic is significant and models for crustal growth should take this substantial contribution from the mantle into account.

KEY WORDS: A-type granite, continental flood basalts, fractionation, melting experiments, rhyolite

Whether silicic magmatic rocks are largely derived by partial melting or crystal fractionation is a much discussed question and one closely linked to debates over the origin of the continental crust. One of the striking observations is that most silica-rich magmatic rocks often occur in bimodal associations. In orogenic settings these include distinctive suites termed A-type rocks (e.g. Collins *et al.* 1982; Eby 1990). Most continental flood basalt provinces contain, and frequently are capped by, extensive rhyolite sequences (see Mahoney & Coffin 1997 for a recent review). The presence of a silica gap in these bimodal suites has been widely regarded as evidence against a liquid line of descent in bimodal magmatic suites, with the lack of intermediate rocks put down to the fact that crustal rocks are broadly granitic in composition and therefore tend to yield rhyolitic melts (e.g. Leeman 1982; Bellieni *et al.* 1986; Sylvester 1989). Instead the higher silica rocks have frequently been interpreted as crustal melts, with the heat for melt generation being derived from the emplacement of the associated basaltic magmas (e.g. Huppert & Sparks 1988). In cases where the higher silica rocks have isotope ratios similar to those of the basalts, it has been argued that they were derived by remelting of the intrusive equivalents of the basalts (e.g. in the Lebombo, Cleverly *et al.* 1984; the Deccan, Lightfoot *et al.* 1987; and the Paraná, Piccirillo *et al.* 1987). In the present paper, it is shown that these rhyolites share many important characteristics with A-type granites and volcanic rocks, and geochemical and experimental data are combined to argue that fractional crystallisation from the basalt itself, not crustal melting of associated metapelite or intermediate rock types, is the most likely mechanism of generation of many of the high-temperature, high-silica magmatic suites.

1. Comparison of A-type granites with Rhyolites from continental flood basalt provinces

Table 1 shows average major element compositions of A-type granites and silicic rocks from continental flood basalt provinces worldwide, along with some estimates of eruption temperatures and volumes. A-type granites and their volcanic equivalents typically occur in bimodal magmatic suites, and at least some can be shown to be the result of fractionation of accompanying basaltic magma (Turner *et al.* 1992; Frost & Frost 1997; McCurry *et al.* 2008; Whitaker *et al.* 2008). In addition to elevated concentrations of SiO_2 and incompatible elements combined with low Al_2O_3 and CaO (see Table 1), A-type rocks are also distinguished from the more common I- and S-type igneous rocks by their high magmatic temperatures and relatively anhydrous mineral assemblages (e.g. Clemens

© 2009 The Royal Society of Edinburgh. doi:10.1017/S1755691009016181

Table 1 Typical compositions of A-type granites, CFB rhyolites (including volumes and average temperatures of rhyolites and associated basalts) and granophyre.

	A-type granite average	low-Ti Paraná	Tasmania granophyre	British Tertiary Province	Keweenawan	Columbia River (glass)	Karoo (central)	Black Hill granophyre	high-T Paraná	Lebombo rhyolite	Deccan Salsette island	Huronian	Yardea dacite
SiO_2 (wt.%)	73·60	68·85	66·69	69·81	71·60	74·40	63·05	73·80	65·90	69·39	65·63	71·02	67·09
TiO_2	0·33	0·89	0·93	0·76	0·39	0·90	0·76	0·31	1·29	0·50	0·66	0·55	0·74
Al_2O_3	12·69	12·72	11·38	12·97	12·28	13·00	16·06	13·07	13·25	12·43	15·39	12·54	14·24
Fe_2O_3	2·90	5·95	4·72	4·07	3·55	1·60	6·31	1·64	7·00	6·26	5·12	5·19	4·08
MnO	0·06	0·10	0·14	nd	nd	nd	0·16	0·05	0·13	0·11	nd	nd	0·10
MgO	0·33	1·05	0·35	0·75	0·43	0·30	2·54	0·01	1·27	0·33	1·24	0·56	0·84
CaO	1·09	2·47	3·72	2·01	0·90	0·50	3·20	0·51	2·73	1·46	1·47	0·67	2·47
Na_2O	3·34	2·88	2·65	3·11	2·97	2·60	2·70	3·52	3·42	3·14	4·51	2·57	3·43
K_2O	4·51	4·23	3·08	4·43	5·46	6·60	2·04	6·20	4·25	4·53	5·05	5·11	4·75
P_2O_5	0·09	0·25	0·25	0·26	0·06	0·40	0·19	0·02	0·40	0·14	0·11	0·29	0·20
Volume (km^3)													
basalt	–	890000	50000	250000	unknown	175000	1000000	14	89000	1000000	500000	unknown	unknown
rhyolite	–	20000	small	15000	unknown	10000	35000	1	20000	35000	500	unknown	3000
Temperature (°C)													
basalt	–	1200	1200	–	–	–	1200	1200	1200	–	1050	–	–
rhylote	940	1000	980	–	–	–	1100	1000	1000	–	900	–	1060
Reference(s)	1,2	3	4	5,6	7,8	9	10	11,12	3	10	13	14	15

1: Collins *et al*. (1982); 2: Clemens *et al*. (1986); 3: Garland *et al*. (1995); 4: Hergt *et al*. (1987); 5: Walsh *et al*. (1979); 6: Gamble *et al*. (1992); 7: Green & Fitz (1993); 8: Nicholson & Shirey (1990); 9: Lambert *et al*. (1989); 10: Milner & Duncan (pers. comm. 1996); 11: Turner (1996); 12: Turner & Foden (1996); 13: Lightfoot *et al*. (1987); 14: Jolly *et al*. (1992); 15: Creaser & White (1991).

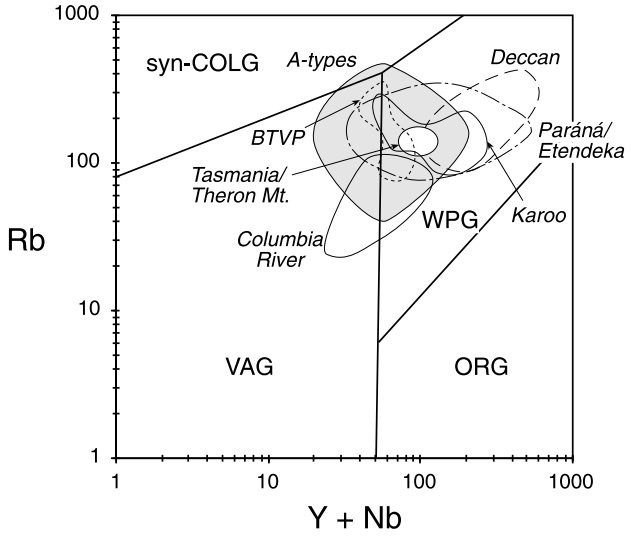

Figure 1 Rb *vs.* Y+Nb granite discrimination diagram from Pearce *et al.* (1984) showing the compositional overlap between A-type granites (data from Collins *et al.* 1982; Turner *et al.* 1992; Turner & Foden 1996) and rhyolites from continental flood basalt provinces (data sources as in Table 1). BTVP=British Tertiary volcanic province; VAG=volcanic arc granites; ORG=orogenic granites; syn-COLG=syn-collision granites; WPG=within-plate granites.

et al. 1986; Turner *et al.* 1992). On trace element discrimination diagrams, A-type granites largely fall in the within-plate granite field of Pearce *et al.* (1984) (Fig. 1). Volumes can be non-trivial and in Australia, for example, the Gawler Range Volcanics are a suite of high temperature A-type volcanic rocks with an estimated volume of >3000 km^3 (e.g. Creaser & White 1991).

Bimodal basalt-rhyolite suites are common in continental flood basalt provinces, generally with high-temperature rhyolite units capping the basalts (the Paraná-Etendeka, the Karoo, the Deccan Trap and the Proterozoic of the Keweenawan and Huronian), but can also contain intrusive silicic equivalents at lower temperatures (the British Tertiary province, and the Ferrar province of Antarctica and Tasmania). Characteristic features include large aerial extent, generally anhydrous primary mineral assemblages, and often a high proportion of glass in the matrix. The mode of eruption of this distinctive class of rhyolites is not easy to determine, as high silica magmas tend to be highly viscous and unable to flow long distances. Possible causes of the lowered viscosity are either an abundance of volatiles (Holtz & Johannes 1994), or unusually high eruption temperatures or effusion rates (Henry *et al.* 1988). Alternatively the rhyolite units could have been emplaced as pyroclastic eruptions, or as hybrid 'rheoignimbrites' in which the initially pyroclastic material is rewelded on contact with the ground due to the sustained high temperatures (Fig. 2). Where large calderas are found with the high-temperature rhyolites, a pyroclastic origin is favoured (e.g. Milner & Ewart 1989), but in a number of cases there is no such evidence (e.g. Ekren *et al.* 1984). Rhyolites associated with continental flood basalt provinces tend to be devoid of traces of eruptive centres, thus their mode of eruption is not easy to explain.

Whilst it is obviously difficult to generalise about the chemistry of high-temperature rhyolites world-wide, there are a number of major element features which characterise this group. In particular, the high-temperature rhyolites tend to have moderate silica contents, low Al_2O_3, TiO_2, MgO and FeO* that are often almost identical to those of A-type granites (see Table 1). They also have elevated incompatible trace element concentrations and overlap with A-type granites (Fig. 1). It is these many similarities which suggest the likelihood of a common petrogenesis which we now explore through comparison with experimental data. Initial comparisons are made with the well documented low-Ti rhyolites from the Paraná-Etendeka province. These have incompatible trace element and isotopic characteristics which are nearly identical to underlying low-Ti basalts and which both Garland *et al.* (1995) and Ewart *et al.* (2004) have used to argue for a fractional crystallisation origin for the rhyolites.

2. Experimental investigation of crustal melting

Numerous experimental studies have been performed which should allow the distinction of partial melts of different crustal lithologies. The likely source materials of crustal melts are metasediments and quartzo-felspathic, intermediate rock types (e.g. tonalite) in the mid–upper crust, and granulites, basalts or amphibolites in the lower crust. Experimental work on partial melting of such rocks with varying source composition, pressure, water content and temperature has been carried out in a number of studies, and the major element composition of the melt determined (e.g. Helz 1976; Spulber & Rutherford 1983; Rutter & Wyllie 1988; Vielzeuf & Holloway 1988; Beard & Lofgren 1989, 1991; Rapp *et al.* 1991; Rapp & Watson 1995; Rushmer 1991; Patiño-Douce & Johnston 1991; Skjerlie & Johnston 1993, Sisson *et al.* 2005). The liquid composition is controlled by the melting reactions in the source, which are in turn determined by factors such as water content, pressure and fO_2. Water content of the source arguably plays the most fundamental role in determining the specific melting reactions, and hence the liquid composition (Beard & Lofgren 1991). Three main scenarios exist: (i) water-saturated melting, where there is free water present; (ii) dehydration or fluid-absent melting, in which water is contained in hydrous phases such as micas and amphiboles, but is not of a sufficient quantity to saturate the melt; and (iii) dry melting in which no hydrous phases are involved. The presence of water lowers the granite solidus (Holtz & Johannes 1994), therefore the water content in the source region determines the temperature at which the first melt will be produced. Water content also affects the percentage of melt obtained, for example during fluid-absent melting, an assemblage containing micas is more water-rich than one containing an equivalent proportion of amphibole as the only hydrous phase, and this results in 50% as opposed to 20% melt under the same pressure-temperature conditions (Clemens & Vielzeuf 1987). Alternatively, increases in pressure serve to reduce the melt proportion, because at higher pressures, the solubility of water is increased in the melt phase and this reduces melt volume. The effects of fO_2 are allied to the water content, as water increases the fO_2 by introducing more oxygen into the system (Morse 1980).

Figure 3 compiles FeO *vs.* Al_2O_3 experimental data from amphibolite melting experiments (Beard & Lofgren 1989, 1991; Spulber & Rutherford 1983; Helz 1976; Rapp *et al.* 1991; Rushmer 1991; Sisson *et al.* 2005), tonalites (Rutter & Wyllie 1988; Skjerlie & Johnston 1993) and metasediments (Patiño-Douce & Johnston 1991; Vielzeuf & Holloway 1988). Within the amphibolite melting region, most data show general trends from low FeO and Al_2O_3 to higher FeO and Al_2O_3 as a function of increasing temperature and melt fraction (with the exception of Rapp *et al.* 1991, where the trends are not as clear). The present authors compare data where fO_2 is approximately QFM (Sisson *et al.* 2005 show the effects of changing fO_2). This is also true for Spulber & Rutherford 1983, where experiments are performed at $P_{H_2O} \leq P_{total}$ (region labelled 1); for the P_{H_2O}=1 kb P_{total} of Beard & Lofgren (1989; region

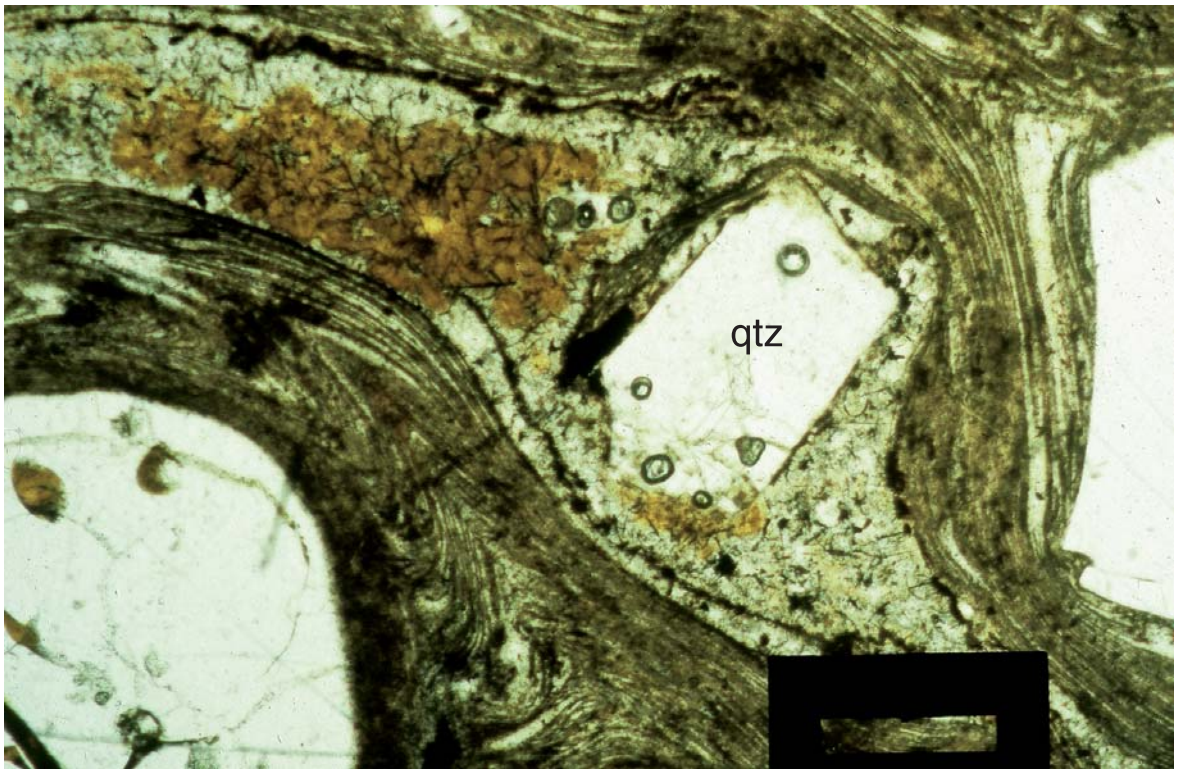

Figure 2 Photomicrograph of a rhyolite from part of the Paraná continental flood basalt province in Uruguay showing rheoignimbritic textures (note quartz phenocryst in flattened pumice fragment). Scale bar = 1 mm, plane polarised light.

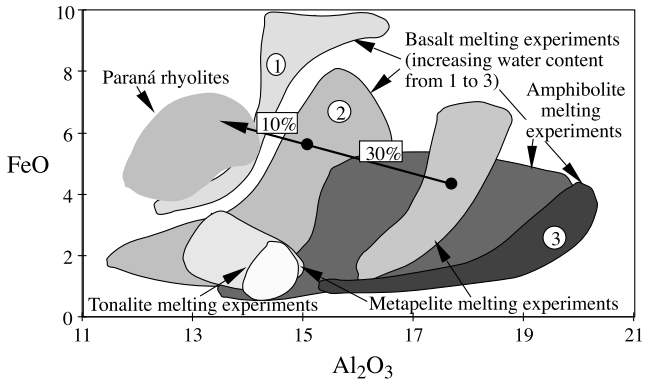

Figure 3 Al_2O_3 *vs.* FeO plot for experimental data on basalts (Helz 1976; Spulber & Rutherford 1983; Beard & Lofgren 1989, 1991; Rapp *et al.* 1991; Rushmer 1991), tonalites (Rutter & Wyllie 1988; Skjerlie & Johnston 1993) and metasediments (Vielzeuf & Holloway 1988; Patiño-Douce & Johnston 1991). Increasing water content in the numbered experimental source basalts: (1) $P_{H_2O} \leq P_{total}$ (Spulber & Rutherford 1983); (2) $P_{H2O} = P_{total}$ (Beard & Lofgren 1989); (3) $P_{H_2O} = 5$ kb (Heltz 1976). The Paraná rhyolites plot at low Al_2O_3, and moderately high FeO, coinciding with the least wet basalt experiments. Alternatively low pressure plagioclase crystallisation and removal allows the Paraná rhyolite composition to be reached either by 10% plagioclase crystallisation from the basalts with intermediate water content (2), or by 30% plagioclase crystallisation from the metapelite. See text for further discussion.

labelled 2) and for $P_{H_2O} = 5$ kb of Heltz (1976; region labelled 3). Tonalite partial melts have lower FeO and Al_2O_3 and are comparable to the metapelite melting experiments of Patiño-Douce & Johnston (1991). Vielzeuf & Holloway's (1988) metapelite partial melts are distinctly higher in FeO and Al_2O_3. Both show an increase in FeO and Al_2O_3 as a function of increasing temperature (see below for further discussion). The Paraná rhyolites are also plotted, as discussed below.

2.1. Metasedimentary and quartzo-felspathic source materials

The effect of higher water content in the source is known to increase the Al_2O_3, and decrease the FeO abundances of the melt (e.g. Thy *et al.* 1990). This is due to the decreased stability of plagioclase under wet conditions, while pyroxene stability is correspondingly increased (Beard & Lofgren 1991). Metasedimentary sources tend to contain a substantial proportion of micas (both muscovite and biotite) which are rich in water compared to quartzo-felspathic sources such as tonalite (Clemens & Vielzeuf 1987; Rutter & Wyllie 1988); therefore melts derived from metapelites have higher Al_2O_3 contents than melts derived from tonalites (Fig. 3). A series of experiments carried out on a metapelite source deficient in plagioclase (Patiño-Douce & Johnston 1991) resulted in low Al_2O_3 abundance (white field in Fig. 3), despite a high proportion of mica in the source (40%). However, this can be explained by the production of garnet during the biotite fluid-absent melting reaction, which withholds some Al_2O_3 from the melt. Despite the variation in Al_2O_3 content, the metapelites all tend to yield melts with low FeO abundances (generally <3 wt.% FeO), similar to the abundance of FeO in wet melts of basalt sources (Helz 1976). The exception is the melts produced at high temperatures (1050–1250°C) from the metapelitic source as shown by Vielzeuf & Holloway (1988), which started with a high FeO content. This appears to be due to the breakdown of garnet to spinel and quartz, liberating FeO into the melt (in addition to Al_2O_3, giving a relatively high abundance of both elements).

In comparison with the Paraná rhyolites, melts from metapelites and tonalites are high in Al_2O_3 and low in FeO, making them unsuitable analogues for the rhyolites. However, the rhyolite magma could also have undergone fractional crystallisation in the crust prior to eruption, in which case the original melt composition would have been more primitive than the samples analysed. The main mineral phase likely to fractionate

from silicic magmas over the temperature range 950–1200°C is plagioclase (Skjerlie & Johnston 1993), which would result in a decrease in abundance of Al_2O_3, CaO and Na_2O. On that basis, the high temperature melts from the metapelites of Vielzeuf & Holloway (1988) would appear to be the most suitable parental magma for the rhyolites in terms of Al_2O_3 and FeO. The Paraná rhyolites might then reflect 30% plagioclase crystallisation from such melts (Fig. 3). However, the CaO and Na_2O abundances of the metapelite melts are already low compared to the rhyolites, and are therefore inconsistent with subsequent plagioclase removal. The low FeO content of the metapelite melts of Patiño-Douce & Johnston (1991) and the tonalite melts of Skjerlie & Johnston (1993) at similar Al_2O_3 contents to the rhyolite magmas would require accumulation of pyroxene or Fe–Ti oxides in order to achieve similarity to the rhyolites, which is not considered likely. Thus, none of these sedimentary/quartzo-feldspathic melts satisfy the chemical requirements of the Paraná rhyolites, and they are considered to be unsuitable source materials for the rhyolite magmas.

2.2. Basalt source

An alternative source for the Paraná rhyolites is derivation from basaltic material, or its hydrated and metamorphosed equivalent (amphibolite). The geographic association of low-Ti rhyolites with low-Ti basalts and high-Ti rhyolites with high-Ti basalts strongly suggests a link between the mafic and felsic lavas. Experiments on basalts have been carried out under varying degrees of hydration, with a range in Al_2O_3 content as mentioned above. The hydrous experiments of Helz (1976) were undertaken at a water pressure of 5 kb, giving rise to melts very rich in Al_2O_3 (generally $\geq$19 wt.% Al_2O_3) due to the lowered stability of plagioclase (Fig. 3, region 3). Beard & Lofgren (1989) performed experiments on a range of predominantly tholeiitic amphibolites in which $P_{H_2O}=P_{total}$ (1 kb) (Fig. 3, region 2). Spulber & Rutherford (1983) used tholeiitic basalts, with experiments carried out over a range of pressures, in which $P_{H_2O}\leq P_{total}$, making them less water-rich than the experiments of Beard & Lofgren (1991) at pressures greater than 1 kb (Fig. 3, region 1).

The high Al_2O_3 content of the water-saturated melts discounts them as being parental to the Paraná rhyolites, whilst the melts from the experiments of Spulber & Rutherford (1983) and Beard & Lofgren (1989, 1991) are both potential candidates (regions 1 and 2 respectively in Figure 3). In both cases, the basaltic starting material is broadly similar to the Paraná basalts, in that they are tholeiitic and fairly evolved (Mg# of 35–60 compared to Mg# of 35–65 for the Paraná basalts). One significant difference in the starting composition between the experimental and Paraná samples is the K_2O abundance, which is markedly lower in the experimental starting material than the Paraná basalts (<0·45 wt.% K_2O as opposed to an average value of >1·3 wt.% K_2O for the Paraná basalts: Peate *et al.* 1992). Since K acts as an incompatible element throughout melting (neither amphibole or alkali-feldspar are residual solid phases in the melting reactions reported by Beard & Lofgren (1991), the abundance of K_2O in the melt will depend on the concentration in the source, as well as on the degree of melting. Thus, the low K_2O abundance of the experimental melts relative to the Paraná rhyolites (<1 wt.% K_2O *vs.* >3 wt.% K_2O in the rhyolites) could reflect the different K_2O contents of their respective source rocks.

The Paraná rhyolites have high eruption temperatures of >1000°C (e.g. Garland *et al.* 1995), therefore the melt is required to be at equivalent or higher temperatures at the lowest observed silica content ($\sim$65 wt.% SiO_2), assuming that temperatures are likely to decrease with increasing silica. The

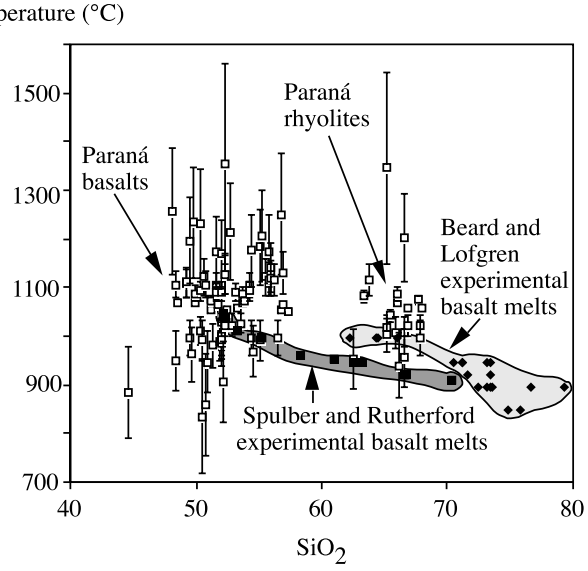

Figure 4 SiO_2 *vs.* temperature plot for the low-Ti Paraná basalts and rhyolites (data from Piccirillo & Melfi 1988; Garland *et al.* 1995). Temperatures calculated by pyroxene thermometry (Kretz 1982), with errors. Both basalts and rhyolites lie mainly within the temperature range 950–1100°C. SiO_2–temperature fields for the experimental data of Beard & Lofgren (1989) and Spulber & Rutherford (1983) are shown for comparison.

experiments of Spulber & Rutherford (1983) were carried out over a temperature range of 913–1050°C, but the temperatures drop rapidly from 52–60 wt.% SiO_2, and at 65 wt.% SiO_2 the temperature is <950°C (Fig. 4). This is at the lower end of the range of calculated temperatures for the rhyolites, whilst the experiments of Beard & Lofgren (1989, 1991) at 1000°C yield a melt with up to 66 wt.% SiO_2. This makes the slightly higher P_{H_2O} experiments of Beard & Lofgren the preferred melting model for the Paraná rhyolites. It is shown on Figure 3 that the Beard & Lofgren experiments (region 2) are offset to consistently higher Al_2O_3 than the Paraná rhyolites, but this can be accounted for by $\sim$10% plagioclase crystallisation. Further, this is consistent with the slightly higher CaO content in the experimental melts compared to the rhyolites, suggesting that the plagioclase removed was anorthite-rich, as opposed to albitic (plagioclase in the Paraná basalts have the range $An_{86–59}$: Bellieni *et al.* 1988).

It must be borne in mind that whilst the basalt experiments have all been considered in terms of partial melting, the experiments are reversible, and therefore apply equally to crystallisation from a basalt melt of the same composition, under the same conditions of temperature and pressure (Spulber & Rutherford 1983). The Paraná rhyolites could, in principle, be modelled either as partial melts of basaltic material, or as the result of crystallisation from a basalt. However, crystallisation processes are more energetically efficient and thermal models for production of silicic melts via re-melting in the crust predict a secular change from silicic to mafic magmatism over time (Annen *et al.* 2006) – the opposite of that observed in most continental flood basalt sequences. Thus, it seems likely that the low-Ti Paraná rhyolites reflect extended fractionation of associated low-Ti basalts (Garland *et al.* 1995).

2.3. Comparison with other CFB rhyolites

In the light of a strong link between the Paraná rhyolites and experimental melts/fractionates from moderately water-undersaturated basalts, we now turn to rhyolites from other continental flood basalt provinces world-wide to consider

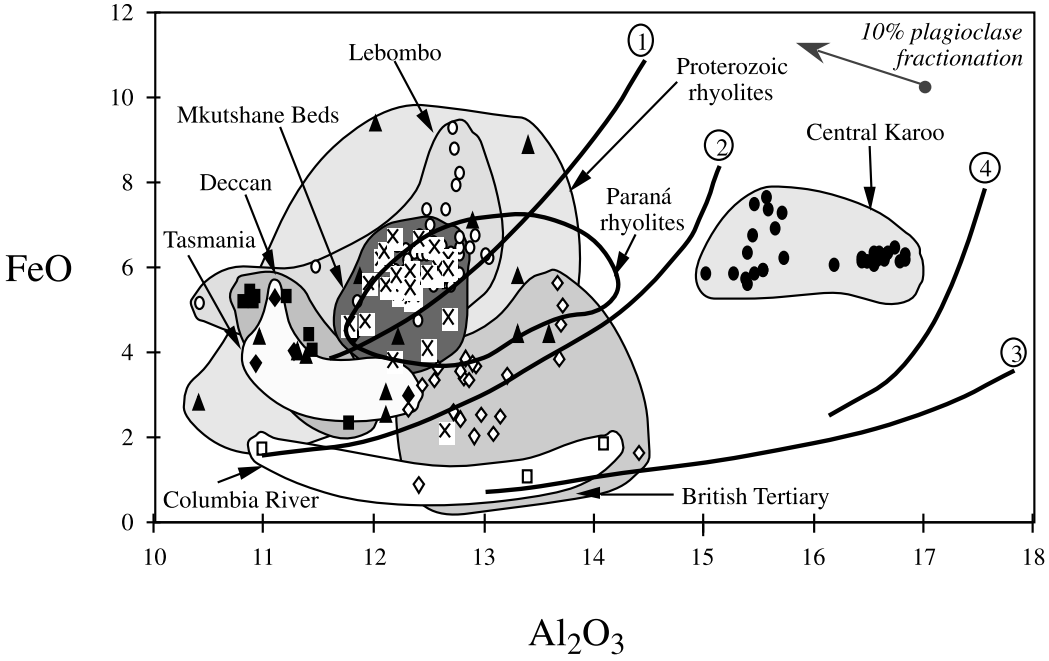

Figure 5 Al_2O_3 *vs.* FeO plot for rhyolites from continental flood basalt provinces world-wide (see text for data sources). The trends marked 1 to 3 are best-fit lines through the basalt melt fields shown in Figure 3, whilst (4) represents a best-fit through the metapelite melt field of Vielzeuf & Holloway (1988). For trend 2, the basalt melts of Beard & Lofgren (1989), temperatures in °C are shown for experiments carried out over the pressure range of 1–3 kb, with the low-temperature experiments resulting in relatively low FeO and low Al_2O_3 melts. The majority of the rhyolites lie close to the experimental trend of moderately dry basalts (1 and 2). Exceptions are the Columbia River rhyolite glasses, at the low temperature end of the wet basalt trend (3); and the Central Karoo silicics close to the metapelite melting field (4). The vector for 10% plagioclase crystallisation is shown in the top right hand corner.

whether they have similar petrogenetic relations. The Karoo continental flood basalt province has a highly voluminous rhyolite succession in the east of the province (Cleverly *et al.* 1984), where the Lebombo monocline is comprised almost entirely of rhyolite units (~35 000 km^3). They can be divided into a northern high-Ti group, and a southern low-Ti group, with the lowermost flow units (the Mkutshane Beds) constituting a separate low-Ti group with raised $^{87}Sr/^{86}Sr$ values, indicative of crustal contamination (Cleverly *et al.* 1984). There are volumetrically insignificant evolved flows in the Central Karoo, which also have higher $^{87}Sr/^{86}Sr$ than the associated basalts, and have been modelled as crustal melts (Marsh & Eales 1984). Other continental flood basalt provinces which contain silicic flows, albeit in less impressive volumes than found in the Paraná–Etendeka and Karoo, are the Huronian (Jolly *et al.* 1992), the Keweenawan (Nicholson & Shirey 1990), and the Deccan provinces (Lightfoot *et al.* 1987). The British Tertiary province contains abundant evidence of intrusive silicic activity (e.g. Gamble *et al.* 1992), which is found on a smaller scale in the Tasmanian dolerites (McDougall 1962) and the Columbia River basalts (Lambert *et al.* 1989), the latter two being interpreted as *in-situ* differentiates from basic magma. The majority of erupted rhyolites in continental flood basalt provinces share the same high temperatures as the Paraná rhyolites (>1000°C: e.g. Cleverly *et al.* 1984; Green & Fitz 1993), and the majority have an anhydrous mineralogy, consisting of plagioclase, clinopyroxene, Fe–Ti oxides and rare quartz and alkali feldspar. These petrographic and thermal similarities between these rocks suggest that they were generated under broadly similar conditions of source composition, pressure and water content. In general, the rhyolites have eruption temperatures ~200°C lower than their associated mafic rocks and such a temperature drop would result in 70–80 crystallisation, sufficient to yield a rhyolite from a basaltic precursor (Turner *et al.* 1992). These petrographic and thermal similarities between these rhyolites suggest that they were generated under broadly similar conditions of source composition, pressure and water content. In order to make further comparison with the Paraná rhyolites, and the experimental data reviewed above, the continental flood basalt rhyolites are plotted on an Al_2O_3 versus FeO diagram (Fig. 5).

The Lebombo rhyolites of the Karoo province, together with the Mkutshane Beds, plot very close to the Paraná rhyolites, whilst the Huronian, Keweenawan and Deccan rhyolites plot on parallel trends adjacent to this same cluster (Fig. 5). A number of Deccan samples from Lightfoot *et al.* (1987) have been omitted from Figure 5 in order to avoid unnecessary cluttering for the following reasons: (i) samples with higher Al_2O_3 and FeO are interpreted as mixing with the associated basalts (noted for trace elements by Lightfoot *et al.* 1987); and (ii) samples with very high Al_2O_3 contents (16–17 wt.% Al_2O_3) are thought to be the result of plagioclase accumulation (these samples are plagioclase-phyric, and have high Sr/Zr ratios: Lightfoot *et al.* 1987). The British Tertiary and Tasmanian silicic rocks plot at the low temperature end (lower Al_2O_3 and FeO) of the Beard & Lofgren (1989, 1991) experimental melts, consistent with the slower cooling of these rocks in intrusive bodies. By comparison with the composition of the experimental melts at pressures of 1–3 kb (Fig. 5), the British Tertiary rocks range in temperature from 900°C to 950°C, whilst the Tasmanian granophyres are marginally cooler at ≤900°C. Both the British Tertiary and the Tasmanian silicic rocks plot at the same Al_2O_3 contents as the Beard and Lofgren experimental melts, implying that subsequent plagioclase removal was not necessary to generate the observed magma composition. The Columbia River silicic glasses (found as interstitial melt pockets within the majority of basalt flows, generally comprising ~10% of the bulk flow volume: Lambert *et al.* 1989) plot at the lowest FeO abundances (<2 wt.% FeO). They lie along the experimental melts

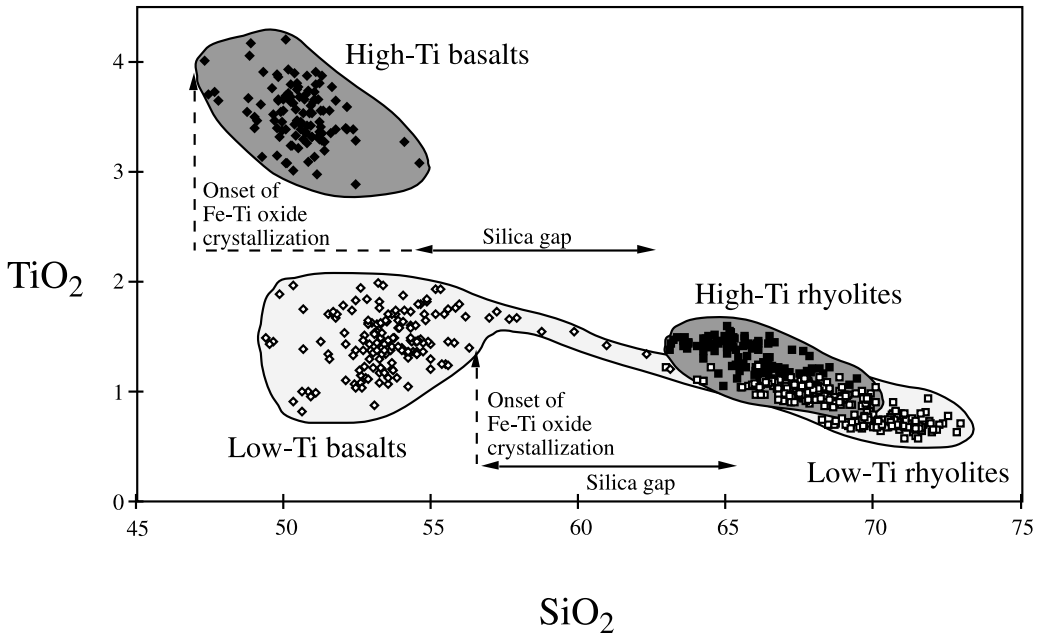

Figure 6 SiO_2 *vs.* TiO_2 plot contrasting the high- and low-Ti Paraná basalts. The low-Ti basalts show an initial increase in TiO_2, whilst the high-Ti basalts show a consistent decrease in TiO_2, indicating that titanomagnetite was crystallising from an early stage. Basalt data from Peate *et al.* (1992).

of the amphibolite source of Rapp *et al.* (1991), in which the melting reactions were fluid-absent. The pressures at which the experiments were carried out are at higher pressures, ranging from 8 kb to 32 kb, and not as applicable to the lower pressures that would have been present for the emplacement conditions of the Columbia River Basalt province (Helz 1976). More applicable are the water-undersaturated basalt melting experiments of Holloway & Burnham (1972) in which $P_{H_2O}=0{\cdot}6P_{total}$ over the pressure range 5–8 kb. The fact that the Columbia River glasses lie along this possibly more water-enriched trend is indicative of the fact that water, along with slightly higher pressures when compared to those of Beard & Lofgren (1989, 1991) and Spulber & Rutherford (1983), plays an important role in changing phase stabilities and therefore FeO content of the melt.

The only marked outlier from the rhyolite groups is the Central Karoo, which lies at high Al_2O_3 and moderate FeO relative to the rhyolites from other continental flood basalt provinces. The rhyolites from the Central Karoo lie at very slightly lower Al_2O_3 contents than the high temperature experimental melts from metasediments of Vielzeuf & Holloway (1988), and are distinct from the other basalt melting trends. Marsh & Eales (1984) interpreted the Central Karoo silicic rocks as crustal melts based on a combination of composition and isotope ratios, and indeed melting of a two-mica metasedimentary rock at temperatures of $\geq 1150°C$ gives a melt of appropriate composition, although a slightly lower temperature melt, followed by 5–10% plagioclase removal would give a similar composition.

3. Crystallisation models and the lack of intermediate compositions

The preceding discussion is based on reversible, equilibrium experiments which strictly only constrain equilibrium crystallisation. However, the differences between equilibrium and fractional crystallisation are generally trivial for major elements. The difference becomes more important for incompatible trace elements which are not the focus of the present paper, but can be used to distinguish between partial melting and fractional crystallisation in some high silica magmas (e.g. Halliday *et al.* 1991). Therefore, it is now considered how fractional crystallisation processes may produce bimodal magmatic suites. Silica saturated basaltic magmas with a quartz–diorite composition, that typify continental flood basalt provinces, tend to undergo continuous SiO_2 enrichment with on-going crystallisation (e.g. Mahoney & Coffin 1997). By definition, intermediate compositions are rarely observed in bimodal suites, but this remains a weak argument against a fractionation origin for the silicic rocks (Brophy 1991; Turner *et al.* 1992; Bonnefol *et al.* 1995). In tholeiites, early iron-enrichment is due to plagioclase (an iron-poor phase) dominating the early fractionating assemblage (Grove & Baker 1984), and FeO* abundance is then primarily controlled by Fe–Ti oxide crystallisation and removal. Due to the absence of silica from Fe–Ti oxides, removal of this phase significantly increases SiO_2 in the residual liquid. Within the low-Ti Paraná basalts, TiO_2 and Fe_2O_3 broadly increase with differentiation up to $\sim$56% SiO_2, and the onset of Fe–Ti oxide crystallisation is then marked by an abrupt decrease in TiO_2 and Fe_2O_3 with increasing SiO_2, and the start of the silica gap (Fig. 6). Once Fe–Ti oxides begin to crystallise out, the calculated SiO_2 content of the fractionating assemblage in the low-Ti basalts decreases from $\sim$48% to $\sim$42%. The onset of Fe–Ti oxide crystallisation is thus critical in determining the evolution of the silica content in the liquid. A gradual increase in silica, as demonstrated by the calc–alkaline series, is brought about because Fe–Ti oxides appear at high temperature, which also restricts iron-enrichment. The entry of Fe–Ti oxides into the crystallising assemblage is determined largely by temperature (Thy & Lofgren 1994) and fO_2 (Snyder *et al.* 1993). High fO_2 also leads to the early appearance of Fe–Ti oxides, particularly magnetite. Oxygen fugacities calculated for the Paraná lavas using magnetite–ilmenite pairs generally lie along the QFM buffer (Bellieni *et al.* 1986, 1988), with the high-Ti magmas at marginally higher fO_2 than the low-Ti magmas. This results in saturation of titanomagnetite earlier in the high-Ti magmas than in the low-Ti magmas.

Recently, some workers have argued for the production of high silica magmas via the extraction of interstitial liquid from

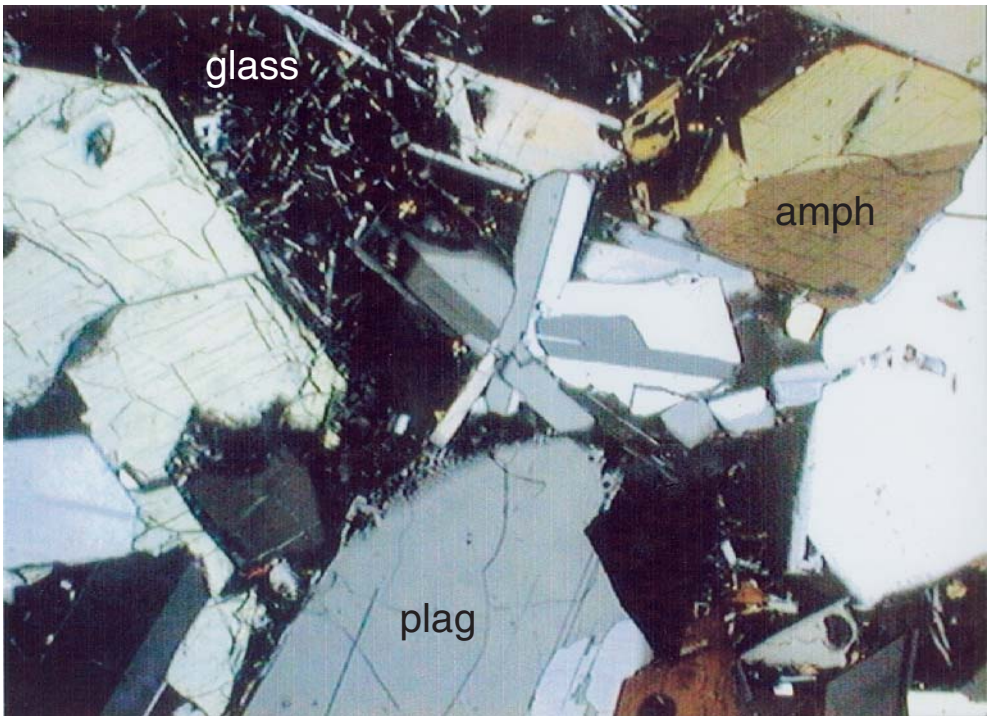

Figure 7 Photomicrograph of a Tasmanian dolerite containing residual silicic interstitial glass with a major element composition very similar to associated granophyric sills. Crossed polars; width = 4 mm.

a cooling gabbroic crystal mush (Turner & Foden 1996; Marsh 2002; Bachmann & Bergantz 2004), providing a somewhat different physical process for explaining the bimodal melt production. This is effectively an equilibrium crystallisation process and can thus be directly linked to the experiments discussed above. A significant observation is the occurrence of granophyre on various scales from interstitial segregations to larger sills and pods in continental flood basalts and many mafic intrusions such as the Tasmanian dolerites (Fig. 7) and even basaltic lavas flows (Martin & Sigmarsson 2007). In the study of Turner & Foden (1996) of the Mannum region in South Australia, the granophyre is similar in composition to many of the rhyolites in question, and overlaps the chemical and isotopic range of comagmatic A-type granites and volcanic rocks. This observation is a good example of the physical process of bimodal melt production suggested by Marsh (2002). In this model, it is the cooling of basaltic sills and gabbroic intrusions that drives instabilities and pressure gradients that allow concentration of silicic melts. Therefore, the coalescing of interstitial granophyric magma provides one possible petrogenetic model. Interstitial liquid in cumulates becomes enriched in components incompatible with the cumulus matrix of olivine, pyroxene and plagioclase. Intermediate compositions are not produced in this system because the components for intermediate compositions are removed by diffusion to become incorporated in overgrowths on the cumulus phases. Alkalis and incompatible elements will not readily become incorporated in these overgrowths and thus become enriched in a rhyolitic residua that develops into the interstitial granophyric phase. This A-type granitic liquid will have a lower solidus (800–725°C, Clemens *et al.* 1986) than the surrounding solid cumulate (cf. ~1000°C), and thus will remain liquid for longer periods. It seems likely that such interstitial liquid, which is well documented from the Tasmanian Dolerites and other layered gabbroic plutons, should be capable of coalescing and/or gravitational separation. Compaction of the cumulate pile (e.g. Sparks *et al.* 1985) could force expulsion of this liquid to form sills at the top of the pile. Interestingly Lambert *et al.* (1989) calculated that, if coalesced, the interstitial rhyolitic glass present in the Columbia River basalts would total some 10,000 km^3 of rhyolite (although, in this case, no contemporaneous rhyolites were erupted).

4. Volumes and significance for crustal growth

For a given starting mass of basalt (liquid or solid), both crystallisation of a basaltic liquid or partial melting of a solid basalt will produce the same relative volumes of mafic residue and a more silicious product. For example, the production of a siliceous melt with ~70 SiO_2 requires either >70% crystallisation of a basalt (e.g. Turner *et al.* 1992) or <30% partial melting of a basalt (e.g. Sisson *et al.* 2005). Thus, both the partial melting and crystallisation scenarios require that significant volumes of basalt are emplaced into the crust during the formation of the rhyolites being discussed. Table 1 shows that all the of the provinces considered contain sufficient volumes of basalt to account for the rhyolites. In this context, it has long been noted that continental flood basalts contribute significant volumes ($\sim 8 \times 10^{-1}$ km^3/yr) of new mafic material to the continental crust (e.g. Hawkesworth *et al.* 1999). However, the associated volumes of rhyolite are also non-trivial. Table 1 lists the approximate volumes of rhyolite associated with some of the major Phanerozoic continental flood basalts, and the calculated rate of addition of this silicic material ($\sim 4 \times 10^{-4}$ km^3/yr) to the continental crust compares favourably, for example, with an estimate of $4{\cdot}4 \times 10^{-4}$ km^3/yr for the Central Andes (Crisp 1984).

5. Summary and conclusions

It has long been inferred that the major site of production of silicic continental crust is active magmatic convergent margins. However, the importance of silica-rich magmas that are produced during differentiation of continental flood basalts may be underestimated. The present authors suggest that the

rhyolites that are found associated with continental flood basalts (Paraná in particular) may be formed by fractional crystallisation during cooling. Geochemical data from the natural rhyolites and experimental studies of melts formed from basaltic starting material (performed under low to moderate pressures at $P_{H_2O}<P_{total}$) show good agreement. It is proposed that crystallisation of basaltic magma, possibly in conjunction with physical segregation processes, can be an important process to generate significant volumes of continental crust.

6. Acknowledgements

It is a pleasure to thank Francis Garland, John Foden and Chris Hawkesworth for many interesting discussions on this topic over the years. We also thank Eric Christiansen and John Shervais for detailed reviews, and Carol Frost for editorial handling. Simon Turner was funded by an ARC Federation Fellowship.

7. References

Annen, C., Blundy, J. D. & Sparks, R. S. J. 2006. The genesis of intermediate and silicic magmas in deep crustal hot zones. *Journal of Petrology* **47**, 505–39.

Bachmann, O. & Bergantz, G. W. 2004. On the origin of crystal-poor rhyolites: extracted from batholithic crystal mushes. *Journal of Petrology* **45**, 1565–82.

Beard, J. S. & Lofgren, G. E. 1989. Effects of water on the composition of partial melts of greenstone and amphibolite. *Science* **244**, 195–7.

Beard, J. S. & Lofgren, G. E. 1991. Dehydration melting and water-saturated melting of basaltic and andesitic greenstones and amphibolites at 1·3 and 6·9 kbar. *Journal of Petrology* **32**, 365–401.

Bellieni, G., Comin-Chiaramonti, P., Marques, L. S., Melfi, A. J., Nardy, A. J. R., Papatrechas, C., Piccirillo, E. M., Roisenberg, A. & Stolfa, D. 1986. Petrogenetic aspects of acid and basaltic lavas from the Paraná plateau (Brazil): geological, mineralogical and petrochemical relationships. *Journal of Petrology* **27**, 915–44.

Bellieni, G., Piccirillo, E. M., Comin-Chiaramonti, P., Melfi, A. J. & Da Roit, P. 1988. Mineral chemistry of continental stratoid volcanics and related intrusives from the Paraná Basin (Brazil). *In* Piccirillo, E. M. & Melfi, A. J. (eds) *The Mesozoic flood volcanics of the Paraná Basin: petrogenetic and geophysical aspects*, 73–92. São Paulo: IAG–USP Press.

Bonnefol, C. C., Provost, A. & Albarede, F. 1995. The 'Daly gap' as a magmatic catastrophe. *Nature* **378**, 270–2.

Brophy, J. G. 1991. Composition gaps, critical crystallinity, and fractional crystallization in orogenic (calc–alkaline) magmatic systems. *Contributions to Mineralogy and Petrology* **109**, 173–82.

Collins, W. J., Beams, S. D., White, A. J. R. & Chappell, B. W. 1982. Nature and origin of A-type granites with particular reference to south-eastern Australia. *Contributions to Mineralogy and Petrology* **80**, 189–200.

Clemens, J. D., Holloway, J. R. & White, A. J. R. 1986. Origin of A-type granite: Experimental constraints. *American Mineralogist* **71**, 317–24.

Clemens, J. D. & Vielzeuf, D. 1987. Constraints on melting and magma production in the crust. *Earth and Planetary Science Letters* **86**, 287–306.

Cleverly, R. W., Betton, P. J. & Bristow, J. W. 1984. Geochemistry and petrogenesis of the Lebombo rhyolites. *Geological Society of South Africa Special Publication* **13**, 171–94.

Creaser, R. A. & White, A. J. R. 1991. Yardea Dacite – Large volume, high-temperature felsic volcanism from the Middle Proterozoic of South Australia. *Geology* **19**, 48–51.

Crisp, J. A. 1984. Rates of magma emplacement and volcanic output. *Journal of Volcanology and Geothermal Research* **20**, 177–211.

Eby, G. N. 1990. The A-type granitoids: A review of their occurrence and chemical characteristics and speculations on their petrogenesis. *Lithos* **26**, 115–34.

Ekren, E. B., McIntyre, D. H. & Bennett, E. H. 1984. High temperature, large volume, lavalike flow tuffs without calderas in southeastern Idaho. *US Geological Survey Professional Paper* **1272**, 1–73.

Ewart, A., Marsh, J. S., Milner, S. C., Duncan, A. R., Kamber, B. S. & Armstrong, R. A. 2004. Petrology and geochemistry of early Cretaceous bimodal continental flood volcanism of the NW Etendeka, Namibia. Part 2: Characteristics and petrogenesis of the high-Ti latite and high-Ti and low-Ti voluminous quartz latite eruptives. *Journal of Petrology* **45**, 107–38.

Frost, C. D. & Frost, B. R. 1997. Reduced rapakivi-type granites: the tholeiite connection. *Geology* **25**, 647–50.

Gamble, J. A., Meighan, I. G. & McCormick, A. G. 1992. The petrogenesis of Tertiary microgranites and granophyres from the Slieve Gullion central complex, NE Ireland. *Journal of the Geological Society, London* **149**, 93–106.

Garland, F., Hawkesworth, C. J. & Mantovani, M. S. M. 1995. Description and petrogenesis of the Paraná rhyolites. *Journal of Petrology* **36**, 1193–227.

Green, J. C. & Fitz, T. J. 1993. Extensive felsic lavas and rheoign-imbrites in the Keweenawan Midcontinent Rift plateau volcanics, Minnesota: petrographic and field recognition. *Journal of Volcanology and Geothermal Research* **54**, 177–96.

Grove, T. L. & Baker, M. B. 1984. Phase equilibrium controls on the tholeiitic versus calc–alkaline differentiation trends. *Journal of Geophysical Research* **89**, 3253–74.

Halliday, A. N., Davidson, J. P., Hildreth, W. & Holden, P. 1991. Modelling the petrogenesis of high Rb/Sr silicic magmas. *Chemical Geology* **92**, 107–14.

Hawkesworth, C., Kelley, S., Turner, S., Le Roex, A. & Storey, B. 1999. Mantle processes during Gondwana break-up and dispersal. *Journal of African Earth Sciences* **28**, 239–61.

Helz, R. T. 1976. Phase relations of basalts in their melting ranges at $P_{H_2O}=5$ kbar. Part II. Melt compositions. *Journal of Petrology* **17**, 139–93.

Henry, C. D., Price, J. G., Rubin, J. N., Parker, D. F., Wolff, J. A., Self, S., Franklin, R. & Barker, D. S. 1988. Widespread, lavalike silicic volcanic rocks of Trans-Pecos Texas. *Geology* **16**, 509–12.

Hergt, J. M. 1987. *The origin and evolution of the Tasmanian dolerites.* PhD Thesis. The Australian National University, Canberra.

Holloway, J. R. & Burnham, C. W. 1972. Melting relationships of basalt with equilibrium water pressure less than total pressure. *Journal of Petrology* **13**, 1–29.

Holtz, F. & Johannes, W. 1994. Maximum and minimum water contents of granitic melts: implications for chemical and physical properties of ascending magmas. *Lithos* **32**, 149–59.

Huppert, H. E. & Sparks, R. S. J. 1988. The generation of granitic magmas by intrusion of basalt into continental crust. *Journal of Petrology* **29**, 599–624.

Jolly, W. T., Dickin, A. P. & Wu, T.-W. 1992. Geochemical stratigraphy of the Huronian continental volcanics at Thessalon, Ontario: contributions of two-stage crustal fusion. *Contributions to Mineralogy and Petrology* **110**, 411–28.

Kretz, R. 1982. Transfer and Exchange equilibria in a portion of the pyroxene quadrilateral as deduced from natural and experimental data. *Geochimica et Cosmochimica Acta* **46**, 411–21.

Lambert, R. St. J., Marsh, I. K. & Chamberlain, V. E. 1989. The occurrence of interstitial granite-glass in all formations of the Columbia River Basalt Group and its petrogenetic implications. *Geological Society of America Special Paper* **239**, 321–32.

Leeman, W. P. 1982. Rhyolites of the Snake River Plain–Yellowstone Plateau Province, Idaho and Wyoming: a summary of petrogenetic models. *In* Bonnischen, B. & Breckenridge, R. M. (eds) *Cenozoic Geology of Idaho. Idaho Bureau of Mines and Geology Bulletin* **26**, 63–6.

Lightfoot, P. C., Hawkesworth, C. J. & Sethna, S. F. 1987. Petrogenesis of rhyolites and trachytes from the Deccan Trap: Sr, Nd and Pb isotope and trace element evidence. *Contributions to Mineralogy and Petrology* **95**, 44–54.

McCurry, M., Hayden, K. P., Morse, L. H. & Mertzman, S. 2008. Genesis of post-hotspot, A-type rhyolite of the Eastern Snake River Plain volcanic field by extreme fractional crystallization of olivine tholeiite. *Bulletin of Volcanology* **70**, 361–83.

McDougall, I. 1962. Differentiation of the Tasmanian dolerites: Red Hill dolerite-granophyre association. *Geological Society of America Bulletin* **73**, 279–316.

Mahoney, J. J. & Coffin, M. F. (eds) 1997. *Large igneous provinces: continental, oceanic, and planetary flood volcanism. Geophysical Monograph* **100**, 438 pp. Washington, DC: American Geophysical Union.

Marsh, B. D. 2002. On bimodal differentiation by solidification front instability in basaltic magmas, part 1: Basic mechanics. *Geochimica et Cosmochimica Acta* **66**, 2211–29.

Marsh, J. S. & Eales, H. V. 1984. The chemistry and petrogenesis of igneous rocks of the Karoo Central Area, Southern Africa. *Geological Society of South Africa Special Publication* **13**, 27–69.

Martin, E. & Sigmarsson, O. 2007. Low-pressure differentiation of tholeiitic lavas as recorded in segregation veins from Reykjanes (Iceland), Lanzarote (Canary Islands) and Masaya (Nicaragua). *Contributions to Mineralogy and Petrology* **154**, 559–73.

Milner, S. C. & Ewart, A. 1989. The geology of the Goboboseb Mountain volcanics and their relationship to the Messum Complex, Namibia. *Communications of the Geological Survey of Namibia* **5**, 31–40.

Morse, S. A. 1980. *Basalts and phase diagrams: an introduction to the quantitative use of phase diagrams in igneous rocks*. Berlin, Heidelberg, New York: Springer-Verlag. 493 pp.

Nicholson, S. W. & Shirey, S. B. 1990. Midcontinent Rift volcanism in the Lake Superior region: Sr, Nd, and Pb isotopic evidence for a mantle plume origin. *Journal of Geophysical Research* **95**, 10851–68.

Patiño Douce, A. E. & Johnston, A. D. 1991. Phase equilibria and melt productivity in the pelitic system: implications for the origin of peraluminous granitoids and aluminous granulites. *Contributions to Mineralogy and Petrology* **107**, 202–18.

Pearce, J. A., Harris, N. B. W. & Tindle, A. G. 1984. Trace element discrimination diagrams for the tectonic interpretation of granitic rocks. *Journal of Petrology* **25**, 956–83.

Peate, D. W., Hawkesworth, C. J. & Mantovani, M. S. M. 1992. Chemical stratigraphy of the Paraná lavas, South America: classification of magma types and their spatial distribution. *Bulletin of Volcanology* **55**, 119–39.

Piccirillo, E. M., Bellieni, G., Cavazzini, G., Comin-Chiaramonti, P., Petrini, R., Melfi, A. J., Pinese, J. P. P., Zantadeschi, P. & De Min, A. 1987. Bimodal fissural volcanic suites from the Paraná Basin (Brazil): K–Ar age, Sr-isotopes and geochemistry. *Geochemica Brasiliensis* **1**, 53–69.

Piccirillo, E. M. & Melfi, A. J. 1988. *The Mesozoic flood volcanism of the Paraná Basin: petrogenetic and geophysical aspects*. São Paulo: IAG–USP Press. 600pp.

Rapp, R. P., Watson, E. B. & Miller, C. F. 1991. Partial melting of amphibolite/eclogite and the origin of Archaean trondhjemites and tonalites. *Precambrian Research* **51**, 1–25.

Rapp, R. P. & Watson, E. B. 1995. Dehydration melting of metabasalt at 8–32 kbar: implications for continental growth and crust-mantle recycling. *Journal of Petrology* **36**, 891–931.

Rushmer, T. 1991. Partial melting of two amphibolites: contrasting experimental results under fluid-absent conditions. *Contributions to Mineralogy and Petrology* **107**, 41–59.

Rutter, M. J. & Wyllie, P. J. 1988. Melting of vapour-absent at 10 kb to simulate dehydration-melting in the deep crust. *Nature* **331**, 159–60.

Sisson, T. W., Ratajeski, K., Hankins, W. B. & Glazner, A. F. 2005. Voluminous granitic magmas from common basaltic sources. *Contributions to Mineralogy and Petrology* **148**, 635–61.

Skjerlie, K. P. & Johnston, A. D. 1993. Fluid-absent melting behaviour of an F-rich tonalitic gneiss at mid-crustal pressures: implications for the generation of anorogenic granites. *Journal of Petrology* **34**, 785–815.

Snyder, D., Carmichael, I. S. E. & Wiebe, R. A. 1993. Experimental study of liquid evolution in an Fe-rich, layered mafic intrusion: constraints of Fe–Ti oxide precipitation on the T–fO_2 and T–p paths of tholeiitic magmas. *Contributions to Mineralogy and Petrology* **113**, 73–86.

Sparks, R. S. J., Huppert, H. E., Kerr, R. C., McKenzie, D. P. & Tait, S. R. 1985. Post cumulus processes in layered intrusions. *Geological Magazine* **122**, 555–68.

Spulber, S. D. & Rutherford, M. J. 1983. The origin of rhyolite and plagiogranite in oceanic crust: an experimental study. *Journal of Petrology* **24**, 1–25.

Sylvester, P. J. 1989. Post-collisional alkaline granites. *Journal of Geology* **97**, 261–80.

Thy, P., Beard, J. S. & Lofgren, J. E. 1990. Experimental constraints on the origin of Icelandic rhyolites. *Journal of Geology* **98**, 417–21.

Thy, P. & Lofgren, G. E. 1994. Experimental constraints on the low-pressure evolution of transitional and mildly alkalic basalts: the effect of Fe–Ti oxide minerals and the origin of basaltic andesites. *Contributions to Mineralogy and Petrology* **116**, 340–51.

Turner, S. P. 1996. Petrogenesis of the late-Delamerian gabbroic complex at Black Hill, South Australia: implications for convective thinning of the lithospheric mantle. *Mineralogy and Petrology*, **56**, 51–98.

Turner, S. P., Foden, J. D. & Morrison, R. S. 1992. Derivation of some A-type magmas by fractionation of basaltic magma and an example from the Padthaway Ridge, South Australia. *Lithos* **28**, 151–71.

Turner, S. P. & Foden, J. D. 1996. Magma mingling in late-Delamerian A-type granites at Mannum, South Australia. *Mineralogy and Petrology* **56**, 147–69.

Vielzeuf, D. & Holloway, J. R. 1988. Experimental determination of the fluid-absent melting relations in the pelitic system. *Contributions to Mineralogy and Petrology* **98**, 257–76.

Walsh, J. N., Beckinsdale, R. D., Skelhorn, P. R. & Thorpe, R. S. 1979. Geochemistry and petrogenesis of Tertiary granitic rocks from the Island of Mull, northwest Scotland. *Contributions to Mineralogy and Petrology* **71**, 99–116.

Whitaker, M. L., Nekvasil, H., Lindsley, D. H. & McCurry, M. 2008. Can crystallization of olivine tholeiite give rise to potassic rhyolites? – An experimental investigation. *Bulletin of Volcanology* **70**, 417–34.

MS received 27 December 2007. Accepted for publication 13 May 2008 (Stellenbosch); 15 January 2009 (RSE).

Structural controls on melt segregation and migration related to the formation of the diapiric Schwerin Fold in the contact aureole of the Bushveld Complex, South Africa

Luke Longridge[1], Roger L. Gibson[1] and Paul A. M. Nex[1,2]

[1] School of Geosciences, University of the Witwatersrand, Johannesburg, PVT Bag 3, Wits, 2050, South Africa
Email: luke.longridge@wits.ac.za

[2] Umbono Group of Companies, Isle of Houghton, Johannesburg, South Africa

ABSTRACT: Partial melting of metapelitic rocks beneath the mafic–ultramafic Rustenburg Layered Suite of the Bushveld Complex in the vicinity of the periclinal Schwerin Fold resulted in a structurally controlled distribution of granitic leucosomes in the upper metamorphic aureole. In the core of the pericline, subvertical structures facilitated the rise of buoyant leucosome through the aureole towards the contact with the Bushveld Complex, with leucosomes accumulating in en-echelon tension gashes. In a subhorizontal syn-metamorphic shear zone to the southeast of the pericline, leucosomes accumulated in subhorizontal dilational structural sites. The kinematics of this shear zone are consistent with slumping of material off the southeastern limb of the rising Schwerin pericline. The syndeformational timing of leucosome emplacement supports a syn-intrusive, density-driven origin for the Schwerin Fold. Modelling of the cooling of the Rustenburg Layered Suite and heating of the floor rocks using a multiple intrusion model indicates that temperatures above the solidus were maintained for >600,000 years up to 300 m from the contact, in agreement with rheological modelling of floor-rock diapirs that indicate growth rates on the order of 8 mm/year for the Schwerin Fold.

KEY WORDS: diapiric fold, granite leucosomes, thermal modelling

The role of deformation in the initial segregation, migration and accumulation of leucosomes has been investigated in a wide variety of regional metamorphic terrains (e.g. Brown 1994 and references therein; Brown & Solar 1998; Kisters *et al.* 1998). Additionally, studies have demonstrated the weakening effect of melt on the rheology of rocks (e.g. Bai *et al.* 1997; Gleason *et al.* 1999; Holyoke & Rushmer 2002). Although many studies exist that demonstrate the relationship between deformation and melting in an orogenic context, few studies exist where melting and deformation relationships have been examined in contact metamorphic aureoles (e.g. Rosenberg & Berger 2000; Vernon *et al.* 2003). In the northeastern parts of the contact aureole to the Bushveld Complex, South Africa, a number of kilometre-scale periclinal fold structures are found in the upper amphibolite- to granulite-grade floor rocks underlying the Bushveld Complex. The Schwerin Fold is one of these periclinal structures developed in migmatitic rocks of the upper Transvaal Supergroup. Here, the interplay of deformation and anatexis and, particularly, the positive feedback loop between deformation-enhanced melt accumulation and migration, and the rheological consequences of deformation in partially molten rocks, can be investigated.

1. Melting sites and melt migration in metamorphic terranes

The importance of deformation in the migration and ascent of granitic magmas in orogens has been noted repeatedly (e.g. Brown 1994, 2005; Kisters *et al.* 1998) and, although the buoyancy of low-density granitic magma is a primary driving force for the ascent of the magma, fault systems and shear zones are needed as conduits. In addition to gravity-driven ascent of buoyant magma, non-hydrostatic stresses and pressure gradients may also drive melt into, and along structures. Strain localisation in migmatite terrains is a key factor in the accumulation, segregation and transport of granitic melt, and a positive feedback exists between deformation-initiated melt mobilisation, melt accumulation promoting ductile deformation processes and enhancing bulk strain partitioning, and the buoyant rise of segregated melts (Kisters *et al.* 1998). In orogenic terrains, where heating of rocks to upper amphibolite to granulite facies conditions is generally accompanied by progressive deformation, this deformation can result in the formation of low-pressure sites where melt can preferentially accumulate. These low-pressure sites can include boudin necks (Vernon *et al.* 2003), extensional shear bands (Brown *et al.* 1995), shear zones (Bhadra *et al.* 2007), and fold axial planes (Hand & Dirks 1992). These low-pressure sites also play a key role in the segregation of mafic selvedges from leucosome (Sawyer 1991). This melt accumulation leads to a localised increase in the ductility of the rocks in the vicinity of the melt, which in turn increases strain partitioning in the vicinity of the melt.

2. Regional geological setting and previous work

The intrusion of the ~8 km-thick, 2·06 Ga (Walraven *et al.* 1990) sill-like mafic-ultramafic Rustenburg Layered Suite (RLS) of the Bushveld Complex (Fig. 1) into the sedimentary

© 2009 The Royal Society of Edinburgh. doi:10·1017/S1755691009016119

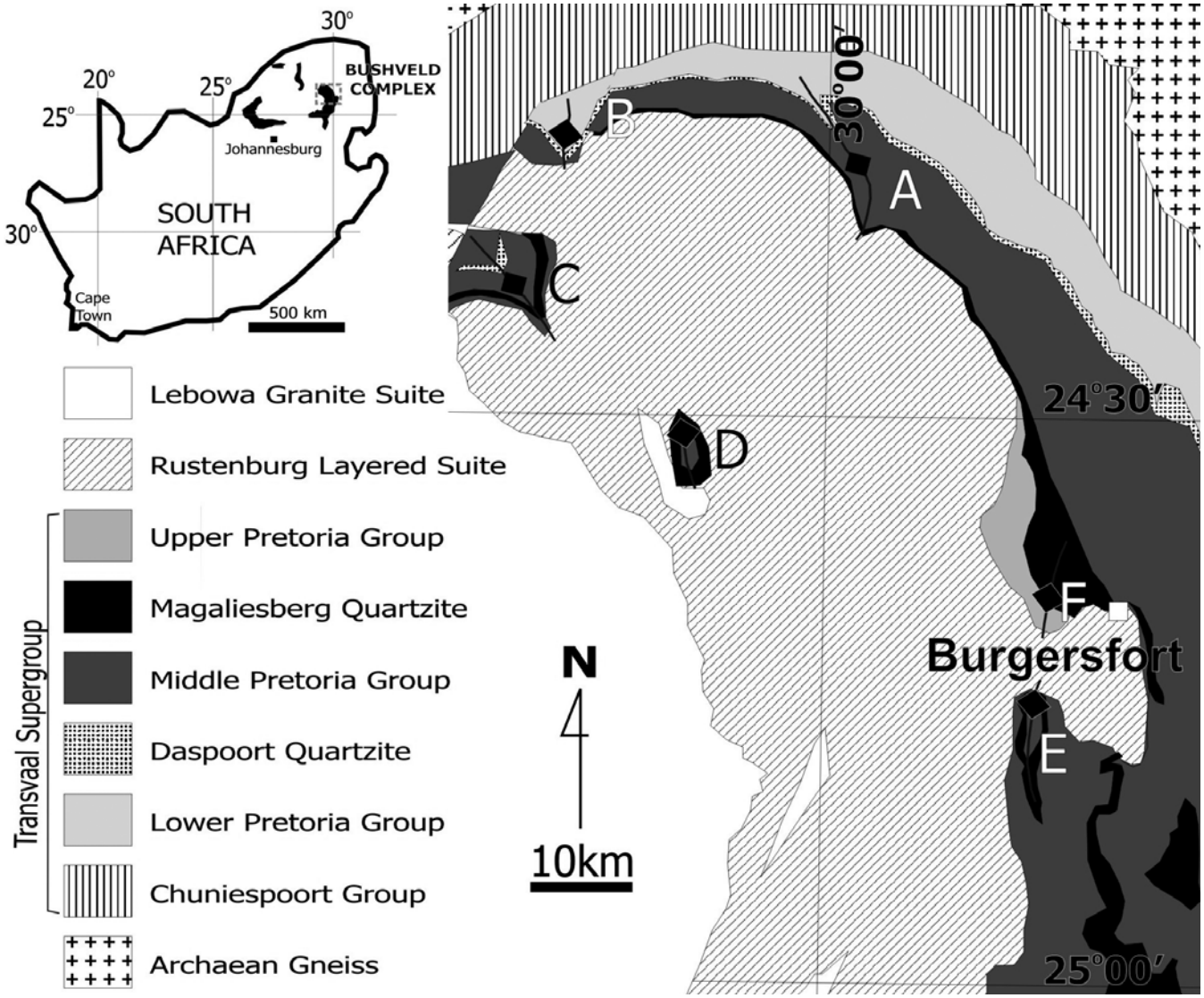

Figure 1 Geological map of the northeastern limb of the Bushveld Complex, showing locations of the Schwerin Fold (A) and other fold structures: B=Katkloof; C=Phosiri; D=Phepane; E=Steelpoort; F=Derde Gelid. After 1:250 000 Geological Series sheets 2429B (Chuniespoort) and 2430A (Wolkberg) (Schwellnus *et al.* 1962).

rocks of the Transvaal Supergroup formed a metamorphic aureole in the floor rocks that extends up to tens of kilometres from the RLS contact. Since the RLS intruded horizontally, the term 'upper aureole' is used to describe the highest-grade rocks that lie immediately below the contact with the RLS. In the upper aureole, metamorphic grade reached granulite grade (indicated by the presence of metamorphic orthopyroxene locally in rocks proximal to the RLS contact; Uken 1998; Johnson *et al.* 2003), and migmatites formed in pelitic and psammitic rocks. Mapping of the floor rocks to the RLS in the northeastern Bushveld Complex has revealed a number of domes and periclines within both these high-grade migmatites and the lower-grade unmigmatised metapelites (Fig. 1). Early workers suggested that these structures formed as a result of regional compression and modification of pre-Bushveld folds during the intrusion of the RLS (Sharpe & Chadwick 1982; du Plessis and Walraven 1990; Hartzer 1995), but more recent work (Uken & Watkeys 1997; Uken 1998; Johnson *et al.* 2004) has suggested that these structures are the result of gravity-induced diapiric rise of low-density argillaceous, arenaceous and calcareous rocks into the dense mafic magmas of the RLS (Uken & Watkeys 1997), a mechanism initially proposed by Button (1978). The Schwerin Fold (located ~60 km NNW of the town of Burgersfort; Fig. 1) is one such pericline and is developed in rocks of the upper Pretoria Group (Transvaal Supergroup; Fig. 2).

Contact metamorphic effects beneath the RLS in the northeastern Bushveld Complex extend throughout the Pretoria Group, with temperatures of ~450°C in rocks of the lower Pretoria Group (Waters & Lovegrove 2002), and up to ~750°C near the contact with the RLS (Johnson *et al.* 2003, 2004). Bulk compositional variation, as well as metamorphic grade, controls mineral assemblages in the aureole. A regional study of anatectic migmatites in the eastern Bushveld Complex aureole by Johnson *et al.* (2003) emphasised the role of deformation in the migration and ascent of melts. They noted that, throughout the upper aureole, migmatites occur in rocks that are gently folded on a m-scale, with a moderate to weak foliation, and that are locally more intensely strained (particularly in the vicinity of the km-scale periclines). In the zone closest to the contact with the RLS, Johnson *et al.* (2003) described migmatites associated with a variety of structural features. These include quartz-sillimanite veins, approximately parallel to the subhorizontal bedding in the area, which are folded into cm- to dm-scale open to tight, locally ptygmatic folds, and which contain a foliation similar to that in the host

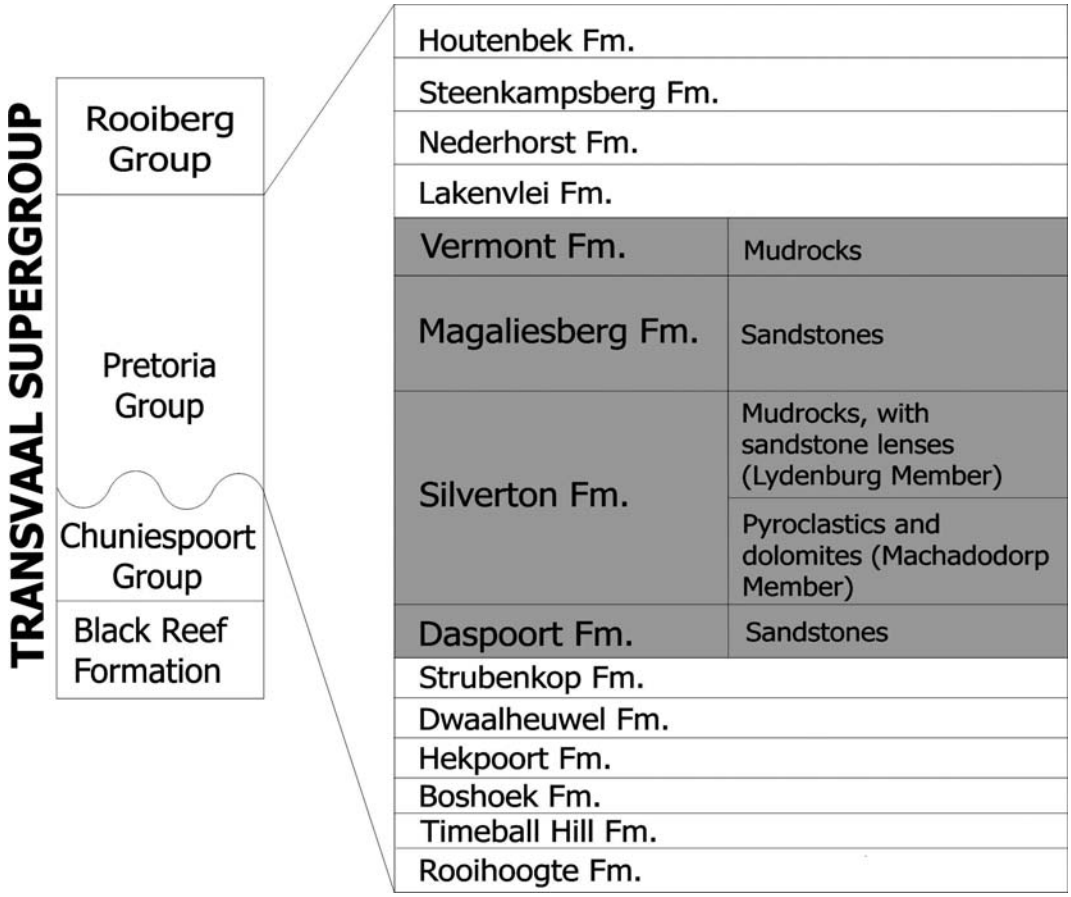

Figure 2 Stratigraphy of the Transvaal Supergroup showing the detailed stratigraphy and lithologies of the Pretoria Group in the study area. Formations which dominate the study area are shaded in grey. Modified after Eriksson *et al*. (1993).

rocks. They interpreted these features as channels for H_2O- and volatile-rich melts. Also noted were higher-strain domains commonly associated with discordant leucosomes, that are commonly located above the small antiformal closures of folded quartz-sillimanite veins. The significance of this contemporaneous relationship between melting and deformation is explored further below.

3. Geology of the Schwerin Fold

The Schwerin Fold (Figs 1, 3) is a kilometre-scale, upright to steeply inclined, gently- to moderately-plunging periclinal structure that is developed in the arenaceous to argillaceous rocks (with minor pyroclastic and calcareous rocks) of the Pretoria Group (uppermost Transvaal Supergroup; Fig. 2). The contact with the RLS is at the level of the Vermont Formation. The Schwerin Fold has a maximum wavelength of ~8 km and an amplitude of ~5 km, but is disharmonic, and the interlimb angle decreases to that of a tight fold in the stratigraphically-highest layers closest to the RLS. The fold is asymmetric, with steeper dips (70–80°) on the western limb and shallower dips (20–40°) on the eastern limb (Fig. 3). The regional dip of the rocks in the area is towards the RLS (~25°SW), subparallel to the magmatic layering in the RLS. The Schwerin Fold differs from other periclines in the floor to the RLS in its asymmetry, and in that it has a curved axial trace, which is perpendicular to the contact with the RLS at the contact but curves to subparallel to the RLS strike away from the contact. However, like the other periclines in the RLS aureole (Uken & Watkeys 1997; Uken 1998), it has gentle to open synclinal areas adjacent to both limbs. For simplicity of structural analysis, the Schwerin Fold has been divided into three sub-domains.

3.1. Domain 1 – metasediments in the contact aureole away from the Schwerin Fold

At a distance of 3–6 km from the contact with the RLS, in the NE of the study area, pelitic rocks of the Lydenburg Member (Silverton Formation; Fig. 2) dip shallowly (~25°) SW. The rocks retain original sedimentary compositional layering, defined by layers which are more or less biotite-rich (Fig. 4A). A moderately SE-dipping (~35°), moderate to weak foliation defined by biotite occurs oblique to bedding (Fig. 4B). The rocks are not migmatised and contain the assemblage andalusite–biotite–cordierite–quartz–ilmenite/magnetite. The matrix consists of fine (0·01–0·2 mm) quartz, biotite and ilmenite/magnetite. Andalusite porphyroblasts are generally stubby to elongate, 1–5 cm long, chiastolitic, and lie with their longest dimensions within the bedding plane (indicating a compositional control). Andalusite contains graphite and small (0·05–0·1 mm) muscovite and quartz inclusions towards the core, and larger (0·1–0·2 mm) quartz and biotite inclusions near the rim. Cordierite porphyroblasts are 0·5–5 mm in size, and some cordierite porphyroblasts are texturally zoned, with an inclusion-rich core and an inclusion-free rim. Cordierite contains fine (0·01–0·1mm) inclusions of quartz, biotite and ilmenite/magnetite, which are aligned parallel to the foliation observed in the matrix. Andalusite has inclusions aligned parallel to the foliation, although this is less distinctive owing to the generally inclusion-free nature of andalusite relative to cordierite. No pressure shadows exist adjacent to either andalusite or cordierite (which, together with alignment of inclusions, supports post-tectonic growth). This contrasts with

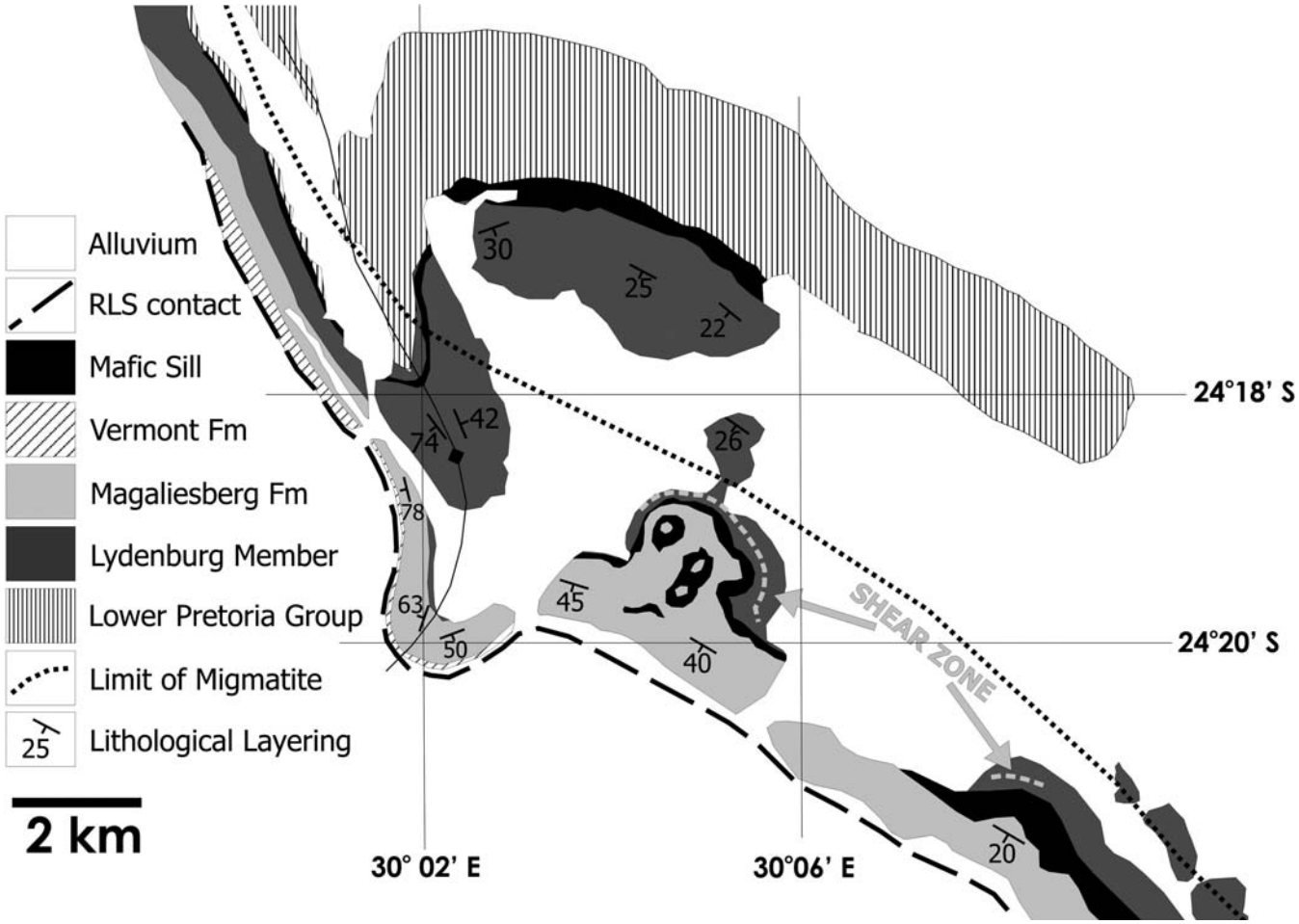

Figure 3 Geological map of the Schwerin Fold, showing the lower limit of migmatite development in the contact aureole. Note the change in strike of the axial surface and the steeper dip of strata on the western limb. Modified after Uken (1998).

textures further from the RLS contact reported by Uken (1998), which show flattening of the bedding-parallel foliation around andalusite porphyroblasts.

3.2. Domain 2 – metasediments from the Schwerin Fold

The second domain includes metapelites (Lydenburg Member) in the core of the Schwerin Fold, as well as the quartzites (Magaliesberg Formation) closer to the contact with the RLS (Fig. 3). Closest to the contact with the RLS, the Magaliesberg Formation quartzite forms a prominent ridge. This quartzite describes a moderately SW-plunging anticlinal fold with a 3 km wavelength. Bedding dip varies from ~70°WSW to vertical on the western limb of the fold to ~40°S to SSE on the southeastern limb of the fold. The quartzites are well bedded, and retain numerous original sedimentary features, including trough cross-bedding and ripple marks. Cross-bedding confirms that the rocks have not been overturned. The rocks are coarsely recrystallised and 2–3 cm long euhedral quartz crystals are found filling vugs in the quartzite, consistent with hydrothermal fluid activity. In places on the western limb a weak foliation is defined by elongate quartz grains. This foliation is slightly oblique to bedding, striking 010° and dipping steeply at 70°W. Gentle to open folds, with a 2–5 m wavelength and 0·5 m to 1 m amplitude are present in the quartzites, and plunge steeply NW.

The core of the Schwerin Fold is defined by a ridge of pelitic to semi-pelitic rocks of the Lydenburg Member (Figs 2, 3) and calc-silicates and volcanic breccias of the Machadodorp Member (Fig. 2). Bedding is defined by mm- to cm-thick siliceous layers and sedimentary structures (graded, flaser and rare trough cross-bedding) that indicate a right-way-up sequence. Bedding is generally moderately dipping, but has a variable orientation caused by dm- to m-scale open to tight folds. A penetrative subvertical foliation is present which, at distances of >2 km from the contact with the RLS, is defined by biotite.

The northeastern parts of Domain 2 straddle the lower limit of migmatite development, and contain the assemblage andalusite–biotite–cordierite–plagioclase–muscovite–quartz in lower-grade metapelites, and andalusite–biotite–cordierite–plagioclase–muscovite–fibrolite–quartz in higher-grade samples. Biotite occurs as 0·5–1 mm grains with 0·02–0·1 mm inclusions of quartz, although it is generally inclusion-free. It is locally retrogressed to chlorite. Texturally-late muscovite is present as large (>1 mm) vermicular grains, which overgrow the foliation. Cordierite is 0·5–1 mm in size, and contains fine (0·01 mm) inclusions of quartz and coarser (0·1 mm) inclusions of biotite (Fig. 4H). It is commonly texturally zoned, with inclusion-free rims surrounding inclusion-rich cores, and may show sector twinning. Cordierite porphyroblasts are commonly lensoid and aligned with the foliation (indicating syntectonic growth). In higher-grade samples, fibrolite is developed around biotite, and appears to form at the expense of biotite (Fig. 4G). Where fibrolite is developed, it is not distributed throughout the sample, but occurs as discrete 'seams' within the sample, along which it replaces biotite. Locally, 1–3 cm-long andalusite porphyroblasts are aligned parallel to the biotite and fibrolite foliations, supporting

syn-tectonic growth, although textural evidence indicates that fibrolite postdates andalusite.

A thin garnet-bearing horizon below the migmatite zone contains the assemblage garnet–biotite–cordierite–muscovite–ilmenite–quartz, with 0·2–1 mm subhedral garnet porphyroblasts preferentially developed in ilmenite-rich beds. Garnet contains 0·01–0·02 mm inclusions of quartz and ilmenite, and the moderate biotite foliation may bend gently around the garnet porphyroblasts, although generally it does not wrap around garnet, suggesting late- to post-tectonic growth of the latter.

Within ~2 km of the outcrop of the RLS contact, the pelitic rocks are cut by coarse-grained to pegmatitic quartz–feldspar–fibrolite–tourmaline–muscovite leucosomes, which may contain peritectic cordierite (see also Johnson *et al.* 2003). As the contact is approached, a progressive increase in the volume of leucosome is seen. In the lowermost migmatite zone, the leucosomes develop within metapelites adjacent to quartz-sillimanite veins (originally more psammitic beds; Johnson *et al.* 2003) as 1–5 cm long, 0·5–2 cm wide veins (Fig. 4D) but, with decreasing distance from the contact, they develop into tension gashes up to 30 cm in length and ~5 cm wide (Fig. 4E). As the volume of leucosome increases, the leucosomes become more pod-like, and cross-cut the pelite bedding, forming an interconnected network (Fig. 4F). The leucosomes are coarsely crystalline (quartz grains ~5 mm) to pegmatoidal (quartz grains ~20 mm). Leucosomes with the finest grain size retain a relict fibrolite foliation within them, with a similar orientation to that observed in the pelites, but this foliation is absent in the coarser pegmatites. Granophyric textures are observed; these commonly overgrow fibrolite aggregates, which also occur as inclusions in quartz. Although the leucosomes appear in structurally controlled sites, there is no evidence that deformation continued following leucosome crystallisation. Minerals within the leucosomes are unstrained, and leucosomes show no penetrative fabric.

The modal proportion of fibrolite increases in tandem with the volume of leucosome towards the RLS contact. Textural evidence suggests that fibrolite development was at the expense of biotite, rather than andalusite, and that fibrolite-rich seams correspond to pathways recording the passage of an H_2O-rich volatile phase, which may have been responsible for the fluid-fluxed incongruent melting of biotite (Johnson *et al.* 2003). Johnson *et al.* (2003) suggested that the reaction Pl+Bt+Qtz=Kfs+Crd+L is the most likely melt-producing reaction for typical Lydenburg Member metapelite compositions, although melt-producing reactions vary with temperature and X_{Mg}, and an influx of H_2O may have generated the congruent melting reaction Kfs+Pl+Bt+Crd+Qtz+H_2O=L.

A mafic sill is found at the base of the Lydenburg Member in both the migmatites and lower grade rocks and (like the stratigraphy) is cut by the isograds in the aureole (Fig. 3). This sill has no obvious chill margin, but field evidence (textural and mineralogical variation) suggests that it may be a composite sill composed of at least two phases. It is metamorphosed, with an assemblage tremolite–actinolite–plagioclase–quartz indicating significant rehydration, and does not preserve any original igneous textures.

3.3. Domain 3 – migmatitic shear zone east of the Schwerin Fold

Domain 3 is found in the southeastern part of the study area, on the southeastern limb of the syncline flanking the Schwerin Fold (Fig. 3). Here the uppermost rocks (Silverton Formation) contain a 50 m to 100 m-wide subhorizontal to gently SW-dipping bedding-parallel shear zone (Fig. 3). Below the shear zone, metapelites preserve compositional banding as alternating biotite-rich and quartz-feldspar-rich layers, or as staurolite-rich layers. In less competent lithologies in the shear zone, bedding appears transposed, with rootless tight to isoclinal cm-scale folds of either quartz–feldspar or biotite-rich layers, indicating remnant bedding (Fig. 5A).

Assemblages in more biotite-rich layers are generally quartz–biotite–plagioclase feldspar, with some perthitic K-feldspar, cordierite and muscovite. Generally the rock consists of fine (0·02–0·1 mm) quartz, plagioclase and biotite with a strong foliation, and 0·5–1 mm vermicular muscovite overgrowing the foliation. Cordierite is 0·5–1 mm in size, and contains 0·01 mm inclusions of biotite and quartz. Andalusite is rare, and no fibrolite is developed in these rocks. A shallow WNW-dipping foliation, defined by biotite, wraps around low strain lenses that contain a relict foliation with an obliquity of 15° to 70° relative to the main foliation (Fig. 5B). Pressure shadows around these low strain lenses contain slightly coarser (0·2–0·4 mm) quartz and feldspar (Fig. 5B). No change in assemblage is observed between these low strain lenses and the foliated matrix.

The shear zone is characterised by open, tight and isoclinal m-scale folding (Fig. 5A, C), with fold vergence typically towards the S, SW or W, and an axial planar foliation, defined by biotite, which typically dips shallowly WNW (Fig. 5C). Locally, mullions are present in fold hinges. Listric extensional shear bands (ESBs) are widespread, and are filled with coarse to pegmatoidal quartz–feldspar–tourmaline–muscovite leucosomes, containing 0·5–5 cm biotite schlieren. ESBs range in size from a few cm long and a few mm wide to metres in length and >10 cm wide. Boudins are found rarely in the more competent psammitic layers, and are generally symmetrical, with only weak local asymmetry, indicating an approximately top-to-the-SE sense of shear.

Folds vary from cm-scale recumbent isoclinal folds to gently inclined open m-scale folds, to upright ptygmatic m-scale folds, although most folds are ~0·5 m to 1 m in wavelength, and are tight to isoclinal, gently plunging, and moderately to gently inclined (Fig. 5C). Although there is a large variation in fold hinge azimuth, no sheath folds were found. The foliation is refracted by compositional layering. Deformation styles vary within the shear zone, depending upon the lithology. In pelitic rocks, which are the predominant lithology towards the base of the shear zone, the rocks are highly foliated. In this zone of less competent lithologies, folds are rare and, where seen, are cm-scale and isoclinal (Fig. 5A), consistent with extreme transposition. Towards the top of the shear zone, a more competent psammitic lithology predominates, and larger-scale folds, ESBs and boudins are common. Below the shear zone, where only minor leucosome veins are found in boudin necks, the rocks lack evidence of shear-related deformation. The shear zone can be traced over a strike length of ~10 km southeastwards from the hinge of the Schwerin Fold; however it has not been found near the hinge or on the northern limb of the Schwerin Fold.

Leucosomes from ESBs within the shear zone have an assemblage comprising quartz–microcline–biotite–muscovite–plagioclase–tourmaline ± cordierite. Microcline is extremely coarse (>5 mm) and contains ~0·2 mm rounded to subidioblastic inclusions of quartz, plagioclase, muscovite and biotite (Fig. 5F). Biotite occurs either as small (~0·5 mm) euhedral flakes or as larger (~3 mm) schlieren, which are unlikely to be crystallisation products, but appear to have been entrained during anatexis and leucosome movement (see Fig. 5E). This biotite is slightly more magnesian (Mg#=50–53) than that from the host rocks (Mg#=33–39; Longridge 2006), and may be the restitic product of the partial melting which formed the leucosomes. Muscovite is commonly poikilitic. Leucosomes

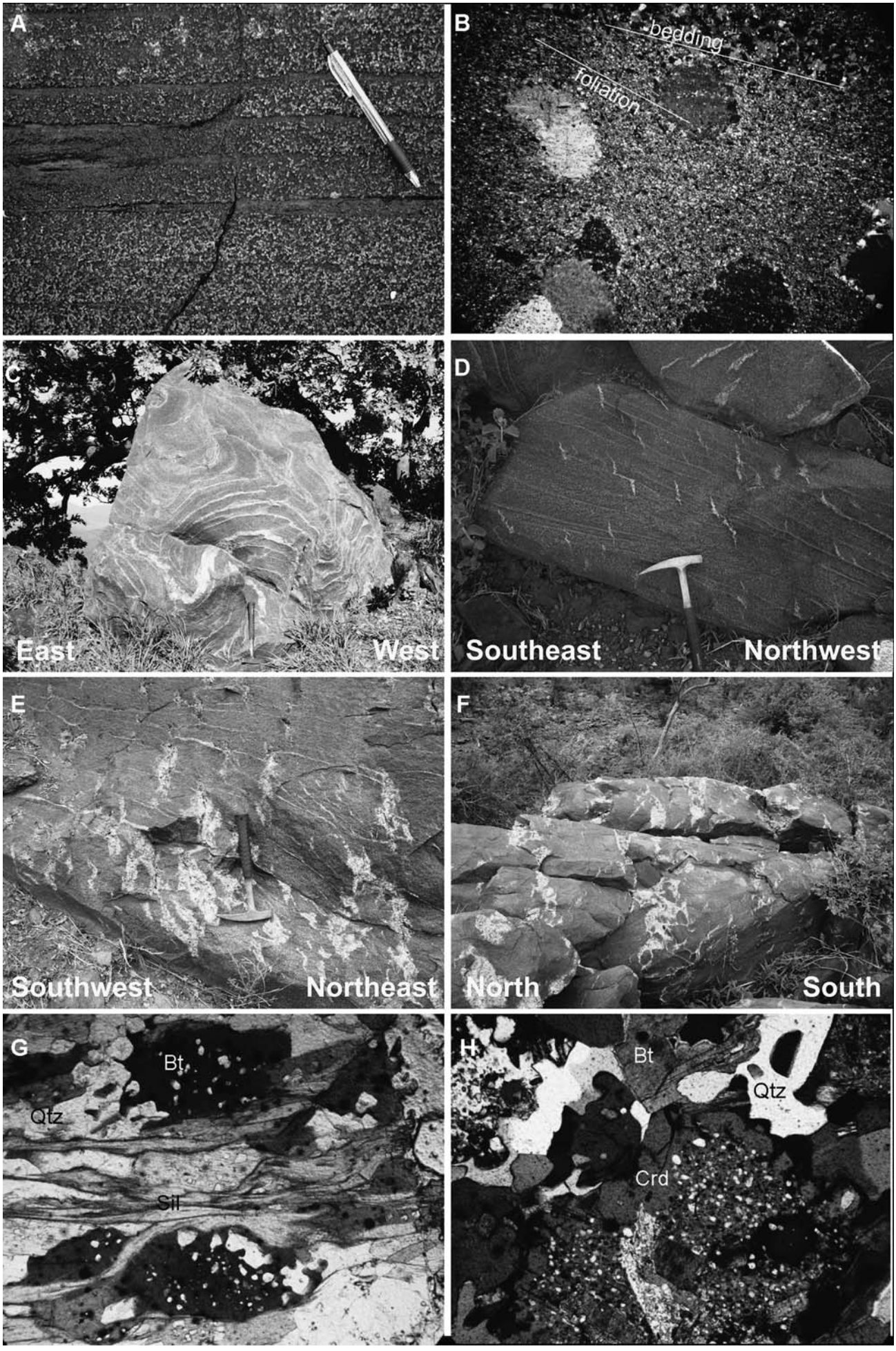
A
B
bedding
foliation
C
East
West
D
Southeast
Northwest
E
Southwest
Northeast
F
North
South
G
Bt
Qtz
Sil
H
Bt
Qtz
Crd

may contain biotite selvedges at their margins. These leucosomes are similar to the small granite sheets found in the migmatite zone in the eastern Bushveld Complex metamorphic aureole, which Harris *et al*. (2003) attributed to incongruent melting of biotite in the pelites of the Silverton Formation. No post-crystallisation deformation features or any evidence for strain is observed in the leucosomes, indicating that deformation had ceased in the shear zone by the time the leucosomes had crystallised.

4. Structural geology of the Schwerin Fold

The broad structure of the Schwerin Fold differs from other comparable structures such as the Katkloof Fold (Fig. 1), in that it has a strongly curved axial trace. At the contact with the RLS, the Schwerin Fold hinge plunges towards the SW, whereas the fold hinge in the core of the fold has a SSE plunge (Fig. 6). Both the eastern and western limbs of the Schwerin Fold give way to open synclines, where the strike of the rocks adjacent to the pericline gently curves into the regional NW–SE strike of the Pretoria Group rocks.

A structural investigation by Uken (1998) focused primarily on the non-migmatitic core of the Schwerin Fold, where he noted boudinaged calc–silicate layers and cuspate–lobate folds with radially oriented fold axes. These folds were noted to have an associated axial planar cleavage, and slickenside lineations on bedding surfaces, consistent with a flexural slip fold mechanism (Uken 1998). Also noted was a non-penetrative bedding-parallel S_2 cleavage in the limbs of the fold.

4.1. Low-grade metapelites away from the Schwerin Fold

In the northeast of the study area, low-grade metapelites are not affected by the Schwerin Fold, and structures are more representative of the regional trends in the floor rocks to the RLS. In this area, the bedding in metapelites of the Lydenburg Member dips moderately towards the RLS (average orientation 124°/18°SW) and the oblique foliation defined by biotite has an average orientation of 232°/32°SE (Fig. 6B[II]).

4.2. Quartzites adjacent to the RLS contact

Adjacent to the RLS contact, competent Magaliesberg Formation quartzites appear to inhibit foliation formation, with the foliation only locally developed and defined by an elongation of quartz grains. Bedding orientations in the hinge of the fold define a π-pole girdle, which gives a fold axis plunge of 47° on an azimuth of 227° (Fig. 6D[II]). Bedding data from the northwestern limb are more scattered than those from the southeastern limb. A best-fit partial π-pole girdle through these data defines a fold plunge of 52° on 346° (Fig. 6D[II]). A progressive change in bedding orientation occurs from ~170°/78°W in the north to ~195°/62°W in the south. Bedding orientations on the northwestern limb are steeper than those on the southeastern limb.

4.3. Metasediments from the core of the Schwerin Fold

In the core of the Schwerin Fold, bedding data from the Lydenburg Shale Member show more scatter than data from the quartzites adjacent to the contact. The data define a π-pole girdle with a fold axis plunge of 26° on 188° (Fig. 6A[II]). This is slightly shallower than the hinge-line orientations of m-scale outcrop folds, but the azimuths nonetheless correspond well. Foliations from metapelites of the Lydenburg Member are approximately vertical to steeply W-dipping and N–S trending in the centre of the pericline, but some variation in orientation occurs.

4.4. Shear Zone

Within and adjacent to the shear zone to the east of the Schwerin Fold, a number of structural elements are present. Bedding and foliation orientations are variable, but, on average, they are 146°/16°SW and 202°/20°W, respectively (Fig. 6C[II]).

Extensional shear band (ESB) orientations are also variable, owing to their listric nature, and give an average orientation of 106°/22°S (Fig. 6C[II]; given the curved character of the ESBs, an average value is likely to be the best representation of their orientation). ESBs are not present as a conjugate set, but display a consistent vergence towards the SSW. Boudin axes plunge shallowly to the east or west. Lineations are also sub-horizontal, and plunge either shallowly NNW or SSE, with the exception of a single outlier, which has an orientation of 30° on 225°. Most lineations are located on bedding surfaces, and are mineral stretching lineations. Fold hinges have highly variable orientations. The plunge of most folds is quite shallow, but azimuths vary from N to W and S.

5. Structural interpretation of the Schwerin Fold

In order to understand the orientation of structures in the Schwerin Fold, consideration must be given to the orientation of rocks in the adjacent RLS. A recent re-evaluation of the palaeomagnetism of the Bushveld Complex (Letts 2007), indicates that the RLS acquired its remnant magnetisation (i.e. passed through the Curie temperature) whilst still horizontal. If the fold and shear zone formed before this (see below; also Uken & Watkeys 1997; Uken 1998), then their geometry can only be determined by back-rotating them by an amount equivalent to the average dip of the RLS. Thus, by removing the effects of the regional ~20°SW dip of the RLS and its floor rocks, one can obtain the 'original' orientation of the Schwerin Fold.

Figure 4 (A) Hornfels from the lower aureole (below the migmatite zone) showing lithological layering defined by variable biotite content. Spots are chiastolite porphyroblasts. (B) Photomicrograph of (A) showing cordierite and andalusite porphyroblasts, and a weak foliation slightly oblique to bedding (crossed polars; width of field of view=4 mm). (C) Folding of migmatitic metapelites in the core of the Schwerin Fold. Note the subvertical orientation of the axial plane to the folds, which mirrors the large-scale structure of the pericline. (D) En-echelon tension gashes oriented oblique to bedding in metapelite from the core of the pericline, in the lower migmatite zone. (E) Enlargement of tension gashes in rocks closer to the contact with the RLS than (D), on the western limb of the fold. (F) Patchy leucosome network no longer restricted to tension gashes (upper migmatite zone). (G) Photomicrograph of metapelite from the pericline core, showing fibrolite seams developed at the expense of biotite (uncrossed polars, width of field of view 2 mm). (H) Photomicrograph of metapelite from the core of the pericline, showing a large cordierite porphyroblast with an inclusion-rich core and clear rim, in addition to biotite and corroded quartz, indicating melting (crossed polars; width of field of view=2 mm). Mineral abbreviations after Kretz (1983).

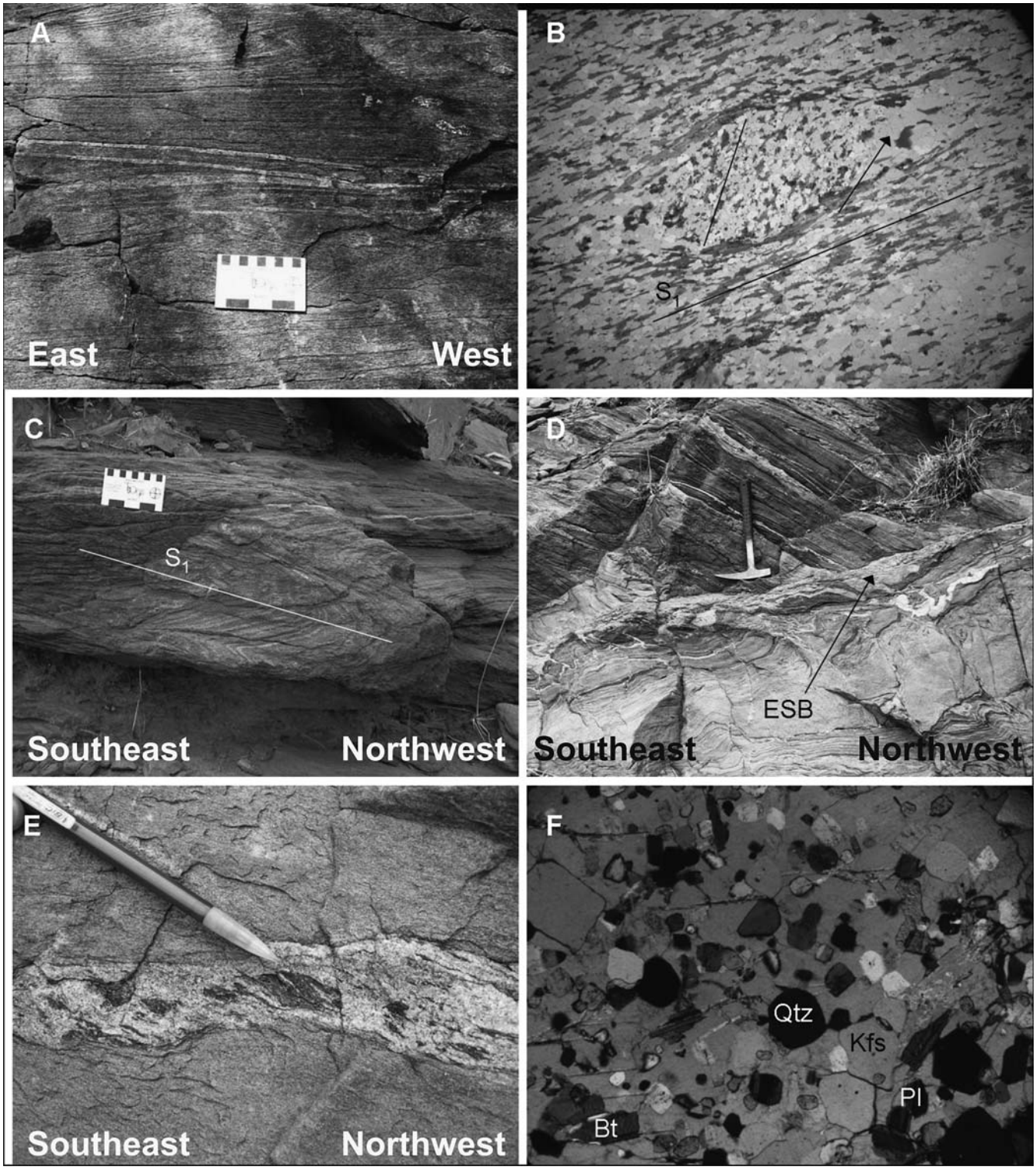

Figure 5 Outcrop and microscopic structural characteristics of the shear zone: (A) Isoclinal intrafolial folds and transposed bedding in semi-pelitic schist; (B) Oblique earlier foliation in a low-strain lens within quartz-biotite schist. Note coarse quartz grains in the pressure shadow formed by this lens. This texture is interpreted as a composite foliation due to progressive shearing deformation rather than overprinting deformation events (uncrossed polars, width of field of view = 5 mm); (C) Tight SE-verging folds with a shallow NE-dipping axial planar foliation; (D) Shallow SE-verging extensional shear bands filled with granitic leucosome; (E) Close-up view of a leucosome within an extensional shear band, containing biotite schlieren which indicate vergence towards the southeast; (F) Photomicrograph of a granitic leucosome, showing a large (~5mm) K-feldspar with euhedral to subhedral quartz, plagioclase and biotite inclusions, indicating crystallisation from a melt (crossed polars; width of field of view = 2 mm). Mineral abbreviations after Kretz (1983).

5.1. Low grade metapelites away from the Schwerin Fold

Metapelites in the contact aureole distal to the Schwerin Fold contain a penetrative subhorizontal cleavage that is typical of the RLS aureole away from periclinal structures (Uken 1998). This fabric is generally subparallel to bedding, but becomes axial planar to periclinal structures towards the core of these structures, creating a distinctive upward-closing fan pattern (Uken & Watkeys 1997; Fig. 9).

Rotation of the structural data through rotation by 20° around a horizontal axis trending 135° results in an

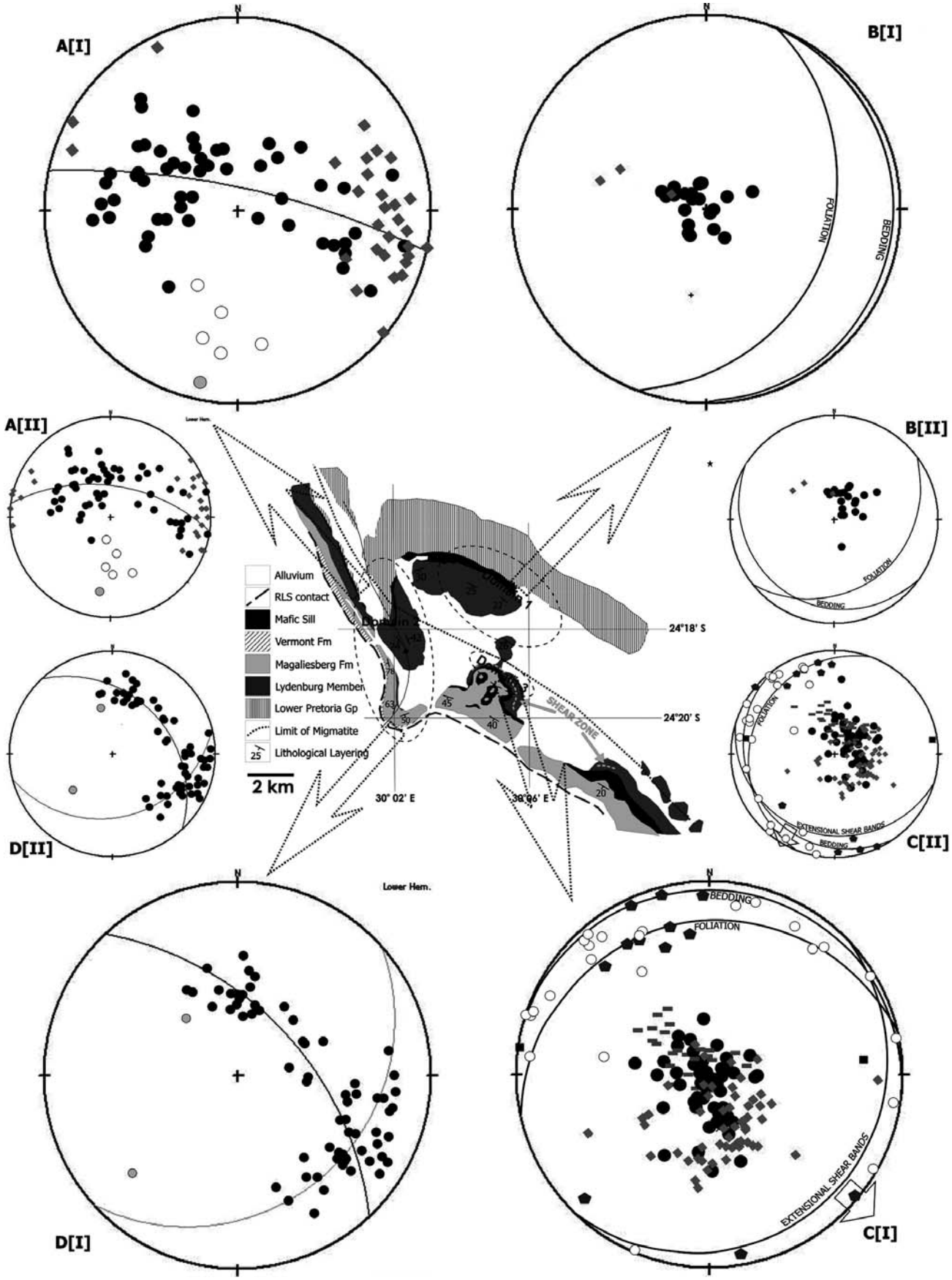

Figure 6 Geological map of the Schwerin Fold, showing stereonets for the various structural domains. Small stereonets [II]=original data. Large stereonets [I]=original data rotated 20° about a horizontal axis trending 135°. A – Core of the Schwerin anticline; B – Lower-grade schists below migmatite zone; C – Shear zone east of the anticline; D – Fold hinge within the Magaliesberg Formation adjacent to the contact with the RLS. Black circles=bedding; grey diamonds=foliation; white circles=measured fold hinge lines; grey circles=fold hinge lines from π-pole girdles; grey horizontal lines=extensional shear bands; grey pentagons=lineations; black squares=boudin long axes. B and C show average orientations for foliation, bedding, and extensional shear bands. The arrow on C[I] indicates the approximate shear direction of the shear zone.

approximately horizontal bedding dip, and a fabric which dips shallowly away from the Schwerin Fold (Fig. 6B[I]), as expected from the fanning cleavage model (Uken & Watkeys 1997).

5.2. Quartzites adjacent to the RLS contact

The scatter of bedding data from the northwestern limb of the fold in the quartzites adjacent to the contact with the RLS may be due to broad curvature of this limb of the fold (Fig. 3), or to smaller, m-scale folding observed rarely on this limb. A m-scale open fold located on the northwestern limb may reflect this. It has a hinge orientation of 78° on 337° (Fig. 6D), which is similar to the pole to the best-fit π-pole girdle through the bedding data of 52° on 346°. This suggests that the small-scale folding of these quartzites is a consequence of broad-scale warping of the northwestern limb. Rotation of the data does not significantly affect the geometry of this domain, but does result in a shallower plunge for the fold axis in this domain.

5.3. Metasediments from the core of the Schwerin Fold

Bedding data from the Lydenburg Shale Member show more scatter than data from the quartzites adjacent to the contact with the RLS, because bedding in this domain is rotated by dm- to m-scale folds, and chaotic deformation has occurred, probably reflecting melt-assisted strain localisation. Additionally, the variability in the orientation of the fibrolitic foliation is probably due to disruption by melt-assisted strain localisation. On a broad scale, the subvertical fabric present in the core of the Schwerin Fold rotates to the more general shallowly-dipping fabric orientation, subparallel to bedding, that is present throughout the lower-grade parts of the RLS aureole (Uken 1998; Fig. 9). It is interesting to note that, whilst the present geometry of the Schwerin Fold is asymmetric, with steeper dips on the northwestern limb and shallower dips on the southeastern limb, rotation of the data to remove post-RLS tilting creates a more symmetric fold, with dips on the northwestern limb similar to those on the southeastern limb (Fig. 6A). Such symmetry would be more consistent with diapir development.

5.4. Shear Zone

The shallow E or W plunge of boudins from the shear zone (Fig. 6C) is consistent with a broadly N–S extension direction, and this does not change significantly following the rotation of the data. Lineation data also remain largely unaffected by the rotation, and the single outlier in lineation measurements (30° on 225°) coincides with the bedding-cleavage intersection orientation. There is no geographic control on the variability of fold axis orientations, and so plotting a π-pole girdle through these data would be meaningless. One possibility is that leucosome veins could have facilitated disruption and shearing-induced rotation of a set of SSE-verging folds (see below).

Apart from the folds, the orientation of structures in the shear zone indicates vergence towards the south prior to rotation. This orientation is subparallel to the axial trace in the core of the Schwerin Fold, and does not appear to be consistent with gravity-induced shedding of material off the flanks of a rising fold, which should be perpendicular to the axis of the fold. The high strains indicate substantial flattening normal to the RLS contact and subhorizontal extension. However, the ESBs and leucosome-filled shears are not conjugate, but verge asymmetrically to the south and, together with the overall fold asymmetry, indicate a significant non-coaxial strain component.

Following back-rotation to correct for the RLS dip, the vergence of the shear zone is towards the southeast (SE-dipping ESBs, NW-dipping axial planar foliation – Fig. 6C[I]). This is somewhat more compatible with gravity-induced shedding of material from a rising Schwerin Fold with a SW-trending axis, which is the axial trace of the Schwerin Fold at the contact with the RLS, even following rotation. The sense of shear for this shear zone (verging top-to-the-SE, away from the core of the fold) is the opposite of that expected for typical fold formation via a flexural slip or flexural flow mechanism, where shear sense would be expected to be reverse and top-to-the-NW towards the fold axis. However, diapirism of the floor rocks and slumping of material from the limb of the rising diapir is consistent with the vergences observed.

6. Structural relationships of the leucosomes

The leucosomes within the migmatite zone show abundant evidence of representing crystallised anatectic melts (e.g., Johnson *et al.* 2003). They are found in a wide variety of structural settings that indicate an intimate timing relationship between deformation and melting. These structural relationships vary according to structural context within the larger Schwerin Fold and shear zone.

Within the core of the pericline, leucosomes occur in en-echelon tension gashes, as discordant pods, or as diktyonitic interconnected networks (see also Johnson *et al.* 2003) between leucocratic bedding layers. Leucosomes intrude sites of localised high strain, where the bedding and foliation are displaced, truncated and rotated (Fig. 7B). Elsewhere, they occur subparallel to the subvertical foliation (Fig. 7A), as well as subparallel to bedding, but they may also be discordant to both bedding and foliation. Leucosome veins that are subparallel to the bedding and the foliation may form a network connecting these two planes. Elsewhere, smaller shear planes with 0·5–1 cm-wide leucosomes displace and rotate bedding.

In the shear zone to the southeast of the anticlinal core, leucosome orientations are generally subhorizontal, contrasting with the predominantly subvertical orientation of leucosomes in the core of the Schwerin Fold. Leucosomes are found subparallel to bedding and foliation, and locally pool below more competent psammitic layers (Fig. 7C). They truncate fold hinges along the axial planar fabric, and fill the cores of cm- to dm-scale folds (Fig. 7D). They commonly appear to have intruded preferentially along extensional shear bands (Fig. 5D). Locally, they contain disrupted schlieren of biotite (Fig. 5E) caught up during leucosome movement, that typically display geometries similar to mica 'fish', indicating movement on ESBs with a vergence towards the southeast (SSW prior to rotation). Leucosomes are also locally ptygmatically folded on a cm-scale, and develop in rare boudin necks.

7. Interpretation of the structural relationships of the leucosomes

In the core of the Schwein Fold the rocks are dominated by a subvertical axial planar fabric and upright, moderately plunging m-scale folds. Leucosomes occur in en-echelon tension gashes and evidence also exists for melt movement having occurred along the subvertical fibrolite seams (Figs 4D–E, 7B). These features are consistent with melt having been lost upwards along the steep axial planar fabric and bedding in the fold limbs, with only limited entrapment in a few extensional sites.

In the shear zone, most structures are much less steep than in the antiform. A number of syn-shearing extensional sites

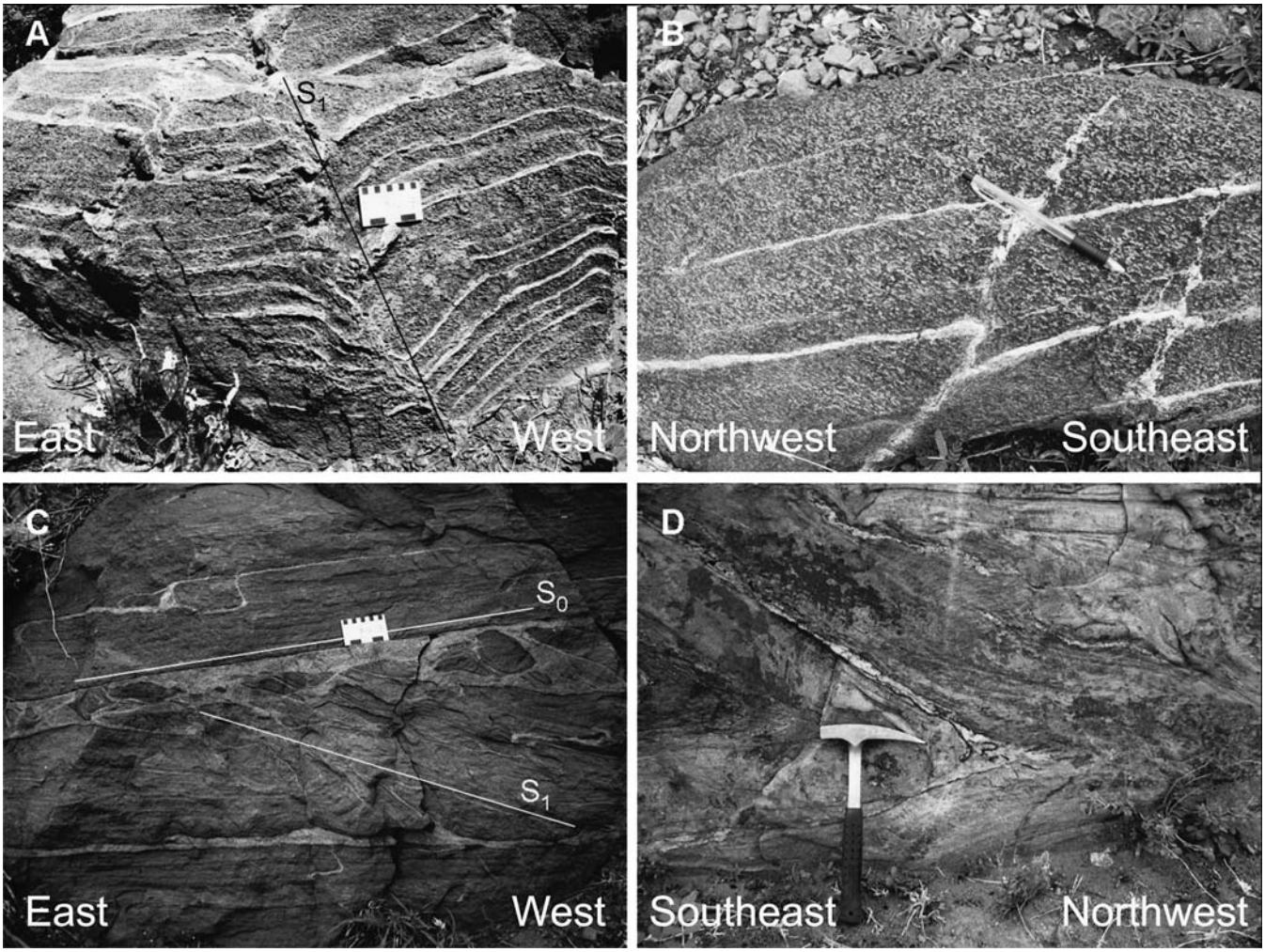

Figure 7 Leucosome structural sites: (A) Subvertical axial planar cleavage with leucosome from the migmatite zone in the core of the anticline; (B) Leucosomes within shear planes displacing lithological layering in the core of the anticline. Pencil parallel to axial planar foliation defined by fibrolite and aligned andalusite; (C) Leucosomes aligned along the NW dipping foliation in the shear zone, and along bedding; (D) Leucosome-filled dilational areas in the hinge zone of a recumbent fold in the shear zone.

(fold hinges, ESBs, boudin necks) were exploited by the melt. Additionally, the shear zone is overlain by a thick, competent quartzite layer, which may have acted as a trap for upward-migrating melts. This, in turn, would have enhanced ductility, concentrating shear strain further and possibly explaining the variable fold orientations as isolated hinges were able to rotate along slip surfaces lubricated by melt.

8. Modelling of the Bushveld Complex thermal aureole

Gerya *et al*. (2003, 2004) numerically modelled diapir development in the floor rocks beneath the RLS in two dimensions, based on the three-dimensional conceptual model of Uken & Watkeys (1997). This two-dimensional model assumes a 200–300 kg/m^3 density contrast between the dense mafic magmas of the RLS and the underlying sedimentary Pretoria Group. The rheological properties and relationships of the model depend on composition, temperature, pressure, strain rate and degree of melting and, hence, resemble the physical properties of the rocks quite well. This is evident in the sensitivity of the model to changes in the initial properties of the rocks (temperature of the floor rocks and RLS, rheological strength, lateral box size, and amplitude of the initial pericline from which these structures nucleate). A timeframe of ~800,000 years was estimated for diapir growth, and a corresponding growth rate of 8 mm/year for the most well-developed diapirs (e.g. the Phepane Dome; Fig. 1) was calculated based on the amplitude of the diapirs and the maximum timeframe for growth. The results of this modelling are considered to be robust, accurate estimates, which correspond well to the initial estimates of an ~6 mm/year growth rate made by Uken & Watkeys (1997). Since field evidence does not indicate any diapir-related structural overprint of the leucosomes in the Schwerin Fold, and there is no evidence that the lower limit of migmatite development has been significantly folded by the Schwerin Fold (isograds cut lithological boundaries and are essentially parallel to the RLS contact; Fig. 3), it can be assumed that migmatite development should have occurred over at least a similar timeframe to diapir growth. However, previous thermal modelling for the heating of the Bushveld Complex aureole using a simple one-dimensional conductive cooling approach, where the RLS is intruded as a single sill into the sediments of the Pretoria Group at ~3 km depth with a temperature of 1200–1300°C (Johnson *et al*. 2003; Harris *et al*. 2003), does not indicate such a lengthy timeframe for migmatite development. The model of Harris *et al*. (2003), in fact, assumed a RLS sill thickness of only 1500 m, and the model does not simulate temperatures sufficient to account for the melting in the aureole if conductive heating occurred. Instead, they suggested extensive fluid circulation could have accelerated the heating rate and, thus, maintained suprasolidus temperatures over significant

Table 1 Parameters used for the multiple intrusion thermal modelling using Thermos 2·0 (© 1996 Raven Applications).

Geothermal Gradient	30°C/km
Model Depth	20 km
Cell Dimension	100 m (2000 cells)
Time Interval	1 year
Depth of Initial Intrusion	3 km
$T_{intrusion}$	1160°C to 1300°C
Time for Emplacement	75,000 years
Thermal Conductivity	6×10^{-3} cal/deg/cm^2

distances from the contact. Johnson *et al.* (2003) assumed a more realistic 7 km thickness for the RLS, and their model simulated temperatures above the solidus at orthogonal distances of >350 m from the contact. However, this model suggested that, at these distances from the contact, supra-solidus temperatures would be maintained for only ~350,000 years. Consequently, the heating model of Johnson *et al.* (2003) would require a growth rate of over 12 mm/year for the Schwerin Fold. This growth rate is double that of the initial estimates made by Uken & Watkeys (1997), and 50% greater than that calculated by Gerya *et al.* (2003).

In response to this divergence between the results from the thermal and rheological modelling the present authors have developed a thermal model of the aureole based on the intrusion of the RLS magmas in multiple pulses, rather than as a single event. This model follows Cawthorn & Walraven (1998) who developed an intrusive–crystallisation sequence based on trace element compositions and isotopic ratios of the RLS, and calculations of the amount of magma required to form the layered chromitite bands in the RLS. Their model suggests that the RLS sill was progressively inflated during distinct periods of magma addition interspersed with periods dominated by fractionation (Cawthorn & Walraven 1998).

8.1. Model setup

The thermal model was set up using similar parameters to Cawthorn & Walraven (1998) (see Table 1). The modelling was performed using the program Thermos 2·0 (© 1996 Raven Applications). Cell dimensions and time intervals were optimised to give the maximum resolution capable by the program. The total emplacement time is based on the calculations of Cawthorn and Walraven (1998).

8.2. Model results

A revised heating history for the RLS aureole has been derived using this setup. These results predict that anatexis would have extended to an orthogonal distance of >500 m from the contact and that, at a distance of 300 m from the contact, anatexis would have persisted until at least 600,000 years after intrusion. Anatexis would have continued for more than 500,000 years at a distance of ~400 m from the RLS contact (Fig. 8). This incremental intrusion model predicts higher temperatures over longer timeframes than the thermal effects of a single intrusion, and this increase in the calculated width of the migmatite zone is more compatible with the observed extent of anatexis in the aureole (>500 m, Fig. 3; although the lower limit of anatexis does vary somewhat along strike). More significantly, however, the calculated timeframe for melt generation more closely approximates the rheological modelling results for diapiric fold formation obtained by Gerya *et al.* (2003, 2004).

9. Discussion

Deformation is well known as a key factor in creating mechanisms and pathways by which buoyant anatectic melt can segregate from its source rocks and escape upwards in orogenic terrains (e.g. Brown 1994; Kisters *et al.* 1998). The Schwerin Fold region shows that similar relationships can also apply in a contact metamorphic environment. The leucosome geometries in the migmatites from the Schwerin Fold core and the area to the southeast suggest that highly variable local stresses were an important controlling factor in the movement and emplacement of granitic melts beneath the Bushveld Complex intrusion.

Both in the anticlinal core of the Schwerin Fold, as well as in the shear zone, leucosome distribution is structurally controlled. In the anticlinal core, en-echelon tension gashes provided low pressure sites where leucosome accumulated. However, the subvertical axial planar foliation and upright folds characteristic of the core of anticline provided pathways for leucosome to migrate upwards. The limited preservation of leucosomes in these features (apart from the tension gashes, only the melt escape pathways are preserved as fibrolite seams) suggests very effective melt migration once it entered these structures. This is perhaps not surprising, as the thermal gradient in the aureole is inverted, so that melts migrating upwards were actually entering hotter rocks. In the shear zone to the east of the Schwerin Fold, leucosomes are clearly located in dilational structural features such as boudin necks and ESBs that formed during subhorizontal shearing. The generally subhorizontal nature of the lithological layering and structural fabrics in this area has resulted in pooling of leucosome below more competent lithologies, with only limited upwards migration possible along the shallowly-dipping axial planar foliation in the shear zone. This concentration of leucosome in the shear zone would have increased ductility, thus concentrating further deformation in the shear zone.

It is clear from Figure 9 that the stress pattern in and around the Schwerin Fold during Bushveld metamorphism was highly variable and cannot be readily explained by a simple NW–SE compression mechanism as proposed by, e.g., Sharpe & Chadwick (1982). The leucosomes provide evidence that subvertical and subhorizontal foliations were developing simultaneously in different parts of the structure, and the foliation in the subsolidus part of the aureole displays similar syn-peak timing to the other structures but has a significantly different orientation (shallow dip obliquely away from the RLS contact). Uken & Watkeys (1997) noted similar complex fabric relationships in and around the Katkloof Fold (Fig. 1), with a subvertical axial planar fabric in the fold core rotating outwards to shallower dips until, in the interdomal areas, it is approximately bedding-parallel. These interdomal areas contain extensional features, such as boudins and conjugate ESBs, that are indicative of predominantly vertical compression and horizontal extension via pure shear (Uken 1998). In contrast, the core of the Katkloof Fold contains a variety of constrictional fold and mullion structures in addition to the subvertical foliation. Such observations suggest that fold development was driven by buoyancy, rather than regional compression.

Uken & Watkeys (1997) proposed that the diapiric folds nucleated in the necks between NE-trending finger-like intrusions of the RLS. More recently, Clarke *et al.* (2009) have demonstrated the link between aureole structures and intrusion geometry on a smaller scale around Burgersfort (Fig. 1). They attributed the strain heterogeneity in the aureole rocks to the twin causes of the stepped nature of the intrusive contact, which locally cuts across the Pretoria Group stratigraphy, and subsequent magmatic inflation of the individual fingers of

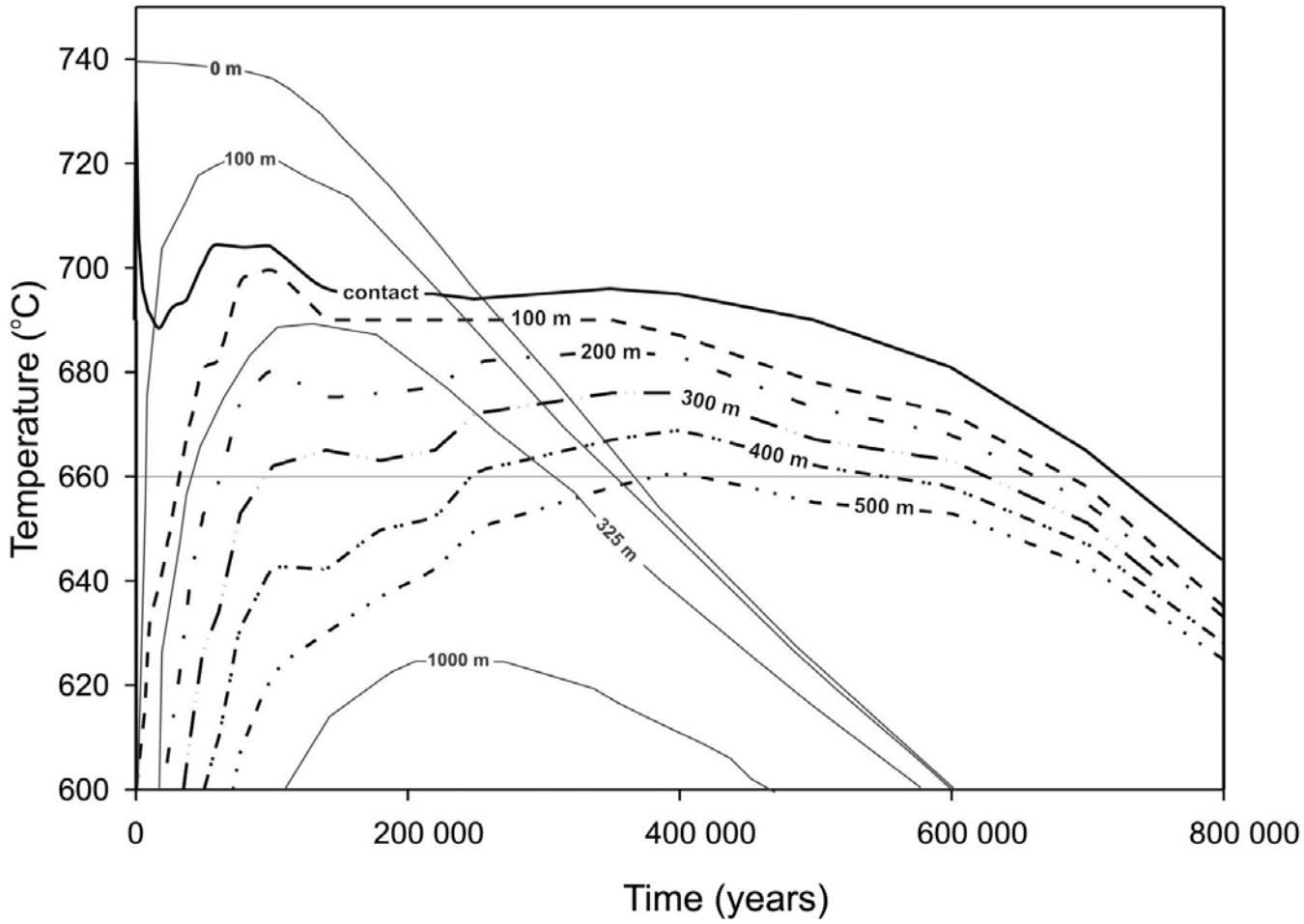

Figure 8 Results of thermal modelling of the RLS aureole, using the single intrusion model of Johnson *et al.* (2003) (grey lines), and the multiple intrusion model of Cawthorn & Walraven (1998) (black lines). Note that for the single intrusion model peak temperatures are higher and are achieved earlier, but cool below the solidus quicker (<400,000 years after the intrusion of the RLS). In the case of the multiple intrusion model the solidus is exceeded further from the contact and, at 300 m from the contact, suprasolidus temperatures are maintained for ~600,000 years. Irregularities in the curves are due to the periodic emplacement of magma into the RLS chamber, as described in Cawthorn & Walraven (1998).

the RLS sheet intrusion. Where the intrusion fingers were separated by country rock, or where a step occurred, lateral inflation induced compressional stresses in the country rock, generating symmetric or asymmetric structures depending on the exact intrusion geometry. A local stress regime induced by the geometry of the intrusion can more readily explain such features as the curvature of the Schwerin Fold axial trace and the restricted extent of the shear zone orthogonal to the Schwerin Fold axis. It could also explain the subsolidus foliation in the northeastern part of the study area, which dips obliquely away from, rather than towards, the main RLS contact. If Clarke *et al*'s (2009) model is applied, this foliation was induced by a (now-eroded) transgressive RLS contact dipping southeast and lying southeast of the study area. The exact timing of development of this lower-grade foliation relative to the axial planar and shear foliations is a matter of debate. Figure 8 shows that the metamorphic peak is attained progressively later in rocks further from the RLS contact; however, it is likely that peak conditions were reached before termination of deformation related to the formation of the fold. The fact that the andalusite, cordierite and garnet porphyroblasts in the lower-grade rocks show a late- to post-kinematic timing relative to this foliation (compared with the pre- to syn-kinematic relationships in both the fold and the shear zone), may reflect the delayed thermal response in the lower aureole compared with the rapid transfer of stresses that would ultimately have driven foliation development once appropriate metamorphic conditions were reached.

The Schwerin Fold is, thus far, the only periclinal structure in the Bushveld Complex aureole that appears to be associated with a large shear zone. As shown in the diagrammatic representation of the structures in the Schwerin Fold (Fig. 9), the development of the shear zone to the east of the pericline is compatible with slumping of ductile material from the flanks of a rising diapir. This is supported by the restricted areal distribution of the shear zone, which disappears towards the southeast away from the fold. Similar slumping effects have been noted by Clarke *et al.* (2005) adjacent to the Steelpoort Pericline, but only in magmatic RLS rocks. The western limb of the Schwerin Fold appears to be extremely attenuated (Fig. 3) but contains no evidence of shearing, although outcrop of non-quartzitic rocks is poor. If the Schwerin shear zone is unique, the reason may lie in the proximity of the thick quartzite unit of the Magaliesberg Formation to the RLS contact in the Schwerin area. This unit may have acted both as a barrier to rising anatectic melts and as a coherent structural unit which then slid southeastwards off the diapirically rising Schwerin pericline, thus focusing shear stresses in the melt-weakened unit immediately below it. In other periclines, the RLS contact cuts across more-finely-bedded, less refractory, lithologies which would have undergone general melt-induced weakening that, together with their original rheological

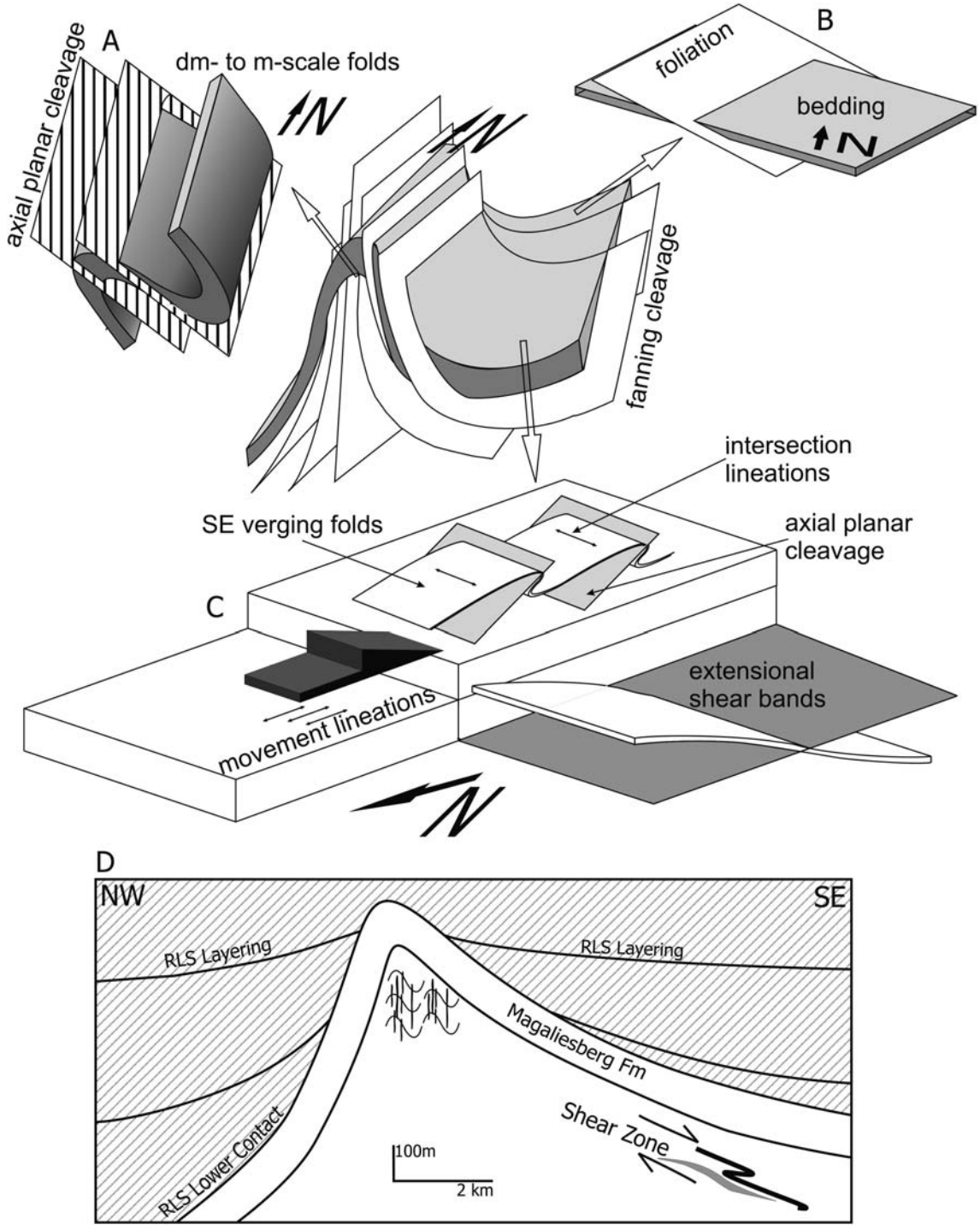

Figure 9 Diagrammatic summary of the structural features found within the study area: (A) The NE domain furthest from the RLS contains a weak ESE-dipping foliation and subhorizontal bedding; (B) The core of the anticline contains dm- to m-scale folds and a subvertical axial planar cleavage; (C) The shear zone contains SE-verging, tight to isoclinal folds with an axial planar cleavage. Bedding-cleavage intersection lineations and movement (mineral extension) lineations are present on bedding surfaces. ESBs have a SE vergence. Bedding is subhorizontal (following restoration by rotation – see Fig. 6); (D) Schematic representation of the Schwerin Fold showing subvertical leucosomes oriented axial planar to folds in the core of the pericline, with the top-to-the-SE shear zone resulting from gravitational slumping of material off the eastern limb of the fold, and RLS layering truncated and folded by the diapiric fold.

properties, would have distributed the limb shear stresses more homogeneously.

Another question which arises from the Schwerin Fold is whether the leucosome present in the migmatites contributed to the overall buoyancy of the fold, and accelerated the diapiric rise of the floor rocks. Johnson *et al.* (2003) noted that Marginal Zone norites of the RLS are brecciated and invaded by significant quantities of leucosome near the Derde Gelid Pericline south of the study area (Fig. 1). A similar concentration of leucosomes is not seen in the quartzites or RLS in the hinge of the Schwerin Fold, but the efficiency of melt segregation and migration attested to by the fibrolite seams in the core of the fold makes it most likely that such an accumulation did form in the now-eroded crest of the fold. Notwithstanding this, when a buoyant melt is created and segregated from its source rock, a denser residue/restite is

left behind. In this case, the overall density of the rock volume does not change, as the buoyancy of the magma is counteracted by the increased density of the restite. Field relations indicate that the Schwerin Fold encompasses the entire volume of suprasolidus rock and, thus, that no significant buoyancy effect is likely to have existed due to melt extraction. Furthermore, Johnson *et al*. (2003) estimated that overall melting in the Schwerin Fold is unlikely to have exceeded 10 vol%. The primary impetus for diapirism must, thus, have been the density contrast (200–300 kg/m^3; Gerya *et al*. 2003) between the upper Pretoria Group floor rocks and the overlying RLS, with an irregular lower RLS contact created by the finger-like geometry of the magma intrusions (Uken & Watkeys 1997; Clarke *et al*. 2009).

The interrelationship between the thermal and deformation effects in the upper contact aureole caused by the intrusion of the RLS must be evaluated within the context of a model that acknowledges the multi-stage nature of inflation of the Bushveld magma chamber (Cawthorn & Walraven 1998). In contrast to the single-stage intrusion models (e.g., Johnson *et al*. 2003; Harris *et al*. 2003), which would require doming rates double that calculated by Gerya *et al*. (2003), the multiple-intrusion model generates slightly lower peak temperatures but a longer-lived metamorphic effect that achieves very good agreement with the timescale for diapiric fold development deduced by Gerya *et al*. (2003).

10. Conclusions

The segregation and migration of melt in the contact aureole beneath the RLS is intimately linked to the structural development of the aureole, particularly in areas such as the Schwerin Fold, where structures are more pronounced, and where deformation is clearly contemporaneous with metamorphism and migmatisation within the aureole. Of additional importance is the absolute timing of metamorphism, migmatisation and diapir development in the contact aureole. The Schwerin Fold developed over ~600 000 years, with a growth rate of ~8 mm/year, which is consistent with modelled estimates for the duration of diapir development elsewhere in the aureole (Gerya *et al*. 2003). A simple, one-dimensional, cooling model of a 7–8 km-thick sill does not account for this – rather, a model of multiple intrusive pulses for the RLS is more consistent with the longer duration of diapir development. It is evident that migration and accumulation of buoyant leucosome is controlled by the structural geometry of the area in which migmatisation is occurring – subvertical structures allow these leucosomes to escape upwards, whilst subhorizontal structures result in the accumulation of leucosome, in turn triggering a local increase in ductility. The latter may well have led to slumping along the diapir flank being localised in a broad extensional shear zone.

11. Acknowledgements

We are grateful to Anglo Platinum for logistical support during field work for this study. Tim Johnson and Chris Gerbi are thanked for constructive reviews which improved the quality of the manuscript.

12. References

Bai, Q., Jin, Z.-M. & Green II, W. 1997. Experimental investigation of the rheology of partially molten peridotite at upper mantle pressures and temperatures. *In* Holness, M. B. (ed.) *Deformation-enhanced Fluid Transport in the Earth's Crust and Mantle*, 40–61. *The Mineralogical Society Series* **8**. London: Chapman & Hall.

Bhadra, S., Das, S. & Bhattacharya, A. 2007. Shear Zone-hosted Migmatites (Eastern India): the Role of Dynamic Melting in the Generation of REE-depleted Felsic Melts, and Implications for Disequilibrium Melting. *Journal of Petrology* **48**, 435–57.

Brown, M. 1994. The generation, segregation, ascent and emplacement of granite magma: the migmatite-to-crustally-derived granite connection in thickened orogens. *Earth Science Reviews* **36**, 83–130.

Brown, M. 2005. Synergistic effects of melting and deformation: an example from the Variscan belt, western France. *In* Gapais, D., Brun, J. P. & Cobbold, P. R. (eds) *Deformation Mechanisms, Rheology and Tectonics: from minerals to the Lithosphere*, 205–26. *Geological Society, London, Special Publication* **243.** Bath, UK: The Geological Society Publishing House.

Brown, M., Averkin, Y. A., McLellan, E. L. & Sawyer, E. W. 1995. Melt segregation in migmatites. *Journal of Geophysical Research* **100**, 15655–79.

Brown, M. & Solar, G. S. 1998. Shear zone systems and melts: feedback relations and self-organization in orogenic belts. *Journal of Structural Geology* **20**, 211–27.

Button, A. 1978. Diapiric structures in the Bushveld, north-eastern Transvaal. *Information Circular, Economic Geology Research Unit* **96.** Johannesburg, South Africa: University of the Witwatersrand. 13 pp.

Cawthorn, R. G. & Walraven, F. 1998. Emplacement and crystallization time for the Bushveld Complex. *Journal of Petrology* **39**, 1669–87.

Clarke, B. M., Uken, R., Watkeys, M. K. & Reinhardt, J. 2005. Folding of the Rustenburg Layered Suite adjacent to the Steelpoort pericline: implications for syn-Bushveld tectonism in the eastern Bushveld Complex. *South African Journal of Geology* **108**, 397–412.

Clarke, B. M., Uken, R. & Reinhardt, J. 2009. The geometry and emplacement mechanics of a Bushveld Complex peridotite body. *South African Journal of Geology* **112**, 141–62.

Eriksson, P. G., Schweitzer, J. K., Bosch, P. J. A., Schereiber, U. M., Van Deventer, J. L. & Hatton, C. J. 1993. The Transvaal Sequence: an overview. *Journal of African Earth Sciences* **16**, 25–51.

Gerya, T. V., Uken, R., Reinhardt, J., Watkeys, M. K., Maresch, W. V. & Clarke, B. M. 2003. Cold fingers in hot magma: numerical modeling of country rock diapirs in the Bushveld Complex, South Africa. *Geology* **31**, 753–6.

Gerya, T. V., Uken, R., Reinhardt, J., Watkeys, M. K., Maresch, W. V. & Clarke, B. M. 2004. 'Cold' diapirs triggered by intrusion of the Bushveld Complex: Insight from two-dimensional numerical modeling. *In* Whitney, D. L., Teyssier, C. & Siddoway, C. S. (eds) *Gneiss Domes in Orogeny*, 117–27. *Geological Society of America Special Paper* **380.** Boulder, Colorado & Lawrence, Kansas: Geological Society of America & University of Kansas Press.

Gleason, G., Bruce, V. & Green, H. W. 1999. Experimental investigation of melt topology in partially molten quartzofeldspathic aggregates under hydrostatic and non-hydrostatic stress. *Journal of Metamorphic Geology* **17**, 705–22.

Hand, M. & Dirks, P. H. G. M. 1992. The influence of deformation on the formation of axial-planar leucosomes and the segregation of small melt bodies within the migmatitic Napperby Gneiss, central Australia. *Journal of Structural Geology* **14**, 591–604.

Harris, N., McMillan, A., Holness, M., Uken, R., Watkeys, M., Rogers, N. & Fallick, A. 2003. Melt generation and fluid flow in the thermal aureole of the Bushveld Complex. *Journal of Petrology* **44**, 1031–54.

Hartzer, F. J. 1995. Transvaal Supergroup inliers: geology, tectonic development and relationship with the Bushveld Complex, South Africa. *Journal of African Earth Sciences* **21**, 521–47.

Holyoke, C. W. & Rushmer, T. 2002. An experimental study of grain scale melt segregation mechanisms in two common crustal rock types. *Journal of Metamorphic Geology* **20**, 493–512.

Johnson, T. E., Gibson, R. L., Brown, M., Buick, I. S. & Cartwright, I. 2003. Partial Melting of metapelitic rocks beneath the Bushveld Complex, South Africa. *Journal of Petrology* **44**, 789–813.

Johnson, T., Brown, M., Gibson, R. & Wing, B. 2004. Spinel-cordierite symplectites replacing andalusite: evidence for melt-assisted diapirism in the Bushveld Complex, South Africa. *Journal of Metamorphic Geology* **22**, 529–45.

Kisters, A. F. M., Gibson, R. L., Charlesworth, E. G. & Anhaeusser, C. R. 1998. The role of strain localization in the segregation and ascent of anatectic melts, Namaqualand, South Africa. *Journal of Structural Geology* **20**, 229–42.

Kretz, R. 1983. Symbols for rock-forming minerals. *American Mineralogist* **68**, 277–79.

Longridge, L. 2006. *Structural and metamorphic evolution of the Schwerin Fold, northeastern Bushveld Complex, Limpopo Province.* Honours Thesis, University of the Witwatersrand, Johannesburg, South Africa. 42p.

Letts, S. A. 2007. *The palaeomagnetic significance of the Bushveld Complex and related 2 Ga magmatic rocks in ancient continental entities*. PhD Thesis, University of the Witwatersrand, Johannesburg, South Africa. 228 pp.

du Plessis, C. P. & Walraven, F. 1990. The tectonic setting of the Bushveld Complex in southern Africa, part 1. Structural deformation and distribution. *Tectonophysics* **179**, 305–19.

Rosenberg, C. L. & Berger, A. 2000. Syntectonic Melt Pathways in Granitic Gneisses, and Melt-Induced Transitions in Deformation Mechanisms. *Physics and Chemistry of the Earth* **26**, 287–93.

Sawyer, E. W. 1991. Disequilibrium melting and the rate of melt-residuum separation during migmatization of mafic rocks from the Grenville Front, Quebec. *Journal of Petrology* **32**, 701–38.

Schwellnus, J. S. I., Engelbrecht, L. N. J., Coertze, F. J., Russell, H. D., Malherbe, S. J., van Rooyen, D. P. & Cooke, R. 1962. *The geology of the Oliphants River area*. Explanation to Sheets 2429B (Chuniespoort) and 2430A (Wolkberg). Geological Survey of South Africa.

Sharpe, M. R. & Chadwick, B. 1982. Structures in Transvaal Sequence rocks within and adjacent to the eastern Bushveld Complex. *Transactions of the Geological Society of South Africa* **85**, 29–41.

Uken, R. 1998. *The Geology and Structure of the Bushveld Complex metamorphic aureole in the Olifants River area.* PhD Thesis, University of Natal, Durban, South Africa. 277 pp.

Uken, R. & Watkeys, M. K. 1997. Diapirism initiated by the Bushveld Complex, South Africa. *Geology* **25** 723–6.

Vernon, R. H., Collins, W. J. & Richards, S. W. 2003. Contrasting magmas in metapelitic and metapsammitic migmatites in the Cooma Complex, Australia. *Visual Geosciences* **8**, 1–22.

Walraven, F., Armstrong, R. A. & Kruger, F. J. 1990. A chronostratigraphic framework for the north-central Kaapvaal craton, the Bushveld Complex and Vredefort structure. *Tectonophysics* **171**, 23–48.

Waters, D. J. & Lovegrove, D. P. 2002. Assessing the extent of disequilibrium and overstepping of prograde metamorphic reactions in metapelites from the Bushveld Complex aureole, South Africa. *Journal of Metamorphic Geology* **20**, 135–49.

MS received 12 December 2007. Accepted for publication 10 June 2008 (Stellenbosch); 15 January 2009 (RSE).

Parental magmas of Grenville Province massif-type anorthosites, and conjectures about why massif anorthosites are restricted to the Proterozoic

Jean H. Bédard

Geological Survey of Canada, CGC-Québec, 490 de la Couronne, Québec, Canada, G1K 9A9
Email: jbedard@rncan.gc.ca

ABSTRACT: Trace element inversion modelling of Grenvillean anorthosite massifs and associated rocks yield NMORB-normalised trace element profiles enriched in highly incompatible elements; commonly with negative Nb and Th anomalies. Model melts can be divided into subtypes that cannot be linked through fractional crystallisation processes. Most model melts are depleted in the heavy rare-earth elements and can be explained by partial melting of arc basaltic sources (5–60 melting %) with garnet-bearing residues. Some of the model melts have flat NMORB-normalised profiles (for rare-earth elements), have high compatible element contents, and might have been derived from mantle fertilised by arc magmatism, followed by low-pressure fractional crystallisation. Intermediate Ce/Yb types may represent mixtures of these end-members, or less probably, variations in the crustal source composition and residual assemblage. The active tectonic context now favoured for the Grenville Province appears to be inconsistent with plume or thermal insulation models. The heat source for crustal and mantle melting could record either post-orogenic thermal relaxation of a tectonically-thickened arc crust, or basaltic underplating caused by delamination of a mantle root or subduction slab beneath this arc crust. In this context, pre-Proterozoic anorthosites may be lacking, because prior to ca. 2·5 Ga, the crust may have been too weak to be thickened tectonically. The absence of post-Proterozoic anorthosites may be due to the secular decrease in radiogenic heating and cooling of the mantle and crust.

KEY WORDS: apatite, crust, gabbro, granite, ilmenite, immiscibility, melting, tectonics, trace elements

The Proterozoic Eon is characterised by voluminous anorthositic massifs (Fig. 1; $An_{30–70}$), that are associated with mangerite and granite batholiths, with bodies of gabbro, troctolite and norite, and with minor Fe-rich ferrodiorite to monzonorite (e.g. Morse 1975, 1982; Emslie 1978, 1980, 1985; Wiebe 1992; Ashwal 1993). These rocks can be grouped together as the AMCG suite (anorthosite, mangerite, charnockite, granite or gabbro: Emslie 1985). The petrogenesis of this suite and reason for the restricted age spectrum of massif-type anorthosites (2·5–0·9 Ga: see review in Ashwal 1993 and in Scoates & Chamberlain 1997) are enduring problems (Bowen 1917). In its simplest form, the problem can be summarised as: if anorthosites form by a conventional petrogenetic mechanism (basaltic underplating, plumes, crustal anatexis . . .), then why are they restricted to the Proterozoic?

Historically, mantle-derived tholeiitic or high-Al basalt parents for the anorthosites were favoured (e.g. Morse 1969, 1982; Emslie 1980, 1985; Emslie *et al*. 1994; Wiebe 1990a, b; Olson 1992; Mitchell *et al*. 1995, 1996; Icenhower *et al*. 1998). However, a growing minority favour crustal sources (Michot 1965; Berg 1969; Philpotts 1969; Frith & Currie 1976; Simmons & Hanson 1978; Taylor *et al*. 1984; Demaiffe *et al*. 1986; Duchesne *et al*. 1989; Schärer *et al*. 1996; van der Auwera *et al*. 1998; Longhi *et al*. 1999; Duchesne *et al*. 1999; Peck & Valley 2000; Schiellerup *et al*. 2000; Selbekk *et al*. 2000; Bédard 2001; Peck *et al*. 2004).

To account for the extensive volumes of feldspar, those favouring a crustal origin consider that the source is either inherently aluminous (e.g. feldspar-rich meta-cumulates: Berg 1969; Duchesne *et al*. 1999; Selbekk *et al*. 2000), or becomes so as a result of prior anatexis (e.g. Frith & Currie 1976). Among advocates of a mantle origin, many suggest that the feldspar was concentrated as a flotation cumulate during extensive fractionation of aluminous basalt in the lowermost crust (e.g. Emslie 1980, 1985; Duchesne 1984; Longhi *et al*. 1993; Ashwal 1993; Scoates & Frost 1996).

Another way of helping plagioclase to form in abundance is through combined fractionation–assimilation of aluminous crustal rocks (Bowen 1922; Buddington 1936; Michot 1965; Philpotts 1969; Emslie & Hegner 1993; Emslie *et al*. 1994; Brandriss & Cawthorn 1996; Dempster *et al*. 1999; Li *et al*. 2000). Once formed, this concentration of plagioclase could be remobilised and ascend as a crystal-rich mush (Martignole & Schrijver 1970; Woussen *et al*. 1981). In contrast, others have proposed that the accumulation process is not mechanical, but chemical, a consequence of delayed nucleation (Morse 1982) or prior resorption of feldspar (Wiebe 1988, 1990b; Markl & Frost 1999), with feldspar then being produced in great abundance when it does begin to crystallise upon ascent and emplacement.

The lack of superimposed deformation in some anorthosite provinces led to an early consensus for an anorogenic setting (Bridgwater & Windley 1973; Berg 1977; Emslie 1978, 1985;

© 2009 Her Majesty The Queen in right of Canada. doi:10.1017/S1755691009016016

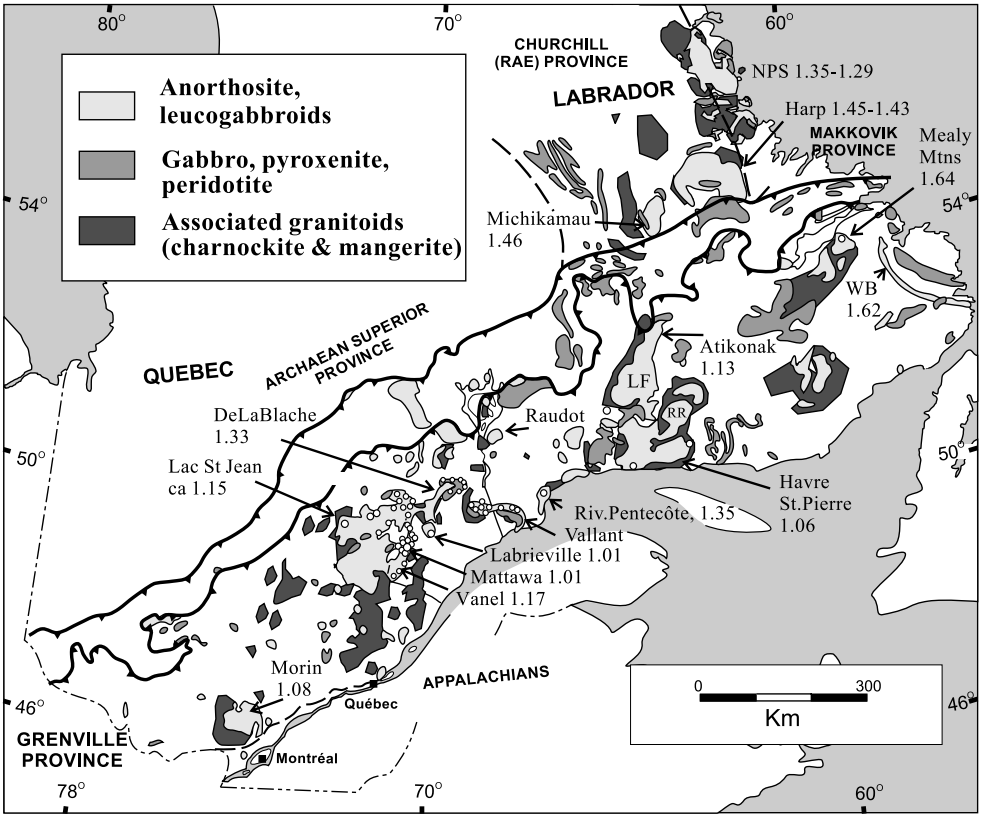

Figure 1 Location map, adapted from the Grenville map of Tony Davidson (1998), complemented with other sources (Tom Clark, MRNFQ; David Corrigan, GSC, pers. comm.; and a variety of sources quoted in the reference list). SIGÉOM samples are the small dots. Other data locations and source of age data are in the original papers (see text). WB=White Bear Arm anorthosite (Kamo *et al.* 1996), LF=Lac Fournier lobe, RR=rivière Romaine lobe.

Morse 1982; Olson 1992; Schärer *et al.* 1996; Amelin *et al.* 1997). However, convincing evidence of rifting is typically absent (Emslie 1978), leading to suggestions of an origin from mantle plumes (Morse *et al.* 1988) or mantle superswells produced by thermal insulation under a supercontinent (Anderson 1983; Hofmann 1989; Vigneresse 2005). Recent work challenges the anorogenic consensus; suggesting that most anorthosites are late- to post-orogenic (Martignole 1996); related to crustal thickening and delamination (Scoates & Chamberlain 1997; Corrigan & Hanmer 1997), and/or to crustal imbrication (Duchesne *et al.* 1999).

Perhaps the most serious obstacle to progress on all aspects of anorthosite petrogenesis is the lack of liquid compositions amenable to quantitative modelling and testing. This paper corrects this lacuna by calculating the trace element contents of the melts from which Grenville Province anorthosite suite rocks crystallised; complementing a previous study of Nain Plutonic suite rocks (Bédard 2001). The anorthositic massifs of the Grenville Province are the largest and most voluminous on Earth, and epitomise the anorthosite problem. With such model liquid data in hand, quantitative tests are designed to ascertain whether or not different facies are related by fractionation, and melting models are constructed to test whether mantle or crustal sources are most plausible.

1. The Grenville Province and its anorthosites

The emerging picture for the tectonic evolution of the Proterozoic Grenville Province is of an active history of cratonward subduction, punctuated by periodic back-arc rifting and accretion of oceanic arc terranes, and terminated by continent–continent collision (e.g. Martignole 1996; Rivers 1997; Rivers & Corrigan 2000; Hanmer *et al.* 2000; Culshaw *et al.* 2000; Ketchum *et al.* 2002; Gower & Krogh 2002; Dickin & McNutt 2007; Corriveau *et al.* 2007; Schulz & Cannon 2007; Davidson 2008). When considered in this context, the widespread Grenville Province AMCG complexes appear to record: (a) distal extensional events linked to an active margin setting; (b) back-arc rifting; or (c) are related to post-orogenic collapse of the collisional orogen and delamination of its lithospheric root (e.g. Corrigan & Hanmer 1997; McLelland *et al.* 1996; Rivers & Corrigan 2000; Gower & Krogh 2002).

Ages of AMCG massifs modelled herein range from ca. 1·62 Ga Post-Labradorian (Mealy Mountains complex: James *et al.* 2000), to ca. 1·36–1·33 Ga Post-Pinwarian (Rivière Pentecôte, De La Blache: Nantel & Martignole 1991; Gobeil *et al.* 2002), to ca. 1·18–1·13 Ga Post-Shawinigan (Vanel, Lac St. Jean, Havre St. Pierre: van Breemen & Higgins 1993; Higgins *et al.* 2002; Hébert & van Breemen 2004a, b), and ca. 1·02–1·008 Post-Ottawan (Mattawa, Labrieville: Owens *et al.* 1994; Hébert *et al.* 2005); and thus spans nearly the entire age-range of Grenville Province AMCG magmatism. The Baie-Comeau or Vallant anorthosite massif is undated, and could belong to any of the post-1·36 Ga series. Individual anorthosite massifs in the Grenville can be over 100 km in diameter, and the giant Lac St. Jean complex underlies 20 000 km^2 (Fig. 1). The anorthosite massifs are spatially associated with granitic rocks, commonly pyroxene-bearing high-temperature types, which locally form sheaths around the anorthosites (Fig. 1; e.g. Emslie 1991; Emslie & Hunt 1990). Mafic cumulate rocks are also commonly associated spatially and temporally with the anorthosites (Fig. 1). These range from various types of leuco-gabbroic rocks, to mela-gabbros, pyroxenites and peridotites, which are commonly rather

Fe-rich (e.g. Olson & Morse 1990; Francis *et al*. 2000). Concentrations of Fe–Ti-oxide minerals, some economic, are also present in and around the anorthositic massifs (e.g. Owens & Dymek 1992; Dymek & Owens 2001; Hébert *et al*. 2005; Corriveau *et al*. 2007); and some are associated with sulphide mineralisation (Corriveau *et al*. 2007). Altogether, rocks of the AMCG suite occupy more than 20% of the Grenville Province (Martignole 1996); and any geotectonic model must account for their presence.

2. Methodology

2.1. The equilibrium distribution method (EDM)

The chemistry of many plutonic rocks reflects the nature and proportions of accumulated minerals when the proportion of melt entrapped in the cumulate framework is small. Bédard (1994, 2001) developed the equilibrium distribution method (EDM) to calculate the composition of trace elements in the liquid from which cumulates formed. Its application requires: a set of trace element crystal/liquid partition coefficients (Table 1); a whole-rock trace element analysis (Table 2; for data see Appendix Table A1 – Supplementary Material); a mode (Table 2; Table A1); and an assumed value for the trapped melt fraction (TMF). Uncertainty with regard to the TMF has a significant effect on absolute abundances of trace element contents, but has little effect on trace element ratios (Fig. 2b). A TMF value of 0 was assumed for analysed plagioclase megacrysts (e.g. Owens & Dymek 2001).

A judicious choice of partition coefficients is paramount. It is now understood that D values vary with melt and mineral chemistry, and it is of critical importance that the D values should be appropriate to the rock being modelled. Each model in this paper was calculated with its own D dataset pinned by the plagioclase An-content. An example for An_{50} plagioclase is given as Table 1. Since most samples being modelled were not analysed for their mineral chemistry, the An-content of the plagioclase (needed to calculate Ds for plagioclase using the equations in Bédard (2006a), Table 1) was estimated from norm calculations. Where mineral–chemical data exist, only small differences from the normative values were observed, validating the use of normative plagioclase compositions for this purpose. The impact of uncertainties in the An content on computed values of D is considered in Figure 2a, and is small. Aside from analytical uncertainty, the largest source of uncertainty in the EDM models computed here is uncertainty in the D regressions vs. An-content (Fig. 2c), which nonetheless is small enough that the main conclusions of this paper are not affected.

To calculate values of D for olivine (Bédard 2005) and orthopyroxene (Bédard 2007), it is necessary to estimate melt SiO_2 and MgO contents. Since most analyses are of cumulate rocks that do not represent frozen liquids, melt compositions must somehow be estimated. Francis *et al*. (2000) analysed a set of gabbroic chilled margins and dykes that they inferred were related to AMCG magmatism. Normative plagioclase compositions from these were regressed against melt MgO, allowing melt MgO content to be calculated as follows:

$$\text{MgO (wt\%) of melt} = \text{An (molar fraction)} \times 14{\cdot}066\ (\pm 3{\cdot}951) + 0{\cdot}3663\ (\pm 0{\cdot}8966) \quad (1)$$

with an R^2 of 0·6788 for N = 8. The trend of melt SiO_2 vs. An content is not systematic for this dataset and the Francis *et al*. (2000) dyke data yield a very low average SiO_2 of 45·6 wt%. As will become apparent, a crustal derivation is inferred for many melts, and so a more evolved melt SiO_2 of 55 wt% was used for all calculations where SiO_2 was needed. These are only needed for DZn in Cpx and for apatite Ds. Some of the D values for clinopyroxene (MS in preparation) and orthopyroxene require that the Al^{iv} content be known. The average Al^{iv} contents of clinopyroxene and orthopyroxene from the Labrieville massif analysed by Owens & Dymek (2001) are 0·02 and 0·05, respectively, and these values were used throughout. More precise models would result if mineral–chemical data were available, but the uncertainty in Opx Al^{iv} content only affects D values for Nb and Cu (Table 1). On the other hand, many Cpx D values are controlled by Cpx Al^{iv} content (Table 1). However, since Cpx is rarely present as a model residual phase, few models are affected by this uncertainty. D values for magnetite, ilmenite, apatite and zircon are either constants taken from the compilation of Bédard (2006b); or are newly derived (unpublished data, >'T2′ in Table 1). To this end, mineral partitioning data were compiled from the literature and values of LnD were regressed against MgO or SiO_2 in the liquid; or where no regression was possible, simple averages were computed. The DREE–Y (REE = rare earth elements) data were smoothed using the Lattice Strain Model of Blundy & Wood (1994; for method see Bédard 2007), and values of these constants will be published elsewhere.

Since thin sections and other petrographic details were not generally available, and grain sizes are commonly so coarse as to make thin sections unrepresentative, modes were estimated on the basis of CIPW norm calculations, adjusted for minor elements (see Bédard 2001 for the method). Specifically, small proportions of orthoclase were added to plagioclase, pyroxene modes were redistributed to compensate for exsolution, and small amounts of normative chromite, ilmenite and magnetite were distributed among the dominant ferromagnesian silicates. Where larger proportions of magnetite, ilmenite or apatite are present in the norm, a cumulus origin was inferred and integrated into the inverse models. Where reported in the original study, modal data were used to guide reconstruction of the mode. Note that small changes in geochemistry can lead to large variations in normative olivine/orthopyroxene ratios. Furthermore, peritectic and subsolidus reactions may change the orthopyroxene/olivine ratio. However, variations of the olivine/orthopyroxene ratio have only a minor impact on the computed melt trace element distribution because of the general similarity of orthopyroxene and olivine D profiles and values.

The basis of the EDM (Bédard 1994) is a mass balance equation that reconstructs the composition of the melt from which the cumulus minerals were derived, at the point where this assemblage of cumulates + trapped melt was sealed off from the main body of magma and became a closed system. It is assumed that equilibrium prevailed; that most of the intercumulus melt was quickly expelled from the cumulus framework at near-liquidus temperatures (before it could differentiate significantly); that melt entrapped in the pores of the cumulate framework crystallised *in situ*; and that there are no complicating post-cumulus percolation or metasomatic effects. If these assumptions hold true, then the EDM yields the trace element composition of the liquidus melt. The pertinent equations and the methodology are explained in Bédard (1994, 2001), and a revised set of equations that consider the structure-forming role of TiO_2 in ilmenite, P_2O_5 in apatite and ZrO_2 in zircon are presented in Bédard *et al*. (2009).

To preserve mass, a proportion of minerals equivalent to the trapped melt fraction (TMF) needs to be subtracted from the solid assemblage. This backstripping of the solid assemblage is conceptually identical to non-modal melting, and leaves a residual mode complementary to the model melt. As backstripping progresses solid phases may disappear, and so the melting mode must change accordingly. The melting modes used here are either experimentally-determined cotectic proportions, or approximations derived from phase proportions in common

Table 1 Example of one of the mineral/liquid partition coefficient datasets used in this paper, corresponding to an An50 plagioclase. Cpx=clinopyroxene; Plag=plagioclase; Opx=orthopyroxene; Ol=olivine; Cte=chromite; Mt=magnetite; Ilm=ilmenite; Ap=apatite; Zirc=Zircon. Columns to the right of the D values record the way that D was calculated, or gives the source of the data or equations used. For example, '29, An' implies that D values were calculated from plagioclase An-content using equation #29. Plag Ds were calculated using equations in Bédard 2006a. Opx and Ol Ds were calculated using equations in Bédard 2007 and Bédard 2005, respectively. Values for Ds in Cpx and Ap are from mss in preparation. Values for chromite, magnetite and ilmenite are from the compilation of Bédard 2006b unless otherwise specified, or were calculated from the constants given in Bédard *et al*. 2009. 'MgO' implies that D values were calculated from the melt MgO content, itself calculated from the plagioclase An-content (MgOwt% of melt=An (molar fraction) × 14·066+0·3663; see text). For An=0·5, then MgO=7·4%. Melt FeO and SiO_2 contents were assumed constant at 11% and 55%, respectively, and so in this case MgO#=MgO/(MgO+FeOt)=0·402. The tetrahedral Al-contents of Opx and Cpx (Al^{iv}) are assumed constant at 0·05 and 0·02 respectively. For Plag, MSAn=calculated from MgO, SiO_2 and An-contents using multiple regression analysis. SAn=calculated from SiO_2 and An-contents using multiple regression analysis. Av.=average of experimental and natural data. L means that the Ds for the rare-earth elements and Y were calculated using the lattice strain model of Blundy and Wood (1994) from the variable associated with it (e.g., '135–7, L, MgO' means that the D value was calculated using equations 135 to 137, using the Lattice strain model calibrated against the MgO content of the melt). For Ap, AvSM means that the value of D is the average of Ds calculated from regressions against MgO and SiO_2. HD=calculated using the equation of Hart & Davis (1978: DNi=124/(MgO) − 0·9). Values of DZircon Ga, Ni, Cu, Zn and V are unknown and were set=1.

	Cpx		Plag		Opx		Ol		Mt		Ilm		Ap		Zirc
DCs	0·00046	Al^{iv}	0·0918	16, An	0·0110	63, MgO	0·00236	MgO	0·001		0·025		0·00372	SiO	0·005
DK	0·0116	MgO	0·242	15c, An	0·0100	set=DBa	0·00236	MgO	0·001		0·167	T2	0·0255	Av.	0·005
DRb	0·00046	Al^{iv}	0·0602	17, An	0·0100	set=DBa	0·00236	MgO	0·001		0·029	T2	0·0255	set=DK	0·006
DBa	0·0085	Av.	0·540	18a, An	0·0100	65, MgO	0·00097	MgO	0·001		0·024	T2	0·0724	SiO_2	0·005
DTh	0·0112	MgO	0·104	37, An	0·00334	18, MgO	0·00962	MgO	0·0044	T2	0·0637	T2	344	MgO	62
DU	0·0054	Av.	0·0755	38a, An	0·0035	21, MgO	0·0139	MgO	0·443	T2	0·063	T2	67	MgO	800
DNb	0·0080	MgO	0·0941	32a, An	0·00691	28, Al^{iv}	0·00181	MgO	0·0424	T2	0·530	T2	0·0393	SiO_2	189
DTa	0·0141	MgO	0·0184	33, MSAn	0·00686	29, MgO	0·0497	MgO	0·119	T2	1·054	T2	0·0603	SiO_2	44·4
DLa	0·0853	L, Al^{iv}	0·125	64, L, An	0·00224	135–7, L, MgO	0·00006	L, MgO	0·015		0·0005	T2	4·47	L, SiO_2	26·6
DCe	0·136	L, Al^{iv}	0·121	64, L, An	0·00386	135–7, L, MgO	0·00014	L, MgO	0·016		0·001	T2	6·39	L, SiO_2	23·5
DPr	0·202	L, Al^{iv}	0·114	64, L, An	0·00645	135–7, L, MgO	0·00032	L, MgO	0·018		0·002	T2	8·30	L, SiO_2	20·0
DPb	0·290	Av.	0·657	20, An	0·0570	97, MgO	0·00336	MgO	0·022		0·0006	T2	0·0580	Av.	0·06
DSr	0·0138	Av.	3·06	19a, An	0·00331	60, MgO	0·00404	MgO	0·022		0·0003	T2	1·304	SiO_2	0·03
DP	0·0411	Av.	0·107	39, An	0·0252	23, MgO	0·00550	MgO	0·0944		0·0016	T2	41 wt%		2·4

Table 1 *Continued.*

	Cpx		Plag		Opx		Ol		Mt		Ilm		Ap		Zirc
DNd	0·283	L, Al^{iv}	0·105	64, L, An	0·0104	135–7, L, MgO	0·00070	L, MgO	0·026		0·0036	T2	9·83	L, SiO_2	21·7
DSm	0·442	L, Al^{iv}	0·0885	64, L, An	0·0223	135–7, L, MgO	0·00240	L, MgO	0·024		0·0093	T2	10·64	L, SiO_2	17·7
DZr	0·0214	MgO	0·0184	34b, An	0·0156	31, MgO	0·0180	MgO	0·0631	T2	0·218	T2	123	MgO	66 wt%
DHf	0·0466	MgO	0·0537	40a, SAn	0·0354	32, MgO	0·0110	MgO	0·042	T2	0·356	T2	506	MgO	2640
DTi	0·178	MgO	0·110	8, An	0·172	15, MgO	0·0330	MgO	0·837	T2	51 wt%		0·0465	Av.	0·056
DEu	0·0302	MgO	0·275	46b, An	0·0184	42a, MgO	0·00841	MgO	0·025		0·0004	T2	5·59	AvSM	12·1
DGd	0·563	L, Al^{iv}	0·0731	64, L, An	0·0400	135–7, L, MgO	0·00614	L, MgO	0·018		0·0188	T2	9·18	L, SiO_2	15·0
DTb	0·606	L, Al^{iv}	0·0656	64, L, An	0·0521	135–7, L, MgO	0·00939	L, MgO	0·019		0·0258	T2	7·94	L, SiO_2	37·3
DDy	0·631	L, Al^{iv}	0·0583	64, L, An	0·0666	135–7, L, MgO	0·0140	L, MgO	0·018		0·0346	T2	6·55	L, SiO_2	60·0
DY	0·638	L, Al^{iv}	0·0540	64, L, An	0·0769	135–7, L, MgO	0·0176	L, MgO	0·018		0·0409	T2	5·69	L, SiO_2	80·0
DHo	0·638	L, Al^{iv}	0·0519	64, L, An	0·0824	135–7, L, MgO	0·0197	L, MgO	0·018		0·0443	T2	5·27	L, SiO_2	120
DEr	0·630	L, Al^{iv}	0·0464	64, L, An	0·0988	135–7, L, MgO	0·0264	L, MgO	0·018		0·0546	T2	4·18	L, SiO_2	200
DTm	0·612	L, Al^{iv}	0·0417	64, L, An	0·115	135–7, L, MgO	0·0340	L, MgO	0·018		0·0652	T2	3·30	L, SiO_2	300
DYb	0·587	L, Al^{iv}	0·0378	64, L, An	0·132	135–7, L, MgO	0·0420	L, MgO	0·018		0·0755	T2	2·61	L, SiO_2	490
DLu	0·560	L, Al^{iv}	0·0344	64, L, An	0·147	135–7, L, MgO	0·0502	L, MgO	0·018		0·0853	T2	2·08	L, SiO_2	632
DGa	0·339	MgO	0·964	25a, MgO	0·186	95, MgO	0·103	Av.	3·20	T2	0·0863	T2	0·280	set = DCu	1
DCr	4·32	MgO	0·116	23, An	8·25	79, MgO	1·037	MgO	63·7	T2	8·89	T2	9·0	Av.	9
DCo	1·61	MgO	0·165	29, An	1·87	84, MgO	4·21	MgO	5·85	T2	1·05	T2	0·17	Av.	16
DNi	0·796	MgO	0·440	24, An	1·95	87, MgO	15·9	HD	19·65	T2	9·72	T2	0·0468	set = DFeO	1
DCu	0·164	Al^{iv}	0·00017	30, MSAn	0·0671	94, Al^{iv}	0·11	Av.	0·114	T2	3·16	T2	0·28	Av.	1
DZn	0·621	SiO_2	0·0112	31, MgO	1·22	88, MgO	1·42	MgO	4·24	T2	0·214	T2	1·79	Av.	1
DV	0·388	MgO	0·0436	27, An	0·385	91, MgO	0·15	Median	0·104	T2	10·34	T2	0·022	set = DAl	1
DSc	0·934	MgO	0·00148	28, MgO	0·858	81, MgO	0·238	MgO	0·656	T2	0·859	T2	0·05	AvSM	57·5

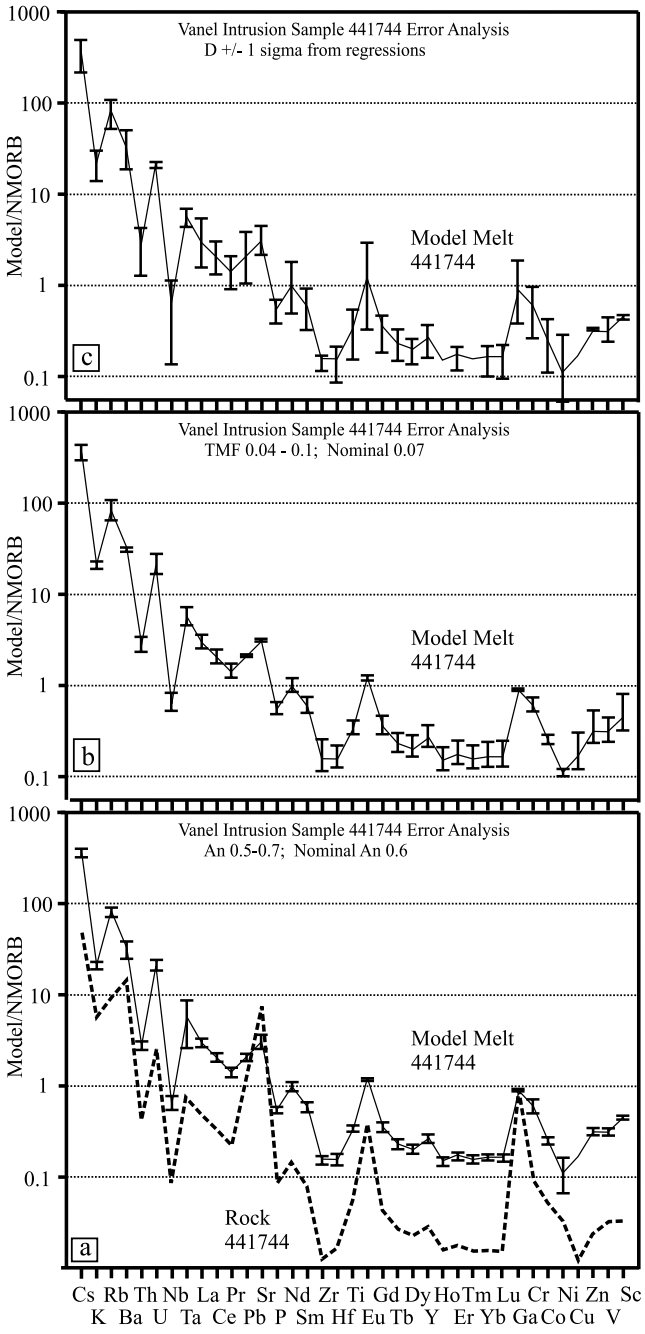

Figure 2 Error analysis applied to a Vanel anorthosite (441744, with a few elements interpolated from other rocks), showing consequences of varying. (a) An-content from An50 to An70 (the rock analysis is also shown); (b) the assumed trapped melt fraction from 0·04 to 0·1; and (c) plagioclase/melt D values by 1 sigma, from the equations in Bédard 2006a. Values in this and forthcoming graphs are normalised to N-MORB of Sun & McDonough 1989, except K (600 ppm), U (0·047 ppm) and Th (0·12 ppm) as per Jochum *et al.* 1983, and compatible elements which are modified from Pearce & Parkinson 1993 by comparison with compiled data: Ga (16 ppm), Cr (275 ppm), Co (47 ppm), Ni (135 ppm), Cu (100 ppm), Zn (83 ppm), V (250 ppm), Sc (40 ppm). Elements where no error bars are shown were not computed from the An-content.

cumulate rocks (see table e2 in Bédard 2001). The point of disappearance of minor silicate, phosphate or oxide phases during backstripping was used to constrain the TMF in most models calculated in the present paper. For most anorthosites, an assumed TMF of about 5–10% completely eliminates all phases except feldspar. Most mafic cumulate models were reduced to simple two- or three-phase assemblages between 10 and 15% TMF. In a few cases, the TMF was increased beyond this point to bring models into congruence with other models from the same intrusion. Where a cumulus origin is inferred for magnetite, ilmenite or apatite, more complex oxide–apatite melting modes were used to calculate the residual mode. A cumulus proportion of 0·1 was assumed for both magnetite and ilmenite, and 0·08 for apatite, with the proportions of the better-known silicate phases being reduced by dilution. Other assumptions and detailed procedures involved in the modelling were discussed at length in Bédard (1994, 2001) and are not repeated here.

2.2. Data sources

Modern whole-rock trace element data were gleaned from the literature (Labrieville *in* Owens & Dymek 2001; Mattawa *in* Owens & Dymek 2005; Raudot, DeLaBlache and Rivière Pentecôte *in* Francis *et al.* 2000), and from Québec Government studies supplied through the courtesy of Daniel Lamothe and Claude Hébert (Ministère des Resources Naturelles et de la Faune du Québec), who extracted all available anorthosite-related whole-rock data from the SIGÉOM database. Older data that showed spiky normalised trace element patterns were discarded. An anorthosite from the Mealy Mountains complex of Labrador (sample L5) was collected during a fieldtrip led by C. Gower in 1989, and was analysed (Table 2) as described in Bédard (2001).

3. Results of inverse models

3.1. Conventions, and the presence of positive Zr–Ti–P peaks

The modelled rocks were subdivided both by intrusion and lithology. Lithological subtypes include anorthosites (ss) with >90% plagioclase (normative), leuco-gabbroids with 90–65% plagioclase, gabbroids with 65–40% plagioclase, melagabbroids with 40–30% plagioclase, pyroxenites with <30% plagioclase and >50% pyroxene, and peridotites with >50% olivine. Average values for each suite are shown in Table 3. The input data, calculated norms, and individual models are available as an electronic Appendix (Table A1 – Supplementary Material).

Many inverse models yielded normalised melt profiles with positive Ti–P–Zr anomalies (vs. adjacent REE). There are 18 models (including some calculated from plagioclase megacrysts) which have positive Zr anomalies, which are too large to be due to use of an overly low D value, or to analytical imprecision. They may reflect a nugget effect caused by analysis of samples which are too small to include a representative proportion of post-cumulus zircon. Alternatively, some of the analysed rocks and feldspar megacrysts may contain xenocrystic zircon. Inherited zircon occurs in other anorthosite provinces (e.g. Schärer *et al.* 1996) and may also be present in Grenvillian anorthosites. Since these zircons contribute to the Zr-budget, addition of zircon to the residual mode can erase this signature. Most samples require 0·001% to 0·002% zircon, with a maximum of only 0·013%.

Positive P-anomalies are seen in 22 model melts (e.g. Fig. 3). In many cases, very small changes in the abundance of residual apatite smooth out the profile. The simplest explanation is therefore that the modal proportion of apatite used during backstripping (8%) differed from the real proportion of crystallising apatite in some cases. Similarly, positive Ti anomalies occur in 35 models (e.g. Fig. 3). Some may reflect small differences between model and real proportions of ilmenite in the crystallising melt. However, in some examples, extremely large proportions of residual ilmenite are needed to drag down the Ti peak (up to 13%). A primary positive Ti and/or P

Table 2 Analysis of L-5 anorthosite from the Mealy Mountains massif of Labrador. Major elements and Sr, Cr, Ni, Cu, Zn, and V by ICP-ES, with all other trace elements by ICP-MS. Data generated at the Institut National de la Recherche Scientifique – Eau, Terre et Environnement, in Québec City, with methods and accuracies as discussed in Bédard 2001.

Major elements (wt%)		Trace elements in rock (ppm)		Model melt (ppm)	
SiO_2	54·14				
TiO_2	0·14	Cs	0·1352	Cs	0·7925
Al_2O_3	28·11	K	6890	K	22985
Fe_2O_3	1·06	Rb	6·24	Rb	43·5
MnO	0·02	Ba	603	Ba	1207
MgO	0·61	Th	0·0094	Th	0·052
CaO	10·78	U	0·0272	U	0·177
Na_2O	4·47	Nb	0·386	Nb	2·32
K_2O	0·83	Ta	0·01	Ta	0·073
P_2O_5	0·02	La	2·47	La	12·5
LOI	0·79	Ce	4·76	Ce	24·5
Total	100·97	Pr	0·656	Pr	3·49
CIPW Norm		Sr	1325	Sr	528
		P	87·3	P	464
Anhydrous		Nd	2·39	Nd	13·2
		Sm	0·488	Sm	2·92
$Fe^{2+}/Fet=0·9$		Zr	1·58	Zr	14·4
		Hf	0·042	Hf	0·305
Quartz	0·42	Ti	839	Ti	4354
Corundum	0·31	Eu	0·608	Eu	1·73
Orthoclase	4·90	Gd	0·899	Gd	5·81
Albite	37·79	Tb	0·037	Tb	0·248
Anorthite	53·31	Dy	0·198	Dy	1·38
Hypersthene	2·81	Y	0·801	Y	5·75
Magnetite	0·15	Ho	0·035	Ho	0·251
Chromite	0·01	Er	0·084	Er	0·629
Ilmenite	0·27	Tm	0·010	Tm	0·080
Apatite	0·05	Yb	0·061	Yb	0·477
		Lu	0·009	Lu	0·0740
An/An+Ab+Or (molar)		Cr	35	Cr	191
54·2		Ni	30	Ni	82·9
		Cu	26	Cu	260
Residual Mode		Zn	18	Zn	172
		V	3	V	19·7
Plag 90%		Sc	3	Sc	25·7
TMF 10%					

anomaly in the melt is unlikely, and these peaks are most plausibly explained by either: heteradcumulus growth of these phases, or post-cumulus metasomatism by a Ti–P-enriched immiscible melt (e.g. Philpotts 1966, 1976; Veksler *et al.* 2007). Adding small amounts of apatite or ilmenite to the residual mode can correct for these effects. The adjustment for ilmenite has only a very small effect on the calculated abundances of most trace elements, but adjustment of modal apatite and zircon can have significant impact on calculated REE (Fig. 3). Nevertheless, if no corrections were made, the basic conclusions of the present paper would remain identical.

3.2. Labrieville massif

The Labrieville alkalic anorthositic pluton (ca. 300 km^2) was emplaced at 1·01 Ga (Owens *et al.* 1984). The Labrieville models are considered at some length to illustrate the methodology. This pluton has been divided by Owens & Dymek (2001) into an inner core sodic anorthosite (An<32), an outer core anorthosite that is more calcic (An>32), and a leucogabbroic marginal/border facies. Paradoxically, the sodic core has the most magnesian pyroxenes, whilst the calcic margin has the least magnesian pyroxenes. The pluton also contains a hemo–ilmenite/nelsonite deposit (Dymek & Owens 2001; Hébert *et al.* 2005). Most Labrieville data are from Owens & Dymek (2001). Although these analyses lack U and many REE, they are useful because they include data on plagioclase megacrysts which are (*a priori*) single crystals. As such, their TMF must be=0, unless disequilibrium crystallisation allowed incorporation of abundant melt inclusions (e.g. Bédard 2001). Assuming that these megacrysts were originally at equilibrium, then models derived from the megacrysts assuming TMF=0 can be compared to models calculated from whole-rock data on cumulates (composites of minerals + trapped melt), to constrain the TMF for this suite of rocks.

Figure 4a shows the NMORB-normalised (normal mid-ocean ridge basalt) trace element profiles of melt calculated from inner core megacryst 285p, as compared to the model melt calculated from Labrieville inner core anorthosite 285. Both model melts are fractionated, with relative L/H REE enrichment (light and heavy rare earth elements, respectively), LILE-enrichment (large ion lithophile elements), prominent positive Sr–Eu anomalies, a negative Th-anomaly, a spiky

Table 3 Average compositions of model liquids for the different Suites. PSAS and ESAS are primitive and enriched steep anorthositic suites, respectively. FAGS is the flatter anorthositic-gabbroic suite, ES and VES are the enriched and very enriched suites, respectively. The number in brackets is the number of rocks attributed to this suite. Av.=average; Std=Standard deviation; N=number of data.

	Low-Sr P–SAS (31)			High-Sr P–SAS (13)			Low-Sr FAGS (20)			High-Sr FAGS (5)			U (2)			Low-Sr E–SAS (12)			High-Sr E–SAS (7)			Low-Sr ES (16)			High-Sr ES (4)			VES (3)		
	Av.	Std	N	Av.	Std	N	Av.	Std	N	Av.	Std	N	Av.	Std	N	Av.	Std	N	Av.	Std	N	Av.	Std	N	Av.	Std	N	Av.	Std	N
Cs	1·438	1·127	16	0·186	0·127	5	2·27	2·61	8	0·236	—	1	—	—	0	3·55	4·36	10	—	—	0	3·54	2·27	8	1·275	—	1	2·226	1·089	3
K	13370	5814	31	45700	9327	13	12690	6895	14	36062	2430	5	7414	1724	2	21480	9693	12	26300	7857	9	20017	8783	16	33290	2178	4	81675	37161	3
Rb	31·3	27·5	28	39·3	11·9	13	64·8	74·5	11	33·0	7·0	5	—	—	0	83·8	76·6	12	30·4	17·1	8	30·7	17·2	14	29·7	8·98	4	213	57	3
Ba	289	105	31	1095	220	13	268	133	14	921	116	5	350	—	1	373	153	12	940	448	9	695	395	16	1105	138	4	5595	3307	3
Th	1·49	1·36	9	0·096	0·015	4	2·87	3·020	7	0·183	0·042	5	—	—	0	5·14	7·31	9	3·57	3·65	4	4·17	12·2	12	0·458	0·244	3	4·76	4·58	3
U	1·04	0·53	9	—	—	0	1·46	1·079	4	—	—	0	—	—	0	3·30	2·22	7	1·614	1·183	2	0·518	0·174	3	—	—	0	3·53	1·97	2
Nb	7·4	6·4	10	6·8	5·0	3	14·1	18·3	11	—	—	0	—	—	0	9·0	6·1	9	8·0	3·6	6	15·8	7·2	15	15·8	4·48	3	30·6	24·6	3
Ta	0·993	0·300	5	0·777	0·814	10	1·71	1·89	8	1·24	1·19	5	1·55	—	1	1·99	1·76	8	1·29	0·81	3	2·34	2·20	7	1·97	0·61	3	2·84	0·54	2
La	9·46	3·01	30	13·6	3·38	13	12·4	3·42	14	17·3	4·99	5	6·47	2·75	2	33·5	18·3	12	40·9	15·2	9	29·4	8·95	16	51·3	17·8	3	315	143	3
Ce	17·3	5·22	30	25·3	5·88	13	23·2	6·51	14	35·7	11·2	5	10·7	4·05	2	65·9	33·3	12	80·0	30·8	9	57·5	16·4	16	108	33·5	3	611	276	3
Pr	2·09	0·56	30	2·94	0·85	4	3·01	0·88	14	—	—	0	1·28	0·52	2	7·70	4·02	11	9·33	2·87	7	8·24	1·78	5	20·4	—	1	66·7	—	1
Pb	2·90	6·65	22	3·11	3·54	5	1·59	0·38	6	7·12	0·20	2	—	—	0	1·91	1·00	11	0·858	0·598	7	2·45	—	1	0·788	—	1	1·258	—	1
Sr	252	54·8	31	480	53·5	13	279	57·4	12	498	38·3	5	338	—	1	247	29	12	501	126	9	201	41	15	518	64	44	73	59	3
P	517	234	26	1046	531	13	698	301	11	1784	730	5	286	53·3	2	1733	942	10	3269	1411	8	2860	997	14	5725	2647	4	9794	2540	3
Nd	8·56	2·32	30	12·5	4·47	4	12·9	4·07	14	—	—	0	4·98	1·85	2	30·7	16·1	12	46·1	14·1	8	37·0	11·6	15	101	—	1	316	118	3
Sm	1·58	0·45	29	2·08	0·557	13	2·68	1·00	14	4·36	1·94	5	0·960	0·304	2	6·53	2·80	11	8·35	2·45	9	9·61	2·39	16	15·2	4·22	3	56·1	15·6	3
Zr	34·4	23·4	25	58·1	19·4	12	75·0	43·8	14	126	73·8	5	24·0	—	1	161	168	12	245	184	9	99	107	15	274	73	4	969	777	3
Hf	0·930	0·427	3	1·460	1·011	10	2·525	1·285	8	2·707	1·824	5	—	—	0	5·13	2·36	7	5·90	1·31	6	1·71	2·21	13	4·77	1·36	3	19·9	18·0	3
Ti	3826	1207	31	3702	1320	13	6346	2788	14	8514	2235	5	2211	399	2	7248	5160	12	12055	6807	9	16820	7854	16	18270	2274	4	24566	11440	3
Eu	1·842	0·561	30	2·94	0·672	13	2·193	0·879	14	3·30	0·648	5	1·22	0·59	2	2·75	1·19	12	3·75	1·21	9	3·98	1·35	16	5·61	0·32	3	13·8	5·53	3
Gd	1·512	0·552	30	1·506	0·743	4	2·90	1·257	14	—	—	0	1·06	0·32	2	4·88	2·99	11	7·18	2·37	7	10·46	5·11	6	18·0	—	1	40·8	—	1
Tb	0·196	0·074	29	0·181	0·074	13	0·487	0·208	14	0·557	0·321	5	0·217	0·034	2	0·766	0·564	12	0·898	0·268	7	1·394	0·623	14	1·963	0·468	3	3·53	2·48	3
Dy	0·975	0·343	30	1·164	0·435	4	2·44	1·13	14	—	—	0	1·25	0·26	2	4·42	3·14	11	4·57	1·30	7	8·88	4·89	5	13·5	—	1	31·5	—	1
Y	5·96	2·64	29	3·66	1·76	4	13·8	5·9	11	40·5	—	1	12·6	—	1	29·2	15·8	11	24·7	7·11	8	47·0	20·9	16	49·7	15·4	4	99·6	56·1	3
Ho	0·196	0·106	11	0·247	—	1	0·496	0·242	13	—	—	0	0·384	0·036	2	0·964	0·576	10	0·938	0·302	6	2·16	1·02	9	2·56	—	1	4·28	1·69	2
Er	0·581	0·255	24	0·438	0·217	3	1·45	0·66	14	—	—	0	1·11	0·10	2	2·45	1·49	11	2·39	0·81	7	5·13	2·88	5	5·71	—	1	14·7	—	1
Tm	0·079	0·025	7	0·086	—	1	0·175	0·129	10	—	—	0	0·206	0·044	2	0·664	0·342	3	0·426	0·083	4	0·874	0·414	7	0·816	—	1	2·39	—	1
Yb	0·559	0·295	23	0·343	0·112	9	1·29	0·61	14	1·46	1·23	5	1·50	0·029	2	2·81	1·54	11	2·23	0·65	9	4·48	1·80	16	3·90	0·65	3	7·33	3·85	3
Lu	0·113	0·051	16	0·072	0·041	6	0·212	0·108	13	0·227	0·199	5	0·272	0·025	2	0·409	0·247	12	0·316	0·168	6	0·724	0·309	14	0·627	0·126	3	1·093	0·580	2
Ga	18·1	2·5	28	22·8	1·6	13	22·3	3·6	10	23·0	2·2	5	—	—	0	20·7	2·2	12	24·1	3·6	9	23·5	4·4	13	28·5	2·7	4	31·2	4·9	3
Cr	178	282	28	19·4	28·9	11	118	68	10	12·2	5·9	5	97·8	9·4	2	130	160	10	158	312	7	162	220	8	37·7	35·7	2	56·5	46·3	3
Co	40·7	23·6	19	9·59	9·39	12	54·1	22·8	10	30·2	11·6	5	—	—	0	22·9	19·6	11	17·9	7·3	8	42·7	23·3	12	29·9	11·8	3	23·3	0·81	2
Ni	55·1	50·3	22	4·1	2·4	4	56·2	42·7	14	20·8	7·1	4	80·3	11·7	2	30·0	33·5	12	16·0	9·7	7	76	84	9	7·3	3·1	3	4·7	—	1
Cu	32·7	30·3	16	21·8	16·1	3	88·6	73·5	6	127	47	2	—	—	0	42·9	32·3	11	26·9	11·8	8	267	408	6	52·4	8·8	2	140·6	—	1
Zn	37·8	34·2	17	59·6	33·7	8	109	90	9	188	67	5	—	—	0	67	40	12	88	43	8	151	86	6	174	71	4	166	—	1
V	130	98	16	149	64	5	223	178	7	162	11·7	3	262	—	1	132	113	11	139	64	8	355	233	5	224	34	4	468	—	1
Sc	14·7	8·4	18	6·84	4·83	12	25·3	9·7	6	24·9	15·6	5	—	—	0	18·9	8·9	11	17·6	7·6	8	40·5	16·7	13	22·3	11·4	3	58·8	3·0	3

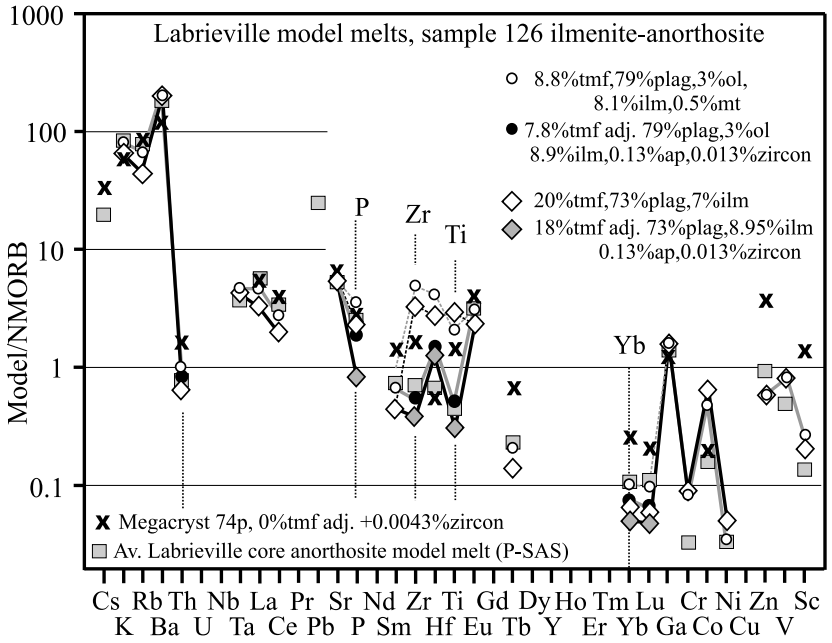

Figure 3 Inverse models for a Labrieville ilmenite-anorthosite 126 (Owens & Dymek 2001) are shown for ca. 20% and ca. 8% trapped melt fractions (TMF). The residual mode is shown, with the 'adj.' or adjusted mode resulting from the addition of residual apatite, ilmenite and zircon to eliminate positive P–Ti–Zr peaks. These adjustments also impact on the concentration of HREE, Hf and Th, elements compatible in zircon and apatite. Only minor effects are seen on the model concentration of other elements, however. Also shown for comparison is the average adjusted model melt from Labrieville core anorthosites (grey squares; see Fig. 4b), and the adjusted model melt from marginal gabbroic feldspar megacryst 74p (see Fig. 4c). Note that the 126 models show an overall decrease of incompatible element abundances as the assumed TMF increases. The average PSAS anorthosite (grey squares) shows a close match to the 8% TMF models, but the 20% TMF models are too low in M–HREE Zr–Hf–Ti. Conversely, the 74p models are too enriched in M and HREE–Ti–Zr to match the adjusted 8% TMF models.

Zr–Hf–Ti segment, high Ga and low Cr. The similarity implies a cosanguineous relationship. The whole-rock anorthosite model has positive Zr–Ti spikes, while the megacryst model also shows a positive P-spike. These can be corrected by adding modest amounts of ilmenite, apatite and zircon to the residual assemblage (labelled adj. (adjusted) on the Figures). This implies that the megacryst contains xenocrystic zircon, apatite and ilmenite as inclusions. In comparison with the adjusted megacryst model melt, the adjusted whole-rock model melt calculated for a TMF of 3% (anorthosite residue) has slightly lower P–REE–Zr–Hf, but there is an almost perfect match for K–Rb–Ba–Sr–Ti–Eu–Ga. The slight difference in P–REE–Zr–Hf could indicate that the melt from which the rock crystallised was slightly less evolved than the melt from which the megacryst crystallised. In a broader sense, both models (megacryst and whole-rock) for sample 285 are similar to model melts from other Labrieville core anorthosites (Fig. 4b), implying that all belong to a common suite.

Model melts from other Labrieville inner core anorthosites are shown on Figure 4b. The %TMF was fixed at the point where the residual assemblage became pure anorthosite in all cases. Most samples show positive Ti spikes, and half have positive Zr spikes. The non-adjusted values for sample 108 are shown for comparison. All model melts resemble models derived from megacryst 285P and anorthosite 285 (Fig. 4a), and from ilmenite–anorthosite 126 (Fig. 3); and probably belong to a cosanguineous suite, which is defined here as the *primitive steep anorthositic suite* (PSAS). This refers to the steepness of the normalised trace element profile and the modest enrichment of LREE and MREE (middle REE). On the basis of major and trace element trends, Owens & Dymek (2001) inferred that Labrievielle rocks contain very low TMF. The inverse models presented in Figure 4b, validated by comparison with the megacryst model (285p, Fig. 4a), corroborate this inference. This conclusion can guide the choice of whether high-TMF or low-TMF models should be preferred in what follows.

Figure 4c examines model melts calculated from feldspar megacryst 74p and its host gabbro 74, which are located in the marginal zone of the pluton. The figure also compares these models to the average inner core anorthosite PSAS model melt, and a model melt from a marginal anorthosite (442007). The model melt calculated from megacryst 74p (diamonds) shows some resemblance to average inner core PSAS model melts (grey squares), but has a shallower HREE profile, and so may not be strictly cosanguineous with this suite (in accord with the proposals of Owens & Dymek 2001). Because of the shallower HREE profile and lower L/H REE ratio, this suite will be referred to as the *flatter anorthositic-gabbroic suite* (FAGS). The contrast between PSAS and FAGS is subtle, and there may be a continuous variation between the two suites. Model melts calculated for outer core samples (36, 107 and 218) closely resemble models for megacryst 74p (Fig. 5a) and can also be classed with the FAGS.

The host to megacryst 74p is an ilmenite-rich gabbro (74) from the margin of the intrusion. Several model melts from this gabbro are shown (5, 10, 37% TMF), all adjusted slightly to eliminate positive Zr–Ti–P spikes. Note that small changes in the assumed TMF (e.g. from 5% to 10%) have modest impacts on the trace element contents and slope of the model melt profiles. Significant changes in trace element content of model melts are only seen for large variations in the assumed TMF (e.g. to 37%). If such a high (37%) TMF is chosen, then the model melt for gabbro 74 approaches values for models calculated from megacryst 74p for the REE–Zr, suggesting that it might have crystallised from a melt cosanguineous with the megacryst (FAGS). However, the 37%TMF model melts from gabbro 74 are too low in K–Rb, and TMF>40% are

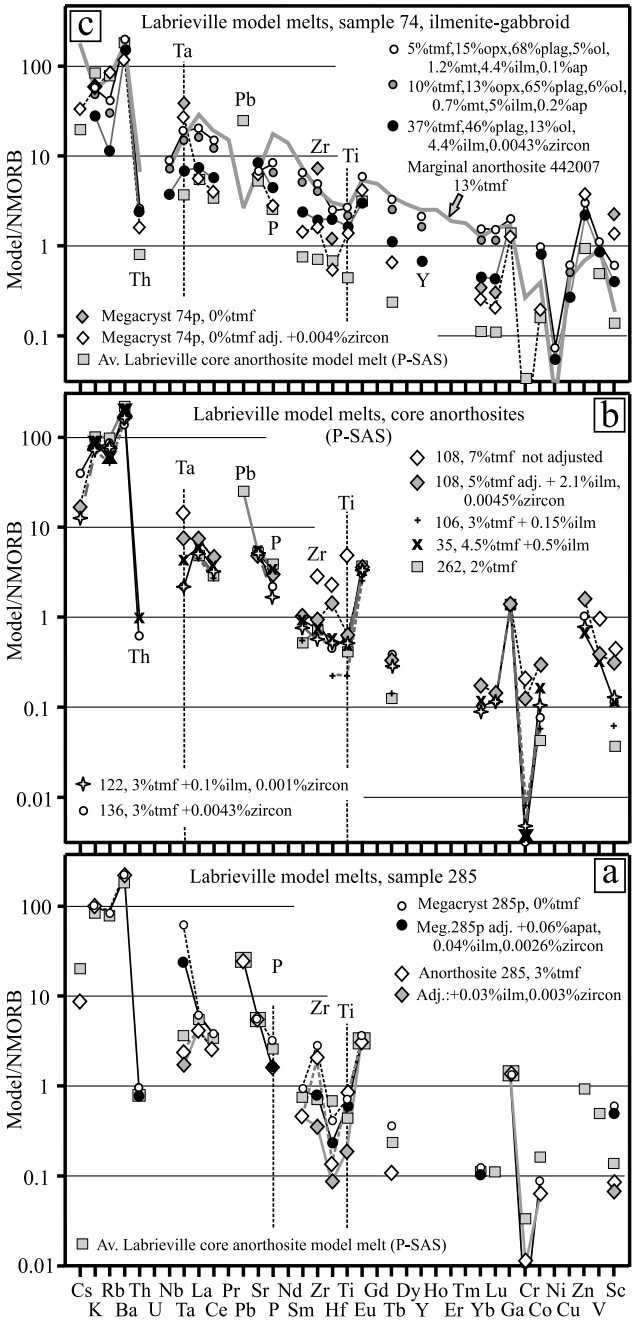

Figure 4 (a) Inverse models for a Labrieville anorthosite 285 and plagioclase megacryst 285p (Owens & Dymek 2001). Models are shown with and without added apatite, ilmenite and zircon. These phases were added to the residual assemblage to eliminate positive P–Ti–Zr peaks. Only models that differ from the unadjusted values are shown. Note the close resemblance of megacryst (285p) and whole-rock (285) models, suggesting a cosanguineous relationship, and that both resemble the average core anorthosite model melts (PSAS). (b) Inverse models for a series of Labrieville core anorthosites 285 (Owens & Dymek 2001). Only the adjusted models are shown. All are similar and, together with sample 126, were averaged to yield the average core anorthosite model melt (PSAS) shown in the other figures. (c) Inverse models for a Labrieville ilmenite–gabbro 74 and plagioclase megacryst 74p (Owens & Dymek 2001). Adjusted models are shown, with added apatite, ilmenite and zircon. Note that the megacyst models are too enriched in HREE to match the average core anorthosite model. Three models for gabbro 74 are shown, at 5%, 10% and 27% TMF. Note that the 37% TMF model approaches but does not attain the megacryst models; whilst the 5–10% TMF models closely resemble the evolved model melt calculated from the marginal anorthosite (sample 442007).

needed to obtain a close match for the REE. Rocks with such high TMF are rarely found in large plutons (Bédard *et al.* 2003a), being more characteristic of diabasic-textured hypabyssal intrusions, and so this high-TMF model seems implausible. A much simpler explanation is provided through comparison with a model melt calculated from an anorthosite (442007) located at the margin of the Labrieville pluton. Values of TMF of 5–10% for gabbro 74 yield enriched model melts that closely resemble 13%TMF model melts calculated from anorthosite 442007 (except for Co–Ni–Zn–Sc); suggesting that gabbro 74 crystallised from a relatively enriched melt similar to the one that generated anorthosite 442007. If this is correct, then the relatively depleted nature of the melt in equilibrium with megacryst 74p implies that this feldspar crystal must have formed from a depleted melt and was entrained into the enriched melt from which gabbro 74 crystallised, but did not fully equilibrate with it. Other samples (89, 153, 74, 99) from the marginal zone yield similar solutions, and are now defined as the *enriched suite* (ES, Fig. 5b).

The differences between the model melt trace element profiles of the Labrieville complex (Figs 3–5) imply that the margin (ES), outer core (FAGS), and inner core (PSAS) of the intrusion were not strictly cosanguineous. The origin of the core-to-margin trace element enrichment (PSAS to ES) is problematic, since it is coupled to outwardly increasing An-content, with the most enriched marginal samples having the highest An-contents. Owens & Dymek (2001) favoured a pressure effect to explain the zoning, but also speculated that this may be due to progressive buildup of H_2O during differentiation. The origin of this enrichment will be discussed below. Owens & Dymek (2001) also inferred that Labrieville rocks crystallised from unusually alkalic melts. The models developed in the present paper support this conclusion, since the average core anorthosite model melt (PSAS) contains 6·1wt% K_2O, 43 ppm Rb, 1181 ppm Ba and 478 ppm Sr; the average FAGS model melt has 4·4wt% K_2O, 34 ppm Rb, 919 ppm Ba and 509 ppm Sr; and the average ES model melt has 4 wt% K_2O, 30 ppm Rb, 1104 ppm Ba and 518 ppm Sr. The model K_2O contents are imprecise, since D K is poorly controlled in ternary feldspars, but the model Sr and Ba contents are robust.

3.3. Lac St. Jean and Vanel complexes

The giant Lac St. Jean anorthosite complex (>20 000 km^2) was emplaced between 1160 and 1140 Ma (Higgins *et al.* 2002; Hébert & van Breemen 2004a). The eastern border of this massif has recently been attributed to a distinct, but roughly coeval (1180–1160 Ma) massif called the Vanel complex (Hébert & van Breemen 2004b; Hébert *et al.* 2009). There are 16 analyses of the Lac St. Jean complex and 24 of the Vanel complexes in the SIGÉOM database. The assumed TMF of most of these was fixed where the residual mode became anorthositic.

Nine anorthosites from the Vanel complex yield steeply fractionated model melts (Fig. 6a) that are grouped together as the Vanel *primitive steep anorthositic suite* (PSAS). In contrast to the Labrieville PSAS, Vanel PSAS have lower overall alkali contents (Av. model K_2O=1·42 wt%, Rb=21 ppm, Ba=248 ppm, Sr=270 ppm), but are otherwise quite similar. Ten Vanel rocks (most anorthositic) yield model melts that have a shape very similar to the PSAS models (Fig. 6b), but with higher overall abundances of incompatible elements, and slightly lower L/H REE. This suite will be referred to as the Vanel *enriched steep anorthositic suite* (ESAS). Several Vanel rocks yielded PSAS or ESAS-type model melts with markedly higher contents of Sr, Ba and K. These signatures are characteristic of the nearby Mattawa intrusion (see section 3.9) and these samples may represent offshoots from its younger intrusion (C. Hébert, pers. comm. 2007). Two Vanel rocks yielded model liquids with trace element profiles that are flatter and

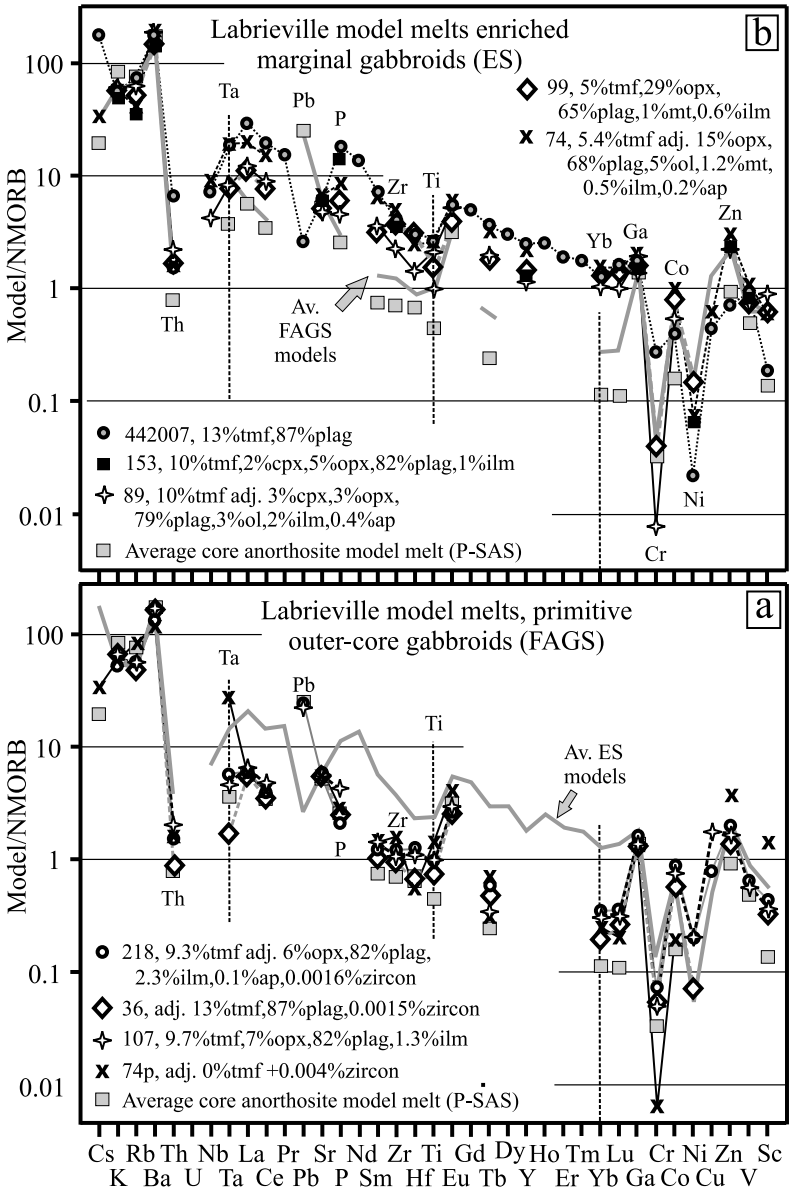

Figure 5 (a) Inverse models for a series of Labrieville primitive gabbroids from the outer core of the complex (Owens & Dymek 2001). Only adjusted models are shown. Note the close similarity of all models, that they resemble the model melt from megacryst 74p, and that they have shallower L/H REE slopes than the core anorthosite PSAS melts. The evolved suite gabbroid model melt (ES) from (b) is shown. (b) Inverse models for a series of Labrieville evolved gabbroids from the margin of the complex (Owens & Dymek 2001). Only adjusted models are shown. Note the close similarity of all models, and that they resemble the model melt from sample 442007. The average primitive outer core gabbroid model melt from (a) is shown (FAGS).

slightly less enriched overall than the Vanel ESAS (Fig. 6c). They most closely resemble the Labrieville FAGS (Fig. 6c), and so these two rocks are tentatively classified as a Vanel FAG suite. A single Vanel rock (441881) yielded an ES-type profile (see Fig. 7b).

Among the Lac St. Jean rocks, three anorthosites yielded steep fractionated trace element profiles very similar to Vanel PSAS model melts (Fig. 7a). This suite probably constitutes much of the Lac St. Jean complex, but is under-represented in the dataset. Twelve rocks from the margin of the Lac St. Jean complex contain abundant modal ilmenite and/or apatite, and yield model melt profiles characterised by overall enrichment and a flat profile shape (Fig. 7b). These will be referred to as the Lac St. Jean *enriched suite* (ES) henceforth. Most are leucogabbroids, but three have different modes, one being a mela-gabbronorite (442409), another an ilmenite harzburgite (442421), and a third being anorthositic (441881). Nonetheless, despite wide variation in residual modes, all yield very similar model melts. The pattern for ES model melts is commonly very spiky, with negative Zr, Hf, Ti and Sr troughs. Note that these profiles were not adjusted by adding ilmenite, and so the Ti and P-peaks have significance. One Lac St. Jean rock (237171) yielded a very enriched model trace element profile that does not appear to fit in with the ES, and which is classed as the very enriched suite (VES, see Fig. 9c). This VES model has many of the same troughs and peaks, as do the ES models, but has a more fractionated L/H REE profile and extremely high alkali contents similar to those of the Mattawa intrusion VES. It may represent an offshoot from the Mattawa intrusion.

3.4. Vallant complex

The Vallant complex is undated. Twelve anorthositic to troctolitic rocks from this complex yield steeply fractionated PSAS type profiles that closely resemble Lac St. Jean and Vanel PSAS models in most respects (Fig. 8a). Four yielded extremely high model Cu (up to 15713 ppm Cu for sample

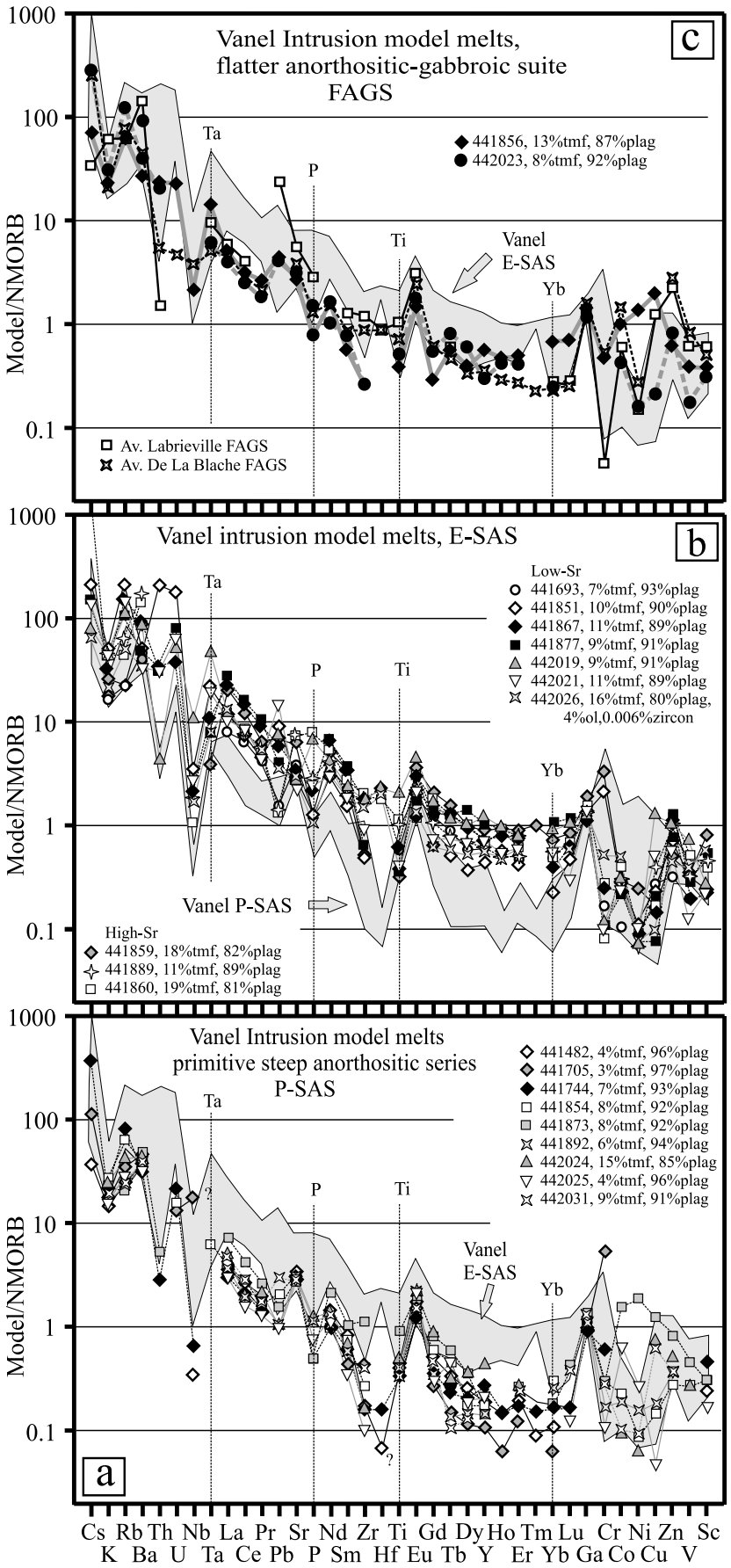

Figure 6 Inverse models for a series of Vanel complex anorthosites and leucotroctolites that define the primitive (a) and enriched (b) steep anorthositic suites (PSAS and ESAS, respectively), and (c) the flatter anorthositic-gabbroic suite (FAGS).

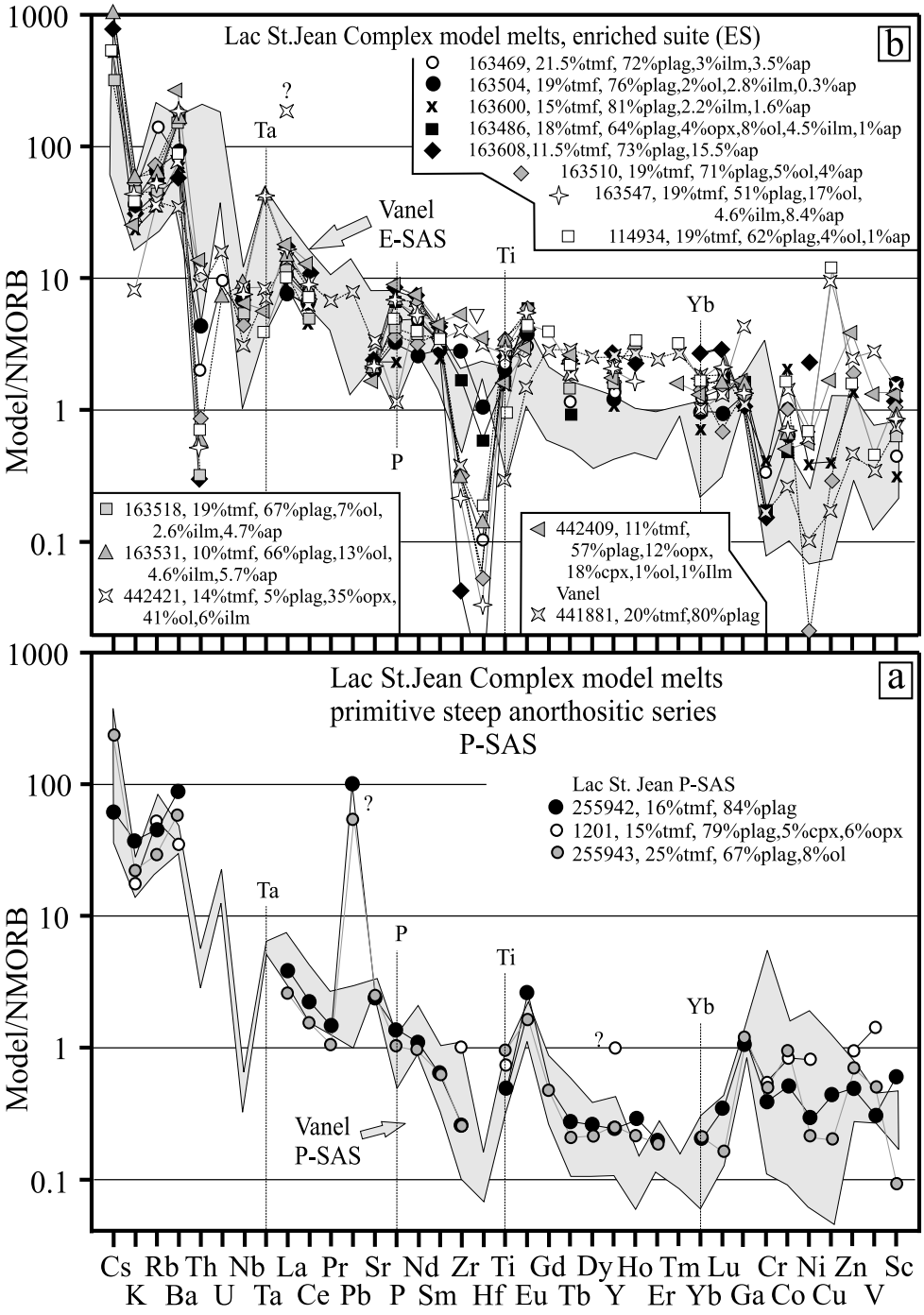

Figure 7 (a) Inverse models for Lac St. Jean rocks yielding primitive steep anorthositic suite (PSAS) model melts. (b) Inverse models for Lac St. Jean rocks (and one Vanel rock) that yielded flat, enriched trace element profiles, classed as the enriched series (ES). The field of Vanel ESAS models from Figure 6b is shown for comparison.

625280), and Co–Ni (up to 1369 ppm Ni, and 277 ppm Co for 625280); far above the range observed in the Lac St. Jean and Vanel models. The anomalous Vallant rocks contain high S (1·44% for 625280) and the anomalous models probably contain sulphides (Corriveau *et al*. 2007). The Co–Cu–Zn–V–Ni averages for this intrusion do not include these anomalous rocks. Four Vallant anorthosites and troctolites yielded more enriched model melts that closely resemble Vanel ESAS models (Fig. 8b); whilst five other anorthosites and troctolites yielded flatter, generally more depleted models similar to the Vanel FAGS (Fig. 8c).

3.5. De La Blache complex

The De La Blache troctolite–anorthosite complex has been dated at 1·327 Ga by Gobeil *et al*. (2002), and has fine-grained margins and dykes that Francis *et al*. (2000) interpreted as quenched melts. Two of the troctolites provided by Francis *et al*. (2000), together with two leucotroctolite analyses from the SIGÉOM database, yield model melts that are similar to the average Vanel and Lac St. Jean PSAS model melt (Fig. 9a) and are classed as the De La Blache PSA Suite. Another five analyses yield slightly flatter profile shapes with higher overall HREE contents (not shown) that are very similar to the Labrieville FAGS average and are grouped together as the De La Blache FAG Suite (Fig. 9b). Two feldspar-poor rocks from the Blache complex yield flatter enriched profiles (ES) (Fig. 9c).

3.6. Rivière Pentecôte intrusion

The Rivière Pentecôte troctolite–anorthosite complex has been dated at 1·36 Ga (Nantel & Martignole 1991; Martignole *et al*.

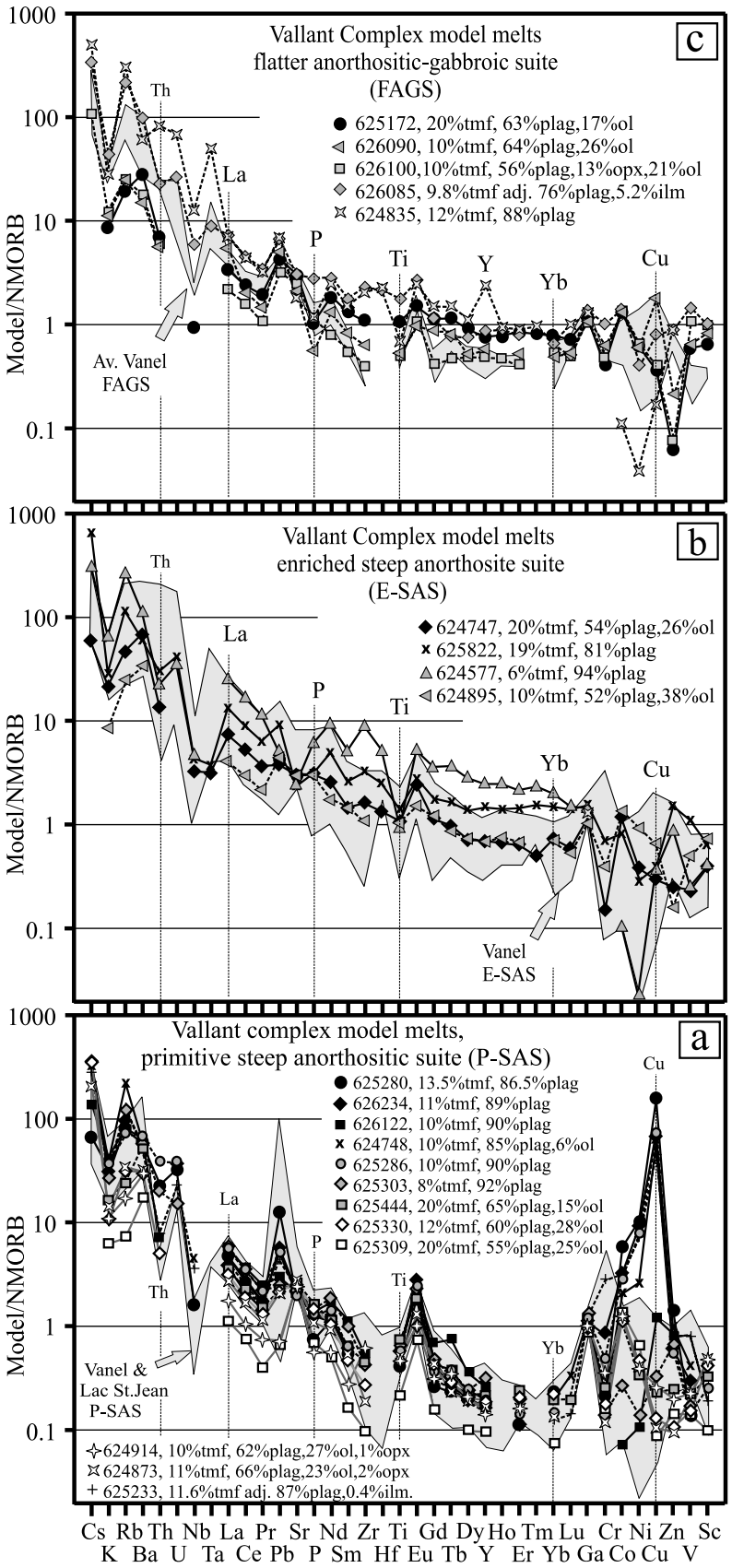

Figure 8 (a) Inverse models for a series of Vallant complex rocks with steep fractionated profiles very similar to the Vanel/Lac St. Jean PSAS models (grey field). Some of the samples are enriched in sulphide and yielded strong Cu–Ni–Co–Zn anomalies. (b) Inverse models for four Vallant complex rocks with more enriched and fractionated melt profiles very similar to the Vanel ESAS models (grey field). (c) Inverse models for five Vallant complex rocks with flatter profiles very similar to the Vanel FAGS models (grey field).

1993). Two analyses are provided by Francis *et al.* (2000). Troctolite PC31 (An63) yields a 5%TMF model melt that closely resembles the average Lac St. Jean and Vanel PSAS models (Fig. 9a), and is classed as a PSAS-type rock.

3.7. Havre St. Pierre complex

The Havre St. Pierre anorthosite is dated at ca. 1·062 Ga (van Breemen & Higgins 1993). The Rivière Romaine (RR in Fig. 1) and Lac Fournier (LF in Fig. 1) lobes may be related, but are undated. The Atikonek massif (1·13 Ga) appears to be slightly older, but the date is from an associated granite (Emslie & Hunt 1990). These massifs are poorly represented in the database, with only three anorthosite analyses from the SIGÉOM compilation. All three yield model melts that are similar to average Vanel ESAS, albeit with a very slightly flatter shape (Fig. 9b).

3.8. Mealy Mountains anorthosite

A single anorthosite analysis from the ca. 1·65–1·62 Ga (James *et al.* 2000) Mealy Mountains anorthosite is presented here (Table 2). The data was generated as outlined in Bédard (2001). The inverse model is very similar to the average Lac St. Jean and Vanel PSAS model (Fig. 9a).

3.9. Mattawa complex

The 1·012 Ga (Hébert *et al.* 2005) Mattawa andesine–anorthosite intrusion is of nearly the same age as the Labrieville intrusion, and the two may be related (Owens & Dymek 2005). It is also characterised by a predominance of andesine anorthosite and contains hemo-ilmenite deposits and inclusions of labradorite anorthosite. Six anorthosites (two ilmenite-rich) and one leuco-troctolite yielded PSAS-type model melts (Fig. 9a). Most have low An-contents and are high in Sr and LILE, and represent a high-Sr alkaline PSAS end-member similar to the Labrieville high-Sr alkaline PSAS. Others have higher An and lower Sr-contents and may represent enclaves of the adjoining Vanel anorthosite. Three anorthosites yielded ESAS type melts somewhat similar to Vanel ESAS (Fig. 9b), though with higher overall Sr-contents. Data are incomplete (Owens & Dymek 2005), but model melts from these andesine anorthosites are generally similar to the ESAS models, and they are grouped together henceforth. Two rocks yielded VES-type melts (Fig. 9c).

3.10. Raudot intrusion

The undated, 300 m-thick, Raudot intrusion from the Manicouagan region contains dunitic to leucotroctolitic rocks (Francis *et al.* 2000), and has fine-grained margins that Francis *et al.* (2000) interpreted to be quenched melts. The availability of near-liquid compositions has allowed the relationship between melt MgO content and feldspar An-content to be constrained (see above). Six analyses of cumulate rocks from the Raudot intrusion are available (Francis *et al.* 2000), and yield model melts of the FAG and ES type (Fig. 9b and c), with a dunite yielding a depleted, U-shaped model melt similar to a boninite (e.g. Bédard 1999, Fig. 10a).

4. Comparisons and inferences about processes

The average values of the different model melt suites from each pluton or massif are compared in Figures 9 to 11. The different lineages share many traits in common. All are LREE–LILE-enriched, and most have negative Th–Nb anomalies and positive Eu anomalies. The absolute values of the Eu anomalies may not be significant, since the D values for Eu in plagioclase in the present models are under-constrained. Conversely, the prominent positive Sr-anomalies that characterise PSAS and FAGS melts are much less prominent in the other magma types (Figs 9 and 10). The Grenville PSAS averages define a homogeneous population (Fig. 9a) that is very similar to the average normal anorthosite model melt from the Nain Plutonic Suite (Fig. 11a) calculated by Bédard (2001). The similarity suggests that this magma type is common to both the NPS and Grenville Province; and that use of constant Ds for the NPS calculations has not led to a major error. On the other hand, the small apparent enrichment in LREE and LILE in the Nain models probably reflects the effect of the older set of D values that were used. Similarly, the FAGS averages (Fig. 9b) also define a fairly homogeneous population essentially indistinguishable from the flat anorthosite model melt from the NPS (Fig. 11a). The similarity in the shape of the PSAS and FAGS profiles (Fig. 11a) suggests a common source. The increasing divergence for the HREE segments suggests that the petrogenesis of the steeper PSAS melts may involve larger proportions of a more HREE-compatible phase such as garnet, amphibole or clinopyroxene; or admixture with a component having higher HREE-contents.

The Grenville ESAS averages seem to represent a distinct population (Fig. 10b) that has a lower L/H REE ratio and higher overall trace element abundances in comparison to the FAGS (Fig. 10a). The Grenville ES also form a fairly coherent population (Fig. 9b), that resembles the average enriched mafic model melt from the NPS (Bédard 2001; Fig. 11b). The main differences are that the Grenvillean model melts have higher overall LILE–Th–Eu concentrations in comparison to the NPS mafic model melt. Bédard (2001) interpreted the enriched mafic model melts from the NPS as possibly belonging to a continental tholeiitic lineage. Interestingly, the Grenville ESAS and ES are almost indistinguishable for elements to the left of Zr (Fig. 11b). This might imply a common source, but involvement of different proportions of a more HREE-compatible phase such as garnet, amphibole or clinopyroxene. The Labrieville mica lamprophyres analysed by Owens & Tomascak (2002; Fig. 11b) are distinct in having slightly steeper profiles, but otherwise show some resemblances, suggesting some link.

The VES (Figs 9c & 10a) have very steep profiles, not unlike those of the PSAS. Is it possible that they may represent fractionated melts derived therefrom? The two U-shaped models (Fig. 10a) may perhaps reflect involvement of amphibole, or genesis from refractory arc mantle. In view of the limited number of analyses available, these two subgroups (VES and U-type) are not discussed further.

Figure 12a shows the calculated liquid Sr-content vs. the normative An-content of the individual rocks modelled; whilst Figure 12b shows the NMORB-normalised Sr-anomaly (in log units) calculated by interpolating to the nearest available REE. It is apparent that there are two main data clusters. The andesine-anorthosites of the Labrieville and Mattawa intrusions constitute a high-Sr/low-An group, in accord with the suggestion of Owens & Dymek (2001), who pointed out that Labrieville was unusually alkaline. In contrast, the Vallant, Blache, Lac St. Jean, Vanel, Raudot and Pentecôte intrusions constitute a low-Sr/high-An group. The high- and low-Sr averages are compared in Figure 10b and c. On average, the high-Sr subgroups have slightly steeper profiles (higher L/H REE) and are slightly enriched in Ba and P in comparison with the equivalent low-Sr suites. Models calculated from the very enriched suite (VES) rocks from Mattawa (and Lac St. Jean) plot with the high-Sr group (Fig. 12a). The single analysis from the Mealy Mountains massif is anomalous in showing high-Sr contents at high-An contents. This may represent a difference

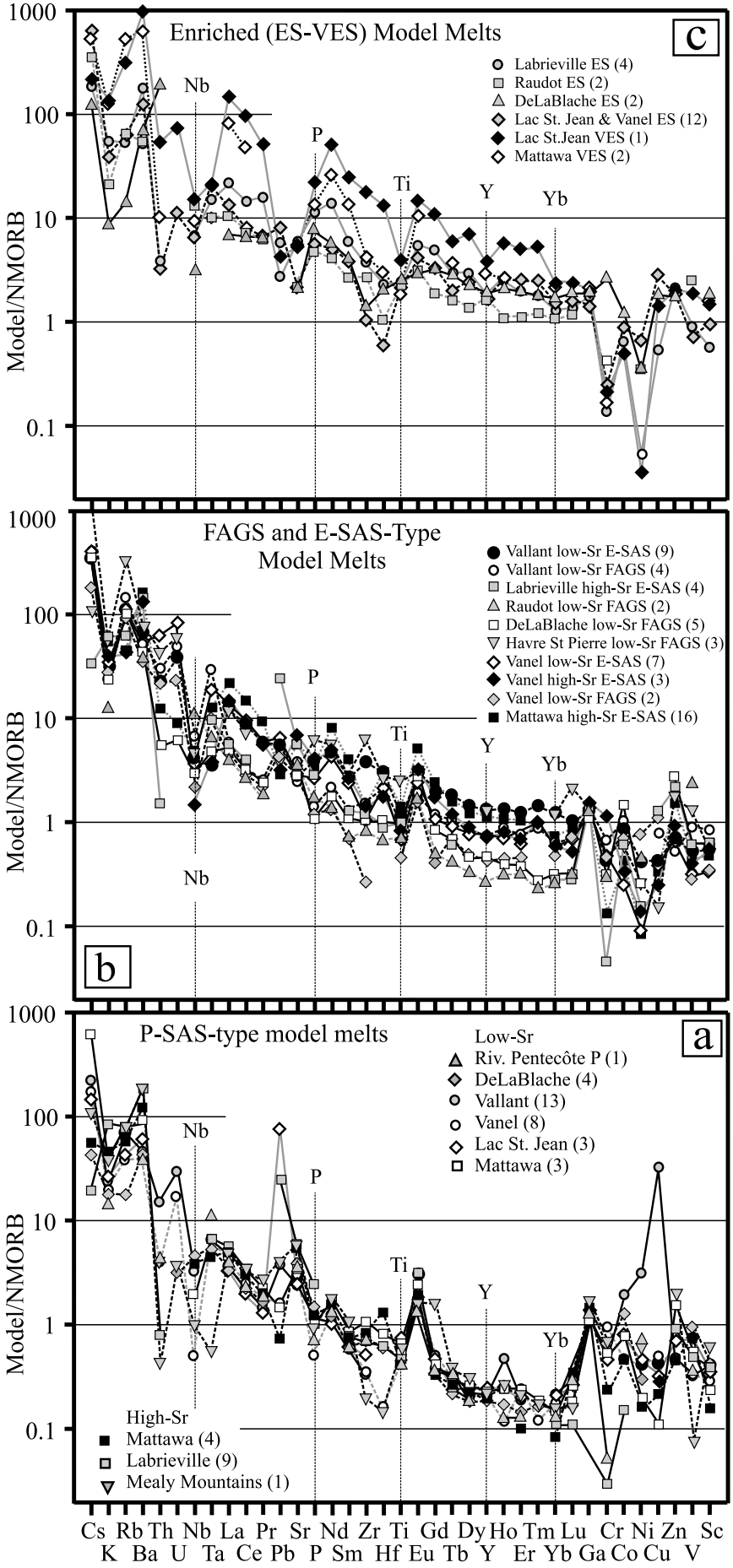

Figure 9 Compares results for the different intrusions and Suites. The number between brackets is the number of models in each average. (a) PSAS, (b) FAGS and ESAS and (c) ES and VES models.

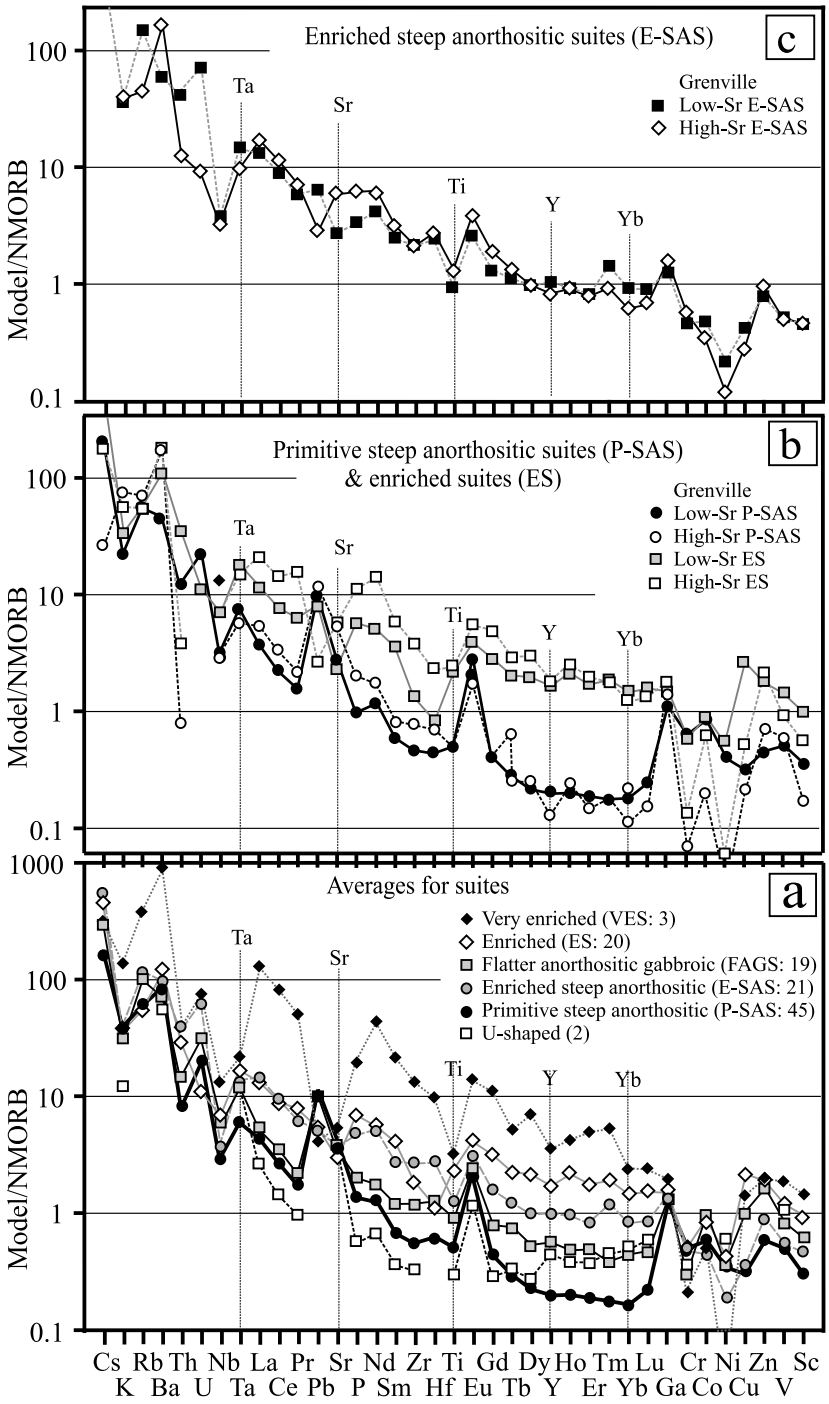

Figure 10 (a) Compares averages for PSAS, FAGS, ESAS, ES, VES and U-Shaped models from all Grenville intrusions. (b) Compares average Low-Sr and High-Sr PSAS and ES models. (c) Compares average low-Sr and high-Sr ESAS models.

in source composition. Two data from Havre St. Pierre fall between the low- and high-Sr groups, while a third model from this intrusion plots with the low-Sr/high-An group. Finally, the two labradorite–anorthosite enclaves from Mattawa are distinct, since one is high-Sr, while the other is low-Sr. Figure 12a also shows how model melt Sr varies with changes in assumed TMF (the ticked curve 10–20–30%). The differences between the two groups is far beyond what could be expected from errors in assumed TMF or plagioclase/liquid D variations, and so this distinction into low-Sr/high-An *vs.* high-Sr/low-An appears to be a robust result.

At Labrieville, the gradation from a PSAS-dominated core through a FAGS-dominated margin to an ES rim (Owens & Dymek 2001) is associated with an increase in An-content (Fig. 12a). This could perhaps be misinterpreted as a rim-to-core fractional crystallisation series, were it not for the fact that: (1) the Mg# of mafic phases decreases from the intrusion core to its rim (Owens & Dymek 2001), as do the compatible elements in the model melts (Figs 4 and 5), the opposite of what is expected from fractional crystallisation; (2) the size of the positive Sr (Fig. 12b) and Eu anomalies increase from intrusion rim to core, precluding significant plagioclase fractionation; and (3) ES and FAGS melts are more enriched in incompatible elements than the PSAS melts, and so are unlikely to be parental to PSAS (Figs 4 and 5). The high-Sr PSAS to ESAS melts from the Mattawa complex show a similar evolutionary pattern, and presumably share a common genetic scenario.

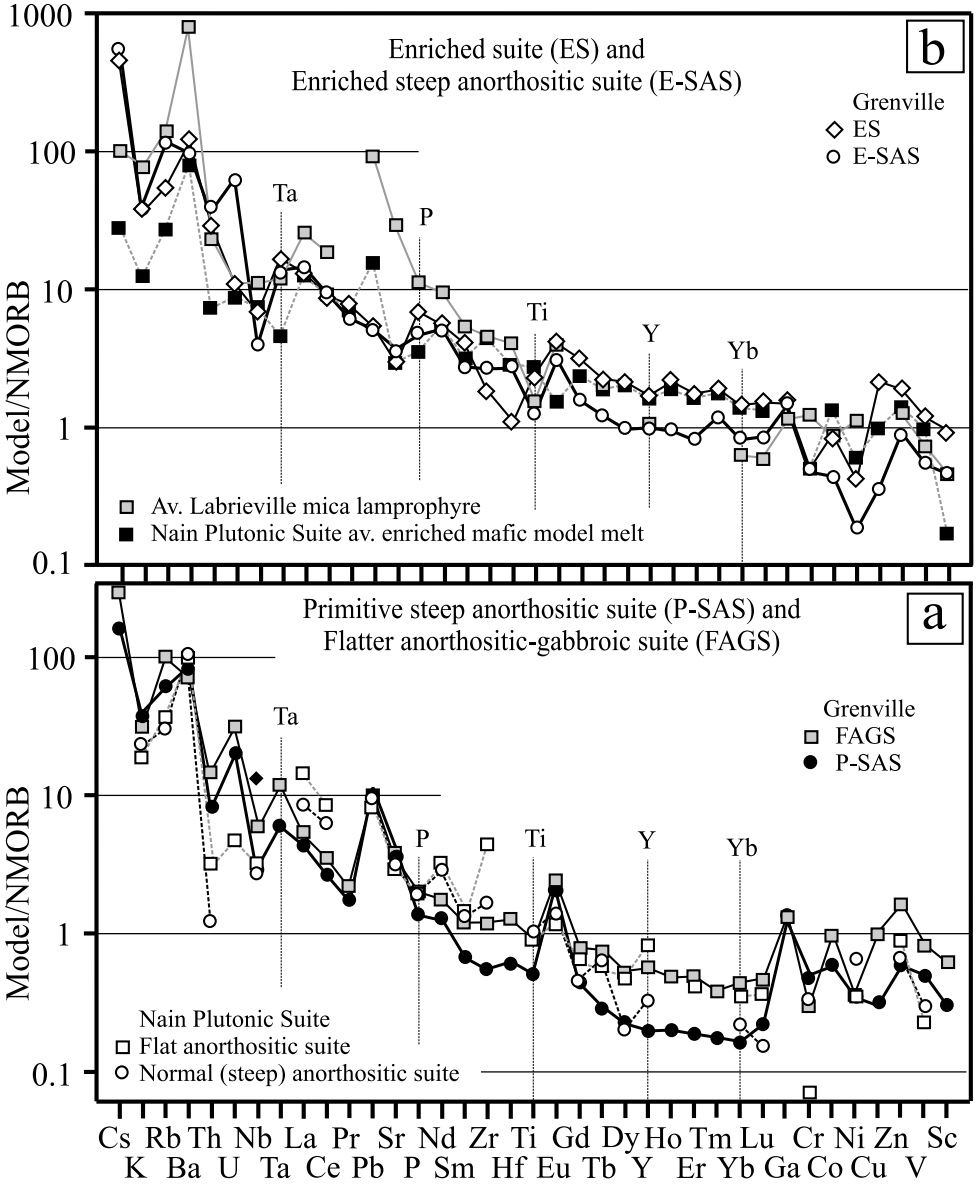

Figure 11 (a) Compares averages for Grenville PSAS and FAGS to equivalent Nain Plutonic Suite (NPS) anorthositic model melts (Bédard 2001). (b) Compares average Grenville ES and ESAS models to average NPS mafic enriched model melts, and to the average Labrieville biotite lamprophyre from Owens & Tomascak (2002).

In contrast, the low-Sr model melts appear to show a simpler trend of systematically decreasing Sr, and a change from positive to negative Sr anomalies as An decreases (Fig. 12b); which would be consistent with a plagioclase-dominated fractional crystallisation scenario. A series of simple equilibrium melting and fractional crystallisation models are developed in the next section to test possible evolutionary processes. A full petrogenetic model has yet to be developed, but it is hoped that these tentative first steps can at least eliminate impossible hypotheses and rough out a plausible scenario for more rigorous evaluation in the future.

5. Fractional crystallisation models

A series of simple fractional crystallisation models using constant D values (Table 1, Fig. 13) were set up to see whether it is possible for a low-Sr PSAS parent to evolve through a low-Sr FAGS or a low-Sr ESAS intermediate melt to a low-Sr ES residual melt. Figure 13a shows model residues from 60% fractionation of the average low-Sr PSAS (black circles) model melt. Residues from anorthositic (open circles) and troctolitic (black squares) fractionation assemblages are shown. Note that the troctolitic residue models are only shown where they differ from the anorthositic models. Through trial and error, reasonable matches with the target FAGS (grey squares) for the HREE were produced, but the LREE and LILE are always over-enriched in the models *vs* the target. Notably, the residual melt generated by anorthosite fractionation shows extreme Sr-depletion, rendering this an implausible hypothesis. The troctolitic fractionation model can improve the fit for Sr, but shows excessive Ni–Co depletion, and the LREE–LILE misfit remains. The misfit in the overall pattern implies that it is implausible to derive FAGS from a PSAS parental melt by simple fractional crystallisation. Coupled assimilation–fractionation (AFC) models involving interaction with continental crust cannot resolve this problem, since the LREE–LILE fit would worsen.

A similar set of models test whether low-Sr ESAS (grey squares) and ES (grey diamonds) model melts can be derived from low-Sr PSAS parents (black circles, Fig. 13b). Anorthositic (open circles), and feldspathic websterite (black squares) fractionation assemblages were found to yield fairly

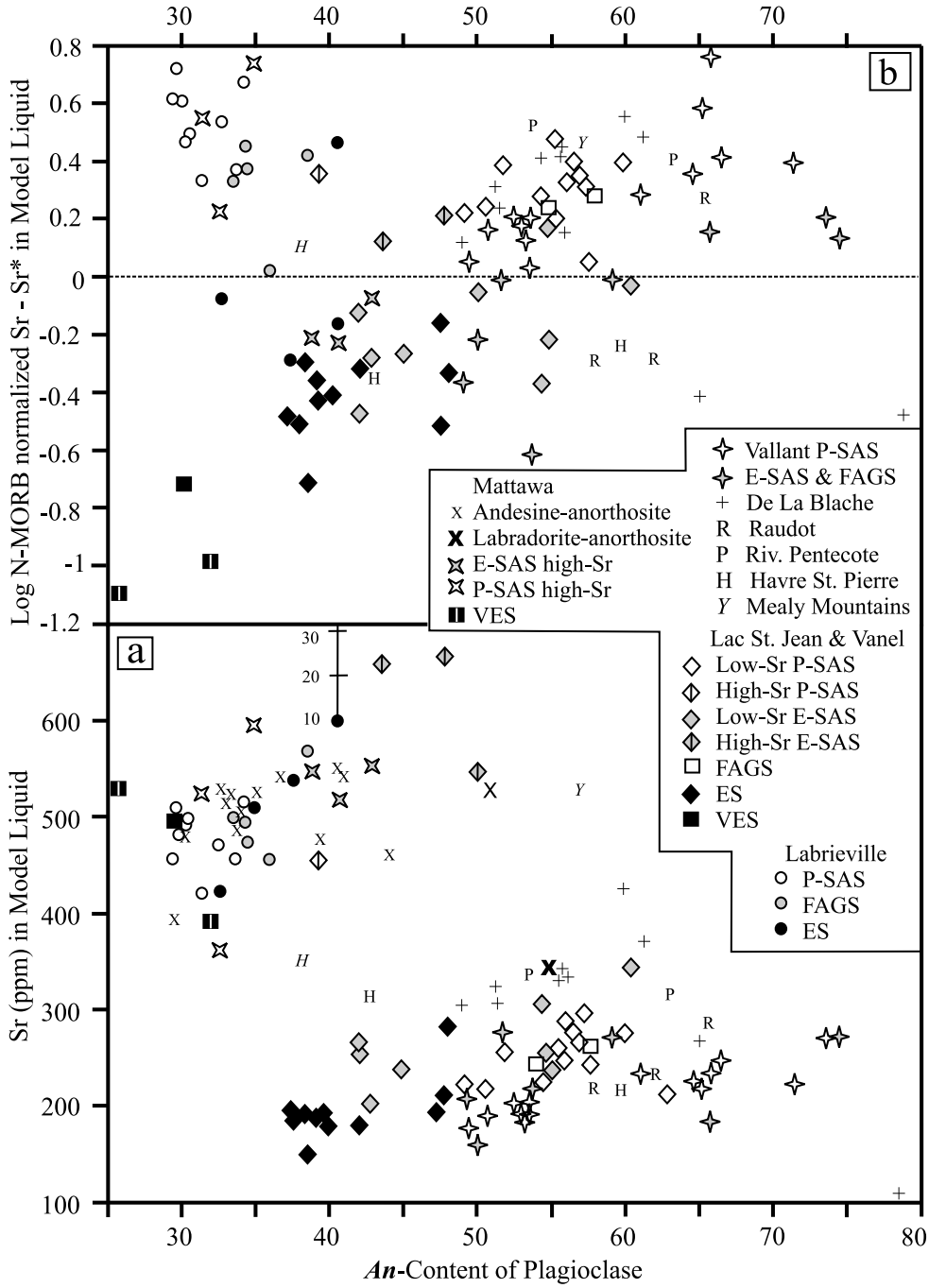

Figure 12 (a) Sr (ppm) of model melts, and (b) Log of N–MORB-normalised Sr anomaly in model melts (interpolated to nearest REE) *vs* normative An-content of rock. Note the existence of two trends.

close matches with the ESAS model melt REE at 80% crystallisation, but both fractionation assemblages lead to over-enrichment of the LILE. Note that only feldspathic websterite models that differ from the anorthosite models are shown. Furthermore, the residue from anorthosite fractionation shows excessive Sr-depletion, and over-enrichment in Cr–Co–Cu–Zn–Sc; whilst the residue from pyroxenite fractionation shows excessive Ni–Co depletion. Extraction of gabbroic assemblages (black diamonds) shares many of these defects and worsens the HREE fit. About 20% biotite fractionation would be needed to suppress LILE-enrichment, which seems implausible. Thus, it does not seem possible to derive an ESAS residue from a PSAS parent by simple fractional crystallisation.

Finally, the previously outlined fractionation models (Fig. 13b) yield reasonable fits to the LREE–MREE–Sr–Ti abundances of ES model melts for 80% crystallisation; but cannot generate the requisite HREE enrichment, or generate residual melts that are over-enriched in the LILE, and cannot account for the fact that ES model melts generally have compatible element abundances equal to or higher than is observed in the PSAS model melts. Consequently, ES melts cannot be the residua of a PSAS to ESAS to ES fractionation series.

6. Partial melting models

The prominent positive Sr–Eu peaks of the model melts calculated from the Grenville anorthosites might suggest a feldspar-enriched, possibly cumulate source (e.g. Duchesne *et al*. 1999). This type of source might also impose an unusually aluminous nature to the melt and explain the abundance of plagioclase that eventually crystallises. Three equilibrium melting models (Fig. 14a) were calculated using depleted

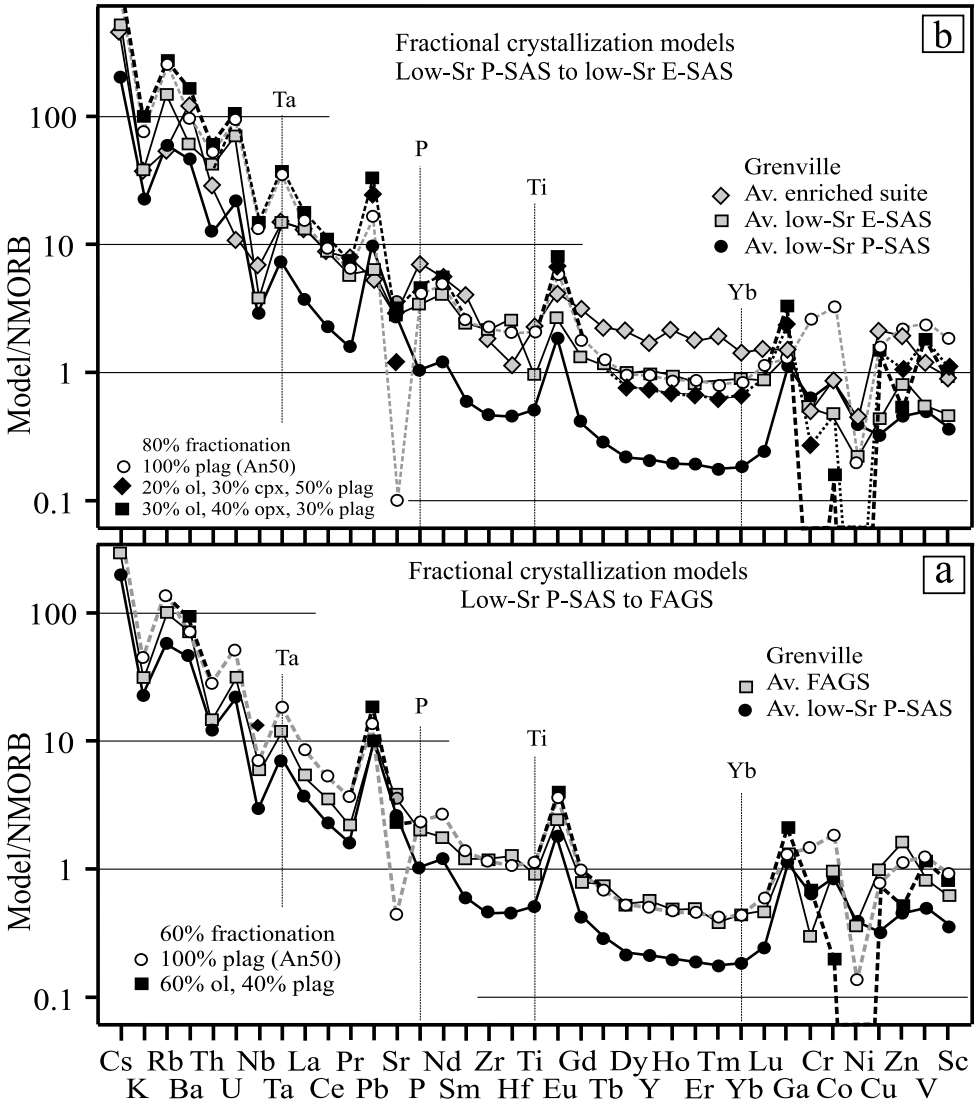

Figure 13 Fractional crystallisation models using the constant D values of Table 1 attempting to relate the average low-Sr PSAS parental melt to (a) av. FAGS and (b) av. Low-Sr ESAS and ES model melts.

aluminous cumulate (1722A4), and an enriched aluminous and ferruginous (1722A2) gabbro–norite cumulate from the Talkeetna Arc (Greene *et al.* 2006) as sources. D-values used were those of Table 1, with garnet Ds from Bédard (2006a). The open symbols represent garnet-rich residues (needed to fractionate the REE), whilst the grey diamonds shows a variant with a pyroxenitic residue. Comparison with the compositions of the average low-Sr PSAS model melt from the Grenville (grey line on Figure 14a) shows that arc cumulates are too depleted and cannot generate PSAS-type melts at reasonable degrees of melting (ca. 5–30%). The problem is compounded by the steep slope of the PSAS models. To generate a melting model with such a slope requires abundant residual garnet, which creates strongly REE-depleted melts. If smaller proportions of garnet are used (grey diamond), the models yield melts with HREE-contents that begin to approach the PSAS field, but which have very shallow L/H REE slopes. Thus, it seems as though simple batch melting of feldspathic arc cumulates alone cannot produce PSAS or FAGS type melts.

Given the trace element deficit of the arc cumulate sources (Fig. 14a), a typical arc tholeiite protolith was tried. The average composition of the Mount Misery Formation, an Ordovician-age depleted arc-tholeiite sequence from Newfoundland (Bédard 1999) was used. Figure 14a shows a 30% melting model based on this source. Although somewhat *ad-hoc* in terms of its residual mineral assemblage, the model yields a fairly good fit to low-Sr PSAS melts. Small variations in assumed residual mode or degree of melting produce only small changes in melt composition, and so the fit to PSAS is fairly robust. The Ce/Yb *vs.* Yb distribution (Fig. 15) suggests that PSAS melts form by 5–65% melting of an arc tholeiite source with a feldspar-free garnetiferous pyroxenite (eclogitic) residue. Extensive melting of aluminous source rocks where plagioclase is not a stable residual phase can account for the prominent positive Sr–Eu anomalies and steep L/HREE profile of the model melts (Fig. 14a), and could help explain extensive plagioclase crystallisation upon ascent. This should not be taken to imply that only downthrust (subducted) volcanic facies are involved. The huge source volume needed to account for the size Grenville AMCG massifs (at least twice the observed volume of anorthosite and granite) suggests that the melting events may sample 'whole-crust' domains including cumulates and differentiated products also (Fig. 16b).

High-Sr PSAS model melt can also be fitted as a partial melt of the same Mt. Misery source (not shown), but with slightly more pyroxene and less amphibole in the residual mode. The high-Sr PSAS model melts, although generally very similar to the low-Sr model melts (Fig. 10b), have feldspar with much

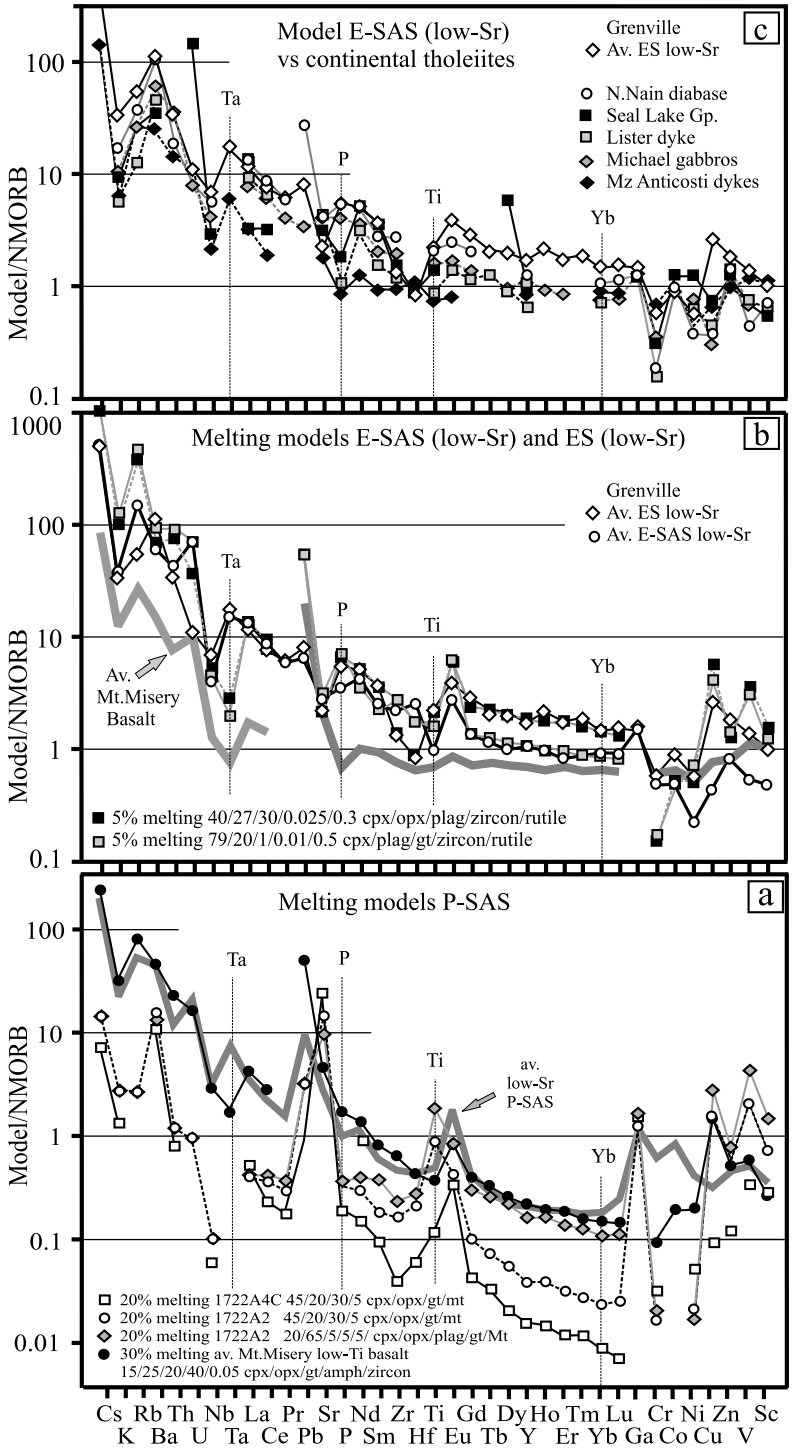

Figure 14 Equilibrium melting models attempting to generate average low-Sr PSAS (a), and low-Sr ESAS and ES (b) from the average Mt. Misery arc tholeiite (Bédard 1999), and from two Talkeetna arc cumulates (Greene *et al.* 2006). (c) Compares the average low-Sr ES melt to different continental flood basalt melt compositions. Proterozoic: North Nain Diabase and Seal Lake Group (Cadman *et al.* 1994, 1995a, 1995b); Michael gabbros (Emslie *et al.* 1997); Mt Lister intra-plutonic Dykes (Emslie *et al.* 1994). Mesozoic Anticosti dykes from Bédard (1992).

lower An contents (Fig. 12), a feature that has yet to be fully explained. One possibility is that high-Sr andesine anorthosites might represent reworked low-Sr labradorite anorthosites (Buddington 1936; Berg 1969; Anderson & Morin 1969).

Figure 14b shows variants of this Mt. Misery melting model that attempt to fit average low-Sr ESAS melts. Apparently reasonable fits are obtained only at low (ca. 5%) degrees of melting, and the residual assemblages are dominated by pyroxene with subordinate plagioclase and minor (1–2%) garnet. The need for such small amounts of garnet suggests that it may not physically exist in the source, but may reflect natural variation in HREE Ds of clinopyroxene and amphibole. Small amounts of residual zircon ± rutile are also needed to produce satisfactory fits for Zr and Ti. The LILE elements are over-estimated in the melting models, possibly indicating that the source had LILE-contents lower than those typifying the Mt. Misery basalts. The average high-Sr ESAS model can also be fitted (not shown), but requires a different residual mode, involving cpx/opx/plag/gt/zircon/rutile = 70/21/7/2/0·01/0·5, i.e. less clinopyroxene and

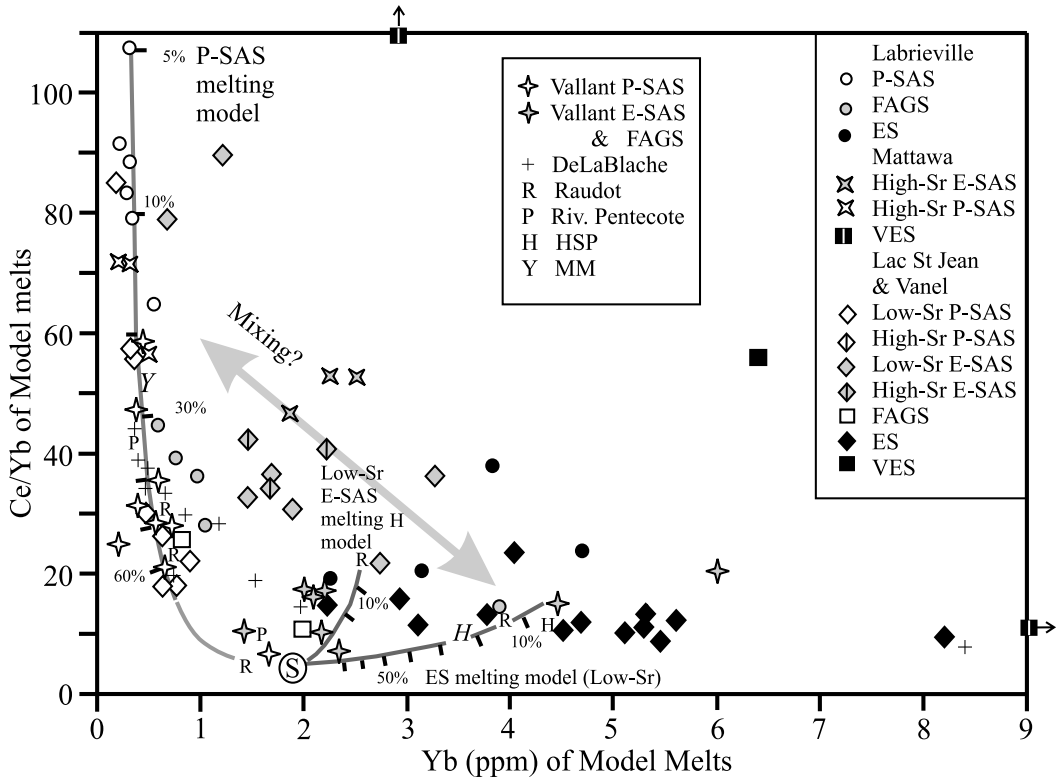

Figure 15 Ce/Yb vs. Yb (ppm) of model melts, compared to the Mt. Misery (S) equilibrium melting curves of Figure 14a and b. See text for discussion.

feldspar and more orthopyroxene. However, to account for the spread of the ESAS data in terms of a melting model (Fig. 15), melting degree is constrained to remain low, while the source volume had to change mode. Figure 14b also shows a melting model for average low-Sr ES melts. Reasonable fits are obtained for small degree melting of the same Mt. Misery basalt source, but here the residue must be gabbronoritic, since abundant plagioclase is needed to buffer the Sr-abundance. The high-Sr ES melts could not be fitted by partial melts of this source and appear to require a less depleted source rock (not shown). As for the ESAS models, the ES models intersect the target melt at low degrees of melting (e.g. Fig. 15), are very sensitive to the residual mode, and are not robust.

The high compatible element abundances (Fig. 10a), the abundance of modal olivine in many ES rocks (Appendix Table A1 – Supplementary Material), and the resemblance of the ES trace element profiles to those of typical continental flood basalts (Fig. 14c) and lamprophyres (Owens & Tomascak 2002; Fig. 11b) suggest that the ES melts may be mantle-derived. This would be consistent with the resemblance between Grenville Province ES model melts and Nain Plutonic Suite enriched mafic series model melts calculated by Bédard (2001; Fig. 11b) that he interpreted as mantle-derived melts. If the ES model melts are mantle-derived, then extensive intracrustal fractional crystallisation is implied to account for the overall trace element enrichment. In this context, the high LILE and negative Nb–Ta–Ti anomalies could imply either extensive assimilation of crust (AFC), or derivation from a mantle previously enriched by arc processes. The constancy of the Ce/Yb ratios (Fig. 15) seems incompatible with the former, and favours derivation from subduction-modified mantle (Fig. 16b). Partial melting of delaminated crustal slabs may also contribute. If a dominant mantle derivation for ES series melts is accepted, then this suggests that ESAS and FAGS may represent mixtures of extensive high-pressure crustal PSAS melts with mantle-derived ES melts (Fig. 15). This mixing scenario for ESAS and FAGS is more plausible than the melting models for these two suites.

7. Why are massif-type anorthosites solely a Proterozoic phenomenon?

The evidence for a crustal arc source for AMCG magmas is consistent with phase equilibrium considerations and isotopic signatures (e.g. Demaiffe *et al.* 1986; Duchesne *et al.* 1989; Duchesne 1990; Van der Auwera *et al.* 1998; Longhi *et al.* 1999; Schiellerup *et al.* 2000), and (locally) inherited zircons (Schärer *et al.* 1996). Heat could be provided either by thermal relaxation of tectonically thickened crust (Duchesne *et al.* 1999; Fig. 16a), or from underplating basaltic intrusions generated by post-tectonic delamination of the underlying mantle/slab (Corrigan & Hanmer 1997, fig. 22b). The absence of AMCG complexes from the Phanerozoic is problematic in this regard, given that active margins abound in the post-Proterozoic record. Three possible explanations can be entertained. (1) The source was ephemeral, and was completely destroyed by ca. 900 my. This seems unlikely, since Archaean cratons persist in the geological record. Another model (2) posits that the anorthosites and associated rocks formed through melting of the base of a long-lived stable supercontinent (e.g. Hoffman 1989; Vigneresse 2005). However, the Grenvillean orogen was far from stable, and is in fact a collage of peri-continental and oceanic arc terranes assembled between ca. 1700 Ga and ca. 1100 Ga. Thermal blanketing scenarios appear to be inconsistent with the active-margin environment favoured by most of the geologists working in the Grenville Province (e.g. Rivers & Corrigan 2000; Hanmer *et al.* 2000; Gower & Krogh 2002). In addition, younger supercontinents (Rodinia and Pangea) are not characterised by anorthosites. It has also been suggested (3) that anorthositic massifs form when underthrust crustal rocks melt during post-orogenic

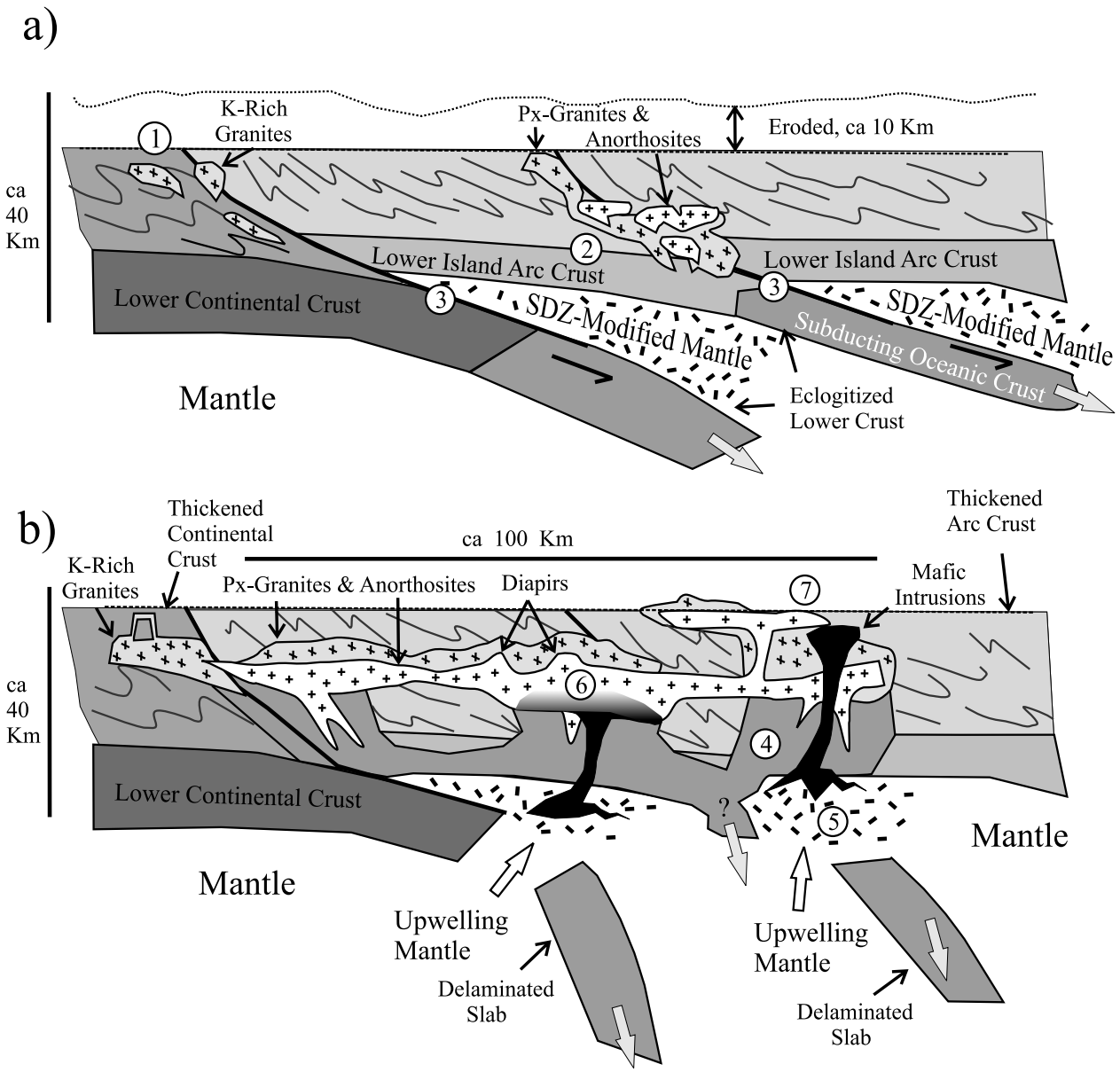

Figure 16 (a) Cartoon illustrating the crustal tongue model of Duchesne *et al.* (1999) in a context of collisional tectonics, with island arc and continental blocks welded together and thickened. (1) High-K granites form above downthrust continental crust. (2) Lower-K granites and jotunitic melt parental to anorthosites form by fusion of juvenile simatic lower crust as it heats up when juxtaposed against hotter mantle (3). (b) Model proposed here, with scale of bodies adapted to Grenville Province AMCG Suite. After collisional orogenesis and crustal thickening, the eclogitised 'oceanic' slabs detach and sink, leading to large-scale mantle upwelling. This transfers abundant heat, which causes large-scale melting of lower crust. Low degrees of melting generate granitoids, whilst extensive melting generates melt parental to anorthosites, leaving behind abundant eclogitic residues (4) which must at least equal the volume of anorthosite+granite, and which may itself become unstable and delaminate. The influx of heat also induces melting of subduction-modified mantle (5) and delaminated crust, so generating the associated mafic intrusions, some of which mix (6) with the anorthosites. Some of the granites may be residual melts expelled from fractionating anorthosite cumulates. Deeply-emplaced anorthosites may develop diapiric instabilities, while more shallowly-emplaced anorthosites (7) are conduit-fed (Royce & Park 2000).

thermal relaxation (Fig. 16; Duchesne *et al.* 1999; Corrigan & Hanmer 1997). In the context of this third model, the restriction of anorthosites to the Proterozoic is difficult to explain. The absence of AMCG rocks from exhumed active margins (e.g. Greene *et al.* 2006; Jagoutz *et al.* 2007) implies that this is not just a sampling/erosional level problem. The only remaining possibility seems to be that the secular decrease in the activity of radioactive elements and mantle temperature (e.g. Kramers *et al.* 2001) has made it unlikely for large-scale remobilisation of the lower crust to occur in Phanerozoic orogens.

If one accepts the post-tectonic model for AMCG genesis postulated above (hypothesis 3; Fig. 16), then the absence of AMCG complexes from the Archaean is also problematic, given that the peripheral parts of many cratons are thought by many to be tectonic terrane collages (e.g. Percival *et al.* 2006; Smithies *et al.* 2007). The absence of pre-1 Ga high-pressure rocks (Stern 2005) and pre-2·5 Ga large-scale basaltic dyke swarms (Yale & Carpenter 1998); results of thermal modelling (Kramers *et al.* 1991); and the recognition of partial convective overturn events in craton cores (Chardon *et al.* 1996; Collins *et al.* 1998; Bédard *et al.* 2003b), all imply that the pre-Proterozoic crust was extremely weak, and was probably not capable of being thickened tectonically (Sandiford 1989; Bailey 1999; Bédard 2006b). This provides a possible explanation for the absence of AMCG magmatism prior to 2·5 Ga.

8. Conclusions

Trace element inversion modelling of Grenvillean anorthosite massifs and associated mafic rocks emplaced from ca. 1·64 Ga to 1 Ga yield model melts with trace element profiles enriched in alkalis and light rare-earth elements (LREE) relative to normal mid-ocean ridge basalt (NMORB); commonly with negative Nb and Th anomalies. More than half of the models have steeply-fractionated trace element profiles with high Ce/Yb, positive Sr–Eu anomalies, and low abundances of HREE (heavy REE), and are named PSAS and FAGS (primitive steep anorthositic suite, and flatter anorthositic-gabbroic suite) that cannot be linked through fractional crystallisation processes. However, PSAS and FAGS can be explained by extensive (5–65%), high-pressure (garnet in residue) partial melting of arc basaltic sources. The second most important model melt subtype generated from Grenvillean anorthosites is the enriched steep anorthositic suite (ESAS), which shares many of the PSAS traits, but at higher overall incompatible element abundances. ESAS melts could not be derived from PSAS parents by fractional crystallisation models. Partial melting models can generate ESAS melts from the same arc basalt source discussed above, but the models are not robust. A third important population of rocks yielded model melts with flatter, more enriched profiles (enriched suite or ES). The incompatible element budgets of ES model melts can be modelled by lesser degrees of melting of the same arc source at low-pressures (plagioclase stable); but this is probably not consistent with the elevated abundances of compatible elements in these models, which suggests that the ES subtype represents partial melts of a mantle fertilised by arc magmatism. Mixing between ES and PSAS could provide a mechanism to generate ESAS- and FAGS-type melts. The active tectonic context now favoured for the Grenville Province appears to be inconsistent with plume or thermal insulation models. The heat source for melting could record either post-orogenic thermal relaxation, or basaltic underplating caused by delamination of a mantle root or subduction slab. This new model can explain the lithological associations, with the basaltic end-members forming from subduction-modified mantle, with anorthosites forming from the downthrust arc crust, and granitoids forming either from the less-depleted crustal segments, or being derived by fractionation of the anorthosite parental melt. In this context, pre-Proterozoic anorthosites may be lacking, because prior to ca. 2·5 Ga, the lower crust was too weak to be thickened tectonically. It is notable that continent-scale dyke swarms are absent prior to 2·5 Ga. Post-Proterozoic anorthosites may be absent due to the secular decrease in radiogenic heating and cooling of the mantle, making extensive reactivation of thickened crust less likely.

9. Acknowledgements

This is Geological Survey of Canada contribution #20080320. Jean-François Moyen and Gary Stevens are thanked for the invitation and means to present this paper at the Hutton Meeting. Louise Corriveau commented on an earlier version. Jean-Clair Duchesne and Lew Ashwal provided useful comments. Daniel Lamothe of the MRNFQ provided data extracts from the SIGÉOM database, and Claude Hébert (MRNFQ) provided unpublished data and valuable discussion. Pierre Brouillette (CGC-Québec) helped with the map and data projection.

10. Supplementary Material

The Appendix Table A1 is published as Supplementary Material with the online version of this paper. This is hosted by the Cambridge Journals Online Service and can be viewed at http://journals.cambridge.org/tre

11. References

Amelin, Y. V., Larin, A. M. & Tuckerm, R. D. 1997. Chronology of multiphase emplacement of the Salmi rapakivi granite–anorthosite complex, Baltic shield: implications for magmatic evolution. *Contributions to Mineralogy and Petrology* **127**, 353–68.

Anderson, A. T. Jr. & Morin, M. 1969. Two types of massif anorthosites and their implications regarding the thermal history of the crust. *In* Isachsen, Y. W. (ed.) *Origin of Anorthosite and Related Rocks. New York State Museum Science Service Memoir* **18**, 57–69.

Anderson, J. L. 1983. Proterozoic anorogenic granite plutonism of North America. *In* Medaris, L. G., Byers, C. W., Mickelson, D. M. & Shanks, W. C. (eds) *Proterozoic Geology. Geological Society of America Memoir* **161**, 133–54.

Ashwal, L. D. 1993. *Anorthosites*. Berlin: Springer-Verlag, 422 pp.

Bailey, R. C. 1999. Gravity-driven continental overflow and Archaean tectonics. *Nature* **398**, 413–15.

Bédard, J. H. 1992. Jurassic high-Titanium quartz tholeiites from Anticosti Island, Québec. *In* Puffer, J. & Ragland P. C. (eds) *Eastern North American Mesozoic Magmatism. Geological Society of America Special Paper* **SP268-09**, 161–7.

Bédard, J. H. 1994. A procedure for calculating the equilibrium distribution of trace elements among the minerals of cumulate rocks, and the concentration of trace elements in the coexisting liquids. *Chemical Geology* **118**, 143–53.

Bédard, J. H. 1999. Petrogenesis of boninites from the Betts Cove ophiolite, Newfoundland, Canada: Identification of subducted source components. *Journal of Petrology* **40**, 1853–89.

Bédard, J. H. 2001. Parental magmas of Nain Plutonic Suite anorthosites and mafic cumulates: A trace element modelling approach. *Contributions to Mineralogy and Petrology* **141**, 747–71.

Bédard, J. H. 2005. Partitioning coefficients between olivine and silicate melts. *Lithos* **83**, 394–419.

Bédard, J. H. 2006a. Trace element partitioning in plagioclase feldspar. *Geochimica et Cosmochimica Acta* **70**, 3717–42.

Bédard, J. H. 2006b. A catalytic delamination-driven model for coupled genesis of Archaean crust and sub-continental lithospheric mantle. *Geochimica et Cosmochimica Acta* **70**, 1188–214.

Bédard, J. H. 2007. Trace element partitioning coefficients between silicate melts and orthopyroxene: Parameterizations of D variations. *Chemical Geology* **244**, 263–303.

Bédard, J. H., Pagé, P. & Lissenberg, J. 2003a. Melt transfer mechanisms in the lower ophiolitic crust: Examples from the Bay of Islands, Thetford-Mines, Betts Cove and Annieopsquotch. *EOS Transactions of the American Geophysical Union* **84**, p. F1540 [Abstract].

Bédard, J. H., Brouillette, P., Madore L. & Berclaz A. 2003b. Archaean cratonization and deformation in the northern Superior Province, Canada: an evaluation of plate tectonic versus vertical tectonic models. *Precambrian Research* **127**, 61–87.

Bédard, J. H., Leclerc, F., Harris, L. & Goulet, N. 2008. Intra-sill magmatic evolution in the Cummings Complex, Abitibi greenstone belt: Tholeiitic to calc-alkaline magmatism recorded in a subvolcanic conduit system. *Lithos* **111**, 47–71.

Berg, J. H. 1977. Regional geobarometry in the contact aureoles of the anorthositic Nain complex, Labrador. *Journal of Petrology* **18**, 399–430.

Berg, R. B. 1969. Petrology of anorthosites of the Bitterroot Range, Montana. *In* Isachsen, Y. W. (ed.) *Origin of Anorthosite and Related Rocks. New York State Museum Science Service Memoir* **18**, 387–98.

Blundy, J. D. & Wood, B. J. 1994. Prediction of crystal-melt partition coefficients from elastic moduli. *Nature* **372**, 452–4.

Bowen, N. L. 1917. The problem of the anorthosites. *Journal of Geology* **25**, 209–43.

Bowen, N. L. 1922. The behaviour of inclusions in igneous magmas. *Journal of Geology* **30**, 513–70.

Brandriss, M. E. & Cawthorn, R. G. 1996. Formation of anorthosite and leucotonalite during magma hybridization in the Koperberg Suite of Namaqualand, South Africa. *South African Journal of Geology* **99**, 135–51.

Bridgewater, D. D. & Windley, B. F. 1973. Anorthosites, post-orogenic granites, acid volcanic rocks and crustal development in the North Atlantic Shield during the Mid-Proterozoic. *In* Lister, L. A. (ed.) *Symposium on Granites, Gneisses and Related Rocks. Geological Society of South Africa Special Publication* **3**, 307–17.

Buddington, A. F. 1936. Origin of anorthosite in the Adirondacks and in general. *Transactions of the American Geophysical Union* **17**, 255–6.

Cadman, A. C., Tarney, J., Baragar, W. R. A. & Wardle, R. J. 1994. Relationship between Proterozoic dykes and associated volcanic sequences: evidence from the Harp Swarm and Seal Lake Group, Labrador, Canada. *Precambrian Research* **68**, 357–74.

Cadman, A. C., Ryan, B., Royse, K. & Noble, S. R. 1995a. An investigation of some metamorphosed dykes of the Nain area: Part 3 – Geochemistry and structural relationships of dykes in the Nukasusutok Island area. *In Current Research, Newfoundland Department of Mines and Energy, Geological Survey Branch Report* **95-1**, 1–14. St. John's, Newfoundland: Newfoundland Department of Mines and Energy.

Cadman, A. C., Tarney, J. & Baragar, W. R. A. 1995b. Nature of mantle source contributions and the role of contamination and *in situ* crystallisation in the petrogenesis of Proterozoic mafic dykes and flood basalts Labrador. *Contributions to Mineralogy and Petrology* **122**, 213–29.

Chardon, D., Choukroune, P. & Jayananda, M. 1996. Strain patterns, decollement and incipient sagducted greenstone terrains in the Archaean Dharwar craton (South India). *Journal of Structural Geology* **18**, 991–1004.

Collins, W. J., Van Kranendonk, M. J. & Teyssier, C. 1998. Partial convective overturn of Archaean crust in the east Pilbara Craton, Western Australia: driving mechanisms and tectonic implications. *Journal of Structural Geology* **20**, 1405–24.

Corrigan, D. & Hanmer, S. 1997. Anorthosites and related granitoids in the Grenville orogen: A product of convective thinning of the lithosphere? *Geology* **25**, 61–4.

Corriveau, L., Perreault, S. & Davidson, A. 2007. Prospective metallogenic settings of the Grenville Province. *In* Goodfellow, W. D. (ed.) *Mineral Deposits of Canada: A Synthesis of Major Deposit-types, District Metallogeny, the Evolution of Geological Provinces, and Exploration Methods. Geological Association of Canada, Special Publication* **5**, 819–48.

Culshaw, N., Ketchum, J. & Barr, S. 2000. Structural evolution of the Makkovik Province, Labrador, Canada: tectonic processes during 200 Myr at a Paleoproterozoic active margin. *Tectonics* **19**, 961–77.

Davidson, A. 1998. Geological map of the Grenville Province, Canada and adjacent parts of the United States of America. *Geological Survey of Canada Map* **1947A**, scale 1:2,000,000.

Davidson, A. 2008. Late Paleoproterozoic to mid-Neoproterozoic history of northern Laurentia: An overview of central Rodinia. *Precambrian Research* **160**, 5–22.

Demaiffe, D., Weis, D., Michot, J. & Duchesne, J.-C. 1986. Isotopic constraints on the genesis of the Rogaland anorthositic suite (southwest Norway). *Chemical Geology* **57**, 167–79.

Dempster, T. J., Preston, R. J. & Bell, B. R. 1999. The origin of Proterozoic massif-type anorthosites: evidence from interactions between crustal xenoliths and basaltic magma. *Journal of the Geological Society, London* **156**, 41–6.

Dickin, A. P. & McNutt, R. H. 2007. The Central Metasedimentary Belt (Grenville Province) as a failed back-arc rift zone: Nd isotope evidence. *Earth and Planetary Science Letters* **259**, 97–106.

Duchesne, J.-C. 1984. Massif anorthosites: another partisan review. *In* Brown, W. L. (ed.) *Feldspar and Feldspathoids. NATO Advanced Study Institute Series* **C137**, 411–33. Dordrecht: Kluwer Academic.

Duchesne, J.-C. 1990. Origin and evolution of monzonorites related to anorthosites. *Schweizerische Mineralogische und Petrographische Mitteilungen Bulletin* **70**, 189–98.

Duchesne, J.-C., Wilmart, E., Demaiffe, D. & Hertogen, J. 1989. Monzonorites from Rogaland (southwest Norway): a series of rocks coeval but not comagmatic with massif-type anorthosites. *Precambrian Research* **45**, 111–28.

Duchesne, J.-C., Liégeois, J. P., Van der Auwera, J. & Longhi, J. 1999. The crustal tongue melting model and the origin of massif anorthosites. *Terra Nova* **11**, 100–5.

Dymek, R. F. & Owens, B. E. 2001. Petrogenesis of apatite-rich rocks (Nelsonites and oxide-apatite gabbronorites) associated with massif anorthosites. *Economic Geology* **96**, 797–815.

Emslie, R. F. 1978. Anorthosite massifs, rapakivi granites and late Proterozoic rifting of North America. *Precambrian Research* **7**, 61–98.

Emslie, R. F. 1980. Geology and petrology of the Harp Lake Complex, Central Labrador: An example of Elsonian magmatism. *Geological Survey of Canada Bulletin* **293**, 236 pp.

Emslie, R. F. 1985. Proterozoic anorthosite massifs. *In* Tobi, A. C. & Touret, J. R. L. (eds) *The Deep Crust in the North Atlantic Provinces. NATO Advanced Study Institute Series* **C158**, 39–60. Dordrecht: D. Reidel.

Emslie, R. F. 1991. Granitoids of rapakivi granite-anorthosite and related associations. *Precambrian Research* **51**, 173–92.

Emslie, R. F., Hamilton, M. A. & Thériault, R. J. 1994. Petrogenesis of a Mid-Proterozoic anorthosite–mangerite–charnockite–granite (AMCG) complex: Isotopic and chemical evidence from the Nain plutonic suite. *Journal of Geology* **102**, 539–58.

Emslie, R. F., Hamilton, M. A. & Gower, C. F. 1997. The Michael Gabbro and other Mesoproterozoic lithospheric probes in southern and central Labrador. *Canadian Journal of Earth Sciences* **34**, 1566–80.

Emslie, R. F. & Hegner, E. 1993. Reconnaissance isotopic geochemistry of anorthosite–mangerite–charnockite–granite (AMCG) complexes, Grenville Province, Canada. *Chemical Geology* **106**, 279–98.

Emslie, R. F. & Hunt, P. A. 1990. Ages and petrogenetic significance of igneous mangerite–charnockite suites associated with massif anorthosites, Grenville Province. *Journal of Geology* **98**, 213–31.

Francis, D., Scowen, P., Panneton, G. & Doig, R. 2000. Contrasting Si-saturation in troctolite–anorthosite intrusions along the Manicouagan corridor of the Abitibi–Grenville transect. *Canadian Journal of Earth Sciences* **37**, 271–89.

Frith, R. A. & Currie, K. L. 1976. A model for the origin of the Lac St. Jean anorthosite massif. *Canadian Journal of Earth Sciences* **13**, 389–99.

Gobeil, A. Hébert, C., Clark, T., Beaumier, M. & Perreault, S. 2002. Géologie de la région du Lac De La Blache (22K03 et 22K04). *Ministère des Ressources Naturelles du Québec, RG* **2002-01**.

Gower, C. F. & Krogh, T. E. 2002. A U–Pb geochronological review of the Proterozoic history of the eastern Grenville Province. *Canadian Journal of Earth Sciences* **39**, 795–829.

Greene, A. R., DeBari, S. M., Kelemen, P. B., Blusztajn, J. & Clift, P. D. 2006. A detailed geochemical study of island arc crust: the Talkeetna Arc section, south-central Alaska. *Journal of Petrology* **47**, 1051–93.

Hanmer, S., Corrigan, D., Pehrsson, S. & Nadeau, L. 2000. SW Grenville Province, Canada: the case against post-1·4 Ga accretionary tectonics. *Tectonophysics* **319**, 33–51.

Hart, S. R. & Davis, K. E. 1978. Nickel partitioning between olivine and silicate melt. *Earth and Planetary Science Letters* **40**, 203–19.

Hébert, C., Cadieux, A. M. & van Breemen, O. 2005. Temporal evolution and nature of Ti–Fe–P mineralization in the anorthosite–mangerite–charnockite–granite (AMCG) suites of the south-central Grenville Province, Saguenay–Lac St. Jean area, Québec, Canada. *Canadian Journal of Earth Sciences* **42**, 1865–80.

Hébert, C., Cadieux, A. M. & van Breemen, O. 2009. Région du réservoir Pipmuacan (SNRC 22E): Synthèse géologique. *Ministère des Ressources Naturelles et de la Faune, Québec. Report* **RG-2009-01** + 1/250,000 scale map.

Hébert, C. & van Breemen, O. 2004a. Mesoproterozoic basement, the Lac St. Jean anorthosite suite and younger Grenvillian intrusions in the Saguenay region (Quebec): structural relationships and U–Pb geochronology. *In* Tollo, R. P., Corriveau, L., McLelland, J. & Bartholomew, M. (eds) *Proterozoic tectonic evolution of the Grenville orogen in North America. Geological Society of America Memoir* **197**, 65–79.

Hébert, C. & van Breemen, O. 2004b. Redefinition of the Lac St. Jean anorthosite, central Grenville Province, Québec, based on compositional, structural, geochronological, and mineral deposit features. *American Geophysical Union meeting*, Montréal. Abstract V53A-03.

Higgins, M. D., Ider, M. & van Breemen, O. 2002. U–Pb ages of plutonism, wollastonite formation, and deformation in the central part of the Lac-Saint-Jean anorthosite suite. *Canadian Journal of Earth Sciences* **39**, 1093–105.

Hoffman, P. F. 1989. Speculations on Laurentia's first gigayear (2·0 to 1·0 Ga). *Geology* **17**, 135–8.

Icenhower, J. P., Dymek, R. F. & Weaver, B. L. 1998. Evidence for an enriched mantle source for jotunite (orthopyroxene monzodiorite) associated with the St. Urbain anorthosite, Québec. *Lithos* **42**, 191–212.

Jagoutz, O., Müntener, O., Ulmer, P., Pettke, T., Burg, J. P., Dawood, H. & Hussain, S. 2007. Petrology and Mineral Chemistry of Lower Crustal Intrusions: the Chilas Complex, Kohistan (NW Pakistan). *Journal of Petrology* **48**, 1895–953.

Jochum, K. P., Hofmann, A. W., Ito, E. Seufert, H. M. & White, W. M. 1983. K, U and Th in mid-ocean ridge basalt glasses and heat production, K/U and K/Rb in the mantle. *Nature* **306**, 431–6.

James, D. T., Kamo, S. & Krogh, T. 2000. Preliminary U–Pb geochronological data from the Mealy Mountains terrane, Grenville Province, Southern Labrador. *In Current Research 2000. Newfoundland Department of Mines and Energy Geological Survey, Report* **2000-1**, 169–78. St John's, Newfoundland: Newfoundland Department of Mines and Energy.

Kamo, S. L., Wasteneys, H., Gower, C. F. & Krogh, T. E. 1996. U–Pb geochronology of Labradorian and later events in the Grenville Province, eastern Labrador. *Precambrian Research* **80**, 239–60.

Ketchum, J. W. F., Culshaw, N. G. & Barr, S. M. 2002. Anatomy and orogenic history of a Paleoproterozoic accretionary belt: the Makkovik Province, Labrador, Canada. *Canadian Journal of Earth Sciences* **39**, 711–30.

Kramers, J. D., Kreissig, K. & Jones, M. Q. W. 2001. Crustal heat production and style of metamorphism: a comparison between two Archean high grade provinces in the Limpopo Belt, southern Africa. *Precambrian Research* **112**, 149–63.

Li, C. S., Lightfoot, P. C., Amelin, Y. & Naldrett, A. J. 2000. Contrasting petrological and geochemical relationships in the Voisey's Bay and Mushuau intrusions, Labrador, Canada. Implications for ore genesis. *Economic Geology* **95**, 771–99.

Longhi, J., Fram, M. S., Van der Auwera, J. & Montieth, J. N. 1993. Pressure effects, kinetics, and rheology of anorthositic and related magmas. *American Mineralogist* **78**, 1016–30.

Longhi, J., Van der Auwera, J., Fram, M. S. & Duchesne, J.-C. 1999. Some phase equilibrium constraints on the origin of Proterozoic (Massif) anorthosites and related rocks. *Journal of Petrology* **40**, 339–62.

Markl, G. & Frost, B. R. 1999. The origin of anorthosites and related rocks from the Lofoten Islands, northern Norway: II. Calculation of parental liquid compositions for anorthosites. *Journal of Petrology* **40**, 61–77.

Martignole, J. 1996. Tectonic setting of anorthositic complexes of the Grenville Province, Canada. *In* Demaiffe, D. (ed.) *Petrology and Geochemistry of magmatic suites of rocks in the continental and oceanic crusts*, 3–18. A volume dedicated to Professor Jean Michot, Université Libre de Bruxelles. Tervuren, Belgium: Royal Museum for Central Africa.

Martignole, J., Machado, N. & Nantel, S. 1993. Timing of intrusion and deformation of the Rivière-Pentecôte anorthosite (Grenville Province). *Journal of Geology* **101**, 652–8.

Martignole, J. & Schrijver, K. 1970. Tectonic setting and evolution of the Morin anorthosite, Grenville Province, Quebec. *Geological Society of Finland Bulletin* **42**, 165–209.

McLelland, J., Daly, J. S. & McLelland, J. M. 1996. The Grenville orogenic cycle (ca. 1350–1000 Ma): An Adirondack perspective. *Tectonophysics* **265**, 1–28.

Michot, P. 1965. Le magma plagioclasique. *Geologische Rundschau* **55**, 956–76.

Mitchell, J. N., Scoates, J. S. & Frost, C. D. 1995. High-Al gabbros in the Laramie anorthosite complex, Wyoming: Implications for the composition of melts parental to Proterozoic anorthosite. *Contributions to Mineralogy and Petrology* **119**, 166–80.

Mitchell, J. N., Scoates, J. S., Frost, C. D. & Kolker, A. 1996. The geochemical evolution of anorthosite residual magmas in the Laramie Anorthosite Complex, Wyoming. *Journal of Petrology* **37**, 637–60.

Morse, S. A. 1969. Layered intrusions and anorthosite genesis. *In* Isachsen, Y. W. (ed.) *Origin of Anorthosite and Related Rocks. New York State Museum Science Service Memoir* **18**, 175–87.

Morse, S. A. 1975. Plagioclase lamellae in hypersthene, Tikkoatokah Bay, Labrador. *Earth and Planetary Science Letters* **26**, 331–6.

Morse, S. A. 1982. A partisan review of Proterozoic anorthosites. *American Mineralogist* **67**, 1087–100.

Morse, S. A., Olson, K. E. & Hamilton, M. A. 1988. Massif anorthosite as a key to Proterozoic megatectonics. *Geological Association of Canada Program with Abstracts* **13**, 87.

Nantel, S. & Martignole, J. 1991. Le complexe anorthositique de Rivière-Pentecôte (Côte-Nord). *Ministère de l'Énergie et des Ressources, Québec Report* **MM89–02**, 83 pp.

Olson, K. E. 1992. The petrology and geochemistry of mafic igneous rocks in the anorthosite-bearing Adirondack Highlands, New York. *Journal of Petrology* **33**, 471–502.

Olson, K. E. & Morse, S. A. 1990. Regional Al–Fe mafic magmas associated with anorthosite-bearing terranes. *Nature* **344**, 760–2.

Owens, B. E., Dymek, R. F., Tucker, R., Brannon, J. C. & Podosek, F. A. 1984. Age and radiogenic isotopic composition of a late- to post-tectonic anorthosite in the Grenville Province: the Labrieville Massif, Quebec. *Lithos* **31**, 189–206.

Owens, B. E. & Dymek, R. F. 1992. Fe–Ti–P-rich rocks and massif anorthosite: Problems of interpretation illustrated from the Labrieville and St-Urbain Plutons, Quebec. *Canadian Mineralogist* **30**, 163–90.

Owens, B. E. & Dymek, R. F. 2001. Petrogenesis of the Labrieville alkalic anorthosite massif, Grenville Province, Quebec. *Journal of Petrology* **42**, 1519–46.

Owens, B. E. & Dymek, R. F. 2005. Rediscovery of the Mattawa Anorthosite Massif, Grenville Province, Quebec. *Canadian Journal of Earth Sciences* **42**, 1699–718.

Owens, B. E. & Tomascak, P. B. 2002. Mesoproterozoic lamprophyres in the Labrieville Massif, Quebec: clues to the origin of alkalic anorthosites? *Canadian Journal of Earth Sciences* **39**, 983–97.

Pearce, J. A. & Parkinson, I. J. 1993. Trace element models for mantle melting: Application to volcanic arc petrogenesis: *In* Prichard, H. M., Alabaster, T., Harris, N. B.W. & Neary, C. R. (eds) *Magmatic Processes and Plate Tectonics. Geological Society, London, Special Publication* **76**, 373–403. Bath, UK: The Geological Society Publishing House.

Peck, W. H., Valley, J. W., Corriveau, L., Davidson, A., McLelland, J. & Farber, D. A. 2004. Oxygen-isotope constraints on terrane boundaries and origin of 1·18–1·13 Ga granitoids in the southern Grenville province. *In* Tollo, R. P., Corriveau, L., McLelland, J. & Bartholomew, M. J. (eds) *Proterozoic tectonic evolution of the Grenville Orogen in North America. Geological Society of America Memoir* **197**, 163–82. Boulder, Colorado and Lawrence, Kansas: Geological Society of America and University of Kansas Press.

Peck, W. H. & Valley, J. W. 2000. Large crustal input to high $\delta^{18}O$ anorthosite massifs of the southern Grenville Province: new evidence from the Morin Complex, Quebec. *Contributions to Mineralogy and Petrology* **139**, 402–17.

Percival, J. A., Sanborn-Barrie, M., Skulski, T., Stott, G. M., Helmstaedt, H. & White, D. J. 2006. Tectonic evolution of the western superior province from NATMAP and lithoprobe studies. *Canadian Journal of Earth Sciences* **43**, 1085–117.

Philpotts, A. R. 1976. Silicate liquid immiscibility: its probable extent and petrogenetic significance. *American Journal of Science* **276**, 1147–77.

Philpotts, A. R. 1969. Parental magma of the anorthosite–mangerite suite. *In* Isachsen, Y. W. (ed.) *Origin of Anorthosite and Related Rocks. New York State Museum Science Service Memoir* **18**, 207–12.

Philpotts, A. R. 1966. Origin of anorthosite-mangerite rocks of southern Quebec. *Journal of Petrology* **7**, 1–64.

Rivers, T, 1997. Lithotectonic elements of the Grenville Province: review and tectonic implications. *Precambrian Research* **86**, 117–54.

Rivers, T. & Corrigan, D. 2000. Convergent margin on southeastern Laurentia during the Mesoproterozoic: tectonic implications. *Canadian Journal of Earth Sciences* **37**, 359–83.

Royce, K. R. & Park, R. G. 2000. Emplacement of the Nain anorthosite: diapiric versus conduit ascent. *Canadian Journal of Earth Sciences* **37**, 1195–207.

Sandiford, M. 1989. Horizontal structures in granulite terrains: A record of mountain building or mountain collapse? *Geology* **17**, 449–52.

Schärer, U., Wilmart, E. & Duchesne, J.-C. 1996. The short duration and anorogenic character of anorthosite magmatism: U–Pb dating of the Rogaland complex, Norway. *Earth and Planetary Science Letters* **139**, 335–50.

Schiellerup, H., Lambert, R. D., Prestvik, T., Robins, B., McBride, J. & Larsen, R. B. 2000. Re–Os isotopic evidence for a lower crustal origin of massif-type anorthosites. *Nature* **405**, 781–4.

Schulz, K. J. & Cannon, W. F. 2007. The Penokean Orogeny in the Lake Superior region. *Precambrian Research* **157**, 4–25.

Scoates, J. S. & Chamberlain, K. R. 1997. Orogenic to post-orogenic origin for the 1·76 Ga Horse Creek anorthosite complex, Wyoming, USA. *Journal of Geology* **105**, 331–43.

Scoates, J. S. & Frost, C. D. 1996. A strontium and neodymium isotopic investigation of the Laramie anorthosites, Wyoming, USA: Implications for magma chamber processes and the evolution of magma conduits in Proterozoic anorthosites. *Geochimica et Cosmochimica Acta* **60**, 95–107.

Selbekk, R. S., Skjerlie, K. P. & Pedersen, R. B. 2000. Generation of anorthositic magma by H_2O-fluxed anatexis of silica-undersaturated gabbro: an example from the north Norwegian Caledonides. *Geological Magazine* **137**, 609–21.

Simmons, E. C. & Hanson, G. N. 1978. Geochemistry and origin of massif-type anorthosites. *Contributions to Mineralogy and Petrology* **66**, 119–35.

Smithies, R. H., Van Kranendonk, M. J. & Champion, D. C. 2007. The Mesoarchean emergence of modern-style subduction. *Gondwana Research* **11**, 50–68.

Stern, R. J. 2005. Evidence from ophiolites, blueschists, and ultrahigh-pressure metamorphic terranes that the modern episode of subduction tectonics began in Neoproterozoic time. *Geology* **33**, 557–60.

Sun, S.-S. & McDonough, W. F. 1989. Chemical and isotopic systematics of oceanic basalts: implications for mantle compositions and processes. *In* Saunders, A. D. & Norry, M. J. (eds) *Magmatism in the Ocean Basins. Geological Society, London, Special Publication* **42**, 313–45. Bath, UK: The Geological Society Publishing House.

Taylor, S. R., Campbell, I. H., McCulloch, M. T. & McLennan, S. M. 1984. A lower crustal origin for massif-type anorthosites. *Nature* **311**, 372–5.

van Breemen, O. & Higgins, M. D. 1993. U–Pb zircon age of the southwest lobe of the Havre–Saint Pierre anorthosite complex, Grenville Province, Canada. *Canadian Journal of Earth Sciences* **30**, 1453–7.

van der Auwera, J., Longhi, J. & Duchesne, J.-C. 1998. A liquid line of descent of the jotunite (Hypersthene monzodiorite) suite. *Journal of Petrology* **39**, 439–68.

Veksler, I. V., Dorfman, A. M., Borisov, A. A., Wirth, R. & Dingwell D. B. 2007. Liquid immiscibility and the evolution of basaltic magma. *Journal of Petrology* **48**, 2187–210.

Vigneresse, J. L. 2005. The specific case of the Mid-Proterozoic rapakivi granites and associated suite within the context of the Columbia supercontinent. *Precambrian Research* **137**, 1–34.

Wiebe, R. A. 1988. Structural and magmatic evolution of a magma chamber: The Newark Island Layered Intrusion, Nain, Labrador. *Journal of Petrology* **29**, 383–411.

Wiebe, R. A. 1990a. Dioritic rocks in the Nain Complex, Labrador. *Schweizerische Mineralogische und Petrographische Mitteilungen Bulletin* **70**, 199–208.

Wiebe, R. A. 1990b. Evidence for unusually feldspathic liquids in the Nain Complex, Labrador. *American Mineralogist* **75**, 1–12.

Wiebe, R. A. 1992. Proterozoic anorthosite complexes. *In* Condie, K. C. (ed.) *Proterozoic Crustal Evolution*, 215–61. Amsterdam: Elsevier.

Woussen, G., Dimroth, E., Corriveau, L. & Archer, P. 1981. Crystallization and emplacement of the Lac St-Jean anorthosite massif (Quebec, Canada). *Contributions to Mineralogy and Petrology* **76**, 343–50.

Yale, L. B. & Carpenter, S. J. 1998. Large igneous provinces and giant dike swarms: proxies for supercontinent cyclicity and mantle convection. *Earth and Planetary Science Letters* **163**, 109–22.

MS received 18 December 2007. Accepted for publication 22 July 2008 (Stellenbosch); 15 January 2009 (RSE).

Granite formation: Stepwise accumulation of melt or connected networks?

Paul D. Bons[1], Jens K. Becker[1], Marlina A. Elburg[2] and Kristjan Urtson[3]

[1] Mineralogy and Geodynamics, Institute for Geosciences, Eberhard Karls University Tübingen, Wilhelmstr. 56, 72074 Tübingen, Germany
Email: paul.bons@uni-tuebingen.de; becker@jkbecker.de

[2] Department of Geology and Soil Science, Ghent University, Krijgslaan 281 S8, 9000 Ghent, Belgium
Email: Marlina.Elburg@UGent.be

[3] Institute of Geology, Tallinn University of Technology, Ehitajate tee 5, 19086 Tallinn, Estonia
Email: urtson@gi.ee

ABSTRACT: Several authors have proposed that granitic melt accumulation and transport from the source region occurs in networks of connected melt-filled veins and dykes. These models envisage the smallest leucosomes as 'rivulets' that connect to feed larger dykes that form the 'rivers' through which magma ascends through the sub-solidus crust. This paper critically reviews this 'rivulets-feeding-rivers' model. It is argued that such melt-filled networks are unlikely to develop in nature, because melt flows and accumulates well before a fully connected network can be established. In the alternative stepwise accumulation model, flow and accumulation is transient in both space and time. Observations on migmatites at Port Navalo, France, that were used to support the existence of melt-filled networks are discussed and reinterpreted. In this interpretation, the structures in these migmatites are consistent with the collapse and draining of individual melt batches, supporting the stepwise accumulation model.

KEY WORDS: leucosomes, melt accumulation, melt networks, migmatite, Port Navalo, stepwise accumulation

The transport of crustally-derived magma, from mid/lower-crustal source rocks to (commonly) upper crustal emplacement levels, is one of the most important mass and heat transfer processes in the crust. The whole process, from initial melt formation, segregation, accumulation, to emplacement, spans an enormous range of length scales: about nine orders of magnitude from ~10 μm initial melt pockets to ~10 km-scale plutons. The volume concentration factor is a staggering 10^{27}. This large range in scales hampers the study of the complete process. One approach is to regard the whole process as a chain of distinct sub-processes, each operating on a typical length scale. This approach would separate the initial melt segregation into veins as one step, followed by accumulation of the melt in larger volumes, and then by ascent of the magma, typically in dykes, which finally leads to emplacement.

Research over the past decades has had a tendency to investigate these four steps separately, possibly because their typical length scales necessitate different research methods. The smallest scale is amenable to laboratory experiments (Rutter & Neumann 1995; Holtzman *et al.* 2003a, b; Walte *et al.* 2005; etc.), whereas the next step is best studied in the field in migmatite terrains (e.g. Allibone & Norris 1992; Marchildon & Brown 2003; Sawyer 1996). As active dykes are difficult to study in the field, they have been mostly subject to geophysical modelling (e.g. Emerman & Marrett 1990; Rubin 1995a; Mériaux *et al.* 1999; etc.). Pluton emplacement, finally, is again mostly studied in the field (e.g. Zorpi *et al.* 1989; Paterson & Fowler 1993; Koukouvelas & Kokkolas 2003). The fact that different research communities addressed different steps in the process has left transitions from one step to another relatively neglected.

Another approach is to consider a single mechanism that covers the whole range from initial melt segregation to final emplacement. Several mechanisms have been proposed: diapirism (e.g. Weinberg & Podladchikov 1994; Paterson & Vernon 1995), porous flow (e.g. Jackson *et al.* 2003), fracture networks/dykes (e.g. Weinberg & Searle 1998; Nicolas & Jackson 1982; Weinberg 1999; Olson *et al.* 2004) and step-wise accumulation (e.g. Maaløe 1987; Bons & van Milligen 2001; Bons *et al.* 2001a, b, 2004). Diapirism mostly 'avoids' the problem of segregation and accumulation by envisaging wholesale mobilisation of partially molten rock. However, most workers nowadays regard diapirism as a non-viable mechanism for crustal pluton formation (Clemens & Mawer 1992; Vigneresse 2004).

Most modelling of dykes has not considered the question of how the dykes are supplied with magma, as it is normally assumed that there is either a constant magma pressure or flux at the base (Emerman *et al.* 1986; Spence *et al.* 1987; Rubin 1995a; Mériaux & Jaupart 1998). Weinberg (1999) has been among the few authors to address this question. He and others proposed the formation of fracture networks where small fractures feed larger ones. This 'rivulets-feeding-rivers' or 'rooted vein network' model has been applied to both the mantle (Nicolas 1986; Hart 1993; Maaløe 2003) and the crust (Brown & Solar 1998; Petford & Koenders 1998; Weinberg 1999). The concept is appealing in that a single process can span the whole process from large dykes that feed plutons down to the smallest fractures that tap melt from between grains. However, the present paper will discuss several problems with the rivulets-feeding-rivers model. The paper will address field evidence and theoretical problems of the model,

© 2009 The Royal Society of Edinburgh. doi:10.1017/S175569100901603X

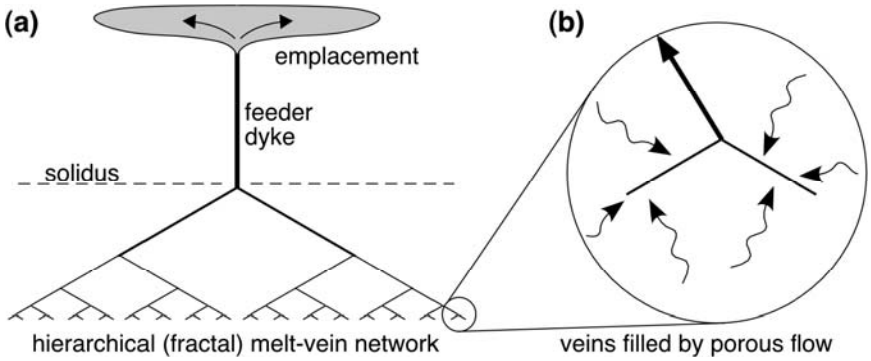

Figure 1 Schematic overview of the transport steps in the RFR model. A developing granite pluton is fed by a feeder dyke, which in turn taps a hierarchical network of melt-filled veins. This network spans the scale range from the feeder dyke down to the smallest veins that are fed by porous flow and/or diffusion with melt from grain boundaries (inset).

and it will be argued that discontinuous connectivity of melt-filled fractures in a stepwise accumulation model is a preferred model. The discussion will be limited to the formation and transport of purely crustally-derived melts, as an end member of granite petrogenesis, even though it is recognised that many granites contain at least some mantle input (Elburg 1996; Soesoo & Nicholls 1999).

The word 'leucosome' will be used for the first stage of melt vein that accumulates although it is recognised that some leucosomes, as found in outcrop, do not represent melt compositions, but cumulates (Sawyer 1987; Ellis & Obata 1992; Brown *et al*. 1999; Solar & Brown 2001; Johannes *et al*. 2003). Furthermore, the term 'melt' will be used for the material inside leucosomes, even though it may contain solid material, such as residue or newly formed crystals.

1. Fracture networks

The rivulets-feeding-rivers (RFR) model can be summed up by citing Weinberg (1999): '*In order to produce a transporting dyke, the source must evolve to a stage of maturity in which an extensive tributary dyke network is capable of maintaining the high flow rates in the transporting dyke*'. In 1994, Brown had already proposed essentially the same model: '*Melt is extracted from the accumulation networks by porous flow down gradients in pressure to ductile opening mode fractures and shear zones, where ascent is buoyancy driven. Extraction occurs at some critical combination of melt fraction and distribution, most probably as the developing accumulation network reaches the percolation threshold*'. Both authors envisaged a connected network of tributary melt-filled fractures that must reach a state of maturity to enable flow to occur from the source towards one or more dykes that transport the magma through the crust. To address the viability of this model, one must consider the following questions:

- Can such a mature, extensive tributary dyke network form?
- Is the model feasible, not only considering length scales, but also time scales?
- What is the field evidence for connecting networks?

These questions will be addressed in the following sections.

1.1. Can extensive melt-filled fracture networks exist?

In the RFR model, the process from melting at grain boundaries to formation of a pluton is generally divided in five steps (e.g. Brown 2004) (Fig. 1):

1. melting of the source rock,
2. transport of melt along grain boundaries towards melt-filled veins (leucosomes),
3. transport of the melt towards a large conduit (feeder dyke),
4. transport of magma across subsolidus crust through the conduit,
5. emplacement of the magma.

Some authors combine steps 3 and 4 into one, effectively regarding the final conduit, or feeder dyke, as the largest melt-filled vein in a single system of connecting veins (e.g. Weinberg 1999; Harris *et al*. 2000; Vigneresse 2004). The time and length scale of step 4 is probably the one constrained best, because transport through the feeder dyke must be fast enough to inhibit freezing of the ascending magma in the subsolidus crust. Critical dyke width and magma ascent rate depend on buoyancy and viscosity of the magma. Estimated minimum dyke widths are in the order of metres and flow rates up to cm/s, meaning that a pluton may be filled in a matter of tens to thousands of years in a single event (Clemens 1998).

For the very efficient dyke transport step to work, enough melt must be able to drain into the base of the feeder dyke (Weinberg 1999). This is envisaged to occur by the formation of a percolating network of melt-filled fractures. This network must be able to support a sufficient flux to keep the magma in the final conduit flowing without freezing and clogging the system. To achieve this, and to provide a link from the smallest veinlets up to the largest dyke, a hierarchical or self-organised network is envisaged (Weinberg 1999; Vanderhaeghe 2001; Brown 2004; Moyen *et al*. 2003; Maaløe 2003) (Fig. 1). Many small veins feed fewer veins that are one order in size larger. These connect to even fewer of the next order up, and so on. This idea is supported by Tanner (1999), who suggested that melt-vein networks have a fractal structure that is similar to a Menger Sponge.

The present paper will not question whether a melt-filled network can feed a feeder dyke (which it can if the decrease in number of higher-order dykes is balanced by their increased width), but whether such a network is actually likely to form in nature. A critical point is that the network must first develop before it can feed a pluton. The first step in forming a pluton is the formation of melt, which is controlled by heat diffusion or decompression rates, depending on the cause of melting. The time scale of melt formation is thus controlled by the duration of tectono-metamorphic events, which is in the order of 1–10 million years. This time scale is much larger than the time needed to fill a pluton (Petford *et al*. 2000 and references therein). One possibility is that the heating events themselves are caused by underplating/intraplating events of hot basaltic magma into the crust, causing a relatively short burst of

melting. Petford & Koenders (1998) suggest a time frame in the order of 10^5 years. If melting is not in such short bursts, magma-extraction events are separated by prolonged periods in which melt is formed, but no melt escapes from the source. In the RFR model, the networks form during these intervals, implying that the networks must be sustainable, without significant flow, for a prolonged period of time.

1.2. The percolation threshold

Several authors have used the concept of a percolation threshold to determine the melt fraction at which melt can flow (see e.g. citation above of Brown 1994; Vigneresse *et al.* 1996; Weinberg 1999; Vigneresse & Burg 2000). In this concept, the percolation threshold (PT) or 'melt escape threshold' (Vigneresse *et al.* 1996) is the fraction of melt at which the melt-filled conduits (pores, veins) link up to form a percolating network, through which melt can flow over large distances (relative to the size of single pores or veins). Percolation thresholds or critical melt fractions of around 10–20% are usually quoted (Vigneresse *et al.* 1996). The actual value of the PT depends on several factors, such as shape and orientation of the conduits. Randomly oriented fractures have the highest chance of intersecting, and hence the lowest PT. However, there is abundant field evidence that melt-filled veins are generally aligned parallel to structures and foliations, or are oriented by the stress field, thus decreasing their chance of intersecting and increasing the PT. Deformation, however, may also aid in creating connectivity and probably lowers the PT.

Some authors assume that there is no flow below the PT or *critical melt percentage* (e.g. Brown 1994; Weinberg 1999; Vigneresse 2007). Other authors make no specific statement on how a percolating network develops, and how much transport takes place during this stage, as their modelling is based on the assumption that the network has developed (Hart 1993; Maaløe 2003). A fully percolating network, of whatever geometry (rooted vein network or other), would develop by the formation of more and more melt-filled veins as the melt fraction increases. Contrary to the statement of Weinberg (1999) that '*the permeability is zero below a critical value*' (the PT), the permeability of the system below the PT is non-zero and increases as more melt produces more melt-filled veins that have an increasing chance of intersecting (Petford & Koenders 1998; Petford *et al.* 2000). This means that melt can start to flow and change the developing network before it reaches the PT. Flow from one vein into another may lead to effective closure of the first vein, thus reducing the number of melt-filled veins and, hence, the permeability. To achieve a fully percolating network, connectivity creation by melting must outpace connectivity reduction by flow.

A rough estimate of the rate of connectivity, and hence permeability destruction can be made by considering a limited cluster of connected veins. One driving force for flow within a limited cluster of connected veins is the buoyancy of the melt. This will drive melt from a lower vein into a vein higher up, to which it is connected. If the slow buoyancy-driven flow can be shown to be efficient enough to inhibit the development of a fully percolating network, there is no need to consider the additional effect of deformation. The rate at which melt would flow from one vein into a second one is limited by the ductile flow of the matrix, which must accommodate the closure of the first and opening of the second vein. A simple geometry of connected fractures may serve to estimate the time-scale of network collapse by ductile flow of the solid matrix.

Consider a volume of rock, with dimensions $2L \times L \times L$, in the source zone. There is a thin horizontal sill at the base of the box, as depicted in Figure 2a. The sill has a horizontal extent

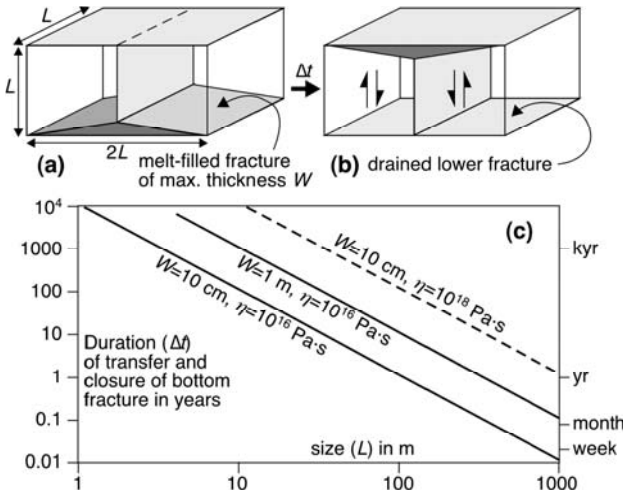

Figure 2 (a) Idealised simple fracture network, consisting of horizontal fractures at the top and bottom of the box that are connected by a vertical fracture. The bottom fracture is filled with melt and has a maximum width W, which is much smaller than the size of the box, defined by L. (b) After time Δt, all melt is transferred to the top fracture and the bottom fracture is closed. Transfer rate is controlled by the shear rate of the solid matrix. (c) Duration (Δt) to transfer all melt from bottom to top fracture as a function of size of the network, for three different combinations of width of the melt-filled fracture (W) and viscosity (η) of the solid matrix. A tall network (tens to hundreds of meters) cannot be maintained for more than a few (hundreds of) years.

of $2L \times L$ and a maximum thickness $W << L$. The sill is connected to another not-yet-filled fracture at the top of the cube. How long will it take for the melt to flow from the bottom to the top (Fig. 2b), thus closing the fracture at the base and destroying connectivity of the network? This question can be answered by equating the potential energy gained by transferring the buoyant melt up by a distance L, and the work done by ductile deformation to close the bottom sill, while opening the top sill.

The potential energy gain (ΔE_p) is the product of the volume of the sill, its density difference ($\Delta\rho$) with the matrix, the height of the cube (L) and the gravitational acceleration (g):

$$\Delta E_p = g\Delta\rho W L^3 \tag{1}$$

For this idealised geometry, the deformation (induced by the flow of the melt) of the matrix can be approximated by simple shear in the solid matrix with a vertical shear plane. The duration (Δt) to full closure of the bottom sill is determined by the simple shear rate simple shear rate $\dot{\gamma}$:

$$\dot{\gamma} = \frac{W}{L\Delta t} \tag{2}$$

The work done (ΔE_τ) to close the bottom sill is a function of the shear rate, the shear stress (τ), the volume of the deforming material and the duration:

$$\Delta E_y = \dot{\gamma}\tau L^3 \Delta t \tag{3}$$

Inserting equation (2) into (3), and relating the strain rate to the shear by the viscosity ($\tau = \eta\dot{\gamma}$) then gives the work done by shearing of the matrix:

$$\Delta E_y = \eta\dot{\gamma}^2 L^3 \Delta t = \frac{\eta W^2 L}{\Delta t} \tag{4}$$

Finally, the time needed to transfer the melt from the bottom sill to the top sill can be found by equating ΔE_p and ΔE_τ, and rearranging:

$$\Delta E_p = \Delta E_\gamma \Leftrightarrow g\Delta\rho WL^3 = \frac{\eta W^2 L}{\Delta t} \Leftrightarrow \Delta t = \frac{\eta W}{g\Delta\rho L^2} \quad (5)$$

Clearly the time needed for the transfer increases with increasing viscosity of the matrix and width of the fracture (amount of melt). The time decreases with increasing buoyancy of the melt ($\Delta\rho$, here taken at 300 kg/m^3) and vertical extent of the connected fractures (L). Considering that the solid matrix is in or close to the source region of magma, it can be regarded as relatively weak. The matrix viscosity is conservatively estimated at $\eta = 10^{16}$–10^{18} Pa·s.

Figure 2c shows that the time to close the local network is in the order of years to hundreds of years for a vertical extent in the order of tens to hundreds of meters. This means that it is difficult to build or maintain a tall network of connected melt-filled fractures over a prolonged period of time (>> thousands of years). One could argue that a fracture cannot fully close because an infinite time is needed to squeeze out a viscous fluid from between two parallel (elastic) plates. However, in nature, especially under the high metamorphic conditions applicable here, ductile flow, dissolution–precipitation processes and dynamic recrystallisation would enable fractures to effectively close.

1.3. Hydraulic fracturing

The fully percolating network invoked by the RFR model would have a large vertical and horizontal extent. The vertical extent would be approximately the height of the partially molten zone, estimated at ≥ 1 km. This implies that, before the PT, developing clusters should reach vertical extents of at least hundreds of metres. Such clusters would not be stable. Weertman (1971) first suggested that vertical fractures that are filled with a buoyant liquid have a maximum vertical extent. Above the critical height, the fracture becomes unstable and starts to propagate upwards (Takada 1990; Secor & Pollard 1975). The critical height depends on several parameters, such as the density difference between melt and matrix and the fracture toughness (or fracture energy: Rubin 1995b). It can be estimated to be about ≥ 100 m (Secor & Pollard 1975), which means that a developing fracture network would become unstable well before it has reached its full vertical extent. Instead, developing clusters would start to propagate upwards, draining the melt from below and destroying connectivity.

2. Stepwise accumulation

A feasible model for the extraction of magma from the source regions in the lower to middle crust must reconcile the relative long duration of melt formation with occasional short 'bursts' of draining and transport of magma to pluton emplacement levels. Field evidence suggests that initial melt tends to drain into melt-filled veins (leucosomes) from the 1–10 cm scale upwards. Veins generally develop parallel to existing foliations (layering, cleavage) and in dilatant sites, such as boudin necks, as has been extensively described by e.g. Brown *et al.* (1995), Brown (2005a), Vanderhaeghe (2001), etc.

There seems to be general consensus that after initial segregation of melt into veins (by porous flow or diffusion), most transport and accumulation takes place through these veins. With increasing number and volume of the veins, transport and accumulation of melt can commence, well below the PT. Vertical flow can be driven by buoyancy of the melt, filling the uppermost veins in a locally connected vein cluster. The buoyancy of the melt may also induce upwards propagation of fractures, but only if a critical length of >100 m is exceeded. However, deformation may induce fracture propagation of much shorter veins, because the normal stress gradients acting on a vein can be much larger (up to about one MPa/m) than those resulting from the density difference between melt and matrix ($\leq$0·003 MPa/m). The effect of these processes is to form ever-larger volumes of melt. These 'batches' are mostly isolated, because any connectivity would lead to melt flow and accumulation. Connectivity is therefore transient, with the duration of local connectivity decreasing with increasing size of the connected system (Fig. 2).

The process of transient flow and accumulation without ever reaching full percolation is illustrated by the highly simplified ('toy') experiment of Bons & van Milligen (2001). In the experiment, yeast is added to loose sand that is saturated with sugar water. Fermentation of the dissolved sugar produces alcohol and CO_2 gas. As the amount of gas increases, horizontal gas-filled hydrofractures appear (Fig. 3). These hydrofractures appear, grow, and then collapse again by draining into other hydrofractures higher up in the tank. There is never a fully percolating network of gas-filled fractures, yet there is an upward flux of gas. Upward flow takes place by short transient events when local connectivity is briefly established, and subsequently destroyed as the gas flows from one hydrofracture to another.

As stated above, the process of stepwise accumulation and ascent (Bons *et al.* 2001b) leads to the formation of ever-larger volumes of melt (or gas in the experiment). This effect is enhanced by the occurrence of transport avalanches, which are also observed in the experiment. The collapse of one hydrofracture may trigger a chain reaction of interactions between other hydrofractures. Such a chain reaction can suddenly drain a large fraction of the gas within the tank. Numerical modelling by Bons *et al.* (2004) showed that power–law size distributions of accumulated volumes result from this process. A power–law distribution of the volumes of gas-filled experimental hydrofractures was also reported by Urtson & Soesoo (2007). Field evidence for power–law size distributions will be discussed below.

3. Field observations

Both the RFR and the stepwise accumulation (SA) models should be testable in the field. Evidence for connecting melt networks is expected for the RFR model, but not for the SA model. The SA model predicts that (1) former melt-filled veins have a power–law size distribution, and (2) structures should be present that represent collapsed former melt volumes. Migmatite outcrops near Port Navalo on the South Brittany coast (France) were chosen to investigate this, because these outcrops have been studied in detail by Brown (1983), Marchildon & Brown (2003) and Johnson & Brown (2004). The reader is referred to these papers for a thorough description of the local geology, which is only briefly recapitulated here.

The study area is located in the Southern Brittany Metamorphic (or Migmatite) Belt (SBMB), which is part of the Variscan Armorican arc. The area was deformed and metamorphosed during the Paleozoic Variscan orogeny, reflecting interaction (subduction, collision and intra-continental deformation, followed by extension and exhumation) between Laurasia and Gondwana (Matte 2001). The area is located to the southwest of the South Armorica shear zone, which separates South from Central Armorica. It is separated from lower-grade rocks to the south by a late-orogenic extensional detachment (Gapais *et al.* 1993). The study area is dominated by metapelites, but amphibolites are present too. Both lithologies display signs of partial melting, but migmatisation is better

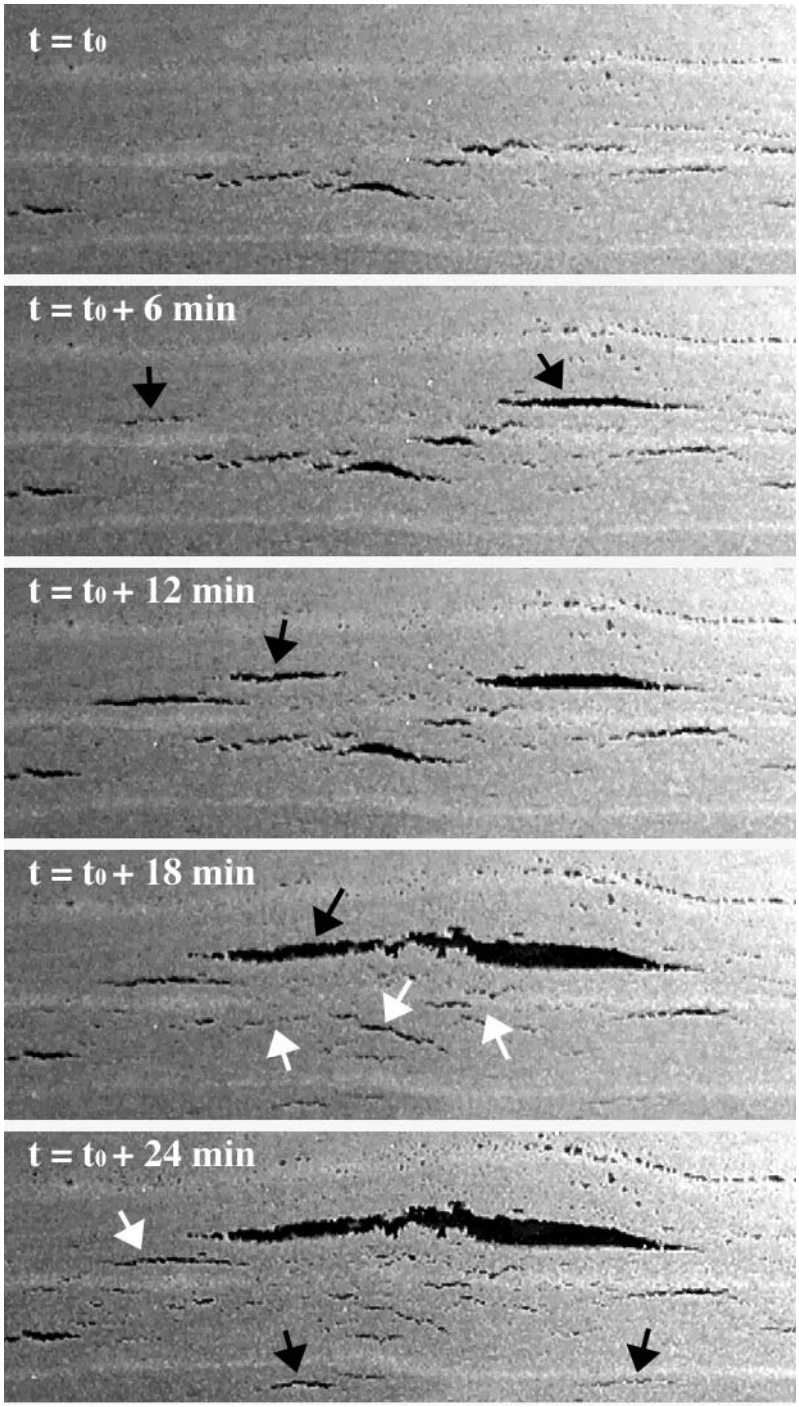

Figure 3 Five stages (six-minute intervals) in an experiment where CO_2 gas is produced by fermentation in sand that is saturated with sugar water (Bons & van Milligen 2001). The buoyant gas props open hydrofractures (black arrows) that subsequently become unstable and drain (white arrows) into other hydrofractures higher up in the system. Full percolation of the gas phase is never reached, yet there is a non-zero upwards flux of gas. First image is after about t_0=2 hours after onset of fermentation. Width of view about 15 cm. See Bons & van Milligen (2001) for a detailed description of the experiment.

developed in the metapelites. Leucosomes and granitic dykes consist of plagioclase, quartz, perthitic K-feldspar, myrmekitic intergrowths and biotite with red-brown to straw-yellow pleochroism. Zircon and apatite occur as minor accessory phases. The melanosomes consist of the same phases plus cordierite or garnet, and contain higher proportions of biotite and accessory phases. Peak metamorphic conditions associated with a first phase of melting have been estimated at 8 kbar and 800°C, whilst a second phase of melting resulted from near-isothermal decompression (at 700°C) to ~4 kbar (Johnson & Brown 2004). Ar–Ar cooling ages for hornblende and muscovite from the area are 303–298 Ma and 306–305 Ma respectively (Brown & Dallmeyer 1996). Three deformation phases have been recognised in the area (Marchildon & Brown 2003).

3.1. Leucosomes and granite dykes

The subhorizontal wave platforms along the coast provide an ideal perpendicular section through the subvertical structures in the stromatic migmatites that contain former melt. There are three types of such structures:

- Leucosomes parallel to bedding and bedding-parallel foliation, together S_{01}, contain most of the former melt (up to

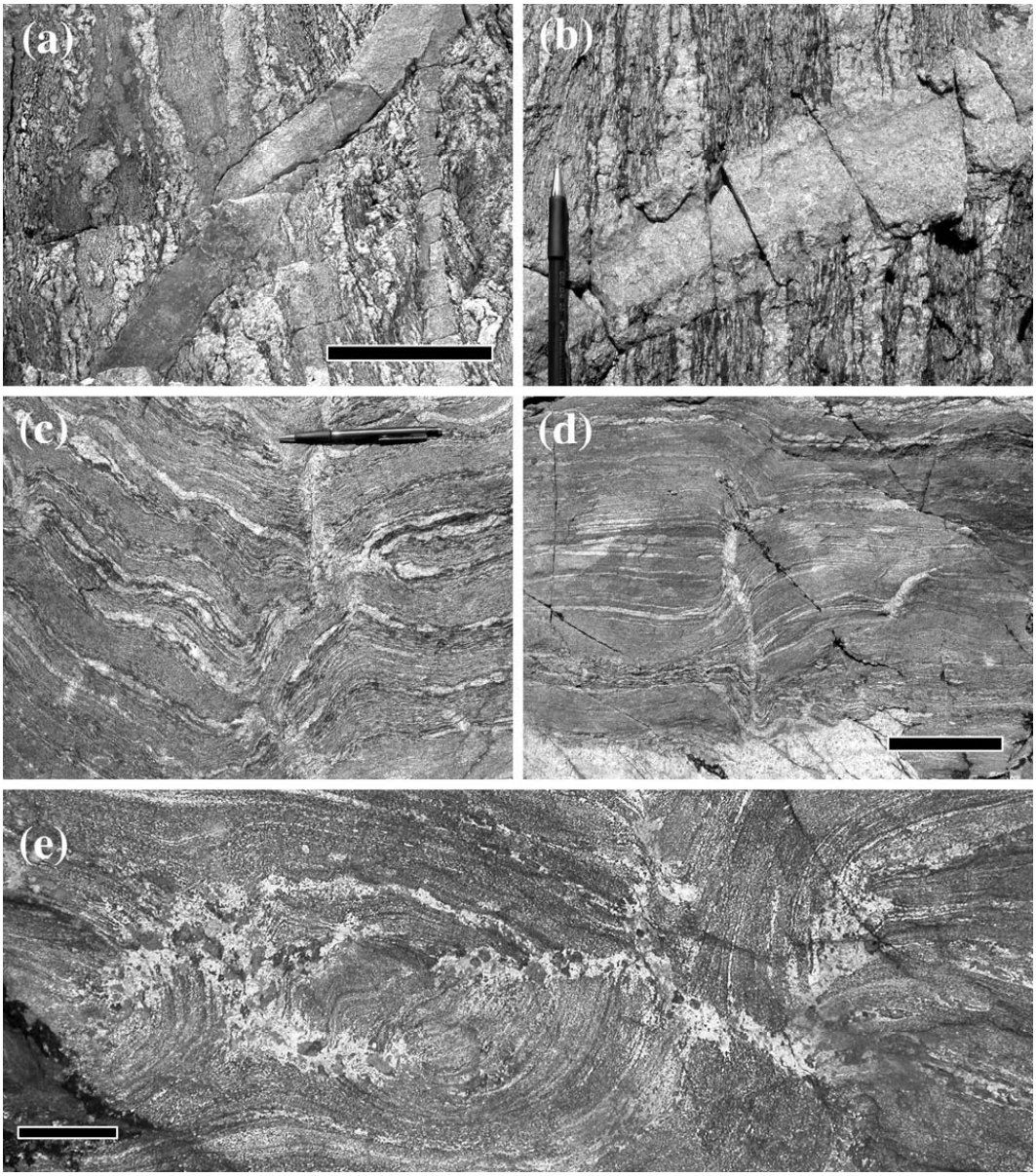

Figure 4 Images from the subhorizontal migmatite outcrops at Port Navalo, France: (a) Coarse-grained, bedding-parallel leucosomes are cut by a younger aplite dyke. There is clear petrographic discontinuity between leucosomes and aplite dyke. Some of the leucosomes on the left show isoclinal folding. Scale bar = 50 cm; (b) Second example of an aplite dyke cutting coarser-grained, bedding-parallel leucosomes, again with a clear petrographic discontinuity; (c) Cross-cutting leucosome in boudin-like structure; (d) Cross-cutting leucosome with dextral shear, displaying both reverse and normal drag folds of the adjacent foliation. Scale bar = 20 cm; (e) Boudin-like structure in amphibolite layer. The strong bending of the layering can only be explained by collapse of a melt volume by melt loss (Brown 2005b). Scale bar = 5 cm.

about 40%). Leucosomes are folded together with the S_{01} foliation. Most folds are open folds, attributed to D_3 (Marchildon & Brown 2003). Isoclinally folded leucosomes with an axial plane parallel to S_{01} can sometimes be observed (Fig. 4a).

- Discordant leucosomes have a similar composition and internal texture as the bedding-parallel leucosomes (Fig. 4c–d). These leucosomes typically form boudin- and shear band-like structures, where the S_{01} foliation is deflected. Boudins show typical fish-mouth structures where the foliation pinches in towards the boudin neck. The foliation bends into shear band-like leucosomes (Fig. 4d), whereby the drag direction can be both normal (synthetic with sense of shear) and reverse (antithetic with respect to sense of shear) (Grasemann & Stüwe 2001; Exner *et al*. 2004).
- Granitic and aplitic dykes cut all the previously mentioned leucosomes (Fig. 4a–b). The dykes have a finer grain size than the leucosomes. The dykes have widths of tens of centimetres to metres, are steeply dipping, but can have variable strikes, which means they sometimes intersect. The dykes are mostly straight and appear not or only little affected by the latest folding. These dykes therefore formed late in the history of the migmatites, and must post-date at least part of the leucosome formation.

Marchildon & Brown (2003) and Brown (2004, 2005a) argue that the dykes and the layer-parallel leucosomes show 'petrographic continuity', implying they both contained the same melt at the same time (e.g. figure 3D in Marchildon & Brown 2003). They also argued that the intersecting dykes show no clear crosscutting relationships (figure 6A in Marchildon & Brown 2003), again suggesting that the intersecting dykes were all filled with melt at the same time. These interpretations lead to a model whereby melt flows from bedding-parallel

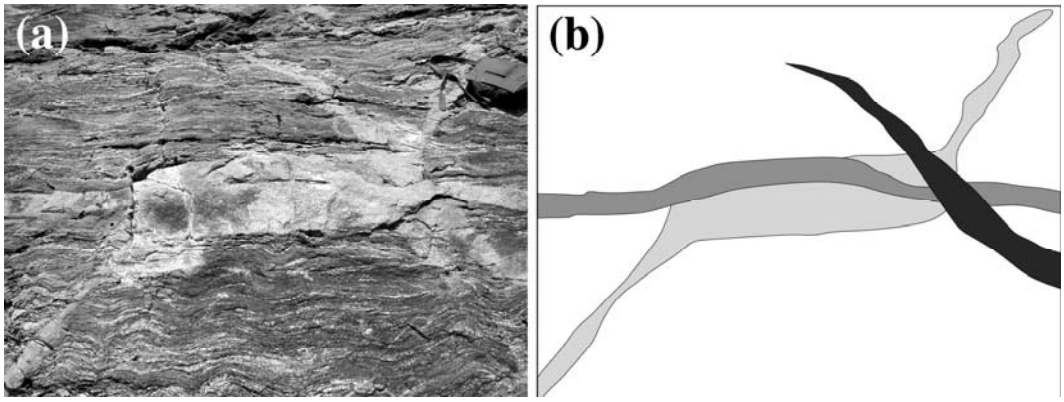

Figure 5 (a) Intersecting granite dykes in subhorizontal outcrop at Port Navalo. Dykes are steeply dipping (same intersection as shown in figure 6A of Marchildon & Brown 2003). Bag for scale in upper-right corner. (b) Close observation shows that the intersection is of three dykes of different generations, each cutting older dykes and the wavy stromatic layering.

leucosomes into dilatant discordant leucosomes (both shear bands and boudin necks), which subsequently feed into a network of dykes. Flow would have been perpendicular to the current horizontal outcrops, focussed in tubular intersections of dykes.

Close observation of the outcrops leads the present authors to disagree with the above interpretation. Dykes do clearly crosscut the leucosomes and show a petrographic discontinuity, with the dykes having a different grain size and colour (Fig. 4a–b). Furthermore, dykes cut isoclinally folded leucosomes, whereas they themselves are not folded (Fig. 4a). It is therefore concluded that the dykes and the leucosomes (both bedding parallel and discordant) belong to different generations and were not filled with melt at the same time. This two-stage melting scenario is supported by the petrological work of Johnson & Brown (2004). The present authors, however, see no indication that the rocks remained molten throughout these two melting events. There is little variation in composition and texture of the dykes, which makes it difficult to distinguish generations where dykes cut each other, as in Figure 5a. Yet, even there, subtle textural differences and the geometry of the dykes show that different generations of dykes intersected each other (Fig. 5b). The straight and sharp boundaries between the different generations indicate that the older dyke was already solidified when cut by a younger one. Therefore, no evidence is seen for a melt-filled network of dykes at the Port Navalo migmatite outcrops.

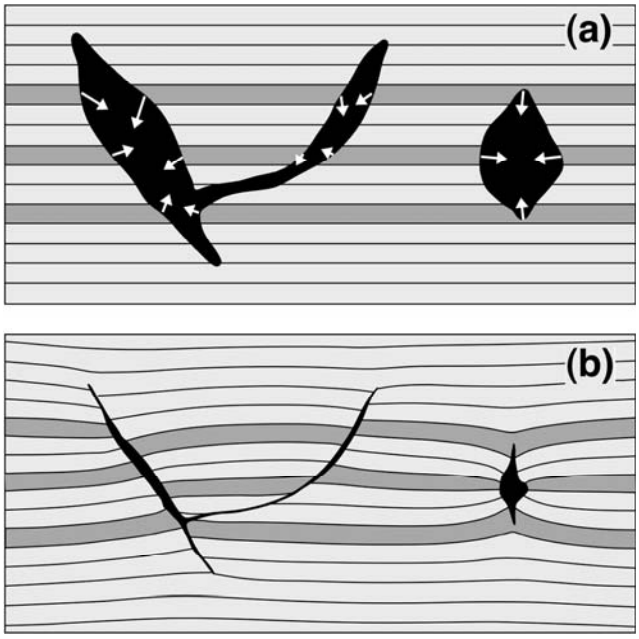

Figure 6 Cartoon showing the formation of boudins and shear bands by removal of melt. (a) Situation before melt loss, where melt is black. White arrows show convergence direction of the wall rock when the melt pockets collapse. (b) Situation after melt removal, showing a typical fish mouth boudin (right) and shear bands with reverse drag folds (left). Notice that there is no bulk extension.

3.2. Interpretation of the discordant leucosomes

Discordant leucosomes, both shear bands and boudin necks, are commonly interpreted as dilational structures (e.g. Hollister & Crawford 1986; Oliver & Barr 1997; Kisters *et al.* 1998; Brown 2004). For boudin necks, this interpretation seems obvious at first sight, as the separation of boudins creates a pressure gradient that could suck in melt (Allibone & Norris 1992). Depending on orientation, shear fractures may also induce pressure gradients that lead the melt to flow towards them (Sleep 1988). The concentration of melt in shear zones is furthermore observed in grain-scale experiments (e.g. Rosenberg & Handy 2001; Holtzmann 2003a, b; Walte *et al.* 2005). Despite the apparent plausibility of the interpretation that the discordant veins represent dilatant structures, the possibility should also be considered that these structures are in fact the opposite: namely contraction structures.

When melt drains from an accumulated volume of melt, the surrounding rocks converge. Figure 6 shows that, depending on the original shape of the melt volume, a variety of structures may form, ranging from shear band-type leucosomes to apparent boudins (Bons 1999; Kriegsman 2001). Shrinkage of equidimensional melt volumes produces boudin-like structures as the surrounding foliation converges from all sides. This produces the typical fish-mouth boudin necks, so commonly observed in migmatites, and which Kriegsman (2001) used to quantify the amount of melt loss. Shrinkage of lenticular veins that are oblique to the foliation produces shear band-like leucosomes, which are typically flanked by reverse drag folds (bending of the foliation opposite to the apparent sense of shear, Grasemann & Stüwe 2001). The deflection of the foliation is, however, normal (synthetic with the apparent offset) at the tips of the collapsing veins. The combination of both reverse and normal drag at the centre and tips of a leucosome, respectively, is commonly observed in migmatites (Fig. 4d). Experiments by Druguet & Carreras (2006) show that deformation enhances this effect. The collapse of irregular melt volumes leads to more complex structures with the remaining melt left in irregular, spider-like leucosomes (Fig. 4e). It is of interest to note that Brown (2005b) actually

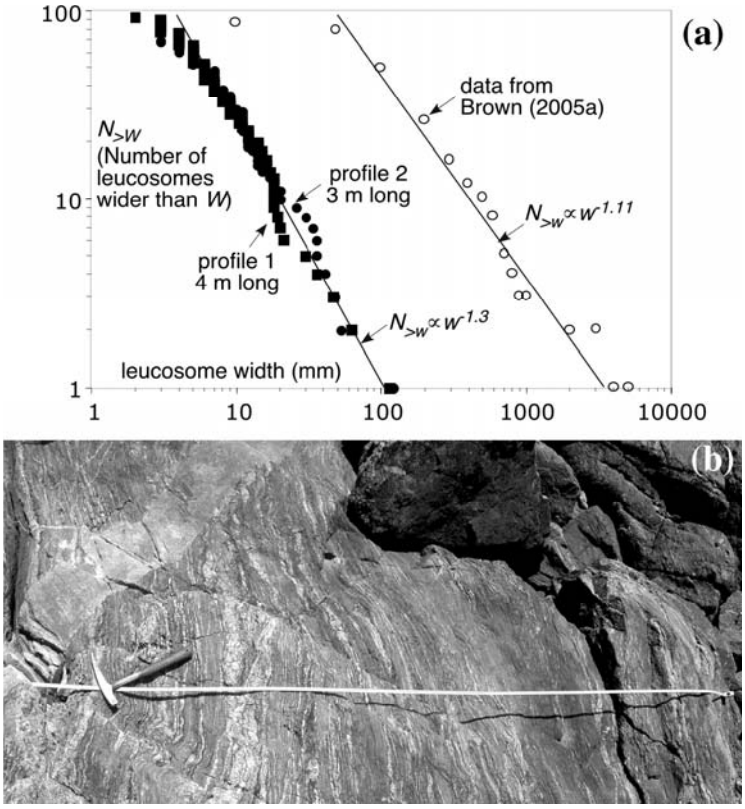

Figure 7 (a) Width distribution of leucosomes in migmatites near Port Navalo in a log–log graph of number ($N_{>W}$) of leucosomes wider than a width W against that width in mm. Our data (filled circles & squares) are from two parallel profiles that were logged perpendicular to the leucosomes. The leucosome fraction was 31%. Leucosomes wider than about 5 mm follow a power–law distribution. Note the similarity in distribution with the data from Brown (2005b), extracted from his figure 8 (open circles). It is however not certain that his measurements are on the same generation dykes as the leucosomes analysed by the present authors. (b) Photograph of the 3 m-long section. Note that the crosscutting aplite dyke was not included in the log.

interpreted this structure as indicating melt loss, but the other discordant veins at the same location as dilatant sites.

Is it possible to distinguish dilatant from collapse structures? There are unambiguous cases, such as is shown in Figure 4e. However, in many other cases both interpretations seem to be permissible. Shearing along a fracture or vein in a ductile matrix leads to the formation of both normal and reverse drag folds by geometric necessity (Gomez-Rivas *et al.* 2007). Similarly, extensional boudinage leads to pinching in of the foliation. These structures as such are therefore not sufficient to distinguish dilation or contraction. What needs to be considered is whether the amount of deflection of layers is consistent with either model. Unfortunately, the formation of collapse structures has not yet been investigated in any detail. The strong deflections for relatively short shear band-type leucosomes (Fig. 4d), as well as the presence of unambiguous collapse structures (Fig. 4e) lead the present authors to favour melt loss and contraction as the origin of these structures. The fact that leucosomes often have a cumulate composition supports the model of melt loss, whereby solid cumulate material would preferentially remain behind (Ellis & Obata 1992; Brown *et al.* 1999; Johannes *et al.* 2003).

3.3. Power–law distributions

Having established that melt-loss structures are found in migmatites, we now turn to the prediction that melt volumes should exhibit power–law volume distributions. In the field it is virtually impossible to measure volume distributions of leucosomes, as one normally only has one-dimensional (drill core) or two-dimensional (surface) outcrops. However, if leucosomes have a power–law volume distribution, they are also expected to have a power–law width distribution. This was indeed observed in migmatites from South Finland (outcrop) and the Estonian basement (drill core) (Bons *et al.* 2004; Soesoo *et al.* 2004). Power–law width distributions were also reported by Kruhl (1994) for a range of scales from small leucosomes to dykes.

A power-law distribution of vein widths can be described by the following equation, where $N_{>W}$ is the number of veins wider than W, and n is an exponent:

$$N_{>W} \propto W^{-n} \tag{6}$$

Brown (2005a) reports a power–law exponent of $n=1{\cdot}11$ for dykes wider than about 10 cm at Port Navalo. Marchildon & Brown (2003) measured width distributions of thinner leucosomes at Port Navalo, and conclude that these do not follow a power law. Their conclusion is, however, based on all recorded leucosomes, down to a width of one mm. Such widths are in the order of the grain size in the rock, which means it is difficult to record them all. This is one of the truncation effects from which this technique invariably suffers, and which are most pronounced at the lower end of the measured spectrum (Bonnet *et al.* 2001). The present authors analysed two profiles (3 m and 4 m long, respectively), in the same migmatites at Port Navalo, and observed a power–law width distribution ($n=1{\cdot}3$) for leucosomes wider than 5 mm (Fig. 7). Both these data (widths 5 mm to ~100 mm) and those of veins/dykes wider than 100 mm of Brown (2005a) each span less than two orders of magnitude, which is a small range to confidently prove a power–law distribution. The fact that both data sets show a power law indicates that the observed power–law distribution extends over a wider range than the individual

analyses. It is, however, unclear whether the veins and dykes in the two data sets are of the same generation.

The observed power–law width distributions are consistent with the model of Bons *et al*. (2004), but should also arise from the fractal-tree or fractal Menger–Sponge models of Tanner (1999), Weinberg (1999) and Maaløe (2003). A power–law distribution should, however, not be equated with a fractal distribution. Whereas the data do show power–law width distributions, the analyses of Marchildon & Brown (2003) show that the melt veins do not have a fractal geometry.

4. Discussion and conclusions

Several arguments have been presented in the present paper that speak against the RFR for melt accumulation. The main argument is that a large-scale percolating network is unlikely to form in partially molten rocks, because (1) melt will start to flow in smaller connected clusters, controlled by ductile flow of the matrix, and (2) melt-filled fractures have a limited stability and can propagate driven by the melt buoyancy or applied stress gradients. Both processes have the effect of destroying connectivity before a percolating network forms. Both processes also lead to accumulation of melt in ever-larger volumes.

The field evidence that has been used to support melt-filled networks has also been considered, focusing on the migmatite outcrops at Port Navalo, subject of studies by Brown and co-workers (Marchildon & Brown 2003; Brown 2004, 2005a). It has been shown that the apparent networks actually consist of different generations of melt-filled veins and dykes. Cross-cutting relationships indicate that previous generations of melt structures had already solidified when intruded by younger generations. The interpretation of discordant leucosomes as dilatant structures that form part of the network must also be reconsidered, as these are more probably contraction structures formed by the escape of melt.

Both the theoretical arguments and the field evidence speak against percolating melt networks in which melt flows from little rivulets (leucosomes) to large rivers, the dykes that feed plutons. Instead, the present authors argue for a stepwise accumulation process, whereby batches of melt interact and accumulate locally (e.g. Maaløe 1987; Bons & van Milligen 2001; Bons *et al*. 2001a, b, 2004). Whereas the whole process of melt accumulation, and finally extraction, may span the entire thermal phase, individual accumulation events take place on a much shorter time scale. This model is consistent with the observed collapse structures found in the field, which represent sites where batches of melt once resided, but which have now moved elsewhere. The power–law distributions of leucosome widths, observed in several migmatite terrains, is also consistent with a stepwise accumulation of melt batches (Bons *et al*. 2004).

5. Acknowledgements

This project was partly funded by a German Research Foundation grant to Bons and Becker (DFG-project BO1776/4). Urtson acknowledges travel support by the German DAAD. We are grateful to Mike Brown for introducing us to the migmatite outcrops at Port Navalo. The manuscript benefited from constructive reviews by Mike Brown and Nick Petford, and editorial handling by John Clemens.

6. References

Allibone, A. H. & Norris, R. J. 1992. Segregation of leucogranite microplutons during syn-anatectic deformation: an example from the Taylor valley, Antarctica. *Journal of Metamorphic Geology* **10**, 589–600.

Bonnet, E., Bour, O., Odling, N. E., Davy, P., Main, I., Cowie, P. & Berkowitz, B. 2001. Scaling of fracture systems in geological media. *Reviews of Geophysics* **39**, 347–83.

Bons, P. D. 1999. Apparent extensional structures due to volume loss. *Proceedings of the Estonian Academy of Sciences, Geology* **48**, 3–14.

Bons, P. D., Dougherty-Page, J. & Elburg, M. A. 2001a. Analogue modelling of segregation and ascent of magma (*on-line*). *Journal of the Virtual Explorer* **3**: Animations in Geology – visualising the Earth.

Bons, P. D., Dougherty-Page, J. & Elburg, M. A. 2001b. Stepwise accumulation and ascent of magmas. *Journal of Metamorphic Geology* **19**, 627–33.

Bons, P. D., Arnold, J., Elburg, M. A., Kalda, J., Soesoo, A. & van Milligen, B. P. 2004. Melt extraction and accumulation from partially molten rocks. *Lithos* **78**, 25–42.

Bons, P. D. & van Milligen, B. P. 2001. A new experiment to model self-organized critical transport and accumulation of melt and hydrocarbons from their source rocks. *Geology* **29**, 919–22.

Brown, M. 1983. The petrogenesis of some migmatites from the Presqu'ile de Rhuys. *In* Atherton, M. P. & Gribble, C. (eds) *Migmatites, Melting and Metamorphism*, 174–200. Nantwich: Shiva Publications.

Brown, M. A. 1994. The generation, segragation, ascent and emplacement of granite magma: the migmatite- to crustally-derived granite connection in thickened orogens. *Earth-Science Reviews* **36**, 83–130.

Brown, M. A. 2004. The mechanism of melt extraction from lower continental crust of orogens. *Transactions of the Royal Society of Edinburgh: Earth Sciences* **95**, 35–48.

Brown, M. A. 2005a. Synergistic effects of melting and deformation: an example from the Variscan belt, western France. *In* Gapais, D., Brun, J. P. & Cobbold, P. R. (eds) *Deformation Mechanisms, Rheology and Tectonics: from Minerals to the Lithosphere. Geological Society, London, Special Publication* **243**, 205–26. Bath, UK: The Geological Society Publishing House.

Brown, M. A. 2005b. 'Comment' in Brown, M. A., Pitcher, W. S., Vernon, R. H. & Clemens, J. D. Invited comments on Clemens's 'Granites and granitic magmas'. *Proceedings of the Geologists' Association* **116**, 17–32.

Brown, M., Averkin, Y. A., McLellan, E. L. & Sawyer, E. W. 1995. Melt segregation in migmatites. *Journal of Geophysical Research* **100**, 15655–79.

Brown, M. A., Brown, M., Carlson, W. D. & Denison, C. 1999. Topology of syntectonic melt-flow networks in the deep crust: Inferences from three-dimensional images of leucosome geometry in migmatites. *American Mineralogist* **84**, 1793–818.

Brown, M. & Dallmeyer, D. 1996. Rapid Variscan exhumation and the role of magma in core complex formation: southern Brittany metamorphic belt, France. *Journal of Metamorphic Geology* **14**, 361–79.

Brown, M. & Solar, G. S. 1998. Shear-zone systems and melts: feedback and self-organization in orogenic belts. *Journal of Structural Geology* **20**, 211–27.

Clemens, J. D. 1998. Observations on the origins and ascent mechanisms of granitic magmas. *Journal of the Geological Society, London* **155**, 843–51.

Clemens, J. D. & Mawer, C. K. 1992. Granitic magma transport by fracture propagation. *Tectonophysics* **204**, 339–60.

Druguet, E. & Carreras, J. 2006. Analogue modelling of syntectonic leucosomes in migmatitic schists. *Journal of Structural Geology* **26**, 1734–47.

Elburg, M. A. 1996. Evidence of isotopic equilibration between microgranitoid enclaves and host granodiorite, Warburton Granodiorite, Lachlan Fold Belt, Australia. *Lithos* **38**, 1–22.

Ellis, D. J. & Obata, M. 1992. Migmatite and melt segregation at Cooma, New South Wales. *Transactions of the Royal Society of Edinburgh: Earth Sciences* **83**, 95–106.

Emerman, S. H., Turcotte, D. L. & Spence, D. A. 1986. Transport of magma and hydrothermal solutions by laminar and turbulent fluid fracture. *Physics of Earth and Planetary Interiors* **41**, 249–59.

Emerman, S. H. & Marrett, R. 1990. Why dykes? *Geology* **18**, 231–3.

Exner, U., Mancktelow, N. S. & Grasemann, B. 2004. Progressive development of s-type flanking folds in simple shear. *Journal of Structural Geology* **26**, 2191–201.

Gapais, D., Lagarde, J. L., Lecorre, C., Audren, C., Jegouzo, P., Sainz, A. C. & Vandendriessche, J. 1993. The Quiberon Shear Zone – Evidence for Carboniferous Extension in the Variscan Belt

of South Brittany (France). *Comptes Rendus de l'Academie des Sciences Serie II* **316**, 1123–9.

Gomez-Rivas, E., Bons, P. D., Griera, A., Carreras, J., Druguet, E. & Evans, L. 2007. Strain and vorticity analysis using small-scale faults and associated drag folds. *Journal of Structural Geology* **29**, 1882–99.

Grasemann, B. & Stüwe, K. 2001. The development of flanking folds during simple shear and their use as kinematic indicators. *Journal of Structural Geology* **23**, 715–24.

Harris, N., Vance, D. & Ayres, M. 2000. From sediment to granite: timescales of anatexis in the upper crust. *Chemical Geology* **162**, 155–67.

Hart, S. R. 1993. Equilibrium during mantle melting: a fractal tree model. *Proceedings National Academy of Sciences USA* **90**, 11914–18.

Hollister, L. S. & Crawford, M. L. 1986. Melt-enhanced deformation: A major tectonic process. *Geology* **14**, 558–61.

Holtzman, B. K., Groebner, N. J., Zimmerman, M. E., Ginsberg, S. B. & Kohlstedt, D. L. 2003a. Stress-driven melt segregation in partially molten rocks. *Geochemistry, Geophysics, Geosystems* **4**, 8607.

Holtzman, B. K., Kohlstedt, D. L., Zimmerman, M. E., Heidelbach, F., Hiraga, T. & Hustoft, J. 2003b. Melt segregation and strain partitioning: implications for seismic anisotropy and mantle flow. *Science* **103**, 1227–30.

Jackson, M. D., Cheadle, M. J. & Atherton, M. P. 2003. Quantitative modeling of granitic melt generation and segregation in the continental crust. *Journal of Geophysical Research* **108**(B7), 2332–53.

Johannes, W., Ehlers, C., Kriegsman, L. M. & Mengel, K. 2003. The link between migmatites and S-type granites in the Turku area, southern Finland. *Lithos* **68**, 69–90.

Johnson, T. M. & Brown, M. 2004. Quantitative constraints on metamorphism in the Variscides of Southern Brittany – a complementary pseudosection approach. *Journal of Petrology* **45**, 1237–59.

Kisters, A. F. M., Gibson, R. L., Charlesworth, E. G. & Anhaeusser, C. R. 1998. The role of strain localization in the segregation and ascent of anatectic melts, Namaqualand, South Africa. *Journal of Structural Geology* **20**, 229–42.

Koukouvelas, I. K. & Kokkolas, S. 2003. Emplacement of the Miocene west Naxos pluton (Aegean Sea, Greece): a structural study. *Geological Magazine* **140**, 45–61.

Kriegsman, L. M. 2001. Quantitative field methods for estimating melt production and melt loss. *Physics and Chemistry of the Earth* **26**, 247–53.

Kruhl, J. H. 1994. The formation of extensional veins: an application of the Cantor-dust model. *In* Kruhl, J. H. (ed.) *Fractals and dynamic systems in geoscience*, 95–104. Berlin: Springer Verlag.

Maaløe, S. 1987. The generation and shape of feeder dykes from mantle sources. *Contributions to Mineralogy and Petrology* **96**, 47–55.

Maaløe, S. 2003. Melt dynamics of a partially molten mantle with randomly oriented veins. *Journal of Petrology* **44**, 1193–210.

Marchildon, N. & Brown, M. 2003. Spatial distribution of melt-bearing structures in anatectic rocks from Southern Brittany, France: implications for melt transfer at grain- to orogen-scale. *Tectonophysics* **364**, 215–35.

Matte, P. 2001. The Variscan collage and orogeny (480–290 Ma) and the tectonic definition of the Armorica microplate: a review. *Terra Nova* **13**, 122–8.

Mériaux, C., Lister, J. R., Lyakhovsky, V. & Agnon, A. 1999. Dyke propagation with distributed damage of the host rock. *Earth and Planetary Science Letters* **165**, 177–85.

Mériaux, C. & Jaupart, C. 1998. Dike propagation through an elastic plate. *Journal of Geophysical Research* **103**, 18295–314.

Moyen, J.-F., Nédélec, A., Martin, H. & Jayananda, M. 2003. Syntectonic granite emplacement at different structural levels: the Closepet granite, South India. *Journal of Structural Geology* **25**, 611–31.

Nicolas, A. 1986. A melt extraction model based on structural studies in mantle peridotites. *Journal of Petrology* **27**, 999–1022.

Nicolas, A. & Jackson, M. 1982. High temperature dikes in peridotites: origin by hydraulic fracturing. *Journal of Petrology* **23**, 568–82.

Oliver, N. H. S. & Barr, T. D. 1997. The geometry and evolution of magma pathways through migmatites of the Halls Creek Orogen, Western Australia. *Mineralogical Magazine* **14**, 3–14.

Olson, S. N., Marsh, B. D. & Baumgartner, L. P. 2004. Modelling mid-crustal migmatite terrains as feeder zones for granite plutons: the competing dynamics of melt transfer by bulk versus porous flow. *Transactions of the Royal Society of Edinburgh: Earth Sciences* **95**, 49–58.

Paterson, S. R. & Fowler, T. K. 1993. Re-examining pluton emplacement processes. *Journal of Structural Geology* **15**, 191–206.

Paterson, S. R. & Vernon, R. H. 1995. Bursting the bubble of ballooning plutons: a return to nested diapirs emplaced by multiple processes. *Geological Society of America Bulletin* **107**, 1356–80.

Petford, N., Cruden, A. R., McCaffrey, K. J. W. & Vigneresse, J.-L. 2000. Granite magma formation, transport and emplacement in the Earth's crust. *Nature* **408**, 669–73.

Petford, N. & Koenders, M. A. 1998. Self-organisation and fracture connectivity in rapidly heated continental crust. *Journal of Structural Geology* **20**, 1425–34.

Rosenberg, C. L. & Handy, M. R. 2001. Mechanisms and orientation of melt segregation paths during pure shearing of a partially molten rock analog (norcamphor–benzamide). *Journal of Structural Geology* **23**, 1917–32.

Rubin, A. M. 1995a. Propagation of magma-filled cracks. *Annual Review of Earth and Planetary Science* **23**, 287–336.

Rubin, A. M. 1995b. Why geologists should avoid using 'fracture toughness' (at least for dykes). *In* Baer, G. & Heimann, A. A. (eds) *Physics and Chemistry of Dykes*, 53–63. Rotterdam: Balkema.

Rutter, E. H. & Neumann, D. 1995. Experimental deformation of partially molten Westerly granite under fluid-absent conditions with implications for the extraction of granitic magmas. *Journal of Geophysical Research* **100**, 15697–715.

Sawyer, E. W. 1987. The role of partial melting and fractional crystallization in determining discordant migmatite leucosome compositions. *Journal of Petrology* **28**, 445–73.

Sawyer, E. W. 1996. Melt segregation and magma flow in migmatites: implications for the generation of granite magmas. *Transactions of the Royal Society Edinburgh: Earth Sciences* **87**, 85–94.

Secor, D. T. & Pollard, D. D. 1975. On the stability of open hydrofractures in the Earth's crust. *Geophysical Research Letters* **2**, 510–13.

Sleep, N. H. 1988. Tapping of melt by veins and dikes. *Journal of Geophysical Research* **93**, 10255–72.

Soesoo, A., Kalda, J., Bons, P. D., Urtson, K. & Kalm, V. 2004. Fractality in geology: a possible use of fractals in the studies of partial melting processes. *Proceedings of the Estonian Academy of Sciences, Geology* **53**, 13–27.

Soesoo, A. & Nicholls, I. A. 1999. Mafic rocks spatially associated with Devonian felsic intrusions of the Lachlan Fold Belt: a possible mantle contribution to crustal evolution processes. *Australian Journal of Earth Sciences* **46**, 725–34.

Solar, G. S. & Brown, M. 2001. Petrogenesis of migmatites in Maine, USA: possible source of peraluminous leucogranite in plutons? *Journal of Petrology* **42**, 789–823.

Spence, D. A., Sharp, P. W. & Turcotte, D. L. 1987. Buoyancy-driven crack propagation: a mechanism for magma migration. *Journal of Fluid Mechanics* **174**, 135–53.

Takada, A. 1990. Experimental study on propagation of liquid-filled crack in gelatin: shape and velocity in hydrostatic stress condition. *Journal of Geophysical Research* **95**, 8471–81.

Tanner, D. C. 1999. The scale-invariant nature of migmatite from the Oberpfalz, NE Bavaria and its significance for melt transport. *Tectonics* **302**, 297–305.

Urtson, K. & Soesoo, A. 2007. An analogue model of melt segregation and accumulation processes in the Earth's crust. *Estonian Journal of Earth Sciences* **56**, 3–10.

Vanderhaeghe, O. 2001. Melt segregation, pervasive melt migration and magma mobility in the continental crust: the structural record from pores to orogens. *Physics and Chemistry of the Earth (A)* **26**, 213–23.

Vigneresse, J. L. 2004. A new paradigm for granite generation. *Transactions of the Royal Society of Edinburgh: Earth Sciences* **95**, 11–22.

Vigneresse, J. L. 2007. The role of discontinuous magma inputs in felsic magma and ore generation. *Ore Geology Reviews* **30**, 181–216.

Vigneresse, J. L., Barbey, P. & Cuney, M. 1996. Rheological transitions during partial melting and crystallization with application to felsic magma segregation and transfer. *Journal of Petrology* **37**, 1579–600.

Vigneresse, J. L. & Burg, J. P. 2000. Continuous vs. discontinuous melt segregation in migmatites: insight from a cellular automaton model. *Terra Nova* **12**, 188–92.

Walte, N. P., Bons, P. D. & Passchier, C. W. 2005. Deformation of melt-bearing systems – insight from *in situ* grain-scale analogue experiments. *Journal of Structural Geology* **27**, 1666–79.

Weertman, J. 1971. Theory of water-filled crevasses in glaciers applied to vertical magma transport beneath ocean ridges. *Journal of Geophysical Research* **76**, 1171–83.

Weinberg, R. F. 1999. Mesoscale pervasive felsic magma migration: alternatives to dyking. *Lithos* **46**, 393–410.

Weinberg, R. F. & Podladchikov, Y. Y. 1994. Diapiric ascent of magmas through power law crust and mantle. *Journal of Geophysical Research* **99**, 9543–59.

Weinberg, R. F. & Searle, M. P. 1998. The Pangong Injection Complex, Indian Karakoram: a case of pervasive granite flow through hot viscous crust. *Journal of the Geological Society, London* **155**, 883–91.

Zorpi, M. J., Coulon, C., Orsini, J. B. & Cocirta, C. 1989. Magma mingling, zoning and emplacement in calc-alkaline granitoid plutons. *Tectonophysics* **157**, 315–29.

MS received 18 October 2007. Accepted for publication 1 April 2008 (Stellenbosch); 15 January 2009 (RSE).

Earth and Environmental Science Transactions of the Royal Society of Edinburgh, **100**, 117–132, 2010 (for 2009)

Emplacement and assembly of shallow intrusions from multiple magma pulses, Henry Mountains, Utah

Eric Horsman[1]*, Sven Morgan[2], Michel de Saint-Blanquat[3], Guillaume Habert[3], Andrew Nugent[2], Robert A. Hunter[1] and Basil Tikoff[1]

[1] University of Wisconsin–Madison, Madison, Wisconsin, USA

*Current address: East Carolina University, Greenville, North Carolina, USA
Email: horsmane@ecu.edu

[2] Central Michigan University, Mt Pleasant, Michigan, USA

[3] CRNS-LMTG, Observatoire Midi-Pyrénées, Université Paul-Sabatier, Toulouse, France

ABSTRACT: This paper describes three mid-Tertiary intrusions from the Henry Mountains (Utah, USA) that were assembled from amalgamation of multiple horizontal sheet-like magma pulses in the absence of regional deformation. The three-dimensional intrusion geometries are exceptionally well preserved and include: (1) a highly lobate sill; (2) a laccolith; and (3) a bysmalith (a cylindrical, fault-bounded, piston-like laccolith). Individual intrusive sheets are recognised on the margins of the bodies by stacked lobate contacts, and within the intrusions by both intercalated sedimentary wallrock and formation of solid-state fabrics. Finally, conduits feeding these intrusions were mostly sub-horizontal and pipe-like, as determined by both direct observation and modelling of geophysical data.

The intrusion geometries, in aggregate, are interpreted to reflect the time evolution of an idealised upper crustal pluton. These intrusions initiate as sills, evolve into laccoliths, and eventually become piston-like bysmaliths. The emplacement of multiple magma sheets was rapid and pulsed; the largest intrusion was assembled in less than 100 years. The magmatic fabrics are interpreted as recording the internal flow of the sheets preserved by fast cooling rates in the upper crust. Because there are multiple magma sheets, fabrics may vary vertically as different sheets are traversed. These bodies provide unambiguous evidence that some intrusions are emplaced in multiple pulses, and that igneous assembly can be highly heterogeneous in both space and time. The features diagnostic of pulsed assembly observed in these small intrusions can be easily destroyed in larger plutons, particularly in tectonically active regions.

KEY WORDS: fabric analysis, laccolith, magma flow, pluton emplacement, sill

A subtle but fundamental shift is occurring in our perception of how igneous bodies intrude into the crust. Specifically, it involves the concept of assembly, which recognises that all plutons may not have existed as a single large magma bodies (e.g. Coleman *et al*. 2004; Glazner *et al*. 2004). Rather, plutons may grow through amalgamation of sequentially intruded sheets (e.g. Mahan *et al*. 2003; Michel *et al*. 2008) or relatively small magma pulses with a variety of geometries (e.g. Matzal *et al*. 2006).

A brief historical review provides the context for this issue. During the past two decades, much work has concentrated on a four-part sequence of magma generation, segregation, ascent, and emplacement (Petford *et al*. 2000). This sequence developed partially in response to the increasing lack of evidence for the upward movement of magma through the crust as diapirs. Diapiric transport of magma inherently combines both the ascent (vertical movement) and emplacement (transition to sub-horizontal movement) of magma bodies. The concept of diapirism is no longer generally regarded as a major ascent process in the upper crust, but the concept of intrusion of magma as a single large pulse lingers. While large magma bodies must exist to result in large-volume ignimbrite flows (e.g. Lipman 1984, 2007), there is no compelling reason to make the *a priori* assumption that all plutons were single magma bodies.

For the purposes of this article, *emplacement* is described as the displacement of the surrounding rocks that allows a pluton to attain its three-dimensional geometry (Fig. 1). For this reason, emplacement mechanisms typically describe space-making mechanisms (e.g. roof lifting, floor depression, stoping), and it is generally recognised that multiple emplacement mechanisms facilitate the emplacement of any pluton (Hutton 1988, 1997; Paterson & Fowler 1993). *Assembly* is defined as the process of pluton construction through magmatic addition. Assembly can occur in a single magmatic pulse or as an amalgamation of sequentially emplaced magma pulses. Within the context of these definitions, emplacement and assembly are different concepts. A pluton emplaced by roof lifting could have been assembled from a single pulse of magma or a series of pulses (Fig. 1).

A major problem remains: the assembly of plutonic bodies is often cryptic. Glazner *et al*. (2004) argue that the range of ages in the Tuolumne Intrusive Suite in the Sierra Nevada batholith, California, is larger than would be expected from a

© 2009 The Royal Society of Edinburgh. doi:10.1017/S1755691009016089

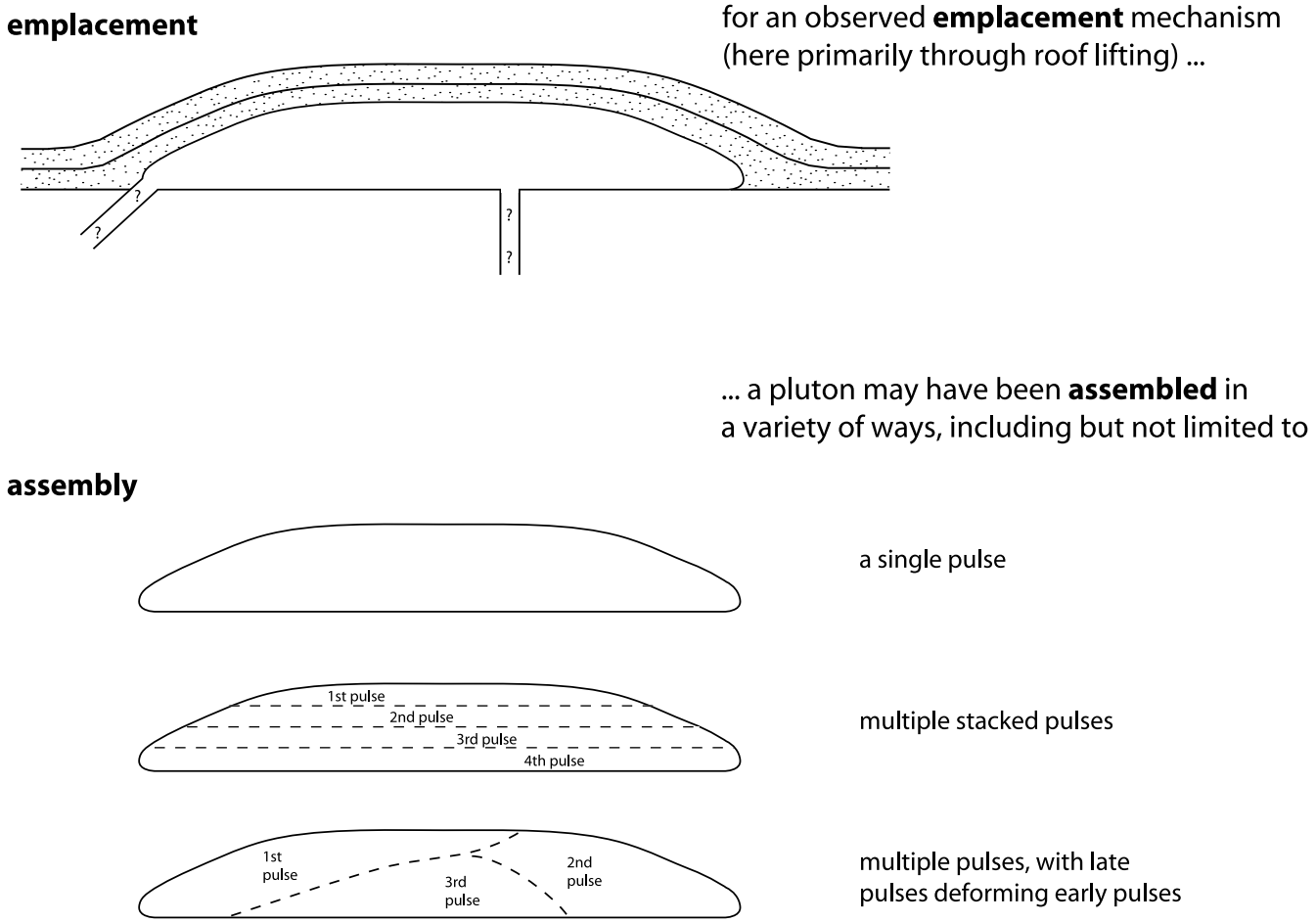

Figure 1 Diagram illustrating the distinction between emplacement and assembly, as used in this paper. For a given observed emplacement geometry, multiple assembly histories are possible.

single, cooling magma body. Consequently, periodic influxes of magma are required to explain the observed trends. However, direct observation of multiple magma pulses is often difficult. For example, recognition of multiple pulses within plutons is only straightforward when a major compositional difference exists (e.g. Wiebe & Collins 1998; Matzal *et al.* 2006). Similarly, primary fabrics within plutons can result from both emplacement-related and assembly-related processes, and separation of these effects is often difficult. Lastly, regional deformation can dramatically influence both pluton geometry and fabric patterns, making inferences of assembly history equivocal (Paterson *et al.* 1998).

Results are presented of a detailed study of intrusions in the Henry Mountains of southern Utah, a location ideally suited for separating emplacement from assembly of igneous bodies. First, the primary emplacement mechanism for these small intrusions is roof lifting, as first proposed by Gilbert (1877) and supported by subsequent workers (e.g. Hunt 1953; Johnson & Pollard 1973; Pollard & Johnson 1973; Jackson & Pollard 1988). Secondly, the intrusions exist at a shallow crustal level where cooling was sufficiently rapid that magmatic fabrics and evidence of multiple magma pulses are preserved. Thirdly, the intrusions are exceptionally well exposed, as the surrounding sedimentary rocks are distinctly more susceptible to erosion than the igneous bodies. Finally, emplacement of the intrusions occurred on the Colorado Plateau during a time of tectonic quiescence, and therefore the fabrics are not affected by regional deformation.

The results demonstrate that assembly occurred by intrusion of a series of sub-horizontal igneous sheets that contain complex internal fabrics. These sheets are locally fed by sub-horizontal tube-shaped conduits, which also exhibit evidence for multiple magmatic pulses. Evidence for magmatic pulses becomes increasingly cryptic as the size of the intrusion increases. Using this evidence, constraints are summarised from numerical modelling on the time scale of the magma intrusion. Finally, the paper discusses how assembly influences emplacement models and provides insights into how intrusions grow in the upper crust.

1. The Henry Mountains

The mid-Tertiary igneous bodies of the Henry Mountains intrude the flat-lying stratigraphy of the Colorado Plateau (Fig. 2). Displacement of the wallrock therefore directly records intrusion geometry. The intrusions post-date the minor Laramide-age deformation that affected this region. Therefore, fabrics within the intrusion reflect emplacement processes and lack a tectonic overprint. The magmas have a geochemical signature typical of volcanic arcs above a subduction zone (Nelson *et al.* 1992; Nelson 1997; Saint Blanquat *et al.* 2006; Bankuti 2007) and are part of a diffuse pattern of simultaneous magmatism throughout the region, which is interpreted to reflect arc-like magmatism above a shallowly dipping slab (Nelson *et al.* 1992) filtered through the thick crust of the Colorado Plateau (Thompson & Zoback 1979). Combined with the 3–4 km original depth of emplacement (Jackson & Pollard 1988), these features make the Henry Mountains an ideal location to study shallow igneous emplacement processes of arc magmas in a relatively simple system. Complications associated with regional tectonism, found in essentially all arcs, are absent.

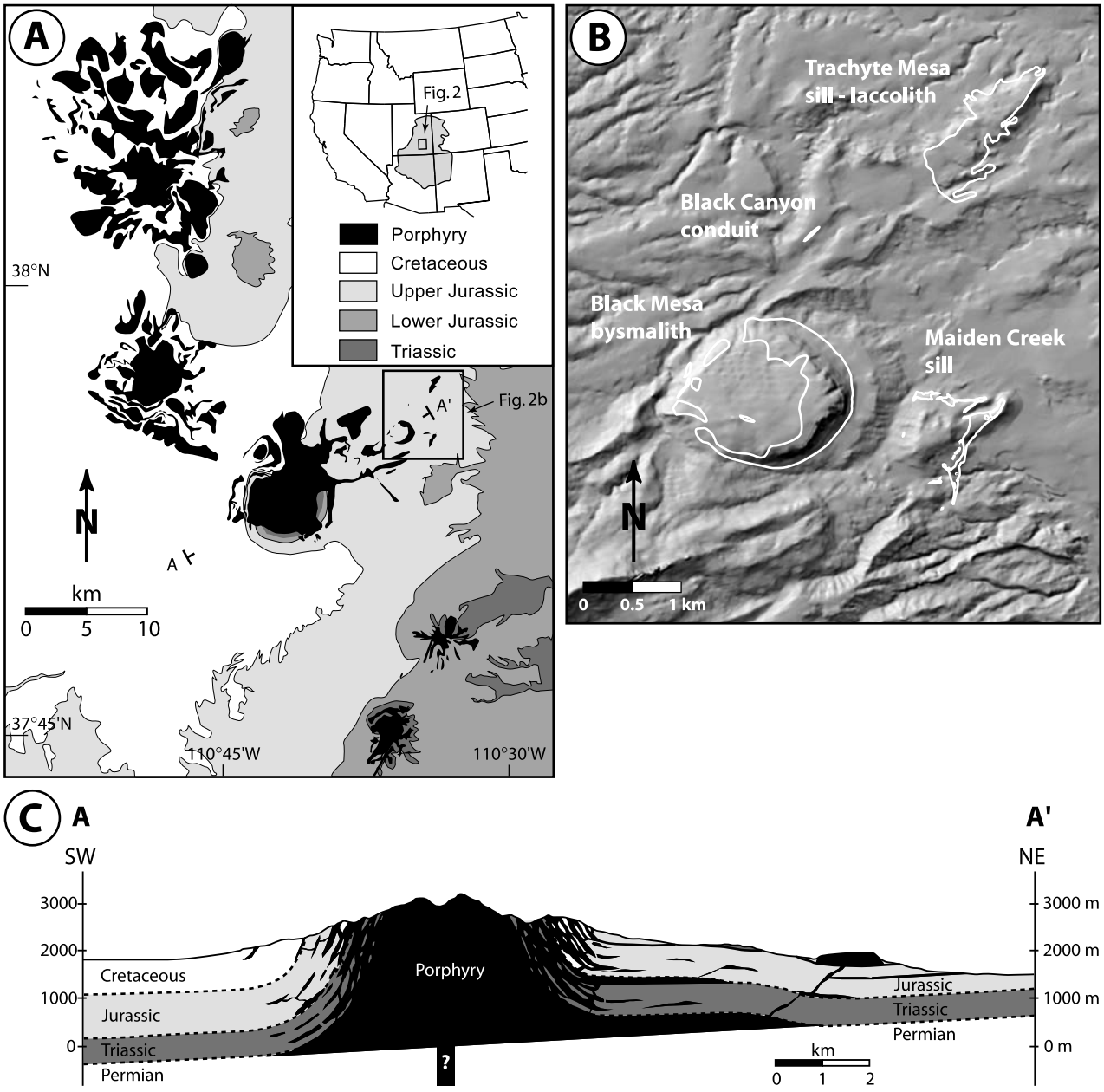

Figure 2 (a) Simplified geologic map of the Henry Mountains region. Box shows the location of (b). Location of cross section shown in (c) is also indicated. Inset shows the location of (a) on the Colorado Plateau in the western United States cordillera. (b) Shaded relief map of the eastern portion of Mt Hillers. Outlines of the three intrusions and the conduit discussed in this paper are shown in white. (c) Schematic cross section through Mt Hillers, oriented NE–SW.

Five intrusive centres comprise the Henry Mountains (Fig. 2). Each intrusive centre is a large and complex laccolithic body (Jackson & Pollard 1988, 1990), made of dozens of interconnected component intrusions with a wide range of geometries. All three of the intrusions studied on the eastern margin of the Mt Hillers intrusive centre (Fig. 2b) are in a unique state of erosion. Numerous upper, lower and lateral contacts with the surrounding sedimentary rock are preserved. The level of detail of intrusion geometry preserved helps to illuminate the complex emplacement and assembly processes of the igneous bodies.

1.1. Composition, fabric, and wallrock deformation

The intrusions are composed of plagioclase-hornblende porphyry whose bulk chemistry is consistently similar throughout the range (Nelson *et al.* 1992; Bankuti 2007). Primary phenocryst populations include 30–35% by volume 0·5–1·5 cm-diameter euhedral plagioclase laths, and 5–15% by volume 0·1–0·5 cm-long hornblende needles. Other phenocrysts include <2% euhedral to subhedral oxides (principally magnetite) and <1% euhedral apatite and sphene. The matrix commonly makes up 50% or more of the rock and is composed primarily of very fine-grained plagioclase, hornblende, and oxides.

Field fabric is variably well developed in the intrusions (Morgan *et al.* 2005), as described in more detail for each body below. In general, fabrics are strongest near intrusion margins and decrease in intensity away from the margins. A carapace of solid-state fabric is locally preserved in the outermost few centimetres of each intrusion. Where the carapace is well preserved, it grades smoothly into magmatic fabric away from the wallrock contact. Asymmetry of the solid state and magmatic fabric relative to the contact provides a useful shear sense indicator (e.g. Horsman *et al.* 2005).

Further from contacts, fabric is less well developed. To characterise these weak fabrics, the anisotropy of magnetic

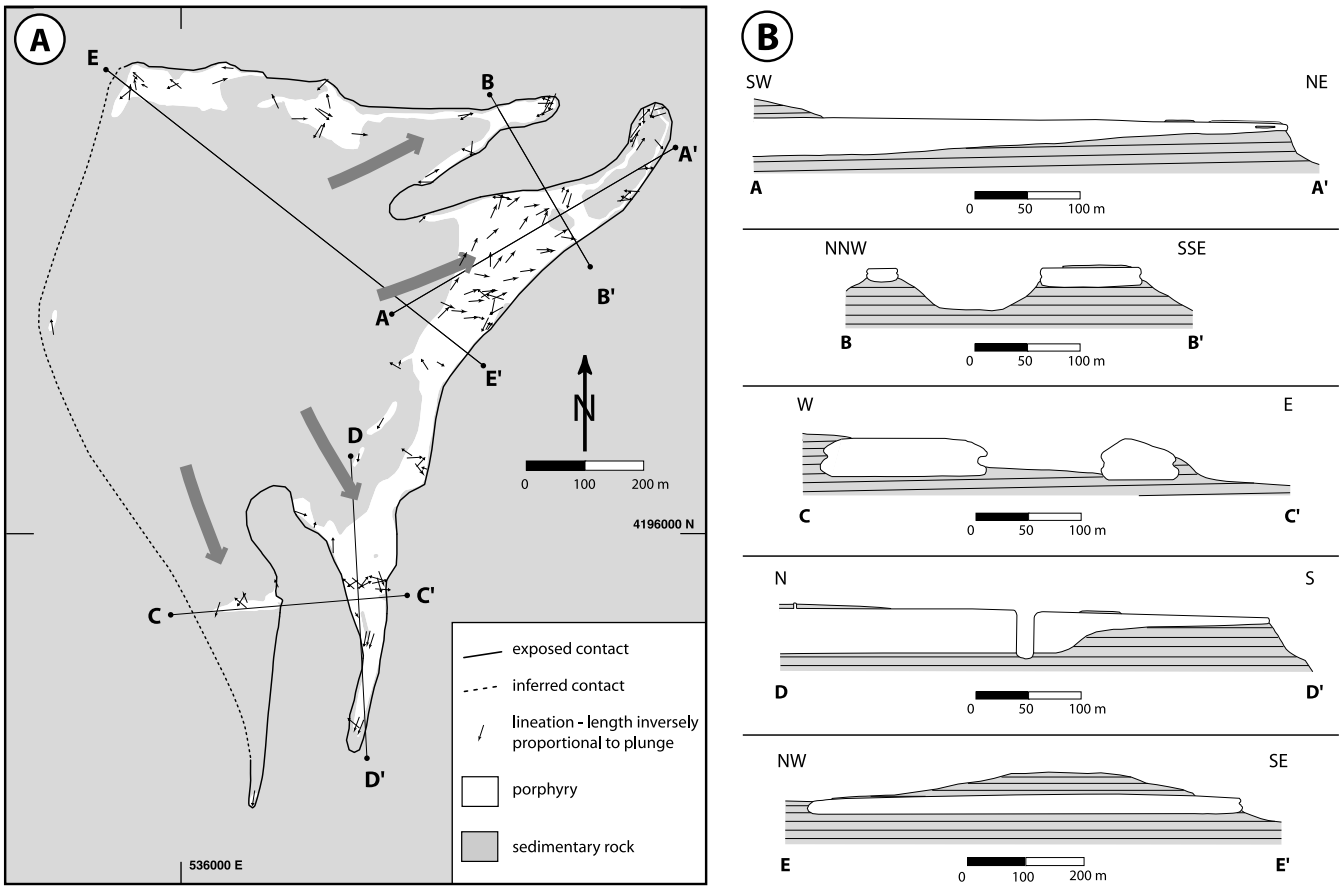

Figure 3 (a) Geologic map of the Maiden Creek sill. Lineations shown with black arrows include field measurements and magnetic fabric results, with arrow length inversely proportional to plunge. Locations of cross-sections shown in (b) are indicated. Large grey arrows indicate inferred primary magma flow directions based on intrusion geometry and fabric patterns. UTM zone 11. (b) Cross-sections through the intrusion. Note that the scale of cross-section E–E′ is different from that of the others.

susceptibility (AMS) was measured at numerous stations in each intrusion. Where detailed comparisons have been made, AMS orientations agree well with both field measurements and three-dimensional laboratory fabric analysis results (Horsman *et al*. 2005). The AMS signal in the porphyry is carried principally by multi-domain and pseudo-single-domain magnetite (Habert & de Saint Blanquat 2004; Horsman *et al*. 2005; Morgan *et al*. 2008), allowing for normal interpretation of results; the maximum eigenvector of the magnetic susceptibility tensor is the magnetic lineation and the minimum eigenvector is the pole to magnetic foliation.

Both field-based measurements and magnetic fabric data provide constraints on magma flow patterns during emplacement. The intrusions are small and occur in an upper crustal setting, suggesting that they cooled quickly and do not record any structural overprinting. In fact, three-dimensional intrusion geometries are so well constrained that the first-order magma flow patterns can be inferred directly from the geometry and then tested against the observed fabrics.

Aside from fabric analysis, wallrock deformation provides information on the emplacement and assembly history of each intrusion. Analysis of fault and fracture orientations and offset sometimes allows for inference of detailed emplacement history (e.g. Pollard & Johnson 1973; Morgan *et al*. 2008). Interpretation of wallrock deformation and igneous fabrics together provides a more complete picture of emplacement and assembly history. Each data set records distinct processes and these data are integrated in the present paper to provide a more complete analysis of emplacement and assembly.

2. Maiden Creek sill

2.1. Three-dimensional geometry

The Maiden Creek sill (Fig. 3) represents the initial stage of igneous emplacement with a relatively small volume of magma (<0·03 km^3). A more thorough description of the intrusion in provided by Horsman *et al*. (2005).

Numerous upper, lower and lateral contacts with wallrock sandstone are preserved. These contacts tightly constrain a complex three-dimensional geometry. In map view, the sill has an elliptical main body from which protrude several finger-like, 100 m-scale lobes. Similar lobate sill geometries have been observed in detailed three-dimensional seismic reflection studies in the North Sea (Thomson & Hutton 2004; Hansen & Cartwright 2006).

In detail, the cross sectional geometry of the intrusion is similarly complex. Whilst the main body has a simple sill-like cross sectional geometry with concordant upper and lower contacts, cross sections along the length of the two best-exposed finger-like lobes (Fig. 3b) show that the base of the intrusion cuts up through the stratigraphic section. Along the easternmost finger this process was gradual (cross section A–A′ on Fig. 3b), while along the SE finger the process was more step-like (cross section D–D′ on Fig. 3b).

2.2. Internal fabric and wallrock deformation

Solid-state fabric exists in the outermost few centimetres of the intrusion near every exposed contact with wallrock, and this

carapace is preserved in some locations where the sedimentary rock has eroded, suggesting that the erosion is relatively recent. This solid-state fabric grades smoothly into a similarly oriented magmatic fabric over a few centimetres. Further from the contact magmatic fabric becomes weaker.

Foliation is consistently sub-horizontal and lineation has a fanning radial map pattern in the elliptical main body (Fig. 3). In each finger-like lobe, lineation has a more restricted fanning map pattern generally aligned with the long axis of the lobe. The tightly constrained intrusion geometry requires that magma flowed from the main body into the lobes (Fig. 3).

2.3. Evidence for multiple magma pulses

Several lines of evidence demonstrate that the sill is composed of two stacked horizontal sheets of magma that intruded sequentially. Several cross-sections through the lateral margin of the intrusion are preserved and everywhere show two stacked bulbous terminations (figs 4a and 4b in Horsman *et al.* 2005). Additionally, the sub-horizontal boundary between the two sheets is marked locally by either metre-scale lenses of intercalated sandstone or centimetre-scale zones of solid-state fabric.

The combination of strong fabric at the intrusion margins and weak fabric in the interior suggests that a significant portion of the emplacement-related strain in the intrusion was accommodated in the outer few centimetres of each sheet. This fabric also suggests that emplacement of each sheet occurred rapidly. The two sheets were probably emplaced in rapid succession, because the sheet-sheet contact is commonly difficult to recognise, except where marked by intercalated wallrock. The well-preserved lateral margins of each sheet are bulbous in cross-section, rather than pointed as predicted by many mechanical models of sheet intrusions (e.g. Pollard 1973).

2.4. Summary

The Maiden Creek intrusion is a sill with a complex geometry. It is lobate in map view and the bottom contact cuts upward in cross-section. Both solid-state and magmatic fabrics closely preserve magma flow patterns. These fabric patterns correspond well with the complex intrusion geometry and demonstrate that magma flowed from the main body out into the finger-like lobes to produce fanning lineation and arcuate foliation patterns that reflect progressive growth of the intrusion. The sill is composed of two stacked sheets that were emplaced sequentially as separate magma pulses.

3. Trachyte Mesa laccolith

3.1. Three-dimensional geometry

The Trachyte Mesa laccolith (Fig. 4) has at least twice the volume of magma ($\sim$0·05 km^3) as the Maiden Creek sill. The intrusion is elongate along a line pointing radially away from the main Mt Hillers intrusive centre. Morgan *et al.* (2008) provide a more detailed description of this intrusion. Numerous upper contacts of this intrusion with flat-lying wallrock are well preserved, and lower contacts are locally preserved. These contacts indicate that the intrusion has a broadly sill-like cross-sectional geometry (Fig. 4b).

A well-preserved lateral contact on the NW margin indicates that the intrusion grew in a laccolithic manner. In this location, wallrock layers are bent upward and thinned over the intrusion. Strain analyses of these sandstone layers demonstrate that deformation of the overlying rock was localised at the intrusion margins through vertical growth of the intrusion. There is also evidence for multiple (>10) stacked igneous sheets at this margin, identified by bulbous terminations, solid-state fabrics and intercalated sandstone. Cross-cutting relationships between sheets demonstrate a complex stacking history, but are consistent with a general pattern of emplacement of younger sheets below older sheets. For example, some of these igneous sheets at the margin are rotated with the sedimentary layering, suggesting that they were intruded horizontally and rotated by subsequent emplacement of underlying sheets. However, late horizontal igneous sheets locally intrude the rotated sedimentary beds and earlier igneous sheets.

Although the main body of the intrusion is essentially laccolithic, at several locations on the margins of the intrusion complex, finger-like lobes are preserved (Fig. 4). These 100-m-scale, highly elongate lobes commonly project out from the margin of the main Trachyte Mesa intrusion. These lobes are similar to the finger-like lobes observed within the Maiden Creek intrusion. However, the lobes make up only a small portion of the Trachyte Mesa intrusion volume instead of the majority they make up on the Maiden Creek intrusion.

3.2. Internal fabric and wallrock deformation

Field and magnetic foliation data for the Trachyte Mesa intrusion are consistently sub-horizontal (Fig. 4). Lineation plunges are also consistently sub-horizontal, but trend values have a bilaterally symmetric geometry. Along a central axis, lineation is parallel to the length of the intrusion. Away from that axis, lineation trends perpendicular to the axis and points toward the intrusion margins. Flow patterns with this bilaterally symmetric geometry have traditionally been ascribed to flow away from a central dike-like feeder below the intrusion (e.g. Ferré *et al.* 2002). However, data is presented (see section 5) indicating that the intrusion is fed by a sub-horizontal conduit from the direction of the main Mt Hillers intrusive centre. The average foliation on top of the intrusion also dips approximately 10° to the NE (Fig. 4a), parallel to the long axis of the intrusion, and is used as a bulk magma flow indicator (Morgan *et al.* 2008). Therefore, it is suggested that this pattern represents magma flow out along the length of the intrusion in a sub-horizontal conduit, which then feeds magma out to the lateral margins (see Morgan *et al.* 2008). A similar flow pattern has been inferred for other sills (Thomson & Hutton 2004; Hansen & Cartwright 2006).

Wallrock deformation is documented by Morgan *et al.* (2008). Little deformation is observed on the few outcrops of wallrock on the top of the intrusion, suggesting primarily vertical translation of these rocks. Deformation at the exposed lateral contact on the NW side of the intrusion is consistent with the sedimentary layering being translated upward and over the top of an upward- and outward-propagating hinge. Sedimentary layers immediately above the contact locally show evidence for layer-parallel shortening, which is inferred to result from coupling with the underlying sheets as they moved outward. Further from the contact, sedimentary layers show up to 20% layer-parallel thinning due to bulk roof lifting, accommodated by fracture-induced porosity collapse and faulting. These zones are decoupled from each other by a thin layer of intensely sheared sandstone.

3.3. Evidence for multiple magma pulses

Although cross-cutting relationships clearly demonstrate the importance of pulsed assembly at the margins of the Trachyte Mesa intrusion, exposures of the interior have only equivocal evidence of sheets. In particular, the top of the intrusion has two distinct plateau-like levels, which are thought to

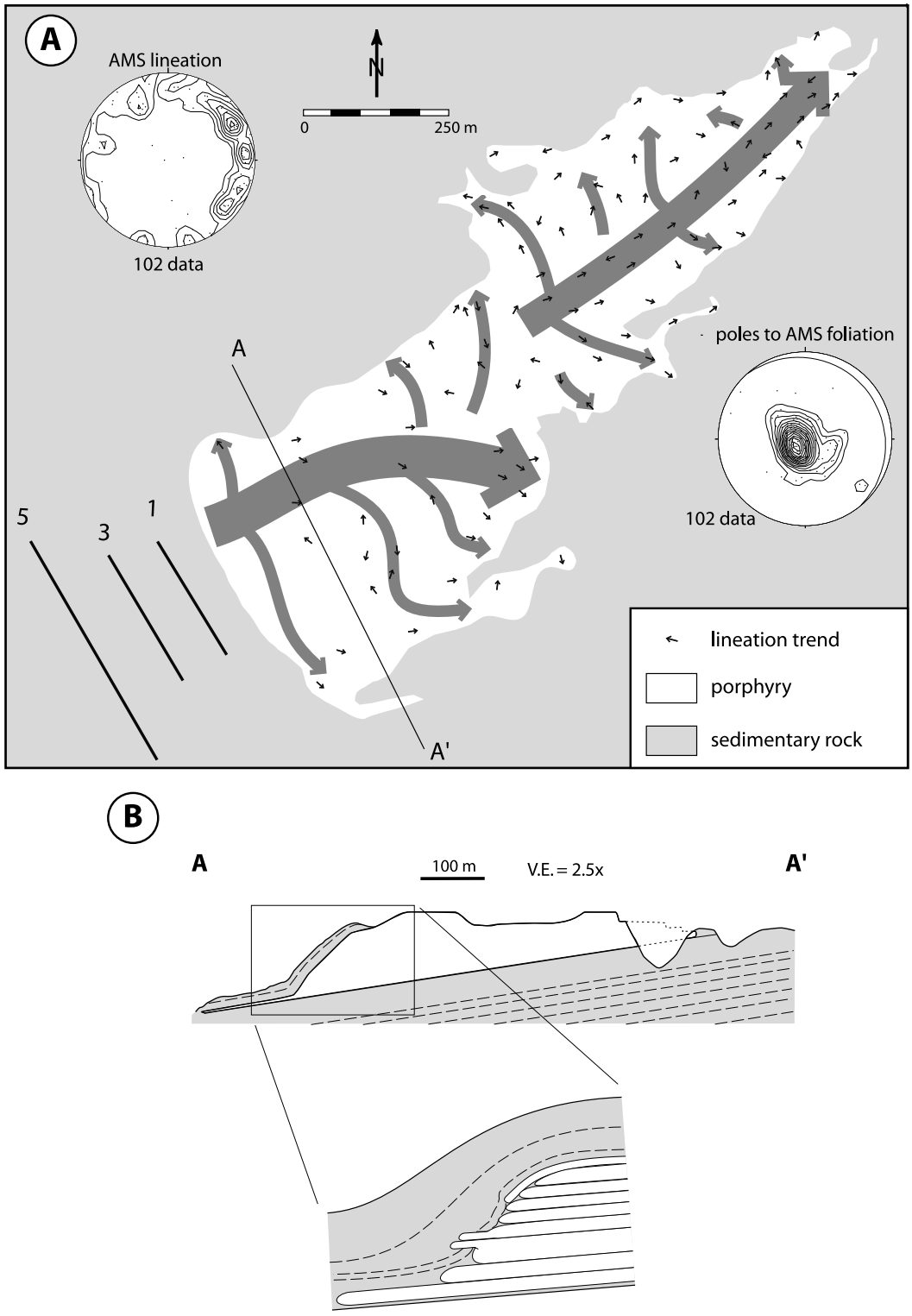

Figure 4 (a) Geologic map of the Trachyte Mesa laccolith. Lineations shown with black arrows are magnetic fabric results and all have sub-horizontal plunges. Equal-area lower hemisphere plots show orientations of magnetic lineation and poles to foliation. Note that foliation dips shallowly to the NE, parallel to the length of the intrusion. Grey arrows indicate inferred primary magma flow directions based on intrusion geometry and fabric patterns. Numbered lines SW of the intrusion indicate locations of magnetic anomaly traverses described in Figure 7. UTM zone 11. (b) Cross-section through the intrusion. 2·5 times vertical exaggeration.

correspond to different sheets. This inference is corroborated by slightly different fabric patterns that occur at those different levels. The lack of distinct sheet–sheet contacts suggests assembly was rapid enough for emplaced pulses to stay above the solidus before the next sheet intruded.

These observations can be interpreted in a variety of ways. First, late-stage magmatic processes may have obscured evidence of earlier pulsed assembly. Alternatively, sheets could form only near the margins of the intrusion while the interior was a single magma body. The latter hypothesis is not consistent with the emplacement, rotation, and pre-intrusion of sheets on the margins or the different flow fields on top of the intrusion. Consequently, it is inferred that late magmatic processes obscured evidence of earlier pulsed assembly.

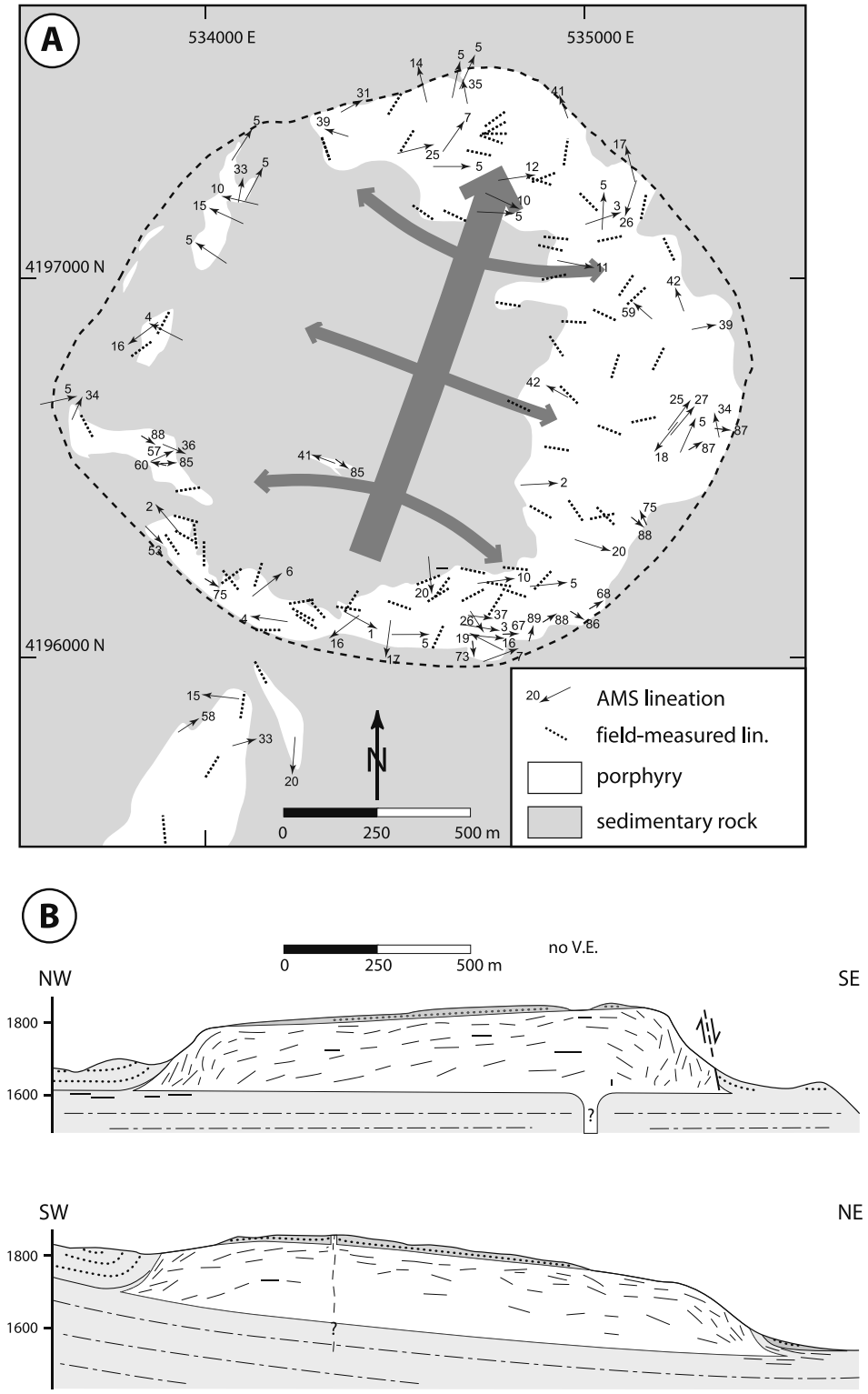

Figure 5 (a) Geologic map of the Black Mesa intrusion. Lineations shown with black arrows are magnetic fabric results, with plunge indicated. Lineations shown with black lines are field measurements of lineation trend. Grey arrows indicate primary magma flow directions based on intrusion geometry and fabric patterns. UTM zone 11. (b) Cross-sections through the intrusion, with schematic trace of foliation indicated.

3.4. Summary

The Trachyte Mesa laccolith is an elongate body in map-view. In cross-section it exhibits sub-horizontal, sill-like upper and lower contacts, along with laccolithic margins. Magma in the intrusion flowed out along a central axial conduit that fed flow to the lateral margins. Numerous magma pulses contributed to assembly of the intrusion. Evidence of these pulses as distinct sheets is clear at the lateral margins of the intrusion, but cryptic in the centre of the body.

4. Black Mesa bysmalith

4.1. Three-dimensional geometry

The relatively voluminous ($\sim$0·4 km^3) Black Mesa bysmalith (Fig. 5) is the largest of the studied intrusions. Habert & Saint Blanquat (2004) and Saint Blanquat *et al*. (2006) provide more detailed descriptions of this intrusion. As with the other two intrusions studied, numerous preserved top and lateral contacts allow the geometry of the intrusion, which is $\sim$1·7 km in

diameter and roughly circular in map view, to be clearly constrained. The eastern margin is a sub-vertical fault along which the sub-horizontal wallrock is displaced upward ~200 m. This vertical offset is determined from stratigraphic relationships between sub-horizontal shale and sandstone on the top of the intrusion and similar wallrock exposed at the base of the intrusion. This type of relation occurs on the margin of a bysmalith, which is defined as an intrusion with a flat floor and flat roof that lifts the overburden in a piston-like manner along a curved, steeply dipping fault. In contrast, the western margin of the intrusion is a monocline. Taken together, the intrusion resembles a trapdoor, with a hinge along the western side and a discrete, faulted offset along the eastern side. Consequently, the Black Mesa intrusion represents a transitional stage of development between a laccolith and a bysmalith.

4.2. Internal fabric and wallrock deformation

There is little information available about the internal fabric of the Black Mesa intrusion, because the current exposures record almost exclusively the outermost margins of the body. Along the steep, faulted eastern margin of the intrusion, solid-state and magmatic lineations are both steeply plunging. Immediately adjacent to wallrock contacts, the fabric is solid-state and defined by cataclastically deformed phenocrysts. Further from this contact, the fabric is magmatic and defined by phenocryst shape-preferred orientation. The observed fabrics are consistent with syn-magmatic shearing on the sub-vertical bounding fault along the eastern margin of the intrusion.

Where exposure exists, the top of the intrusion is also characterised by both solid-state and magmatic fabrics. Solid-state fabrics occur in the outer few centimetres and grade inward to magmatic fabrics, similar to the other intrusions. Foliation is sub-horizontal in both the solid-state and magmatic fabrics. Lineation orientation changes with distance from the top contact. The solid-state and magmatic lineations at the upper contact are oriented WNW, while the magmatic lineations are oriented NNE several centimetres below the contact. Saint Blanquat *et al.* (2006) interpret this fabric to indicate NNW stretching during divergent ENE-oriented magma flow. They attribute the pattern to intrusion from below, perhaps by a dike-like feeder striking approximately NNE. The similarity of this fabric pattern to that observed in Trachyte Mesa intrusion suggests that a lateral pipe-like feeder at the base of the intrusion is also possible. However, no feeder conduit, is exposed.

Outcrops of wallrock on the top of the intrusion are relatively undeformed. Minor fracturing exists as conjugate sets, with orientations generally consistent with regional trends away from the Henry Mountains. This observation is similar to overburden rocks atop both the Maiden Creek and Trachyte Mesa intrusions.

4.3. Evidence for multiple magma pulses

Several observations provide indirect evidence of multiple pulses. In the upper portion of the intrusion, sub-horizontal textural layering and cataclastic zones can be traced for tens of metres. The remainder of the intrusion displays no internal contacts, although exposures of the interior are very rare. Additionally, petrologic and geochemical zonation exists along vertical profiles through the intrusion (Bankuti 2007). None of these observations provides unequivocal evidence of multiple magma pulses. However, together they strongly suggest that the intrusion was amalgamated from multiple magma pulses.

4.4. Summary

The Black Mesa intrusion has an approximately cylindrical geometry. The western margin of the intrusion is monoclinal, while the eastern margin is a vertical fault with a displacement of ~200 m. Magma in the intrusion flowed out along a central axial conduit before flowing laterally out to the margins. Multiple pulses of magma likely contributed to the assembly of the intrusion, but evidence for these pulses is more cryptic than in the two smaller intrusions studied.

5. Magma conduits

Dikes are rare in the Henry Mountains. Instead, isolated sub-horizontal igneous bodies with approximately elliptical cross sections are observed, similar to the elongate lobes of the Maiden Creek body. Following Hunt (1953), it is suspected these were pipe-like feeders that locally provided magma for the separate intrusive bodies. Two examples are described below: (1) an exposed example of one of these feeders (section 5.1); and (2) geophysically imaged conduits that act as feeders to the Trachyte Mesa intrusion (section 5.2). In the absence of a purely descriptive geometric name defined in the literature, these igneous bodies are referred to as conduits. These conduits presumably feed magma from the main Mt Hillers intrusive centre to the satellite bodies and represent the final stage of a longer ascent process that principally involves vertical movement.

5.1. Black Canyon conduit

Approximately 5 km SW of the Trachyte Mesa intrusion, a highly elongate igneous body is exposed for ~150 m as a series of isolated outcrops in Black Canyon (Fig. 6). The composition and texture are similar to the larger igneous bodies in the area. This intrusion was originally reported by Hunt (1953), and is herein referred to as the Black Canyon conduit.

For several of the individual outcrops, both the top and side contacts of the Black Canyon conduit are well exposed (Fig. 6). In general, the top contact is sub-horizontal, while the lateral contacts are sub-vertical. These observations constrain the width of the intrusion to less than ~5–10 m along the length of the exposure. The absence of continuous outcrop indicates that the intrusion cannot be a continuous tabular body (e.g. a dike or sill). Rather, the intersection of the topography and the igneous body is most consistent with a pipe-like conduit, with the base of the intrusion oriented near the current exposure level of the body. Consequently, the Black Canyon conduit likely represents a pipe-like feeder transporting magma radially away from the main Mt Hillers intrusive centre.

Hunt (1953) noted the Black Canyon conduit was located between the Trachyte Mesa intrusion and the Mt Hillers intrusive centre, with an orientation toward Trachyte Mesa. Hunt consequently suggested that the conduit might be an exposure of the feeder for the Trachyte Mesa intrusion. The present authors disagree with this interpretation for two principal reasons. First, the conduit is located higher in the stratigraphic section than the Trachyte Mesa intrusion. It is unlikely that a magma conduit would cut downsection, particularly given our observation of the upward-sloping bottom contact in the finger-like lobes of the Maiden Creek intrusion. Secondly, as described below (see section 5.2), geophysical studies suggest that multiple tube-like conduits feed the Trachyte Mesa intrusion below the current level of exposure.

Fabric in the conduit is magmatic in the middle of the body and solid-state on the edges (Fig. 6). Magmatic fabrics farther from the wallrock contact are dominated by lineation, with

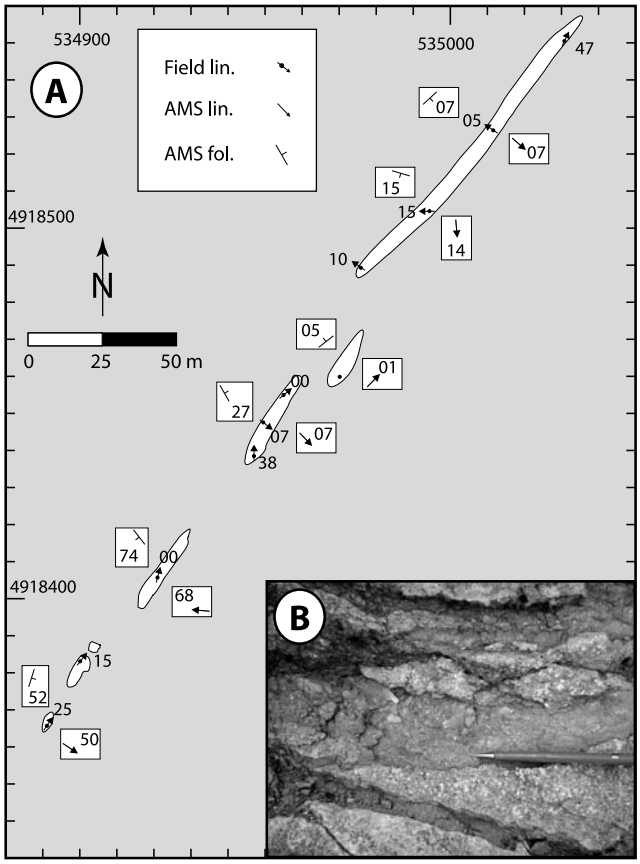

Figure 6 (a) Simplified geological map of the Black Canyon conduit. Field-measured lineation shown at the station locations. AMS lineation and foliation results, plotted nearby in white boxes, are from the same stations. UTM zone 11. (b) Field photograph of several generations of breccia veins. Composition of clasts in the breccia include porphyry, sandstone, and older breccia.

local, poorly developed foliation. In general, solid-state and magmatic lineations near wallrock contacts trends perpendicular to the length of the intrusion, while magmatic lineation further from contacts trends roughly parallel to the length of the intrusion. The first lineation, oriented NS–SE and subparallel to the long axis of the intrusion, is interpreted as recording flow along the length of the conduit. Magmatic flow presumably went from the SW to the NE, away from the Mt Hillers intrusive centre. The second lineation is interpreted as recording the radial expansion of the conduit during pulsed growth of the body.

Six oriented samples were collected for AMS analysis. Samples were taken from rocks containing only magmatic fabrics and were processed similarly to those from the other intrusions (e.g. Horsman *et al.* 2005). Similar to the field lineation, AMS results display an irregular lineation in the magnetic fabric that varies in both trend and plunge along the length of the intrusion (Fig. 6a), although the field and magnetic lineation locally disagree. Magnetic foliation is generally flat-lying, consistent with the one observed field foliation. Magnetic fabrics are dominantly plane strain, which appears inconsistent with the strong field-based linear fabric.

Veins of fine-grained, green breccia are locally preserved along the outcrop (Fig. 6b). These roughly planar veins generally strike sub-parallel to the trend of the intrusion and contain clasts of both porphyry and sandstone. Evidence of multiple cross-cutting diking events suggests multiple episodes of brecciation. The presence of these zones suggests multiple injections of magmas, with either very high strain rates or sufficient cooling of the intrusion to cause fracturing. Kinematic indicators present within the breccia zones potentially indicate oblique slip, but this inferred shear sense varies from vein to vein. These structures are interpreted as recording the relative displacement between individual magma pulses.

In summary, the Black Canyon conduit records dominantly linear fabrics in a tube-like body, suggesting outward magma flow from the Mt. Hillers intrusive centre. The observed breccia veins, field fabrics, and AMS results are consistent with the intrusion of multiple magma pulses through the conduit. The complicated lineation pattern likely records simultaneous magma flow and intrusion growth within this small, geometrically complex body.

5.2. Trachyte Mesa feeder

Magnetic anomaly data were collected along five traverses on the alluvial plateau SW of the Trachyte Mesa intrusion to provide constraints on the feeder system for the body. Data are presented from three of these traverses (1, 3, 5) in Figure 7 and locations are shown on Figure 4. Data from the two traverses not presented (2, 4) show patterns similar to the discussed traverses. The length and placement of the traverses were governed by the size of the accessible plateau area, eliminating any changes in the magnetic field that might occur due to changes in elevation. The traverses were oriented NW–SE, perpendicular to an axis connecting Mt Hillers to the intrusion. The closest traverse is 110 m SW from the nearest exposure of the intrusion (Fig. 4). The first and third traverses are 170 m long. The fifth traverse, which is furthest from the intrusion, is 290 m long and is ~320 m from the SW edge of the intrusion. Magnetic data were collected every three metres along each traverse using two magnetometers separated on a pole in the gradiometer mode. The data from each traverse were smoothed.

Traverses one and three each reveal two to four anomalies, two of which can be traced between the traverses. Each of these two traverses has a relatively large anomaly near the NW end (Fig. 7). Traverse five, the most distant from the exposed intrusion, has numerous smaller anomalies. The magnitude of the anomalies varies considerably between the five traverses. Traverse one has anomalies that vary between positive and negative 10 γ/m, whereas traverse three has a positive anomaly close to 100 γ/m and traverse five has negative anomalies of similar magnitude.

To test possible intrusion geometries, the observed anomaly profiles were forward modelled as dikes, sills, and finger-like bodies using GM-SYS software. Each 2·5-dimensional model simulates a block of country rock Entrada Sandstone that was intruded by various shapes of porphyry. The susceptibility and remanence of samples from the porphyry and from the country rock Entrada Sandstone were determined using rock magnetic facilities at Lake Superior State University and the University of Michigan. The sills and finger-like bodies were modelled to be at a depth of 12 m below the surface, based on the elevation of the observed base to the intrusion 300 m to the NE. Shapes of the modelled finger-like bodies were modified in order to have the greatest correspondence between the observed and calculated (model) magnetic intensities. Dikes were placed at various positions and with various dips for the best fit. Dike widths and sill thicknesses were also modified for the best fit.

The models illustrate that along each traverse, a series of finger-like bodies more accurately matches the observed anomalies than one sill or a set of dikes. The models also show that a thick finger-like shape of porphyry, somewhat similar to the projected cross-sectional shape of the Black Canyon conduit, may exist on the NW end of the closest two traverses.

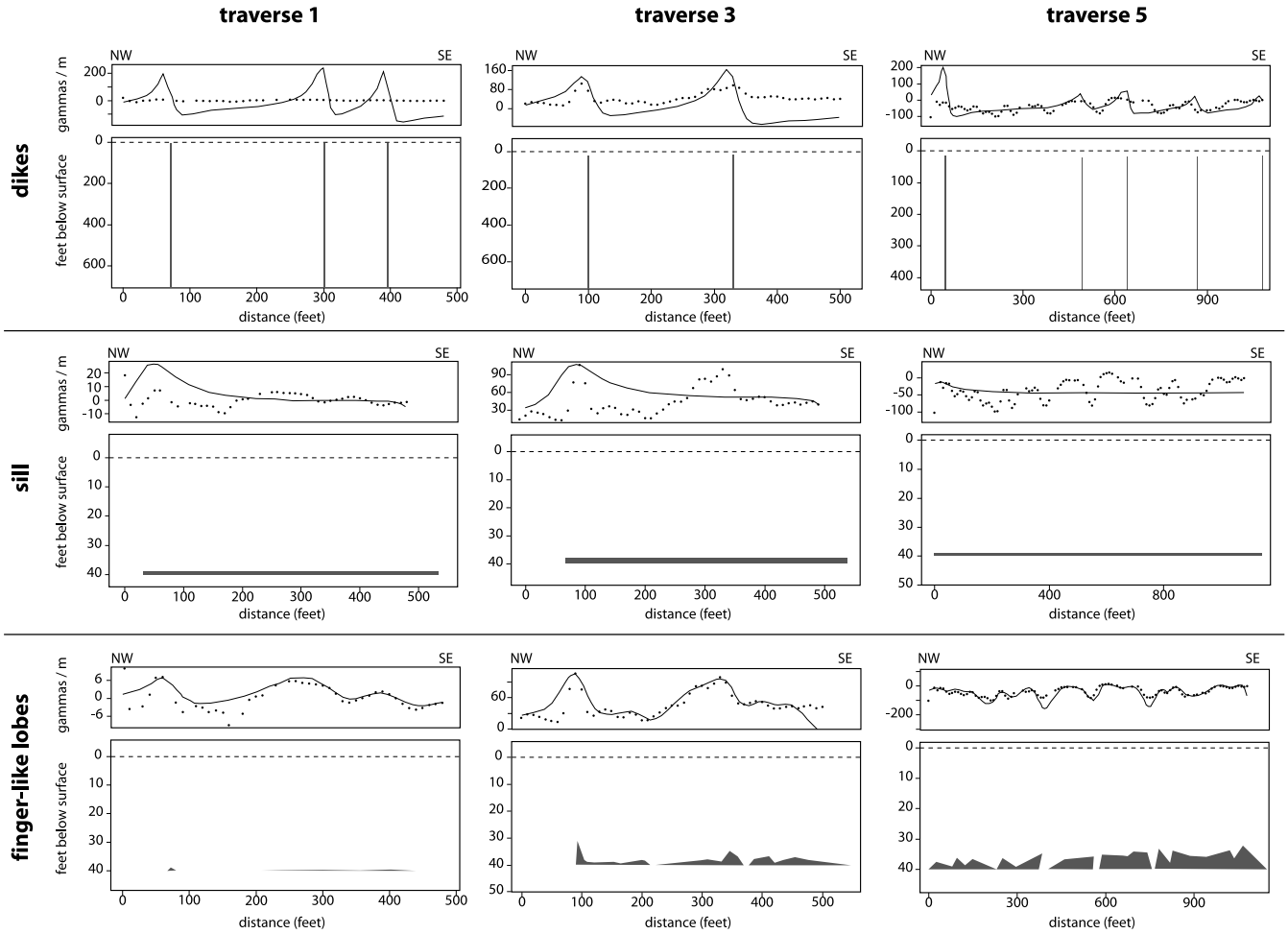

Figure 7 Magnetic anomaly data from traverses SW of the Trachyte Mesa laccolith. Forward models of the data test possible feeder geometries for each magnetic anomaly traverse. Tested feeder geometries include dikes, sills and finger-like bodies. Finger-like feeder bodies best match the observed anomaly data. Note that scales and vertical exaggeration differ for each plot. Locations of the traverses are shown on Figure 4.

Correlation from traverse to traverse suggests that a network of finger-like lobes may anastomose at a particular bedding horizon and finally converge near the SW exposure of the Trachyte Mesa intrusion.

6. Discussion

The geometries of the three intrusions studied lie along the hypothesised evolution of an upper crustal intrusion from sill to laccolith to bysmalith. Individually, each intrusion provides insight into different aspects of shallow magma emplacement. Together, the intrusions provide a framework to consider several aspects of emplacement and assembly, including: (1) evolution of pluton geometry; (2) fabric patterns and magma flow evolution; (3) times scales of emplacement and assembly; and (4) heterogeneity of magma pulses in space and time.

6.1. Evolution of pluton geometry

The exceptional preservation of intrusion geometry in the Henry Mountains provides an informative view of the geometries of the three igneous bodies. Using observations of the intrusions as a guide, a hypothetical history of pluton assembly is presented during growth from sill to laccolith to bysmalith. Figure 8 shows idealised intrusion geometries for a sill, laccolith, and bysmalith with pulsed assembly histories. Figure 9 schematically shows both the primary emplacement mechanism (vertical displacement of the wallrock) and the preferred assembly histories for the three intrusions studied.

The Maiden Creek intrusion demonstrates the early stages of sill formation, which presumably involved a relatively small magma pulse spreading away from a pipe-like feeder in the form of finger-like lobes. In the immediate vicinity of the feeder, these lobes coalesced to form a sill-like body with a roughly elliptical shape in map view. A second magma pulse of approximately the same volume followed the same emplacement path, so that two stacked sheets comprise the intrusion.

The Trachyte Mesa intrusion demonstrates how a pluton can evolve into a sill-like body and begin to inflate into a laccolith. Further magma pulses (or larger initial pulses) spread beyond the nascent sill observed at the Maiden Creek intrusion to produce a larger and more mature sill. This more developed intrusion maintains the tabular cross-sectional geometry, but exhibits a more simple map-view geometry, in which finger-like lobes constitute a small portion of the total volume. Late magma pulses followed emplacement paths similar to early pulses. Additionally, the pulses thickened the intrusion a few metres at a time. Eventually, earlier emplaced sheets were rotated upward and sometimes intruded by subsequent sheets to form a laccolithic margin. Assembly of the Trachyte Mesa intrusion ceased at this stage with characteristics of both sill and laccolith geometries.

The Black Mesa intrusion illustrates further development of an igneous body with increased magma supply. As the number of emplaced sheets grew, the margins of the laccolith steepened. Eventually, a fault formed along the E margin of the

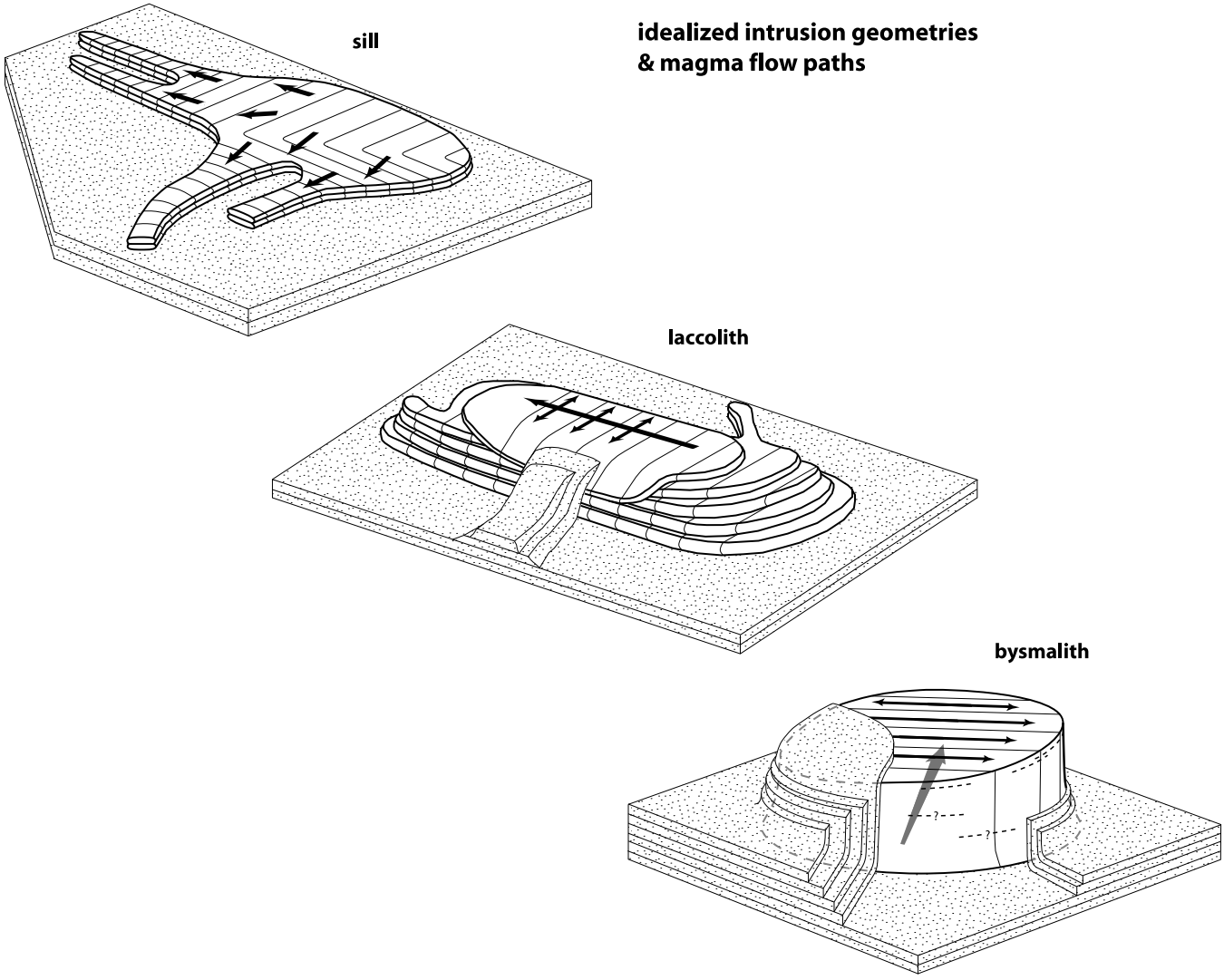

Figure 8 Schematic block diagrams of idealised intrusions, including magma sheets, inferred primary magma flow directions and relationships with sedimentary wallrock. These diagrams show characteristic features of intrusions with sill, laccolith and bysmalith geometries assembled from multiple pulses. Although the sketches are somewhat similar to the observed intrusions in the Henry Mountains, they do not accurately reflect those observations.

laccolith and the overburden was lifted in a piston-like manner to produce a bysmalith. The circular map pattern minimises the area of the intrusion-bounding fault, maximising the efficiency of overburden uplift. Additionally, the different geometries on the eastern and western margins of the Black Mesa intrusion provide clear evidence of the transitional nature of the change from laccolith to bysmalith. Emplacement of additional magma pulses would presumably have produced further roof uplift and eventually a fault around the entire pluton margin. Examples of well-developed bysmaliths are seen elsewhere in the Henry Mountains (e.g. Bull Mountain and Table Mountain on the Mt Ellen intrusive centre; Hunt 1953).

The main distinctions between the different types of intrusion appear to be (1) the amount of magma that is emplaced and (2) the manner in which the wallrock accommodates emplacement. The amount of magma appears to correspond to the specific number of magma pulses, recognisable as horizontal sheets at the periphery of the intrusion where cooling is rapid. The magma pulses must have similar volumes, within an order of magnitude, as they have similar thicknesses over approximately the same map area. The Maiden Creek intrusion consists of two magma pulses, the Trachyte Mesa intrusion consists of at least ten magma pulses, and thermal modelling suggests the Black Mesa consists of at least ten pulses (Saint Blanquat *et al.* 2006).

The Black Mesa intrusion also demonstrates the importance of the evolution of emplacement mechanisms as pluton volume grows. In fact, this intrusion preserves the transition of primary emplacement mechanism from wallrock rotation and distortion seen on the laccolithic western margin to wallrock uplift through faulting, as seen at the bysmalithic eastern margin. This transition is likely related to mechanical limits on the amount of strain the wallrock can accommodate, and perhaps to rates of deformation, with both high strain and high strain rates leading to localisation and faulting.

During the progression from sill to laccolith to bysmalith, the volumetric importance of peripheral lobes decreases as total pluton volume increases. For example, a large portion of the intrusive volume of the Maiden Creek sill occurs as lobes radiating away from a relatively small central main body. The Trachyte Mesa laccolith, finger-like lobes exist only at the margin of the relatively large main body of the intrusion. No such lobes are exposed as part of the approximately cylindrical Black Mesa intrusion. This decrease in the volumetric importance of finger-like lobes may reflect increasing stability of pluton geometry; emplacement of additional magma produces vertical pluton growth rather than lateral growth. Similarly,

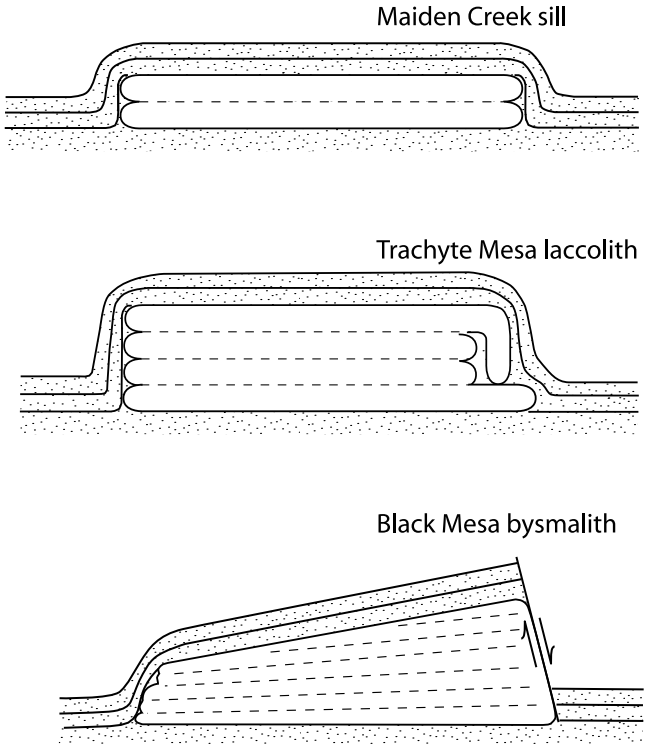

Figure 9 Schematic cross-sections through the Maiden Creek, Trachyte Mesa, and Black Mesa intrusions to illustrate idealised emplacement mechanisms and our preferred assembly histories. Intrusions are not drawn to scale. The number of pulses shown is intended to demonstrate relationships between successive pulses rather than actual number.

the cylindrical shape of the Black Mesa intrusion may have evolved from a less volumetrically efficient elongate laccolith, similar to the Trachyte Mesa intrusion, at an earlier stage.

6.1.1. Comparison with previous models. Pollard & Johnson (1973) developed a model of the evolution of pluton geometry that was mainly based on wallrock geometry. This model involves the following three stages: (1) Intrusion of an initial sill and growth by lateral propagation; (2) When a critical length/thickness ratio is achieved, the sill begins to inflate vertically by overburden bending to produce a laccolith, which is also still growing laterally; (3) Finally, fracturing of wallrocks over the periphery of the intrusion permits the uplift of both the wallrock and older igneous sheets. This fault-controlled roof uplift results in vertical growth and transforms the laccolith into a bysmalith.

The observations of the present authors are in general agreement with this succession of events (sill to laccolith to bysmalith), but not in agreement with the proposed mechanisms. First, no clear evidence is found for a true laccolithic stage of growth, for the three following reasons: (1) Each intrusion has a tabular, nearly flat roof, not a dome-like shape predicted by laccolithic growth; (2) Profiles of the contacts on the margins of all three intrusions (including the W side of Black Mesa) have a staircase-like shape rather than a smooth progressive bending predicted by classic laccolith models; and (3) The existence of simultaneous vertical and lateral propagation is not supported by the data. The initial sill of the Trachyte Mesa laccolith, for example, had a size similar to the final horizontal size of the pluton.

The idea of the achievement of the maximum horizontal size before the beginning of vertical growth is also supported by structural data from the wallrock. First, the absence of faults (i.e. 'remnant' hinges) in wallrock above all the intrusions shows that deformation remained localised more or less at the same place (along the margins) during growth. Thus, the vertical growth began after lateral growth, and consequently vertical growth was not accompanied by significant lateral growth. Secondly, in the marginal wallrock around the Black Mesa intrusion, not only sub-vertical, but also sub-horizontal and shallowly dipping fractures and faults have been measured, with normal and reverse slip sense (Saint Blanquat *et al.* 2006). These can be interpreted as remnants of flexural hinges developed during the beginning of the vertical growth, before the loss of continuity of the bedding (see fig. 16 of Corry 1988).

The question remains as to what factors control the change from sill-like emplacement to bysmalith-like emplacement during the growth of a large intrusion. As stated above, the present authors' observations contradict Pollard & Johnson's (1973) suggestion that the switch occurs once a laccolith reaches a particular radius relative to its thickness. Another possible controlling factor may be wallrock lithology, as suggested by the emplacement of the Black Mesa intrusion within relatively compliant shale (the Summerville formation), whereas the two smaller intrusions both formed within relatively stiff sandstone (the Entrada formation). Additional possibilities include an increase in magma emplacement rate, or variations in feeder position and geometry.

6.2. Fabric and magma flow patterns

The rapid cooling of the intrusions due to their small size and shallow depth ensures that the fabrics preserved in the plutons reflect magma flow patterns. Thus, by combining detailed knowledge of intrusion geometry with fabric data from the intrusions, the evolution of magma flow during emplacement and assembly can be considered. Additionally, the observations of feeder conduit geometry allow the examination of relationships between magma flow patterns and the magma supply.

Bulk magma flow patterns evolve as intrusion geometry progresses from sill to laccolith to bysmalith. In the Maiden Creek sill, a direct correlation is observed between the complex, lobate intrusion geometry and fabric patterns. Magma flowed radially out from an unexposed feeder into the main body and then was channelised into the lobate finger-like regions. The observed correspondence between geometry and fabric pattern thus provides a useful test of the utility of fabric analysis in these rocks. These complex, lobate geometries are not confined to the upper crust; Stevenson *et al.* (2007) inferred assembly of a mid-crustal pluton through emplacement of numerous finger-like magma pulses.

Magma flow patterns in the Trachyte Mesa intrusion reflect more organisation of the magma distribution system than developed in the Maiden Creek intrusion. Rather than flowing radially away from the feeder source in numerous sinuous lobes, magma flowed from the several sub-horizontal feeder pipes and, once in the intrusion, out along the central axial magma channel. From this channel, magma flowed out laterally to supply the margins of the intrusion. This bilaterally symmetric magma flow pattern bears a striking resemblance to inferred magma flow patterns in large, complex sills analysed in detailed three-dimensional seismic reflection studies (Thomson & Hutton 2004; Hansen & Cartwright 2006) and to physical models of magma flow by Kratinová *et al.* (2006). Although these patterns are commonly interpreted as resulting from flow away from a steeply dipping feeder dike (e.g. Ferré *et al.* 2002), these examples demonstrate that feeder geometry cannot be inferred from fabric data alone.

Magma flow patterns in the Black Mesa intrusion have a bilateral symmetry similar to that observed in the Trachyte Mesa intrusion. Both intrusions have central axial conduits

trending radially away from the main Mt Hillers intrusive centre. Additionally, the lateral margins of the both intrusions were presumably fed by flow away from an axial conduit. This similarity suggests that the magma distribution system may be similar in both the laccolith and the bysmalith. However, little fabric data from the interior of the Black Mesa intrusion is available, so this hypothesis is not well constrained. Nonetheless, the similarity suggests that early in its assembly history (i.e. preserved in fabrics near the roof) the Black Mesa intrusion went through a stage similar to that observed on the Trachyte Mesa intrusion. By extension, if the transition from laccolith to bysmalith involved vertical inflation and progression toward a cylindrical shape, it is consistent with the magma distribution system remaining stable throughout that geometric evolution. Thus, it appears that with increasing maturity of the magma distribution system, flow patterns evolve and become progressively more stable and efficient.

This analysis of correspondence between evolving intrusion geometry and magma flow patterns was possible only because the conditions were ideal for preservation of fabric in these small intrusions.

6.3. Pulsed assembly

Evidence of pulsed assembly exists in each of the three intrusions. This evidence is unequivocal in the Maiden Creek and Trachyte Mesa intrusions. In the Black Mesa intrusion, the sub-horizontal textural layering and cataclastic zones near the top of the intrusion suggest that early stages of assembly involved multiple magma pulses. The importance of magma pulses during the late stages of assembly of the Black Mesa intrusion is less clear, but vertical variation in geochemistry suggests that pulses existed throughout assembly (Bankuti 2007). Assuming that pulsed assembly continued throughout the growth of the intrusion, a threshold governing sheet contact preservation was crossed at some point. This threshold is of considerable interest because of the ongoing debate regarding possible pulsed assembly of large intrusions.

Several factors govern the preservation of evidence for pulses. Differences in composition of juxtaposed pulses result in the most easily recognisable contacts. A large temperature contrast between the pulse and the host rock (i.e. wallrock or a previous magma pulse) favours the development of solid-state fabric and makes pulse contacts more easily recognisable. The strain rate in the intruding magma must however be sufficiently high to produce solid-state fabric. A long time-lag between pulses allows the previous pulse to cool and favours strong fabric development. These several factors are interdependent and govern processes like annealing of emplacement-related fabric and reworking of pulse margins, both of which can destroy evidence of pulses.

For example, Tuffen & Dingwell (2005) demonstrate how early cataclastic fabrics in shallow volcanic conduits were modified and eventually destroyed by subsequent annealing and ductile deformation. They note that in some cases it is possible to recognise multiple generations of such overprinting structures. This cyclical brittle–ductile deformation may be a consequence of temperature variations moving the melt across liquid–glass transition. Thus, a new pulse of magma may reheat older solidified magma, including solid-state fabric, resulting in annealing and renewed flow deformation of the older magma. Matzal *et al.* (2006) present further evidence of reworking of pulse margins deeper in the crust. In their model, as a magma pulse is emplaced and begins to cool, the volumetric crystal percentage increases, and the remaining melt is largely trapped inside a crystal-rich carapace. Subsequent pulse emplacement reheats the margin of the previous sheet, partially incorporating some of the other material, and blurring the transition between the pulses both chemically and texturally.

The question remains at to why sheeting is clearly preserved in the Maiden Creek and Trachyte Mesa intrusions, but cryptic in the Black Mesa intrusion. Both the shallow depth of emplacement and the relatively small volume of all three intrusions contribute to rapid cooling. The lack of preservation in the Black Mesa intrusion demonstrates the ephemeral nature of such features, even with rapid cooling. The lack of field evidence of pulsed assembly in some deeper, larger intrusions (e.g. Glazner *et al.* 2004) is therefore not surprising. Pulsed assembly is, however, apparent in some plutons, despite the factors working against preservation of evidence. Most examples of large intrusions with pulsed assembly are composite plutons where pulses of different composition make recognition straightforward (Wiebe 1993, 1994; Wiebe & Collins 1998; Wiebe *et al.* 2002; Matzal *et al.* 2006; Michel *et al.* 2008), although evidence can be cryptic even in composite plutons (Mahan *et al.* 2003).

Host rock deformation can provide indirect evidence of magma pulses. Albertz *et al.* (2005) suggest that moderate background strain rates in pluton aureoles may be punctuated by high strain rate excursions associated with emplacement of magma pulses. Fernández & Castro (1999) called upon similar processes. These pulses of intense deformation can produce localisation of strain as shear zones or faults in the vicinity of plutons. This intense deformation is superposed upon the background deformation of host rock associated with pluton emplacement.

Several hypotheses exist for the formation of magma pulses and can be broadly divided into mechanisms due to: (1) ascent processes; (2) emplacement processes; or (3) source region processes. Ascent-related mechanisms suggest that interaction between magma ascending in sub-vertical dike-like or pipe-like channels results in formation of magma pulses (e.g. Denlinger & Hoblitt 1999). Emplacement-related mechanisms attribute magma pulses to similar interactions during pluton assembly rather than in the feeder conduit. The processes of magma generation and segregation in the source region operate an order of magnitude more slowly than the processes of ascent and emplacement (Petford *et al.* 2000). Thus, even minor cyclical processes in the source region can result in more dramatic cyclicity in the upper crust.

Regardless of the mechanisms leading to pulse formation, the existence of pulses may largely invalidate existing mechanical models of the growth of shallow intrusions (e.g. Pollard & Johnson 1973; Kerr & Pollard 1998; Zenzri & Keer 2001), which rely on entire igneous bodies acting as a single mechanical entity throughout assembly. Future theoretical models should account for empirical evidence for pulsed assembly and actual geometric shapes (e.g. flat rather than domed tops) of the intrusions. Further field-based work needs to concentrate on how magma flows during a single pulse, which can in turn constrain mechanical models of emplacement and assembly.

6.4. Time scales of emplacement and assembly

Recognition of the pulsed nature of the assembly of many upper-crustal plutons leads to the question of the time scales on which these processes operate. Few timing constraints exist for the Henry Mountains, but radiometric ages constrain timing at the scale of the entire range and, to a lesser extent, in individual intrusive centres (Nelson *et al.* 1992). For example, ages throughout the Henry Mountains span $\sim$9 Myr from 30 Ma to 21 Ma. Individual intrusive centres have age ranges restricted to $\sim$3 Myr or less. Other data provide evidence of the relative ages of component intrusions in intrusive centres. For example, Jackson & Pollard (1988) used palaeomagnetism

to demonstrate that early sills on Mt Hillers were rotated and uplifted by later magmatism that formed the underlying main laccolithic body.

Thermal modelling can provide additional constraints on assembly times for individual plutons (e.g. Annen *et al*. 2006). The present authors use one-dimensional thermal modelling of the Black Mesa intrusion by Habert & Saint Blanquat (2004) and Saint Blanquat *et al*. (2006) to provide a conservative maximum duration of pulsed assembly. Several assumptions and observations ensure that this thermal modelling provides a maximum estimate of the duration of assembly. First, the assumption of cooling solely through conduction provides a maximum estimate of the time necessary to cool through the solidus, because the advection of heat due to interaction with groundwater, or to the release of intrusion-related fluids, would cool the intrusion more rapidly than conduction alone. Secondly, the lack of evidence of clear contacts between separate magma pulses in the pluton constrains the time between pulses to be no longer than the time for the margin of last pulse to cool through the solidus. Results of the thermal model suggest that the lack of internal contacts can be explained if the intrusion formed in less than 100 years through the amalgamation of numerous sheets. This result implies that the roof lifted at least 2 m/yr during assembly. The less voluminous Maiden Creek and Trachyte Mesa intrusions were likely assembled in much shorter periods of time.

The time scales of the emplacement of individual component magma pulses are difficult to assess directly. However, individual pulses in each intrusion must be short lived, particularly if individual plutons are emplaced within 100 years (e.g. the Black Mesa intrusion). The magma supply clearly persisted for a lengthy period of time relative to the lifespan of a single pluton, or even a single intrusive centre. At the scale of the Mt Hillers intrusive centre, magma may have ascended in a few relatively large batches. However, the satellite intrusions studied in the present paper were likely assembled in myriad small, laterally fed pulses from the adjacent larger body.

Evidence from other studies reinforces the observations made in the Henry Mountains. Examples of the pulsed nature of assembly come from studies of both modern and ancient upper-crustal magmatism. Interferometric synthetic aperture radar studies demonstrate that sub-volcanic magma chambers inflate and deflate on time scales of weeks to months (e.g. Voight *et al*. 1998; Pritchard & Simons 2004). Henry *et al*. (1997) note that the Solitario laccolith-caldera is composed of three distinct episodes of magmatism, and demonstrate that these episodes are each composed of numerous magma pulses. Evans *et al*. (1993) used seismic reflection to recognise that the Lake District batholith is composed of numerous sub-horizontal sheets. Similarly, radiometric dating of such intrusions suggests that magmatism feeding a single intrusion can last a million years or even a few million years (Harrison *et al*. 1999; Glazner *et al*. 2004; Matzal *et al*. 2006). Such time spans are considerably longer (often by an order of magnitude) than it takes a shallow pluton assembled as a single large pulse to solidify.

Thus, several independent lines of evidence suggest that pluton assembly in the upper crust is not a continuous and gradual process. Rather, many plutons grow through the amalgamation of numerous pulses of magma. These pulses tend to be obscured even under conditions ideal for preserving evidence of magma pulses: high crustal levels, fast cooling rates, and no regional deformation. The characterisation of pulses likely depends on both the temporal and the spatial scales of observation.

6.5. Emplacement versus assembly

The exceptional exposure and ideal conditions for preserving evidence of magma pulses in the Henry Mountains allow us to make some statements about emplacement and assembly of plutons that are generally applicable to intrusions. The first concerns the difference between emplacement and assembly. The intrusions of the Henry Mountains inspired Gilbert (1877) to coin the term *laccolite*, which he used to describe a pluton that made space for itself by uplifting the overlying rocks. For the last 100 years, there has been no argument about the *emplacement* of the small intrusions in the Henry Mountains. The *assembly* of these plutons, in contrast, has not been understood. Although previously inferred to have formed from a single pulse of magma, the present work demonstrates that they occurred in multiple magma pulses. Thus, emplacement and assembly can be distinguished. The process of assembly by multiple pulses opens new fields of research. For instance, how does an individual magma pulse flow either into a pre-existing chamber or into wall rock? How do these patterns and processes evolve as subsequent pulses are emplaced? At present, these processes are largely unstudied.

Another unique aspect of the Henry Mountains is the well-exposed intrusion geometries, which allow the present authors to recognise that none of the three intrusions studied fits neatly into a common idealised geometry category. The Maiden Creek sill has a highly complex map-view geometry, despite its simple cross-sectional geometry. The Trachyte Mesa laccolith is largely tabular, similar to a sill, only bending the wallrocks on the margins of the intrusion. This pattern is consistent with most laccoliths, which commonly have flat rather than domed tops (Corry 1988). The Black Mesa intrusion is clearly transitional between a laccolith (on the west side) and a bysmalith (on the east side). These details of true intrusion geometry provide essential information about emplacement and assembly history. While idealised models provide a useful reference frame, they can lead to oversimplification of the mechanisms of emplacement, assembly, and magma flow.

Finally, there is the historical aspect of pluton emplacement and assembly. Many plutons assembled from multiple pulses change geometry considerably over time, as emplacement mechanisms accommodating sequential pulses evolve (e.g. McNulty *et al*. 2000; Belcher & Kisters 2006). The complexities inherent in analysing plutons in tectonically active regions (e.g. overprinting of fabrics, incomplete data sets, unknown three-dimensional geometries, etc.) make it difficult to directly compare them with the Henry Mountains intrusions. However, many of the same features are found in both cases, suggesting that similar processes operate during emplacement and assembly, regardless of differences in scale or the presence of tectonic activity (e.g. McCaffrey & Petford 1997; Saint Blanquat *et al*. in press).

7. Conclusions

The three intrusions studied in the Henry Mountains represent successive snapshots of the emplacement of an upper crustal pluton during geometric evolution from sill to laccolith to a piston-like bysmalith. Assembly of each of these intrusive bodies occurred through a series of magma pulses, manifested locally as distinct magma sheets. The exceptionally well-preserved intrusion geometries demonstrate that idealised models of intrusion shape are overly simplistic. These bodies appear to be fed by sub-horizontal, pipe-like conduits emanating from the main intrusive centre, located several kilometres away.

Magma flow patterns are well preserved because of rapid cooling due to the small intrusion volumes, rapid assembly, and shallow depth of emplacement. These magma flow patterns correspond well with observed complex intrusion geometries. Early magma flow in the sill involved radial flow away from a pipe-like feeder and into several finger-like lobes. As intrusion volume grew, the magma distribution system stabilised through the formation of a central axial conduit that fed magma laterally out to the pluton margins. During further growth this magma distribution system remained stable, and consistent magma flow patterns reflect this stability. Increasing intrusion volume also resulted in the evolution of the primary emplacement mechanism: from wallrock uplift; through rotation; to distortion at intrusion margins; to wallrock uplift through faulting.

Evidence of the magma pulses comprising each body becomes more cryptic as intrusion volume grows. Many processes can obscure evidence of pulses and these processes typically become more effective at deeper crustal levels. Thus, a lack of evidence does not necessarily imply a lack of pulsed assembly.

It is concluded that assembly of these igneous intrusions occurs through the amalgamation of numerous pulses of magma, which may be a common occurrence in upper crustal intrusions. These pulsed emplacement and assembly processes operate at many spatial and temporal scales. The conditions in the Henry Mountains – shallow crustal levels, fast cooling rates, and no regional deformation – were ideal for the preservation of internal structures. As the conditions of emplacement and assembly for most plutons are considerably more complex, preservation of primary internal structures is less likely.

8. Acknowledgements

We thank participants from the 2005 G.S.A. field trip to observe these intrusions for numerous thoughtful discussions and an abundance of constructive criticism. Buzz Rackow at the Hanksville B.L.M. office and Dave Dilloway provided logistical assistance. Sandy Cruden and an anonymous reviewer helped improve the manuscript substantially. This work was funded by NSF grant EAR-0003574 to BT and SM. Additional funding came from CNRS/NSF grant 12971 to MSB, NSF grant EAR-0510893 grant to BT, a FRCE-CMU grant to SM, and a Shell Undergraduate Fellowship at the University of Wisconsin to RAH.

9. References

Albertz, M., Paterson, S. R. & Okaya, D. 2005. Fast strain rates during pluton emplacement: magmatically folded leucocratic dikes in aureoles of the Mount Stuart Batholith, Washington, and the Tuolumne Intrusive Suite, California. *Geological Society of America Bulletin* **117**, 450–65.

Annen, C., Scaillet, B. & Sparks, R. S. J. 2006. Thermal constraints on the emplacement rate of a large intrusive complex: the Manaslu Leucogranite, Nepal Himalaya. *Journal of Petrology* **47**, 71–95.

Bankuti, M. 2007. *Pétro-généalogie des intrusions du Mont Hillers, Utah, USA*. Unpublished M.S. Thesis, Université Paul-Sabatier, Toulouse, France. 57 pp.

Belcher, R. W. & Kisters, A. F. M. 2006. Syntectonic emplacement and deformation of the Heerenveen Batholith; conjectures on the structural setting of the 3·1 Ga granite magmatism in the Barberton granite-greenstone terrain, South Africa. *Geological Society of America, Special Paper* **405**, 211–32.

Coleman, D. S., Gray, W. & Glazner, A. F. 2004. Rethinking the emplacement and evolution of zoned plutons; geochronologic evidence for incremental assembly of the Tuolumne Intrusive Suite, California. *Geology* **32**, 433–6.

Corry, C. E. 1988. Laccoliths: Mechanics of emplacement and growth. *Geological Society of America, Special Paper* **220**, 110 pp.

Denlinger, R. P. & Hoblitt, R. P. 1999. Cyclic eruptive behavior of silicic volcanoes. *Geology* **27**, 459–62.

Fernandez, C. & Castro, A. 1999. Pluton accommodation at high strain rates in the upper continental crust; the example of the Central Extremadura Batholith, Spain. *Journal of Structural Geology* **21**, 1143–9.

Evans, D. J., Rowley, W. J., Chadwick, R. A. & Millward, D. 1993. Seismic reflections from within the Lake District Batholith, Cumbria, Northern England. *Journal of the Geological Society, London* **150**, 1043–6.

Ferré, E. C., Bordarier, C. & Marsh, J. S. 2002. Magma flow inferred from AMS fabrics in a layered mafic sill, Insizwa, South Africa. *Tectonophysics* **354**, 1–23.

Gaffney, E. S., Damjanac, B. & Valentine, G. A. 2007. Localization of volcanic activity: 2. Effects of pre-existing structure. *Earth and Planetary Science Letters* **263**, 323–8.

Gilbert, G. K. 1877. *Report on the Geology of the Henry Mountains*. U.S. Geological Survey. 170 pp.

Glazner, A. F., Bartley, J. M., Coleman, D. S., Gray, W. & Taylor, R. Z. 2004. Are plutons assembled over millions of years by amalgamation from small magma chambers? *GSA Today* **14**, 4–11.

Habert, G. & de Saint-Blanquat, M. 2004. Rate of construction of the Black Mesa bysmalith, Henry Mountains, Utah. *In* Breitkreuz, C. & Petford, N. (eds) *Physical Geology of High-level Magmatic Systems. Geological Society, London, Special Publication* **234**, 163–730. Bath, UK: The Geological Society Publishing House.

Hansen, D. M. & Cartwright, J. 2006. Saucer-shaped sills with lobate morphology revealed by three-dimensional seismic data: implications for resolving a shallow-level sill emplacement mechanism. *Journal of the Geological Society, London* **163**, 509–23.

Harrison, T. M., Grove, M., Lovera, O. M., Catlos, E. J., D'Andrea, J. & McKeegan, K. 1999. Origin and episodic emplacement of the Manaslu Intrusive Complex, Central Himalaya. *Journal of Petrology* **40**, 3–19.

Henry, C. D., Kunk, M. J., Muehlberger, W. R. & McIntosh, W. C. 1997. Igneous evolution of a complex laccolith-caldera, the Solitario, Trans-Pecos Texas: implications for calderas and subjacent plutons. *Geological Society of America Bulletin* **109**, 1036–54.

Horsman, E., Tikoff, B. & Morgan, S. 2005. Emplacement-related fabric and multiple sheets in the Maiden Creek Sill, Henry Mountains, Utah, USA. *Journal of Structural Geology* **27**, 1426–44.

Hunt, C. 1953. *Geology and geography of the Henry Mountains region, Utah. US Geological Survey Professional Paper* **228**.

Hutton, D. H. W. 1988. Granite emplacement mechanisms and tectonic controls; inferences from deformation studies. *Transactions of the Royal Society of Edinburgh: Earth Sciences* **79**, 245–55.

Hutton, D. H. W. 1997. Syntectonic granites and the principle of effective stress. *In* Bouchez, J. L., Hutton, D. H. & Stephans, W. E. (eds) *Granite: From segregation of melt to emplacement fabrics*, 189–98. Dordrecht: Kluwer.

Jackson, M. D. & Pollard, D. D. 1988. The laccolith-stock controversy: new results from the southern Henry Mountains, Utah. *Geological Society of America Bulletin* **100**, 117–39.

Jackson, M. D. & Pollard, D. D. 1990. Flexure and faulting of sedimentary host rocks during growth of igneous domes, Henry Mountains, Utah. *Journal of Structural Geology* **12**, 185–206.

Johnson, A. M. & Pollard, D. D. 1973. Mechanics of growth of some laccolithic intrusions in the Henry Mts, Utah, I: Field observations, Gilbert's model, physical properties and the flow of magma. *Tectonophysics* **18**, 261–304.

Kerr, A. D. & Pollard, D. D. 1998. Toward more realistic formulations for the analysis of laccoliths. *Journal of Structural Geology* **20**, 1783–93.

Kratinová, Z., Zavada, P., Hrouda, F. & Schulmann, K. 2006. Non-scaled analogue modelling of AMS development during viscous flow: A simulation on diapir-like structures. *Tectonophysics* **418**, 51–61.

Lipman, P. W. 1987. The roots of ash-flow calderas in western North America: windows into the tops of granitic batholiths. *Journal of Geophysical Research* **89**, 8801–41.

Lipman, P. W. 2007. Incremental assembly and prolonged consolidation of Cordilleran magma chambers: evidence from the Southern Rocky Mountain volcanic field. *Geosphere* **3**, 42–70.

Mahan, K. H., Bartley, J. M., Coleman, D. S., Glazner, A. F. & Carl, B. 2003. Sheeted intrusion of the synkinematic McDoogle pluton, Sierra Nevada, California. *Geological Society of America Bulletin* **115**, 1570–82.

Matzel, J. E. P., Bowring, S. A. & Miller, R. B. 2006. Time scales of pluton construction at differing crustal levels; examples from the Mount Stuart and Tenpeak Intrusions, north Cascades, Washington. *Geological Society of America Bulletin* **118**, 1412–30.

McCaffrey, K. J. W. & Petford, N. 1997. Are granitic intrusions scale invariant? *Journal of the Geological Society, London* **154**, 1–4.

McNulty, B. A., Tobisch, O. T., Cruden, A. R. & Gilder, S. 2000. Multistage emplacement of the Mount Givens Pluton, central Sierra Nevada Batholith, California. *Geological Society of America Bulletin* **112**, 119–35.

Michel, J., Baumgartner, L., Putlitz, B., Schaltegger, U. & Ovthcarova, M. 2008. Incremental growth of the Patagonian Torres del Paine laccolith over 90 k.y. *Geology* **36**, 459–62.

Morgan, S. S., Stanik, A., Horsman, E., Tikoff, B., de Saint-Blanquat, M. & Habert, G. 2008. Emplacement of multiple magma sheets and wallrock deformation: Trachyte Mesa intrusion, Henry Mountains, Utah. *Journal of Structural Geology* **30**, 491–512.

Morgan, S. S., Horsman, E., Tikoff, B., de Saint-Blanquat, M. & Habert, G. 2005. Sheet-like emplacement of satellite laccoliths, sills and bysmaliths of the Henry Mountains, southern Utah. *Geological Society of America Field Guide* **6**, 283–309.

Nelson, S. T., Davidson, J. P. & Sullivan, K. R. 1992. New age determinations of central Colorado Plateau laccoliths, Utah: Recognizing disturbed K–Ar systematics and re-evaluating tectonomagmatic relationships. *Geological Society of America Bulletin* **104**, 1547–60.

Nelson, S. T. 1997. Reevaluation of the Central Colorado plateau laccoliths in the light of new age determination. *US Geological Survey Bulletin* **2158**, 37–9.

Paterson, S. R., Fowler, T. K., Jr., Schmidt, K. L., Yoshinobu, A. S., Yuan, E. S. & Miller, R. B. 1998. Interpreting magmatic fabric patterns in plutons. *Lithos* **44**, 53–82.

Paterson, S. R. & Fowler, T. R., Jr. 1993. Re-examining pluton emplacement processes. *Journal of Structural Geology* **15**, 191–206.

Petford, N., Cruden, A. R., McCaffrey, K. J. W. & Vigneresse, J. L. 2000. Granite magma formation, transport and emplacement in the Earth's crust. *Nature* **408**, 669–73.

Pollard, D. D. 1973. Derivation and evaluation of a mechanical model for sheet intrusions. *Tectonophysics* **19**, 233–69.

Pollard, D. D. & Johnson, A. M. 1973. Mechanics of growth of some laccolithic intrusions in the Henry Mountains, Utah, Part II: Bending and failure of overburden and sill formation. *Tectonophysics* **18**, 311–54.

Pritchard, M. E. & Simons, M. 2004. An InSAR-based survey of volcanic deformation in the Southern Andes. *Geophysical Research Letters* **31**, L15610. doi:10.1029/2004GL020545.

Saint Blanquat, M. (de), Habert, G., Horsman, E., Morgan, S., Tikoff, B., Launeau, P. & Gleizes, G. 2006. Mechanisms and duration of non-tectonically assisted magma emplacement in the upper crust, the Black Mesa pluton, Henry Mountains. *Tectonophysics* **428**, 1–31.

Saint-Blanquat, M. (de), Horsman, E., Habert, G., Law, R. D., Morgan, S., Tikoff, B. & Vanderhaeghe, O. in press. Multiscale magmatic cyclicity, duration of pluton construction and the paradoxical relationship between tectonism and plutonism in continental arcs. *Tectonophysics*.

Stevenson, C. T. E., Owens, W. H. & Hutton, D. H. W. 2007. Flow lobes in granite: the determination of magma flow direction in the Trawenagh Bay granite, NW Ireland, using AMS. *Geological Society of America Bulletin* **119**, 1368–86.

Thompson, G. A. & Zoback, M. L. 1979. Regional geophysics of the Colorado Plateau. *Tectonophysics* **61**, 149–81.

Thomson, K. & Hutton, D. H. W. 2004. Geometry and growth of sill complexes: insights using 3-d seismic from the North Rockall Trough. *Bulletin of Volcanology* **66**, 364–75.

Tuffen, H. & Dingwell, D. B. 2005. Fault textures in volcanic conduits: evidence for seismic trigger mechanisms during silicic eruptions. *Bulletin of Volcanology* **67**, 370–87.

Voight, B., Hoblitt, R. P., Clarke, A. B., Lockhart, A., Miller, A. D., Lynch, L. & McMahon, J. 1998. Remarkable cyclic ground deformation monitored in real-time on Montserrat and its use in eruption forecasting. *Geophysical Research Letters* **25**, 3405–8.

Weinberg, R. F. 1996. Ascent mechanism of felsic magmas: news and views. *Geological Society of America, Special Paper* **315**, 95–103.

Wiebe, R. A. 1993. The Pleasant Bay layered gabbro-diorite, coastal Maine; ponding and crystallization of basaltic injections into a silicic magma chamber. *Journal of Petrology* **34**, 461–89.

Wiebe, R. A. 1994. Silicic magma chambers as traps for basaltic magmas; the Cadillac Mountain intrusive complex, Mount Desert Island, Maine. *Journal of Geology* **102**, 423–37.

Wiebe, R. A. & Collins, W. J. 1998. Depositional features and stratigraphic sections in granitic plutons: Implications for the emplacement and crystallization of granitic magma. *Journal of Structural Geology* **20**, 1273–89.

Wiebe, R. A., Blair, K. D., Hawkins, D. P. & Sabine, C. P. 2002. Mafic injections, *in situ* hybridization, and crystal accumulation in the Pyramid Peak granite, California. *Geological Society of America Bulletin* **114**, 909–20.

Zenzri, H. & Keer, L M. 2001. Mechanical analyses of the emplacement of laccoliths and lopoliths. *Journal of Geophysical Research* **106**, 13781–92.

MS received 18 January 2008. Accepted for publication 3 June 2008 (Stellenbosch); 15 January 2009 (RSE).

Four-stage building of the Cambrian Carion pluton (Madagascar)

M. O. M. Razanatseheno[1], A. Nédélec[2], M. Rakotondrazafy[1], J. G. Meert[3] and B. Ralison[1]

[1] Department of Earth Sciences, BP 906, Antananarivo University, Madagascar

[2] LMTG – OMP, Toulouse University – CNRS-IRD, 14 avenue Edouard Belin, 31400 Toulouse, France
Email: nedelec@lmtg.obs-mip.fr

[3] Department of Geological Sciences, 241 Williamson Hall, Gainesville University, Florida 32611, USA

ABSTRACT: The 532 ± 5 Ma old Carion pluton is a dark, porphyritic ferro-potassic granitoid emplaced near the late Pan-African Angavo mega-shear zone. A rough normal zoning from tonalitic to granitic compositions can be recognised in the field. Steep magmatic foliations are evidenced by K-feldspar megacryst preferred orientations. Microstructures are either magmatic or typical of incipient solid-state deformation in near solidus conditions. Magnetic susceptibility magnitudes (K) range from 11 to 111×10^{-3} SI in the pluton and can be correlated to the petrography (highest K values in the tonalites; lowest K in the granites; granodiorites in between). The susceptibility magnitudes display a complex zoning pattern. Combined with the arrangement of magnetic foliation trajectories, it is possible to delineate four nested sub-units, regarded as four magmatic pulses successively emplaced from the west to the east of the pluton. The four pulses are characterised by very similar magma geochemistry, but variable magmatic differentiation. The highest degrees of magnetic susceptibility anisotropies (up to 1·6) are observed along internal contacts between sub-units and along the borders of the pluton. The magnetic lineations are also steeply plunging in some places in each sub-unit, possibly imaging the different feeder zones. Magma emplacement occurred at the end of the activity of the Angavo shear zone, hence avoiding re-orientation of the magmatic structures by the late Pan-African transcurrent tectonics. The diachronicity of the four magmatic pulses is consistent with previously determined palaeomagnetic data, because only the two older sub-units display a magnetic reversal sequence, whereas the two youngest sub-units lack any reversion. Emplacement of these four magmatic batches was responsible for a strain aureole and suggests a diapiric mode of ascent.

KEY WORDS: anisotropy of magnetic susceptibility, diapir, granitoid, magnetic reversal, zoned pluton

Granitic plutonism is particularly active in collision orogens in which both the thermal conditions necessary for magma genesis and the loci for magma ascent and emplacement in the crust are present. In such collisional settings, granite magma production follows continental suturing by a few tens of Mys and remains often voluminous until the last stages of orogeny (Thompson & Connolly 1995). In a pre-drift reconstruction of Gondwana (Fig. 1a), Madagascar is located in the East African Orogen, a collisional orogen formed by the closure of the Mozambique Ocean at the end of Neoproterozoic times (Stern 1994; Meert 2003). A number of granitoid plutons were emplaced in Madagascar at various stages. The late-Pan-African history of Madagascar is dominated by transcurrent tectonics along major shear zones, especially in the southern and eastern parts of the island (Martelat *et al.* 1997; Ralison & Nédélec 1997; Nédélec *et al.* 2000).

This present study focuses on the Carion pluton (Fig. 1b, c), located near the Angavo shear zone, a lithospheric-scale transcurrent shear zone (Ralison & Nédélec 1997), that has been active at around 550 Ma, as can be inferred from the ages of spatially-related syntectonic and deformed granitic rocks (Kröner *et al.* 1999; Grégoire *et al.* 2008). The Angavo shear zone is associated with low-pressure granulitic parageneses and prograde charnockitisation, whose P and peak T conditions were calculated at 790 (± 10)°C and 330 (± 30) MPa by Nédélec *et al.* (2000). The Carion pluton itself crystallised at about 320 (± 10) MPa (i.e. at about 10 km depth) after Al-in-hornblende barometric calculations using the calibration of Schmidt (1992). It has been dated at 532 (± 5) Ma by SHRIMP zircon age (Meert *et al.* 2001b). Hence, it was slightly younger than the transcurrent tectonics along the Angavo shear zone, therefore representing one of the latest stage of Pan-African magmatism in Madagascar. On the geological map of Besairie (1969), it is classified as a post-tectonic pluton.

Since the pioneer work of Ellwood & Whitney (1980), anisotropy of magnetic susceptibility (AMS) has been proven the most efficient tool in determining the internal fabric of granitic plutons, as recently reviewed by Bouchez (1997; 2000 and references therein). This method is here applied to the Carion pluton. Preliminary AMS results were already provided by Nédélec *et al.* (2000). These authors observed well-defined magnetic/magmatic foliations and steeply plunging magnetic/magmatic lineations, in sharp contrast with the sub-horizontal N–S lineations of the nearby Angavo shear zone, hence confirming the late- to post-tectonic character of the pluton. The present paper provides a more detailed AMS study

© 2009 The Royal Society of Edinburgh. doi:10.1017/S1755691009016156

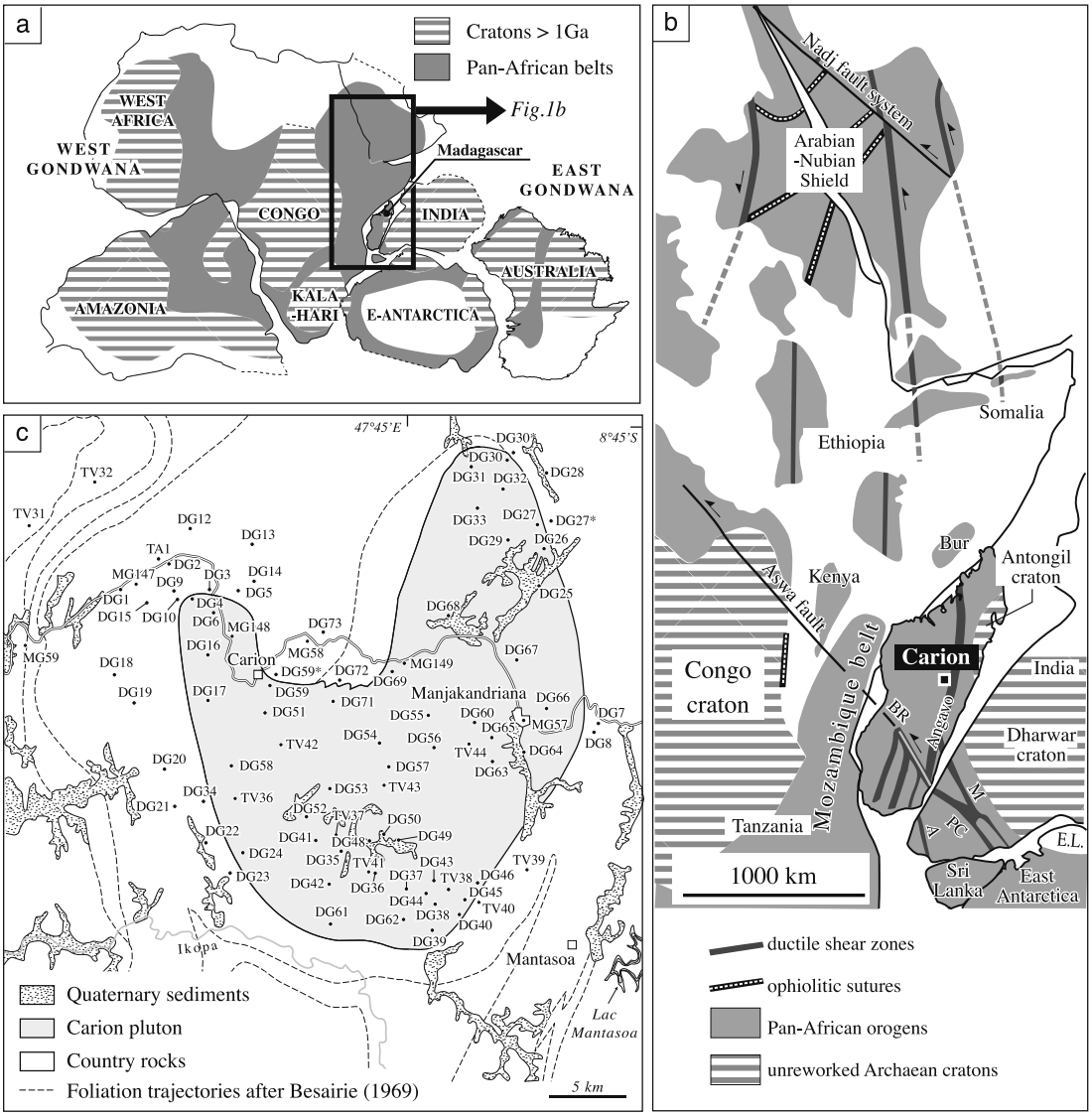

Figure 1 (a) Gondwana reconstruction at 550 Ma after Lawver *et al.* (1998). (b) The East African Orogen at 550 Ma after Abdelsalam & Stern (1996), Nédélec *et al.* (2000) and Reeves & de Wit (2001). Shear zones: A=Achankovil: BR=Bongolava-Ranostsara: M=Moyar; PC=Palghat–Cauvery: E.L.=Enderby Land. (c) Location of AMS sampling sites.

of the pluton and its wall rocks. Combined with field geology and petrology data, it reveals the internal structure of the pluton. These data are in turn used to infer the magma emplacement mode. In addition, they highlight previous observations related to former palaeomagnetic results and Ar–Ar geochronology of Meert *et al.* (2001b).

1. Field and petrology data

The Carion pluton extends over $\sim$370 km^2 and its elliptical shape is deeply indented to the north (Fig. 1c). Country rocks are made of migmatites, pink biotite granites, hornblende gneisses and charnockites, that all belong to the Ambatolampy Group of the Graphite System (Besairie 1969; Hottin 1976). On the maps, foliations of the country rocks were drawn parallel with the massif contours, except in the northern indentation, where they seem to be crosscut by the intrusion, hence the post-tectonic setting first proposed by Lautel (1953). The pluton area is rather hilly (Fig. 2a), with good outcrops (some of them used as quarries), due to the fact that the granitic rocks are less weatherable than their gneissic host rocks. The Carion pluton does not show any contact metamorphism at its margins, evidencing the lack of thermal contrast between the magma and its host rocks. When observed, contacts are not sharp. There is often a transition zone up to 1 km in width, where the granitic magma formed conformable sheets within the country rocks. To the northwest, the magma was intruded as a sinuous veining network in the nearby migmatites (Fig. 2e), suggesting that the country rocks were still hot and soft. Rafts and xenoliths of migmatites of various sizes can be observed in the southern margin of the pluton (Fig. 2d). Hence, the pluton contours drawn in the maps represent a simplification.

The first detailed petrographic account of the Carion Massif was given by Hottin (1975). This author underlined the foliated nature of the granite, but failed to recognise the mainly magmatic nature of the foliation, and, for this reason, regarded the intrusion as an orthogneissified body, a contention that is no longer tenable in the light of microscopic observations (Fig. 3). As observed by Hottin (1975), the main rock type is a mesocratic (medium to dark grey) porphyritic granitoid containing K-feldspar megacrysts with an average length of 3 cm. The feldspar preferred orientation is responsible for the conspicuous magmatic foliation observed in the field (Fig. 2b). Apart from the megacrysts, rocks are medium- to coarse-grained, with an average grain-size of about 5 mm.

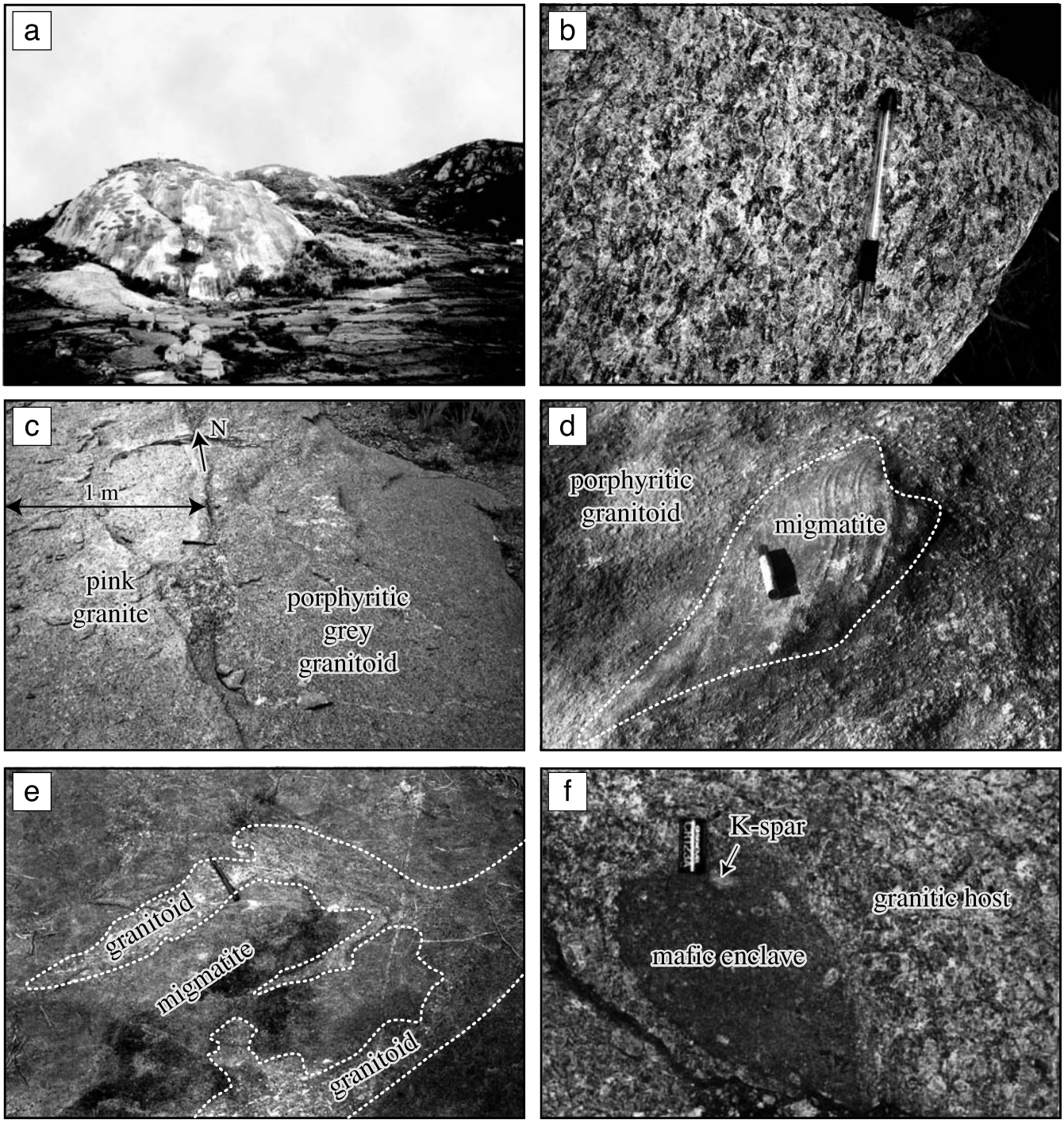

Figure 2 (a) Characteristic dome outcrop in Carion pluton. (b) Typical porphyritic Carion granitoid with conspicuous foliation. (c) Contact between prophyritic grey granitoid and pink granite at site DG52. (d) Elongate xenolith of migmatite at site DG 5. (e) Veining network of porphyritic granitoid in wall rock migmatite at site DG 9. (f) Microgranumlar mafic enclave within a granitic host at site DG 5.

Scarce mafic microgranular enclaves are globular in shape and no more than a few tens of centimetres in length. Feldspar megacrysts were mechanically introduced from the host granitic magma into these enclaves before their complete crystallisation, pointing to their co-magmatic nature (Fig. 2f).

Towards the margins of the intrusion, feldspar megacrysts are smaller and less abundant, and plagioclase prevails over alkali feldspar, hence a tonalitic composition. In the centre of the pluton, rocks are lighter in colour (light grey to pink), due to less abundant ferro-magnesian minerals and to the pink colour of the K-feldspar megacrysts; they have a granitic composition. A pink leucogranite sometimes forms magmatic dykes or larger hectometric stocks, but its porphyritic texture is very similar to the texture of the main petrographic type (Fig. 2c).

Mineral abundances and compositions are determined in thin sections and by electron microprobe analyses. Feldspars, both as megacrysts and as interstitial grains, constitute about 60% of the rocks. The K-feldspar megacrysts are made of perthitic orthose or microcline (Fig. 3a). Plagioclase are nearly unzoned, with a usually restricted composition in the range An_{26-20}. Quartz is present as large crystals, sometimes elongate parallel to the magmatic foliation (Fig. 3b). The grains often display chessboard patterns due to both prismatic and basal subgrain boundaries, attesting for incipient solid-state deformation in near solidus conditions. However, the lack of

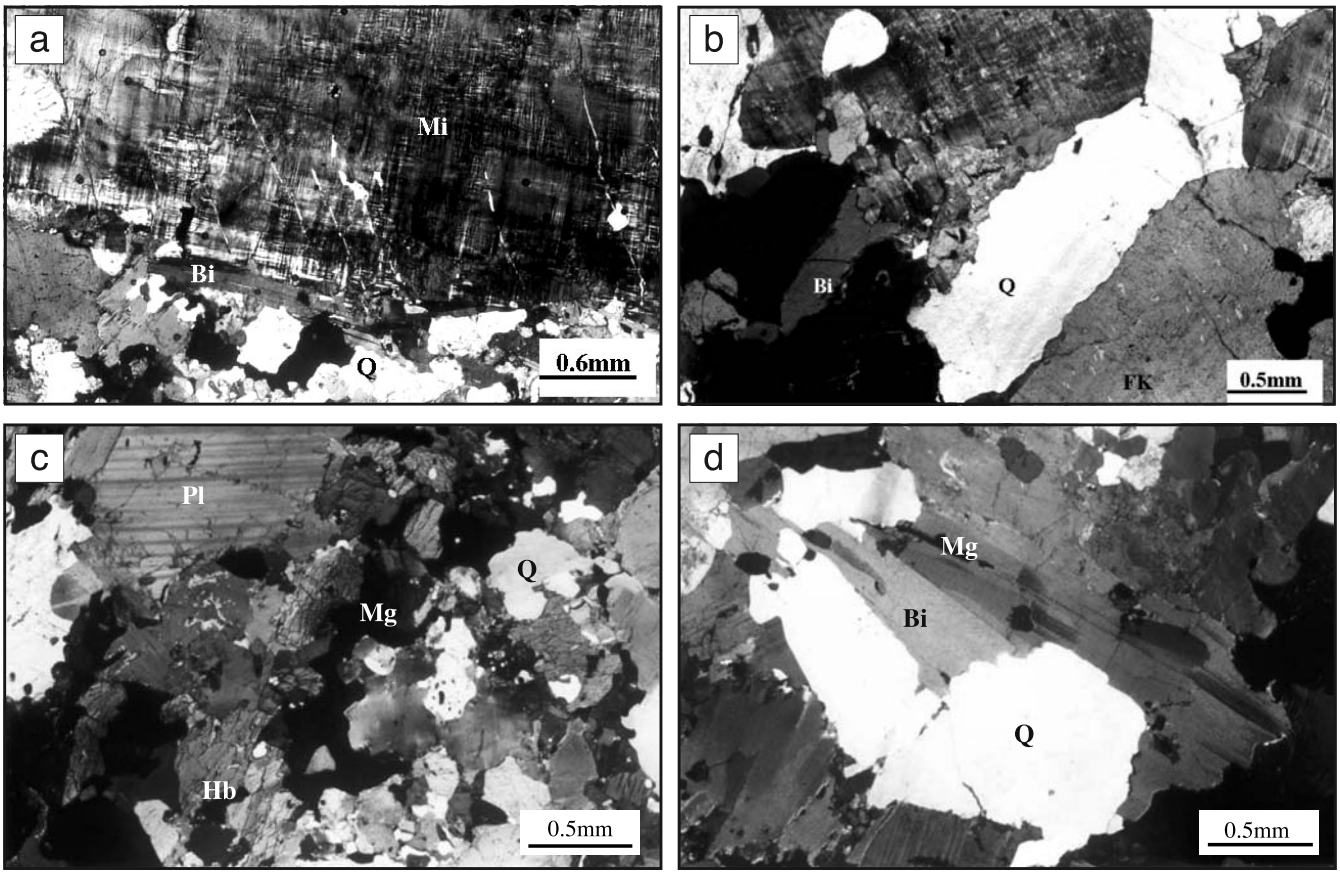

Figure 3 (a) Microcline megacryst (Mi), biotite (Bi) and quartz (Q) in sample DG 62 (crossed polars). (b) Elongate quartz grain (Q), slightly perthitic K-feldspar (FK) and biotite (Bi) in sample DG60 (crossed polars). (c) Cluster of hornblende (Hb) and magnetite (Mg) along the boundary of a subautomorphic plagioclase (Pl) in sample DG 52 (crossed polars). (d) Quartz (Q) (large undeformed grain), biotite (Bi) and associated magnetite (Mg) in sample DG 60 (crossed polars).

recrystallised grains testifies that no significant deformation occurred after the solidification of the magma. Ferro-magnesian silicate minerals are hornblende, actually edenite or magnesio-hornblende after the classification of Leake *et al.* (1997), and biotite. They often form clusters with accessory minerals (Fig. 3c). Biotite is ubiquitous (Fig. 3b–d), whereas hornblende is rare or absent in the most evolved (granitic) rocks. Whatever the rock type, hornblende and biotite contain a relatively high magnesium fraction (XMg=0·6–0·7) and are also characterised by a relatively high fluorine content (XF=0·3–0·5), as can be seen in Table 1. Accessory minerals are ilmenite, magnetite, titanite, apatite and zircon. The iron oxide compositions were determined by electron microprobe analysis (Table 1). Ilmenite is the most abundant accessory mineral and forms aggregates, together with titanite and apatite, in the interstitial spaces surrounding the large feldspar and quartz grains (Fig. 3a, c). Ilmenite crystals sometimes contain a few haematite exsolution lamellae. Magnetite is less abundant than ilmenite and is also observed as inclusions in feldspars and ferro-magnesian silicates, pointing to its earlier crystallisation in the magma.

Whole-rock compositions of seven representative samples are given in Meert *et al.* (2001a). The darkest tonalites from the eastern and western sides have silica contents in the 61–63% range and total iron oxide contents of about 6%, whereas the most evolved rock, a pink granite from the southern central area of the pluton, has a silica content of about 70% and an iron oxide content of 2·6%. Other samples display major element contents in between these endmembers. All analysed rocks are metaluminous and follow the sub-alkaline magmatic trend in the R1–R2 diagram of La Roche *et al.* 1980 (Fig. 4a). More precisely, they are highly potassic (shoshonitic) and ferriferous magmatic rocks (Meert *et al.* 2001a; Rakotondrazafy *et al.* 2001). On the basis of field and geochemical data, the Carion pluton had been regarded so far as a simple normally zoned pluton (Fig. 4b).

2. AMS data

2.1. Material and methods

Internal fabrics of granitic rocks are generally difficult to measure through classic techniques based on direct observation. For instance, lineations are difficult to determine in the field, even in the case of a well foliated porphyritic granite like the Carion granite. AMS measurements provide scalar parameters as well as foliation and lineation maps that, combined with petrographic and microstructural data, make it possible to refine the internal structure of the Carion pluton and to infer its emplacement history. Preliminary structural data on the Carion pluton was based on ten sampling sites in the pluton and seven sites in its wall rocks, that were part of an extensive AMS and metamorphic study in an area extending over 150 km by 70 km around Antananarivo city (Nédélec *et al.* 2000). This first data set was augmented by 48 sites in the plutons and 25 in the country rocks, resulting in a total of 58 sampling sites within the Carion pluton and 32 sites in the surroundings (Fig. 1c). A sampling station is characterised by two to eleven (median value: four) oriented cylinder specimens (22 mm in length and 25 mm in diameter). AMS was determined using a Kappabridge KLY 2 susceptometer (AGICO, Brno, Czech Republic) with a detection limit of about

Table 1 Representative compositions of iron-bearing minerals. Structural formulae on the basis of 13 cations (+Ca, Na, K) for amphiboles, 22 O for biotites, three cations for magnetite and two cations for ilmenite and hematite. ∞=calculated; FeO*=total Fe as FeO.

Amphiboles				Biotites		
Rock type	Tonalites		Granite	Rock type	Tonalite	Granite
Sample no.	GC 24	DG 62	GC 12	Sample no.	GC 24	GC 12
SiO_2	43·00	44·03	43·87	SiO_2	37·64	37·86
TiO_2	1·44	1·40	1·10	TiO_2	3·73	2·33
Al_2O_3	8·96	8·63	8·07	Al_2O_3	13·05	12·29
Fe_2O_3 ∞	2·59	5·14	3·90	FeO*	14·13	15·42
FeO ∞	13·66	10·38	13·86	MnO	0·41	0·45
MnO	0·48	0·38	0·66	MgO	15·4	14·81
MgO	11·45	12·63	10·91	Na_2O	0·12	0·07
CaO	11·78	11·19	11·67	K_2O	10·24	9·53
Na_2O	1·94	1·85	1·64	F	2·72	2·63
K_2O	1·48	1·56	1·25	Cl	0·00	0·20
F	1·08	1·72	1·75	Total	0·00	0·00
Cl	0·15	0·16	0·16			
Total	99·06	99·45	98·58	Si	5·68	5·77
				Al^{IV}	2·32	2·23
Si	6·54	6·58	6·66	Al^{VI}	0·00	0·00
Al^{IV}	1·46	1·42	1·34	Ti	0·42	0·41
Al^{VI}	0·14	0·11	0·11	Fe	1·78	1·96
Ti	0·17	0·16	0·13	Mn	0·05	0·06
Fe^{3+}	0·30	0·58	0·45	Mg	3·46	3·36
Fe^{2+}	1·74	1·30	1·76	Na	0·04	0·02
Mg	2·59	2·81	2·47	K	1·97	1·85
Mn	0·06	0·05	0·09	Sum cations	15·74	15·68
Ca	1·92	1·79	1·90	F	1·27	1·23
Na(B)	0·08	0·21	0·10	Cl	0·00	0·05
Na(A)	0·49	0·33	0·38	OH ∞	2·73	2·85
K	0·29	0·30	0·24			
Sum cations	15·78	15·63	15·62	X Mg	0·66	0·63
F	0·61	0·81	0·93	X F	0·32	0·30
Cl	0·09	0·041	0·09			
OH ∞	1·30	1·15	0·98			
XMg	0·60	0·68	0·58			
XF	0·31	0·41	0·47			

Magnetite		Ilmenite		Haematite exsolved lamellae in ilmenite)	
Rock type	Tonalite	Rock type	Tonalite	Rock type	Tonalite
Sample no.	MG 57	Sample no.	MG 57	Sample no.	MG 57
SiO_2	0·03	SiO_2	0·03	SiO_2	0·09
TiO_2	0·00	TiO_2	50·20	TiO_2	12·34
Al_2O_3	0·14	Fe_2O_3 ∞	6·59	Al_2O_3	0·14
Fe_2O_3 ∞	68·76	FeO ∞	42·67	Fe_2O_3	88·61
FeO	30·81	MnO	1·47	MnO	0·18
MnO	0·12	MgO	0·57	Total	101·35
NiO	0·18	Total	101·53		
Total	100·04			Si	0·00
		Si	0·00	Ti	0·23
Si	0·00	Ti	0·94	Al	0·00
Ti	0·00	Fe^{3+}	0·12	Fe^{3+}	1·68
Al^{VI}	0·01	Fe^{2+}	0·89	Mn^{2+}	0·00
Fe^{3+}	1·99	Mn^{2+}	0·03	Sum Cations	1·92
Fe^{2+}	0·99	Mg	0·02		
Mn^{2+}	0·00	Sum Cations	2·00		
Ni	0·01				
Sum Cations	3·00	Ilmenite	88·63		
		Hematite	6·16		

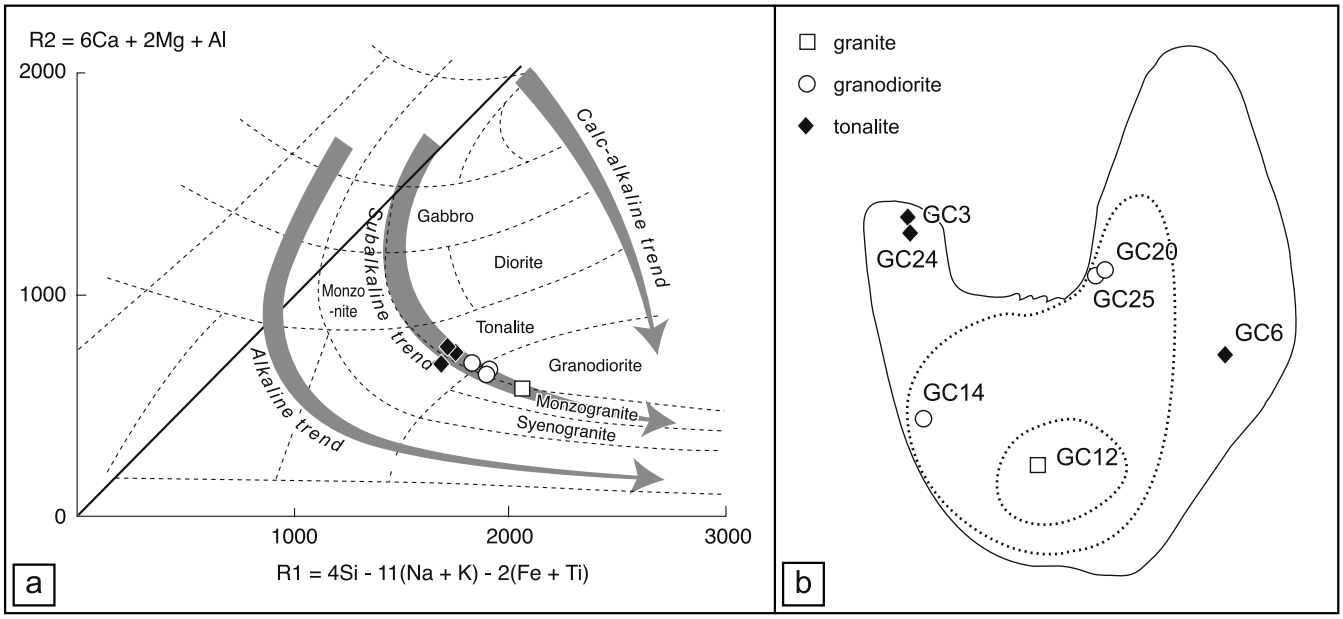

Figure 4 (a) Plot of Carion whole-rock compositions in the R1–R2 diagram of La Roche *et al.* (1980). (b) Location of analysed samples and inferred normal concentric zoning.

4×10^{-8} SI. The magnetic susceptibility magnitude (or bulk magnetic susceptibility) is the arithmetic mean defined by K=1/3 (k1+k2+k3), where k1, k2 and k3 are the respective magnitudes of the principal axes of the AMS ellipsoid (Nagata 1961). The anisotropy degree is given by P=K1/K3, and the linear and planar anisotropies are L=K1/K2 and F=K2/K3 respectively. The results are presented in Table 2. Averages of magnetic foliations and lineations from each site can be seen in the projection diagrams of Figure 5. Foliations and lineations are generally well-defined in most sites, with average F values (1·14) comparable to average L values (1·10). In a few cases, some scattering of data is observed, corresponding to average angular departures from the mean axis a(Ki) >5° (Table 2). This is attributed to the porphyritic nature of the rocks, with large feldspar megacrysts that can locally disturb the mineral fabric at the specimen scale.

2.2. Magnetic susceptibility magnitudes

Magnetic susceptibility magnitudes (K) range from 11 to 111×10^{-3} SI, with an average at 62×10^{-3} SI in the Carion pluton (Table 2). These large magnetic susceptibilities are typical of magnetite-bearing granitoids. Indeed, Rochette *et al.* (1992) recognised that magnetite-free granitoids are characterised by K values generally less than $0{\cdot}5 \times 10^{-3}$ SI. The susceptibility magnitudes of Carion granitoids are in the highest observed range for granitic rocks (Bouchez 2000). Ilmenite, that is abundant in the Carion granitoids, can also have contributed efficiently to the susceptibility magnitudes, as this oxide has a rather high susceptibility (Borradaile & Henry 1997; Diot *et al.* 2003). Thermomagnetic curves (K *vs.* temperature) obtained from representative samples show a fast susceptibility decrease at about 580°C, the Curie temperature of pure magnetite (Fig. 6). This is evidence of the ferrimagnetic nature of these rocks, where magnetite is indeed the main susceptibility carrier in addition to ilmenite, hornblende and biotite.

Outside the limits of the Carion pluton, the country rocks have generally lower susceptibilities (Fig. 7a). Within the pluton, the magnetic susceptibility map displays a pattern more complicated than the expected simple normal zoning. In paramagnetic (magnetite-free) granites, the susceptibility magnitudes are directly proportional to the iron contents of the rocks, thus providing a reliable petrographic indicator (Gleizes *et al.* 1993). In ferrimagnetic rocks, the magnetic susceptibility magnitude is less straightforward to use, but it often displays some relationships with the petrography, as it mainly depends on the amounts of magnetite (in addition to other iron-bearing minerals). In intermediate to felsic metaluminous rocks such as the Carion pluton, it is expected that the amount of Fe–Ti oxides decreases as a result of magmatic differentiation. The susceptibility map confirms that a differentiated area does exist in the centre of the pluton, corresponding to the pink granite type. Other minor areas with relatively low susceptibilities are also correlated to the most felsic granites. In the Carion pluton, the susceptibility values display a zoning pattern (Fig. 7a), where the lowest values correspond to the previously recognised granitic core and the highest values correspond to the tonalitic compositions near the city of Manjakandriana. However, the zoning pattern is not a simple concentric one, such as the first pattern suggested from whole-rock geochemistry (Fig. 4b). This complex zoning pattern is explained by comparison with the foliation map (Fig. 7c). Indeed, the whole set of scalar and directional susceptibility data is consistent with the recognition of four sub-units, as discussed hereafter.

The magnetic fabric of magnetite-bearing plutonic rocks has been demonstrated to parallel the shape-preferred orientation of magnetite grains (Archanjo *et al.* 1995; Grégoire *et al.* 1998). Moreover, in the case of the Carion pluton, the consistency of the magnetic foliation with the mineral foliation due to the preferred orientations of feldspar megacrysts has been checked locally in the field (Nédélec *et al.* 2000). The magnetic fabric is therefore a good proxy for the mineral fabric. In the Carion pluton, foliations are rather steep and arranged in patterns that locally crosscut each other and help to delineate four nested sub-units inside the pluton (Fig. 7c). The emplacement order of the sub-units is derived from the crosscutting relationships of the foliation trajectories. The sub-units are numbered 1 to 4 from east to west according to their nesting relationships, hence their temporal relationships. The steepest dips generally coincide with external or internal contacts. Foliation trajectories are rather consistent with the limits of the pluton, with the exception of the northern central indentation, where they seem to be at a high angle to the pluton contour. In fact, in this case, foliation trajectories outside the pluton can also be

Table 2 AMS data for Carion pluton and its country rocks. K=susceptibility magnitude; K1=magnetic lineation; K3=magnetic lineation; 'P, L, F=anisotropy parameters; n=number of measured specimens; a(K1)=average angular departure from the mean K1 at 95% confidence level; a(K3)=average angular departure from the mean K3 at 95% confidence level.

Sample	n	K	K1			K3			P=K1/K3	L=K1/K2	F=K2/K3
		($\times 10^{-3}$ SI)	Trend	Plunge	a (K1)	Trend	Plunge	a (K3)			
Carion pluton											
DG 4	2	51	97	36	1	0	8	4	1·18	1·12	1·06
DG 6	2	73	116	49	2	263	36	2	1·25	1·11	1·14
DG 16	3	45	131	67	7	294	29	1	1·23	1·03	1·20
DG 17	1	57	124	41	0	257	38	0	1·38	1·09	1·29
DG 24	4	44	83	49	5	235	34	1	1·24	1·04	1·20
DG 25	7	63	226	54	1	73	43	1	1·28	1·12	1·16
DG 26	5	75	159	37	2	37	30	3	1·16	1·07	1·09
DG 27	5	64	296	64	2	116	26	1	1·16	1·05	1·11
DG 29	4	73	200	45	2	28	45	2	1·26	1·11	1·15
DG 30	3	67	94	71	2	217	10	1	1·31	1·10	1·20
DG 31	3	88	144	67	1	20	13	2	1·36	1·23	1·13
DG 32	4	58	161	44	1	345	46	1	1·27	1·10	1·17
DG 33	5	74	200	49	2	0	42	1	1·27	1·08	1·19
DG 35	4	24	193	29	2	295	54	2	1·08	1·04	1·04
DG 36	4	47	107	35	3	14	11	2	1·14	1·06	1·08
DG 37	3	101	127	25	5	23	37	2	1·16	1·05	1·11
DG 38	4	58	69	72	2	306	11	2	1·13	1·07	1·06
DG 39	6	59	355	70	1	185	21	1	1·32	1·16	1·16
DG 40	3	61	74	73	2	302	23	2	1·22	1·11	1·11
DG 41	8	76	94	68	1	268	21	1	1·41	1·14	1·27
DG 42	3	69	217	67	2	41	23	1	1·62	1·19	1·43
DG 43	4	14	61	22	3	161	7	1	1·09	1·02	1·07
DG 44	4	86	172	20	1	354	67	5	1·15	1·09	1·06
DG 45	3	43	191	35	3	38	69	6	1·07	1·04	1·03
DG 46	4	31	351	26	5	154	65	1	1·17	1·04	1·13
DG 48	4	42	173	47	3	320	39	2	1·14	1·06	1·08
DG 49	3	42	223	13	3	323	38	4	1·11	1·06	1·05
DG 50	2	29	88	28	2	332	36	2	1·43	1·22	1·21
DG 51	4	64	304	25	5	121	65	2	1·15	1·05	1·10
DG 52	4	62	76	71	3	272	18	2	1·27	1·07	1·20
DG 53	4	56	147	37	1	285	43	2	1·19	1·10	1·09
DG 54	3	30	87	35	2	307	50	1	1·30	1·10	1·20
DG 55	4	73	191	70	1	73	9	1	1·26	1·11	1·15
DG 56	3	59	91	76	1	231	10	1	1·31	1·15	1·16
DG 57	4	82	206	22	9	303	18	2	1·18	1·06	1·12
DG 58	2	91	146	52	3	279	28	1	1·37	1·06	1·31
DG 59	4	64	134	49	5	303	31	4	1·28	1·08	1·20
DG 60	3	100	89	43	1	338	23	3	1·22	1·12	1·10
DG 61	3	32	12	68	3	211	22	1	1·39	1·09	1·30
DG 62	2	71	152	8	1	327	81	1	1·22	1·12	1·10
DG 63	3	56	136	64	1	253	12	1	1·21	1·11	1·10
DG 64	5	111	119	85	1	310	6	9	1·23	1·15	1·08
DG 65	5	73	159	74	1	343	15	1	1·32	1·16	1·16
DG 66	5	103	119	75	2	277	12	1	1·18	1·06	1·12
DG 67	3	83	168	46	4	51	22	1	1·21	1·04	1·17
DG 68	5	81	158	44	1	40	25	4	1·30	1·21	1·09
DG 69	4	45	116	32	1	275	58	2	1·64	1·43	1·21
DG 71	2	58	94	44	1	289	45	1	1·46	1·21	1·20
MG 57	6	51	129	53	-	253	23	-	1·24	1·14	1·09
MG 148	4	78	147	51	1	287	32	1	1·17	1·13	1·14
MG 149	4	73	180	49	3	308	30	1	1·22	1·06	1·14
TV 36	3	64	74	59	3	279	35	1	1·33	1·06	1·27
TV 37	3	11	89	8	2	343	29	1	1·11	1·03	1·08
TV 38	4	65	0	76	2	164	12	1	1·21	1·14	1·07
TV 41	2	44	129	52	1	42	11	2	1·16	1·09	1·07
TV 42	2	53	175	70	3	287	7	1	1·27	1·05	1·22
TV 43	4	52	168	48	2	305	34	2	1·15	1·06	1·09
TV 44	4	88	343	67	1	105	14	3	1·22	1·15	1·07
averages		*62*							*1·25*	*1·10*	*1·14*

Table 2 *Continued.*

Sample	n	K	K1			K3			P=K1/K3	L=K1/K2	F=K2/K3
		($\times 10^{-3}$ SI)	Trend	Plunge	a (K1)	Trend	Plunge	a (K3)			
Country rocks											
DG 1	3	52	18	40	11	122	22	2	1·27	1·06	1·21
DG 2	3	55	357	67	1	177	29	1	1·50	1·29	1·21
DG 3	3	9	118	16	4	258	68	2	1·35	1·09	1·26
DG 5	2	20	77	7	2	212	80	1	1·23	1·06	1·17
DG 7	4	26	160	37	10	26	46	2	1·14	1·04	1·10
DG 8	4	24	213	23	2	75	58	3	1·16	1·09	1·07
DG 9	3	35	39	49	2	246	32	2	1·45	1·21	1·24
DG 10	2	7	53	12	2	295	66	2	1·09	1·04	1·03
DG 12	10	7	268	19	15	159	30	10	1·40	1·19	1·21
DG 13	3	35	329	17	2	192	67	1	1·29	1·08	1·21
DG 14	2	18	291	9	5	193	53	2	1·19	1·04	1·15
DG 15	3	28	350	37	6	177	53	1	1·29	1·04	1·25
DG 18	6	9	314	29	3	220	5	6	1·11	1·07	1·04
DG 19	5	13	157	8	2	287	78	5	1·39	1·26	1·13
DG 20	6	13	144	13	1	6	73	1	1·38	1·16	1·22
DG 21	11	18	156	13	2	269	60	1	1·49	1·18	1·31
DG 22	5	18	146	20	2	265	52	1	1·55	1·15	1·40
DG 23	4	20	145	15	7	246	39	2	1·35	1·06	1·29
DG 27	11	58	208	48	2	303	2	1	1·25	1·09	1·16
DG 28	4	43	341	45	4	75	12	1	1·18	1·06	1·12
DG 30	5	46	145	68	2	45	3	1	1·31	1·10	1·21
DG 34	2	5	54	27	2	254	63	1	1·14	1·05	1·09
DG 59	4	17	115	54	5	303	31	4	1·27	1·08	1·19
DG 72	2	3	217	8	1	126	2	2	1·09	1·05	1·04
DG 73	3	37	107	34	1	335	46	2	1·29	1·16	1·13
MG 58	4	13	219	20	-	320	32	-	1·20	1·02	1·17
MG 59	4	6	192	1	-	281	13	-	1·27	1·07	1·18
TAN 1	3	62	358	37	4	269	3	1	1·46	1·10	1·32
TV 31	4	18	351	67	2	176	22	4	1·19	1·13	1·06
TV 32	2	51	350	32	1	191	64	2	1·35	1·17	1·18
TV 39	4	30	239	46	5	132	13	1	1·26	1·05	1·21
TV 40	4	13	339	66	2	162	20	1	1·11	1·05	1·06
averages		*25*							*1·28*	*1·10*	*1·14*

traced inside and parallel the contact between sub-units 2 and 3. The low-susceptibility leucocratic granite core is included in sub-unit 3 that presents the widest range of susceptibilities, likely recording the largest magmatic differentiation. However, there is some overlap of magnetic susceptibility magnitudes in the four sub-units, due to their very similar petrographic nature. Sub-units 1 and 2 display a lateral zoning due to an evolution from high to medium susceptibilities, that seems to witness a magmatic differentiation from tonalitic to granodiortic compositions. Sub-unit 4 display only high susceptibilities; it is mainly made of tonalites and represents the last-emplaced magmas.

The degree of anisotropy (P) ranges from 1·05 to 1·64 (Fig. 7b), with an average of 1·25. This is rather high for granitoids that are almost free of solid-state deformation microstructures, despite the fact that magnetite-bearing granites are known to be generally more anisotropic that magnetite-free granites (Bouchez 2000). The lowest values characterise the granitic core of sub-unit 3. High values characterise the eastern contact between the pluton and its country rocks. In addition, high anisotropies are also observed inside the pluton and correspond to the previously-inferred contact of sub-unit 3 against sub-unit 2. These highly anisotropic zones possibly record the forcible intrusion of magma of sub-unit 3 with respect to the more crystallised unit 2 inside the pluton, as well as some ballooning effect of the first emplaced magma against its wall rocks. Linear and planar anisotropies are both rather high, but with a predominance of the planar anisotropies (1·14 in average for F, against 1·10 for L) suggesting the predominance of flattening with respect to constrictional strain.

Magnetic lineations are most valuable as evidence of mineral lineations that are generally difficult to determine precisely in plutonic rocks. In the Carion pluton, magnetic lineation plunges are rather steep; this is confirmed by local field observations of the mineral lineation. Each sub-unit contains at least one zone where lineation plunges are higher than 60° (Fig. 7d). Such zones are generally regarded as the indication of magma-feeding zones (Amice & Bouchez 1989; Naba *et al.* 2004).

3. Interpretation

3.1. Four-pulse emplacement of the Carion magmas

The Carion pluton displays a complex susceptibility zoning, that cannot fit the simple normal zoning derived from preliminary geochemical studies. Moreover, the foliation pattern suggests that the pluton is made of four sub-units consistent with the distribution of susceptibility values. These sub-units are regarded as four successive magmatic pulses emplaced in a

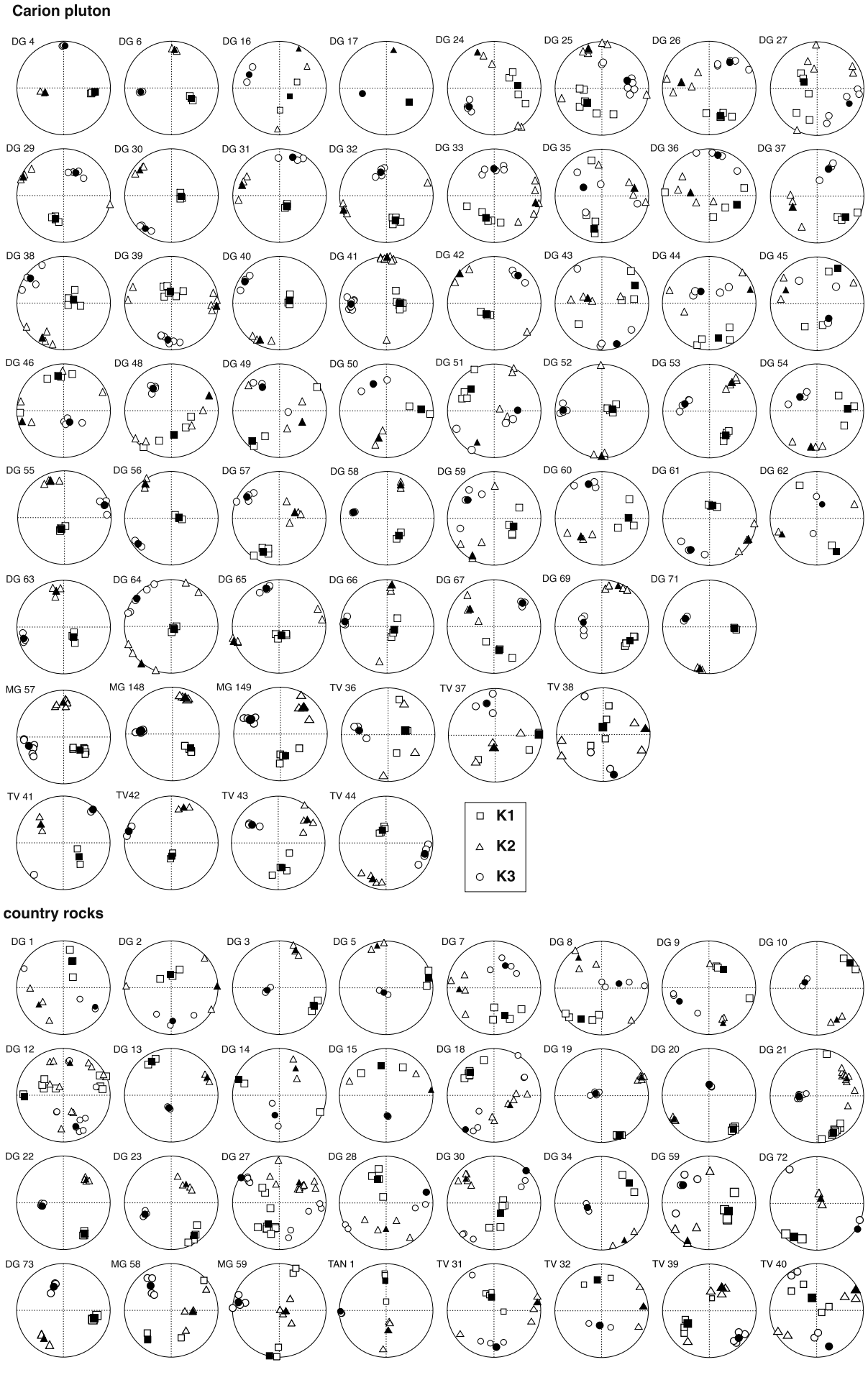

Figure 5 Projection diagrams (lower hemisphere) for all Carion pluton and country rock sampling sites. Open symbols=AMS results for each specimen; solid symbols=averages for each site.

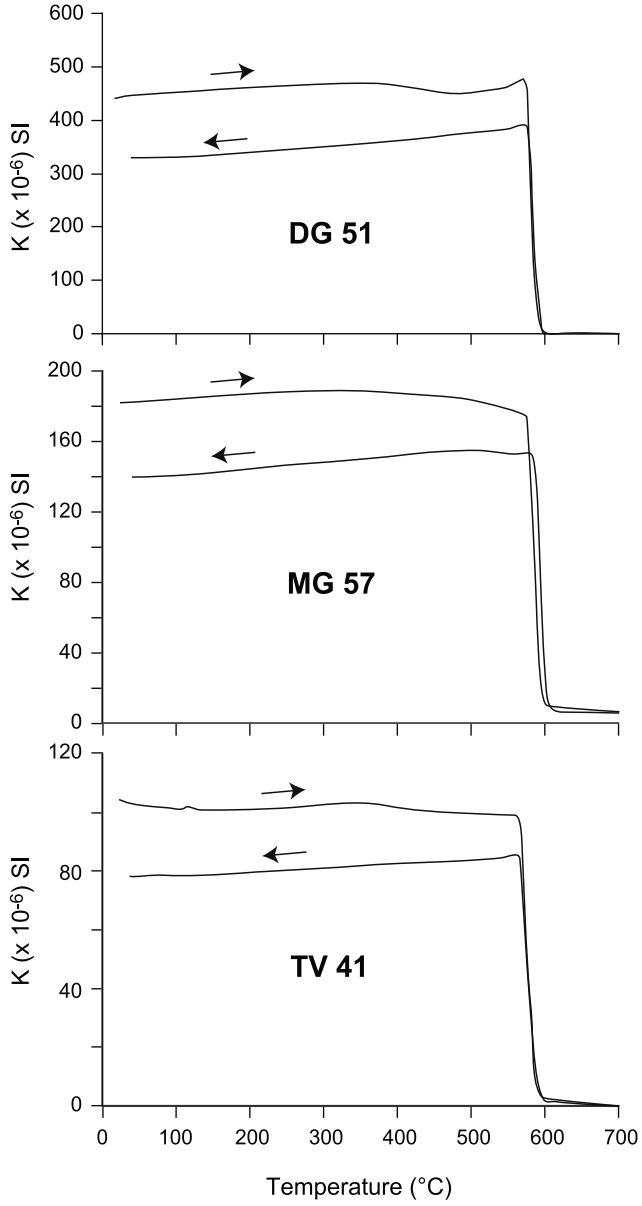

Figure 6 Thermomagnetic curves (K *vs.* temperature) of representative samples from the Carion pluton.

nested fashion. Each sub-unit contains at least one zone where highly plunging lineations likely indicate the location of a magma feeder zone.

Nested granites are not uncommon, but sometimes correspond to unrelated magmas with independent emplacement kinematics (Bouchez & Diot 1990). In the Carion pluton, the four magmatic pulses represent very similar magmas of intermediate composition that underwent some variable magmatic differentiation (either at depth or at emplacement level). Only in the case of sub-unit 3 did magmatic differentiation reach a proper granitic composition. Nevertheless, the whole pluton is made of co-genetic magmas as deduced from petrographic observations, very similar mineral compositions (Table 1) and whole-rock geochemistry (Fig. 4a). The magmas were likely tapped from the same source or from the same magma chamber at depth. The Carion pluton is different from some other cases where a complex distribution pattern of susceptibility magnitudes corresponds to bimodal intrusions with mixing/mingling interactions (e.g. Déléris *et al.* 1996; Asrat *et al.* 2003). Indeed, the recurrence of petrogenetic processes leading to the incremental building of large plutons has been recently admitted even in the absence of conspicuous internal contacts (Glazner *et al.* 2004).

3.2. Chronology of magma emplacement

The crosscutting relationships between foliation patterns of the four sub-units enable their emplacement order to be determined. Nevertheless, the time lag between two successive sub-units remains difficult to estimate. Due to the warm environment evidenced by amphibolite to granulite facies conditions in the country rocks, the older sub-units may have remained highly ductile and even only partly crystallised until the emplacement of the younger sub-units. However, the time lag between emplacements of sub-units 2 and 3 may have been longer than in the other cases, because these sub-units are separated by a highly anisotropic area (Fig. 7b).

The relative chronology of the four sub-units is consistent with the palaeomagnetic data of Meert *et al.* (2001b). The Carion pluton provided a good-quality palaeomagnetic pole dated at 509 ($\pm$ 11) Ma. It was demonstrated that the remanence was a TRM carried by nearly pure magnetite, because of oven unblocking temperatures in the 560–600°C range. The 3-axis IRM experiments confirmed the lack of haematite. In addition, the palaeomagnetic samples exhibit either a dual polarity, or a single reverse polarity, with an apparent spatial bias (Fig. 8). Whereas sites from the country rocks and sites from plutonic sub-units 1 and 2 display mixed polarities with reversal sequences from normal to reverse, the younger parts of the pluton, thus the latest cooled areas, i.e. the granitic core of sub-unit 3 and the sub-unit 4, only display the reverse component. Curie runs on samples that carried the reverse, normal and mixed directions showed nearly reversible heating and cooling curves with well-defined Curie temperature in the magnetite range, pointing to the same type of remanence in all samples; that is, mainly a TRM carried by magnetite. Assuming parallel and rather slow cooling paths for all sub-units (a realistic assumption in such a metamorphic environment), the lack of dual polarity in the youngest parts of the plutons is evidence that these areas were slightly warmer than the others, hence too warm to register the change from 'normal' (negative) to 'reverse' (positive) inclination of the magnetic field. Nevertheless, the lack of any significant difference in normal and reverse polarity directions suggests that the different plutonic sub-units (and their respective cooling paths) were separated only by relatively short time intervals. Indeed, the motion of Gondwana during the 530–490 Ma interval was quite rapid (Meert *et al.* 2001b) and a 5–10 Myr resolution would have been possible. Therefore, it is concluded that the whole Carion pluton was built in less than five Myrs.

3.3. Pluton-related strain *vs.* tectonic strain

At the time of Carion pluton emplacement (532 $\pm$ 5 Ma), transcurrent tectonics along the Angavo shear zone was in its waning stage or already finished, as the Carion pluton is nearly devoid of any solid state deformation and its structures did not come into parallelism with the foliations and lineations of the shear zone. Moreover, a strain aureole with a maximum thickness of 3 kilometres can be traced in many places around the pluton. This aureole is responsible for a conspicuous foliation triple point to the south (Fig. 1c). Formation of such a triple point requires that the wall rocks were still ductile at the time of pluton emplacement (Guglielmo 1993). Indeed, new Ar–Ar ages from the Angavo shear zones point to temperatures well above 500°C at that time (Grégoire *et al.* 2008). In addition, a higher degree of anisotropy is observed in the country rocks along the western border of the pluton (Fig. 7b) and is also regarded as the result of pluton-related strain.

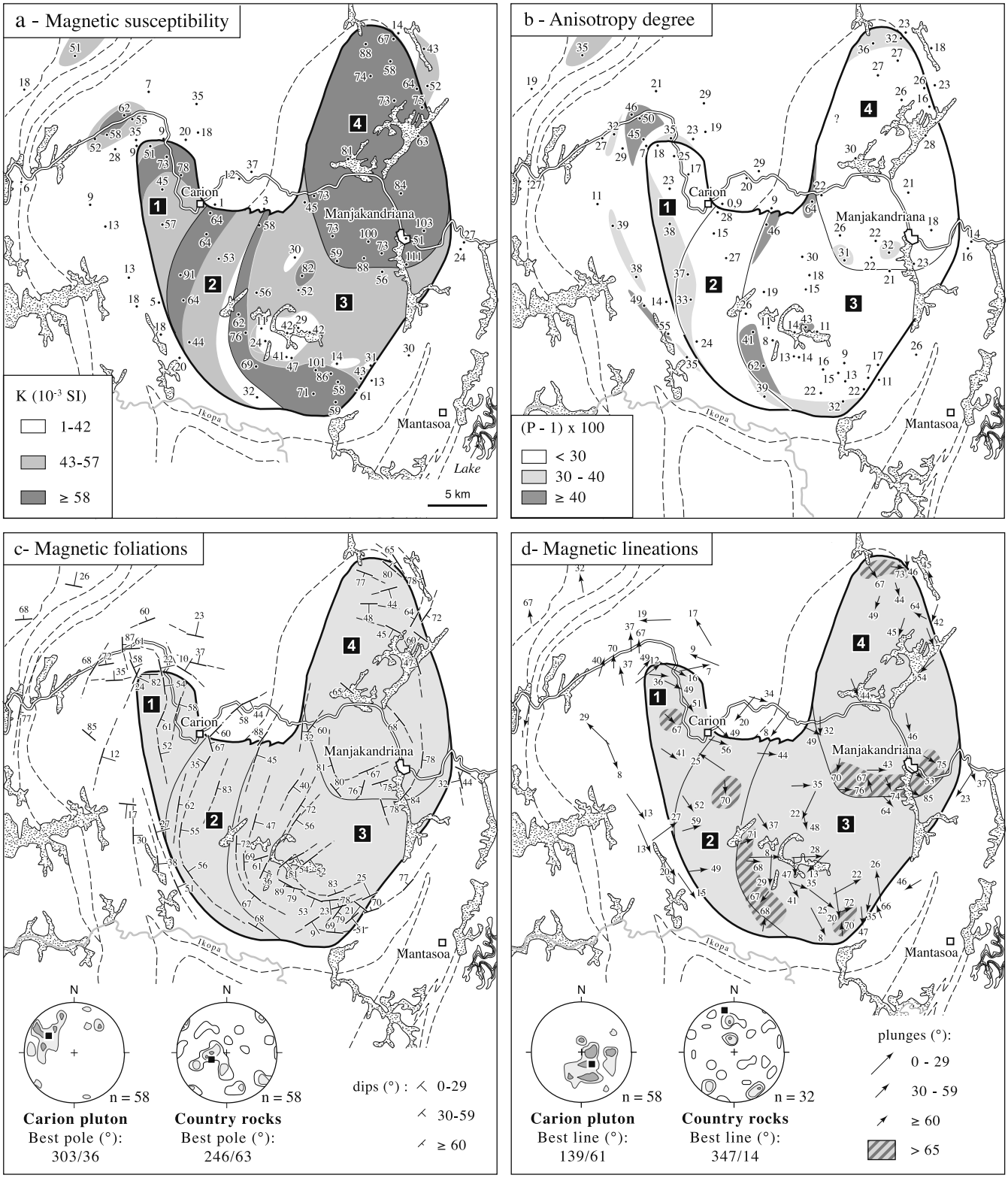

Figure 7 (a) Magnetic susceptibility map and location of the four sub-units. (b) Magnetic anisotropy degree map: values are presented as (P-1) × 100 for sake of clarity. (c) Magnetic foliation map and projection diagram of foliation poles (lower hemisphere; contour lines at 4% and 8% for the pluton and at 2%, 4% and 8% for the country rocks). (d) Magnetic lineation map and projection diagram (lower hemisphere: contour lines at 4% and 8% for the pluton and at 2%, 4% and 8% for the country rocks).

The strain aureole is not observed along the whole northern border of the pluton. There, foliations in the wall rocks come into parallelism only with those of the last sub-unit, in agreement with its last-emplaced character. In the nearby Angavo shear zone (further East from the pluton), steeply dipping foliations are striking to the north and lineations are also trending to the north with subhorizontal to gentle plunges (Nédélec *et al.* 2000). Close to the Carion pluton, foliations display variable dips and lineations are more scattered (Fig. 7c–d). These observations are consistent with pluton-related strain around a post-tectonic intrusion.

The pluton-related strain aureole can have resulted from a ballooning effect. However, the rather steep lineations observed in the pluton also suggest that the different magmatic

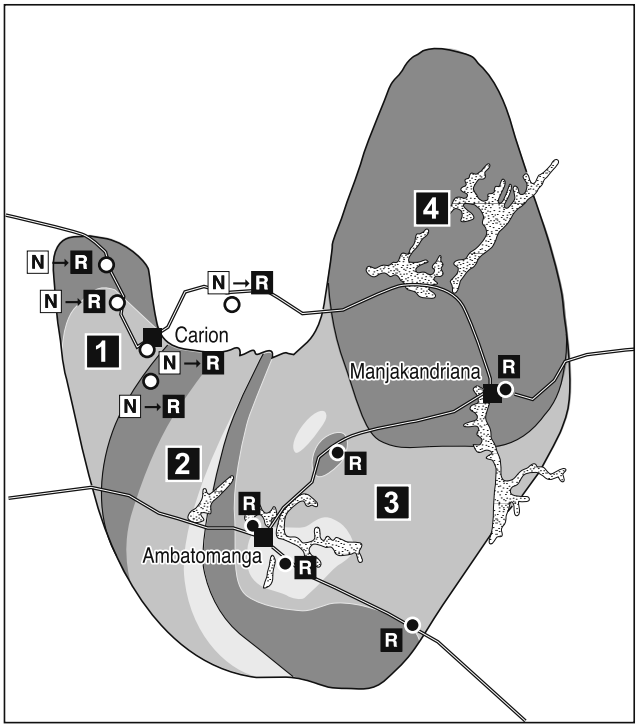

Figure 8 Location of the mixed and single polarity sites of Meert *et al*. (2001b) with respect to the four sub-units defined in the present paper.

pulses may have been emplaced as individual diapirs. Diapiric emplacement cannot be advocated for granitic magmas emplaced in the brittle upper crust (Petford 1996). Here, due to the sustained high temperature conditions in the country rocks, diapiric emplacement was possible. The first diapirically-emplaced sub-unit would have favoured the emplacement of the following magma batches, because of additional heat advection and country rock softening due to magma ascent and emplacement. Then, in agreement with the model of sequential diapirism of Weinberg (1997), the subsequent magma diapir rises into and across the former one, finally building a nested intrusion.

4. Conclusions

The Carion pluton, east of Antananarivo, was emplaced as four nested magmatic sub-units identified by their magnetic foliation patterns, the complex zoning of magnetic susceptibility magnitudes and the location of the highest magnetic anisotropies along some internal contacts. Their relative chronology of emplacement is consistent with previous palaeomagnetic data showing that crystallisation of the pluton covered a time interval sufficient for at least one magnetic reversal, resulting in a dual polarity (from normal to reverse) in the oldest parts of the pluton and a single reverse polarity in the youngest parts of the pluton. Steep lineations and lack of solid-state deformation point to magma ascent and emplacement occurring in the waning stage of the transcurrent tectonics along the Angavo shear zone. A pluton-related strain aureole is possibly due to the diapiric ascent of the sequential magmas batches.

5. Acknowledgements

The Madagascan authors received financial support from the French Ministry of Cooperation through the Campus project 'Geology of the Precambrian basement of Madagascar and its mineralisations'. J. Meert received support from a NSF grant EAR98–05306. J. L. Bouchez, K. Benn and an anonymous reviewer contributed to the substantial improvement of the manuscript. C. Cavaré-Hester, P. Lespinasse, F. de Parceval and A. M. Roquet are warmly acknowledged for technical assistance.

6. References

Abdelsalam, M. G. & Stern, R. J. 1996. Sutures and shear zones in the Arabian-Nubian shield. *Journal of African Earth Sciences* **23**, 289–310.

Amice, M. & Bouchez, J. L. 1989. Susceptibilité magnétique et zonation du batholithe granitique de Cabeza de Araya (Extremadura, Espagne). *Comptes Rendus de l'Académie des Sciences de Paris* **308**, 1171–8.

Archanjo, C., Launeau, P. & Bouchez, J. L. 1995. Magnetic fabric *vs*. magnetite and biotite shape fabrics of the magnetite-bearing granite pluton of Gameleras (Northeast Brazil). *Physics of the Earth and Planetary Interiors* **89**, 63–75.

Asrat, A., Gleizes, G., Barbey, P. & Ayalew, D. 2003. Magma emplacement and mafic-felsic magma hybridization: structural evidence from the Pan-African Negash pluton, northern Ethiopia. *Journal of Structural Geology*, **25**, 1451–69.

Besairie, H. 1969. *Carte géologique de Madagascar à 1/500000: feuille nº 5: Tananarive*. Anatananarivo, Madagascar: Service Géologique.

Borradaile, G. J. & Henry, B. 1997. Tectonic applications of magnetic susceptibility and its anisotropy. *Earth-Science Reviews* **42**, 49–93.

Bouchez, J. L. 1997. Granite is never isotropic: an introduction to AMS studies in granitic rocks. *In* Bouchez, J. L., Hutton, D. H. W. & Stephens, W. E (eds) *Granite: from emplacement of melt to segregation fabric*, 95–112. Dordrecht: Kluwer Academic Publishers.

Bouchez, J. L. 2000. Anisotropie de susceptibilité magnétique et fabrique des granites. *Comptes Rendus de l'Académie des Sciences de Paris* **330**, 1–14.

Bouchez, J. L. & Diot H. 1990. Nested granites in question: contrasted emplacement kinematics of independent magmas in the Zaër pluton, Morocco. *Geology* **18**, 966–9.

Déléris, J., Nédélec, A., Ferré, E., Gleizes, G., Ménot, R. P., Obasi, C. K. & Bouchez, J. L. 1996. The Panafrican Toro Complex (northern Nigeria): magmatic interactions and structures in a bimodal intrusion. *Geological Magazine* **133**, 535–52.

Diot, H., Bolle, O., Lambert, J. M., Launeau, P. & Duchesne, J. C. 2003. The Telnes ilmenite deposit (Rogaland, South Norway): magnetic and petrofabric evidence for a Ti-enriched noritic crystal mush in a fracture zone. *Journal of Structural Geology* **25**, 481–501.

Ellwood, B. B. & Whitney, J. A. 1980. Magnetic fabrics of the Elberton granite, NE Georgia. *Journal of Geophysical Research* **85**, 1481–6.

Glazner, A. F., Bartley, J. M., Coleman, D. S., Gray, W. & Taylor, R. Z. 2004. Are plutons assembled over millions of years by amalgamation from small magma chambers. *GSA Today* **14**, 4–11.

Gleizes, G., Nédélec, A., Bouchez, J. L., Autran, A. & Rochette, P. 1993. Magnetic susceptibility of the Mont-Louis Andorra ilmenite-type granite (Pyrenees): a new tool for the petrographic characterisation and regional mapping of zoned granite plutons. *Journal of Geophysical Research* **98**, 4317–31.

Grégoire, V., Darrozes, J., Gaillot, P., Nédélec, A. & Launeau, P. 1998. Magnetite grain shape fabric and distribution anisotropy *vs*. rocks magnetic fabric: a three-dimensional case study. *Journal of Structural Geology* **20**, 937–44.

Grégoire, V., Monié, P., Nédélec, A. & Bouchez, J. L. 2008. Structure and thermochronology of central Madagascar: a consequence of deformation and heat advection along the late-Panafrican Angavo shear zone. *Réunion des Sciences de la Terre*, Nancy, April 2008.

Guglielmo, G. Jr. 1993. Magmatic strains and foliation triple points of the Merrimac plutons, northern Sierra Nevada, California: implications for pluton emplacement and timing of subduction. *Journal of Structural Research* **15**, 177–89.

Hottin, A. M. 1975. *Le Massif de Carion et son environnement à l'Est de Tananarive*. Thèse de Doctorat de 3ème cycle, Université Paris VI, France.

Hottin, G. 1976. Présentation et essai d'interprétation du Précambrien de Madagascar. *Bulletin du Bureau de Recherches Géologiques et Minières* **IV**, 117–53.

Kröner, A., Windley, B. F., Jaeckel, P., Brewer, T. S. & Razakamanana, T. 1999. Precambrian granites, gneisses and granulites from Madagascar: new zircon ages and regional significance for the evolution of the Pan-African orogen. *Journal of the Geological Society, London* **156**, 1125–35.

La Roche, H (de), Leterrier, J. Grande Claude, P. & Marchal, M. 1980. A classification of volcanic and plutonic rocks using R1–R2 diagrams and major element analysis: relationships and current nomenclature. *Chemical Geology* **29**, 183–210.

Lautel, R. 1953. *Etude géologique du socle cristallin à la latitude de Tamatave*. Doctoral Thesis, University of Clermont-Ferrand, France.

Lawver, L. A., Gahagan, L. M. & Dalziel, I. W. D. 1998. A tight fit-early Mesozoic Gondwana: a plate reconstruction perspective. *Memoir of the National Institute of Polar Research, Special Issue* **53**, 214–29.

Leake, B. E., Wooley, A. R., Birch, W. D., Burke, E. A. J., Ferraris, G., Grice, J. D., Hawthorne, F. C., Kisch, H. J., Krivovichev, V. G., Schumacher, J. C., Stephenson, N. C. N. & Whittaker, E. J. W. 1997. Nomenclature of the amphiboles: Report of the Subcomittee on Amphiboles of the International Mineralogical Association, Commission on New Minerals and Mineral Names. *Canadian Mineralogist* **35**, 219–46.

Martelat, J. E., Nicollet, C., Lardeaux, J. M., Vidal, G. & Rakotondrazafy, R. 1997. Lithospheric tectonic structures developed under high-grade metamorphism in the Southern part of Madagascar. *Geodinamica Acta* **10**, 94–114.

Meert, J. G. 2003. A synopsis of events related to the assembly of eastern Gondwana. *Tectonophysics* **362**, 1–40.

Meert, J. G., Hall, C., Nédélec, A. & Madison Razanatseheno, M. O. 2001a. Cooling of a late-synorogenic pluton: evidence from laser K-feldspar modelling of the Carion granite, Madagascar. *Gondwana Research* **4**, 541–50.

Meert, J. G., Nédélec, A., Hall, C., Wingate, M. & Rakotondrazafy, M. 2001b. Paleomagnetism, geochronology and tectonic implications of the Carion granite, central Madagascar. *Tectonophysics* **340**, 1–21.

Naba, S., Lompo, M., Debat, P., Bouchez, J. L. & Béziat, D. 2004. Structure and emplacement model for late-orogenic Paleoproterozoic granitoids: the Tenkodogo–Yamba elongate pluton (Eastern Burkina Faso). *Journal of African Earth Sciences* **38**, 41–57.

Nagata T. 1961. *Rock magnetism*. Tokyo: Maruzen. 350 pp.

Nédélec, A., Ralison, B., Bouchez, J. L. & Grégoire, G. 2000. Structure and metamorphism of the granitic basement around Anatananarivo: a key to the Pan-African history of central Madagascar. *Tectonics* **19**, 997–1020.

Petford, N. 1996. Dykes and diapirs? *Transactions of the Royal Society of Edinburgh: Earth Sciences* **87**, 105–14.

Rakotondrazafy, M., Madison Razanatseheno, M. O., Nédélec, A., Ralison, B., Fitzsimons, I., Wingate, M. & Meert, J. G. 2001. The Cambrian Carion granite of Madagascar: a case of late Pan-African shoshonitic magmatism. *Gondwana Research* **4**, 746–7.

Ralison, B. & Nédélec, A. 1997. Contrasted Pan-African structures near Antananrivo (Madagascar). *Gondwana Research Group Miscellaneous Publications (Osaka)* **5**, 83–4.

Reeves, C. V. & de Wit, M. J. 2001. Making ends meet in Gondwana: retracing the transforms of the Indian Ocean and reconnecting continental shear zones. *Terra Nova* **12**, 272–80.

Rochette, P., Jackson, M. & Aubourg, C. 1992. Rock magnetism and the interpretation of anisotropy of magnetic susceptibility. *Review of Geophysics* **30**, 209–26.

Schmidt, M. W. 1992. Amphibole classification in tonalite as a function of pressure: an experimental calibration of the Al-in-hornblende barometer. *Contributions to Mineralogy and Petrology* **110**, 304–10.

Stern, R. J. 1994. Arc assembly and continental collision in the Neoproterozoic East African Orogen: implications for the consolidation of Gondwana. *Annual Review of Earth and Planetary Sciences* **22**, 319–51.

Thompson, A. B. & Connolly, J. A. D. 1995. Melting of the continental crust: some thermal and petrological constraints on anatexis in continental collision zones and other tectonic settings. *Journal of Geophysical Research* **100**, 15565–79.

Weinberg, R. 1997. Diapir-driven crustal convection: decompression melting, renewal of the magma source and the origin of nested plutons. *Tectonophysics* **271**, 217–29.

MS received 22 October 2007. Accepted for publication 12 April 2008 (Stellenbosch); 15 January 2009 (RSE).

Earth and Environmental Science Transactions of the Royal Society of Edinburgh, **100**, 147–158, 2010 (for 2009)

Anisotropy of magnetic susceptibility fabrics in syntectonic plutons as tectonic strain markers: the example of the Canso pluton, Meguma Terrane, Nova Scotia

Keith Benn

Ottawa-Carleton Geoscience Centre and Department of Earth Sciences, University of Ottawa, Ottawa, ON K1N6N5, Canada
Email: kbenn@uottawa.ca

ABSTRACT: The anisotropy of magnetic susceptibility (AMS) is widely and routinely used to measure the preferred orientations of Fe-rich minerals in undeformed and weakly deformed granite plutons. The interpretation of the mapped AMS fabrics depends on rock-textural observations, on the map patterns of the fabrics in plutons, and on comparisons of the pluton fabrics to tectonic structures in the country rocks. The AMS may document emplacement-flow related fabrics, but the emplacement fabrics may be reworked or completely overprinted by rather weak tectonic strains of the magma mush or the cooling pluton, especially in syntectonic intrusions. The Late Devonian Canso granite pluton is an excellent example of overprinting of emplacement fabrics by weak tectonic strains. The Canso pluton was emplaced ca. 370 Ma along the boundary between the Meguma and Avalon tectonic terranes, in the northern Appalachian orogen. The AMS was mapped along two traverses that cross the pluton and that are perpendicular to the terrane boundary. Textural evidence suggests the rocks underwent very modest post-full crystallisation strains. The AMS records the dextral transcurrent shearing that occurred on the terrane boundary during emplacement and cooling of the Canso pluton, supporting interpretations that weakly deformed syntectonic granites can be used as indicators of regional bulk kinematics. AMS fabrics in Late Devonian granites of the Meguma Terrane suggest partitioning of the non-coaxial shearing into the terrane bounding fault, with pure-shear dominated deformation further from the fault. Numerical simulations suggest that the kinematics recorded by the fabrics in the Canso pluton was simple-shear, or transpression or transpression with small components of pure shear oriented perpendicular to the bounding shear zone.

KEY WORDS: AMS, Appalachians, granite, strain partitioning, syntectonic, transpression

It is common practice amongst structuralists and granitologists to classify granitic plutons as pre-, syn- and post-tectonic, referring to emplacement prior to, during or following the cessation of orogenic deformation and metamorphism of the country rocks. Such a classification is useful in the practice of putting chronological brackets on tectonic events by isotopic dating of pluton emplacement. Interpretations of pre-, syn- and post-tectonic intrusions are also important in developing pluton emplacement models. Structural interpretations of pre, syn- and post-tectonic emplacement are based on observations of rock textures, the fabric pattern mapped within plutons and comparisons of pluton fabric patterns with the regional-scale structures that record tectonic events.

This present paper presents new data from a syntectonic granite pluton that show tectonic overprinting of magmatic fabrics by small strains related to shearing on a nearby transcurrent terrane boundary. The Canso pluton is a granite of Late Devonian age that was emplaced near the boundary of the Meguma and Avalon terranes, in the Northern Appalachian orogen. The goals of the study are to demonstrate that the fabrics in weakly deformed plutons can provide excellent kinematic indicators of orogenic deformations, and to make the point that the fabrics must be considered in the tectonic context before they can be potentially interpreted to be markers of magma emplacement flow. Numerical simulations are also presented in order to constrain the kinematics of the tectonic overprint of magmatic fabrics in the Canso pluton.

First, interpretations of fabrics in granite plutons are discussed. Then the tectonic setting of the Canso pluton is explained, the new fabric data are presented and the tectonic overprint of the igneous fabrics is argued. The numerical simulations are presented and used to constrain the kinematics along the Meguma–Avalon terrane boundary.

1. Interpreting pluton fabrics

Mineral fabrics in granite plutons can be interpreted in a kinematic framework related to magma dynamics or to regional tectonics (Paterson *et al.* 1998). In the first case, mineral alignments record magma dynamics driven by body forces related to transport and emplacement of the magma, or to convection driven by thermal gradients within the mostly liquid intrusion. The kinematic history recorded by the fabrics can then be interpreted to record buoyancy-driven magma flow (Cruden & Launeau 1994; Tobisch & Cruden 1995) and possibly the mechanics of intrusion. In the second case, the fabric records post-emplacement tectonic deformation of the crystallising magma mush, or of the solidified pluton as it

© 2009 The Royal Society of Edinburgh. doi:10.1017/S1755691009016028

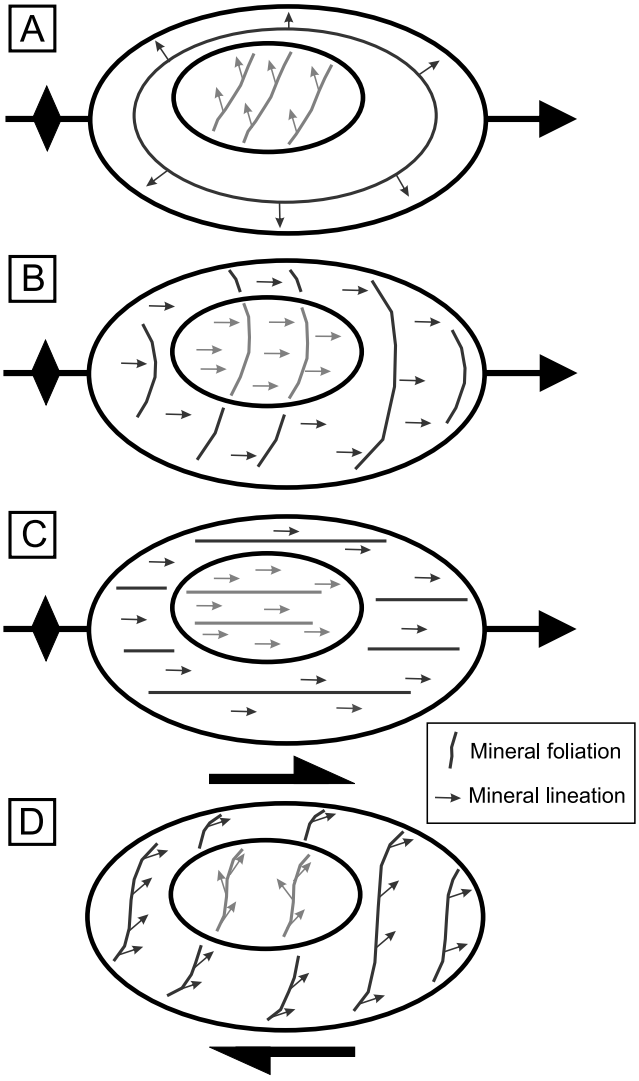

Figure 1 Examples of relationships between fabrics in granite plutons and structures in the country rocks: (A) pluton fabrics are unrelated to country rock structure; (B) probable emplacement-related fabric is folded by regional deformation and lineation is reoriented parallel to the fold hinge; (C) fabric in the pluton is completely overprinted by the regional deformation; (D) pluton emplaced within a region that is undergoing bulk shearing, resulting in partial overprint of the fabric.

cooled from the solidus. The granite fabric then provides information on some (probably small) increment of the regional tectonic strain, and may also be used to infer the tectonic stress field (Benn *et al.* 2001). These two cases are considered to be end-member models. In many published examples of detailed pluton-fabric studies, there is evidence of a partial tectonic overprint of a first generation of mineral alignments that was formed during emplacement flow (Bouchez & Gleizes 1995; Pignotta & Benn 1999; Žák *et al.* 2005; Čečys & Benn 2007).

Figure 1 depicts four examples of fabric patterns in plutons and the relationships of the fabrics to tectonic structures in their host rocks. The precise fabric orientations that are represented in the diagrams are not of primary significance to this discussion. The focus is on the geometric relationships of the fabrics in different nested parts of plutons and on the relationships of pluton fabrics to the tectonic structures. The diagrams in Figure 1 are used to discuss first order interpretations of pluton fabrics. Figure 1A–C depicts plutons emplaced into folded, or folding, country rocks, as indicated by the anticlinal axial surface trace in each figure. Figure 1D shows another example where emplacement occurred during bulk shearing of the host rocks. Cases A and C are similar to pluton fabric development 'completely decoupled' from host rock deformation, and pluton fabric development 'completely coupled' to host rock deformation, as illustrated in figure 13A and C of Paterson *et al.* (1998). Figure 1 includes the necessary analyses of the mineral lineations in plutons which, in practice, are usually determined using the anisotropy of magnetic susceptibility. The interpretation of pluton fabrics is incomplete and risks being erroneous if only the mineral foliations are considered.

In Figure 1A, the pluton fabrics show no geometric relationship to the regional-scale fold. There are also distinct fabric orientations in the nested portions of the pluton that would represent separate magma pulses, indicating the fabrics record the flow kinematics in the two pulses. The structural relationships in Figure 1A suggest that the pluton fabrics record magma flow that was decoupled from deformation in the host rocks, so they can be interpreted to indicate emplacement of the successive magma batches (Vigneresse & Bouchez 1997; Dehls *et al.* 1998; Siegesmund & Becker 2000; Becker *et al.* 2000; Molyneux & Hutton 2000; D'Eramo *et al.* 2006; Razanatseheno *et al.* 2009). This is an example of fabric in a post-tectonic pluton that can be used to infer an emplacement mechanism.

Figure 1 illustrates examples where the fabrics in the plutons are reworked to varying degrees by tectonic deformation. Figure 1B shows a pluton where the foliation is rotated about the regional fold hinge, and the mineral lineation is aligned parallel to the regional hinge. This type of fabric pattern is interpreted to represent folding of a pre-existing foliation in the pluton by regional deformation and reorientation of the lineation parallel to the fold hinge. Figure 1C illustrates a foliation in the pluton that is axial-planar to the regional fold and a lineation that is parallel to the fold hinge. That example represents a stronger tectonic overprint that has resulted in parallelism of the foliation and the lineation in the pluton with the regional structures. Published examples of structural relationships as shown in Figure 1B and C have shown them to indicate emplacement during the regional folding event (Benn *et al.* 1997, 1998; Bolle *et al.* 2003; Čečys & Benn 2007; Pignotta & Benn 1999). The fabrics in the plutons cannot be used to directly infer the kinematics of emplacement flow, or mechanisms involved in pluton emplacement.

In Figure 1D the pluton is emplaced within shearing country rocks. There is an early-formed fabric in the central parts of the pluton that may record magma emplacement flow and it is variably overprinted by the regional shear. The tectonic overprint may begin as the magma in the pluton reaches some threshold of crystallisation, when the solid fraction forms a contiguous framework with increasing strength that transmits anisotropic stresses from the deforming country rocks. Examples like Figure 1D have also been shown to be indicative of syntectonic emplacement (Leblanc *et al*. 1996; Djouadi *et al.* 1997; Gleizes *et al*. 1998; Czeck *et al*. 2006; Gebelin *et al.* 2006).

In examples such as Figure 1B and D, there may be regions of a pluton where igneous textures are preserved; but in no case should the fabrics be interpreted to indicate emplacement flow kinematics, because the fabrics have likely been reworked to some degree by tectonic deformation. The following study serves to illustrate and strengthen the interpretation that, even in granites that would generally be referred to as 'undeformed' or 'weakly deformed', the fabrics may serve as tectonic strain markers.

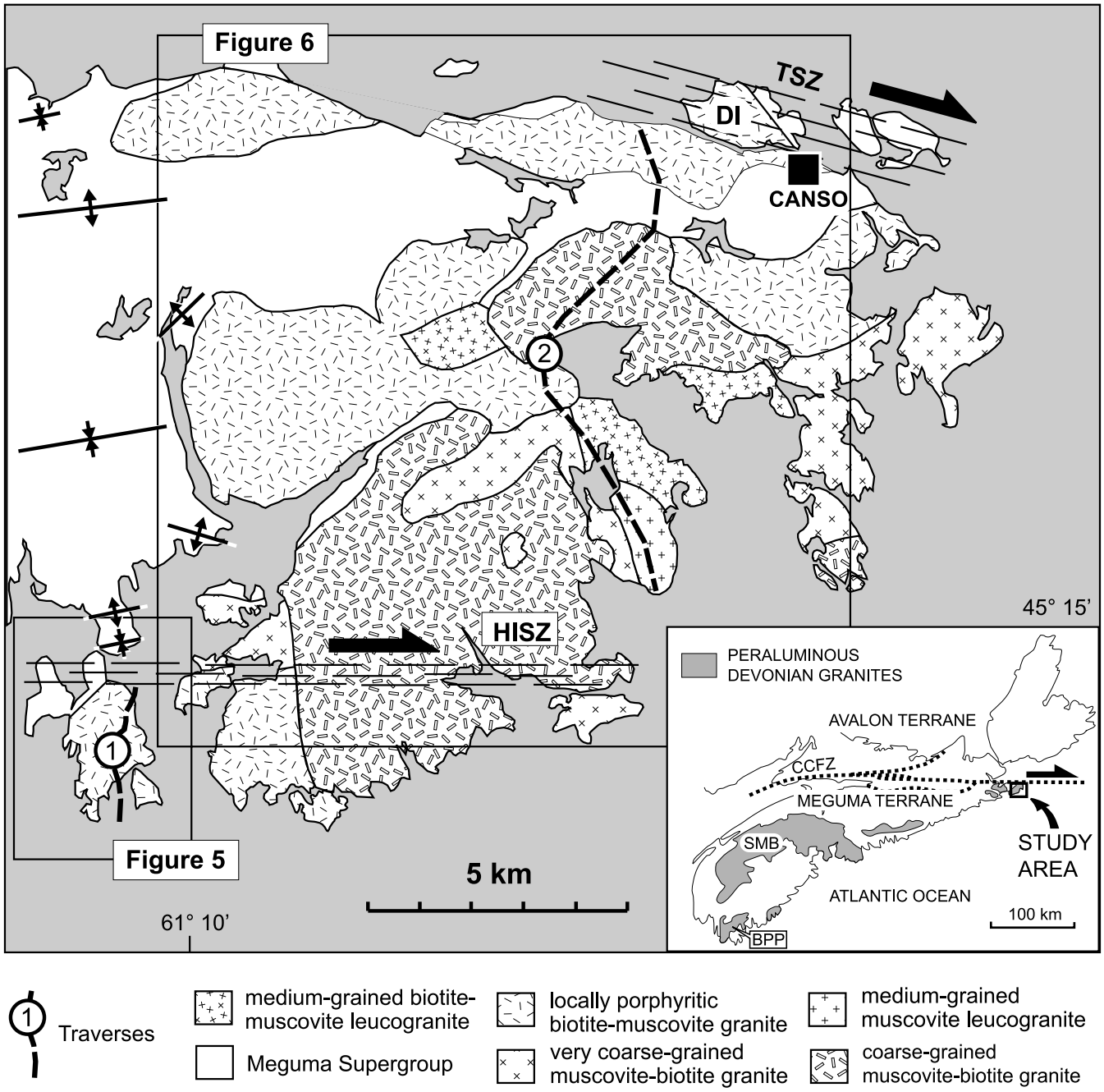

Figure 2 Geological map of the study area, modified from Hill (1991): TSZ, Tittle shear zone; HISZ, Harbour Island shear zone, DI, Durrell's Island. Inset: location map of the Meguma Terrane and the study area: CCFZ, Cobequid–Chedabucto fault zone; SMB, South Mountain batholith; BPP, Barrington Passage pluton.

2. Tectonic setting of the Canso pluton

The Meguma Terrane of southern Nova Scotia (Fig. 2 inset) represents the most internal allochthon recognised within the northern Appalachians (Keppie 1993). The supracrustal rocks are predominantly greenschist to lower amphibolite-grade Cambro-Ordovician metaturbidites of the Meguma Supergroup, which are thought to represent detritus eroded from the Saharan Shield and deposited on the continental slope of northwestern Africa (Schenk 1971, 1995). Collision of the Meguma Terrane with the eastern margin of ancestral North America, represented by the Avalon Terrane (Fig. 2 inset), occurred in the Middle Devonian (Williams & Hatcher 1982; Keppie & Dallmeyer 1987). In Nova Scotia, the boundary between the Meguma and Avalon terranes is represented by the Cobequid–Chedabucto fault zone (CCFZ), which may be linked to a shallowly southward-dipping sole thrust underlying the Meguma Terrane (Keppie 1993). Detailed studies along the CCFZ have revealed a prolonged history of ductile and brittle deformation related to dextral transcurrent tectonics that continued into the Carboniferous (Mawer & White 1987).

The regional structural pattern within the Meguma Supergroup is dominated by upright, shallowly-plunging regional chevron folds (Horne & Culshaw 2001), and associated foliations that trend NNE–SSW in the southern part of the terrane, and that are ENE–WSW trending close to the CCFZ (Keppie 1982). These structures developed during the dextral transcurrent tectonics associated with the Meguma–Avalon collision which is recognised in Nova Scotia as the Acadian Orogeny. Acadian fabric development commenced at about 415 Ma, corresponding to the oldest $^{40}Ar/^{39}Ar$ dates obtained from whole rocks and separates of fabric-forming minerals (Dallmeyer & Keppie 1987; Keppie & Dallmeyer 1987; Muecke *et al.* 1988). $^{40}Ar/^{39}Ar$ dates as young as 360 Ma

Table 1 Characteristics of textural types.

Textural type	Visible fabric	Microstructure
1	None	• Igneous texture preserved • Undulose extinction and subgrains in quartz
2	Weak, vertical foliation defined by quartz aggregates	• Quartz entirely recrystallised into roughly equant new grains, 0·2 to 0·4 mm in size, with highly lobate grain boundaries • Other minerals essentially undeformed
3	Vertical foliation and horizontal extension lineation, both defined by quartz aggregates	• Quartz entirely recrystallised into elongate new grains, $\leq$0·2 mm in size, with straight or gently curved grain boundaries • Mica and feldspars deformed and locally recrystallised

obtained from the Meguma Supergroup (Keppie & Dallmeyer 1987) probably represent thermal resetting during the emplacement of huge volumes of peraluminous granite magma throughout the Meguma Terrane, including the South Mountain batholith (Clarke *et al.* 1993), the Barrington Passage pluton (Reynolds *et al.* 1987) and the Canso pluton, which is the subject of the present study. Geochronological data indicate that the granitic plutons of the Meguma Terrane crystallised between 380 Ma and 365 Ma (Clarke & Halliday 1980; Reynolds *et al*. 1981; Hill 1988; Keppie *et al.* 1993; Tate *et al.* 1997).

Extensive structural, AMS and gravity modelling studies of the large, composite South Mountain batholith showed it to be composed of tabular intrusions, emplaced within a compressional tectonic stress field, resulting in folding of emplacement-related horizontal foliations, and lineations that are parallel to the regional fold axis (Benn *et al.* 1997, 1999). A detailed fabric and AMS study of the Barrington Passage pluton, in the southwestern Meguma Terrane, revealed a similar fabric pattern to the one depicted in Figure 1B (Pignotta & Benn 1999).

3. The Canso pluton and its host rocks

The study area is located along the southern margin of the CCFZ, near the town of Canso, at the eastern tip of the Nova Scotian mainland (Fig. 2). The country rocks are composed of amphibolite-grade psammites and pelites of the Goldenville and Halifax Groups of the Meguma Supergroup. The rocks were strongly deformed during the Acadian Orogeny, resulting in the formation of several generations of vertical, NE–SW to ENE–WSW-trending foliations associated with tight, upright, shallowly plunging folds (Mawer & Williams 1986; Mawer & White 1987). The Canso pluton is discordant to those regional structures, but the contact-parallel folds mapped by Hill (1991) along its western margin (Fig. 2) may record shortening in the wall rocks due to expansion of the pluton during emplacement, as suggested for pluton margin parallel folds near the contact with the South Mountain batholith (Benn *et al.* 1999). Porphyroblasts of biotite, garnet and andalusite include dextrally crenulated segments of the regional foliation within the metamorphic aureole around the pluton, demonstrating emplacement after the development of the regional foliations (Mawer & Williams 1986; Mawer & White 1987; Hill 1991). Two vertical, E–W to WNW–ESE-striking mylonitic shear zones affect the pluton (Fig. 2). Both contain horizontal extension lineations and consistently dextral shear sense indicators (C-S fabrics), showing that the granites were affected by the regional dextral shearing that continued following full crystallisation, and as the pluton cooled.

The Canso pluton was mapped in detail by Hill (1991), who defined the lithological units shown in Figure 2. The granites tend to be homogeneous in both composition and grain size at the outcrop scale. Comagmatic enclaves are rare, and centimetre-scale feldspar phenocrysts are only locally present; therefore the orientations of those markers cannot be mapped systematically. The horizontal two-dimensional nature of most outcrops (except locally along the Atlantic ocean shoreline) also makes field mapping of mineral-preferred orientations difficult. However, shallowly dipping foliations defined by tabular feldspar crystals were reported for a few outcrops of undeformed granites (Hill 1988).

Where autoliths of one magmatic unit are found within another, they tend to be rounded, and the strike of the pre-full crystallisation feldspar foliation is parallel in the autoliths and in the host granite, suggesting that both host and autoliths were deformed together in the magmatic state. This suggests that the different magmatic units in Figure 2 were emplaced contemporaneously, which is consistent with similar monazite crystallisation dates obtained from the different units of 373 Ma to 367 Ma ($^{207}Pb/^{235}U$; T. Krogh *in* Hill 1991). $^{40}Ar/^{39}Ar$ cooling dates obtained for a relatively undeformed sample of granite vary from 366 Ma to 362 Ma (biotite and muscovite separates (Keppie & Dallmeyer 1987)), indicating that the pluton had cooled to about 300°C within $\leq$11 Ma following monazite crystallisation.

4. Rock textures

Microstructures show whether the rock fabric was formed in response to deformation of the crystallising magma, or if some degree of post-full crystallisation overprint may have reworked the magmatic fabric (Paterson *et al.* 1989; Bouchez *et al.* 1990; Vernon 2000). Three microtextural types are defined here for the Canso pluton. The textural types can be correlated with the strength of the mineral fabrics determined in the field, and also using the AMS, and their distinguishing characteristics are given in Table 1.

Rocks of textural type 1 are found at 14 sites, all at distances greater than 1500 m from the mylonitic shear zones. In the field, the rock has no visible fabric, and in thin section there is evidence of only very limited post-full crystallisation strain. The igneous texture is well preserved, and grain-scale ductile strain features are limited to undulose extinction and minor subgrain development in quartz (Fig. 3A).

Closer to the shear zones, there is a transition in the characteristic microstructures, recording an increase in post-full crystallisation deformation. In textural type 2, quartz is recrystallised, though micas and feldspars show little evidence of intracrystalline strain. Quartz new grains are relatively large (Table 1) and have highly lobate grain boundaries (Fig. 3B), suggestive of grain boundary migration, a high temperature recovery mechanism. The new grains form slightly elongate aggregates that define a weak, vertical foliation as observed in the field.

Closer to the shear zones, in rocks of textural type 3, the quartz aggregates are more elongate (defining an easily

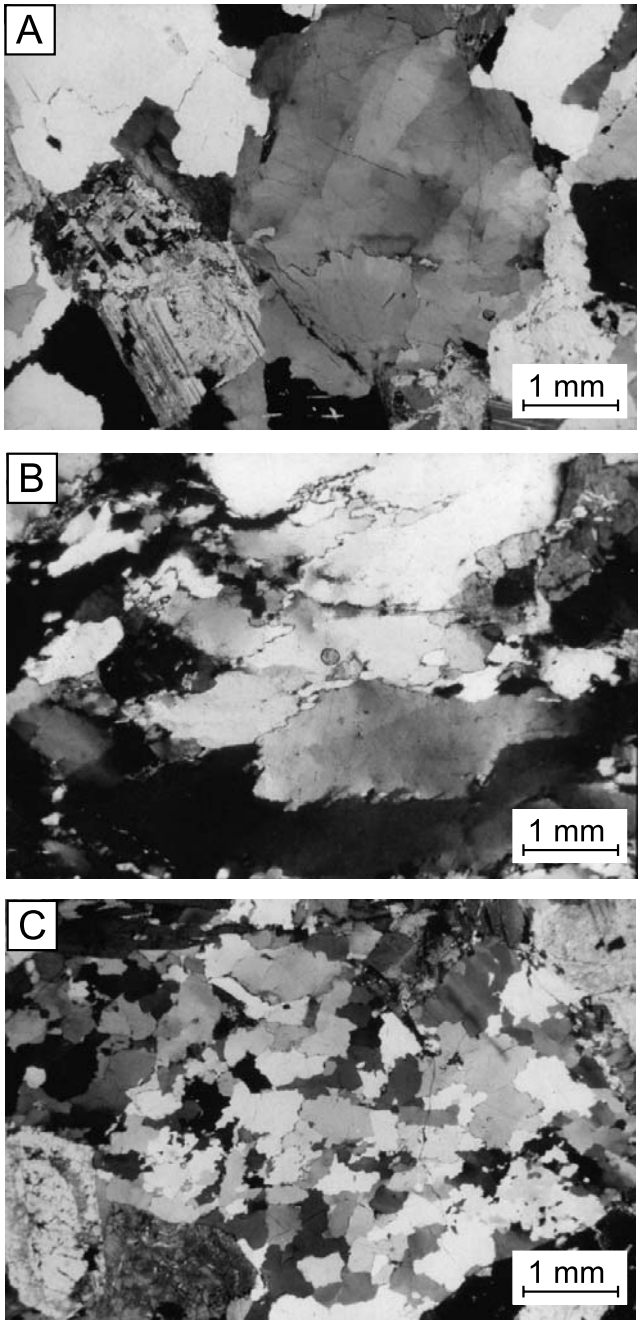

Figure 3 Photomicrographs of the three microstructural types defined in the text: (A) Type 1, from site 19; (B) Type 2, from site 8; (C) Type 3, from site 11.

recognised foliation in the field) and new grains tend to be smaller than in type 2 (compare Fig. 3B and C). The quartz–quartz grain boundaries are lobate, suggesting recrystallisation under fairly high temperature conditions, but the smaller size of quartz new-grains compared to type 2 suggests greater flow stresses (Urai *et al.* 1986) that can be attributed to minor cooling of the pluton during shearing. Some grain-scale shear instabilities (shear bands) are present in type 3 samples which is thought to be indicative of shearing in granites that have cooled to $\approx 500°C$ (Gapais 1989).

The above observations indicate that in rocks of textural type 1, which show no sign of significant subsolidus deformation, the preferred orientations of early formed minerals, such as biotite and euhedral feldspars, will record deformation of the granite magma. On the other hand, the clear imprint of strain and recrystallisation in textural types 2 and 3 shows that fabrics in these rocks have been reworked to some degree, by deformation which occurred after full crystallisation of the magma. The evidence for increasing strain and dynamic recrystallisation under decreasing temperature conditions as the shear zones are approached suggests that fabrics in rocks of textural types 2 and 3 record deformation during subsolidus cooling of the granites, and a progressive localisation of subsolidus strain into the shear zones.

5. Anisotropy of magnetic susceptibility (AMS)

The anisotropy of magnetic susceptibility (AMS) is a method that has proven to be efficient and accurate for measuring the preferred orientations of Fe-minerals in granites, in order to map the fabrics at the pluton-scale (Bouchez 1997, 2000). Sampling for the AMS study was carried out at 30 outcrops along two traverses, mostly following roads and along the Atlantic coastline. No sampling was done for AMS within the mylonitic shear zones, as the fabrics are easily measured in the field, and because the presence of pervasive composite planar fabrics (S-foliation and shear bands) would lead to complex magnetic fabrics (Housen *et al.* 1993; Aranguren *et al.* 1996) that are of no interest in the present study.

Traverse 1 extends from 100 m to 2500 m south of the Harbour Island shear zone (HISZ, Fig. 2), with a maximum spacing between sampling sites of 300 m. Traverse 2 extends from 150 m south of the Tittle shear zone (TSZ, Fig. 2) to 1500 m north of the HISZ, with distances of 125 m to 3000 m between sites. Whereas traverse 1 is entirely within a single intrusive unit of homogeneous muscovite–biotite granite, traverse 2 crosses several internal contacts, and sampling sites therefore represent different intrusive units. Two specimens of 22 mm-length were cut from each of three 25 mm-diameter drill cores collected per sampling site. Thus individual sites are represented by approximately 65 cm^3 of rock. Individual drill cores were separated by several metres in the outcrops in order to obtain a representative sampling.

The AMS was measured at the University of Ottawa using a Kappabridge KLY-2 a.c. bridge (manufactured by AGICO, Czech Republic), in a field strength of 300 A/m at a frequency of 920 Hz. The AMS of each sample is represented by a second order tensor from which the magnitudes of the principal susceptibilities ($K_1 \geq K_2 \geq K_3$), and the orientations of the principal directions (K_n) were obtained. Calculation of site-average AMS tensors and of confidence ellipses about each of the average principal directions was performed using the Hext–Jelinek tensor averaging method (Jelinek 1978, 1981; Borradaile 2003). The confidence ellipses represent the statistical estimates of the areas on the sphere within which 95% of the most probable average orientations of the AMS axes are included.

5.1. Source of the AMS signal

The AMS of a rock sample represents the sum of the intrinsic susceptibility anisotropies of all of the constituent crystals (Hrouda 1982; Borradaile 1988; Rochette *et al.* 1992). The essential minerals of the Canso pluton are biotite+muscovite+plagioclase+K-feldspar+quartz, and accessory minerals include ilmenite, apatite, monazite, garnet and zircon. The mineral assemblage is typical of the ilmenite-series of granites, where titanomagnetite is generally absent (Ishihara 1981; Barbarin 1990). Biotite makes up from 3% to 10% of the rock, and it is the most abundant mineral containing significant amounts of Fe. Its contribution should therefore be predominant in the susceptibility signal of most samples. The susceptibility of ilmenite is greater than that of biotite ($K_{ilmenite} \approx 1$ SI, $K_{biotite} \approx 10^{-3}$ SI; Borradaile 1988), and should this

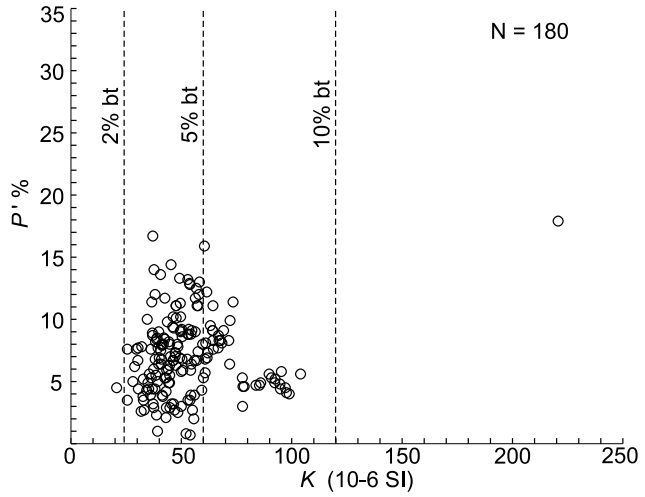

Figure 4 Plot of the degree of magnetic anisotropy (P'%) against the susceptibility (K) for all samples. The dashed lines indicate K values for rocks where the susceptibility is entirely due to 2%, 5%, and 10% biotite, assuming susceptibility $K=1200\times10^{-6}$ SI for biotite.

mineral be locally present in more than trace amounts, it could significantly affect the AMS. We must also consider the presence of very fine grained secondary oxides which may form in association with small amounts of chlorite replacing micas (Benn *et al.* 1993; Borradaile & Werner 1994).

Figure 4 is a plot of the average susceptibility (K) for all samples against P′%=(P′ − 1)*100. P′ is the degree of anisotropy parameter suggested by Jelinek (1981),

$$P'=exp\sqrt{2[(\eta_1-\eta_m)^2+(\eta_2-\eta_m)^2+(\eta_3-\eta_m)^2]},$$

where $\eta_i=ln(K_i)$ (i=1 to 3), and $\eta_m=3\sqrt{\eta_1\cdot\eta_2\cdot\eta_3}$. P′% was calculated following the addition of an isotropic diamagnetic (negative) susceptibility component to the measured AMS. The addition of this component is intended to eliminate the effects of the diamagnetic quartz–feldspar matrix in rocks with weak magnetic susceptibility (Rochette 1987; Bouchez *et al.* 1990). The isotropic component $K_{dia}=-6\times10^{-6}$ SI corresponds to equal contributions from quartz and feldspar, based on susceptibility data reported in Borradaile (1987).

Significant contributions from locally abundant ilmenite, or secondary magnetite, should result in large variations in K in Figure 4. The susceptibilities in the Canso granites are consistently low, with 178 of 180 samples having $K<10^{-4}$ SI, corresponding to expected values for rocks where K is entirely due to the presence of <10% biotite (Fig. 4).

Although the magnetic susceptibility of the specimens can be mostly accounted for by the quantities of biotite present in the rocks, this may not be true for the anisotropy of the susceptibility, which can be strongly affected by the presence of even small amounts of secondary magnetite (Rochette *et al.* 1992, 1999; Borradaile & Henry 1997). Such cases can be recognised by locally anomalous fabric orientations.

To a good approximation, the AMS in the Canso granites can be interpreted in terms of the biotite petrofabric. Since K_3 for biotite monocrystals is close to the [001] crystallographic axis, the measured *magnetic foliation* ($\perp K_3$) will be parallel to the average orientation of biotite basal planes, which defines a structural foliation. As $K_1\cong K_2$ for biotite monocrystals, the measured *magnetic lineation* (K_1) is parallel to the mineral lineation, which is defined by the axis about which the platy biotite crystals are statistically aligned (Bouchez 1997).

5.2. Results

The AMS data, including susceptibilities (K), the degree of anisotropy (P′%), the shape parameter for the average AMS ellipsoids (T, defined in the legend of Table 2), and the orientations of the principal directions for each sampling site, are compiled in Table 2.

Figure 5 presents the AMS orientation data for traverse 1. The strike of the vertical quartz–aggregate foliation, a marker of the weak subsolidus strains that affected some of the sampled granites, is also shown in the orientation diagrams for those outcrops where it is developed (textural types 2 and 3, sites 6–12). Rocks of textural type 1 crop out at the nine sites that are furthest from the HISZ. Site 5 is unique in having an anomalous fabric orientation that is interpreted to indicate a strong magnetic signal from secondary oxides, and it will not be further discussed. At all other sites of textural type 1 (nos. 1–4, 25–28) the orientations of the average principal directions are very consistent. K_{1av} (the magnetic lineation) is horizontal or shallowly plunging, with a NNE–SSW (dominantly) to NE–SW trend, which is consistently oblique in a counterclockwise sense by 50° to 75° to the HISZ. At most of the sites, the K_3 principal direction is well grouped, and K_{3av} plunges steeply, indicating a subhorizontal magnetic foliation.

Approaching the shear zone, in rocks of textural types 2 and 3 the AMS fabrics are rotated in a clockwise sense, and the magnetic foliation steepens progressively. The progressive change in orientations of the fabrics is attributed to the small subsolidus strains that were undergone by the granite at those sites, as indicated by the presence of the vertical quartz–aggregate foliation. It is stressed that the quartz foliation is vertical at all of the sites, but the magnetic (biotite) foliation steepens progressively as the shear zone is approached, and as the solid-state deformation is increased, as shown by the microtextural observations. This is interpreted to indicate that the horizontal foliation that is found in the underformed rocks of textural type 1 was reworked by the solid state deformation associated with dextral shearing, and that the horizontal foliation is completely overprinted with increased strain closer to the shear zone.

On traverse 2 (Fig. 6), the AMS fabric orientations define a pattern similar to the one described for traverse 1. At the sites where the rocks are of textural type 1, K_{3av} is subvertical, indicating horizontal to shallowly-dipping magnetic foliations. K_{1av} is subhorizontal, and trends consistently NE–SW to ENE–WSW. The orientations of K_{1av} are counterclockwise oblique to the HISZ and the TSZ, and it rotates in a clockwise manner in the rocks of textural types 2 and 3 as the TSZ is approached.

The magnetic foliation is horizontal (vertical K_{3av}) at sites 16, 17 and 18, where the vertical quartz foliation is present. The biotite foliation, as indicated by the AMS, is *perpendicular to the vertical quartz aggregate foliation* that represents the superimposed subsolidus strain. This is interpreted to indicate that the subsolidus strain that formed the quartz aggregate foliation was superimposed on a horizontal biotite foliation that likely formed during magmatic deformation. The intensity of the subsolidus strain was apparently insufficient to reorient the biotite foliation at those sites.

5.3. Discussion

Maps of the AMS fabric orientations along two traverses through the Canso granite pluton show that an earlier-formed horizontal biotite fabric in the Canso pluton was reworked and locally overprinted by rather minor amounts of ductile strain as it cooled from the solidus. The ductile strain is certainly related to the well documented dextral shearing along the transcurrent Meguma–Avalon tectonic terrane boundary, the

Table 2 Site average magnetic fabric data.

	Traverse 1						Traverse 2				
		Orientations						Orientations			
Site, Type	$K\ 10^{-6}$ SI	K_1	K_3	Anisotropy P'%	Shape T	Site, Type	$K\ 10^{-6}$	K_1	K_3	Anisotropy P'%	Shape T
1, 1	34·28	199/18	101/25	2·1	0·055	16, 2	55·52	262/02	159/81	9·1	0·088
2, 1	42·02	210/23	315/31	1·7	− 0·826	17, 2	62·08	259/04	008/79	7·9	− 0·259
3, 1	34·16	019/12	132/63	5·2	0·481	18, 2	50·55	272/12	058/75	11·1	− 0·043
4, 1	61·13	046/00	296/89	3·7	− 0·037	19, 1	25·10	231/09	102/76	2·4	0·331
5, 1	40·95	323/56	094/24	2·7	0·401	20, 1	33·58	057/04	310/76	4·8	− 0·598
6, 2	41·51	218/10	343/73	5·3	− 0·565	21, 2	30·09	262/06	170/12	3·4	− 0·734
7, 2	37·85	221/11	320/39	5·7	− 0·456	22, 1	107·1	230/13	124/48	6·7	0·285
8, 2	37·18	225/01	317/45	5·9	− 0·288	23, 1	79·72	241/04	351/79	4·7	− 0·240
9, 2	31·69	231/05	323/28	5·6	− 0·636	24, 1	84·12	264/09	056/80	4·1	− 0·082
10, 2	37·63	243/02	333/01	7·1	0·052	25, 1	34·53	195/04	293/66	6·4	0·440
11, 3	36·77	066/05	157/06	9·4	0·261	26, 1	41·66	254/13	035/74	3·2	0·818
12, 3	40·01	071/03	161/01	10·2	0·071	27, 1	45·51	208/07	034/83	2·0	0·250
13, 2	55·58	088/08	352/37	5·8	− 0·169	28, 1	36·43	217/05	315/54	5·4	0·119
14, 2	46·42	091/02	000/14	7·4	0·176	29, 3	48·82	092/13	353/34	7·6	− 0·771
15, 2	61·79	263/08	166/43	7·4	− 0·025	30, 2	52·21	074/01	164/02	6·7	0·190

Site=sampling site; Type=Textural type (see Table 1); K=magnetic susceptibility; K_1, K_3=principal directions of the anisotropy of magnetic susceptibility; P'%=degree of anisotropy *100 (see text); $T=2(\ln K_2 - \ln K_3/(\ln K_1 - \ln K_3) - 1$ describes the shape of the AMS ellipsoid (Jelinek 1981), where $T=1$ for a perfectly oblate ellipsoid, and $T=-1$ for a perfectly prolate ellipsoid.

CCFZ. The dextral-shear overprint of the fabrics in the Canso pluton confirms that dextral displacements occurred on the CCFZ at 370 Ma. The results also support the use of fabrics in weakly deformed granites to determine the bulk kinematics in orogenic belts, as previously proposed for leucogranites of the Pyrenées mountain belt (Leblanc *et al.* 1996; Gleizes *et al.* 1997).

Previous magnetic fabric studies of the South Mountain batholith (Benn *et al.* 1997) and of the Barrington Passage pluton (Pignotta & Benn 1999), both of which crop out within the Meguma Terrane but far from the transcurrent Meguma–Avalon terrane boundary, showed that the magnetic lineations in the plutons were reworked into orientations parallel to the regional fold axes. In the Canso pluton, which crops out quite close to the transcurrent terrane boundary, the lineations are not parallel to the regional fold hinges; instead, they are oblique to the terrane-bounding shear zone. It is proposed that this difference in the fabric record can be attributed to strain and displacement partitioning in a bulk transpressional orogen (Tikoff & Teyssier 1994). In the South Mountain batholith and the Barrington Passage plutons, the fold-parallel fabrics are indicative of bulk pure shear in the folded rocks far from the terrane bounding shear zone, whereas the fabrics of the Canso pluton record the partitioning of orogen-parallel displacements and bulk non-coaxial strains into the CCFZ.

Another point can be made that is of interest for interpretations of AMS fabrics in granites, in general. The fabrics in the rocks of textural type 2 have certainly been reworked by a weak tectonic strain, resulting in the reorientation of the lineations and a steepening of the foliation. In those rocks the evidence of solid-state strain is limited to the elongation of recrystallised quartz aggregates, whereas feldspar and mica crystals are for the most part undeformed. Therefore, it should be noted that the fabrics in such weakly deformed rocks cannot be easily interpreted as recording only magmatic deformation or emplacement-related strain.

For example, on traverse 1, the AMS measurements of samples from several sites of textural type 1 reveal horizontal foliations and magnetic lineations that are oriented NNE–SSW, making angles as great as 75° with respect to the HISZ. Those fabrics might be interpreted as indicating a horizontal NNE–SSW flow during emplacement of the granitic magma, with the flow trajectory oriented perpendicular to a feeder zone represented by the nearby CCFZ, in a manner similar to the interpretation of magnetic anisotropy fabrics in the Archean Lebel syenite pluton, Canada (Cruden & Launeau 1994). However, given the tectonic overprint of fabrics elsewhere in the Canso pluton, it is stressed that interpretations of the AMS in terms of magma emplacement, in this study, would be highly equivocal.

6. Fabric overprinting in transpression

This section investigates the possibility of constraining the kinematics of the non-coaxial strain that was partitioned into the transurrent terrane boundary during advanced stages of collision of the Meguma and Avalon terranes. A recent study of syntectonic granites in the Vosges Mountains of France proved successful in modelling AMS fabric development and strain partitioning in an overall transtensional regime (Kratinova *et al.* 2007). A slightly different approach to the numerical simulations is taken to the one used by those authors, but the aim of the modelling is similar.

Numerical models can been applied to predict the evolutions of petrofabrics of populations of mineral grains during progressive strain histories, and the modelled petrofabrics can then be used to easily calculate the expected AMS, which can be compared to the measured AMS of rocks to infer strains and strain paths (Richter 1992; Hrouda 1993). The approach used here is similar to that used by Benn 1994, but the progressive strain is transpressional, rather than simple shear and pure shear.

The preferred orientation of the c-axes of biotite crystals was measured for a sample from site CN3 (traverse 1), using a universal stage. Site CN3 is classified as textural type 1, and the AMS indicated a horizontal biotite foliation and a NNE–SSW lineation (Fig. 5). The measured biotite fabric was subjected to successive small strain increments, using the incremental strain matrix,

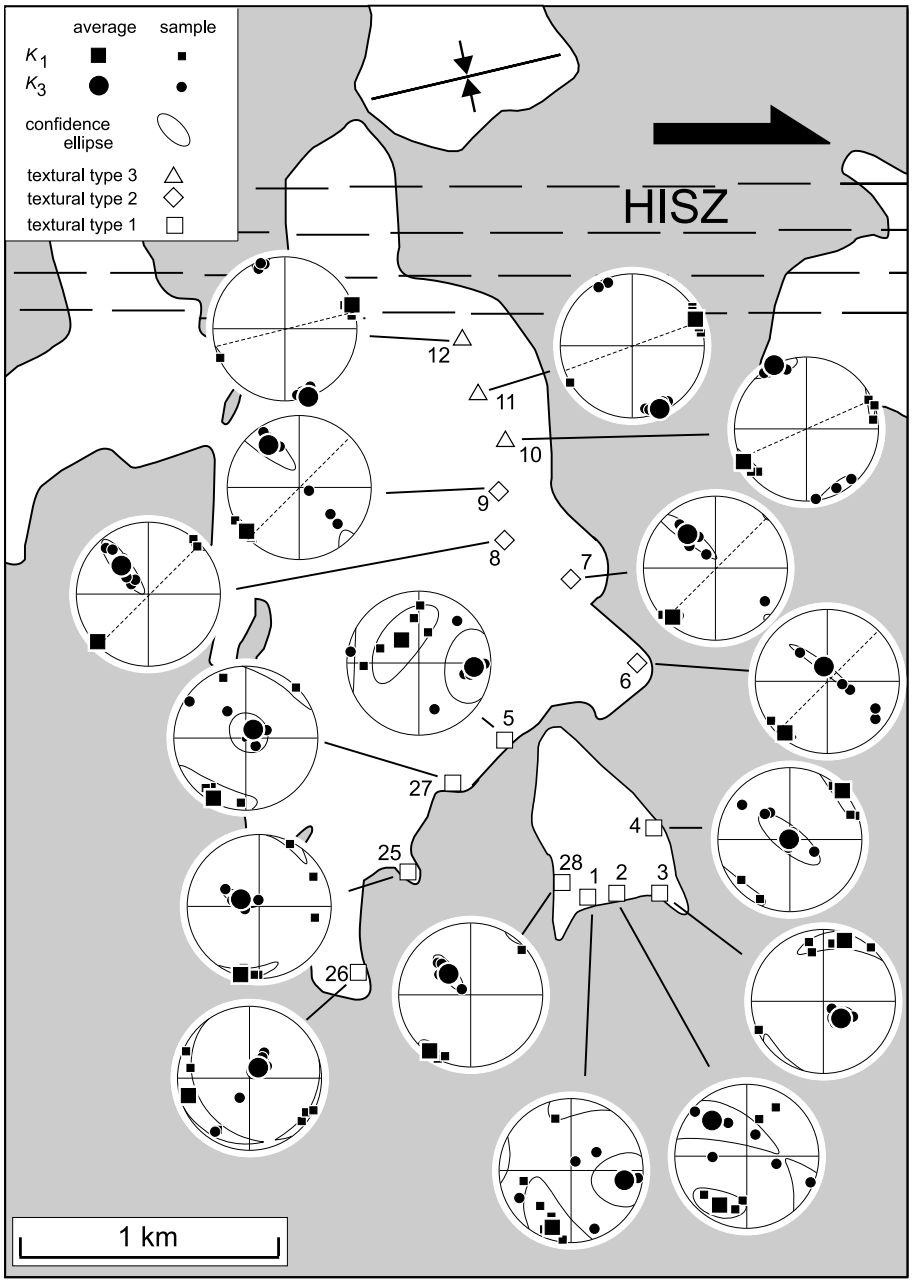

Figure 5 Map of traverse 1, south of the Harbour Island shear zone (HISZ). The number of each sampling site is indicated next to the site. The principal directions of the AMS are shown in lower-hemisphere equal-area projections. Dashed lines in some projections indicate the trace of the vertical quartz–aggregate foliation measured in outcrop. The map area is located in Figure 1.

$$\begin{bmatrix} a & -\gamma & 0 \\ 0 & 1 & 0 \\ 0 & 0 & a^{-1} \end{bmatrix}$$

to simulate progressive, homogeneous strain of the biotite c-axis petrofabric. This is the kinematic model of transpression proposed by Sanderson & Marchini (1984). The dextral simple-shear component of strain takes place along vertical east–west planes, parallel to the CCFZ. γ represents the incremental shear strain. a^{-1} represents the incremental stretch of a line oriented north–south horizontal, and a represents the incremental stretch of a vertical line.

The parameter $T_i = \gamma_i(1 - a_i^{-1})^{-1}$ is used to indicate the relative contributions of incremental pure shear and incremental simple shear (Sanderson & Marchini 1984). Positive values of T_i indicate 'transpression', in the sense that the pure shear component of incremental strain has a vertical X-axis and a horizontal, N–S oriented Z-axis. Negative values of T_i indicate 'transtension', where the pure shear component of incremental strain has the Z-axis vertical and the X-axis N–S horizontal. $|T_i| \rightarrow 0$ indicates an increasing component of incremental pure shear and $T_i = \infty$ indicates simple shear. The incremental strains were calculated with γ held constant at 0·01, and incremental $a^1 = 1 - (\gamma/T_i)$. At each increment in the strain history, the AMS is calculated by summing the susceptibility tensor for each biotite crystal in the petrofabric population, assuming a perfectly oblate AMS for each crystal and an anistropy value (P′) of 1·35 (Hrouda 1993).

One limitation of the approach is that the shapes of biotite crystals are not taken into account; rotations of crystals are governed by the application of the transpressional strain tensor to the vectors defining the orientations of the c-axes of the

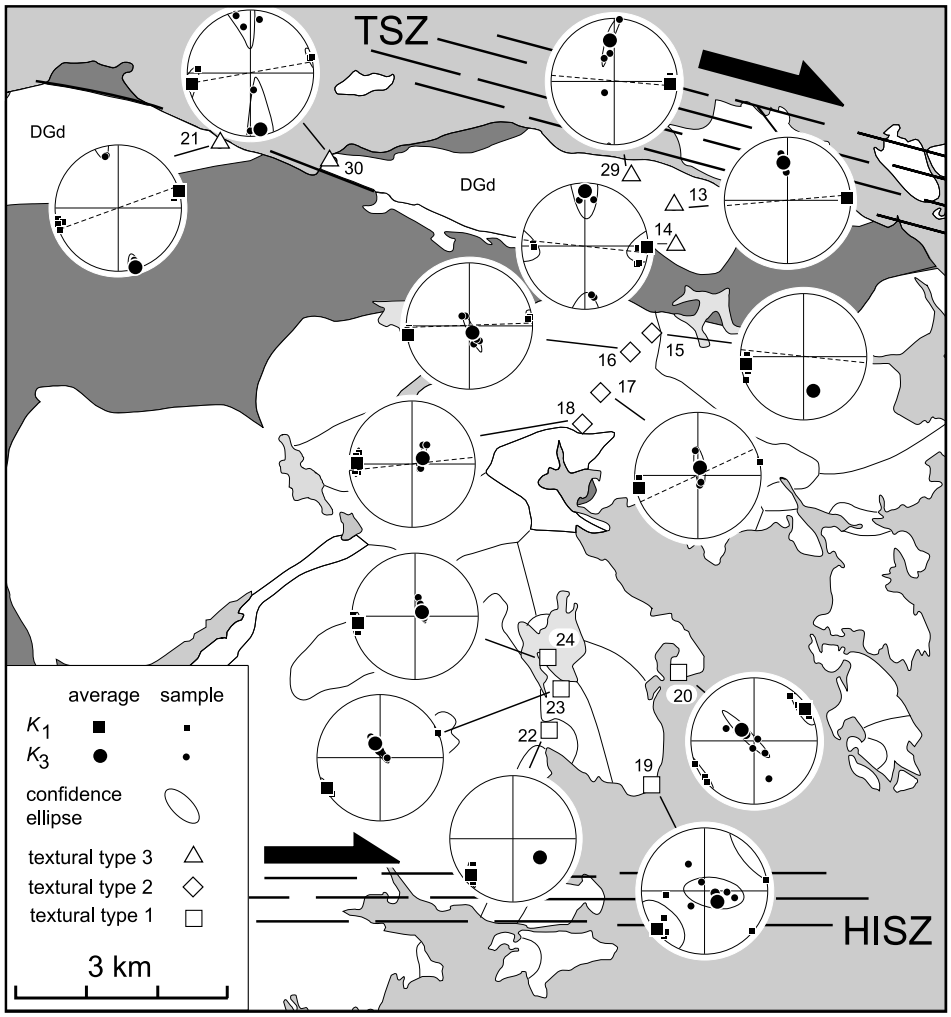

Figure 6 Map of traverse 2, south of the Tittle shear zone (TSZ). The number of each sampling site is indicated next to the site. The principal directions of the AMS are shown in lower-hemisphere equal-area projections. Dashed lines in some projections indicate the trace of the vertical quartz–aggregate foliation measured in outcrop. The map area is located in Figure 1.

crystals. In other words, the biotite crystals are assumed to behave as planes that are reoriented in response to the imposed strain (March 1931). That simplification is not unreasonable for biotite platelets with high aspect ratios. Only small strains are considered here, so that the possibility of periodic petrofabric evolutions which may arise at high strains for populations of crystals with lower aspect ratios (Ildefonse *et al.* 1997) does not need to be taken into account.

The modelling is intended to simulate the variations in the biotite fabric orientations and intensities documented using the AMS, from the undeformed granites of textural type 1 far from the shear zones, through textural types 2 and 3 as the shear zones are approached. An underlying assumption is that the changes in the biotite fabrics along a traverse from type 1 through type 3 represents a time- and strain-progressive overprint of the magmatic fabric at sampling site 3. In support of that interpretation it is noted that strain increases with decreasing distance from the shear zones, as indicated by the intensity of the visible fabric. Also, the microstructures suggest that deformation and dynamic recrystallisation proceeded at slightly lower temperatures as the pluton cooled.

Lower-hemisphere projections of several steps in the progressive evolutions of the strain ellipsoids (modelled extension lineations and foliation poles, Fig. 7A–F) and of the K_1 and K_3 principal directions of the AMS (the magnetic lineation and the pole to the magnetic foliation, Fig. 7G–L) are presented for different strain histories (transpression, transtension and simple shear). The plots show results for steps labelled 1–4, corresponding to strain intensity values of 0·25, 0·50, 1·00, and 1·50. Strain intensities are calculated as (Nadai 1963):

$$\bar{\varepsilon}_s = \sqrt{3}/3[(\varepsilon_1 - \varepsilon_2)^2 + (\varepsilon_2 - \varepsilon_3)^2 + (\varepsilon_3 - \varepsilon_1)^2]^{0.5}$$

For large degrees of incremental N–S shortening, perpendicular to the terrane boundary (transpression, $T_i = 3$, Fig. 7D), there may be a transient stage (steps 2 to 3) where the magnetic fabric path is similar to the pattern mapped in the granites, but at higher strains the magnetic lineation migrates to steeper plunges (steps 3 to 4). The modelled stretching lineation would also be vertical at relatively low strains, as previously shown by Sanderson & Marchini (1984). For large incremental stretches perpendicular to the Minas fault zone (transtension, $T_i = -3$, Fig. 7F), the magnetic foliation would not become vertical and such a strain path could not be responsible for the fabric pattern in the Canso granites.

Progressive simple-shear ($T_i = \infty$, Fig. 7A) and progressive transpressional or transtensional strain histories with small to moderate degrees of incremental pure-shear ($5 \leq T_i \leq 10$, Fig. 7B, C; $T_i = -6$, Fig. 7E) all produce evolutions in the orientations of the strain axes and of the magnetic fabric axes which resemble those mapped across the strain gradients from textural type 1 to textural type 3. In each of these examples the magnetic lineation is oriented close to the stretching lineation at $\bar{\varepsilon}_s \leq 0{\cdot}45$. The magnetic foliation becomes vertical at strain

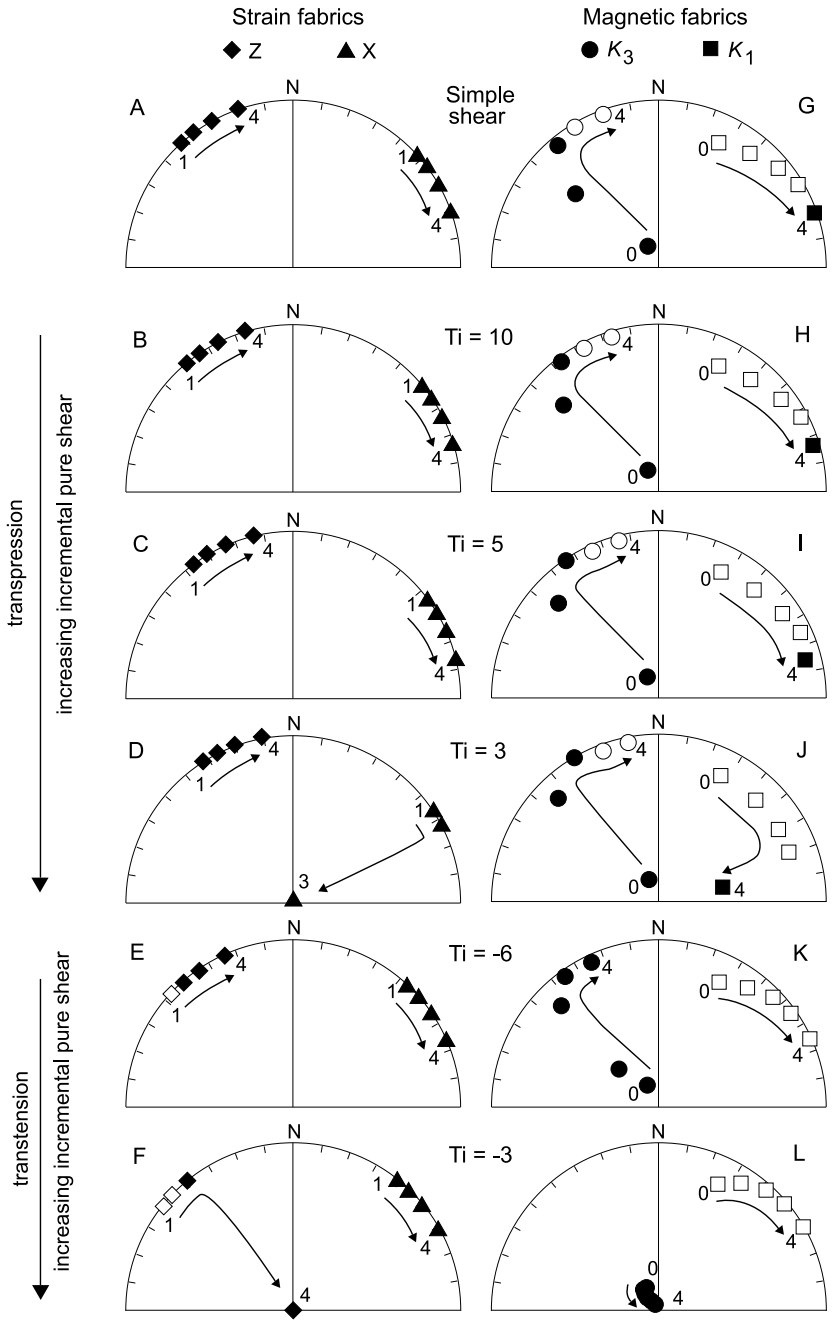

Figure 7 Results of numerical simulations of strain and fabric development during transpression and transtension. The progressive strain histories were applied to an initial biotite petrofabric that was measured for an undeformed granite sample from sample site CN3 (Fig. 5). Equal-area projections. Filled symbols are on the lower hemisphere and open symbols are on the upper hemisphere. Data are plotted for four stages of each strain history. In the magnetic fabrics diagrams, stage 0 is the AMS calculated for the initial petrofabric from sample site CN3.

intensities that are lower during progressive transpressional or simple-shear strain histories than during progressive transtensional strain histories. This is seen by comparing the data for steps 2, $T_i = \infty$, 10 and 5, with that for step 3, $T_i = -6$ (Fig. 7A, B, C and E; Table 2). Increasing progressive transtensional strain could result in verticalisation of the magnetic foliation and in coaxial magnetic and finite strain axes, as seen in more strongly deformed rocks near to the shear-zones (Fig. 7E).

The results of the models presented here suggest that the fabric pattern in the Canso granites could be explained by a progressive strain history represented by simple-shear, or by transpression or transtension with small to moderate components of incremental shortening or stretching perpendicular to the Minas fault zone. The model results indicate that a transtensional strain history would be most likely to preserve the early-formed horizontal magnetic foliation mapped in the rocks of textural type 2, where the magnetic lineation would have rotated to lie in the plane of the mesoscopic quartz-aggregate foliation observed in the field.

7. Conclusions

The anisotropy of magnetic susceptibility (AMS) was used to map the preferred orientations of biotite crystals in a granite pluton that was emplaced during the Late Devonian Acadian Orogeny, in Nova Scotia. The pluton was emplaced near the transcurrent boundary between the Meguma and Avalon tectonic terranes. Careful consideration of the magnetic fabrics in a framework including structural, microstructural and regional tectonic information shows that the AMS fabrics

(inferred to indicate biotite fabrics) preserve a record of syn- to post-emplacement dextral shear on the terrane boundary. The post-emplacement shearing occurred as the pluton cooled from the solidus. An early-formed horizontal fabric, preserved at some sampling sites, was reworked and overprinted by small amounts of tectonic deformation. The results confirm the usefulness of AMS fabrics in weakly deformed syntectonic plutons as markers of the bulk kinematics of orogens. Comparison of the fabrics in the Canso plutons, documented here, with previous results from plutons of similar ages but further from the terrane boundary, within the Meguma Terrane, shows that the fabrics in granites situated within different parts of an orogen can be used to map the partitioning of coaxial and non-coaxial strains that are predicted for transpressional orogens.

Numerical simulations of the fabric evolutions in the Canso pluton suggest that the kinematics of transcurrent shearing along this part of the Meguma–Avalon terrane boundary involved simple-shear or transpression, or transpression with small components of pure shear oriented perpendicular to the bounding shear zone. A markedly transpressional or transtensional progressive strain history is apparently ruled out in this study.

8. Acknowledgements

The field work for this study was funded by a Natural Sciences and Engineering Research Council of Canada (NSERC) research grant to the author. G. S. Pignotta and S. Siegesmund provided reviews that improved the paper.

9. References

Aranguren, A., Cuevas, J. & Tubía, J. M. 1996. Composite magnetic fabrics from S–C mylonites. *Journal of Structural Geology* **18**, 863–9.

Barbarin, B. 1990. Granitoids: main petrogenetic classifications in relation to origin and tectonic setting. *Geological Journal* **25**, 227–38.

Becker, J. K., Siegesmund, S. & Jelsma, H. A. 2000. The Chinamora batholith, Zimbabwe: structure and emplacement-related magnetic fabric. *Journal of Structural Geology* **22** (11–12), 1837–53.

Benn, K. 1994. Overprinting of magnetic fabrics in granites by small strains: numerical modelling. *Tectonophysics* **233**, 153–62.

Benn, K., Rochette, P., Bouchez, J.-L. & Hattori, K. 1993. Magnetic susceptibility, magnetic mineralogy and magnetic fabrics in a late Archean granitoid-gneiss belt. *Precambrian Research* **63**, 59–81.

Benn, K., Horne, R. J., Kontak, D. J., Pignotta, G. & Evans, N. G. 1997. Syn-Acadian emplacement model for the South Mountain Batholith, Meguma Terrane, Nova Scotia: Magnetic fabric and structural analyses. *Geological Society of America Bulletin* **109**, 1279–93.

Benn, K., Ham, N. M., Pignotta, G. S. & Bleeker, W. 1998. Emplacement and Deformation of Granites During Transpression – Magnetic Fabrics of the Archean Sparrow Pluton, Slave Province, Canada. *Journal of Structural Geology* **20** (9–10), 1247–59.

Benn, K., Roest, W. R., Rochette, P., Evans, N. G. & Pignotta, G. S. 1999. Geophysical and structural signatures of syntectonic batholith construction: the South Mountain Batholith, Meguma Terrane, Nova Scotia. *Geophysical Journal International* **136**, 144–58.

Benn, K., Paterson, S. R., Lund, S. P., Pignotta, G. S. & Kruse, S. 2001. Magmatic fabrics in batholiths as markers of regional strains and plate kinematics: example of the Cretaceous Mt. Stuart batholith. *Physics and Chemistry of the Earth* **26** (4–5), 343–54.

Bolle, O., Diot, H. & Trindade, R. I. F. 2003. Magnetic fabrics in the Holum granite (Vest-Agder, southernmost Norway): implications for the late evolution of the Sveconorwegian (Grenvillian) orogen of SW Scandinavia. *Precambrian Research* **121** (3–4), 221–49.

Borradaile, G. 1987. Anisotropy of magnetic susceptibility: rock composition versus strain. *Tectonophysics* **138**, 327–9.

Borradaile, G. J. 1988. Magnetic susceptibility, petrofabrics and strain. *Tectonophysics* **156**, 1–20.

Borradaile, G. J. 2003. *Statistics of Earth Science data.* New York: Springer-Verlag. 351 pp.

Borradaile, G. J. & Henry, B. 1997. Tectonic applications of magnetic susceptibility and its anisotropy. *Earth-Science Reviews* **42**, 49–93.

Borradaile, G. J. & Werner, T. 1994. Magnetic anisotropy of some phyllosilicates. *Tectonophysics* **235**, 223–48.

Bouchez, J.-L. 1997. Granite is never isotropic: an introduction to AMS studies of granitic rocks. *In* Bouchez, J.-L., Hutton, D. H. W. & Stephens, W. E. (eds) *Granite: from segregation of melt to emplacement fabrics*, 95–112. Dordrecht: Kluwer Academic Publishers.

Bouchez, J.-L. 2000. Anisotropie de susceptibilité magnétique et fabrique des granites. *Comptes Rendus à l'Académie des Sciences de Paris, Sciences de la Terre et des planètes* **330**, 1–14.

Bouchez, J.-L., Gleizes, G., Djouadi, T. & Rochette, P. 1990. Microstructure and magnetic susceptibility applied to emplacement kinematics of granites: the example of the Foix pluton (French Pyrenees). *Tectonophysics* **184**, 157–71.

Bouchez, J.-L. & Gleizes, G. 1995. Two-stage deformation of the Mont-Louis-Andorra granite pluton (Variscan Pyrenees) inferred from magnetic susceptibility anisotropy. *Journal of the Geological Society, London* **152**, 669–79.

Čečys, A. & Benn, K. 2007. Emplacement and deformation of the ca. 1.45 Ga Karlshamn granitoid pluton, southwestern Sweden, during ENE–WSW Danopolonian shortening. *International Journal of Earth Sciences* **96**, 397–414.

Clarke, D. B., Chatterjee, A. K. & Giles, P. S. 1993. Petrochemistry, tectonic history, and Sr–Nd systematics of the Liscomb Complex, Meguma Lithotectonic Zone, Nova Scotia. *Canadian Journal of Earth Sciences* **30**, 449–64.

Clarke, D. B. & Halliday, A. N. 1980. Strontium isotope geology of the South Mountain Batholith, Nova Scotia. *Geochimica et Cosmochimica Acta* **44**, 1045–58.

Cruden, A. R. & Launeau, P. 1994. Structure, magnetic fabric and emplacement of the Archean Lebel Stock, SW Abitibi Greenstone Belt. *Journal of Structural Geology* **16**, 677–91.

Czeck, D. M., Maes, S. M., Sturm, C. L. & Fein, E. M. 2006. Assessment of the relationship between emplacement of the Algoman plutons and regional deformation in the Rainy Lake region, Ontario. *Canadian Journal of Earth Sciences* **43** (11), 1653–71.

D'Eramo, F., Pinotti, L., Tubía, J. M., Vegas, N., Aranguren, A. Tejero, R. & Gómez, D. 2006. Coalescence of lateral spreading magma ascending through dykes: a mechanism to form a granite canopy (El Hongo pluton, Sierras Pampeanas, Argentina). *Journal of the Geological Society, London* **163**, 881–92.

Dallmeyer, R. D. & Keppie, J. D. 1987. Polyphase late Paleozoic tectonothermal evolution of the southwestern Meguma Terrane, Nova Scotia: evidence from Ar^{40}/Ar^{39} mineral ages. *Canadian Journal of Earth Sciences* **24**, 1242–54.

Dehls, J. F., Cruden, A. R. & Vigneresse, J. L. 1998. Fracture Control of Late Archean Pluton Emplacement in the Northern Slave Province, Canada. *Journal of Structural Geology* **20** (9–10), 1145–54.

Djouadi, M. T., Gleizes, G., Ferré, E., Bouchez, J. L., Caby, R. & Lesquer, A. 1997. Oblique Magmatic Structures of Two Epizonal Granite Plutons, Hoggar, Algeria – Late-Orogenic Emplacement in a Transcurrent Orogen. *Tectonophysics* **279** (1–4), 351–74.

Gapais, D. 1989. Shear structures within deformed granites: mechanical and thermal indicators. *Geology* **17**, 1144–7.

Gebelin, A., Martelet, G., Chen, Y., Brunel, M. & Faure, M. 2006. Structure of late Variscan Millevaches leucogranite massif in the French Massif Central: AMS and gravity modelling results. *Journal of Structural Geology* **28** (1), 148–69.

Gleizes, G., Leblanc, D. & Bouchez, J.-L. 1997. Variscan granites of the Pyrenees revisited: their role as syntectonic markers of the orogen. *Terra Nova* **9**, 38–41.

Gleizes, G., Leblanc, D., Santana, V., Olivier, P. & Bouchez, J.-L. 1998. Sigmoidal Structures Featuring Dextral Shear During Emplacement of the Hercynian Granite Complex of Cauterets-Panticosa (Pyrenees). *Journal of Structural Geology* **20** (9–10), 1229–45.

Hill, J. D. 1988. Late Devonian peraluminous granitic plutons in the Canso area, eastern Meguma Terrane, Nova Scotia. *Maritime Sediments and Atlantic Geology* **24**, 11–19.

Hill, J. D. 1991. Petrology, tectonic setting, and economic potential of Devonian peraluminous granitoid plutons in the Canso and Forest Hills areas, eastern Meguma Terrane, Nova Scotia. *Geological Survey of Canada Bulletin* **383**. 96 pp.

Horne, R. & Culshaw, N. 2001. Flexural-slip folding in the Meguma Group, Nova Scotia. *Canada Journal of Structural Geology* **23** (10), 1631–52.

Housen, B. A., Richter, C. & van der Pluijm, B. A. 1993. Composite magnetic anisotropy fabrics: experiments, numerical models, and implications for the quantification of rock fabrics. *Tectonophysics* **220**, 1–12.

Hrouda, F. 1982. Magnetic anisotropy of rocks and its application in geology and geophysics. *Geophysical Surveys* **5**, 37–82.

Hrouda, F. 1993. Theoretical models of magnetic anisotropy to strain relationship revisited. *Physics of the Earth and Planetary Interiors* **77**, 237–49.

Ildefonse, B., Arbaret, L. & Diot, H. 1997. Rigid particles in simple shear flow: is their preferred orientation periodic or steady-state? *In* Bouchez, J.-L., Hutton, D. H. W. & Stephens, W. E. (eds) *Granite: from segregation of melt to emplacement fabrics*, 177–85. Dordrecht: Kluwer Academic Publishers.

Ishihara, S. 1981. The granitoid series and mineralization. *Economic Geology, 75th Anniversary Volume*, 458–84.

Jelinek, V. 1978. Statistical processing of anisotropy of magnetic susceptibility measured on groups of specimens. *Studia Geophyzika et Geodetika* **22**, 50–62.

Jelinek, V. 1981. Characterization of magnetic fabric of rocks. *Tectonophysics* **79**, 563–7.

Keppie, J. D. 1982. *Tectonic Map of the Province of Nova Scotia*. Nova Scotia, Halifax: Department of Mines and Energy.

Keppie, J. D. 1993. Synthesis of Palaeozoic deformational events and terrane accretion in the Canadian Appalachians. *Geologisches Rundschau* **82**, 381–431.

Keppie, J. D., Dallmeyer, R. D., Krogh, T. E. & Aftalion, A. 1993. Dating mineralization using several isotopic methods: and example from the South Mountain Batholith, Nova Scotia, Canada. *Chemical Geology* **103**, 251–70.

Keppie, J. D. & Dallmeyer, R. D. 1987. Dating transcurrent terrane accretion: an example from the Meguma and Avalon composite terranes in the northern Appalachians. *Tectonics* **6**, 831–47.

Kratinova, Z., Schulmann, K., Edel, J. B., Jezek, J. & Schaltegger, U. 2007. Model of successive granite sheet emplacement in transtensional setting: Integrated microstructural and anisotropy of magnetic susceptibility study. *Tectonics* **26** (6). doi:10.29/2006TC002035.

Leblanc, D., Gleizes, G., Roux, L. & Bouchez, J.-L. 1996. Variscan dextral transpression in the French Pyrenees: new data from the Pic des Trois-Seigneurs granodiorite and its country rocks. *Tectonophysics* **261**, 331–45.

March, A. 1931. Mathematische Theorie der Regelung nach der Korngestalt bei affiner Deformation. *Zeitschrift für Kristallographie* **81**, 285–97.

Mawer, C. K. & White, J. C. 1987. Sense of displacement on the Cobequid–Chedabucto fault system, Nova Scotia, Canada. *Canadian Journal of Earth Sciences* **24**, 217–23.

Mawer, C. K. & Williams, P. F. 1986. Structural study of highly deformed Meguma phyllite and granite, vicinity of White Head village, S.E. Nova Scotia. *Maritime Sediments and Atlantic Geology* **22**, 51–64.

Molyneux, S.J. & Hutton, D. H. W. 2000. Evidence for significant granite space creation by the ballooning mechanism: the example of the Ardara pluton, Ireland. *Geological Society of America Bulletin* **112**, 1543–58.

Muecke, G. K., Elias, P. & Reynolds, P. H. 1988. Hercynian/Alleghanian overprinting of an Acadian terrane. $^{40}Ar/^{39}Ar$ studies in the Meguma Zone, Nova Scotia, Canada. *Chemical Geology* **73**, 153–67.

Nadai, A. 1963. *Theory of flow and fracture of solids*, Volume 2. New York: McGraw-Hill. 705 pp.

Paterson, S. R., Vernon, R. H. & Tobisch, O. T. 1989. A review of criteria for the identification of magmatic and tectonic foliations in granitoids. *Journal of Structural Geology* **11**, 349–63.

Paterson, S. R., Fowler, T. K. Jr., Schmidt, K. L., Yoshinobu, A. S., Yuan, E. S. & Miller, R. B. 1998. Interpreting magmatic fabric patterns in plutons. *Lithos* **44**, 53–82.

Pignotta, G. S. & Benn, K. 1999. Magnetic fabric of the Barrington Passage pluton, Meguma Terrane, Nova Scotia: a two-stage fabric history of syntectonic emplacement. *Tectonophysics* **307** (1–2), 75–92.

Razanatseheno, M. O. M., Nédélec, A., Rakontondrazafy, M., Meert, J. G. & Ralison, B. 2010. Four-stage building of the Cambrian Carion pluton (Madagascar). *Earth and Environmental Science Transactions of the Royal Society of Edinburgh* **100**(for 2009), 133–45.

Reynolds, P. H., Zentilli, M. & Muecke, G. K. 1981. K–Ar and $^{40}Ar/^{39}Ar$ geochronology of granitoid rocks from southern Nova Scotia: Its bearing on the geological evolution of the Meguma Zone of the Appalachians. *Canadian Journal of Earth Sciences* **18**, 386–94.

Reynolds, P. H., Elias, P., Muecke, G. K. & Grist, A. M. 1987. Thermal history of the southwestern Meguma zone, Nova Scotia, from an $^{40}Ar/^{39}Ar$ and fission track dating of intrusive rocks. *Canadian Journal of Earth Sciences* **24**, 1952–65.

Richter, C. 1992. Particle motion and the modelling of strain response in magnetic fabrics. *Geophysical Journal International* **110**, 451–64.

Rochette, P. 1987. Magnetic susceptibility of the rock matrix related to magnetic fabric studies. *Journal of Structural Geology* **9**, 1015–20.

Rochette, P., Jackson, M. & Aubourg, C. 1992. Rock magnetism and the interpretation of anisotropy of magnetic susceptibility. *Reviews of Geophysics,* **30**, 209–26.

Rochette, P., Aubourg, C. & Perrin, M. 1999. Is this magnetic fabric normal? A review and case studies in volcanic formations. *Tectonophysics* **307** (1–2), 219–34.

Sanderson, D. J. & Marchini, W. R. D. 1984. Transpression. *Journal of Structural Geology* **6**, 449–58.

Schenk, P. E. 1971. Southeastern Atlantic Canada, northwestern Africa, and continental drift. *Canadian Journal of Earth Sciences* **8**, 1218–35.

Schenk, P. E. 1995. Meguma Zone. *In* Williams, H. (ed.) *Geology of the Appalachian–Caledonian Orogen in Canada and Greenland. Geology of Canada*, 261–77. Ottawa: Geological Survey of Canada.

Siegesmund, S. & Becker, J. K. 2000. Emplacement of the Ardara pluton (Ireland): new constraints from magnetic fabrics, rock fabrics and age dating. *International Journal of Earth Sciences* **89**, 307–27.

Tate, M. C., Clarke, D. B. & Heaman, L. M. 1997. Progressive hybridisation between Late Devonian mafic-intermediate and felsic magmas in the Meguma Zone of Nova Scotia, Canada. *Contributions to Mineralogy and Petrology* **126**, 401–15.

Tikoff, B. & Teyssier, C. 1994. Strain modeling of displacement-field partitioning in transpressional orogens. *Journal of Structural Geology* **16**, 1575–88.

Tobisch, O. T. & Cruden, A. R. 1995. Fracture-controlled magma conduits in an obliquely convergent continental magmatic arc. *Geology* **23**, 941–4.

Urai, J. L., Means, W. D. & Lister, G. S. 1986. Dynamic recrystallization of minerals. *In* Hobbs, B. E. & Heard, H. C. (eds) *Mineral and Rock Deformation: Laboratory Studies. Geophysical Monograph*, 161–99. Washington: American Geophysical Union.

Vernon, R. H. 2000. Review of microstructural evidence of magmatic and solid-state flow. *Electronic Geosciences* **5** (2): http://link.springer-ny.com/link/service/journals/10069/bibs/0005001/00050002.htm.

Vigneresse, J.-L. & Bouchez, J.-L. 1997. Successive Granitic Magma Batches During Pluton Emplacement – the Case of Cabeza De Araya (Spain). *Journal of Petrology,* **38** (12), 1767–76.

Williams, H. & Hatcher, R. H. J. 1982. Suspect terranes and accretionary history of the Appalachian orogen. *Geology* **10**, 530–6.

Žák, J., Schulmann, K. & Hrouda, F. 2005. Multiple magmatic fabrics in the Sazava pluton (Bohemian Massif, Czech Republic): a result of superposition of wrench-dominated regional transpression on final emplacement. *Journal of Structural Geology* **27** (5), 805–22.

MS received 29 January 20008. Accepted for publication 30 April 2008 (Stellenbosch); 15 January 2009 (RSE).

Chemical structure in granitic magmas – a signal from the source?

J. D. Clemens[1], P. A. Helps[2] and G. Stevens[1]

[1] Department of Earth Sciences, University of Stellenbosch, Private Bag X1, 7602 Matieland, South Africa
Email: jclemens@sun.ac.za

[2] School of Geography, Geology and the Environment, CEESR, Kingston University, Penrhyn Rd, Kingston-upon-Thames, Surrey KT1 2EE, UK

ABSTRACT: Though typically exhibiting considerable scatter, geochemical variations in granitic plutons and silicic volcanic deposits are commonly modelled as products of differentiation of originally homogeneous magmas. However, many silicic igneous bodies, particularly those classified as S-types, are internally heterogeneous in their mineralogy, geochemistry and isotope ratios, on scales from hundreds of metres down to one metre or less. The preservation of these heterogeneities supports recent models for the construction of granitic magma bodies through incremental additions of numerous batches (pulses) of magma derived from contrasting sources. Such pulses result from the sequential nature of the melting reactions and the commonly layered structure of crustal magma sources. Internal differentiation of these batches occurs, but not generally on the scales of whole magma chambers. Rather than being created through differentiation or hybridisation processes, at or near emplacement levels, much of the variation within such bodies (e.g. trace-element or Mg# variation with SiO_2 or isotope ratios) is a primary or near-source feature. At emplacement levels, the relatively high magma viscosities and slow diffusion rates of many chemical components in silicic melts probably inhibit processes that would lead to homogenisation. This permits at least partial preservation of the primary heterogeneities.

KEY WORDS: chemical variation, differentiation, granitic magma, inherited heterogeneity

Granitic and silicic volcanic rocks are a major component of the Earth's continental crust, and occur in a wide variety of tectonic settings. The geochemical variations found within granitic plutons and silicic volcanic deposits are commonly modelled as the result of processes that occur, during ascent and crystallisation, to modify the composition of an originally relatively homogeneous parent magma. Examples of such processes include various magma hybridisation phenomena (e.g. assimilation of wall rocks and magma mixing) and differentiation processes (e.g. crystal fractionation, crystal unmixing and fluid-driven leaching). These processes can result in chemical variation, and the production of a series of genetically related magma fractions. They can and do dominate the production of variation within some suites of mafic to intermediate igneous rocks, in which very well defined chemical variation trends are observed, and are supported by textural evidence for crystal-liquid separation. However, how generally realistic is the common approach of extending this set of models to more silicic magma systems? This paper defines silicic magmas as those that crystallise to 'granitic' rocks that would be classified (Le Maitre 1989) as alkali feldspar granites, syenogranites, monzogranites, granodiorites and trondhjemites. Rocks of this type dominate the world's silicic batholiths and volcanic complexes, in a wide range of ages and tectonic settings. Using a variety of evidence, it will be shown that there is reason to conclude that much geochemical variation in suites of silicic igneous rocks probably has its origin in primary variations inherited from the magma source regions. For silicic magmas, differentiation, hybridisation, etc. are secondary processes, commonly acting only at relatively small scales.

1. Previous work

Numerous previous studies have amply demonstrated the composite character of some silicic volcanic complexes and granitic bodies. In the volcanic context, a notable example is the work of Mills *et al.* (1997), Huysken *et al.* (2001) and Bindeman & Valley (2003) on the large-volume pyroclastic sequences of the SW Nevada Volcanic Field. These authors presented evidence for the eruption of magma batches with contrasting major-element, trace-element and isotopic characteristics, from the same set of vents, over geologically very short times, with aggregate magma volumes of the order of 1000 km^3.

In the plutonic context, Mohr (1991) studied the cryptic variations in Sr and Nd isotope ratios within the sheets that make up the huge, S-type Leinster batholith of Ireland, and concluded that the variations were inherited from the magma source region and that interactions between magma batches were minimal. Structural studies have identified many instances of incremental magma addition to growing plutons, leading to internally sheeted bodies with textural, mineralogical, geochemical and isotopic contrasts between adjacent sheets (e.g. McNulty *et al.* 1996; Paterson & Miller 1998; Wiebe & Collins 1998; Johnson *et al.* 1999; Miller & Paterson 2001; Weinberg *et al.* 2001; Mahan *et al.* 2003; Archanjo & Fetter 2004; Belcher & Kisters 2006). An example of this type of heterogeneity in a body apparently lacking sheeted structure is the Phillips pluton in Maine, studied by Pressley & Brown (1999). This body is composed of leucogranite enclosing centimetric to decametric masses of granodiorite. The two granitic compositions have contrasting Nd isotope ratios, and are

© 2009 The Royal Society of Edinburgh. doi:10.1017/S1755691009016053

inferred to have been derived from different rock types in a single heterogeneous source region. Pressley & Brown concluded that there had been no significant mixing between the magmas. White *et al.* (2001) came to a similar conclusion in considering Sr isotope heterogeneity in the relatively mafic S-type Jillamatong pluton of southeastern Australia. They regarded the lack of correlation between SiO_2 content and initial $^{87}Sr/^{86}Sr$ as evidence against any form of magma mixing. Scaillet *et al.* (1996) calculated the viscosities of Himalayan S-type leucogranites under likely temperature and fluid conditions during the genesis of the magmas by partial melting of metasediments. The viscosity that they found is around 3×10^4 Pa.s. They concluded that laminar flow in feeder dikes of the size actually observed in the Himalaya would cause source-derived heterogeneities in initial $^{87}Sr/^{86}Sr$ to be preserved, even if multiple, contrasting magma batches ascended as a single physical batch in the same conduit. These examples are all from S-type granitic rocks, and perhaps these might be expected to display such heterogeneity, given the strongly chemically layered nature of many clastic sedimentary accumulations. However, examples will be provided of I-type rocks that show similar features. The question posed is whether geochemical variation within these identified, isotopically distinct magma batches could also have a primary origin, rather than represent evidence for fractionation.

2. Geological context of the present study

This study draws on the authors' own petrological and geochemical data from a variety of high-level granitic and volcanic complexes of Archaean and Palaeozoic age, emplaced in tectonic settings varying from transcurrent shearing, to compressional terrane accretion and post-orogenic extension. Both I- and S-type examples are included, that vary in composition from granites and monzogranites to trondhjemites and granodiorites.

The Stolzburg pluton is a 3·45 Ga trondhjemite (Kamo & Davis 1994) that intrudes the Theespruit Formation, the stratigraphically lowermost unit in the Barberton Greenstone Belt of South Africa. Its tectonic setting is somewhat obscured by younger metamorphic events, but it has been suggested to represent a group of syntectonic sheets intruded during 3·45 Ga compressional accretion (de Wit *et al.* 1987; de Ronde & de Wit 1994). The Nelshoogte pluton is a synorogenic 3236 ± 1 Ma trondhjemite/tonalite body (de Ronde & Kamo 2000) that intruded the SW margin of the Belt during terrane amalgamation and metamorphism (Kisters *et al.* 2003). Both the Stolzburg and Nelshoogte plutons are characterised by exceptionally low degrees of strain, in the context of the Greenstone Belt, though both plutons have strong gneissosity in places, predominantly confined to the margins (e.g. Kisters *et al.* 2003).

The composite Criffell pluton was emplaced at 400 Ma into lower Palaeozoic formations of the Scottish Southern Uplands, during post-orogenic extension. It is an essentially undeformed, high-level, I-type body that contains little textural evidence of hybridisation or contamination (e.g. magmatic enclaves or xenoliths). Previous work has revealed an apparently concentric zoning pattern, in the form of a discontinuous outer margin of metaluminous hornblende granodiorite and a core of increasingly peraluminous muscovite-biotite granite (Stephens *et al.* 1985). Stephens & Halliday (1980) suggested that the granodiorite and the granite represent two separate magma pulses, and Stephens (1992) concluded that compositional variations within Criffell represent the aggregated effects of between-pulse and within-pulse variation, the between-pulse variation being generally dominant.

The 373 Ma Violet Town Volcanics of Central Victoria, in SE Australia (Clemens & Wall 1984) are undeformed, garnet- and cordierite-bearing, S-type, rhyolitic to rhyodacitic, intracaldera ignimbrites, emplaced subaerially onto the eroded surface of very low-grade Silurian to mid-Devonian marine metasediments, in a post-orogenic extensional setting, associated with development of red-bed basins.

The Dartmoor pluton, the largest granitic body in the Cornubian batholith of SW Britain, was emplaced into low-grade metasediments of Carboniferous age. Like the previous two groups of rocks, it was emplaced in a setting of post-orogenic extension. This granite is a peraluminous, S-type, emplaced at 280 Ma (Darbyshire & Shepherd 1985). Brammall & Harwood (1923) identified four main, textural facies that were sequentially intruded; a biotite microgranodiorite, a coarse-grained K–feldspar–phyric biotite granite, an equigranular, sparsely megacrystic granite, and various minor aplitic and microgranitic dykes. Contacts between the different facies are sharp.

3. Petrographic and textural evidence

Many granitic intrusions are internally heterogeneous, in the sense that they contain rocks with a wide range of compositions. Contacts between these rock fractions are seldom gradational over more than a few metres. Commonly, these internal contacts are quite sharp and clearly indicate intrusion of one phase by another, or several others. This sort of relationship suggests the successive intrusion of contrasting magma batches. These batches could be interpreted as magma fractions produced by differentiation elsewhere and then successively emplaced at the site of intrusion. However, there is evidence to the contrary, as will be seen below.

Chappell & White (1974) and Chappell (1984) defined S- and I-type granites. Whatever may be thought of that classification, it cannot be denied that different granitic magmas can be derived from quite contrasting source materials. Thus, it is noteworthy that there are numerous examples of granitic intrusions that are composite, in the sense that I- and S-type magma fractions clearly occupied different parts of the shared space in the pluton.

In the context of granitic complexes that are either purely S- or purely I-type, Belusova *et al.* (2006) studied the internal morphology, geochemistry and Hf and Pb isotope systematics of zircons from, amongst other rocks, a sample of the S-type Numbla Vale monzogranite from the Berridale batholith in southeastern Australia. The zoning within the zircons here indicates that there must have been several contrasting magma batches added to the pluton, from at least two contrasting sources. Thus, there is clear evidence that magmas with contrasting sources were involved in the construction of some granitic intrusions, and that the variations are not always readily apparent from field and petrographic examination of the rocks. Certainly, this variability is commonly on a large scale, and it is possible that the smaller magnitude variations, within these regionally extensive magma batches, could be due to differentiation processes. Again, however, evidence will be presented that such smaller-scale variations too are commonly not produced by *in situ* processes.

Large, intrusive, mafic to ultramafic bodies very commonly show signs of regionally extensive layering, sometimes cyclic in character. In these occurrences, less dense minerals commonly occupy the upper parts of the individual layers and the denser phases the lower, with the implication that gravity has played a major role in producing these structures. There are examples of layering caused by repeated injection of fresh magma, but

in situ differentiation seems to be the most plausible explanation for the origins of the stratification within the different layers. In contrast to the mafic and ultramafic intrusions, non-tectonised silicic intrusive rocks only very rarely exhibit any form of igneous layering. When it is present, it occurs on small scales (up to a few metres) and has been interpreted as the result of minor flow segregation of large and dense crystals suspended in the moving magma. Such local segregation processes cannot have been responsible for the production of large-scale variability in the compositions of the rocks within a granitic pluton. There is thus a fundamental difference in the mechanisms controlling crystal distribution within mafic and felsic magmas – probably due to the small but important contrast in the viscosities of the two sorts of magma (e.g. Clemens & Petford 1999), as well the significant difference in density contrast between the major rock-forming minerals in the two types of magmas. As has often been pointed out, and recently in the analysis by Whittington & Treloar (2002), the densities and viscosities of granitic magmas are strong functions of H_2O content in the melt. However, the work of Clemens & Petford (1999) and Clemens & Watkins (2001) showed the fundamental interdependence of temperature and melt H_2O content in the great majority of granitoid magmas. This means that the full range of possible viscosities and densities is not realised in nature and the influences of these parameters is therefore relatively small in purely felsic magma systems.

4. Major- and trace-element evidence

In mafic to intermediate rock series, SiO_2 content is a useful proxy for the degree of fractionation, so Harker plots portray the major- and trace-element variation very well. It is well known that groups of genetically related mafic to intermediate rocks show a strong tendency to form tight arrays in such plots (e.g. for TiO_2, Al_2O_3, FeO*, MgO, CaO and P_2O_5, and trace elements such as Ni, Cr, Sr and Zr). Some scatter is probably caused by differences in proportions of fractionating mineral phases and by analytical errors. Nevertheless, well defined trends are the norm. In contrast, the degree of scatter observed in Harker plots of the same elements in many silicic rock suites is much greater, even when the field relations suggest that the rocks are genetically related. Where it occurs, this scatter should not be dismissed as noise or analytical error. It is suggested that this feature of the geochemical data for silicic series points to magma features or processes that contrast with those in more mafic systems.

The question arises: what should chemical variation look like in a suite of felsic rocks produced by differentiation from a single parent magma? The best way to illustrate this is to examine inter-element plots for intrusive units for which all the geochemical and isotopic evidence points to *in situ* differentiation as the origin of the variation. One well-documented example is the I-type Boggy Plain pluton in south-eastern Australia (Wyborn *et al.* 2001). Figure 1 shows F (total Fe as FeO + MgO) plotted against TiO_2 and K_2O in the Boggy Plain rocks. The tightness of the variation here is shown by a large number of other oxides and elements, and is typical of rock series produced through fractionation processes. It shows more similarity with the variation in mafic suites than it does with typical felsic suites, which exhibit a much greater degree of scatter in the data. Indeed, here it appears that the felsic magmas are the products of differentiation of a parent mafic magma.

Another excellent example for felsic magmas in which crystal fractionation has controlled the chemical variation has

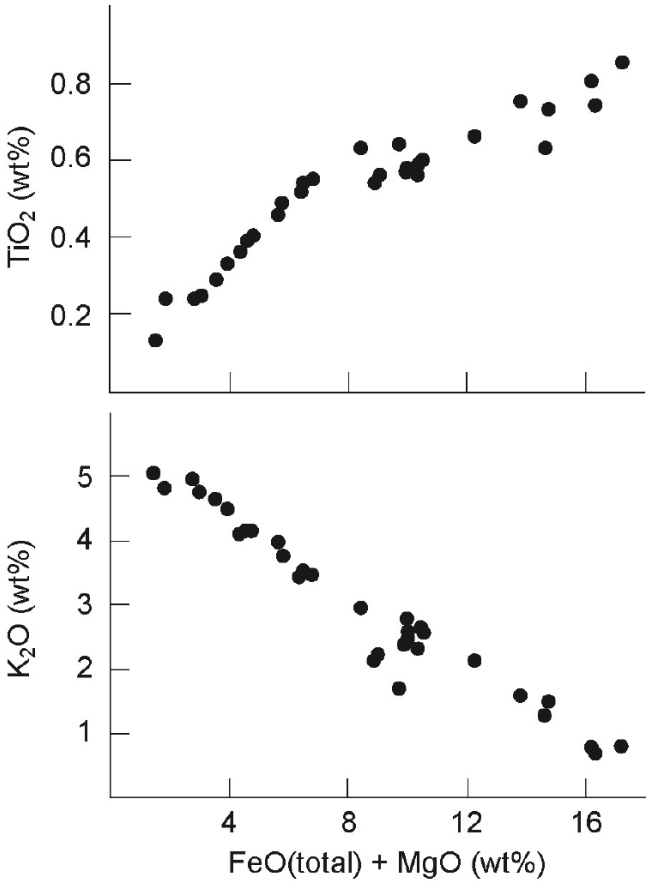

Figure 1 Selected inter-element correlation plots for the Boggy Plain pluton, redrawn from figure 3 of Wyborn *et al.* (2001).

recently been reported by Rodríguez *et al.* (2007). These authors describe isotopically homogeneous dacitic magmas that vary from about 62 to 66 wt% SiO_2. The parent magmas were apparently mantle-derived hybrids of andesitic composition and, like the Boggy Plain pluton, the Harker plots for major- and trace-element variations exhibit tight quasi-linear trends, produced through hornblende fractionation (Fig. 2). This variation was successfully modelled for both major and trace elements, including REE.

The preceding examples of tight chemical variations in felsic magmas, apparently due to differentiation by crystal fractionation, have important features in common. Such variations seem to occur in felsic systems derived by differentiation from mafic to intermediate parent magmas that are either mantle derived or mainly mantle-derived. In contrast, granitic magmas derived from crustal, or mainly crustal, sources typically show far less well-defined variations on a variety of geochemical plots. Some examples are provided below.

Figure 3 shows Harker plots for Mg#, CaO and P_2O_5 for the Stolzburg and Nelshoogte plutons, introduced earlier. The data define the type of rough negative trends that are typical for many crustally-derived granitic rock series. Particularly in the case of the Nelshoogte data, it might be argued that this negative correlation is a magma evolutionary trend of some kind. However, it is noteworthy that the Stolzburg and Nelshoogte data generally plot in the same area of the diagrams, and that the combined dataset defines more definite trends than does that for either individual pluton. The magma batches represented by these two plutons differ in age by ~200 Ma and are related only by the fact that they most probably formed through partial melting of similar, hydrated, metabasic source rocks (Clemens *et al.* 2006). Magmas formed

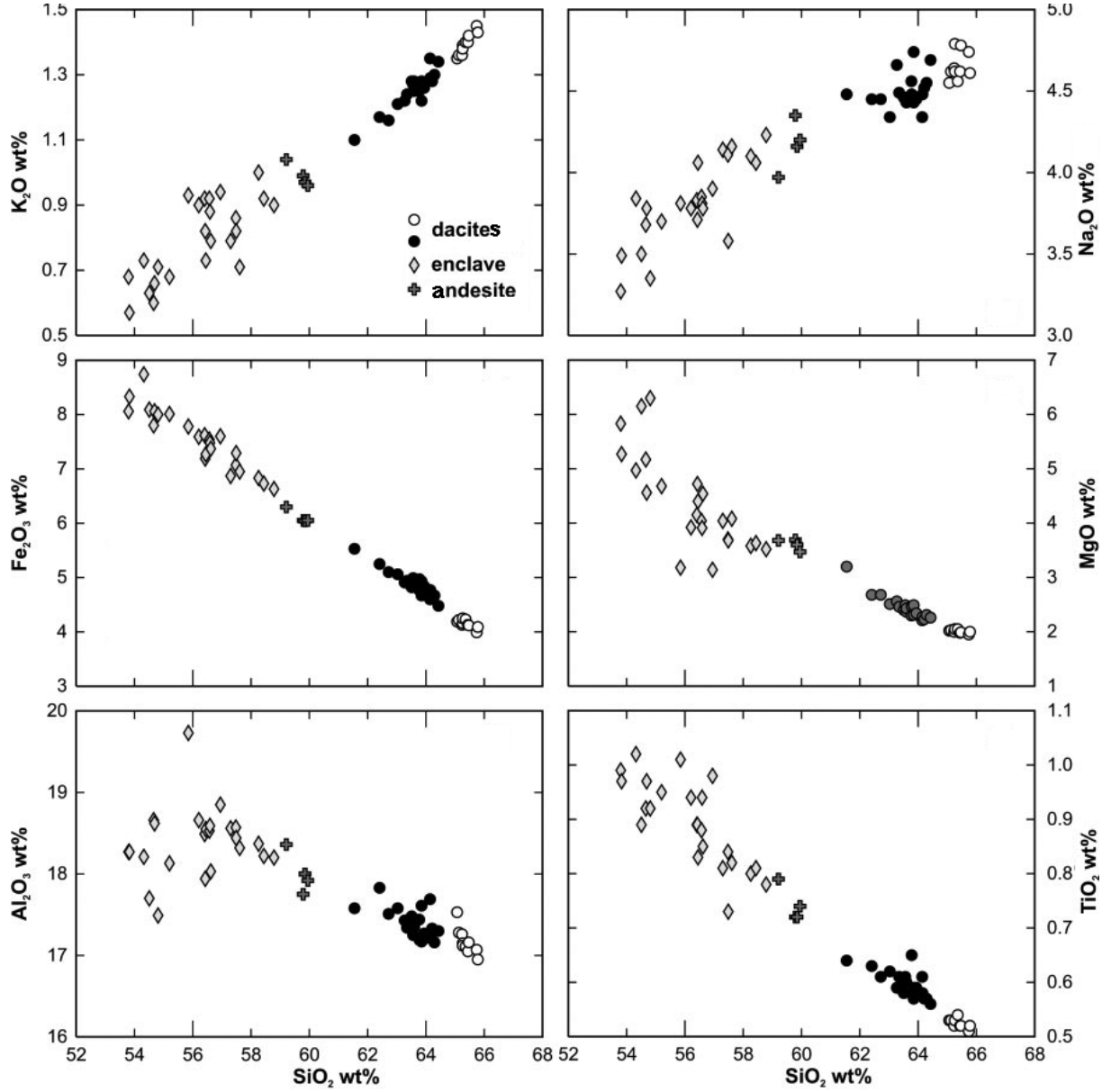

Figure 2 Harker plots showing some major-element variations in the volcanic products of Nevado de Longaví Volcano in central Chile (modified from figure 7 of Rodríguez *et al.* 2007).

from similar sources, under similar conditions will show similar geochemical variations, even if the magmas are unrelated, because the melting equilibria will produce granitic melts, of very similar composition, that coexist with very similar residual mineral assemblages. The variation within and between such bodies as the Stolzburg and Nelshoogte plutons could be controlled by processes that operated at or near the magma sources (rather than at the near-emplacement stage). This possibility is strengthened by the fact that the observed variation in trace elements hosted only by major minerals is difficult to model by fractionation of any combination of the major minerals present in the rocks. In particular, the variations in Rb, Sr and Ba (in feldspars and micas) cannot be modelled satisfactorily as the results of fractionation of any viable phase or mineral assemblage (Clemens *et al.* 2006).

Following on from the approach above, geochemical plots can be used to model the effects of fractionation of the observed crystalline phases in silicic rock suites on major- and trace-element contents of the evolved magmas. This is done by calculating vectors for the fractionation of each mineral and comparing the results to the observed variations, essentially using the approach of Rollinson (1993). Many silicic suites have been tested this way and it has been found that only rarely do predicted trends match the observed data. Usually, no combination of fractionating phases can describe the data adequately. It is emphasised that this problem lies with major elements and trace elements hosted by the major mineral phases, not with trace elements controlled by the distribution of accessory minerals. Thus, in models for the genesis and chemical evolution of granitic magmas, there is a deep systematic mismatch between the trends expected for fractional crystallisation and the actual variations recorded in rocks crystallised from crustally derived granitic magmas.

Figure 4 illustrates this problem for the rocks of the Dartmoor pluton, also introduced earlier. The figure shows the effects of mineral fractionation on the Sr, Rb and Ba concentrations in the residual magma. The plots show the directions and magnitudes of vectors that would be produced by the fractionation of 10% each of biotite, K-feldspar and plagioclase. It must be stressed that there are always uncertainties in the values of crystal–liquid distribution coefficients for natural magma systems, leading to uncertainty in the results of any such modelling. However, the present authors have experimented with the distribution coefficients, varying them within

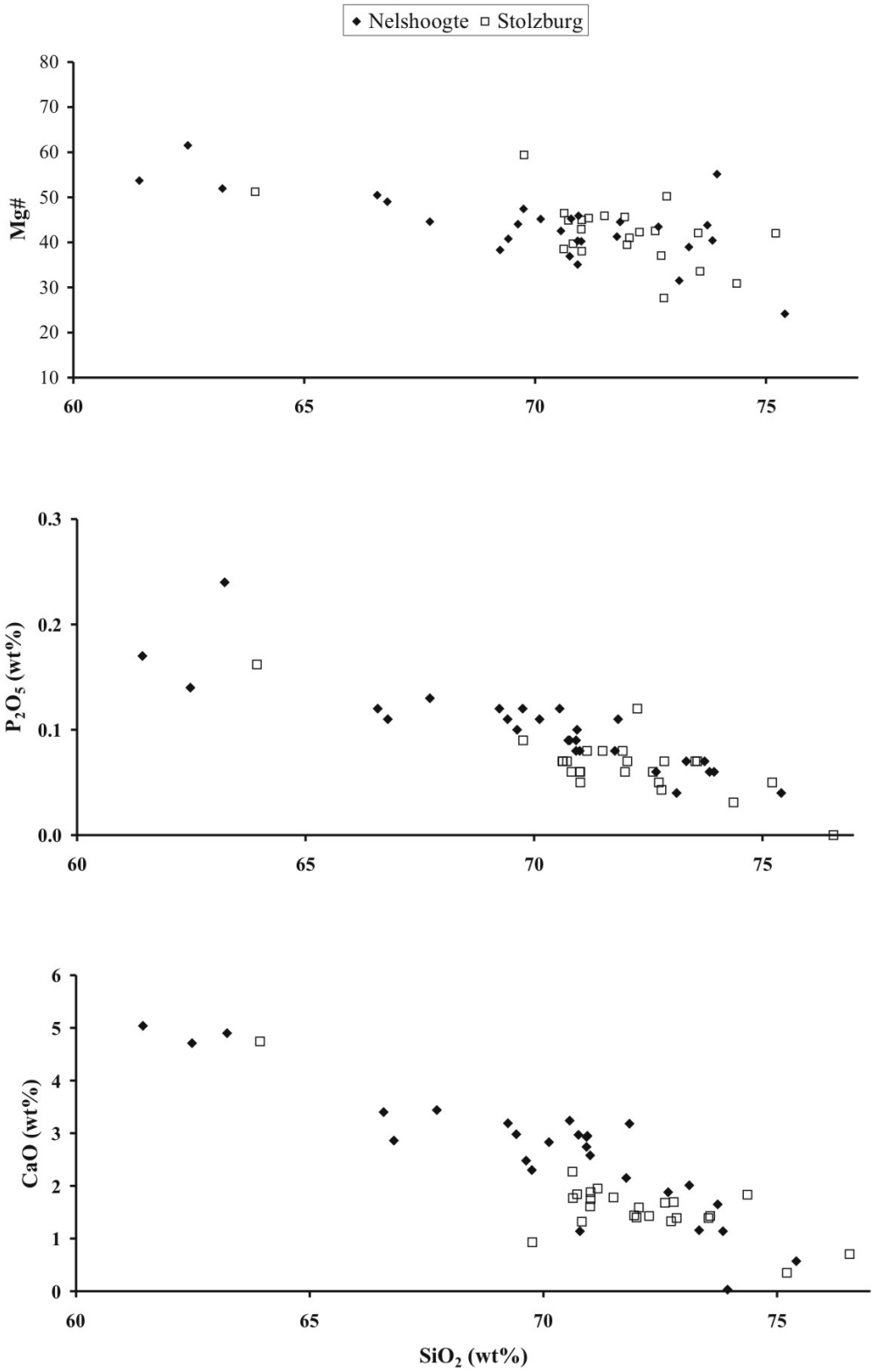

Figure 3 Harker plots for Mg#, CaO and P_2O_5 for the Stolzburg and Nelshoogte plutons.

the bands of quoted values (Whittington & Treloar 2002), and the conclusions reached seem relatively robust.

The Ba–Sr plot (Fig. 4a) rules out biotite and plagioclase fractionation, as enormous degrees of fractionation of any combination of these phases would be required. Orthopyroxene, a near-liquidus phase in many S-type granitic magmas, could be considered as a fractionating phase instead of biotite (with which Opx is replaced during later magma evolution). However, as can be seen from the plot, Opx is even less effective than biotite, producing a trend in the wrong sense. At first sight, Figure 4a suggests the possibility of K-feldspar fractionation. However, it is apparent that >20% K-feldspar fractionation would be required to explain the spread of rock compositions in Dartmoor, something that cannot be the case, given the petrological evidence. First, there is not enough phenocrystal K-feldspar present in the rocks to account for such a trend. Secondly, field observations have not revealed the presence of any strong mechanical accumulations of K-feldspar. Finally, the late crystallisation of K-feldspar in S-type granitic magmas is well established from experimental

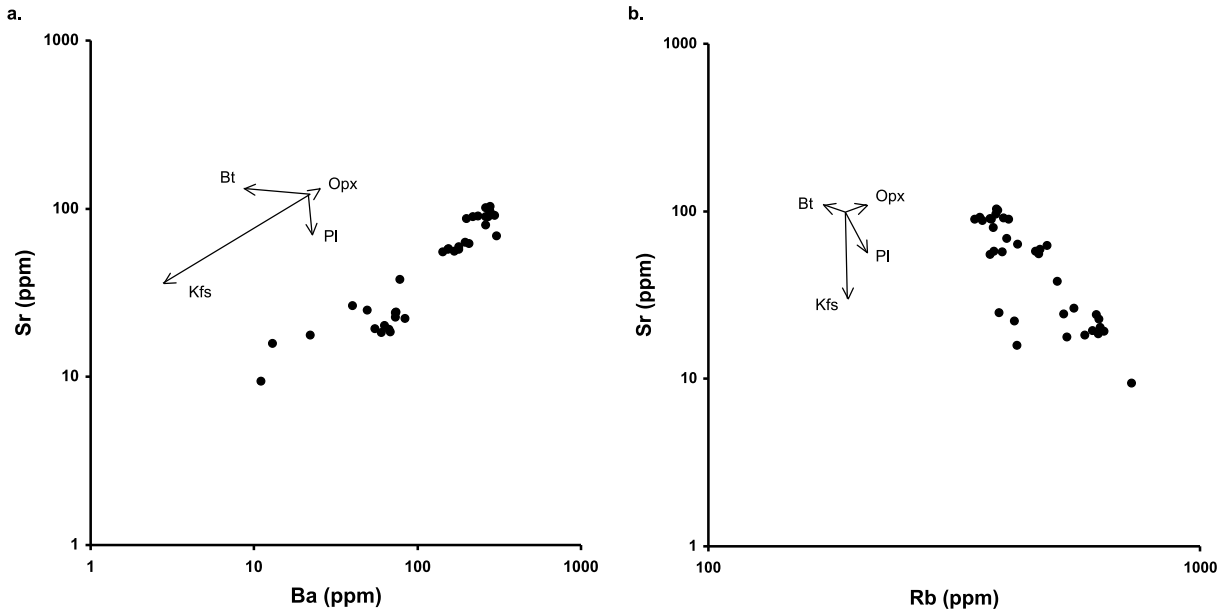

Figure 4 Log–log plots showing (a) Ba–Sr and (b) Rb–Sr variations in the rocks of the Dartmoor pluton of the Cornubian batholith in south-western Britain. Vectors are shown for the effects of fractionation of 10% each of biotite, K-feldspar and plagioclase (minerals present in the rocks) and 10% of orthopyroxene, which might have been present at an earlier stage of magma evolution. The standard Rayleigh fractionation equation was used ($C=C_0.f^{D-1}$), where C is the instantaneous concentration of the element, C_0 is the initial concentration, f is the fraction of liquid remaining (0·9) and D is the crystal–liquid distribution coefficient. Mineral–melt element distribution coefficients for orthopyroxene were taken from Arth (1976). For biotite, the values ($D_{Rb}=2$, $D_{Sr}=0{\cdot}04$) were taken from Icenhower & London (1995), with D_{Ba} set at 10, reflecting the moderate temperature probable for the Dartmoor magmas, and consistent with the Arth (1976) value. For plagioclase, the expressions of Blundy & Wood (1991) were used, with the composition set at An_{36} (the measured composition of the plagioclase crystal cores in the more mafic Dartmoor rocks) and calculated for a magma at 900°C. The resulting values are; $D_{Rb}=0{\cdot}09$, $D_{Sr}=5{\cdot}8$ and $D_{Ba}=0{\cdot}69$. For K-feldspar (Or_{85}), the expressions of Icenhower & London (1995) were used, resulting in $D_{Rb}=0{\cdot}88$, $D_{Sr}=12$ and $D_{Ba}=21{\cdot}3$.

studies (e.g. Clemens & Wall 1981), and is also apparent from the petrographic examination of the Dartmoor rocks. As in most granitic rocks, the majority of the K-feldspar present is interstitial to the earlier plagioclase, quartz and biotite. Crystallising at such a late stage, and from what amounts to an interstitial, residual liquid, it cannot have controlled any fractionation processes. Thus, K-feldspar could not have been present either sufficiently early in the crystallisation of the magmas, or in sufficient quantity to be responsible for fractionation. Any combination of the mineral vectors also results in impossible quantities of fractionated phases.

Figure 4b, the Rb–Sr plot, shows that a combination of plagioclase, K-feldspar and biotite fractionation could theoretically produce the trend but, again, the amounts of fractionated phases are infeasible. Note also the degree of scatter in this plot, despite the fact that the axes are logarithmic. This mismatch between trace-element variations and the mineralogical, petrological and experimental evidence strongly implies a deep, possibly source-inherited origin for much of the geochemical variation within Dartmoor. These major variations are inconsistent with crystal fractionation at any depth. Fractionation of early Opx, Grt, etc. would result in evolutionary trends completely contrary to those observed. Note also that the use of the chosen data sources for construction of Figure 4 results in relatively high distribution coefficients for feldspars, favourable to explanation of the trends as fractionation.

The failure of these models is thus even more telling. Variation due to mineral fractionation is very probably present in these rocks as well, but it seems to have been superimposed on and to be subordinate to the main variations inherited from processes that occurred at deeper levels, prior to magma emplacement. In an intriguing use of a geochemical normal probability plot to study incompatible element variation in silicic ignimbrites from Costa Rica, Vogel *et al.* (2004, p. 155) found that 'The normal probability distributions of Nb/Ta from . . . closely related erupted units are distinct and represent different populations . . . Fractional crystallisation could not have produced this variation among the units . . .'. This finding is in accord with what is presented in the present paper, and it is suggested that this mismatch is a prevalent feature of crustally derived granitic magmas, although this needs to be verified for a wider variety of felsic rock units.

5. Isotope evidence

Ratios of stable isotopes (e.g. $\delta^{18}O$ and $\delta^{34}S$) and radiogenic isotopes (e.g. initial $^{87}Sr/^{86}Sr$, $^{143}Nd/^{144}Nd$ and $^{206}Pb/^{204}Pb$) are well established tracers of rock parentage. For many granitic bodies, true whole-rock Rb–Sr isochrons cannot be produced, and there are commonly significant disagreements between Rb–Sr dates and more accurate and precise Pb–Pb dates based on sub-grain-scale analysis of zircon, monazite, etc. These discrepancies occur in rocks with isotope systems undisturbed by alteration and they are therefore significant. Their existence suggests that the different rock types in many granitic plutons have commonly not been formed by differentiation of any original, homogeneous parent magma (the assumption used in constructing whole-rock isochrons), but are more probably produced from isotopically contrasting magma batches that were aggregated together to form the pluton.

In granitic plutons with overt variation from I- to S-type character, the isotope ratios are usually strongly correlated with the variations in mineral assemblages characteristic of the

two sorts of magma/rock. This clearly indicates that such plutons were filled with contrasting batches of magma derived from different sources. However, there is emerging evidence that significant degrees of isotopic variation (far in excess of typical analytical error) can also be found within what appear to be relatively homogeneous masses of granitic rock, that show no mineralogical signs of multiple parentage. Some examples are provided below.

It is instructive to consider the scales on which such cryptic variation can occur. Helps *et al.* (2003) carried out detailed sampling of a number of granitic plutons, and presented preliminary results of high-precision analyses for initial $^{87}Sr/^{86}Sr$ and $^{143}Nd/^{144}Nd$, and $\delta^{18}O$. In the S-type Dartmoor granite, they discovered variation (an order of magnitude greater than analytical error) on length scales as small as 0·5 m, in rocks with no discernible petrographic variations. In the I-type Criffell pluton similar variation is present, but only at scales >100 m. Further evidence of isotopic heterogeneity in granitic magmas can be found in the study of Waight *et al.* (2000), who used microdrilling techniques to sample zoned plagioclase crystals in granites. These authors discovered significant variations in initial $^{87}Sr/^{86}Sr$ between adjacent zones in the crystals. Such variation shows that these crystals grew from batches of melt that had different isotopic compositions, either by the crystals freely circulating through contrasting magma batches, or by growing from contrasting melts that percolated through a relatively static mush of growing crystals. Such isotopic variability is a clear indication that granitic bodies were constructed by the agglomeration of multiple fractions of contrasting magma. These disparate magma fractions may have been derived from different materials in a heterogeneous magma source, or may result from modification of magma composition by a range of hybridisation mechanisms at some depth greater than the final emplacement level. The implication is that what may appear to be magma fractions generated by differentiation can represent chemically and isotopically distinct magma batches that were produced at or near the magma source region. Mingling and mixing of these magma batches undoubtedly occurs, due to chaotic flow in the composite magma, but the preservation of these heterogeneities highlights the inefficiency of mingling and diffusive re-equilibration in felsic systems.

6. A commentary on some recent literature studies

There have been numerous recent studies of granitic complexes that show isotopic and trace-element heterogeneity, apparently unrelated to physical evidence for magma mingling. Nevertheless, mingling and mixing processes are the most typical models presented for these occurrences. Cristofides *et al.* (2007) studied the 50 Ma, metaluminous Sithonia Plutonic Complex of northern Greece. Here there are dioritic to gabbroic masses, hornblende tonalites with mafic enclaves (monzonitic to dioritic and tonalitic), hornblende tonalites, hornblende and biotite granodiorites, leucogranites, two-mica granites and aplitic to pegmatitic dykes. The published model involves two-stage magma mixing with crystal fractionation – 'The first step explains the chemical variation in the mafic enclave group: a basic magma, represented by the least evolved enclaves, interacted with an acid magma, represented by the most evolved granitoid rocks, to give the most evolved enclaves. The second step explains the geochemical variations of the remaining rocks of the basic group: most evolved enclaves interacted with the same acid magma to give the spectrum of rock compositions with intermediate geochemical signatures.' (Cristofides *et al.* 2007, p. 243). Figure 5 was constructed using the Sr concentration and Sr isotope data presented in table 4 of this reference. Mixing lines can be readily identified using such diagrams, and it is apparent that, although magma mixing might have been involved here, the published scheme is untenable. Interaction between the least evolved enclave magmas and the most evolved granitic magmas would not produce any of the trends observed for the more mafic rocks. However, there may have been mixing between tonalitic host magma and an enclave magma to produce the more evolved enclaves. The second step in the model is equally untenable. The 'acid magma' would appear to be a range of rather contrasting felsic entities. Fractionation of a tonalitic parent could have produced the hornblende–biotite granodiorites, but production of the rest of the series would have to involve mixing with at least three different more felsic end-members (a two-mica granite, a leucogranite and a separate aplitic magma). Aplitic magmas are commonly thought of as differentiates of granitic parents, but here they would appear to have been derived from a separate parent magma, unrelated to the other rocks in the Complex. The dioritic to gabbroic rocks plot in a part of the diagram that suggests that they are unrelated to any of the other rocks in the Complex; they are certainly not candidates for the parents of the enclaves or their host tonalites.

Figure 6 shows the K_2O Harker plot from figure 4 of Cristofides *et al.* (2007). Again, this shows that the diorites and gabbros appear to be a distinct magma, which may have fractionated to produce the range of compositions in this group, but not related to the rest of the magmas. The enclaves show trends that could be related to hybridisation with the tonalites, though this is not a simple relationship. The rest of the graph is not particularly helpful in revealing genetic relationships between the rock groups, and nor are the other Harker plots published in figure 4 of Cristofides *et al.* (2007). As pointed out by Clemens (1989, p. 1315) although they portray the variations very well, 'Harker diagrams are close to impotent as tools for *process* diagnosis'. A significant feature of Figure 6 is the high degree of scatter in the data, typically with 250% variation in K_2O content at any given SiO_2 value. Taken together, these data do not support a fractionation model for the origin of the variation. Indeed, a recent investigation into melt compositions produced from various metasedimentary sources (Stevens *et al.* 2007) has demonstrated that alkali metal and Ca concentrations in the melt vary substantially, reflecting variations in the feldspar mineral assemblage and the feldspar compositions in the sources. Deep mixing processes may have been involved in the evolution of the Sithonia magmas but, if so, there were clearly several end-members. Certainly, the primary heterogeneity here is one of deep, probably near-source origin, rather than something that developed at near-emplacement levels.

Hildreth & Wilson (2007) presented a mass of data on the Bishop Tuff, erupted from the Long Valley magma chamber in eastern California, at 760 ka. The Tuff is zoned in composition, crystal content and temperature, but not due to any shallow differentiation processes. The pre-eruption magma chamber was evidently filled incrementally, with numerous batches of contrasting, crystal-poor rhyolitic magma. These batches were derived from a deep source (or sources), retained their geochemical character during high-level crystallisation (phenocryst formation) and were preserved as distinct pumice units after eruption. The heterogeneity in the chemistry of the pumice magmas is illustrated in Figure 7. The plot shows the variations in CaO, TiO_2, Zr and Ba, all of which are non-volatile elements whose concentrations should not be affected by fluid–fluxed processes. The high degree of scatter is apparent, even within any given textural variety of pumice. Hildreth

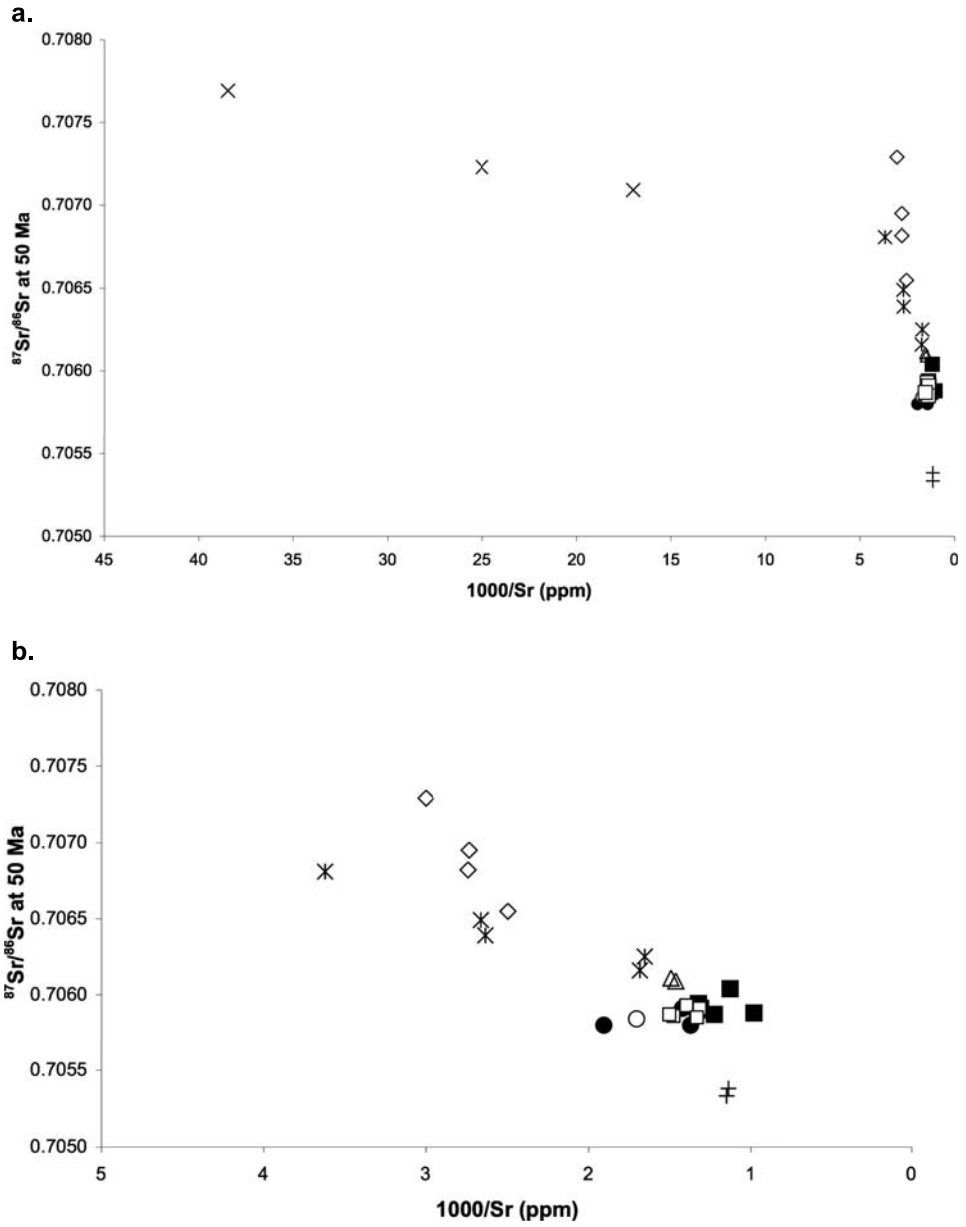

Figure 5 Sr plotted against 1000/Sr for the rocks of the Sithonia plutonic complex (N. Greece), using data from Cristofides *et al.* (2007). Symbols are: +-shaped crosses=diorites and gabbros; filled circles and open circles= monzonitic and dioritic to tonalitic enclaves, respectively; filled squares=tonalites; open squares and triangles=hornblende- and biotite-granodiorites, respectively; stars=leucogranites; diamonds=two-mica granites; ×-shaped crosses=aplites and pegmatites.

& Wilson ascribe this scatter to fractionation processes operating in a mush zone beneath the volcanic magma chamber, within which magma batches evolved and were then delivered, crystal-poor, to a high-level volcanic magma chamber. This mush zone is envisaged to exist at mid-crustal depths. An equally valid view of this would be that the mush zone represents a heterogeneous magma source, with highly variable melt proportions and different degrees of residual solid entrainment into the magmas withdrawn from it. In any case, here too, the primary variation is of deep origin and was not developed through crystal fractionation at or near magma emplacement level.

Recently, Stevens *et al.* (2007) investigated the origin of major-element variations in the S-type, leucogranitic to granodioritic rocks of the Cape Granite Suite, South Africa. These authors proposed that the generally linear trends evident in Harker diagrams for this group of rocks result entirely from processes that operated in the magma source region. In the present paper, the interrelationships between major elements are proposed to result from variable degrees of entrainment, into the magmas, of the peritectic products of the biotite melting reactions that produced the magmas. The more leucocratic granites are proposed to be close to pure melts, bearing only accessory minerals, whilst the more mafic rocks in the suite represent mixtures between melts and up to 20% of the peritectic products (mainly garnet and Fe–Ti oxides). Interestingly, the factors that favour peritectic phase entrainment at the source are also those considered to favour accessory phase entrainment. This would explain the commonly observed correlations between major oxides (e.g. FeO) that could reflect peritectic phase entrainment, and trace elements (e.g. Zr) that reflect accessory phase entrainment and/or dissolution. Stevens *et al.* (2007) make a clear distinction between this highly selective incorporation of peritectic and some accessory minerals and the bulk incorporation of solids, as in the restite unmixing model of Chappell *et al.* (1987). The mechanism proposed by Stevens *et al.* (2007) could produce magmas (and rock series) characterised by tight inter-element correlations,

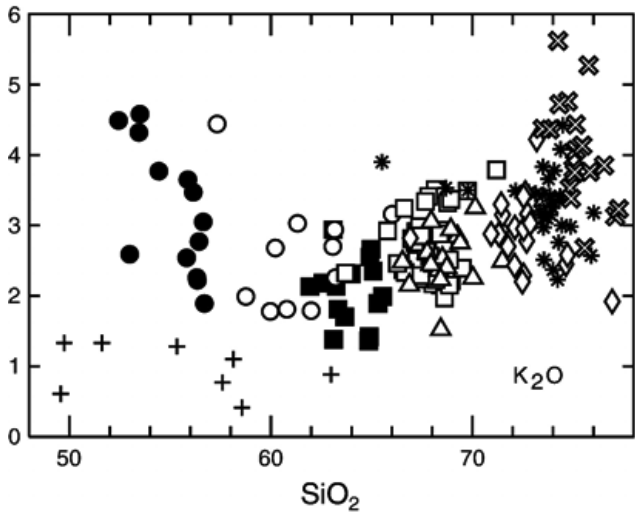

Figure 6 K_2O Harker plot for the rocks of the Sithonia plutonic complex (N. Greece), modified from part of figure 4 of Cristofides *et al*. (2007). Symbols are as in Figure 5.

especially in cases where there is little variation in melt compositions, without the requirement of mechanically segregating minerals. Indeed, the low density contrasts and relatively high viscosities, that hamper fractional crystallisation in felsic magmas, would enhance the efficiency of peritectic phase entrainment, and permit this mechanism to shape the compositions of some granitic rock suites.

7. A magnetic perspective

The evidence above suggests that many granitic plutons were constructed through the aggregation of a number of magma batches or pulses. Similar conclusions were reached by other workers, recently, for example, by Glazner *et al*. (2004). In some cases, these magma batches were derived either from different source regions or from different parts of a heterogeneous source region. Evidently, the processes of magma flow within the pluton, reaction and diffusion are inefficient, and complete homogenisation seems to be uncommon. At least in some felsic magmatic bodies, the persistence of these chemically and isotopically contrasting magma batches probably explains a good deal of the variation. However, although we can sample the rocks and detect the existence of these batches or heterogeneities, unless they have clear mineralogical or structural expressions, it is very difficult or impossible to determine their physical extent and distribution using geochemistry. Using grid sampling it is possible to detect large-scale variations, sometimes cryptic, (e.g. Stephens & Halliday 1980; Stephens *et al*. 1985; Stephens 1992; Glazner *et al*. 2004), but there seems to be evidence of quite small-scale, completely cryptic variation that would not be detected unless outcrop-scale grid sampling and analysis were carried out – an expensive and speculative proposition. The best hope for detecting complex magma heterogeneities and mapping their extent probably lies in geophysics, rather than geochemistry. The aim here would be to map gravity or magnetic variations, not to reveal magma emplacement mechanisms, but to track the extents of magma batches with contrasting properties, and possibly reveal how the magma batches flowed into and round the pluton (magma chamber).

Geophysical imaging from airborne surveys, particularly magnetic imaging, can provide a useful way of examining structures within rock bodies, provided that they contain

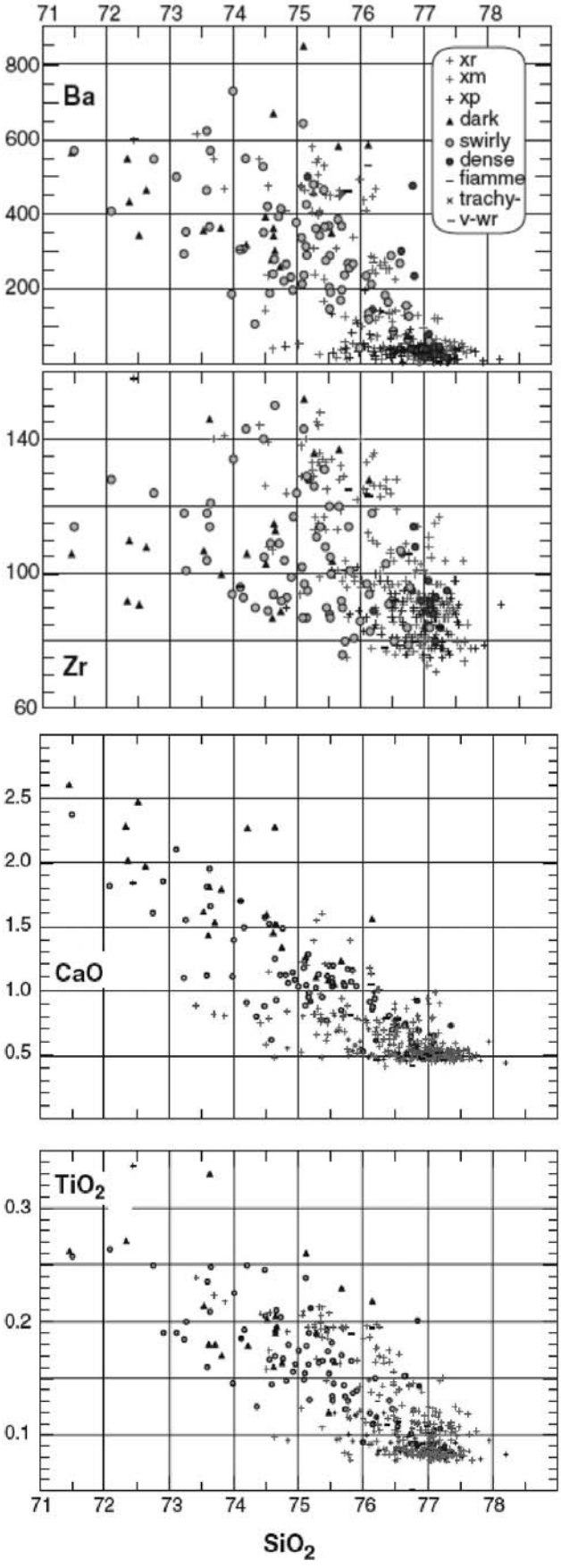

Figure 7 Harker plots for some non-volatile major and trace elements in the Bishop Tuff pumices, modified from parts of figures 9 and 10 of Hildreth and Wilson (2007).

heterogeneities marked by sufficient contrasts in magnetic susceptibility and remanence. This is particularly likely to be the case in composite S-type (ilmenite- and pyrrhotite-bearing)

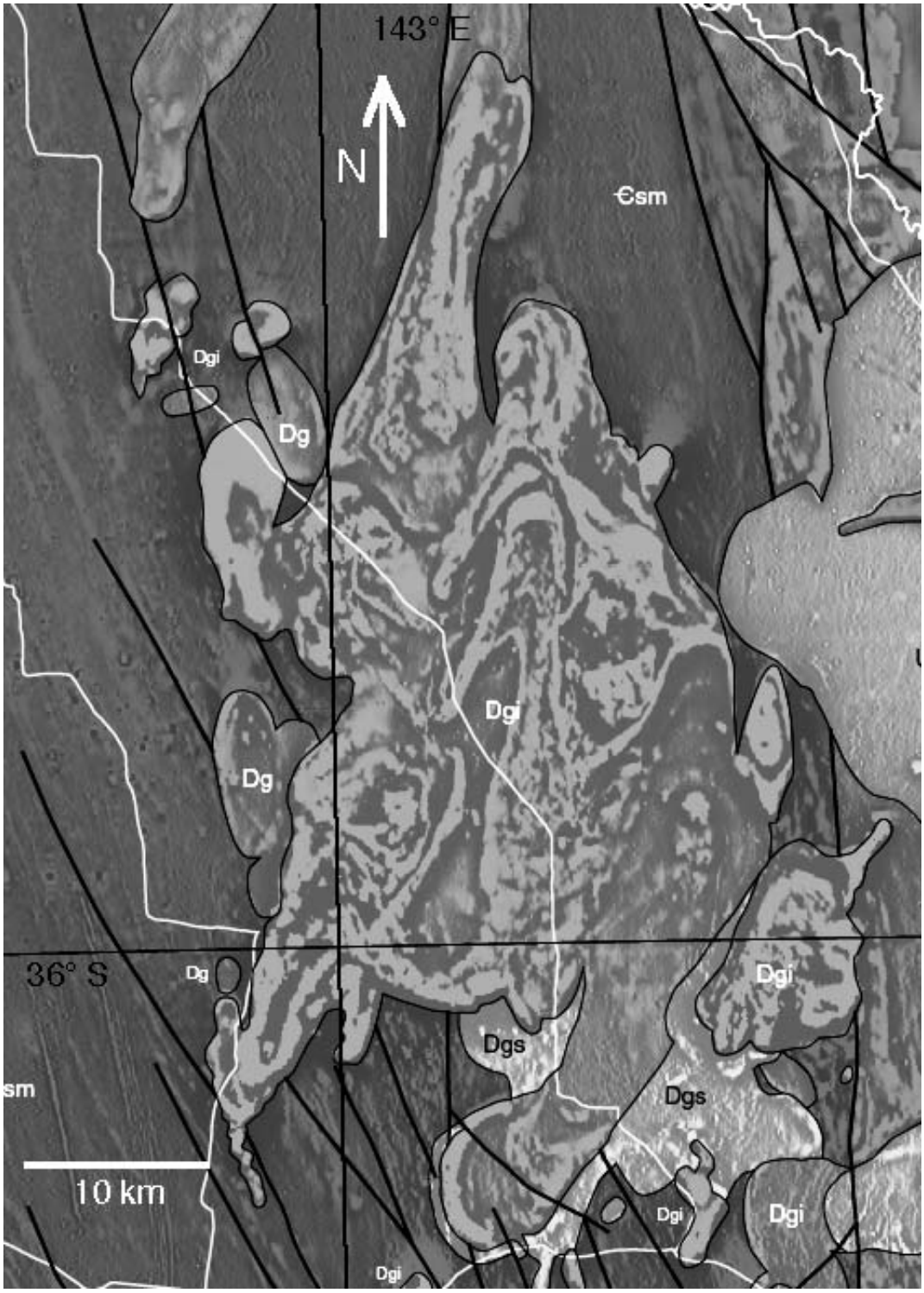

Figure 8 Map of a section of northwestern Victoria, Australia, showing the first vertical derivative of total magnetic intensity. The lighter the grey, the higher the magnetic susceptibility of the rocks. The map shows some of the internal structure of Devonian granitic plutons (Dg=unknown type; Dgi=I-type; and Dgs=S-type) that intrude Cambrian (Csm) and Ordovician (unlabelled) low-grade metasediments. This is a greyscale version of a section of the 1:1 000 000 scale map of Simons and Moore (1999), published as an enclosure in VandenBerg *et al.* (2000).

and some I-type (more oxidised and sometimes magnetite-bearing) plutons. However, this technique has been largely neglected by igneous petrologists working on the genesis of granitic bodies. Figure 8 illustrates the kind of image that could prove rather enlightening in discussions such as that in the present work.

The plutons shown in Figure 8 are Devonian I-type granitic bodies in the northwestern part of the state of Victoria, in Australia. Unfortunately, these plutons are largely unexposed, due to a thin but ubiquitous cover of Quaternary fluvial sediments from the Murray River. The magnetic image cuts through this veil of young sediments to reveal spectacular lobate and concentric ring patterns in the magnetic susceptibility of the underlying granitic rocks. These patterns are due to variations in the magnetic mineral contents of the rocks and are not at all what might be expected to result from *in situ*

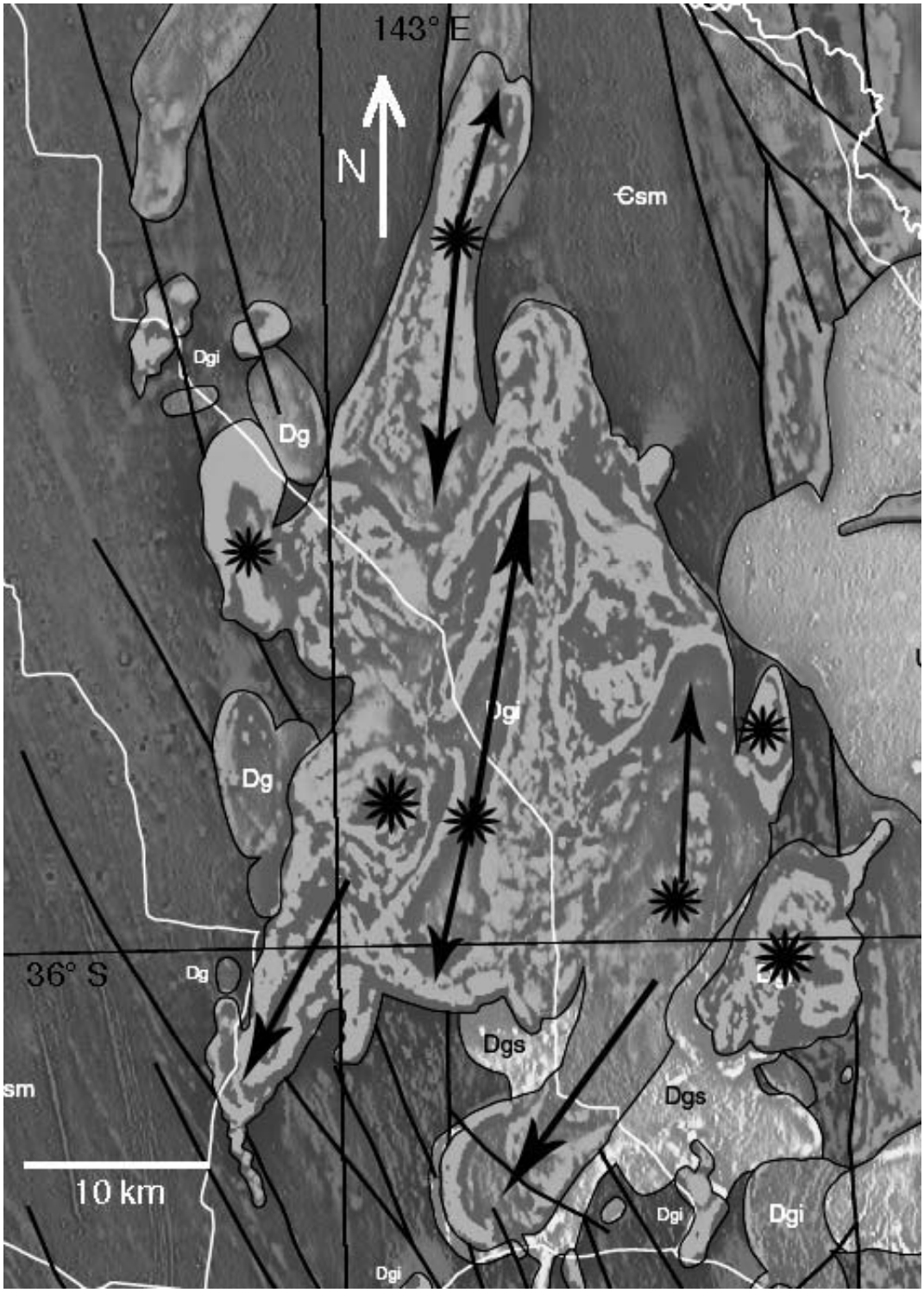

Figure 9 Diagram of the map in Figure 8, showing tentative assignments of magma sources (stars) and flow patterns (arrows). These are highly speculative, but stars without arrows are meant to indicate possible magma upwelling sites at which subsequent magma flow occurred somewhat more equally in all radial directions. Arrows not emanating from stars are meant to suggest the traces of earlier flow patterns, the sources of which appear to have been overprinted by flows from later pulses.

differentiation by gravity or side-wall accretion. The vertical derivative, used in this map of the anomalies, reflects the rate-of-change of anomalies (mainly with depth), as well as their strengths. It is likely to include signals from depths up to a few km, biased toward any shallower features. The banding and blotching in Figure 8 may well be the magnetic signature of the batches or pulses of magma that we have been discussing. Furthermore, the patterns here are strongly reminiscent of flow features in lavas, and it is a simple exercise to identify potential feeder zones from which the magma batches may have emanated and flowed laterally to feed the growing plutons. Tentative assignments of such feeder zones and flow directions are shown in Figure 9. The higher- and lower-susceptibility bands could indicate sub-pulses of magma within the tongues or lobes that may correspond to the main pulses of magma (rather like flow units in lavas). Whatever the case, these features are undeniably of interest and should be further investigated.

8. Conclusions

This survey of characteristics of silicic magmatic rocks shows that granitic plutons and silicic volcanic complexes are very commonly composite bodies, constructed by the accumulation of batches (pulses) of magma derived from different sources. The evidence presented in the present paper suggests that this heterogeneity is independent of the oft-observed magma mingling that is due to the late incorporation of more mafic enclave magmas. It most probably reflects variations in the source rocks that were partially melted to form the various magma batches or deep-seated (near-source) mingling of magmas from different protoliths. Derivation of magma fractions through differentiation of an initially homogeneous parent magma may be common in mafic to intermediate systems, but appears to be less so in silicic systems, especially those formed from magmas generated by crustal melting. This should be no surprise as, even in some mafic magmas, initial, source-related heterogeneities are preserved through later magma evolution (e.g. Bryce & DePaolo 2004).

Differentiation in granitic magmas can lead to production of extreme compositional variants, commonly enriched in Li, Be, B, F, etc. Such differentiation most probably occurs by mechanisms such as crystal fractionation, but the kilometric- to regional-scale variations in many granitic plutons (such as those in Fig. 8) are of deep origin and most commonly primary (source-inherited). This leads to a large degree of scatter in Harker variation diagrams, with the primary heterogeneity further complicated by contrasting differentiation paths that are followed within local magma batches. The heterogeneities involved are sometimes expressed as separate intrusive sheets, dykes or blobs, zoning of plutons or layering of volcanic sequences, or they may be more occult (visible only in the isotopic compositions or with subtle mineralogical expressions). The causes of this primary heterogeneity in silicic magmas include such processes as:

- partial melting of compositionally contrasting sectors of a single source region
- migration (with time) of a melting front into rocks of contrasting composition
- sampling of melts from different levels, by magma ascending in a sub-vertical conduit through a partially molten region
- weakening of a migrating thermal pulse, allowing only more fertile rocks to partially melt as time progresses
- differing degrees of magma mixing and/or wall-rock assimilation at deep levels in the crust.

Whatever combination of these mechanisms may be responsible for the heterogeneity in a given case, it seems that the different magma pulses are commonly channelled upward through the same magma plumbing system, to form a particular pluton or volcanic deposit. If we accept that a good deal of the variation among the rocks of silicic igneous complexes is formed in this way, rather than by differentiation at emplacement levels, we need to be circumspect about the use of whole-rock isochrons for dating such bodies. This is especially so if assembly of the complexes took a significant period of time, within the resolution of the dating technique. In addition, the preservation of pre-emplacement heterogeneities implies that granitic magma chambers commonly do not experience chamber-wide, crystal–liquid processes. It seems more probable that chemical evolution of the magmas occurs within individual magma batches that can have limited volumes and areal extents. At emplacement levels, processes leading to magma homogenisation (e.g. magma mixing, convective stirring and diffusive re-equilibration) must be inefficient; they are probably inhibited by the relatively high magma viscosities and the slow diffusion rates of many chemical components in silicic melts (as discussed, for example, by Sparks & Marshall 1986).

Using field and geophysical evidence, Glazner *et al.* (2004) and Parada *et al.* (2005) also concluded that large and broadly homogeneous plutons can accumulate incrementally, from many smaller magma batches. Such pulses were predicted by Clemens & Mawer (1992), based on consideration of the mechanics of dyke ascent of granitic magma. Bons *et al.* (2004) extended this physical concept in presenting a simple numerical model for melt segregation and batch transport by fracture propagation in a self-organised critical state. Bons *et al.* (2004) also recognised the potential for geochemical complexity in the resulting pluton, if the batches were not subsequently homogenised. However, pulsed melt production (as different hydrous mineral-bearing assemblages successively break down or as the locus of melting shifts in space and time) could also be responsible for magma pulses and heterogeneity (e.g. Clemens 2005). The construction of a pluton from multiple pulses of magma clearly has major implications for the thermal structure and cooling history of the body. Annen *et al.* (2006) emphasised this aspect in their recent paper on the genesis of intermediate to silicic magmas in what they term 'deep crustal hot zones'. Annen *et al.* (2006) did comment (p. 533) that rejuvenation of former magma batches, by later injections, could lead to 'extremely complicated radiometric data'. Glazner *et al.* (2004, p. 4) stated that '. . . many aspects of the petrochemical evolution of magmatic systems (e.g. *in situ* crystal fractionation and magma mixing) need to be reconsidered.' The present authors would agree. There is a general need to reassess the meaning of the geochemical and isotopic data for felsic magmatic systems.

9. Acknowledgements

JC's work for this paper was enabled partly through sabbatical leave support from the Faculty of Science and the Geodynamics and Crustal Processes Research Group (within the Centre for Earth and Environmental Sciences Research) at Kingston University (London, UK). Reviews by Nick Petford, Bill Collins, Steve Sparks, Colin Donaldson, Alan Whittington and Fritz Finger were helpful, but the views expressed here are those of the authors and should not necessarily be ascribed to any of these reviewers.

10. References

Annen, C., Blundy, J. D. & Sparks, R. S. J. 2006. The genesis of intermediate and silicic magmas in deep crustal hot zones. *Journal of Petrology* **47**, 505–39.

Archanjo, C. J. & Fetter, A. H. 2004. Emplacement setting of the granite sheeted pluton of Esperança Brasiliano orogen, Northeastern Brazil. *Precambrian Research* **135**, 193–215.

Arth, J. G. 1976. Behaviour of trace elements during magmatic processes. *United States Geological Survey Journal of Research* **4**, 41–7.

Belcher, R. W. & Kisters, A. 2006. Progressive adjustments of ascent and emplacement controls during incremental construction of the 3·1 Ga Heerenveen batholith, South Africa. *Journal of Structural Geology* **28**, 1406–21.

Belusova, E. A., Griffin, W. L. & O'Reilly, S. Y. 2006. Zircon crystal morphology, trace element signatures and Hf isotope composition as a tool for petrogenetic modelling: examples from eastern Australian granitoids. *Journal of Petrology* **47**, 329–53.

Bindeman, I. N. & Valley, J. W. 2003. Rapid generation of both high- and low-delta O-18, large-volume silicic magmas at the Timber Mountain/Oasis Valley caldera complex, Nevada. *Geological Society of America Bulletin* **115**, 581–95.

Blundy, J. D. & Wood, B. J. 1991. Crystal-chemical controls on the partitioning of Sr and Ba between plagioclase feldspar, silicate melts, and hydrothermal solutions. *Geochimica et Cosmochimica Acta* **55**, 193–209.

Bons, P. D., Arnold, J., Elburg, M. A., Kalda, J., Soesoo, A. & Van Milligen, B. P. 2004. Melt extraction and accumulation from partially molten rocks. *Lithos* **78**, 25–42.

Brammall, A. & Harwood, H. F. 1923. The Dartmoor granite: its mineralogy, structure and petrology. *Mineralogical Magazine* **20**, 39–53.

Bryce, J. G. & Depaolo, D. J. 2004. Pb isotopic heterogeneity in basaltic phenocrysts. *Geochimica et Cosmochimica Acta* **68**, 4453–68.

Chappell, B. W. 1984. Source rocks of I- and S-type granites in the Lachlan Fold Belt, southeastern Australia. *Philosophical Transactions of the Royal Society of London* **A310**, 693–707.

Chappell, B. W., White, A. J. R. & Wyborn, D. 1987. The importance of residual source material (restite) in granite petrogenesis. *Journal of Petrology* **28**, 1111–38.

Chappell, B. W. & White, A. J. R. 1974. Two contrasting granite types. *Pacific Geology* **8**, 173–4.

Clemens, J. D. 1989. The importance of residual source material restite in granite petrogenesis: a comment. *Journal of Petrology* **30**, 1313–16.

Clemens, J. D. 2005. Melting of the continental crust I: fluid regimes, melting reactions and source-rock fertility. *In* Brown, M. & Rushmer, T. (eds) *Evolution and differentiation of the continental crust*, 297–331. Cambridge: Cambridge University Press.

Clemens, J. D., Yearron, L. M. & Stevens, G. 2006. Barberton South Africa. TTG magmas: Geochemical and experimental constraints on source-rock petrology, pressure of formation and tectonic setting. *Precambrian Research* **151**, 53–78.

Clemens, J. D. & Mawer, C. K. 1992. Granitic magma transport by fracture propagation. *Tectonophysics* **204**, 339–60.

Clemens, J. D. & Petford, N. 1999. Granitic melt viscosity and silicic magma dynamics in contrasting tectonic settings. *Journal of the Geological Society, London* **156**, 1057–60.

Clemens, J. D. & Wall, V. J. 1981. Crystallization and origin of some peraluminous S-type. granitic magmas. *Canadian Mineralogist* **19**, 111–31.

Clemens, J. D. & Wall, V. J. 1984. Origin and evolution of a peraluminous silicic ignimbrite suite: the Violet Town Volcanics. *Contributions to Mineralogy and Petrology* **88**, 354–71.

Clemens, J. D. & Watkins, J. M. 2001. The fluid regime of high-temperature metamorphism during granitoid magma genesis. *Contributions to Mineralogy and Petrology* **140**, 600–6.

Cristofides, G., Perugini, D., Koroneo, A., Soldatos, T., Poli, G., Eleftheriadis, G., Del Moro, A. & Neiva, A. M. 2007. Interplay between geochemistry and magma dynamics during magma interaction: An example from the Sithonia Plutonic Complex NE Greece. *Lithos* **95**, 243–66.

Darbyshire, D. P. F. & Shepherd, T. J. 1985. Chronology of granite magmatism and associated mineralization, SW England. *Journal of the Geological Society, London* **142**, 1159–77.

de Ronde, C. E. J. & de Wit, M. J. 1994. Tectonic history of the Barberton greenstone belt, South Africa: 490 million years of Archean crustal evolution. *Tectonics* **13**, 983–1015.

de Ronde, C. E. J. & Kamo, S. L. 2000. An Archaean arc–arc collisional event: a short-lived ca. 3 Myr. episode, Weltevreden area, Barberton greenstone belt, South Africa. *Journal of African Earth Sciences* **30**, 219–48.

de Wit, M. J., Armstrong, R. A., Hart, R. J. & Wilson, A. H. 1987. Felsic igneous rocks within the 3·3 to 3·5 Ga Barberton greenstone belt: high crustal level equivalents of the surrounding tonalite–trondhjemite terrain emplaced during thrusting. *Tectonics* **6**, 529–49.

Glazner, A. F., Bartley, J. M., Coleman, D. S., Gray, W. & Taylor, R. Z. 2004. Are plutons assembled over millions of years by amalgamation from small magma chambers? *GSA Today* **14**, 4–11.

Helps, A., Clemens, J. D. & Petford, N. 2003. Source-related chemical and isotopic heterogeneities in granitoids. *Geophysical Research Abstracts* **5**, 02661.

Hildreth, W. & Wilson, C. J. N. 2007. Compositional zoning of the Bishop Tuff. *Journal of Petrology* **48**, 951–99.

Huysken, K. T., Vogel, T. A. & Layer, W. 2001. Tephra sequences as indicators of magma evolution: Ar-40/Ar-39 ages and geochemistry of tephra sequences in the southwest Nevada volcanic field. *Journal of Volcanology and Geothermal Research* **106**, 85–110.

Icenhower, J. & London, D. 1996. Experimental partitioning of Rb, Cs, Sr, and Ba between alkali feldspar and peraluminous melt. *American Mineralogist* **81**, 719–34.

Johnson, S. E., Paterson, S. R. & Tate, M. C. 1999. Structure and emplacement history of a multiple-center, cone-sheet-bearing ring complex: The Zarza Intrusive Complex, Baja California, Mexico. *Geological Society of America Bulletin* **111**, 607–19.

Kamo, S. L. & Davis, D. W. 1994. Reassessment of Archean crustal development in the Barberton Mountain Land, South Africa, based on U–Pb dating. *Tectonics* **13**, 167–92.

Kisters, A. F. M., Stevens, G., Dziggel, A. & Armstrong, R. A. 2003. Extensional detachment faulting and core-complex formation in the southern Barberton granite-greenstone terrain, South Africa: Evidence for a 3·2 Ga orogenic collapse. *Precambrian Research* **127**, 355–78.

Le Maitre, R. W. 1989. *A classification of igneous rocks and glossary of terms*. Oxford: Blackwell. 193 pp.

Mahan, K. H., Bartley, J. M., Coleman, D. S., Glazner, A. F. & Carl, B. S. 2003. Sheeted intrusion of the synkinematic McDoogle pluton, Sierra Nevada, California. *Geological Society of America Bulletin* **115**, 1570–82.

McNulty, B. A., Tong, W. & Tobisch, O. T. 1996. Assembly of a dike-fed magma chamber: the Jackass Lakes pluton, central Sierra Nevada, California. *Geological Society of America Bulletin* **108**, 926–40.

Miller, R. B. & Paterson, S. R. 2001. Construction of mid-crustal sheeted plutons: examples from the North Cascades, Washington. *Geological Society of America Bulletin* **113**, 1423–42.

Mills, J. G., Saltoun, B. W. & Vogel, T. A. 1997. Magma batches in the timber mountain magmatic system, southwestern Nevada volcanic field, Nevada, USA. *Journal of Volcanology and Geothermal Research* **78**, 185–208.

Mohr, P. 1991. Cryptic Sr and Nd Isotopic Variation Across the Leinster Granite, Southeast Ireland. *Geological Magazine* **128**, 251–6.

Parada, M. A., Roperch, P., Guiresse, C. & Ramirez, E. 2005. Magnetic fabrics and compositional evidence for the construction of the Caleu pluton by multiple injections, Coastal Range of central Chile. *Tectonophysics* **399**, 399–420.

Paterson, S. R. & Miller, R. B. 1998. Mid-crustal magmatic sheets in the Cascades Mountains, Washington: Implications for magma ascent. *Journal of Structural Geology* **20**, 1345–63.

Pressley, R. A. & Brown, M. 1999. The Phillips pluton, Maine, USA: evidence of heterogeneous crustal sources and implications for granite ascent and emplacement mechanisms in convergent orogens. *Lithos* **46**, 335–66.

Rodríguez, C., Sellés, D., Dungan, M., Langmuir, C. & Leeman, W. 2007. Adakitic dacites formed by intracrustal crystal fractionation of water-rich parent magmas at Nevado de Longaví Volcano 36.2°S; Andean Southern Volcanic Zone, Central Chile. *Journal of Petrology* **48**, 2033–61.

Rollinson, H. R. 1993. *Using geochemical data: evaluation, presentation, interpretation*, 352 pp. London: Longman Scientific & Technical.

Scaillet, B., Holtz, F., Pichavant, M. & Schmidt, M. 1996. Viscosity of Himalayan leucogranites: implications for mechanisms of granitic magma ascent. *Journal of Geophysical Research* **B101**, 27691–9.

Simons, B. A. & Moore, D. H. 1999. *Victoria 1:1 000 000 Pre-Permian geology*. Melbourne, Australia: Geological Survey of Victoria.

Sparks, R. S. J. & Marshall, L. A. 1986. Thermal and mechanical constraints on mixing between mafic and silicic magmas. *Journal of Volcanology and Geothermal Research* **29**, 99–124.

Stephens, W. E. & Halliday, A. N. 1980. Discontinuities in the composition surface of a zoned pluton, Criffell, Scotland. *Geological Society of America Bulletin* **91**, 165–70.

Stephens, W. E., Whitley, J. E., Thirlwall, M. F. & Halliday, A. N. 1985. The Criffell zoned pluton – correlated behavior of rare-earth element abundances with isotopic systems. *Contributions to Mineralogy and Petrology* **89**, 226–38.

Stephens, W. E. 1992. Spatial, compositional and rheological constraints on the origin of zoning in the Criffell pluton, Scotland. *Transactions of the Royal Society of Edinburgh: Earth Sciences* **83**, 191–9.

Stevens, G., Villaros, A. & Moyen, J-F. 2007. Selective peritectic garnet entrainment as the origin of geochemical diversity in S-type granites. *Geology* **35**, 9–12.

Vandenberg, A. H. M., Willman, C. E., Maher, S., Simons, B. A., Cayley, R. A., Taylor, D. H., Morand, J., Moore, D. H. & Radojkovic, A. 2000. *The Tasman Fold Belt system in Victoria. Geological Survey of Victoria Special Publication*, 483 pp. Melbourne, Australia: Geological Survey of Victoria.

Vogel, T. A., Patiño, L. C., Alvarado, G. E. & Gans, B. 2004. Silicic ignimbrites within the Costa Rican volcanic front: evidence for the formation of continental crust. *Earth and Planetary Science Letters* **226**, 149–59.

Waight, T. E., Maas, R. & Nicholls, I. A. 2000. Fingerprinting feldspar phenocrysts using crystal isotopic composition stratigraphy: implications for crystal transfer and magma mingling in S-type granites. *Contributions to Mineralogy and Petrology* **139**, 227–39.

Weinberg, R. F., Sial, A. N. & Pessoa, R. R. 2001. Magma flow within the Tavares pluton, northeastern Brazil: compositional and thermal convection. *Geological Society of America Bulletin* **113**, 508–20.

White, A. J. R., Allen, C. M., Beams, S. D., Carr, F., Champion, D. C., Chappell, B. W., Wyborn, D. & Wyborn, L. A. I. 2001. Granite suites and supersuites of eastern Australia. *Australian Journal of Earth Sciences* **48**, 515–30.

Whittington, A. G. & Treloar, P. J. 2002. Crustal anatexis and its relation to the exhumation of collisional orogenic belts, with particular reference to the Himalaya. *Mineralogical Magazine* **66**, 53–91.

Wiebe, R. A. & Collins, W. J. 1998. Depositional features and stratigraphic sections in granitic plutons: implications for the emplacement and crystallization of granitic magma. *Journal of Structural Geology* **20**, 1273–89.

Wyborn, D., Chappell, B. W. & James, M. 2001. Examples of convective fractionation in high-temperature granites from the Lachlan Fold Belt. *Australian Journal of Earth Sciences* **48**, 531–41.

MS received 28 March 2008. Accepted for publication 27 May 2008 (Stellenbosch); 15 January 2009 (RSE).

Causes of compositional diversity in a lobe of the Half Dome granodiorite, Tuolumne Batholith, Central Sierra Nevada, California

R. C. Economos[1], V. Memeti[1], S. R. Paterson[1], J. S. Miller[2], S. Erdmann[3] and J. Žák[4,5]

[1] University of Southern California, Department of Earth Sciences, 3651 Trousdale Parkway, Los Angeles, CA 90089–0740, USA
Email: economos@usc.edu

[2] Department of Geology, San José State University, San José, CA 95192–0102, USA

[3] Department of Earth Sciences, Dalhousie University, Halifax, Nova Scotia, B3H 4R2 Canada

[4] Institute of Geology and Paleontology, Charles University, Albertov 6, Prague, 12843, Czech Republic

[5] Czech Geological Survey, Klárov 3, Prague, 11821, Czech Republic

ABSTRACT: The causes of compositional diversity in the Tuolumne Batholith, whether source heterogeneity, magma mixing, or fractional crystallisation, is a matter of longstanding debate. This paper presents data from detailed mapping and a microstructural and major element, trace element and isotopic study of an elongate lobe of the Half Dome granodiorite that protrudes from the southern end of the batholith. The lobe is normally zoned from quartz diorite along the outer margin to high-silica leucogranite in the core. Contacts are steep and gradational, except for the central leucogranite contact, which is locally sharp: magmatic fabrics overprint contacts. A striking feature of the lobe is the 18 wt% SiO_2 range comparable to that observed for the entire Tuolumne Batholith. Feldspar-compatible elements (Sr and Ba) decrease towards the centre, while Rb increases. Light and middle REEs show a smooth decrease towards the centre of the lobe. Calculated initial isotopic ratios of $^{87}Sr/^{86}Sr_{(i)}$ and $\varepsilon Nd_{(t)}$ have identical values within error across the lobe, except in the central leucogranite, the most silica rich phase, which shows a slightly more crustal signature. Field, structural, geochemical and isotopic data suggest that fractionation was the dominant process causing compositional variation in this lobe. It is envisioned that this fractionation/crystal sorting occurred in a vertically flowing and evolving magma column with the present map pattern representing a cross-section of this column. Thus the areal extent of the lobe represents a minimum size of interconnected melt at the emplacement level of the Tuolumne Batholith and, given its marginal position, limited width and proximity to colder host rocks, implies that fractionation in larger chambers likely occurred in the main Tuolumne Batholith magma chamber(s).

KEY WORDS: fractional crystallisation, magmatic processes, plutons

The ~1100 km^2 Tuolumne Batholith in the central Sierra Nevada, California (Fig. 1), represents a spectacularly exposed, protracted record of plutonic assembly and internal differentiation in a large, open system continental arc magma chamber. Controversies over the assembly and internal differentiation processes in the Tuolumne Batholith persist, despite increasingly large geochronological and geochemical data sets collected from the batholith over the past 25 years. Central to this debate is the long-standing question of whether the compositional diversity preserved in the Tuolumne Batholith largely reflects source region heterogeneity, contamination, internal fractional crystallisation, or a combination of processes. Bateman & Chappell (1979) used geochemical data to argue that compositional diversity in the Tuolumne Batholith formed largely by *in situ* fractional crystallisation of a single, batholith-sized pulse. Kistler *et al.* (1986) used isotopic data to argue that much of the compositional diversity reflects mixing between two separate mantle and crustal derived melts. More recently, Coleman *et al.* (2004) and Glazner *et al.* (2004) argued that a 94–85 Ma intrusion interval requires growth of the Tuolumne Batholith by numerous small increments of magma, although the specific size and longevity of these increments remains contentious. In this model, compositional diversity and elemental variability in the batholith largely reflect variations in partial melt fraction and/or melt source heterogeneity. Based on field studies and published geochemistry, Paterson & Vernon (1995) Žák & Paterson (2006) and Memeti *et al.* (2007a) argued that the diversity was caused by the intrusion of large, nested diapirs derived from different source compositions and that fractional crystallisation occurred within these pulses, and mixing/mingling occurred along the margins between major pulses. The size and longevity of the pulses proposed by these authors was also not specified.

The above also highlights the issue of whether large magma chambers commonly exist in magmatic arcs and the size and number of pulses juxtaposed during batholith construction (Pitcher & Berger 1972; Hutton 1992; Lagarde *et al.* 1990;

© 2009 The Royal Society of Edinburgh. doi:10.1017/S1755691009016065

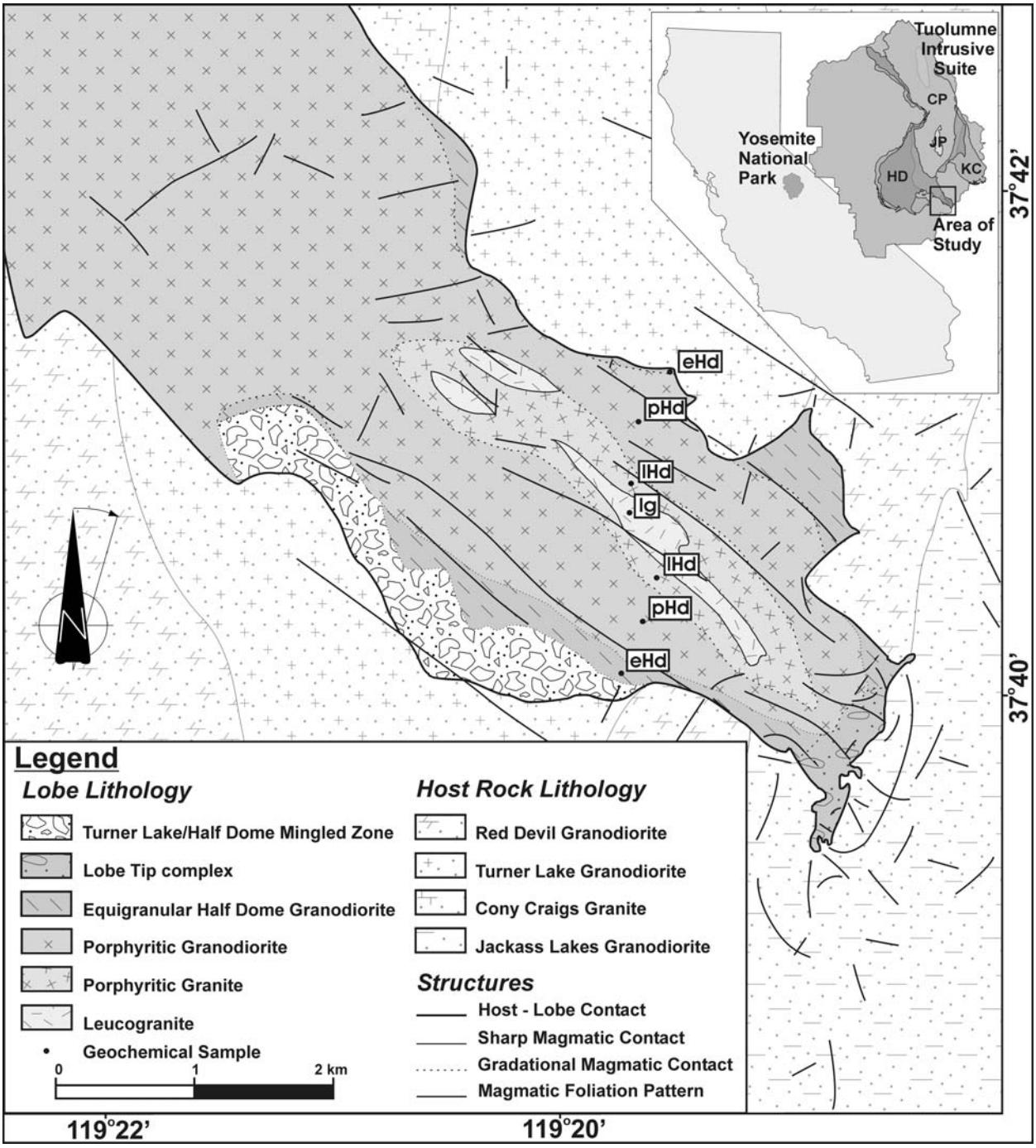

Figure 1 Map of the Half Dome granodiorite lobe and sample locations, with location maps of Yosemite National Park in CA and inset map of the Tuolumne Batholith. Main TIS units are labelled: Kuna Crest (KC); Half Dome (HD); Cathedral Peak (CP); Johnson Porphyry (JP). Lobe units are labelled: equigranular Half Dome granodiorite (eHd); porphyritic Half Dome granodiorite (pHd), leucocratic Half Dome granite to granodiorite (lHd); and leucogranite (lg).

Paterson & Miller 1998; Wiebe & Collins 1998; Johnson *et al.* 1999; Miller & Paterson 2001; Coleman *et al.* 2004; Matzel *et al.* 2005, 2007; Memeti *et al.* 2007b). It is suggested that a useful approach to address these issues is to examine magmatic lobes extending out from the main batholith (Memeti *et al.* 2005). Peripheral lobes in general may offer a relatively simple and short history, and may be more readily amenable to petrogenetic interpretation, in comparison to the larger domains that are complicated by reheating and juxtaposition of later pulses. (Memeti *et al.* 2005; Economos *et al.* 2005; Memeti *et al.* 2007a).

1. Geologic setting

The Tuolumne Batholith, emplaced at a depth of 6–10 km (Ague & Brimhall 1988; Webber *et al.* 2001; Gray 2003), is normally zoned from outer mafic units to inner, progressively more felsic units (Fig. 1) (Bateman 1992). The outer units include the 95–92 Ma Glen Aulin and Glacier Point tonalites and Kuna Crest granodiorite (Bateman 1992; Kistler & Fleck 1994; Coleman *et al.* 2004). Within these is the 91–88 Ma more siliceous Half Dome granodiorite which contains an outer equigranular unit and inner porphyritic unit with K-feldspar

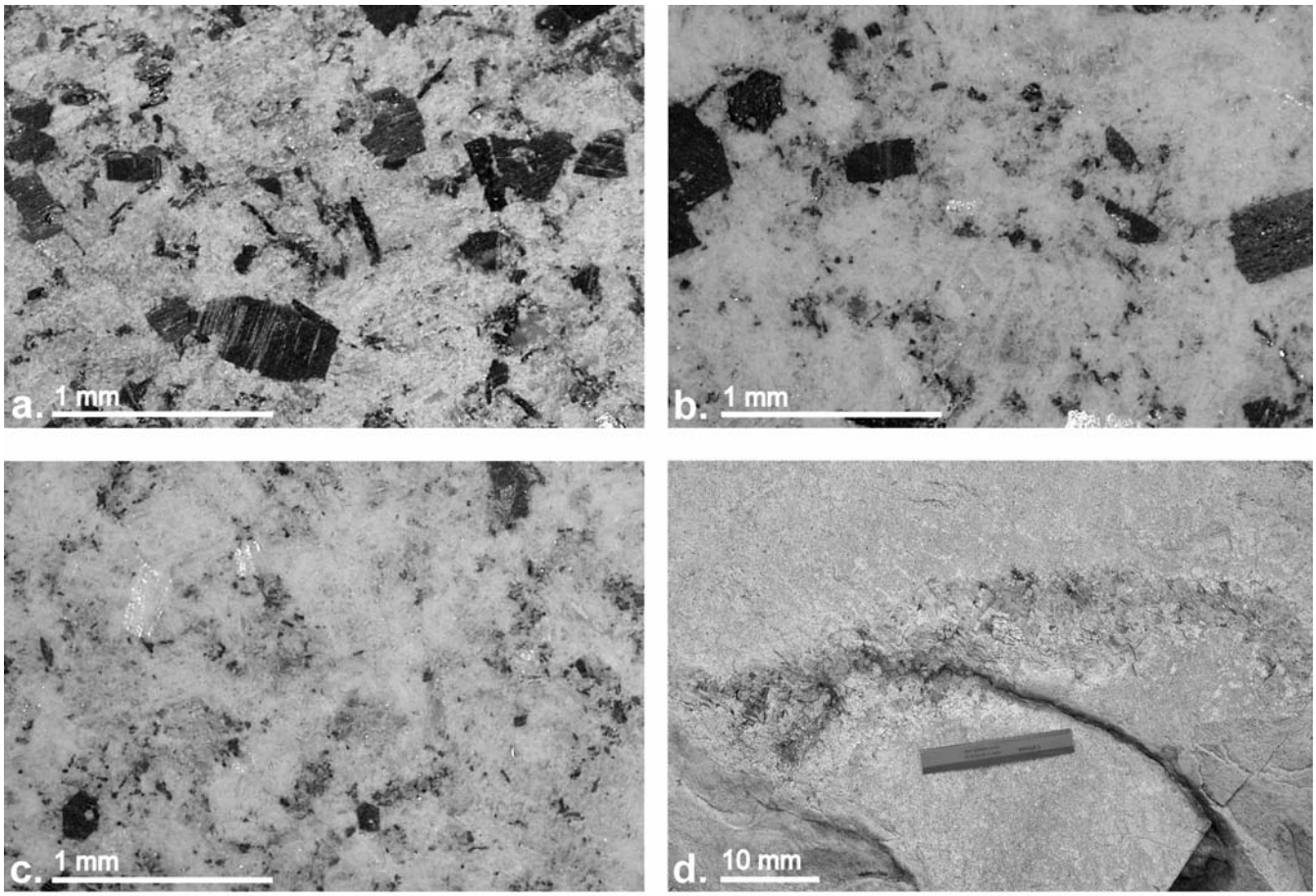

Figure 2 Photographs of Half Dome Lobe units: (a) Equigranular Half Dome granodiorite; (b) Porphyritic Half Dome granodiorite; (c) leucocratic porphyritic Half Dome granodiorite; (d) central leucogranite.

phenocrysts up to 3–4 cm in length (Bateman 1992; Kistler & Fleck 1994; Coleman *et al*. 2004). Further inward is the most aerially extensive unit in the batholith, the 88–85 Ma megacrystic Cathedral Peak granodiorite (Bateman 1992; Kistler and Fleck 1994; Coleman *et al*. 2004, Matzel *et al*. 2005). The small central phase is the ~87 Ma Johnson Granite Porphyry containing local Cathedral Peak inclusions and K-feldspar phenocrysts (Bateman 1992; Titus *et al*. 2005; Bracciali 2008).

This paper focuses on the Half Dome granodiorite. The most distinctive petrographic characteristics of this unit include approximately equal amounts of large (often >1 cm long) euhedral hornblendes and small subhedral biotites and prominent titanite crystals (Bateman 1992). The Half Dome unit dominates the southwestern portion of the main Tuolumne Batholith and has narrow northward and southward protruding lobes (Fig. 1 inset). The southern lobe was originally mapped as Half Dome granodiorite (Peck 1980; Huber *et al*. 1989), but was later assigned to the porphyritic Half Dome phase (Bateman 1992). The lobe intrudes the ~98 Ma Red Devil Lake granodiorite (Tobisch *et al*. 1995), the Turner Lake granite, and the Cony Craigs Porphyry (Bateman 1992). The southern tip of the lobe extends into the 97–98 Ma Jackass Lakes pluton (McNulty *et al*. 1996).

Thermal modelling and $^{40}Ar/^{39}Ar$ thermochronology indicate that the Half Dome lobe may have cooled in a few 10^5 years (Paterson *et al*. 2007), whether emplaced as a single or multiple pulses. An ongoing study of detailed U/Pb zircon geochronology in the lobe yields a 206 Pb/238 U ages of 90·12 ± 0·16 Ma (MSWD of 2·3) for the oldest phase (Fig. 1, 'pHd') and 89·68 ± 0·24 Ma for the youngest phase (Fig.1, 'lg') (Memeti *et al*. 2007c; Memeti *et al*. in press).

2. Results

2.1. Field relationships

The southern Half Dome lobe has been remapped at a 1:10 000 scale. The new mapping shows that the lobe can be divided into four compositionally and texturally distinct phases (Figs 1, 2). The outermost phase is a granodiorite to quartz monzodiorite that is generally equivalent to the equigranular variety of the Half Dome granodiorite in the main batholith (hereafter 'outer phase' [eHd]). It is medium-grained and contains up to 2 cm euhedral hornblende and up to 1 cm euhedral titanite (Figs 1, 2a). This phase grades inwards into a biotite-dominated, porphyritic granodiorite containing K-feldspar megacrysts up to 5 cm in length (hereafter, 'porphyritic phase' [pHd]) (Figs 1, 2b). This phase grades inwards to a more leucocratic, medium-grained biotite granodiorite to monzogranite with 0–2% modal hornblende, 3–5% modal biotite, and sparse, 1–3 cm K-feldspar megacrysts (hereafter, central phase [lHd]) (Figs 1, 2c). The innermost central phase is a fine-grained monzogranite dominated by quartz and K-feldspar with less than 1% modal biotite (hereafter, 'leucogranite' [lg]) (Figs 1, 2d). These units are organised in a symmetrical map pattern with NW-striking contacts aligned parallel to the margins of the lobe (Fig. 1); textural and compositional characteristics of units on the east and west sides of the lobe are identical.

Whilst the compositions within each phase are relatively homogeneous, contacts between the outer, porphyritic, and central phases are gradational over zones 50–60 m wide. As such, contact zones were characterised by gradual changes in

modal mineralogy, microstructure and colour index, and defined in the field as the regions of largest gradients of the above. These gradational contacts remain subvertical across fairly significant changes in topography, and are thus interpreted to be steeply dipping everywhere within the lobe. Cross-cutting dikes from different phases reveal that the outer phase is the oldest, and that phases young towards the centre of the lobe. The contact between the leucogranite and its surrounding central phase is unusual in the lobe in that it is sharp in most localities and has both shallow and steep dips.

The contact between the lobe and its older plutonic host rocks varies dramatically in structure and composition along strike. The tip of the lobe exhibits a highly irregular pattern and is also structurally complex. Compositions range from granite to monzodiorite, with predominantly granodiorite compositions. This tip area contains many randomly oriented blocks of host rock granitic units and rhyolitic to dacitic metatuffs (observed only as blocks) ranging from centimetre- to tens of metres-scales. Enclave swarms tens of metres in diameter that contain hundreds of mafic enclaves are common. Dikes that cross cut host rocks extrude southward away from the very southern tip of the lobe. The southern lobe contact north of the tip is characterised by a 100–200 m-wide structurally complex zone between the equigranular Half Dome granodiorite and the Turner Lake granite (Fig. 1, 'Turner Lake/Half Dome mingled zone'). Common complexities along this contact include mingling between distinctive hornblende-free Turner Lake granite and Half Dome lobe granodiorite, blocks of Turner Lake granite surrounded by Half Dome granodiorite, and abundant schlieren. The northern lobe–host rock contact is generally sharp. Magmatic fabrics in the lobe include a ~NNW–SSE foliation and an ~E–W foliation that overprints all gradational internal contacts in the lobe (Fig. 1).

2.2. Petrography

The outer phase of the Half Dome lobe consists of 53–61% plagioclase, 12–22% quartz, 6% K-feldspar, 10% biotite and 7% hornblende. Accessory minerals include abundant 1·5–3 mm euhedral titanite, apatite, magnetite and zircon. Plagioclase, hornblende and biotite are sub- to euhedral. K-feldspars are large and anhedral, commonly showing perthite exsolution and appear to occupy interstices between more euhedral phases. Plagioclase and hornblende inclusions also commonly occur in K-feldspars. Myrmekite occurs in this phase, and chloritisation of biotites, undulose extinction in quartz and mild deformation of plagioclase twins are also observed.

The porphyritic phase contains 43–54% plagioclase, 20–28% quartz, 14% K-feldspar, 8% biotite and 3% hornblende. Accessory minerals include titanite, apatite, magnetite, zircon and allanite. Titanite is less abundant, but still large and euhedral. K-feldspars have a similar morphology to the outer phase and also show perthite texture, but are occasionally much larger, up to 1·5 cm in length.

The central phase contains 38% plagioclase, 28–32% quartz, 25–29% K-feldspar, 2–5% biotite, and 0–2% hornblende. Titanite and magnetite are present, but less abundant in this phase. K-feldspars are subhedral and perthitic. Whilst K-feldspars are still poikiolitic, they no longer display the interstitial texture from outer phases. Zircon and apatite are also common accessory phases.

The leucogranite phase contains 35% plagioclase, 48% quartz, 16% K-feldspar, and 1% biotite. Titanite is far less abundant than in other phases and is subhedral. Grain sizes in the leucogranite phase are equigranular and markedly smaller than in other phases. Alteration is much more prevalent in this phase, including complete chloritisation of biotite and strong sericitisation of plagioclase crystals. Minor sulfides also occur in this unit.

In summary, modal mineralogy in the lobe shows a clear increase in quartz content and a decrease in plagioclase, hornblende, biotite and titanite toward the centre of the lobe. Total K-feldspar content increases inward and peaks in the megacryst bearing phase.

2.3. Geochemistry

Seven samples for geochemical analyses were collected along a N–S transect across the dominantly NE–SW zoning in the lobe (Fig. 1, Table 1). Samples representative of the main units were selected for analyses.

Whole rock major and trace element data were collected by X-ray flourescence (XRF) and inductively coupled plasma mass spectrometer (ICP-MS) at the Geoanalytical laboratory at Washington State University. Sample chips were selected and ground in a tungsten carbide mill, mixed with dilithium tetraborate, and fused in graphite crucibles for major element analysis and some minor elements. REE analyses of low abundance trace elements were analysed on a quadrupole mass spectrometer with an inductively coupled argon plasma source. Detection limits were at or below chondrite levels. Samples for ICP-MS analysis were ground in an iron bowl in a shatterbox swing mill. Two grams of rock powder were mixed with an equal amount of lithium tetraborate flux, placed into a carbon crucible and fused. The resulting fused bead was re-ground and dissolved in a mixture of HF, HNO_3, and $HCLO_4$. The samples were then dried and re-dissolved and mixed with a standard of In, Re and Ru, used to correct for instrument drift. Measurements were conducted on a Sciex Elan model 250 ICP-MS. Calibration curves were constructed from common silicate rock standards run with the samples for each element and unknown concentrations were computed from these curves.

Whole-rock Nd and Sr isotopic data were also collected for each phase of the lobe (Fig. 3e, f, Table 2). Two hundred mg of rock powder for each sample was dissolved in a mixture of HF and HNO_3 and spiked with mixed ^{150}Nd-^{147}Sm spike in a sealed Teflon bomb at 180°C for 5–7 days. Separation of Rb, Sr and the REE group followed standard cation-exchange procedures. Separation of Sm and Nd used alpha-HIBA on cation exchange resin. Strontium was separated using Sr-spec column chemistry and HNO_3. Neodymium was loaded on single Re filaments with dilute HCl, and Sm were loaded on single-Ta filaments with H_3PO_4. Strontium was loaded with H_3PO_4 and $TaCl_5$ emitter on a single Re filament. All analyses were performed on the Micromass Sector-54 mass spectrometer at the University of North Carolina. Neodymium was analysed in dynamic multicollector mode as NdO using an oxygen bleed valve at 1V, and Sm was analysed in static multicollector mode with $^{147}Sm = 200$ mV. Strontium was analysed in dynamic multicollector mode with $^{88}Sr = 3V$. Neodymium data are normalised to $^{146}Nd/^{144}Nd = 0{\cdot}7219$. Strontium data are normalised to $^{86}Sr/^{88}Sr = 0{\cdot}1194$. During the period of analysis, replication of SRM-987 yielded $^{87}Sr/^{86}Sr = 0{\cdot}710246 \pm 0{\cdot}000010$. Nd data are referenced to La Jolla Nd ($^{143}Nd/^{144}Nd = 0{\cdot}511853$). Replicate analysis of the UNC J-Nd standard during the period of analysis gave $^{143}Nd/^{144}Nd = 0{\cdot}512099 \pm 0{\cdot}000005$. This internal standard is also referenced to LaJolla Nd but is run more frequently. No bias correction has been applied based on repeated measurements of both standards. Initial Sr ratios were calculated using $\lambda^{87}Rb = 1{\cdot}42 \times 10^{-11}$ yr, and using Rb and Sr concentrations measured by ICP-MS. Initial ratios are calculated using a nominal age of 92 Ma for the Half Dome granodiorite (e.g. Coleman *et al.* 2004).

Table 1 Major oxide and trace element data collected at the Geoanalytic Laboratory at Washington State University. Major oxides were measured by XRF and trace elements were measured by ICP-MS.

XRF measurements in wt%:

Sample	SiO_2	AI_2O_3	CaO	MgO	Na_2O	K_2O	Fe_2O_3	MnO	TiO_2	P_2O_5	Cr_2O_3	LOI	Sum
1	58·22	17·97	5·78	2·4	4·17	2·46	6·26	0·11	0·87	0·29	0·02	0·45	98·99
2	67·2	15·88	3·37	0·99	4·17	3·36	3·37	0·07	0·48	0·18	0·02	0·25	99·32
3	74·9	12·9	1·19	0·25	3·28	4·57	1·35	0·02	0·14	0·04	0·03	0·3	98·97
4	76·17	12·86	0·88	0·11	3·57	4·49	1·14	0·02	0·09	0·01	0·03	0·1	99·47
5	68·74	15·44	2·99	0·78	3·97	3·53	2·87	0·06	0·43	0·15	0·02	0·4	99·38
6	66·68	15·9	3·37	1·02	4·04	3·15	3·51	0·07	0·49	0·17	0·02	0·45	98·86
7	61·7	16·17	4·93	1·98	3·73	2·81	5·57	0·09	0·75	0·27	0·02	0·4	98·42

ICP-MS measurements:

Sample	Li (ppm)	Mg (%)	P (%)	Cr (ppm)	Fe (%)	Ni (ppm)	Rb (ppm)	Sr (ppm)	Y (ppm)	Zr (ppm)	Nb (ppm)	Cs (ppm)	Ba (ppm)
1	26	1·52	0·14	114	4·16	10	93·9	872·4	12·6	77·5	9	3·3	889·6
2	26	0·62	0·09	137	2·28	9	130·5	697·2	7·2	124·8	7	5·7	1119·6
3	16	0·14	0·02	182	0·92	8	192·9	151·4	2·4	60·5	5	6·4	194
4	<10	0·06	<0·01	181	0·78	<5	205·4	72·6	2·2	56·8	7	3·9	45·5
5	23	0·48	0·07	127	1·9	7	139·8	624·6	6·2	73·2	7	6·7	825·4
6	26	0·66	0·08	150	2·42	9	118·1	679·1	7·9	138·9	7	4·7	926·5
7	19	1·28	0·12	134	3·84	13	86·2	797·2	11·3	115·1	9	3·8	1107·3

Sample	La (ppm)	Ce (ppm)	Pr (ppm)	Nd (ppm)	Sm (ppm)	Eu (ppm)	Gd (ppm)	Tb (ppm)	Dy (ppm)	Ho (ppm)	Er (ppm)	Tm (ppm)	Lu (ppm)
1	32	63·5	7·36	27·5	4·8	1·24	4·28	0·58	2·4	0·47	1·21	0·17	0·22
2	25·1	46·1	5·29	19·6	3	0·86	2·68	0·37	1·5	0·27	0·78	0·1	0·13
3	15·7	18·9	1·55	4·7	0·7	0·18	0·58	0·08	0·35	0·08	0·2	<0·05	0·08
4	17·1	17·1	1·24	3·4	0·5	0·08	0·47	0·06	0·31	0·07	0·25	<0·05	0·06
5	22·5	40·5	4·92	17·5	2·7	0·77	2·26	0·29	1·16	0·21	0·59	0·08	0·12
6	26·4	48	5·59	20·6	3·4	0·85	2·74	0·36	1·47	0·28	0·79	0·12	0·13
7	29·3	59·2	7·25	27·2	4·5	1·11	3·83	0·49	2·1	0·39	1·23	0·16	0·17

Sample	Yb (ppm)	Hf (ppm)	Pb (ppm)	Th (ppm)	U (ppm)
1	1·1	3	13	11·3	7·92
2	0·7	4	52	11·8	3·84
3	0·3	3	24	19·4	6·12
4	0·3	3	67	21	6·52
5	0·5	2	17	17·1	4·02
6	0·7	4	15	13·3	3·68
7	1	3	13	11·8	4·66

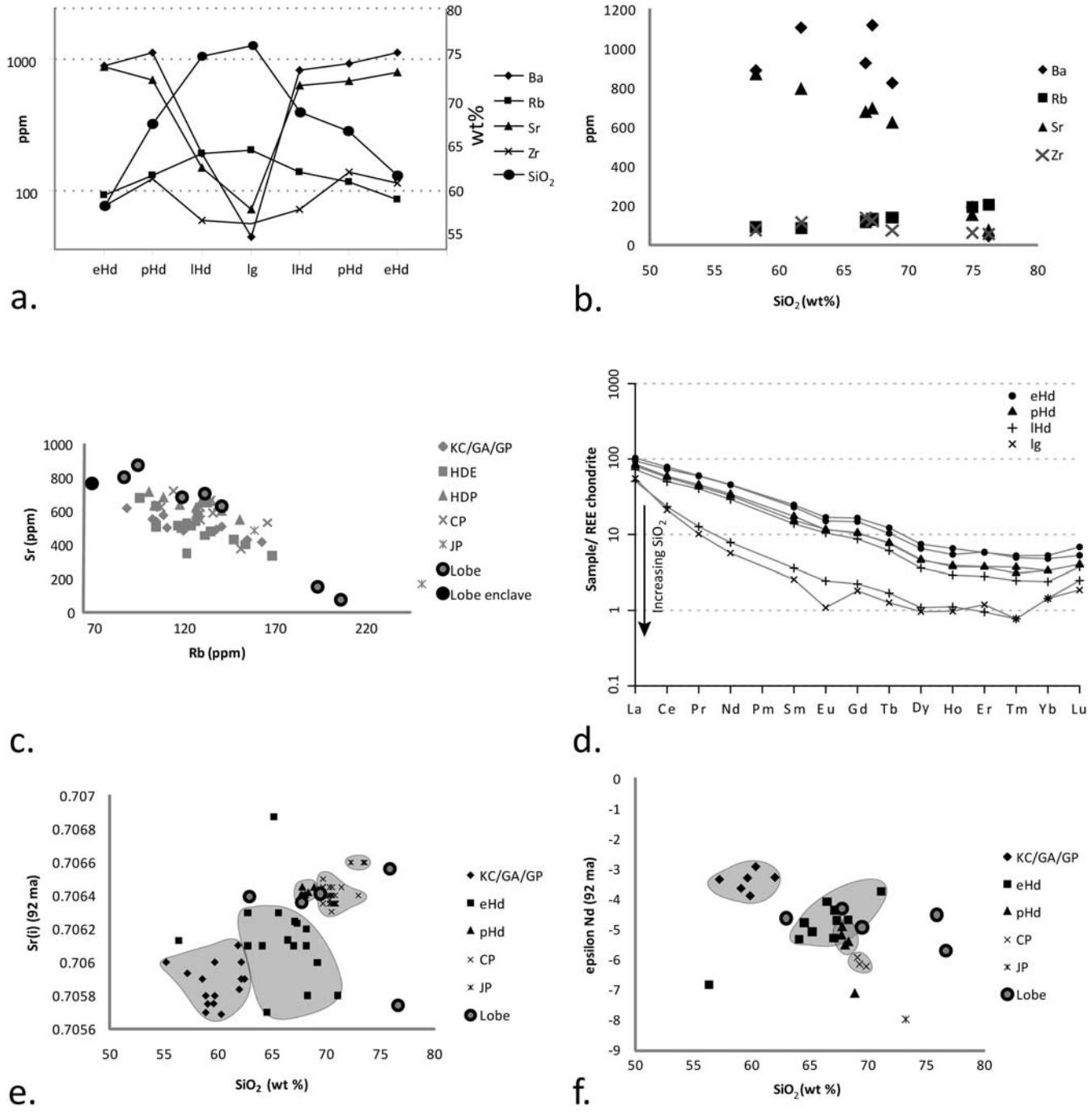

Figure 3 (a) Trace elements Ba, Sr, Rb, Zr and SiO_2 plotted across the lobe to demonstrate symmetrical pattern; (b) The same trace elements plotted against SiO_2; (c) Sr vs. Rb for the Half Dome lobe and the entire Tuolumne Batholith (Bateman & Chappell 1979; Bateman 1992; Gray 2003); (d) Rare Earth Elements normalised to chondrite (Boynton 1984); (e) (f) Sr(i) and εNd vs. SiO_2 for the Tuolumne Batholith (Gray 2003; Kistler *et al.* 1986) and the Half Dome lobe.

The compositional and textural symmetry of the lobe is strongly reflected in geochemical trends. SiO_2 content across the lobe displays a symmetrical inward increase from ~60 wt% SiO_2 in the outer phase to 76 wt% SiO_2 in the leucogranite phase (Fig. 3a). This SiO_2 range is impressive, since it is as large as that of all four mapped units of the main batholith combined (Bateman & Chappell 1979). All major oxide trends in both the lobe and the main batholith show fairly linear relationships with SiO_2 with very little scatter (Bateman & Chappell 1979). CIPW norm calculations (including hornblende) confirm the mineralogical trends identified through point counting, including an increase in K-feldspar in the porphyritic phase of the lobe.

Trace element analyses reveal a symmetrical increase in Rb content towards the centre of the lobe, whereas Ba and Sr decrease toward the centre of the lobe with a major drop off in the leucogranite phase (Fig. 3a). When plotted against SiO_2, Rb and Sr show curvilinear trends, while Ba is more scattered (Fig. 3b). These trace element variations are unlike trends in the main batholith, which tend to show weak or no correlations with SiO_2 (Kistler *et al.* 1986; Fig. 2). Zr displays a more complex trend, increasing from the outer phase to the porphyritic phase and then dropping steeply across the gradational contact between the porphyritic phase and the central phase (Figs 3a, 4a, b). All REE concentrations decrease, with increasing SiO_2 toward the centre of the lobe. Light REEs are more

Table 2 $^{87}Sr/^{86}Sr$ and $^{143}Nd/^{144}Nd$ are measured ratios with 2-sigma analytical errors in parentheses. Initial Sr and Nd ratios are calculated using an age of 92 Ma. Epsilon Nd values at the crystallisation age are calculated using $^{143}Nd/^{144}Nd_{(CHUR,\ 0\ Ma)}=0{\cdot}512638$ and $^{147}Sm/^{144}Nd_{(CHUR,\ 0\ Ma)}=0{\cdot}1967$. Rb and Sr concentration data determined by ICP-MS and Sm and Nd concentration data determined by isotope dilution. Errors in Rb and Sr are within 1% and 0·1% respectively of the amount present. Errors for Sm and Nd are within 2% of the amount present and epsilon values calculated using Sm/Nd from ICP data are within 5% of those calculated by ID-TIMS. Based on these considerations and replication of standards and rocks (e.g. BCR-1; see Miller *et al.* 2000), conservative errors of ± 0·00005 are assigned to initial $^{87}Sr/^{86}Sr$ and ± 0·5 epsilon units to initial εNd values.

Sample	Rb ppm	Sr ppm	$^{87}Sr/^{86}Sr$	$^{87}Sr/^{86}Sr$ (92)	Sm ppm	Nd ppm	$^{147}Sm/^{144}Nd$	$^{143}Nd/^{144}Nd$	εNd (92)	T_{DM} (Ma)
3	193	151	0·711382 (16)	0·706556	0·841	5·642	0·0901	0·512342 (65)	−4·53	871
4	205	73	0·716378 (14)	0·705776	0·427	2·975	0·0867	0·512280 (09)	−5·70	921
5	138	623	0·707197 (16)	0·706361	3·35	20·62	0·0981	0·512326 (09)	−4·93	950
6	118	679	0·707068 (16)	0·706412	3·21	22·89	0·0848	0·512349 (08)	−4·33	823
7	86	797	0·706802 (16)	0·706395	5·27	30·86	0·1032	0·512344 (12)	−4·63	970

enriched than heavy REEs in all samples, and light REE enrichment relative to heavy REEs becomes more pronounced in the central phases (Fig. 3d). Middle REEs show a decrease, particularly in the core aplite, and have a 'scooped' shape that is characteristic of other titanite-bearing Sierran aplites (Glazner *et al.* 2008).

Initial Sr and Nd isotopic compositions (and $\varepsilon Nd_{(t)}$) are invariant within error for the outer, porphyritic and central phases (spanning 15 wt% silica) with $^{87}Sr/^{86}Sr_{(i)}=0{\cdot}7064$ and $\varepsilon Nd_{(t)}=-4{\cdot}6$ (Fig. 3e, f). The leucogranite unit has $^{87}Sr/^{86}Sr_{(i)}=0{\cdot}7058$ and $\varepsilon Nd_{(t)}=-5{\cdot}8$, and is therefore isotopically distinct from the other units.

3. Discussion

A robust petrogenetic model for the southern Half Dome lobe must address: (1) normal zoning from mafic/intermediate to felsic that is symmetrical from margin to centre; (2) gradational, steeply dipping magmatic contacts between all units and sharp and variably dipping contacts with the leucogranite; (3) hornblende-rich 'cumulate-like' zones and local layering and associated mafic enclave swarms at the margin of the lobe; (4) smooth decreases in plagioclase and mafic mineral content and appearance of K-feldspar phenocrysts across a narrow gradational zone; (5) smooth and linear major element variation (excluding Na_2O) with SiO_2; (6) regular trace element variation with SiO_2 and distance for many trace elements (Fig. 3a, b); and (7) invariant Nd and Sr isotopic composition across a wide range of SiO_2 and with distance from the lobe margins with a minor variation in the core leucogranite (Fig. 3e, f).

The symmetric zoning pattern is one of the key compositional aspects of the Half Dome lobe that distinguishes it from the Half Dome elsewhere in the Tuolumne. For example, the much larger mass of the Half Dome granodiorite that comprises most of the southwestern exposure of the Tuolumne (see Fig. 1 inset) is quite homogeneous in mineralogy and major element composition (Gray 2003). In addition, the contacts in the Half Dome lobe are everywhere gradational and are thus markedly simpler than those between the major mapped units in the main batholith, which may change from gradational to sharp along strike (e.g. Bateman 1992).

Compositional zoning of plutons has been attributed to a wide variety of processes including: crystal-liquid fractionation, mixing of compositionally different melts, restite unmixing, and emplacement of compositionally distinct pulses at a more or less constant locus of intrusion (cf. Ragland & Butler 1972; Bateman & Nokelberg 1978; Bateman & Chappell 1979; Halliday *et al.* 1980; Reid *et al.* 1983; Scambos *et al.* 1986; Hill *et al.* 1988; Sawka *et al.* 1990; Walawender *et al.* 1990; Barbey *et al.* 2001; Wyborn *et al.* 2001).

Given the field and petrologic data presented above it is considered unlikely that the lobe was emplaced with abundant restite and/or that restite unmixing was important (e.g., Miller *et al.* 2007). Magma mixing can occur between basaltic melts and felsic melts derived by remelting of mafic underplated materials (e.g. Coleman *et al.* 1992; 1995; Ratajeski *et al.* 2001), and so it cannot be unequivocally ruled out by isotopic data alone. The strikingly linear major element covariation and strong linear correlations with bulk composition are what might be expected for magma mixing, but they could also result from bulk unmixing in the lobe. Magma mixing between the enclave-forming mafic magma with any of the more felsic magmas is precluded by trace element trends (e.g. Rb vs. Sr, Fig. 3c), which clearly show that the enclave has too low Sr to serve as an appropriate mafic end member. Several trace elements display non-linear or curvilinear co-variations (Fig. 4c, d) that preclude a simple two component mixing model. Another first order constraint comes from the whole rock isotopic data, which, for all phases but the central aplite, excludes mixing of melts from two isotopically different sources. This suggests a relatively 'closed-system' process.

Along the margins of the lobe, evidence for the operation of crystal–liquid fractionation processes is indicated by the hornblende and biotite dominated zones and development of schlieren troughs and tubes (e.g. Weinberg *et al.* 2001; Žák & Paterson 2005). Away from the margins of the lobe, where transitions between phases are gradational, outcrop-scale evidence for these processes are also observed in the form of crystal accumulations and crystal-poor leucocratic veins (Paterson *et al.* 2005). These rocks have not been analysed, but within the Half Dome lobe they are the ones most obviously affected by accumulation and/or melt segregation. Their relatively minor volumetric proportion suggests that they are unlikely to form a primary cumulate assemblage for the lobe, and such rocks elsewhere in the Tuolumne Batholith cannot be easily related to the main geochemical trends (Reid *et al.* 1983; Paterson *et al.* 2008). They nevertheless provide evidence for redistribution of crystals and melt, and they are thus regarded as evidence for the operation of at least local crystal-melt movements in a magma chamber at the site of emplacement of the lobe.

All petrographic evidence is also permissive of fractional crystallisation, including increasing quartz and K-feldspar content towards the centre of the lobe and decreasing total plagioclase content. Overgrowth relationships show transitions from clinopyroxene to hornblende to biotite. The leucogranite phase represents a highly evolved melt. A simple least-squares mixing analysis of major element compositions revealed that approximately equal proportions of a residual outer phase and a leucocratic central phase would be produced by fractionating

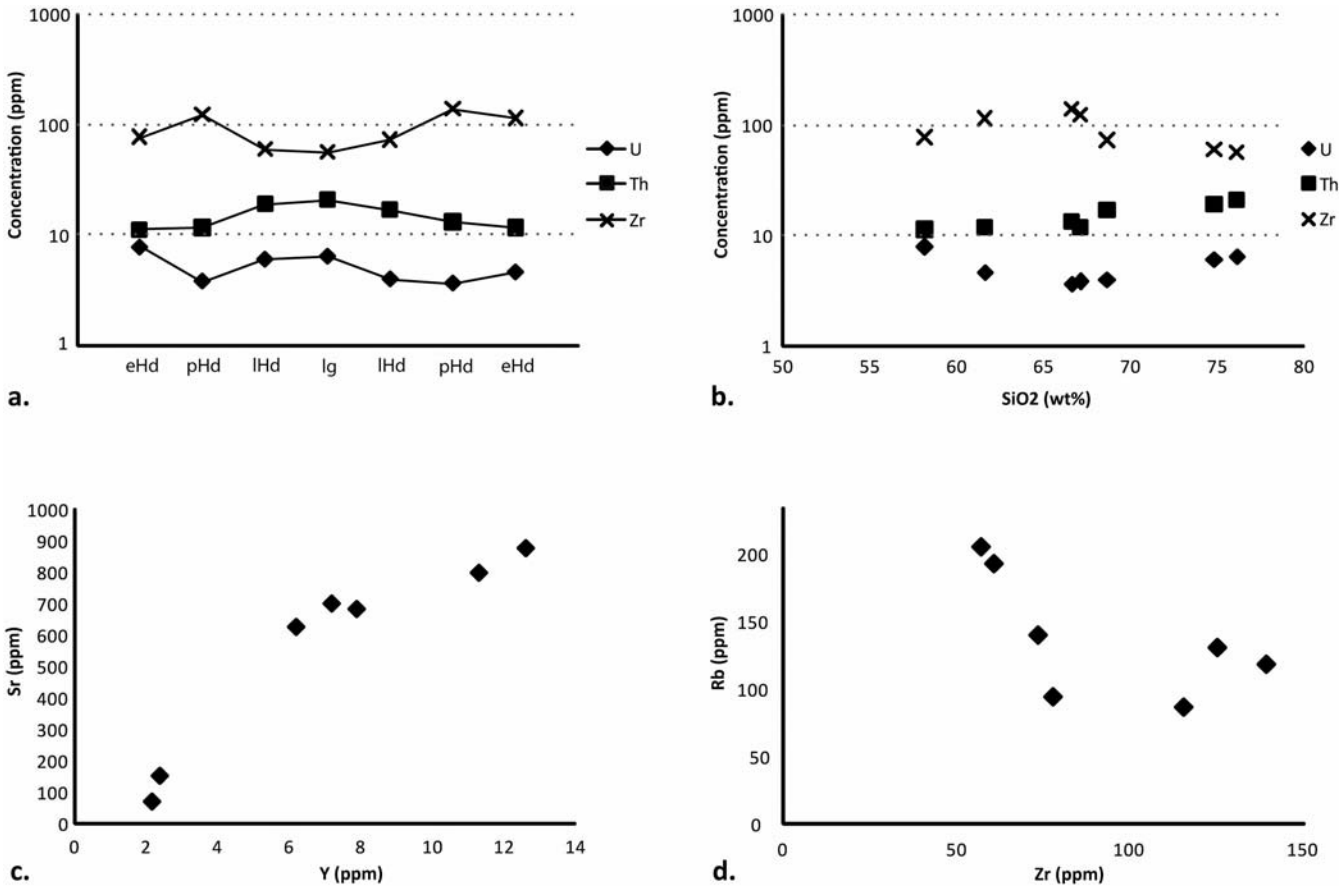

Figure 4 (a) Zircon related elements, U, Th, and Zr, plotted across the lobe showing an inflection point in the porphyritic unit; (b) the same elements plotted vs. SiO_2. (c) (d) Two examples of non-linear trace element trends in the Half Dome lobe: Y vs. Sr and Zr vs. Rb.

the porphyritic phase. However, not enough of the outer phase is present at the level of exposure to account for the fractionation of both the central and leucocratic phase. This is one of several observations that lead the present authors to propose a vertically evolving fractionation system in which some residue resides below the present level of exposure.

Trace element variations are also consistent with fractional crystallisation. Incompatible elements like Rb show an increase with SiO_2 and distance from the host rock contacts, whilst more compatible elements like Sr show a decrease (Fig. 3a), attributed to fractional crystallisation of the major minerals, such as hornblende and plagioclase. These minerals are found in higher abundances in the more marginal phases of the lobe. The pronounced drops in Sr and Ba observed in the leucogranite phase are controlled by feldspar fractional crystallisation, especially K-feldspar, again confirmed by changes in modal mineralogy (Figs 2, 3).

A modest increase in the Ce/Yb ratio is probably indicative of hornblende control until higher SiO_2 values are reached in the interior phases, whereupon Ce/Yb drops markedly. This likely reflects saturation and removal of phase(s) that strongly concentrate the light to middle rare earth elements, and extraction of melt that has been depleted in these elements. The removal of middle REEs that produces the distinctive 'scoop' shape of the rare earth element trend in the leucocratic phases of the lobe is likely attributable to accessory mineral fractional crystallisation, especially titanite (e.g. Glazner *et al.* 2008).

Finally, it is re-emphasised that the isotopic data are a strong indication for dominantly closed-system fractional crystallisation occurring in the Half Dome lobe. Both $^{87}Sr/^{86}Sr_{(i)}$ and $\varepsilon Nd_{(t)}$ values are equal to each other within error over an impressively large variation in SiO_2 content (Fig. 3e, f). This isotopic dataset bears striking similarity to field data, particularly contact relationships. Units that share gradational contacts have identical isotopic values, whilst the single unit with a sharp contact shows a slight isotopic shift.

Geochemical modelling to test the above hypotheses is underway. However, such modelling remains fairly non unique without detailed mineral geochemistry, full consideration of both major, trace, REE, and isotopic data and the roles/volumes of both major and accessory minerals and models designed to test all likely scenarios, and thus is beyond the scope of this paper. Another challenge for geochemical modelling, including modelling of the Tuolumne Batholith, is the increased evidence of recycling and mixing of crystal populations such as now documented for the zircon populations (Matzel *et al.* 2005; Miller *et al.* 2007) and established even at the mesoscale (Paterson *et al.* 2008).

Until these modelling studies are complete, the preferred interpretation is that the lobe represents a frozen cross-section of a vertically evolving and fractionating magma system (Fig. 5). This would allow the possibility that not all of the present exposure in the lobe was laterally connected melt at one time; but if not laterally, it was so vertically. Whilst the percentage of crystallisation beyond the formation of a crystal network is difficult to ascertain, modelling by Bachmann & Bergantz (2004) indicates that relatively crystal-poor magmas can be removed from a mush of 40% to >50% crystals.

The present authors envision a smaller scale version of the upper portions of models presented by Sisson (2005) and Ratajeski *et al.* (2005), in which crystal mush zones along conduit walls grade into a more upwardly mobile crystal mush centre. The chemical gradients, implying chemical communication between magma, cumulates at the host rock contact,

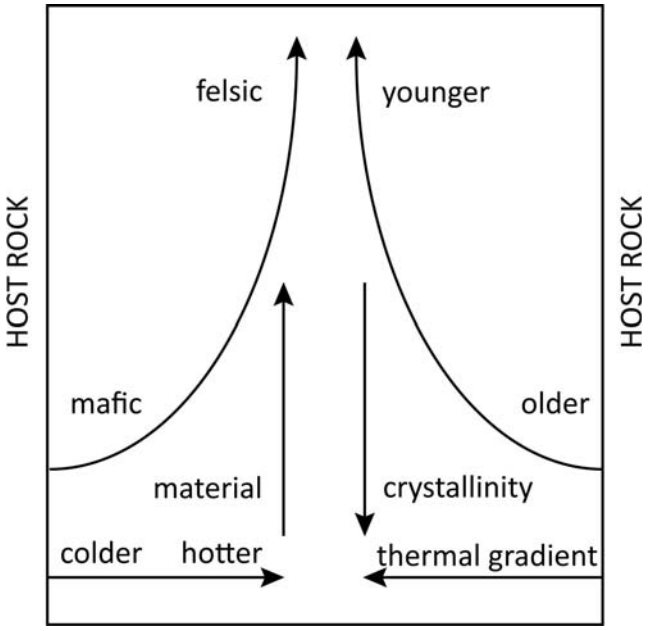

Figure 5 Schematic depicting the major boundary conditions envisioned for a vertically evolving column of fractionating material.

and overprinting magmatic fabrics in this lobe are all time-transgressive (both laterally and vertically); features consistent with this model. Thus, the compositional diversity in the lobe is generated by processes occurring both at and below the level of emplacement, but these processes are linked to each other by interconnected melt in an evolving system. If a similar system operated in the main batholith, in which pulses were disrupted by later intrusions, this nicely explains the difference in isotopic systematics between the Half Dome lobe and the entire Half Dome unit, with the former being isotopically homogeneous while the latter shows a much more complex history (Kistler *et al*. 1986; Kistler & Fleck 1994, Memeti *et al*. 2007b; Matzel *et al*. 2007).

Such a vertically evolving, fractionating system would predict the same or more likely even greater vertical extent than the cross-sectional area of the lobe. If such a volume of interconnected melt is achieved in the thermally less favourable environment of the lobe, larger bodies of interconnected melt should be expected within the main body of the Tuolumne Batholith. This conclusion is supported in the main batholith by magmatic fabrics that overprint all internal contacts (Žák *et al*. 2007), broad zones of mixing/mingling along these contacts and gradations between them (Bateman 1992; Žák & Paterson 2006; Paterson *et al*. 2008), and broad zones of nearly identical U/Pb zircon ages and related geochemistry in the large central Cathedral Peak unit (Burgess & Miller 2008).

One interesting question is why the major oxide diversity in the lobe is greater than that preserved in any unit in the main batholith. Was this signal somehow removed in the main batholith? Or if never achieved by an individual unit in the main batholith, does it imply that the elevated geothermal gradient and rapid crystallisation predicted in the lobes may produce more rather than less fractional crystallisation in natural systems? The most critical differences in boundary conditions between the lobe and the main batholith are thermal gradient during crystallisation (Spera & Bohrson 2001; Paterson *et al*. 2003; Memeti *et al*. 2007a) and presence of additional distinct magma pulses in the main batholith (Spera & Bohrson 2001). The effects of these boundary condition differences on the mechanical separation of crystals and liquid warrants additional discussion.

4. Conclusions

The mapping, structural, chemical and isotopic evidence suggests that a vertically flowing and fractionating column of magma, derived from a largely isotopically homogeneous source, played the dominant role in the formation of compositional diversity in the southern Half Dome granodiorite lobe of the Tuolumne Batholith. This keeps open the possibility that fractional crystallisation may have occurred in the main chamber over length and volume scales significantly larger than that of the lobe, requiring bodies of interconnected melt at least as large as the lobe at the time of emplacement of units in the main batholith.

These results suggest that fractional crystallisation at or near the level of emplacement of the Tuolumne Batholith is capable of producing major oxide heterogeneity of the magnitude seen in the entire batholith. Why this level of fractional crystallisation is not preserved in the main batholith may be that it is masked by subsequent processes (Memeti *et al*. 2007b), or that an elevated thermal gradient in the lobe was a driving factor for the degree of fractional crystallisation. A lower thermal gradient and juxtaposition of different batches in the main batholith may have allowed mixing to play a more significant role.

5. Acknowledgements

This work was supported by funds from the University of Southern California Department of Earth Sciences, by NSF grant EAR-0073943 (to Paterson), NSF EAR-0074099 (to Miller) and by Czech Academy of Sciences Grant No. KJB 3111403 (to Žák). Special thanks to J. Lawford Anderson for his intellectual contribution, and to Claire Wilke and Gayle Hough for their assistance in the field. Thanks to Dr Calvin Miller and Dr Allen Glazner for their constructive, helpful reviews.

6. References

Ague, J. J. & Brimhall, G. H. 1988. Magmatic arc asymmetry and distribution of anomalous plutonic belts in the batholiths of California; effects of assimilation, crustal thickness, and depth of crystallization. *Geological Society of America Bulletin* **100**, 912–27.

Bachmann, O. & Bergantz, G. W. 2004. On the origin of crystal-poor rhyolites extracted from batholithic crystal mushes. *Journal of Petrology* **45** (8), 1565–82.

Barbey, P., Nachit, H. & Pons, J. 2001. Magma–host interactions during differentiation and emplacement of a shallow-level, zoned granitic pluton Tarçouate pluton, Morocco: implications for magma emplacement. *Lithos* **58**, 125–43.

Bateman, P. C. 1992. Plutonism in the central part of the Sierra Nevada Batholith, California. *US Geological Survey Professional Paper* **P 1483**.

Bateman, P. C. & Chappell, B. W. 1979. Crystallization, fractionation, and solidification of the Tuolumne Intrusive Series, Yosemite National Park, California. *Geological Society of America Bulletin* **90** (5), 1465–82.

Bateman, P. C. & Nokelberg, W. J. 1978. Solidification of the Mount Givens Granodiorite, Sierra Nevada, California. *Journal of Geology* **86**, 563–79.

Boynton, W. V. 1984. Cosmochemistry of the rare earth elements: meteorite studies. *In* Henderson, P. (ed.) *Rare Earth Element Geochemistry*, 63–114. Amsterdam: Elsevier.

Bracciali, L., Paterson, S. R., Memeti, V., Rocchi, S., Matzel, J. & Mundil, R. 2008. Build-up of the Tuolumne Batholith, California: the Johnson Granite Porphyry. *In LASI 3 Conference Extended Abstract Volume, Physical Geology of Subvolcanic Systems: Laccolith, Sills and Dykes*. Elba Island, Italy, September 2008.

Burgess, S. D. & Miller, J. S. 2008. Construction, solidification, and internal differentiation of a large felsic arc pluton. Cathedral Peak granodiorite, Sierra Nevada Batholith. *In* Zellmer, G. & Annen,

C. (eds) *Geological Society, London, Special Publication* **304**, 203–33. Bath, UK: The Geological Society Publishing House.

Coleman, D. S., Frost, T. P. & Glazner, A. F. 1992. Evidence from the Lamarck Granodiorite for rapid Late Cretaceous crust formation in California. *Science* **258**, 1924–26.

Coleman, D. S., Glazner, A. F., Miller, J. S., Bradford, K. J., Frost, T. P., Joye, J. L. & Bachl, C. A. 1995. Exposure of a Late Cretaceous layered mafic-felsic magma system in the central Sierra Nevada batholith, California. *Contributions to Mineralogy and Petrology* **120**, 129–36.

Coleman, D. S., Walt, G. & Glazner, A. F. 2004. Rethinking the emplacement and evolution of zoned plutons: Geochronologic evidence for incremental assembly of the Tuolumne Batholith, California. *Geology* **32**, 433–6.

Economos, R. C., Miller, J. S., Paterson, S. R., Memeti, V., Erdmann, S. & Žák, J. 2005. The Role of Fractionation at the Emplacement Level in the Tuolumne Batholith, Sierra Nevada, CA. *Geological Society of America Abstracts with Programs* **37**, 554.

Glazner, A. F., Bartley, J. M., Coleman, D. S., Gray, W. & Taylor, R. Z. 2004. Are plutons assembled over millions of years by amalgamation from small magma chambers? *GSA Today* **14**, 4–11.

Glazner, A. F., Coleman, D. S. & Bartley, J. M. 2008. The tenuous connection between high-silica rhyolites and granodiorite plutons. *Geology* **36**, 183–6.

Gray, W. 2003. *Chemical and thermal evolution of the Late Cretaceous Tuolumne Batholith, Yosemite National Park, California*. Ph.D. Thesis. Chapel Hill, University of North Carolina. 202 pp.

Halliday, A. N., Stephens, W. E. & Harmon, R. S. 1980. Rb–Sr and O isotopic relationships in three zoned Caledonian granitic plutons, Southern Uplands, Scotland: evidence for varied sources and hybridisation of magmas. *Journal of the Geological Society, London* **137**, 329–48.

Hill, M., O'Neil, J. R., Noyes, H., Frey, F. A. & Wones, D. R. 1988. Sr, Nd and O isotope variations in compositionally zoned and unzoned plutons in the central Sierra Nevada Batholith. *American Journal of Science* **288–A**, 213–41.

Huber, N. K., Bateman, P. C. & Wahrhaftig, C. 1989. Geologic map of Yosemite National Park and vicinity, California. *US Geological Survey Report* **I-1874**. Scale 1:125,000, 1 sheet.

Hutton, D. H. W. 1992. Granite sheeted complexes: evidence for the dyking ascent mechanism. *Transactions of the Royal Society of Edinburgh: Earth Sciences* **83**, 377–82.

Johnson, S. E., Paterson, S. R. & Tate, M. C. 1999. Structure and emplacement history of multiple-center, cone-sheet-bearing ring complex: the Zarza Intrusive Complex, Baja California, Mexico. *Geological Society of America Bulletin* **111**, 607–19.

Kistler, R. W., Chappell, B. W., Peck, D. L. & Bateman, P. C. 1986. Isotopic variation in the Tuolumne Batholith, central Sierra Nevada: California. *Contributions to Mineralogy and Petrology* **94**, 205–20.

Kistler, R. W. & Fleck, R. J. 1994. Field guide for a transect of the central Sierra Nevada, California: Geochronology and isotope geology. *US Geological Survey Open-File Report* **94-267**, 51 pp.

Lagarde, J. L., Brun, J. P. & Gapais, D. 1990. Formation of epizonal granitic plutons by *in situ* assemblage of laterally expanding magma. *Comptes Rendus de l'Académie des Sciences Paris* **130**, Serie II, 1109–14.

Matzel, J., Mundil, R., Paterson, S. R., Renne, P. & Nomade, S. 2005. Evaluating pluton growth models using high resolution geochronology: Tuolumne Batholith, Sierra Nevada, CA. *Geological Society of America Abstracts with Programs* **37** (7), 131.

Matzel, J., Mundil, R., Miller, J. S., Wooden, J., Mazdab, F., Paterson, S. & Memeti, V. 2007. Zircon growth and recycling during the assembly of the Tuolumne batholith, Sierra Nevada, California. *Goldschmidt Conference Abstracts* **2007**, A639.

McNulty, B. A., Tong, W. & Tobisch, O. T. 1996. Assembly of a dike-fed magma chamber; the Jackass Lakes Pluton, central Sierra Nevada, California. *GSA Bulletin* **108**, 926–40.

Memeti, V., Paterson, S. R., Economos, R. C., Žák, J. & Erdmann, S. 2005. Deciphering Chamber Growth and Internal Magma Chamber Processes Using Magmatic Lobes as Snapshots of Processes During the Construction of the Tuolumne Batholith, Sierra Nevada. *Geological Society of America Abstracts with Programs* **37** (7), 554.

Memeti, V., Paterson, S. R., Matzel, J. & Mundil, R. 2007a. Magmatic lobes as windows into long lived magma chambers: Tuolumne batholith, Sierra Nevada, California. *In* Miller, J. A. & Kisters, A. F. M. (eds) *6th International Hutton Symposium Abstract Volume and Program Guide*. Stellenbosch, South Africa: Department of Geology, Geography and Environmental Sciences, University of Stellenbosch. 236 pp.

Memeti, V., Paterson, S., Matzel, J., Mundil, R., Ducea, M. & Miller, J. 2007b. Dynamics of a magma chamber: Insights into time and length scales of internal processes in the Tuolumne batholith, CA. *Eos Transactions AGU* **88** (52). Fall Meeting Supplement. Abstract V42C-07.

Memeti, V., Paterson, S. R., Matzel, J., Mundil, R. & Okaya, D. In press. Magmatic lobes as "snapshots" of magma chamber growth and evolution in large, composite batholiths: an example from the Tuolumne Intrusion, Sierra Nevada, CA. *Geological Society of America Bulletin*.

Miller, J. S., Glazner, A. F., Farmer, L., Suayah, I. B. & Kieth, L. 2000. A Sr, Nd, and Pb isotopic study of mantle domains and crustal structure from Miocene volcanic rocks in the Mojave Desert, California. *Geological Society of America Bulletin* **112**(8), 1264–79.

Miller, J. S., Matzel, J. E. P., Miller, C. F., Burgess, S. D. & Miller, R. B. 2007. Zircon growth and recycling during the assembly of large, composite arc batholiths. *Journal of Volcanology and Geothermal Research* **167**, 282–99.

Miller, R. B. & Paterson, S. R. 2001. Construction of mid-crustal sheeted plutons: Examples from the north Cascades, Washington. *Geological Society of America Bulletin* **113**, 1423–42.

Paterson, S. R., Okaya, D. & Žák, J. 2003, Thermal histories of episodically constructed, large volume magma chambers: implications for processes along internal contacts: *Geological Society of America Abstracts with Programs* **35**(6), 93.

Paterson, S. R., Vernon, R. H. & Žák, J. 2005. Mechanical Instabilities and Physical Accumulation of K-feldspar Megacrysts in Granitic Magma, Tuolumne Batholith, California, USA. *Journal of the Virtual Explorer* **18**.

Paterson, S. R., Okaya, D., Matzel, J., Memeti, V., Mundil, R. & Nomade, S. 2007. Size and longevity of magma chambers in the Tuolumne Batholith: A comparison of thermal modeling and cooling thermochronology. *Eos Transactions AGU* **88** (52). Fall Meeting Supplement. Abstract V42C-02.

Paterson, S. R., Žák, J. & Janošek, V. 2008. Growth of complex sheeted zones during recycling of older magmatic units into younger: Sawmill Canyon area, Tuolumne batholith, Sierra Nevada, California. *Journal of Volcanology and Geothermal Research* **177** (2), 457–84.

Paterson, S. R. & Miller, R. B. 1998. Mid-crustal magmatic sheets in the Cascades Mountains, Washington: implications for magma ascent. *Journal of Structural Geology* 20, 1345–63.

Paterson, S. R. & Vernon, R. 1995. Bursting the bubble of ballooning plutons; a return to nested diapirs emplaced by multiple processes. *Geological Society of America Bulletin* **107**, 1356–80.

Peck, D. L. 1980. Geologic map of the Merced Peak Quadrangle; central Sierra Nevada, California. *US Geological Survey Report* **GQ-1531**. Scale 1:62,500. 1 sheet.

Pitcher, W. S. & Berger, A. R. 1972. *The Geology of Donegal: a Study of Granite Emplacement and Unroofing*. New York: Wiley. 435 pp.

Ragland, P. C. & Butler, J. R. 1972. Crystallization of the West Farrington Pluton, North Carolina, USA. *Journal of Petrology* **13**, 381–404.

Ratajeski, K., Glazner, A. F. & Miller, B. V. 2001. Geology and geochemistry of mafic to felsic plutonic rocks in the Cretaceous intrusive suite of Yosemite Valley, California. *Geological Society of America Bulletin* **113**(11), 1486–502.

Ratajeski, K., Sisson, T. W. & Glazner, A. F. 2005. Experimental and geochemical evidence for derivation of the El Capitan Granite, California, by partial melting of hydrous gabbroic lower crust. *Contributions to Mineralogy and Petrology* **149**, 713–34.

Reid, J. B., Evans, O. C. & Fates, D. G. 1983. Magma mixing in granitic rocks of the central Sierra Nevada, California. *Earth and Planetary Science Letters* **66**, 243–61.

Sawka, W. N., Chappell, B. W. & Kistler, R. W. 1990. Granitoid compositional zoning by side-wall boundary layer differentiation: evidence from the Palisade Crest Batholith, Central Sierra Nevada, California. *Journal of Petrology* **31**, 519–53.

Scambos, T. A., Loiselle, M. C. & Wones, D. R. 1986. The Center Pond Pluton; the restite of the story (phase separation and melt evolution in granitoid genesis). *American Journal of Science* **286**, 241–80.

Sisson, T. W. 2005. Solidification, Zoning, and Homogenization in Sierran Plutons. *Geological Society of America Abstracts with Programs* **37** (4), 39.

Spera, F. J. & Bohrson, W. A. 2001. Energy-Constrained Open-System Magmatic Processes 1: General Model and Energy-Constrained

Assimilation and Fractional Crystallization (EC-AFC) Formulation. *Journal of Petrology* **42**, 999–1018.

Titus, S. J., Clark, R. & Tikoff, B. 2005. Geologic and geophysical investigation of two fine-grained granites, Sierra Nevada Batholith, California: Evidence for structural controls on emplacement and volcanism. *Geological Society of America Bulletin* **117** (9), 1256–71.

Tobisch, O. T., Saleeby, J. B., Renne, P. R., McNulty, B. A. & Tong, W. 1995. Variations in deformation fields during development of a large-volume magmatic arc, central Sierra Nevada, California. *Geological Society of America Bulletin* **107**, 148–66.

Walawender, M. J., Gastil, R.G., Clinkenbeard, J. P., McCormick, W. V., Eastman, B. G., Wernicke, R. S., Wardlaw, M. S., Gunn, S. H. & Smith, B. M. 1990. Origin and evolution of the zoned La Posta-Type plutons, eastern Peninsular Ranges batholith, southern and Baja California. *In* Anderson, J. L. (ed.) *The Nature and Origin of Cordilleran Magmatism. Geological Society of America Memoir* **174**, 1–18.

Webber, C. E., Candela, P. A., Piccoli, P. M. & Simon, A. C. 2001. Generation of granitic dikes: can texture, mineralogy, and geochemistry be used as guides to determine the mechanism of diking? *Geological Society of America Abstracts with Programs* **33**, A-138.

Weinberg, R. F., Sial, A. N. & Pessoa, R. R. 2001. Magma flow within the Tavares pluton, northeastern Brazil: Compositional and thermal convection. *Geological Society of America Bulletin* **113**, 508–20.

Wiebe, R. A. & Collins, W. J. 1998. Depositional features and stratigraphic sections in granitic plutons: Implications for the emplacement and crystallization of granitic magma. *Journal of Structural Geology* **20**, 1273–89.

Wyborn, D., Chappell, B. W. & James, M. 2001. Examples of convective fractionation in high-temperature granites from the Lachlan Fold Belt. *Australian Journal of Earth Sciences* **48**, 531–41.

Žák, J., Paterson, S. R. & Memeti, V. 2007. Four magmatic fabrics in the Tuolumne batholith, central Sierra Nevada, California (USA): implications for interpreting fabric patterns in plutons and evolution of magma chambers in the upper crust. *GSA Bulletin* **119**, 194–201.

Žák, J. & Paterson, S. R. 2005. Characteristics of internal contacts in the Tuolumne batholith, central Sierra Nevada, California (USA): Implications for episodic emplacement and physical processes in a continental arc magma chamber. *Geological Society of America Bulletin* **117**, 1242–255.

Žák, J. & Paterson, S. R. 2006. Roof and walls of the Red Mountain Creek pluton, eastern Sierra Nevada, California (USA): implications for process zones during pluton emplacement. *Journal of Structural Geology* **28**, 575–87.

MS received 18 February 2008. Accepted for publication 18 September 2008 (Stellenbosch); 15 January 2009 (RSE).

The evolution of late-Hercynian granites and rhyolites documented by quartz – a review

Axel Müller[1], Alfons M. van den Kerkhof[2], Hans-Jürgen Behr[2], Andreas Kronz[2] and Monika Koch-Müller[3]

[1] Geological Survey of Norway, N-7491 Trondheim, Norway
Email: Axel.Muller@ngu.no

[2] Geowissenschaftliches Zentrum Göttingen, Goldschmidtstr. 3, D-37073 Göttingen, Germany

[3] GeoForschungsZentrum Potsdam, Telegrafenberg, D-14473 Potsdam, Germany

ABSTRACT: The potential of igneous quartz for providing a better understanding of magmatic processes is demonstrated by studying late-Hercynian rhyolites and granites from central and western Europe. Cathodoluminescence (CL) reveals growth patterns and alteration structures within igneous quartz reflecting the magma crystallisation history. The relatively stable and blue-dominant CL of zoned phenocrysts is principally related to variations in the Ti concentration, which is a function of the crystallisation temperature. The Al/Ti ratio of igneous quartz increases with progressive magma differentiation, as Ti is more compatible, compared to Al, Li, K, Ge, B, Fe, P during magma evolution. The red-dominant CL of the anhedral groundmass quartz in granite is unstable during electron bombardment and associated with OH- and H_2O-bearing lattice defects. Thus, CL properties of quartz are different for rocks formed from H_2O-poor and H_2O-rich melts. Both groundmass and phenocrysts in granites are rich in alteration structures as a result of interaction with deuteric fluids during cooling, whereas phenocrysts in extrusive rocks do not usually contain such structures. The combined study of trace elements along with the analysis of quartz textures and melt inclusion inventories may reveal detailed PTX-paths of granite magmas. This study shows that quartz is a sensitive indicator for physico-chemical changes during the evolution of silica-rich magmas. Common growth textures show a wide variety in quartz phenocrysts in rhyolites and some granites. This paper presents a classification of textures, which formed as a result of heterogeneous intra-granular lattice defects and impurities. The alternation of growth and resorption microtextures reflects stepwise adiabatic and non-adiabatic magma ascent, temporary storage of magma in reservoirs and mixing with more mafic, hotter magma. The anhedral groundmass quartz overgrowing early-magmatic phenocrysts in granites is free of growth zoning.

KEY WORDS: adiabatic, cathodoluminescence, crystal resorption, growth textures, late-Hercynian magmatism, quartz

Quartz provides a detailed chronicle of physicochemical changes in granitic melts. Quartz phenocrysts normally grow in different magma batches, which are repeatedly recharged. The solidified granites and rhyolites therefore comprise mixtures of different phenocryst populations embedded in a microcrystalline to coarse-grained groundmass. Feldspars in granites and rhyolites are commonly altered due to the late- to post-magmatic interaction with deuteric and hydrothermal fluids. Quartz is more resistant in this environment, with the consequence that magmatic zoning patterns are commonly preserved. These patterns can be revealed by cathodoluminescence (CL) techniques.

Information about the physicochemical changes during the evolution of granitic magma can be obtained by the study of (1) growth patterns in quartz as visualised by cathodoluminescence; (2) trace element concentrations and distribution within quartz crystals; and (3) melt inclusions hosted by quartz:

1. Laemmlein (1930) examined by optical microscope – probably for the first time – primary growth structures in quartz phenocrysts in rhyolite from Transbaikalia. It was not until the 1980/90s, however, that growth zoning (Schneider 1993; D'Lemos *et al.* 1997; Watt *et al.* 1997) and alteration textures (Sprunt & Nur 1979; Behr 1989; Behr & Frentzel-Beyme 1989) in igneous quartz were studied in more detail by CL microscopy. During the last decade, CL microscopy has become a routine method to visualise growth and alteration patterns in igneous quartz (Müller *et al.* 2000, 2002a, 2003b, 2005; Peppard *et al.* 2001; Ruffini *et al.* 2002; Wark *et al.* 2007; Wiebe *et al.* 2007). CL reveals episodes of quartz crystallisation including crystal nucleation, growth and dissolution, which develop during magma ascent, storage, recharge, and mixing. The effects of late- to post-magmatic quartz alteration also become visible in CL studies.
2. CL colour and intensity are the result of intrinsic lattice defects (e.g., oxygen and silicon vacancies, broken bonds) as well as trace elements in the crystal structure (e.g., Sprunt 1981; Ramseyer *et al.* 1988; Perny *et al.* 1992; Stevens Kalceff *et al.* 2000; Götze *et al.* 2001, 2004, 2005). However, the physical background of quartz luminescence has not been fully understood. The concentration of trace elements in quartz is controlled by their abundance in the melt, the partitioning between different phases, and the thermo-

© 2009 The Royal Society of Edinburgh. doi:10.1017/S17556909016144

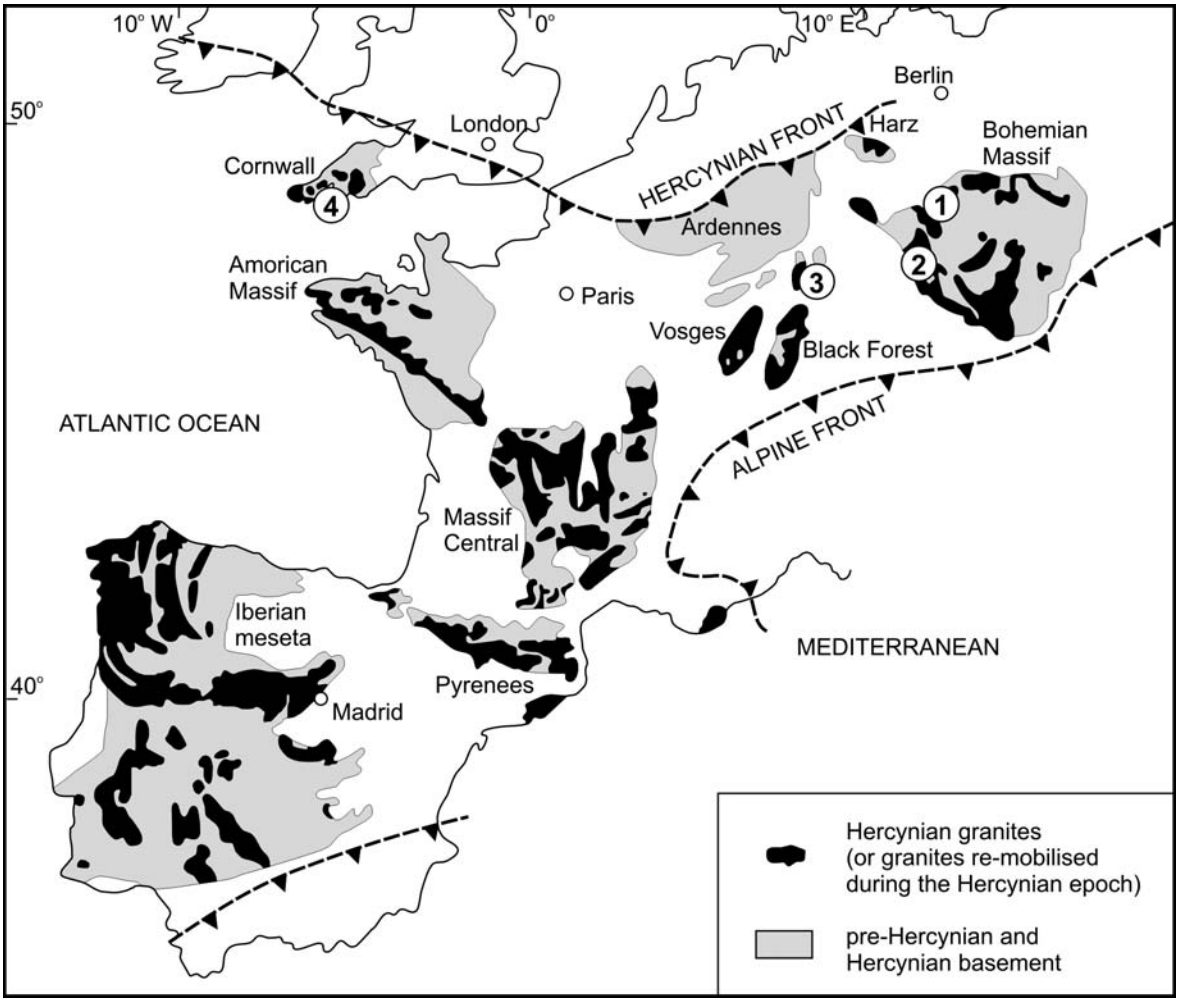

Figure 1 The Hercynian Europe according Rajpoot (1991) with sample locations: 1=Erzgebirge/Krušné Hory; 2=Oberpfalz; 3=Odenwald; 4=Cornwall.

dynamic conditions in the system (Müller *et al*. 2000, 2002a, 2003b; Jacamon & Larsen 2009; Wark *et al*. 2007). Several attempts have been made to combine CL and trace element analysis allowing the quantitative measurement of the Al, Ti, K, and Fe distribution of quartz in relation to CL textures (Watt *et al*. 1997; Müller *et al*. 2000, 2002a, 2003b; Ruffini *et al*. 2002; Wark *et al*. 2007; Wiebe *et al*. 2007). In other studies the total content of Al, Ti, Ge, and Li of igneous quartz has been used to discriminate between magmas of different origin, or in order to better understand the fractionation process (Lyakhovich 1972; Suttner & Leininger 1972; Schrön *et al*. 1988; Gurbanov *et al*. 1999; Larsen *et al*. 2000, 2004; Götze *et al*. 2004; Jacamon & Larsen 2009). Wark & Watson (2006) established the Ti-in-quartz geothermometer, which allows the calculation of the magma temperature at different stages of quartz growth. The incorporation of Al into the quartz lattice is probably controlled by the aluminium saturation index of the magma (Jacamon & Larsen 2009).

3. Igneous quartz, in particular phenocrystic quartz, contains melt inclusions. Melt inclusions comprise a unique record of melt and volatile contents prior to magma emplacement. They record the evolving melt composition and can be used for magma pressure estimates in relation to quartz growth zones. In their study on the Bishop Tuff (eastern California, USA) Peppard *et al*. (2001) related different melt inclusions to growth zones in quartz phenocrysts. Wark *et al*. (2007) continued their work and applied the Ti-in-quartz thermometer to explain variations of the volatile content in melt inclusions. They showed that quartz phenocryst rims containing CO_2-rich melt inclusions document an ~100°C increase of magma temperature shortly prior to eruption.

The aim of the present study is to reveal the magmatogenetic significance of CL properties and textures in relation to the trace element distribution of igneous quartz in late-Hercynian (Upper Carboniferous to Lower Permian) felsic plutonic and volcanic rocks. Furthermore, the paper compiles the results of a number of earlier studies on growth structures and the microchemistry of igneous quartz (Müller 2000; Müller *et al*. 2000, 2002a, 2003b, 2005, 2006a). Samples were collected from the Erzgebirge, Oberpfalz, and Odenwald (Germany), and from Cornwall (SW England; Fig. 1). As a reference, some intermediate to felsic plutonic rocks and associated volcanic rocks of different age and tectonic settings have been included. These rocks (1) are well studied in respect to age, chemical evolution and tectonic setting; (2) cover a wide range of chemical variability from dioritic/dacitic to highly evolved granitic/rhyolitic compositions; (3) include both plutonic and associated volcanic rocks; (4) show well-developed quartz textures (Müller *et al*. 2000, 2002a, 2003b, 2005), and (5) have melt inclusion data available (Thomas 1992, 1994; Müller *et al*. 2006b).

This study combines several visualising and micro-analytical methods, i.e. scanning electron microscope cathodoluminescence (SEM-CL) and optical microscope CL (OM-CL) combined with Fourier-Transform infrared (FTIR) spectroscopy, and electron probe microanalysis (EPMA). FTIR analysis

gives information about the atomic configuration and distribution of hydrogen and structurally bond water in quartz (e.g., Kats 1962; Bambauer *et al.* 1963; Aines & Rossmann 1984; Kronenberg *et al.* 1986; Rovetta *et al.* 1989; Bahadur 1994). The micro-distribution of the trace elements Al, Ti, K and Fe in quartz is determined by EPMA with a spatial resolution down to 5 μm. This combination of analytical techniques allows a crystal-chemical characterisation of igneous quartz and therewith a better understanding of large-scale magmatic processes.

1. Methods

1.1. Optical microscope cathodoluminescence (OM-CL)

CL spectra and colour images were obtained using a hot-cathode luminescence microscope HC3–LM (Neuser *et al.* 1995). The electron gun operates at a voltage of 14 kV under high vacuum (10^5-mbar) and a filament current of 0·18 mA resulting in a current density of ca. 10 mA/mm^2 at the sample surface. Photographic documentation was carried out with a NIKON Microflex UFX-II system equipped with a NIKON FX-35A reflex camera.

The spectral response of the luminescence was recorded with a triple-grating (100 lines/mm, 1200 lines/mm, and 1800 lines/mm) spectrograph TRIAX 320 equipped with a LN_2-cooled CCD-detector. The 100 lines/mm grating was used to acquire emission spectra in the range of 400–900 nm (3·1–1·4 eV); the 1200 lines/mm grating corresponds to a spectral range of 70 nm. The CL-emission was collected for an area of ~0·5 mm^2 using a 20 × /0·40 objective. The integration time for spectrum acquisition was 20 seconds for the 100 lines/mm grating and 30 seconds for the 1200 lines/mm grating. The spectra were corrected for the total detector response. The CL emission spectra are presented as the sum total of Gaussian curves for the different emission lines. These spectra have been deconvoluted using the procedure of Müller *et al.* (2002b). The time-dependent variations of the 1·96 and 2·79 eV emission-line intensities during electron radiation were recorded with a f/3·4 Grating Monochromator at a speed of 10 mm/min.

1.2. Scanning electron microscope cathodoluminescence (SEM-CL)

Two scanning electron microscopes equipped with different CL detectors, the Cambridge Instruments 250-MK3 with a S20-Extended photomultiplier and the JEOL JXA 8900 with a CLD40 R712 photomultiplier, were used for the study of microtextures in quartz. The detectable wavelength for both photomultipliers ranges from 380 to 850 nm (3·26–1·46 eV). SEM-CL allows a better spatial resolution down to 1 μm^2 and the capability of combining CL with back scattered electron (BSE) imaging and electron microprobe analysis (EPMA). The possibility of increasing the power density over small sample areas is useful for samples with low CL intensity. A disadvantage is the monochromatic (grey scale) image. Weakly luminescing quartz corresponds commonly to red to reddish brown CL and bright quartz to blue to violet colours, with the present instrument. Images were collected from the JEOL system using a beam voltage of 30 keV, a filament current of 200 nA, slow beam scan rates of 20 seconds at processing resolution of 1024 × 860 pixels and 256 grey levels. The voltage and sample current for the Cambridge Instruments 250-MK3 was 20 keV and 5–15 nA, respectively. The documentation of the CL images at the 250-MK3 were carried out with a photo camera with Agfapan APX 25 films and by using slow beam scan rates of 250 seconds. The contrast of the images was improved by using the software PhotoShop for Windows.

1.3. Electron probe microanalysis (EPMA)

Trace element abundances of Al, K, Ti, and Fe in quartz were performed with a JEOL 8900 RL electron microprobe with five wavelength dispersive detectors at the Geowissenschaftliches Zentrum Göttingen. Synthetic Al_2O_3 (52·9 wt% Al), orthoclase from Lucerne, Switzerland (12·2 wt.% K), synthetic TiO_2 (59·9 wt.% Ti), and haematite from Rio Marina, Elba (69·9 wt.% Fe) were used for standards. A beam current of 80 nA, an accelerating voltage of 20 kV, diameter of 5 μm, and counting times of 15 seconds for Si, and of 300 seconds for Al, Ti, K, and Fe were used. Raw analyses were converted into concentrations using the phi–rho–Z matrix correction method of Armstrong (1995). Analytical errors were calculated from the counting statistics of peak and background signals, following the Gauss law of error propagation. At low element concentrations the background forms the main part of the total signal. On the other hand, the background signal is nearly constant for a given quartz matrix and the absolute error based on counting statistic is thus nearly constant. Limits of detection by single measurement average (3σ; $n=36$) are 13 ppm for Al, 13 for Ti, 10 for K, and 15 for Fe.

1.4. FTIR spectroscopy

Infrared analysis was performed at the GeoForschungsZentrum Potsdam using a Bruker IFS 66v FTIR-spectrometer coupled with an IR-microscope (Hyperion 1000). The measurements were performed *in situ* at −190 °C using a Linkam FTIR600 heating/freezing stage. The spectra were acquired from 4500 to 2500 cm^{-1} with a resolution of 2 cm^{-1}. Analyses were carried out on doubly-polished wafers of quartz crystals (diameter about 3 mm) with a thickness of 50–80 μm. The beam diameter on the sample ranged from 30 μm to 40 μm and allows the detection of variations within individual quartz crystals. Four to eight points along a line in one crystal could be measured. Thin quartz wafers were used to minimise the risk of encountering fluid inclusions, which are common in quartz from subvolcanic and plutonic rocks. Prior to the analysis the wafers were cleaned with acetone and dried for 10 h at 110 °C. The spectra were corrected for the wafer thickness.

2. Cathodoluminescence of igneous quartz

The cathodoluminescence of igneous quartz commonly shows shades of blue, violet, red and red-brown. These colours mainly result from emissions in the red (1·7–2·2 eV) and blue (2·4–3·1 eV; Fig. 2). Contrary to most other luminescing minerals, the defect structure inventory of quartz, and therewith the cathodoluminescence, is influenced by the electron beam. The ratio of the red and blue emission ranges changes with the irradiation time, whereby the blue emission normally decreases and the red emission increases (Fig. 2). As a consequence, the initial CL signal is difficult to detect. The radiation damage of the upper ca. 5 μm of the quartz sample surface means that the luminescence is non-reproducible.

High-resolution spectral analysis shows that both red and blue emissions are composed of several emission lines. Three emission bands are distinguished in the red emission range (1·73 eV, 1·84 eV, and 1·96 eV), and five bands in the blue emission range (2·47 eV, 2·58 eV, 2·68 eV, 2·79 eV and 2·96 eV). A broad yellow band has been identified at 2·15 eV (Table 1; Fig. 2). The individual CL emission bands can be localised and quantified from best-fit Gaussian curves by working out about ca. 100 spectra (Müller 2000). The CL band positions are reported also in the literature (e.g., Remond *et al.* 1992; Gorton *et al.* 1996; Stevens Kalceff *et al.* 2000 and references therein; Table 1).

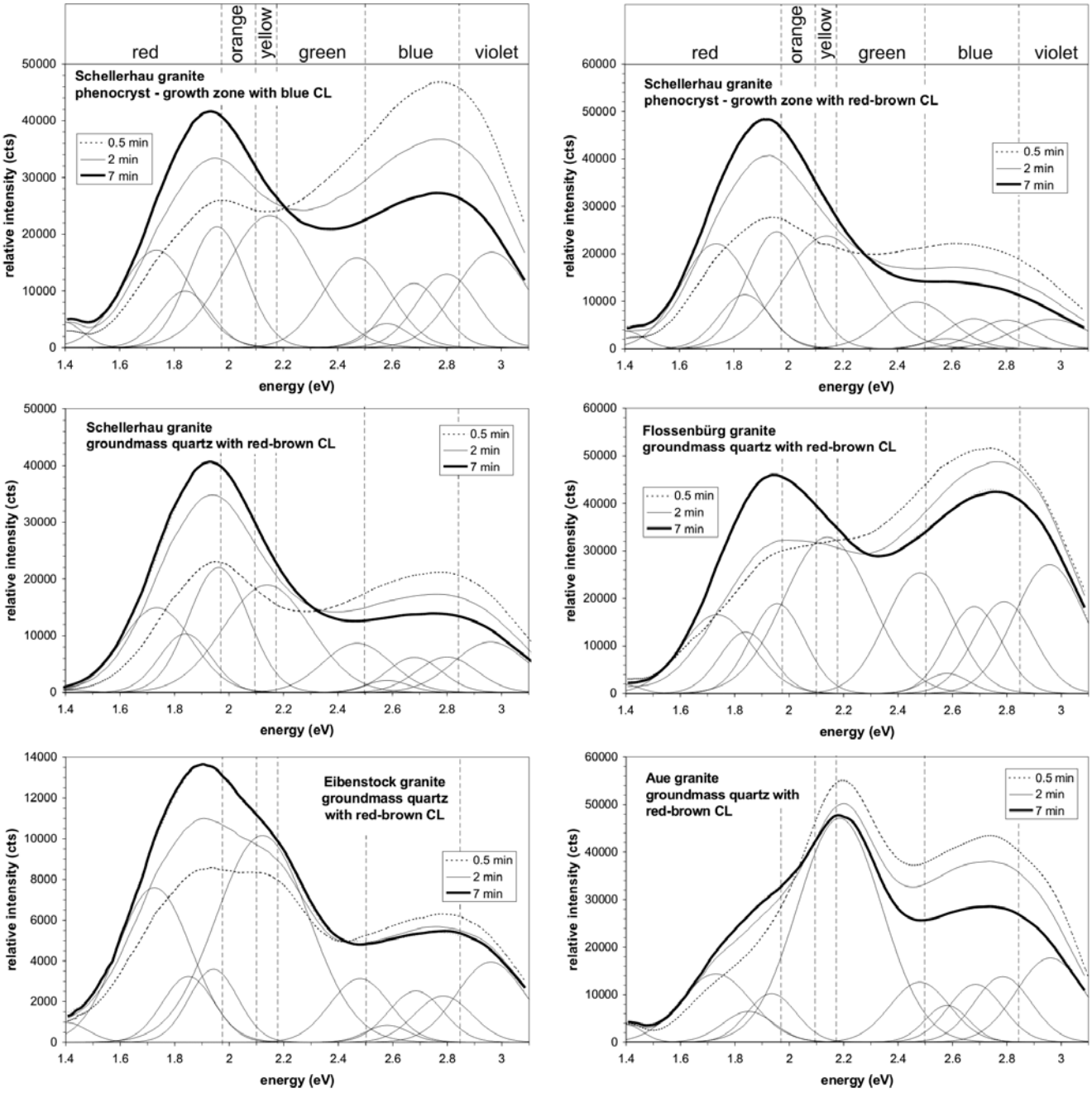

Figure 2 CL spectra of igneous quartz recorded with the 100 lines/mm grating after 30 seconds, two and seven minutes of electron bombardment. The seven-minute-spectra were resolved by best fitting with Gaussian curves.

The blue 2·68 eV and 2·58 eV bands have a constant band area ratio of 1:0·34 ± 0·08. Similar observations were made for the red 1·96 eV and 1·84 eV bands, which show a ratio of 1:0·51 ± 0·17. Predominant emission bands of zoned quartz phenocrysts are the 1·96 eV, 2·58 eV, 2·68 eV, 2·79 eV and 2·96 eV band. Exceptions are the phenocrysts from the Eibenstock and Aue granite from the Western Erzgebirge, which show a characteristic 2·15 eV emission. Some growth zones in the phenocrysts show a marked 1·73 eV emission. The growth zones within quartz phenocrysts correspond to variable intensity of the blue emission, whereas the red emissions are approximately constant.

The blue emission (2·6–3·1 eV) shows high intensity at initial electron bombardment, but a part of the blue emission lines mostly centred at ∼2·8 eV (2·58 eV, 2·68 eV, 2·79 eV and 2·96 eV), drop by 1/2 to 1/3 after a few seconds. However, the 2·79 eV emission decreases much more than the 2·58 eV, 2·68 eV and 2·96 eV emissions (Müller 2000). After 30 seconds to 100 seconds of electron bombardment the CL is stabilised, pointing at a constant number of luminescence centres at the experimental conditions. The applied experimental conditions resulted in a beam current density of ∼10 mA/mm^2 at the sample surface and temperature increase of ca. 110 °C during 100 seconds of initial bombardment. The red emissions (1·75–2·2 eV) show lowest intensity at initial electron bombardment followed by a steep parabolic increase during the first minute of electron radiation followed by a slight increase until a stable luminescence is reached.

Most of the energy of the electron beam is transformed into heat in the sample (e.g., Remond *et al.* 1992). By using the present equipment, the temperature of the sample may increase by up to 140 °C after 10 minutes of electron beam irradiation (Müller 2000). Therefore, thermoluminescence bands may impose CL spectra. Characteristic thermoluminescence bands are at 2·95–2·85 eV, 2·21–2·14 eV and 2·00–1·98 eV (e.g., Jani *et al.* 1983; Rink *et al.* 1993; Yang *et al.* 1994). The intensity

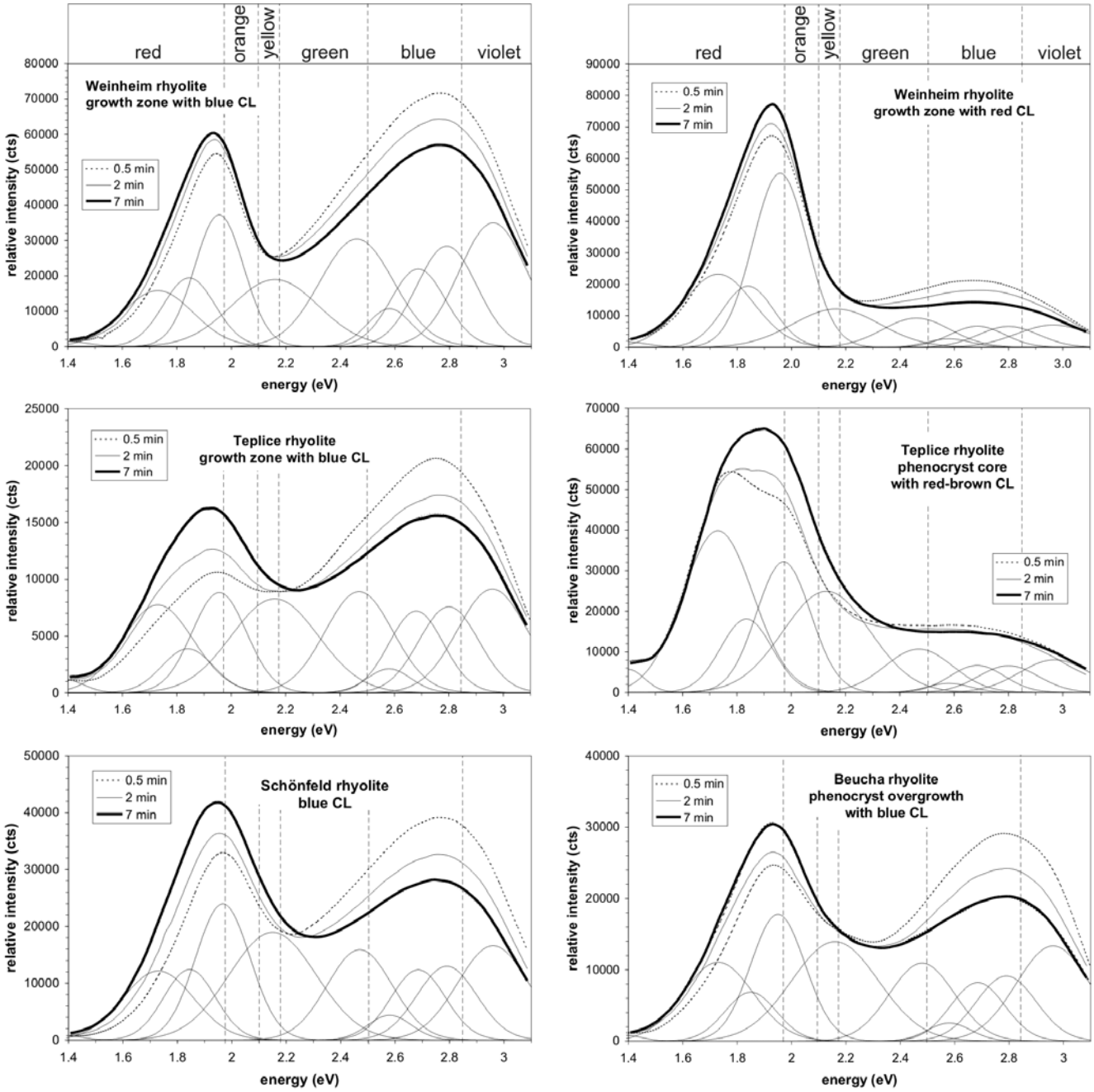

Figure 2 (*Continued*).

maxima of the 2·21–2·14 eV and 2·00–1·98 eV bands lie in the temperature range of the CL measurements. However, the marked different CL for different quartz types in the same temperature range demonstrates that the effect of temperature is relatively small (Müller 2000).

The kinetic law $c=c_0\ e(-kt)$ (c=concentration of the component at time t, c_0=concentration of the component at time $t=0$, and k=velocity [equilibrium] constant) has been applied in order to quantify the changes of CL during electron beam irradiation (Ramseyer *et al.* 1988; Picouet 1999); the increase of the red CL can be described by the reverse equation of the kinetic law. In this way, the CL intensity can be approximately quantified as a function of time. According to Ramseyer *et al.* (1988) and Picouet (1999) the fastly decaying component and the slowly decaying components in the blue CL-range are calculated as the sum of two kinetic law equations:

$$I_b=I_{bs}+I_{b1}\times e(-t/k_{b1})+I_{b2}\times e(-t/k_{b2}) \qquad (1)$$

where I_b=intensity of blue CL at the radiation time t; I_{bs}=intensity of stable blue CL; I_{b1}=intensity of the slow decreasing CL component at $t=0$; k_{b1}=velocity constant of the slow decreasing CL component; I_{b2}=intensity of the fast decreasing CL component at $t=0$; k_{b2}=velocity constant of the fast decreasing CL component; t=radiation time.

The increase of red emission can be described by the equation:

$$I_r=I_{rs}-I_{r1}\times e(-t/k_{r1})-I_{r2}\times e(-t/k_{r2}) \qquad (2)$$

where I_r=intensity of red CL at the radiation time t; I_{rs}=intensity of red CL for $t\rightarrow\infty$; I_{r1}=intensity of the slow increasing CL component for $t\rightarrow\infty$; k_{r1}=velocity constant of the slow increasing CL component; I_{r2}=intensity of the fast increasing CL component for $t\rightarrow\infty$; k_{r2}=velocity constant of the fast increasing CL component; t=radiation time.

The velocity constants k_{r1}, k_{r2}, k_{b1}, and k_{b2} depend on the measurement conditions and are similar for the present

Table 1 Detected CL emission bands of igneous quartz (1·4–3·1 eV) and their possible association with trace elements and defect centres according to literature.

Band position (eV)	Half width (eV)	Proposed origin	Reference with band position
1·73 ± 0·02	0·3 ± 0·02	substitutional Fe^{3+}	Pott & McNicol (1971) – 1·78 eV Kempe *et al.* (1999) – 1·75 eV
1·84 ± 0·01	0·22 ± 0·01	nonbridging oxygen hole centre	Sigel & Marrone (1981) – 1·85 eV
1·96 ± 0·02	0·22 ± 0·02	oxygen vacancy nonbridging oxygen hole centre with OH-groups as precursors	Luff & Townsend (1990) – 1·91 eV Stevens Kalceff & Phillips (1995) – 1·95 eV
2·15 ± 0·02	0·38 ± 0·01	E′ centre $[SiO_3]^{3-}$ associated with substitutional Ge	Götze *et al.* (1999) – 2·1 eV Luff & Townsend (1990) – 2·18 eV
2·47 ± 0·02	0·30 ± 0·03	extrinsic defect $[GeO_4/Li^+]^0$	Stevens Kalceff & Phillips (1995) – 2·46 eV Götze *et al.* (2005) – 2·45 eV
2·58 ± 0·01	0·18 ± 0·005	intrinsic defect	Gritsenko & Lisitsyn (1985) – 2·58 eV
2·68 ± 0·01	0·23 ± 0·01	self trapped exciton combined with E′ centre $[SiO_3]^{3-}$	Stevens Kalceff & Phillips (1995) – 2·68 eV
2·79 ± 0·01	0·26 ± 0·01	self trapped exciton	Itoh *et al.* (1990) – 2·8 eV
2·96 ± 0·015	0·30 ± 0·02	intrinsic defect associated with substitutional Ti	Stevens Kalceff & Phillips (1995) – 2·93 eV Müller *et al.* (2002b) – 2·96 eV

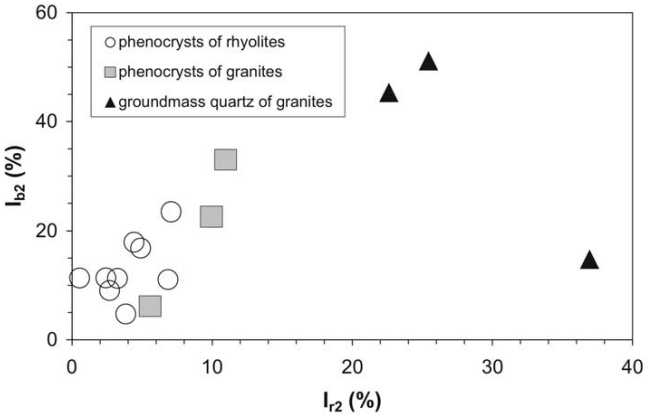

Figure 3 Plot of the fitted parameters I_{r2} and I_{b2} representing fast changing CL components of the red CL (1·96 eV) and blue CL (2·79 eV), respectively. Granitic groundmass quartz exhibit the most unstable CL characterised by a strong increase of the red CL.

samples. Müller (2000) showed that for different quartz types the decay of the luminescence centres causing blue CL is about two times faster than that of those causing red CL. The emission intensities (I) correspond to the concentration of luminescence centres in the interaction volume of the electron beam. The parameters I_{rs}, I_{r1}, I_{r2}, I_{bs}, I_{b1}, and I_{b2} are the intensity portions of all emissions, whereby I_{r1}, I_{r2}, I_{b1}, and I_{b2} are intensity portions of the changeable CL. In granites, zoned quartz phenocrysts have low I_{r2} and I_{b2}, which is indicative of more stable defect structures compared to the groundmass quartz (Fig. 3). The latter quartz exhibits widely varying intensities reflecting a high concentration of unstable defect structures. The high I_{r1} and I_{r2}, which is characteristic for granitic groundmass quartz, demonstrates the predominance of unstable red CL.

3. Intra-granular textures of igneous quartz

3.1. Primary growth textures

The term 'primary growth textures' is used here for intra-granular growth patterns which develop during crystal growth in the magma; secondary structures are the result of alteration.

Primary growth textures may develop in (1) early-magmatic quartz phenocrysts, (2) late snowball quartz in highly evolved albite granites (e.g., Müller & Seltmann 1999), and (3) comb quartz in layered granitic rocks (e.g, Müller *et al.* 2002a).

3.1.1. Early-magmatic quartz phenocrysts. Quartz phenocrysts have been described worldwide from rhyolites, rhyodacites and some dacites with ≥63 wt.% SiO_2. In dacites or other more mafic volcanic rocks, quartz phenocrysts are commonly rounded and sometimes show coronas of hornblende, pyroxene and/or An-rich plagioclase (oscelli texture), indicating disequilibrium with the melt (e.g., Mashima 2004). They must have been inherited from a more felsic magma prior to emplacement or extrusion.

Phenocrysts in volcanic rocks can be easily recognised due to the grain size contrast between them and the micro- to fine-crystalline groundmass. However, groundmass minerals in plutonic rocks are coarser grained and may overgrow phenocrysts. The early magmatic crystals may be not phenocrysts in the strict sense because they may not have shared common histories and crystallised from a melt in which they are now hosted, but rather represent a melt laced with a crystal cargo that has been inherited from melts that existed at different places and times in the magma system (Davidson *et al.* 2007). Neither are they strictly xenocrysts, as they are grown and recycled from closely related progenitor magmas rather than accidentally incorporated from unrelated wallrocks. W. E. Hildreth (pers. comm. in Davidson *et al.* 2007) suggested the term 'antecryst' to denote phases that originate in the magma system, but are not true phenocrysts (*cf.* Charlier *et al.* 2005). Davidson *et al.* (2007) proposed that magmatic rocks can be represented by mixtures of melts, recycled antecrysts, and true phenocrysts. However, in this present study, the dominant early magmatic crystal populations of grantic rock are discussed and, therefore, they are considered as true phenocrysts.

In plutonic rocks phenocrysts are often difficult to identify, but can be identified by their contrasting CL. The majority of the late-Hercynian granites with ≥65 wt.% SiO_2 contain quartz phenocrysts (Müller *et al.* 2000, 2002a, 2003b, 2005, 2006a; Table 2). In some granites the phenocrysts comprise a substantial part of the rock up to 40 vol.% (e.g., Müller *et al.* 2000), whereas in other granites phenocrysts are rare or even absent. A number of late-Hercynian granites with ≥63 wt.% SiO_2 contain exclusively anhedral groundmass quartz without zoning, e.g. the Flossenbürg and Leuchtenberg granite from the Oberpfalz. Groundmass quartz may show euhedral crystal cores with brighter CL, e.g. Rozvadov granite, Oberpfalz. Migmatitic granites, chemically highly evolved albite granites

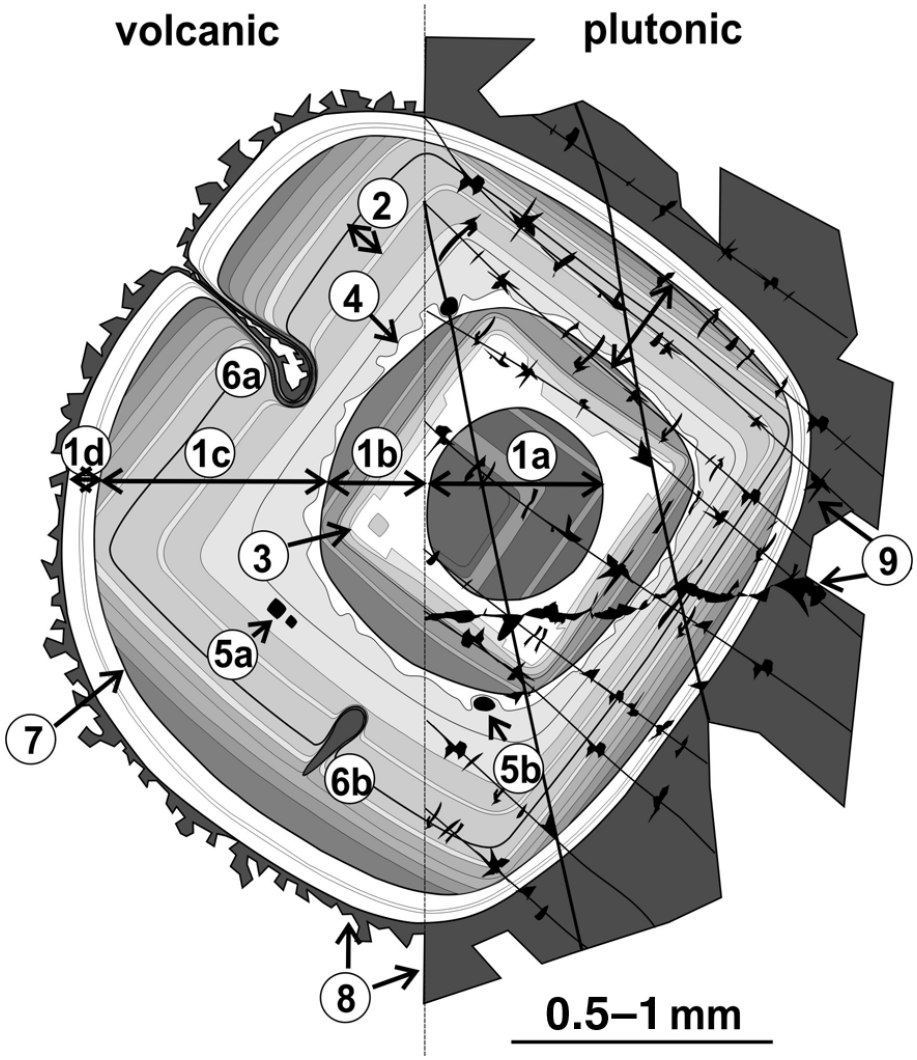

Figure 4 Schematic illustration of growth textures observed in early-magmatic quartz phenocrysts of late-Hercynian felsic igneous rocks. 1a–d=step zones; 2=oscillatory zone; 3=skeletal growth; 4=wavy surface; 5a=melt inclusion with negative crystal shape; 5b=ovoid melt inclusion; 6a=lobate growth embayment; 6b=closed growth embayment; 7=resorption surface; 8=roundmass quartz; 9=secondary structures.

and fluid-enriched aplites and miarolitic granites are generally free of early-magmatic quartz phenocrysts.

The development of zoning in phenocrysts requires that the quartz grew in an evolving magma reservoir. Microscopic growth zone boundaries represent relic crystal-melt interfaces, which develop by fluctuations of growth and diffusion rates. The zoning pattern of the phenocrysts is normally more complex in granites and rhyolites with high SiO_2 content (>70 wt.%). This can be explained by the early SiO_2 saturation with the consequence of a longer period of quartz precipitation prior to final magma emplacement or extrusion. Phenocrysts in granites and rhyolites show similar growth patterns. In some cases, quartz phenocryst populations in granites are similar to populations in the associated rhyolites (e.g., Schellerhau granite and Teplice rhyolite; Müller *et al.* 2005). However, the zoning of granitic phenocrysts is normally less well developed. The zoning may have been quenched or overprinted during slow magma cooling and be destroyed by the interaction with deuteric fluids.

Growth patterns in quartz of granites and rhyolites have been described in Müller *et al.* (2000, 2003b, 2005). The present authors distinguish fine-scale (2–20 μm) oscillatory zoning, large-scale step zoning (compositional zoning), skeletal growth, wavy and resorption surfaces and growth embayments (Fig. 4).

The SEM-CL images of Figures 5 and 6 display characteristic growth textures in igneous quartz from late-Hercynian granites and rhyolites from Central Europe. The images represent a selection of about 1400 pictures taken from more than 260 thin sections. The examples in Figures 5 and 6 represent common features in these rocks. Each igneous system has its own distinctive fingerprint as recorded in the zoning pattern (Table 2).

Textures indicate that epitaxy must be important for quartz nucleation. Quartz nucleates on tiny grains of feldspar, mica, accessory minerals, or on immiscible melt droplets or bubbles occasionally preserved as melt inclusions (Fig. 5b, c). Sometimes two or more quartz crystals grow around one particle. Particularly in granites, these crystals may coalesce to become one crystal or they grow separately forming clusters of two to five crystals (Fig. 5b). Phenocrysts nucleate commonly as dihexagonal β-quartz. Rhombohedral α-quartz has been described by Flick (1987) from rhyolites from the Odenwald. Phenocrysts from the Odenwald show skeletal overgrowths in their cores (Fig. 5c). Skeletal growth reflects a kinematically-driven, non-equilibrium growth phase (e.g., Kirkpatrick 1981; Fenn 1986; Fowler 1990) which is in accordance with the undercooling experiments of Fenn (1977) and Swanson (1977), who showed that growth is controlled by diffusion during rapid crystallisation.

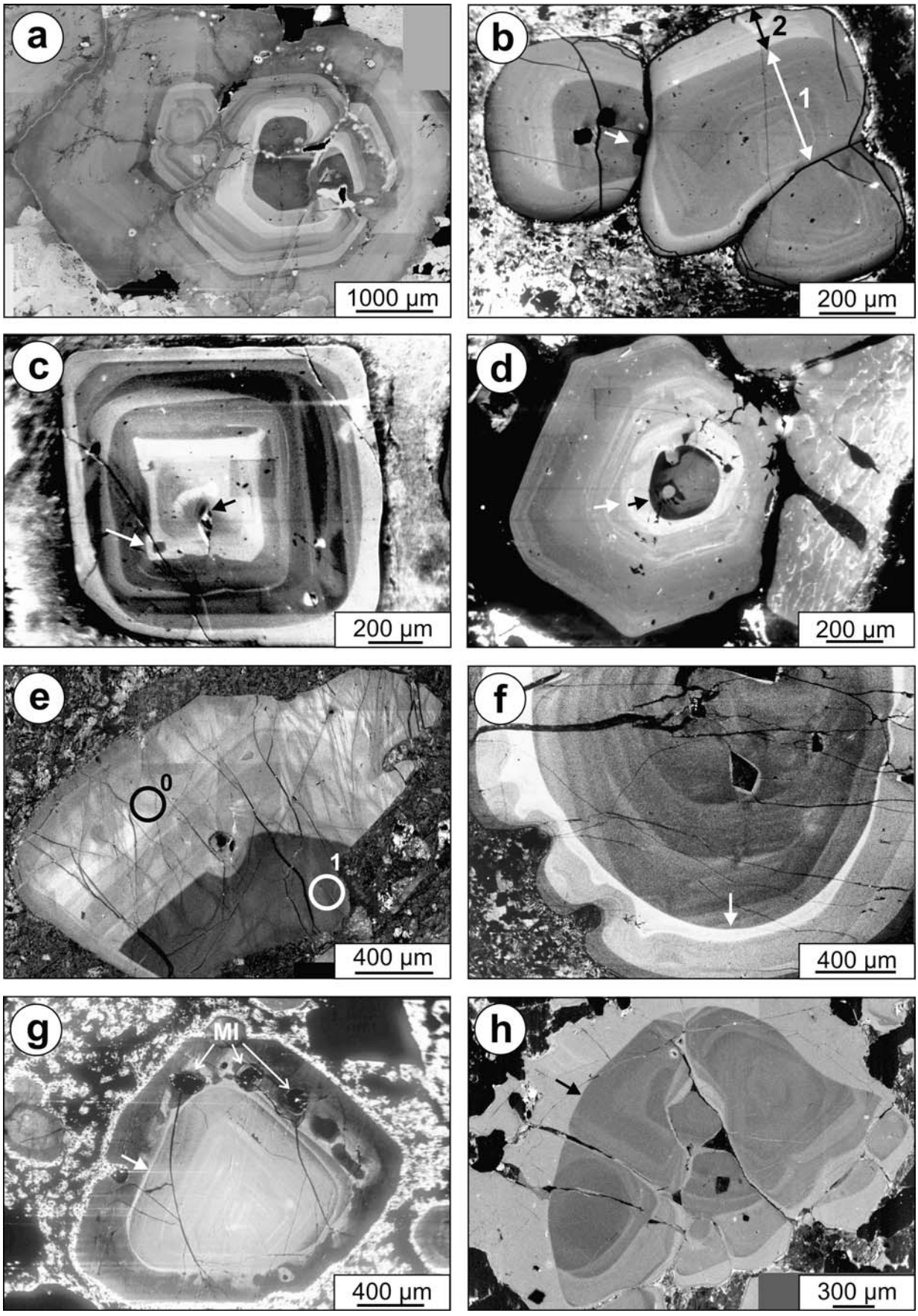
a
1000 µm
b
2
1
200 µm
c
200 µm
d
200 µm
e
0
1
400 µm
f
400 µm
g
MI
400 µm
h
300 µm

Table 2 Characteristic features of quartz phenocrysts in late-Hercynian igneous rocks.

Late-Hercynian igneous province	Investigated igneous rocks	Rock type	SiO_2 wt.%	Characteristic growth structures of phenocrysts	Schemes of growth structures of dominant phenocryst populations (oscillatory zoning is not shown)
Eastern Erzgebirge	Eastern Erzgebirge volcano-plutonic complex	granodiorite, monzogranite, rhyodacite, rhyolite	69–75	phenocryst with complex, contrast-rich zoning, low CL rounded crystal cores, Ti-rich margin (reverse zoning), zoning with β-quartz habit (Figs 5a, d, 6e, g)	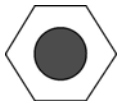
Western Erzgebirge	Eibenstock Nejdek pluton	monzogranite	68–78	phenocrysts with complex, contrast- poor zoning, zoning with β-quartz habit	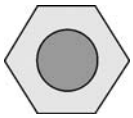
Oberpfalz	Rozvadov, Leuchtenberg, Flossenbürg, and Falkenberg granites	tonalite, diorite, redwitzite, granodiorite, monzogranite	52–76	no phenocryst or phenocrysts with simple, contrast-poor zoning, zoning with β-quartz habit	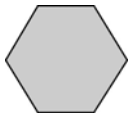
Odenwald	Weinheim, Dossenheim	rhyolite	71–74	phenocryst with complex, contrast- rich zoning, skeletal growth, zoning with α-quartz habit (Fig. 5c)	
Cornwall	Land's End granites	granite	66–77	phenocrysts with contrast-poor zoning, zoning with β-quartz habit	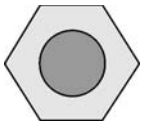

Correlative zoning patterns of quartz phenocrysts from the same magma batch indicate that the crystals of one population nucleated simultaneously and continued growing together (Peppard *et al*. 2001; Müller *et al*. 2000, 2005). Some rocks contain two or more phenocryst populations, whereby one population dominates. Each population represents one nucleation event. In this way the temporal crystallisation history of a magma batch can be reconstructed (Müller *et al*. 2000). Due to multiple magma recharge, quartz populations with a different history can be mingled (Müller *et al*. 2005). This is known from plagioclase in mafic and intermediate rocks (e.g., Davidson *et al*. 2001). The first growth stage of quartz phenocrysts may be interrupted by resorption, resulting in rounding of the crystal nuclei. The resorption surface truncates pre-existing growth zones and results in the rounding of crystals. This process is recorded by rounded crystal cores with weak red-brown CL as commonly found for the Eastern Erzgebirge granites and rhyolites (Fig. 5a, d).

Major resorption surfaces are typically overgrown by bright blue luminescing quartz (Müller *et al*. 2003b). Sometimes the blue luminescing overgrowth is very thin (<10 μm) and may show a dendritic or wavy structure (Fig. 6a). These overgrowths may be enriched in ovoid melt inclusions (Fig. 5g).

Fine-scale (1–5 μm) oscillatory growth zones with low amplitude in CL are sometimes separated by zones recording resorption or skeletal overgrowth, accompanied by a major change of the CL properties. These events with high-amplitude CL superimpose on the oscillatory zoning. Growth stages of low amplitude CL bordered by resorption or skeletal growth are considered step zones (Fig. 5b; Allègre *et al*. 1981). Analogous distinction between low-amplitude (An-content) fine-scale zoning and superimposed high-amplitude large-scale zoning has been made for plagioclase phenocrysts (Pearce & Kolisnik 1990). The quartz phenocryst of Figure 5b shows two step zones. The definition of step zones becomes more complicated for phenocrysts with complex growth patterns. For example, six step zones can be distinguished in the phenocryst shown in Figure 5c.

3.1.2. Late-magmatic snowball and comb quartz. Highly evolved topaz-bearing albite granite contains typically

Figure 5 SEM-CL images of early-magmatic quartz phenocryst from late-Hercynian felsic igneous rocks illustrating the variability of primary growth textures: (a) Zoned quartz phenocryst embedded in groundmass quartz. Schellerhau granite SG2; (b) Cluster of three zoned phenocrysts of the Gattersburg rhyolite (NW Saxony, Germany). The left crystal germinated at melt droplet which is now preserved as melt inclusion (white arrow). The growth pattern is characterised by two step zones with subordinate oscillatory zoning. The relatively homogenous pattern indicates almost undisturbed crystal growth. The phenocrysts show several thin healed contraction cracks (black) caused by shock cooling during eruption; (c) Rhyolitic phenocryst with α-quartz habit with complex growth pattern (Dossenheim, Odenwald). The bright crystal core, which germinates at a melt/volatile droplet (black arrow), shows skeletal growth (white arrow); (d) Rhyolitic phenocryst (Hengstberg, NW Saxony) with dull luminescing, resorbed crystal core (black arrow) with bright overgrowth (white arrow). The euhedral phenocryst is overgrown by almost non-luminescing groundmass quartz (black); (e) Fracture of zoned phenocryst with weak luminescing core (Teplice rhyolite, Erzgebirge). Circles correspond to FTIR absorption sampling spots; (f) Rhyolitic phenocryst (Fichtelgebirge) with a major resorption surface (white arrow). Subsequent wavy growth show bright luminescence; (g) Rhyolitic quartz phenocryst (drill core KB1 Wittichen 263–264 m, Black Forest). The resorption event (white arrow) is followed by irregular growth which result in the entrapment of numerous large melt inclusions (MI); (h) Phenocryst of the Beucha granite porphyry (NW Saxony). The resorbed cluster of zoned phenocrysts (black arrow) is embedded in bright luminescing anhedral groundmass quartz.

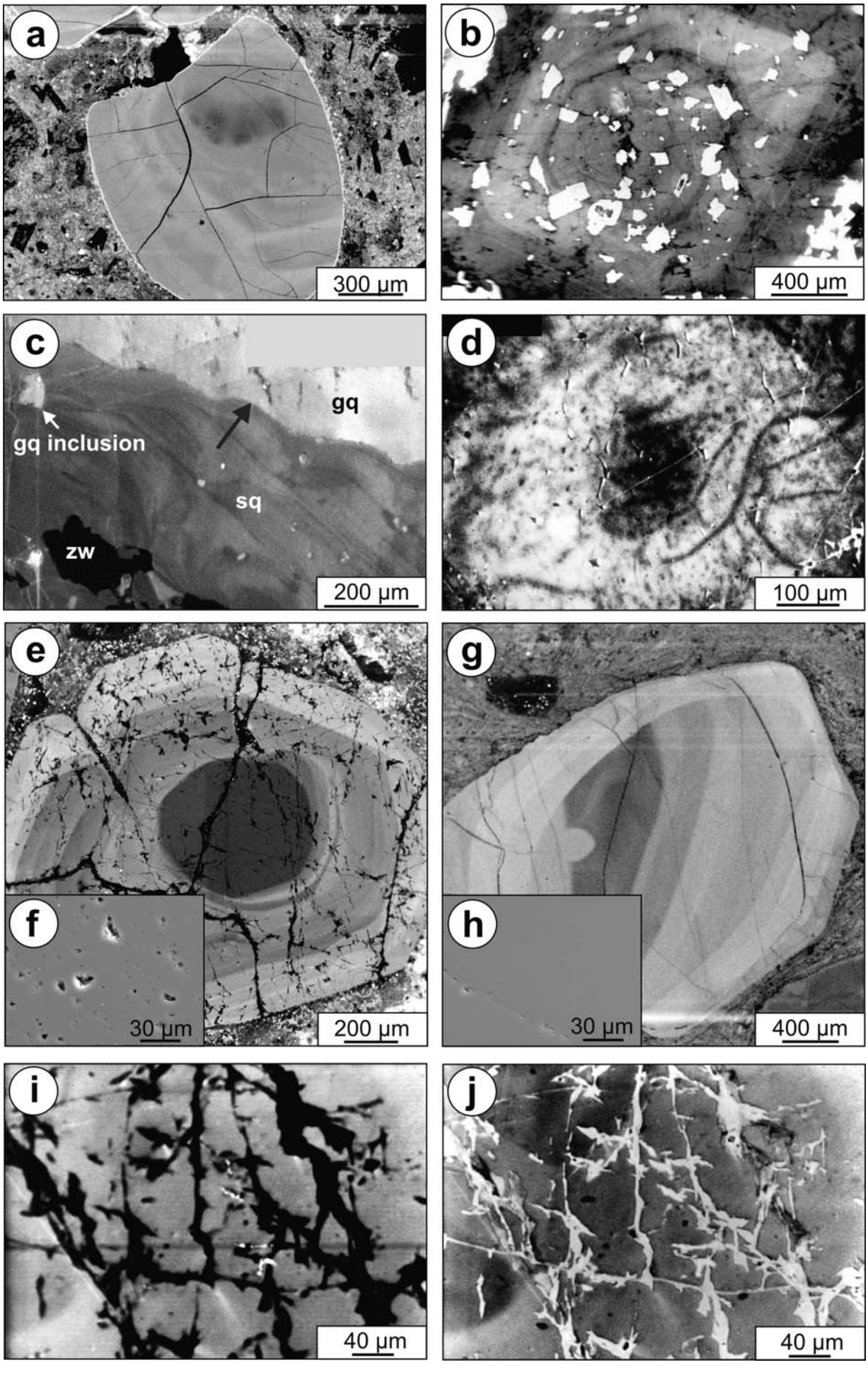
a
300 µm
b
400 µm
c
gq
gq inclusion
sq
zw
200 µm
d
100 µm
e
f
30 µm
200 µm
g
h
30 µm
400 µm
i
40 µm
j
40 µm

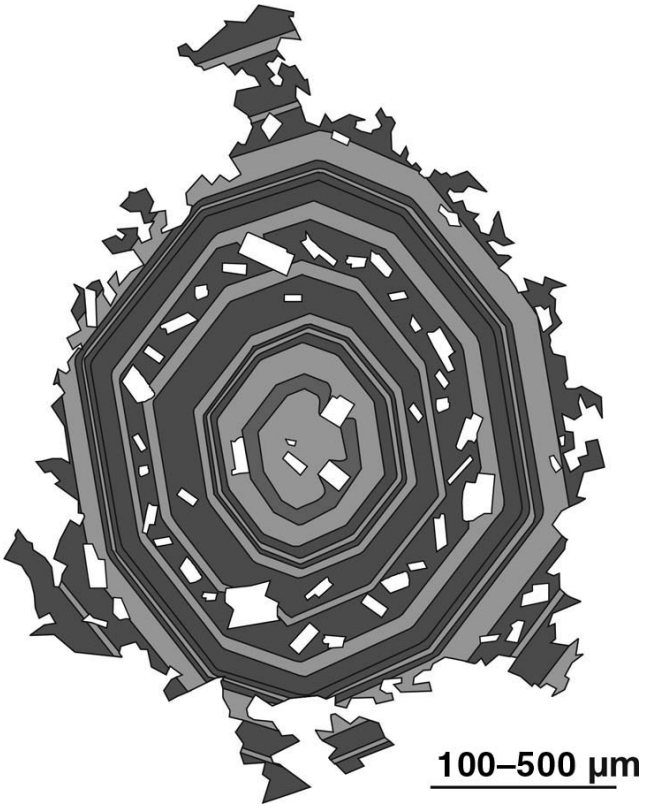

Figure 7 Growth structures of late-magmatic snowball quartz with zonal enclosed albite laths (white). Modified from Müller *et al*. 2002a.

so-called snowball quartz (Beus *et al*. 1962; Kovalenko 1977; Sonyushkin *et al*. 1991; Poutiainen & Scherbakova 1998; Müller & Seltmann 1999; Müller *et al*. 2002a; Fig. 6b, c). These rocks occur in the apical part of sub-volcanic granite complexes and are commonly associated with rare-metal mineralisation. Snowball quartz has a dull red-brown to bright red/orange CL, in contrast to early-magmatic quartz phenocrysts, which have predominantly bluish to violet CL. The crystals show gradual transitions into the ramified dendritic crystal margin and into the matrix quartz without changes of the CL properties. Older quartz generations, which may be present in the albite granites are cannibalised by snowball quartz as shown in Figure 6c. Inclusions of groundmass minerals, such as corroded K-feldspar, mica, zircon, apatite and particularly albite are enriched in the growth zones. Fluid and melt inclusions are abundant throughout the snowball quartz. Lath-shaped albite crystals wrap around the snowball quartz, indicating that the quartz pushed aside the albite laths during growth in a dense crystal mush. The snowball quartz shows oscillatory growth zoning with low CL contrasts. The zone boundaries are characterised by planar growth zones with α-quartz crystal habit. Resorption surfaces, which are characteristic for early-magmatic phenocrysts, have not been observed in the snowball quartz.

Comb quartz occurring typically in granitic line rock nucleates at intra-granite contacts (Breiter *et al*. 2005). It has similar CL properties and structural features as the snowball quartz, with the difference that it does not form double-ended crystals (fig. 3c in Müller *et al*. 2002a).

3.2. Secondary CL structures

Secondary structures in the CL observation mode are principally formed by five processes: (1) micro-cataclasis followed by healing; (2) stress-induced and fluid-driven quartz dissolution and precipitation; (3) stress-induced lattice reorganisation (purification); (4) impurity element diffusion; and (5) α-radiation.

In a cooling magma late- to post-magmatic fluids may result in small-scale quartz dissolution–precipitation along grain boundaries and micro-fractures. Dense healed fractures connecting low-luminescing domains around fluid inclusions are widespread in granitic rocks (Sprunt & Nur 1979; Behr & Frentzel-Beyme 1989; Valley & Graham 1996; D'Lemos *et al*. 1997; Van den Kerkhof & Hein 2001, Van den Kerkhof *et al*. 2001, 2004; Müller *et al*. 2000, 2002b; Rusk & Reed 2002; Fig. 6e, i, j). Micro-fracturing can be attributed to internal stresses at a grain scale, resulting from the thermal contraction of quartz relative to feldspar in the cooling granite (Vollbrecht *et al*. 1991, 1994). The α/β-quartz transformation which causes an anisotropic contraction of 0·86 vol.% vertical to the c-axis and 1·3 vol.% parallel to the c-axis (e.g., Blankenburg *et al*. 1994), imposes additional stress. However, the α/β-quartz transformation is not the dominant process causing the fracture network because these structures are trans-granular, meaning they are independent from the crystallographic orientation of the quartz crystals, and they are absent in phenocrysts from extrusive rocks (Fig. 6e, g).

Müller (2000), Müller *et al*. (2002) and Van den Kerkhof *et al*. (2004) demonstrated the systematic reduction of Al, Ti and K in secondary quartz compared to the host quartz. However, the CL intensity of secondary quartz may increase after several minutes of electron beam exposure using high beam power densities $>10_4$ W/cm^2 (Fig. 6i, j) resulting in contrast reversal. Partially healed radial and concentric contraction cracks caused by shock cooling are common in quartz phenocrysts from volcanic rocks (Fig. 6a).

Groundmass quartz in granites, which is free of primary growth zoning, commonly exhibits non-luminescing 1–5 µm small micropores, which become visible as dark spots in SEM-CL after several minutes of electron bombardment (Van den Kerkhof & Grantham 1999, Müller 2000, Van den Kerkhof & Hein 2001). Figure 6d shows such spots in quartz from the Niederbobritzsch granite, Eastern Erzgebirge.

Igneous quartz sometimes shows halos of pinkish/yellowish white luminescing quartz around zircon inclusions. These textures are caused by α-radiation damage, i.e. metamictisation

Figure 6 SEM-CL images of quartz in igneous rocks illustrating the variability of secondary structures in early-magmatic quartz phenocryst and textures of late-magmatic groundmass and snowball quartz: (a) Rounded (resorbed) quartz phenocryst of the Schönfeld rhyodacite (Eastern Erzgebirge). The internal growth zoning is blurred. The crystal is overgrown by a very thin layer of bright luminescing (white) dendritic groundmass quartz; (b) Snowball quartz of the Schellerhau granite SG3, Erzgebirge, with numerous albite inclusions; (c) Snowball quartz (sq) cannibalising (white arrow) groundmass quartz (gq) in the Podlesí Dyke granite, Erzgebirge. zw=zinnwaldite; (d)Weak luminescent spot-like structures in quartz (Niederbobritzsch granite, Erzgebirge); (e) Zoned quartz phenocryst in a subvolcanic rock (Teplice rhyolite TR3c, Erzgebirge). In contrast to (g), the quartz contains a dense network of secondary structures (black); (f) BSE image of the surface of (e) with high porosity (up to 2 vol.%); (g) Zoned quartz phenocryst from an effusive rock (Teplice rhyolite TR2b, Erzgebirge). (h) Back-scattered electron (BSE) image of the quartz surface of (g) showing very low porosity (<0·2 vol.%); (I) Network of almost non-luminescing domains and healed cracks in the Schellerhau granite (Erzgebirge) at initial electron bombardment (j) The area shown in (i) after 10 minutes focused electron bombardment (20 keV, 15 nA). The luminescence of the secondary quartz had been increased drastically.

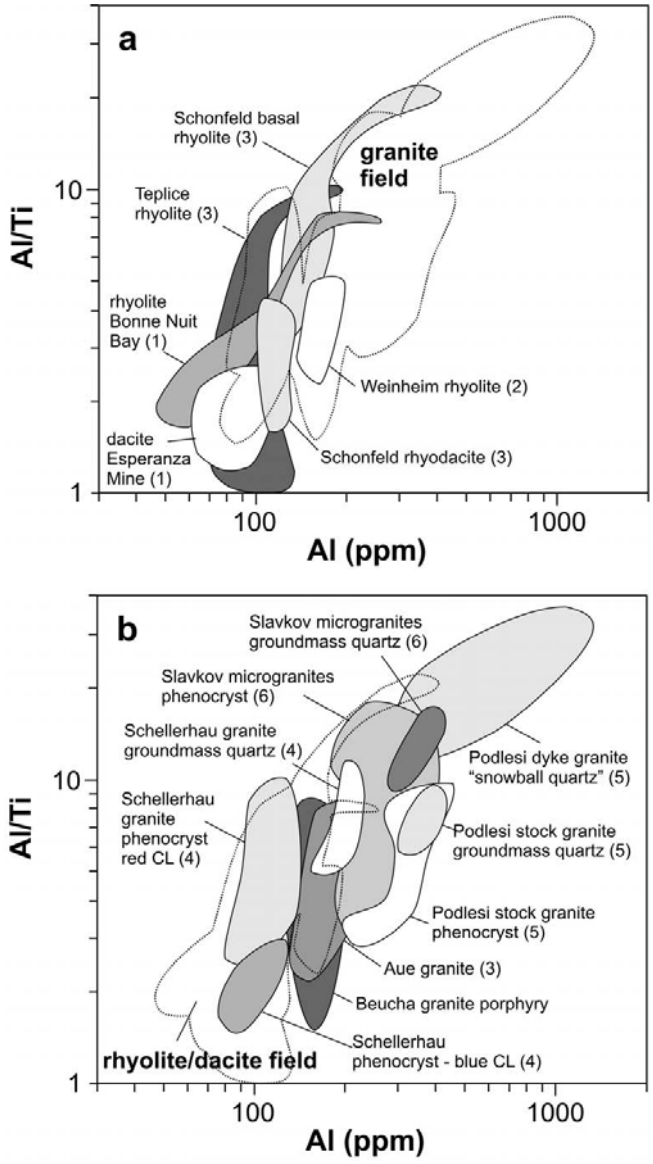

Figure 8 Compilation of Al concentrations and Al/Ti ratios in quartz from (a) dacites and rhyolites and (b) granites. Data were obtained by EPMA and SIMS: (1) Watt *et al*. 1997; (2) Müller *et al*. 2003a; (3) Müller *et al*. 2005; (4) Müller *et al*. 2000; (5) Müller *et al*. 2002a; (6) Müller *et al*. 2003b.

of the quartz crystal structure (e.g., Botis *et al*. 2005). The radius of halos is typically about 40 μm. Each halo is subdivided into a brighter inner zone (~25 μm) and an outer zone (~15 μm). The radius of ~40 μm corresponds to the interaction radius of α-particles in quartz (Owen 1988).

4. Trace elements in igneous quartz

Al and Ti are the most abundant trace elements in igneous quartz (Müller *et al*. 2000, 2002a, 2003a, b). The contrasting behaviour of these two elements during magma differentiation make them suitable for discriminating igneous units. Figure 8 shows Al/Ti *vs*. Ti discrimination diagrams for igneous quartz from dacites, rhyodacites and rhyolites (Fig. 8a) and from granites (Fig. 8b). Quartz in the most primitive rocks (dacites) has the lowest Al and highest Ti (lowest Al/Ti; Fig. 8a). Ti in quartz decreases and Al increases with progressive differentiation. Ti shows maximum concentrations of up to 130 ppm in the bright blue luminescing growth zones in early-magmatic quartz phenocrysts, whereas the Ti concentration in late-magmatic groundmass quartz in granites shows lower concentrations of 20 to 50 ppm (Müller *et al*. 2002a, 2003a, b). An exponential Al/Ti trend can be recognised (linear trend on the log–log plot of Fig. 8), which is however not continuous. The high-Al tails of the data fields of the Schönfeld basal rhyolite, the Teplice rhyolite (Müller *et al*. 2002a) and the rhyolite from Bonne Nuit Bay (Watt *et al*. 1997) are caused by a few out-of-range values (Fig. 8a), which are the result of submicroscopic inclusions (see section 6.1). Taking this into account, Al concentrations in quartz phenocrysts are relatively constant for each volcanic facies, compared to Ti. Al is most variable in evolved granites of the Western Erzgebirge (Podlesí Dyke granite, Aue granite, Slavkov microgranites).

Concentrations of Li, K, Ge, B, Fe, and P in igneous quartz are in the range of 1 to 50 ppm (Schrön *et al*. 1988; Götze *et al*. 2004; Larsen *et al*. 2004; Jacamon & Larsen 2009). All these elements are incompatible and correlate positively with Al, implying that their concentrations increase with progressive differentiation of the magma. Li in quartz may be buffered by Li-bearing micas, which may coexist with quartz at higher degrees of fractionation (Müller *et al*. 2008), whereas B tends to separate into the magmatic vapour phase (e.g., Pichavant 1981). Secondary quartz is typically depleted in Al, Ti, and K (Van den Kerkhof & Müller 1999; Van den Kerkhof *et al*. 2004; Müller *et al*. 2008).

5. FTIR absorption of igneous quartz

The abundance of hydrogen-related defects in igneous quartz has been measured by FTIR spectroscopy. Unpolarised spectra were collected along traverses across quartz crystals (Fig. 9). All spectra show distinct absorption at 3365 cm^{-1} and a minor absorption at 3305 cm^{-1}. Both bands are attributed to hydrogen-compensated Al defects (e.g., Kats 1962). Intense Al absorption was found for the phenocryst cores of the Teplice rhyolite, whereas Al-absorption is less pronounced in quartz from the Schönfeld rhyodacite and from the Åland rapakivi granite. Quartz with blue CL has also relatively low total Al concentrations, as determined by EPMA (80–130 ppm; see Müller *et al*. 2005). On the other hand, the snowball quartz (Podlesí Dyke granite) with highest total Al concentrations (Fig. 8b) shows low Al–H-related absorption.

Quartz from the Podlesí Dyke granite (groundmass quartz), Schellerhau granite and Teplice rhyolite (phase TR1; Müller *et al*. 2005) shows a distinct absorption band at 3474 cm^{-1}, which is caused by a proton-compensated Al defect, perturbed by Li (Kats 1962).

The groundmass quartz of the Podlesí Dyke and Schellerhau granites is characterised by broad absorption bands at 3110 and 3220 cm^{-1}. Both samples show high absorption intensities of both bands, which are assigned to the symmetrical stretching vibrations of frozen molecular water (Aines & Rossman 1984). Low absorption of frozen water exhibits the red luminescing phenocryst core of the Teplice rhyolite (phase TR2b; Müller *et al*. 2005). Blue luminescing quartz and snowball quartz do not show water-related absorption. These bands cannot be attributed to condensated ice in the cooling stage. The bands have been only recognised for secondary quartz and some red luminescing growth zones. Similar absorption bands as frozen molecular water may point at water-bearing micropores; the analysed quartz volume is free of visible fluid inclusions.

Sharp absorption bands at 3365 cm^{-1}, 3305 cm^{-1} and 3474 cm^{-1} and broad absorption bands 3110 cm^{-1} and 3220 cm^{-1} as recorded for the cores and the rims of zoned quartz (phenocrysts, snowball quartz) and in unzoned crystals (groundmass quartz) do not show distinct variation. However,

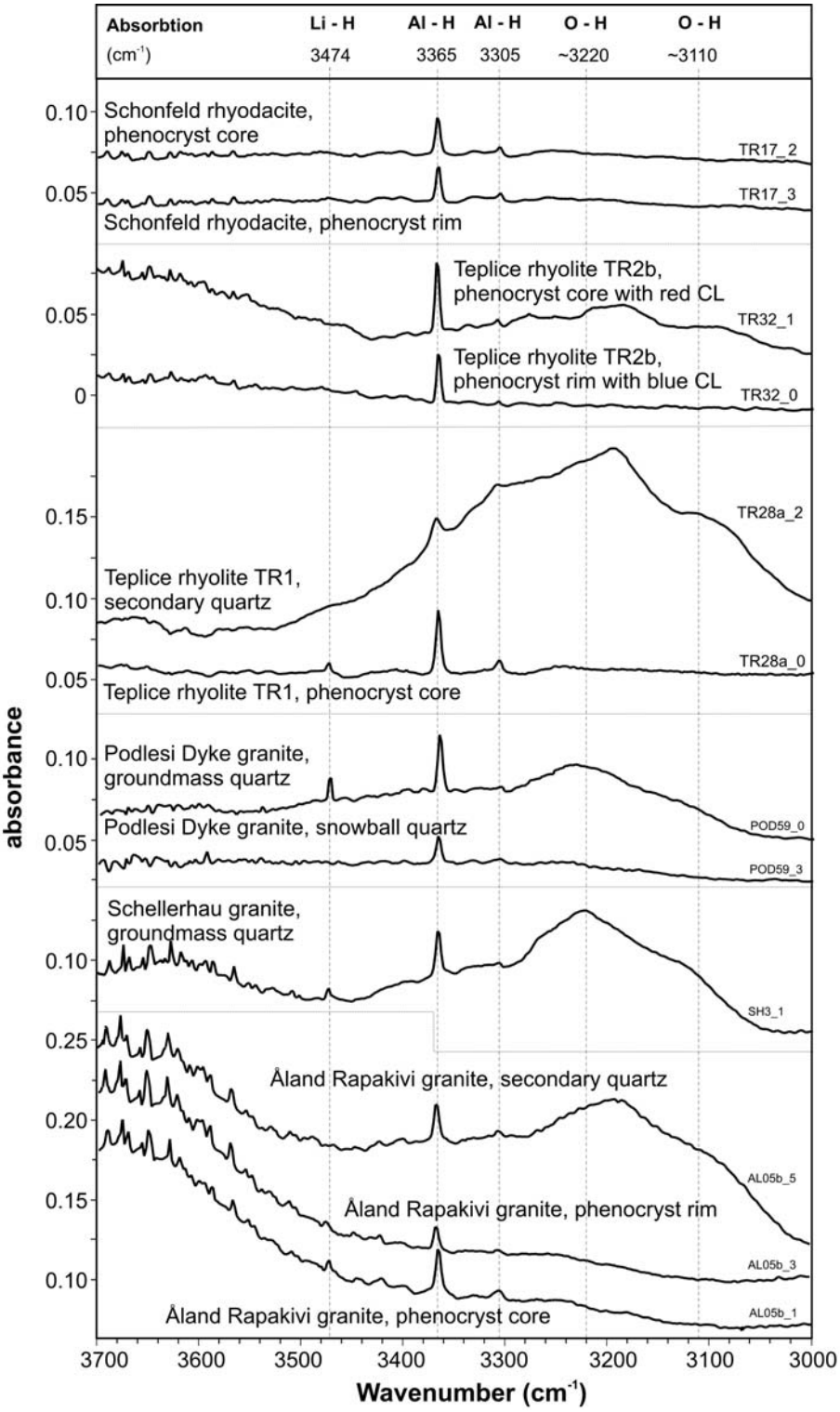

Figure 9 FTIR absorption spectra of igneous quartz. Spectra are offset for clarity.

variations of the absorption pattern were found between different quartz types in the same rock e.g., between groundmass quartz and snowball quartz (Podlesí Dyke granite) and between the primary (igneous) quartz and secondary quartz.

6. Discussion

6.1. CL properties and trace elements of igneous quartz

Cathodoluminescence and trace element studies show that hydrogen-related defect structures are abundant in igneous quartz. According to Stevens Kalceff & Phillips (1995) the red CL emission around 1·96 eV is related to non-bridging oxygen hole centre (NBOHC, an oxygen dangling bond; ≡Si–O·) with hydrogen as precursor (≡Si–OH). Defect structures with hydroxyl are strongly affected by the temperature and ionising radiation: protons and hydroxyl are released and concentrate as molecular water in larger defect structures and micropores (Stenina *et al.* 1984; Heggie 1992). The increase in the red emission of igneous quartz during electron bombardment is explained by radiolysis of hydroxyl groups in the quartz lattice, which results in the formation of NBOHC. The rate of the red CL increase is moderate for early-magmatic quartz phenocrysts, but very high for quartz in the granitic ground mass.

Small, nearly non-luminescing 1–5 μm small spots have been observed in granitic groundmass quartz during electron bombardment at high beam current (e.g., Fig. 6d). Stenina *et al.* (1984) described similar spots in quartz, which was intensively exposed to electron radiation. By using TEM imaging, these authors identified these structures as amorphous (non-crystalline) micro-domains, which contain molecular water. The dull-luminescing spots may be explained by diffusion of protons, hydroxyl and probably also molecular water migrate ('jump') along weak donor-acceptor bonds through the quartz lattice under excitation (Heggie 1992). At defects, hydroxyl and molecular water are trapped, forming water-rich disordered domains. This disorder results in the local quenching of the cathodoluminescence. The elevated concentrations of molecular water in granitic groundmass quartz and secondary quartz as detected by FTIR spectroscopy confirm the existence of water-bearing micropores.

The non-luminescing micro-domains and molecular water have not been detected in early-magmatic phenocrysts with dominant blue CL. The relatively homogeneous concentration of structural hydroxyl in the quartz phenocrysts can be explained by the fact that the amount of structural hydroxyl in quartz correlates with substitutional Al. In summary, the structurally bound hydrogen and water is lowest in the early-magmatic phenocrysts and highest in the granitic groundmass. This observation verifies progressively higher water content of the melt during magma evolution. The strong increase of red-CL and the formation of water-rich disordered micro-domains in granitic groundmass quartz reflects crystallisation from a cool and water-enriched melt. Consequently, late-magmatic snowball quartz should contain highest concentrations of structural water. However, lowest structural water was found here. This unexpected result is related to very rapid quartz crystallisation in F-, B-, and/or P-enriched magmas, because hydrogen diffusion within the quartz lattice requires time to operate. The low-pressure (subsurface) quartz growth would add to the effect of rapid growth, because the hydroxyl content in quartz is a positive function of pressure (e.g., Mosenfelder 2000). In this specific environment quartz incorporates only traces of hydroxyl which are below the detection limit of FTIR spectrometry.

The 'flash' of blue CL commonly observed during the first seconds of electron bombardment is caused by an emission band at 3·18–3·26 eV (Alonso *et al.* 1983; Luff & Townsend 1990; Perny *et al.* 1992; Gorton *et al.* 1996) According to these authors the intensity of the emission band correlates well with the Al content and the concentration of paragenetic $[AlO_4/M^+]$. The band position lies outside the sensitivity range of the spectrometer used in this present study. About 1600 analyses of total Al concentration in quartz do not show a clear correlation with one of the nine emission bands, which were detected for igneous quartz between 1·4 eV and 3·1 eV (Müller 2000; present paper). This lack of correlation may be attributed to the different atomic configurations of Al in the quartz lattice. The substitutional trivalent Al^{3+} can be compensated by coupled substitution of a pentavalent ion e.g. P^{5+}, or by interstitial monovalent ions such as Li^+, H^+, Na^+ and K^+. Therefore, Al in quartz depends on the availability of the compensating ions in the crystallising melt. The different valences of Al in quartz require different uptake conditions. The larger part of the total Al in quartz is probably incorporated in sub-microscopic defect clusters (<0·2 μm) as discussed by Müller *et al.* (2003a). The higher concentration of defect clusters as detected here particularly for quartz with >500 ppm Al, explains the contradictory low Al-H infrared absorption and the high total Al in the snowball quartz from Podlesí.

The intensities of the detected blue emissions at 2·58 eV, 2·68 eV and 2·79 eV also decrease during electron bombardment and contribute to the initial blue 'flash'. Correlations between the 2·58 eV, 2·68 eV and 2·79 eV emissions and the total content of Al, Ti, K, Fe could not be found. The 2·68 eV and 2·79 eV emissions are due to the recombination of a so-called self-trapped exciton (Stevens Kalceff & Phillips 1995), whereas the 2·58 eV band cannot be fully explained (e.g., Gritsenko & Lisitsyn 1985). The self-trapped exciton involves an irradiation-induced electron hole pair (oxygen Frenkel pair consisting of an oxygen vacancy and a peroxy linkage) and is a consequence of strong electron–phonon interactions in the SiO_2 crystal structure (Fisher *et al.* 1990). The CL emission at 2·75–2·80 eV is more or less present in all quartz types (e.g., Müller 2000, Götze *et al.* 2001). Thus the defects related to the 2·58 eV, 2·68 eV and 2·79 eV emissions are not only formed during crystal growth, but also induced by ionising radiation and, therefore not indicative for igneous processes.

Müller *et al.* (2002b) showed that high Ti (>50 ppm) in quartz correlates positively with the intensity of the blue 2·96 eV CL emission. It is still under debate whether Ti is a CL activator or sensitiser (Marshall 1988, Götze 2000). The increasing Al/Ti ratio during magmatic differentiation indicates that Ti is compatible during the formation of igneous quartz, whereas Al is incompatible. Wark & Watson (2006) proved that Ti^{4+}–Si^{4+} substitution is temperature-dependent. The temperature dependence of Ti in quartz explains the higher content in the early-magmatic quartz phenocrysts and the systematic lower concentrations in the younger quartz generations. The relatively stable, blue-dominated CL and the relatively high abundance of Ti in early-magmatic quartz phenocrysts in volcanic rocks and some granites reflect crystallisation from a hot and relatively water-poor melt.

Pott & McNicol (1971) and Kempe *et al.* (1999) found that concentration of bound Fe^{3+} is related to the 1·73 eV CL emission. Some rhyolitic quartz phenocryst margins and the co-genetic fine-grained groundmass quartz show stable red CL at 1·73 eV and elevated Fe concentrations. However, there is no general correlation of total Fe and the 1·73 eV emission intensity found (Müller 2000). It has been frequently observed that quartz adjacent to Fe-rich minerals (biotite, hornblende, tourmaline, etc.) becomes exponentially enriched in Fe towards the grain contact up to several thousands ppm (Penniston-Dorland 2001; Müller *et al.* 2002b, 2003b). However, the diffusing ion is preferentially Fe_2^+, due to its smaller ion radius. Fe diffuses up to 400 μm into the quartz, but the Fe-enrichment of quartz does not necessarily result in changing CL properties. Therefore, the total Fe content in quartz cannot be used to trace magmatic processes.

Schrön *et al.* (1982) introduced the ternary Ti–Al–Ge diagram to discriminate igneous quartz of different origin ('rhyolitic', 'granitic' and 'pegmatitic'). They showed that Ge behaves as an incompatible element during magma differentiation and is a useful quartz fingerprint for magma evolution. Jacamon & Larsen (2009) suggest that the Ge/Ti ratio in quartz is an index of the magmatic evolution of silica-saturated melts. However, the increase of Ge in quartz with increasing differentiation is only minor until the pegmatitic-pneumatolytic stage, making Ge a useful element for identifying pegmatitic quartz (Schrön *et al.* 1988; Götze *et al.* 2004). Götze *et al.* (2005) detected a correlation of the 2·45 eV emission with the concentration of the paramagnetic $[GeO_4/Li^+]^0$ centre in pegmatitic quartz.

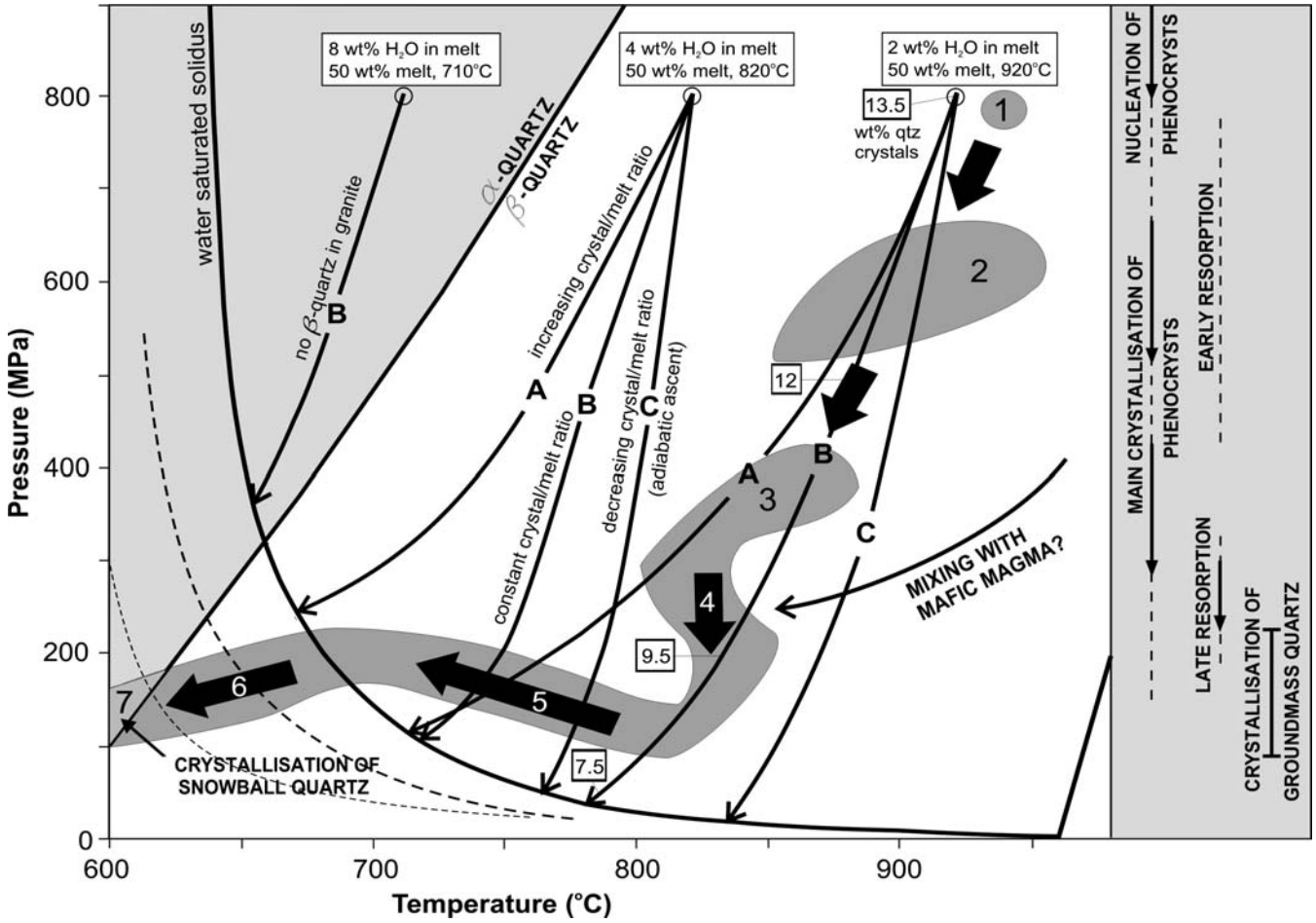

Figure 10 P–T path interpretations for quartz. The grey areas frame thermobarometric results obtained from melt inclusions in felsic igneous rocks from the Erzgebirge, Germany, by Thomas (1994). The data are compiled with experimental PT paths (A, B and C) for haplogranitic magmas with different initial water content (Johannes & Holtz 1996). A paths=increasing crystal/melt ratio (decompression crystallisation); B paths=constant crystal melt ratio; C paths=decreasing crystal/melt ratio (decompression melting). To provide an example the change of the quartz crystal proportion in the ascending magma along the path B with the initial conditions of 920°C and 800 MPa is given according to Johannes & Holtz (1996). The quartz portion decreases but feldspar portion increases and the crystals/melt ratio remains constant. Values for the β-/α-quartz inversion are from Yoder (1950). The dashed solidus lines illustrate the variability of the solidus for different granite compositions. See text for explanation of numbers 1 to 7.

6.2. Resorption of quartz phenocrysts

Major resorption surfaces observed in early-magmatic phenocrysts in extrusive and plutonic rocks are attributed to profound changes in temperature and magma composition. These surfaces are associated with a concentration step of Ti and commonly have wavy (Fig. 5f), dendritic (Fig. 6a), or granophyric textured overgrowth. Foreign particles adhere at the freshly resorbed surface due to its roughness and the high number of free bonds. The particles cause physical shielding, disturbing the planar growth of the crystal face. The hindered growth may cause growth embayments and wavy textures after major resorption events, which can be filled later on with melt droplets and foreign crystals (Fig. 5g). Minor quartz resorption reflects small changes in the same parameters caused by local magma dynamics (convection). Possible causes of major episodes of quartz resorption were previously discussed by Müller *et al*. (2003b) and Müller *et al*. (2005) on the example of the Slavkov microgranites and the igneous rocks of the eastern Erzgebirge volcano-plutonic complex. Two possible processes for major resorption of quartz crystals have been extracted from these discussions. First, isothermal decompression due to *semi-adiabatic magma ascent* and, secondly, *mixing and mingling of different magmas* by injection or recharge. Both processes can be related.

6.2.1. Semi-adiabatic magma ascent. Strong resorption of quartz crystals may occur during semi-adiabatic magma ascent for an energetically closed system (Johannes & Holtz 1996; Fig. 10). Decompression melting during isothermal magma ascent is mainly caused by the decrease of the minimum H_2O content of the melt, leading to the increase of the ratio H_2O_{total}/H_2O_{melt} in the system (Tuttle & Bowen 1958; Carmichael *et al*. 1974; Sykes & Holloway 1987; Holtz & Johannes 1994; Johannes & Holtz 1996). Experimental data of Johannes & Holtz (1996) obtained for the haplogranite system and illustrated in Figure 10 are used here for better understanding the processes of possible quartz resorption during magma ascent. Figure 10 shows the experimental ascent paths of three haplogranitic magmas with 2 wt.%, 4 wt.%, and 8 wt.% H_2O in the melt according Johannes & Holtz (1996). The water-undersaturated magmas start to rise at 800 MPa with 50 wt.% melt and 50 wt.% crystals. During crystallisation along path A, the crystal/melt ratio is increased (decompression crystallisation). Path B represents magma ascent at constant crystal/melt ratio. In the case of an ascending melt along path B with 2 wt.% H_2O in the melt and 920°C initial temperature, the relative proportion of quartz and feldspar changes, but the crystal/melt ratio remains constant. Before the solidus is reached, the proportion of quartz is lowered from

Table 3 Increase of quartz crystallisation temperature after major resorption episodes documented by the chemical zoning of quartz phenocrysts. Ti concentrations were determined by EPMA. α_{TiO2}–TiO_2 activity of magma according to Hayden *et al.* (2005). ΔT = change of magma temperature; n = number of analyses.

Name of igneous rock	Magmatic province	α_{TiO2}	Location of resorption surface within phenocrysts	Ti (ppm) of quartz prior to resorption	Ti (ppm) of quartz after resorption	Minimum ΔT after quartz resorption (°C)
Teplice rhyloite (TR2b)	Eastern Erzgebirge, Germany	0·8	core	<22 (n=2)	58 (n=6)	+97 ± 2
Schellerhau granite	Eastern Erzgebirge, Germany	0·8	core	<22 (n=10)	58 (n=2)	+97 ± 2
Altenberg–Frauenstein microgranite	Eastern Erzgebirge, Germany	1	core	<33 (n=10)	59 (n=11)	+58 ± 1
Altenberg–Frauenstein microgranite	Eastern Erzgebirge, Germany	1	marginal	59 (n=11)	120 (n=4)	+82 ± 1
Beucha granite	NW Saxony, Germany	1	marginal (Fig. 5h)	28 (n=9)	88 (n=26)	+118 ± 2
Hammarudda porphyry	Åland, Finland	1	marginal	154 (n=16)	211 (n=7)	+44 ± 1

13·5 wt.% to 7·5 wt.% (Fig. 10). On the other hand nearly isothermal decompression (path C), corresponding to adiabatic magma ascent, is accompanied by the release of H_2O from the melt in a chemically and energetically closed system. Higher water activities result in melting of the crystals and formation of additional melt (decompression melting). In the C-path example with the initial ascent conditions 800 MPa and 820 °C, about 30 vol.% of quartz and feldspar crystals would dissolve between 800 and 50 MPa (Johannes & Holtz 1996). Crystal resorption is much more intense between 300 and 50 MPa than at higher pressures. The simultaneous fractionation of H_2O-free phases like quartz and feldspar may result in secondary boiling and magma ascent up to the surface. The magma evolution along path B or C is relatively short when it starts to rise at 710 °C, 800 MPa, and 8 wt.% total H_2O, as the magma would crystallise completely at 12 km and 8 km, respectively. The magma would become more or less immobile along the A-path and it would crystallise at 600 MPa or even higher pressures. Therefore the development of major resorption textures in quartz requires an episode of about isothermal decompression, as illustrated for paths B and C.

The P–T path of rhyolite and granite magmas of the Erzgebirge obtained from microthermometric studies of silicate melt inclusions by Thomas (1992, 1994) is illustrated in Figure 10, together with the generalised quartz textures and populations of quartz (Müller *et al.* 2005). The maximum pressure of 780 MPa obtained from melt inclusions represents the minimum crystallisation depth of early magmatic quartz phenocrysts of the Erzgebirge granites and rhyolites (nr. 1 in Fig. 10). It is, however, possible that phenocrysts originate from greater depth. For example, rhombohedric α-quartz phenocrysts in rhyolites of the Odenwald (Dossenheim and Weinheim rhyolite, Germany; Fig. 5c) and other occurrences (Bozen rhyolite, Italy) indicate much deeper quartz crystallisation (Flick 1987). Flick (1987) suggested a minimum crystallisation pressure of the α-quartz phenocrysts at 1250 to 1400 MPa, assuming a magma temperature between 900 °C and 950 °C. The P–T-path of the Erzgebirge granites and rhyolites (Thomas 1992, 1994) follows roughly the experimentally-determined paths A and B for haplogranitic melts with 1·5 wt.% to 2·5 wt.% H_2O in melt (Johannes & Holtz 1996).

The path of the Erzgebirge magmas is not well documented between 800 and 400 MPa, so that ascent parameters may correspond to the path A, B or even C. A number of phenocryst populations in the Eastern Erzgebirge contain rounded crystal cores, which indicate resorption during the early stage of crystallisation (Fig. 5d; Müller *et al.* 2005). This early resorption episode can be attributed to rapid magma ascent or magma mixing. Temporary magma storage probably occurred at a depth of 17–24 km (nr. 2) and in the ductile-brittle transition zone at a depth of 13–10 km (nr. 3; Müller *et al.* 2000, 2005). These stages are documented by significant amounts of quartz growth. Decompression crystallisation (path A) must have occurred between 400 and 300 MPa (between nr. 2 and 3) resulting in higher water contents in the melt. Melt inclusion data indicate adiabatic magma ascent (path C) at a depth of 10–4·5 km (nr. 4) that possibly caused quartz phenocryst resorption. An increase of magma temperature could have been caused by mixing with mafic magma. Most of the Erzgebirge magmas were emplaced at a shallow depth of 5–2·6 km. Here, the solidifying magmas became supersaturated in volatiles and the pressures only slightly increased along the solidus (nr. 5). Melt inclusion data on the left side of the haplogranite solidus (nr. 6) reflect chemistries of highly fractionated magmas enriched in fluorine and other volatiles causing a shift of the solidus. Finally, igneous α-quartz crystallised in topaz-bearing albite granites (nr. 7).

6.2.2. Magma mixing. A number of late-Hercynian rhyolites and granites contain phenocrysts with major resorption surfaces, which were affected by magma mixing and mingling (Müller *et al.* 2005). Rock-forming minerals in these rocks show textures, which indicate magma mixing, such as plagioclase-mantled K-feldspar, sieve-textured plagioclase and mafic micro enclaves (Müller *et al.* 2005). The pre-resorption growth zones in these quartz phenocrysts are in some cases smudged and blurred, whereas the boundaries of post-resorption growth zones are sharp. The smudging of pre-resorption growth zones is explained by the redistribution and healing of defect centres in quartz (Müller *et al.* 2005). Smudging of growth zoning in quartz is, however, a rare phenomenon amongst the late-Hercynian igneous rocks.

The Ti-in-quartz geothermometer of Wark & Watson (2006) provides a tool to determine the quartz crystallisation temperature prior to and after a major phenocryst resorption episode. Table 3 shows calculations of the minimum temperature change after a major resorption episode. The Ti activity αTiO_2 in the magma was determined according Hayden *et al.* (2005). Rutile and titanomagnetite are common accessories in the Altenberg–Frauenstein microgranite, Beucha granite, and Hammerrudda porphyry, indicating Ti saturation of the magma. Rutile is rare in the Teplice rhyolite and Schellerhau granite, which implies slight Ti undersaturation; this is confirmed by the calculation method of Hayden *et al.* (2005). The magma temperature increase in all cases is significant. If the resorption is caused by semi-adiabatic magma ascent, the magma moves into a higher and cooler crustal level and the Ti in quartz would not increase after resorption. The findings support the hypothesis that major resorption of quartz phenocrysts is caused by mixing and mingling with a more mafic magma.

Thus, a number of strong resorption episodes can be related to magma mixing and mingling, particularly, to those observed in igneous rocks of the eastern Erzgebirge volcano-plutonic complex (Müller *et al*. 2005). However, most of the other igneous rocks discussed here show no chemical or textural evidence for magma mixing. These rocks were possibly affected by multiple magma recharge (stepwise magma ascent) resulting in acid-acid magma mixing and mingling. Semi-adiabatic magma ascent theoretically causes major resorption of quartz crystals. At present there is no strong evidence for this theory. However, the injection of a hotter (more mafic) magma at the deeper levels of a magma reservoir may lead to higher gas pressures and trigger magma ascent (e.g., Blake *et al*. 1992, Smith *et al*. 2004). It is suggested that magma mixing and adiabatic magma ascent go normally hand in hand during the magma evolution, as was demonstrated in the example of the Erzgebirge Granites.

7. Summary

CL spectra of igneous quartz in late-Hercynian volcanic and plutonic rocks in central and western Europe commonly comprise nine emission bands between 1·4 eV and 3·1 eV. The decay of blue luminescing centres and the generation of red luminescing centres during electron bombardment have been quantified by applying the kinetic law. Granitic groundmass quartz has more unstable CL, in particular the red 1·85 eV and 1·96 eV emissions, than the CL of early-magmatic quartz phenocrysts. The increase of the 1·85 eV and 1·96 eV emissions during electron radiation is explained by the radiolysis of OH- and H_2O-defects in quartz. The formation of water-rich disordered micro-domains and the strong increase of red-CL in granitic groundmass quartz reflects crystallisation from a water-rich melt in the emplacement level when the melt became rich in water. CL contrasts among growth zones in zoned quartz phenocrysts are essentially related to the distribution of trace elements. Blue luminescing growth zones have high Ti (>50 ppm). High intensity of the relatively stable blue emission at 2·96 eV correlates with high Ti in quartz. As differentiation proceeds, the Ti concentration in quartz decreases, whereas Al in quartz increases. Thus, Ti behaves compatibly during the evolution of igneous quartz, whereas Al behaves more incompatibly. The more stable, blue-dominated CL and the relative high abundance of Ti in quartz phenocrysts in rhyolites and a number of granites reflect higher crystallisation temperatures and a lower crust origin.

CL reveals complex growth patterns of early-magmatic quartz phenocrysts in late-Hercynian volcanic and plutonic rocks. Fine-scale (<10 μm) oscillatory zoning, large-scale step zoning with strong CL contrasts, skeletal growth, resorption surfaces, and growth embayments are distinguished. A few of late-Hercynian granites contain quartz phenocryst populations similar to phenocrysts in associated rhyolites, indicating that the rhyolite is the extrusive equivalent of the underlying granite. Examples are known from the Eastern Erzgebirge volcano-plutonic complex, e.g. the Schellerhau granites and Teplice rhyolites (Müller *et al*. 2005). This phenomenon is presumably much more common, but rhyolites associated with Hercynian granites are either eroded or have not been developed. Phenocrysts in granites are embedded in unzoned anhedral groundmass quartz that makes their identification difficult. A number of major resorption episodes can be related to the mixing of magmas with different physicochemical properties. There is no strong evidence that the observed major resorption surfaces are caused by semi-adiabatic magma ascent. However, both causes can be related, because the injection or recharge of mafic and hotter magmas into the bottom of felsic magma reservoirs may trigger the rise of felsic magma portions.

There are still, however, a number of open questions regarding the petrogenetic significance of the CL properties and the trace element signature of igneous quartz. In particular, the crystallisation parameters, that control the incorporation of Al into the quartz lattice have to be evaluated by experimental work.

8. Acknowledgements

This study was supported by the Deutsche Forschungsgemeinschaft (MU 1717/2–1), the Natural History Museum, London and the Geological Survey of Norway. We are grateful to Marian Holness, Jon Davidson and John D. Clemens for constructive reviews and discussions.

9. References

Aines, R. D. & Rossman, G. R. 1984. Water in minerals? A peak in the infrared. *Journal of Geophysical Research* **89/B6**, 4059–71.

Allègre, C. J., Provost, A. & Jaupart, C. 1981. Oscillatory zoning: A pathological case of crystal growth. *Nature* **294**, 223–8.

Alonso, P. J., Halliburton, L. E., Kohnke, E. E. & Bossoli, R. B. 1983. X-ray induced luminescence in crystalline SiO_2. *Journal of Applied Physics* **54**, 5369–75.

Armstrong, J. T. 1995. CITZAF: A package of correction programs for the quantitative electron microbeam X-ray analysis of thick polished materials, thin films, and particles. *Microbeam Analysis* **4**, 177–200.

Bahadur, H. 1994. Sweeping and irradiation effects on hydroxyl defects in crystalline natural quartz. *IEEE Transactions on Ultrasonics, Ferroelectrics and Frequency Control* **41/6**, 820–33.

Bambauer, H. U., Brunner, G. O. & Laves, F. 1963. Merkmale des OH-Spektrums alpiner Quarze (3 μ-Gebiet). *Schweizerische Mineralogische und Petrographische Mitteilungen* **43**, 259–68.

Behr, H. J. 1989. Die geologische Aktivität von Krustenfluiden. *In* Behr, H. J., Fyfe, W. S., Hoefs, J., Johannes, W. & Touret, J. L. R. (eds) *Gesteinsfluide – Ihre Herkunft und Bedeutung für geologische Prozesse,* **Vol. 1**, 7–42. Hannover: Niedersächsische Akademie der Geowissenschaften Veröffentlichungen.

Behr, H.-J. & Frentzel-Beyme, K. 1989. Permeability and paleoporosity in crystalline bedrocks of the Central European basement-studies of cathodoluminescence. *In* Boden, A. & Eriksson, K. G. (eds) *Exploration of the deep continental crust. Deep drilling in crystalline bedrock*. Vol. 2, 477–97. Berlin, Heidelberg, New York: Springer.

Beus, A. A., Severov, E. A., Sitnin, A. A. & Subbotin, K. D. 1962. *Albitized and greisenized granites (apogranites)*. Moscow: Nauka. [In Russian.]

Blake, S., Wilson, C. J. N., Smith, I. E. M. & Walker, G. P. L. 1992. Petrology and dynamics of the Waimihia mixed magma eruption, Taupo Volcano, New Zealand. *Journal of the Geological Society, London* **149**, 193–207.

Blankenburg, H.-J., Götze, J. & Schulz, J. 1994. *Quarzrohstoffe*. Leipzig-Stuttgart, Germany: Deutscher Verlag für Grundstoffindustrie.

Botis, S., Nokhrin, S. M., Pan, Y., Xu, Y. & Bonli, T. 2005. Natural radiation-induced damage in quartz. I. Correlations between cathodoluminescence colors and paramagnetic defects. *Canadian Mineralogist* **43**, 1565–80.

Breiter, K., Müller, A., Leichmann, J. & Gabašova, A. 2005. Textural and chemical evolution of a fractionated granitic system: the Podlesí stock, Czech Republic. *Lithos* **80**, 323–45.

Carmichael, I. S. E., Turner, F. J. & Verhoogen, J. 1974. *Igneous petrology*. New York: McGraw-Hill.

Charlier, B. L. A., Wilson, C. J. N., Lowenstern, J. B., Blake, S., van Calsteren, P. W. & Davidson, J. P. 2005. Magma generation at a large, hyperactive silicic volcano (Taupo, New Zealand) revealed by U–Th and U–Pb systematic in zircons. *Journal of Petrology* **46**, 3–32.

Davidson, J., Tepley III, F., Palacz, Z. & Meffan-Main, S. 2001. Magma recharge, contamination and residence times revealed by *in situ* laser ablation analysis of feldspar in volcanic rocks. *Earth and Planetary Science Letters* **184**, 427–42.

Davidson, J., Morgan D. J., Charlier, B. L. A., Harlou, R. & Hora, J. M. 2007. Microsampling and isotopic analysis of igneous rocks: Implications for the study of magmatic systems. *Annual Reviews of Earth and Planetary Sciences* **35**, 273–311.

D'Lemos, R. S., Kearsley, A. T., Pembroke, J. W., Watt, G. R. & Wright, P. 1997. Complex quartz growth histories in granite revealed by scanning cathodoluminescence techniques. *Geological Magazine* **134**, 459–552.

Fenn, P. M. 1977. The nucleation and growth of alkali feldspars from hydrous melts. *Canadian Mineralogist* **15**, 135–61.

Fenn, P. M. 1986. On the origin of graphic granite. *American Mineralogist* **71**, 325–30.

Fisher A. J., Hayes W. & Stoneham A. M. 1990. Structure of the self-trapped exciton in quartz. *Physical Reviews Letters* **64**, 2667–70.

Flick, H. 1987. Geotektonische Verknüpfung von Plutonismus und Vulkanismus im südwestdeutschen Variscicum. *Geologische Rundschau* **76**, 699–707.

Fowler, A. D. 1990. Self-organized mineral textures of igneous rocks: the fractal approach. *Earth Sciences Reviews* **29**, 47–55.

Gorton, N. T., Walker, G. & Burley, S. D. 1996. Experimental analysis of the composite blue CL emission in quartz. *Journal of Luminescence* **72–74**, 669–71.

Götze, J. 2000. Cathodoluminescence microscopy and spectroscopy in applied mineralogy. *Freiberger Forschungshefte* **C 485**, 1–128.

Götze, J., Plötze, M., Fuchs, H. & Habermann, D. 1999. Defect structure and luminescence behaviour of agate – results of electron paramagnetic resonance (EPR) and cathodoluminescence (CL) studies. *Mineralogical Magazine* **63/2**, 149–63.

Götze, J., Plötze, M. & Habermann, D. 2001. Origin, spectral characteristics and practical applications of the cathodoluminescence (CL) of quartz – a review. *Mineralogy and Petrology* **71**, 225–50.

Götze, J., Plötze, M. Graupner, T., Hallbauer, D. K. & Bray, C. J. 2004. Trace element incorporation into quartz: A combined study by ICP-MS, electron spin resonance, cathodoluminescence, capillary ion analysis, and gas chromatography. *Geochimica et Cosmochimica Acta* **68**, 3741–59.

Götze, J., Plötze, M. & Trautmann, T. 2005. Structure and luminescence characteristics of quartz from pegmatites. *American Mineralogist* **90**, 13–21.

Gritsenko, B. P. & Lisitsyn, V. M. 1985. Intrinsic short-lived defects in quartz. *Soviet Physics – Solid State* **27**, 1330–1.

Gurbanov, A. G., Chernukha, D. G., Koshchug, D. G., Kurasova, S. P. & Fedyushchenko, S. V. 1999. EPR spectroscopy and geochemistry of rock-forming quartz as an indicator of the superimposed processes in rocks of igneous associations of various ages in the Greater Caucasus. *Geochemistry International* **37**, 519–604.

Hayden, L. A., Watson, E. B. & Wark, D. A. 2005. Rutile saturation and TiO_2 diffusion in hydrous siliceous melts. *EOS Transactions, American Geophysical Union* **86**, Fall meeting supplement, MR13A-0076.

Heggie, M. I. 1992. A molecular water pump in quartz dislocations. *Nature* **355**, 337–9.

Holtz, F. & Johannes, W. 1994. Maximum and minimum water contents of granitic melts: implications for chemical and physical properties of ascending magmas. *Lithos* **32**, 149–59.

Itoh, C., Suzuki, T. & Itoh, N. 1990. Luminescence and defect formation in undensified and densified amorphous SiO_2. *Physical Reviews B* **41/6**, 3794–9.

Jacamon, F. & Larsen, R. B. 2009. Trace element evolution of quartz in the charnockitic Kleivan granite, SW Norway: the Ge/Ti ratio of quartz as an index of igneous differentiation. *Lithos* **107**, 281–91.

Jani, M., Halliburton, L. E. & Kohnke, E. E. 1983. Point defects in crystalline SiO_2: thermally stimulated luminescence above room temperature. *Journal of Applied Physics* **54**, 6321–8.

Johannes, W. & Holtz, F. 1996. *Petrogenesis and experimental petrology of granitic rocks*. Berlin, Heidelberg, New York: Springer.

Kats, A. 1962. Hydrogen in alpha-quartz. *Philips Research Reports* **17**, 133–279.

Kempe, U., Götze, J., Dandar, S. & Habermann, D. 1999. Magmatic and metasomatic processes during formation of the Nb–Zr–REE deposits from Khaldzan Buregte (Mongolian Altai): Indications from a combined CL-SEM study. *Mineralogical Magazine* **63**, 165–77.

Kirkpatrick, R. J. 1981. *Kinetics of crystallization of igneous rocks. Reviews in Mineralogy* **8**, 321–98. Washington DC: Mineralogical Society of America.

Kovalenko, V. I. 1977. *Petrology and geochemistry of rare-metal granitoids*. Novosibirsk: Nauka. [In Russian.]

Kronenberg, A. K., Kirby, S. H., Aines, R. D. & Rossmann, G. R. 1986. Solubility and diffusional uptake of hydrogen in quartz at high water pressures: implications for hydrolytic weakening in the laboratory and within the earth. *Tectonophysics* **172**, 255–71.

Laemmlein, G. 1930. Korrosion und Regeneration der Porphyr-Quarze. *Zeitschrift für Kristallographie* **75**, 109–27.

Larsen, R. B., Polvé, M. & Juve, G. 2000. Granite pegmatite from Evje-Iveland: trace element chemistry and implications for the formation of high-purity quartz. *Norges geologiske undersøkelse Bulletin* **436**, 57–65.

Larsen, R. B., Henderson, I., Ihlen, P. M. & Jacamon, F. 2004. Distribution and petrogenetic behaviour of trace elements in granitic quartz from South Norway. *Contributions to Mineralogy and Petrology* **147**, 615–28.

Luff, B. J. & Townsend, P. D. 1990. Cathodoluminescence of synthetic quartz. *Journal of Physics: Condensed Matter* **2**, 8089–97.

Lyakhovich, V. V. 1972. *Trace elements in rock-forming minerals of granitoids*. Moscow: Izd. Nedra. 200 pp. [In Russian.]

Mashima, H. 2004. Time scale of magma mixing between basalt and dacite estimated for the Saga–Futagoyama volcanic rocks in northwest Kyushu, southwest Japan. *Journal of Volcanology and Geothermal Research* **131**, 333–49.

Marshall, D. J. 1988. *Cathodoluminescence of geological materials*. Winchester, Massachusetts: Allen & Unwin Inc.

Mosenfelder, J. L. 2000. Pressure dependence of hydroxyl solubility in coesite. *Physics and Chemistry of Minerals* **27**, 610–17.

Müller, A. 2000. *Cathodoluminescence and characterisation of defect structures in quartz with applications to the study of granitic rocks*. Ph.D. Thesis, University of Göttingen, Germany.

Müller, A., Seltmann, R. & Behr, H. J. 2000. Application of cathodoluminescence to magmatic quartz in a tin granite – case study from the Schellerhau Granite Complex, Eastern Erzgebirge, Germany. *Mineralium Deposita* **35**, 169–89.

Müller, A., Kronz, A. & Breiter, K. 2002a. Trace elements and growth pattern in quartz: a fingerprint of the evolution of the subvolcanic Podlesí Granite System (Krušné Hory, Czech Republic). *Bulletin of Czech Geological Survey* **77**, 135–45.

Müller, A., Lennox, P. & Trzebski, R. 2002b. Cathodoluminescence and micro-structural evidence for crystallisation and deformation processes of granites in the Eastern Lachlan Fold Belt (SE Australia). *Contributions to Mineralogy and Petrology* **143**, 510–24.

Müller, A., Wiedenbeck, M., Van den Kerkhof, A. M., Kronz, A. & Simon, K. 2003a. Trace elements in quartz – a combined electron microprobe, secondary ion mass spectrometry, laser-ablation ICP-MS, and cathodoluminescence study. *European Journal of Mineralogy* **15**, 747–63.

Müller, A., René, M., Behr, H.-J. & Kronz, A. 2003b. Trace elements and cathodoluminescence of igneous quartz in topaz granites from the Hub Stock (Slavkovský Les Mts, Czech Republic). *Mineralogy and Petrology* **79**, 167–91.

Müller, A., Breiter, K., Seltmann, R. & Pécskay, Z. 2005. Quartz and feldspar zoning in the Eastern Erzgebirge pluton (Germany, Czech Republic): evidence of multiple magma mixing. *Lithos* **80**, 201–27.

Müller, A., Seltmann, R., Halls, C., Jeffries, T., Dulski, P., Spratt, J. & Kronz, A. 2006a. The Land's End granite, Cornwall: the evolution of a composite and mineralised pluton. *Ore Geology Reviews* **28**, 329–67.

Müller, A., Thomas, R., Wiedenbeck, M., Seltmann, R. & Breiter, K. 2006b. Water content of granitic melts from Cornwall and Erzgebirge: A Raman spectroscopy study of melt inclusions. *European Journal of Mineralogy* **18**, 429–40.

Müller, A., Ihlen, P. M. & Kronz A. 2008. Quartz chemistry in polygeneration Sveconorwegian pegmatites, Froland, Norway. *European Journal of Mineralogy* **20**, 447–63.

Müller, A. & Seltmann, R. 1999. The genetic significance of snowball quartz in high fractionated tin granites of the Krušne Hory/Erzgebirge. *In* Stanley, C. J., Rankin, A. H., Bodnar, R. J., Naden, J., Yardley, B. W. D., Criddle, A. J., Hagni, R. D., Gize, A. P., Pasava, J., Fleet, A. J., Seltmann, R., Halls, C., Stemprok, M., Williamson, B., Herrington, R. J., Hill, R. E. T., Prichard, H. M., Wall, F., Williams, C. T., McDonald, I., Wilkinson, J. J., Cooke, D., Cook, N. J., Marshall, B. J., Spry, P., Khin Zaw, Meinert, L., Sundblad, K., Scott, P., Clark, S. H. B., Valsami-Jones, N. J., Beukes, E., Stein, H. J., Hannah, J. L., Neubauer, F., Blundell, D. J., Alderton, D. H. M., Smith, M. P., Mulshaw, S. & Ixer, R. A. (eds) *Mineral deposits: processes to processing* **1**, 409–12. Rotterdam: Balkema.

Neuser, R. D., Bruhn, F., Götze, J., Habermann, D. & Richter, D. K. 1995. Kathodolumineszenz: Methodik und Anwendung. *Zentralblatt für Geologie und Paläontologie Teil 1* **1/2**, 287–306.

Owen, M. R. 1988. Radiation-damage halos in quartz. *Geology* **16**, 529–32.

Penniston-Dorland, S. C. 2001. Illumination of vein quartz textures in a porphyry copper ore deposits using scanned cathodoluminescence: Grasberg Igneous Complex, Irian Jaya, Indonesia. *American Mineralogist* **86**, 652–66.

Pearce, T. H. & Kolisnik, A. M. 1990. Observations of plagioclase zoning using interference imaging. *Earth Science Reviews* **29**, 9–26.

Peppard, B. T., Steele, I. M., Davis, A. M., Wallace, P. J. & Anderson, A. T. 2001. Zoned quartz phenocrysts from the rhyolitic Bishop Tuff. *American Mineralogist* **86**, 1034–52.

Perny, B., Eberhardt, P., Ramseyer, K., Mullis, J. & Pankrath, R. 1992. Microdistribution of aluminium, lithium and sodium in a quartz: possible causes and correlation with shored lived cathodoluminescence. *American Mineralogist* **77**, 534–44.

Pichavant, M. 1981. An experimental study of the effect of boron on water-saturated haplogranite at 1 kbar pressure: geological applications. *Contributions to Mineralogy and Petrology* **76**, 430–9.

Picouet, P. A. 1999. Cathodoluminecence spectroscopy and the orientation of a hydrothermal quartz crystal. *Schweizerische Mineralogische und Petrographische Mitteilungen* **79**, 455–60.

Pott, G. T. & McNicol, B. D. 1971. Spectroscopy study of the coordination and valence of Fe and Mn ions in and on the surface of aluminas and silicas. *Discussions of the Faraday Society* **52**, 121–31.

Poutiainen, M. & Scherbakova, T. F. 1998. Fluid and melt inclusion evidence for the origin of idiomorphic quartz crystals in topaz-bearing granite from the Salmi batholith, Karelia, Russia. *Lithos* **44**, 141–51.

Rajpoot, G. S. 1991. *Controversies in geotectonics of Hercynian Europe*. Prague: Czech Geological Survey.

Ramseyer, K., Baumann, J., Matter, A. & Mullis, J. 1988. Cathodoluminescence colours of α-quartz. *Mineralogical Magazine* **52**, 669–77.

Remond, G., Cesbron, F., Chapoulie, R., Ohnenstetter, D., Rouques-Carmes, C. & Schvoerer, M. 1992. Cathodoluminescence applied to the microcharacterization of mineral materials: a present status in experimentation and interpretation. *Scanning Microscopy* **6/1**, 23–69.

Rink, W. J., Rendell, H., Marseglia, E. A., Luff, B. J. & Townsend, P. D. 1993. Thermoluminescence Spectra of igneous quartz and hydrothermal quartz. *Physics and Chemistry of Minerals* **20**, 353–61.

Rovetta, M. R., Blacic, J. D., Hervig, R. L. & Holloway, J. R. 1989. An experimental study of hydroxyl in quartz using infrared spectroscopy and ion microprobe techniques. *Journal of Geophysical Research* **94**, 5840–50.

Ruffini, R., Borghi, A., Cossio, R., Olmi, F. & Vaggelli, G. 2002. Volcanic quartz growth zoning identified by cathodoluminescence and EPMA studies. *Mikrochemica Acta* **139**, 151–8.

Rusk, B. & Reed, M. 2002. Scanning electron microscope–cathodoluminescence analysis of quartz reveals complex growth histories in veins from the Butte porphyry copper deposit, Montana. *Geology* **30**, 727–30.

Schneider, J. 1993. Das lumineszenzaktive Strukturinventar von Quarzphänokristen in rhyolithen. *Göttinger Arbeiten zur Geologie und Paläontologie* **60**, 1–81.

Schrön, W., Schmädicke, E., Thomas, R. & Schmidt, W. 1988. Geochemische Untersuchungen an Pegmatitquarzen. *Zeitschrift für Geologische Wissenschaften* **16**, 229–44.

Sigel, G. H. Jr. & Marrone, M. J. 1981. Photoluminescence in as-drawn and irradiated silica optical fibres: An assessment of the role of nonbridging oxygen defect centres. *Journal of Non Crystalline Solids* **45**, 235–47.

Smith, V. C., Shane, P. & Nairn, I. A. 2004. Reactivation of a rhyolitic magma body by new rhyolitic intrusion before the 15·8 ka Rotora eruptive episode: implications for magma storage in the Okataina Volcanic Centre, New Zealand. *Journal of the Geological Society, London* **161**, 757–72.

Sonyushkin, V. E., Sukhorukov, Y. T. & Scherbakova, T. F. 1991. P–T environment of crystallization of quartz in granites of the Salmi batholith, Russian Karelia. *In* Haapala, I. & Rämö, O. T. (eds) *Symposium on Rapakivi Granites and Related Rocks. Abstracts, Geological Survey of Finland Guide* **34**, 47.

Sprunt, E. S. 1981. Causes of quartz cathodoluminescence colors. *Scanning Electron Microscopy* **1981**, 525–35.

Sprunt, E. S. & Nur, A. 1979. Microcracking and healing in granites: New evidence from cathodoluminescence. *Science* **205**, 495–7.

Stenina, N. G., Bazarov, L. S., Shcherbakova, M. Y. & Mashkovtsev, R. I. 1984. Structural state and diffusion of impurities in natural quartz of different genesis. *Physics and Chemistry of Minerals* **10**, 180–6.

Stevens Kalceff, M. A., Phillips, M. R., Moon, A. R. & Kalceff, W. 2000. Cathodoluminescence microcharacterization of silicon dioxide polymorphs. *In* Pagel, M., Barbin V., Blanc P. & Ohnenstetter, D. (eds) *Cathodoluminescence in Geosciences*, 193–224 Berlin, Heidelberg, New York: Springer.

Stevens Kalceff, M. A. & Phillips, M. R. 1995. Cathodoluminescence microcharacterization of the defect structure of quartz. *Physical Reviews B* **52**, 3122–34.

Suttner, L. & Leininger, R. K. 1972. Comparison of the trace element content of plutonic, volcanic and metamorphic quartz from Southwestern Montana. *Geological Society of America Bulletin* **83**, 1855–62.

Swanson, S. E. 1977. Relation of nucleation and crystal-growth to the development of granitic textures. *American Mineralogist* **62**, 966–78.

Sykes, M. L. & Holloway, J. R. 1987. Evolution of granitic magmas during ascent: a phase equilibrium model. *In* Mysen, B. O. (ed.) *Magmatic processes: Physicochemical Principles. Geochemical Society, Special Publication* **1**, 447–61. St Louis, Missouri: Geochemical Society.

Thomas, R. 1992. Results of investigations on melt inclusions in various magmatic rocks from the northern border of the Bohemian Massif. *In* Kukal, Z. (ed.) *Proceedings of the 1st International Conference about the Bohemian Massif*. Prague: Czech Geological Survey.

Thomas, R. 1994. Fluid evolution in relation to the emplacement of the Hercynian granites in the Erzgebirge region: a review of the melt and fluid inclusion evidence. *In* Seltmann, R., Möller, P. & Kämpf, H. (eds) *Metallogeny of Collisional Orogens*. Prague: Czech Geological Survey.

Tuttle, O. F. & Bowen, N. L. 1958. Origin of granite in the light of experimental studies in the system $NaAlSi_3O_8$–$KalSi_3O_8$–SiO_2–H_2O. *Geological Society of America Memoir* **74**, 1–153.

Valley, J. W. & Graham, C. M. 1996. Ion microprobe analysis of oxygen isotope ratios in quartz from Skye granite: healed microcracks, fluid flow, and hydrothermal exchange. *Contributions to Mineralogy and Petrology* **124**, 225–34.

Van den Kerkhof, A. M., Kronz, A. & Simon, K. 2001. Trace element redistribution in metamorphic quartz and fluid inclusion modification: observations by cathodoluminescence. XVI ECROFI, Porto 2001, *Departomento Geologica Memória* **7**, 447–50.

Van den Kerkhof, A. M., Kronz, A., Simon, K. & Scherer, T. 2004. Fluid-controlled quartz recovery in granulite as revealed by cathodoluminescence and trace element analysis (Bamble sector, Norway). *Contributions to Mineralogy and Petrology* **146**, 637–52.

Van den Kerkhof, A. M. & Grantham, G. H. 1999. Metamorphe charnockite in contact aureoles around intrusive enderbite from Natal, South Afrika. *Contributions to Mineralogy and Petrology* **137**, 115–32.

Van den Kerkhof, A. M. & Hein, U. 2001. Fluid inclusion petrography. *Lithos* **55**, 27–47.

Van den Kerkhof, A. M. & Müller, A. 1999. Fluid inclusion re-equilibration and trace element redistribution in quartz: observations by cathodoluminescence microscopy. ECROFI XV 1999 Abstracts and Program, Potsdam, *Terra Nostra* **99/6**, 161–2.

Vollbrecht, A., Rust, S. & Weber, K. 1991. Development of microcracks in granites during cooling and uplift: examples from the Hercynian basement in NE Bavaria, Germany. *Journal of Structural Geology* **13**, 787–99.

Vollbrecht, A., Olesen, N. O., Schmidt, N. H. & Weber, K. 1994. Crystallographic microcrack orientation in quartz from a granite – a combined ECP/U stage study. *In* Bunge, H. J., Siegesmund, S., Skrotzki, W. & Weber, K. (eds) *Textures of geological materials*, 345–52. Oberursel: DGM Informationsgesellschaft Verlag.

Wark, D. A., Hildreth, W., Spear, F. S., Cherniak, D. J. & Watson, E. B. 2007. Pre-eruption recharge of the Bishop magma system. *Geology* **35**, 235–8.

Wark, D. A. & Watson, E. B. 2006. TitaniQ: a titanium-in-quartz geothermometer. *Contributions to Mineralogy and Petrology* **152**, 743–54.

Watt, G. R., Wright, P., Galloway, S. & McLean, C. 1997. Cathodoluminescence and trace element zoning in quartz phenocrysts and xenocrysts. *Geochimica et Cosmochimica Acta* **61**, 4337–48.

Wiebe, R. A., Wark, D. A. & Hawkins, D. P. 2007. Insights from quartz cathodoluminescence zoning into crystallization of the Vinalhaven granite, coastal Maine. *Contributions to Mineralogy and Petrology* **154**, 439–53.

Yang, X. H., Townsend, P. D. & Holgate, S. A. 1994. Cathodoluminescence and depth profiles of tin in float glass. *Journal of Physics D* **27**, 1757–62.

Yoder, H. R. 1950. High-low quartz inversion up to 10,000 bars. *Transactions, American Geophysical Union* **31**, 827–35.

MS received 3 December 2007. Accepted for publication 2 June 2008 (Stellenbosch); 15 January 2009 (RSE).

Earth and Environmental Science Transactions of the Royal Society of Edinburgh, **100**, 205–218, 2010 (for 2009)

Trace element constraints on mid-crustal partial melting processes – A garnet ionprobe study from polyphase migmatites (Damara orogen, Namibia)

C. Jung[1], S. Jung[2,3], E. Hellebrand[2,4] and E. Hoffer[1]

[1] Fachbereich Geowissenschaften, Philipps Universität Marburg, 35032 Marburg, FRG

[2] Max-Planck-Institut für Chemie, Abt. Geochemie, Postfach 3060, 55020 Mainz, FRG

[3] Department Geowissenschaften, Mineralogisch-Petrographisches Institut, Universität Hamburg, 20146 Hamburg, FRG
Email: stefan.jung@mineralogie.uni-hamburg.de

[4] SOEST – Department of Geology and Geophysics, University of Hawaii, USA

ABSTRACT: Trace element abundances in garnet from a polyphase migmatite were measured by secondary ion mass spectrometry (SIMS) in order to identify some of the effective variables on the trace element distribution between garnet and melanosome or leucosome. In general, garnet is zoned with respect to REE, in which garnet cores are enriched by a factor of 2–3 relative to the rims. For an inclusion-rich garnet from the melanosome, equilibrium distribution following a simple Rayleigh fractionation is responsible for the decreasing concentrations in REE from core to rim. Inclusion-poor garnet from the same melanosome located in the vicinity of the leucosomes shows distinct enrichment and depletion patterns for REE from core to rim. These features suggest disequilibrium between garnet and the host rock which, in this case, could have been an *in-situ* derived melt. This would probably indicate a period of open-system behaviour at a time when the garnet, originally nucleated in the metamorphic environment reacted with the melt. In addition, non-gradual variation in trace element abundances between core and rim may suggest variable garnet growth rates. Inclusion-free garnet from the leucosome, interpreted to have crystallised in the presence of a melt, has a small core with high REE abundances and a broad rim with lower REE abundances. Here, crystal-liquid diffusion-controlled partitioning is a likely process to explain the trace element variation.

KEY WORDS: *in situ* partial melting, granites, migmatites, trace element composition

Garnet is the major mineral used for the reconstruction of P–T paths because it is involved in a number of reactions useful for thermobarometry (e.g. Essene 1989). Consequently, the major element zoning of garnet has been widely used to investigate the P–T conditions of regional metamorphic terranes (Tracy 1982; Spear & Selverstone 1983; Spear *et al.* 1984). The chemical signatures of the early stages of regional metamorphism are often preserved up to the lower amphibolite facies, due to the slow diffusivities of the major cations Fe, Mg, Mn and Ca. However, prograde chemical zoning is rare in high-grade garnet of amphibolite- to granulite-facies terranes, due to enhanced intracrystalline diffusion at higher temperatures (Spear & Florence 1992). On the other hand, it has been demonstrated that trace element zoning in garnet is often more pronounced than major element zoning (Hickmott *et al.* 1987; Hickmott & Shimizu 1990; Hickmott & Spear 1992; Spear & Kohn 1996; Chernoff & Carlson 1999; Otamendi *et al.* 2002). This implies that trace elements may potentially be less sensitive to chemical changes in rocks than major elements. Accurate interpretation of major and trace element zoning in garnet can therefore lead to significantly improved understanding of the evolutionary path of metamorphism and hence of the tectonic evolution of mountain belts.

Prograde heating of crustal segments will ultimately result in fluid-absent partial melting of metasedimentary rocks, producing a granitic melt and an aluminous residue in which the restitic mineral assemblage will control the trace element concentration of the melt. The mineralogical composition of the residual assemblage is dependent on the nature of the melting reaction and the pressure at which melting occurs. Garnet is a common refractory mineral phase that may be present in the high-grade metasedimentary protolith, or a product of incongruent melting reactions at higher metamorphic grade. A detailed knowledge of the distribution of trace elements between garnet, metamorphic host rock or melt is therefore critical for trace element modelling of anatectic crustal melts. In order to identify some of the effective variables on the trace element distribution between garnet and the host rock, this study presents trace element data on garnet measured by SIMS from a polyphase migmatite terrane from the Damara orogen (Namibia). It is shown that trace element variation during garnet growth during regional metamorphism and melting provides additional constraints on the garnet-forming process with important implications for the geochemical signature of granitic melts.

© 2009 The Royal Society of Edinburgh. doi:10.1017/S1755691009016107

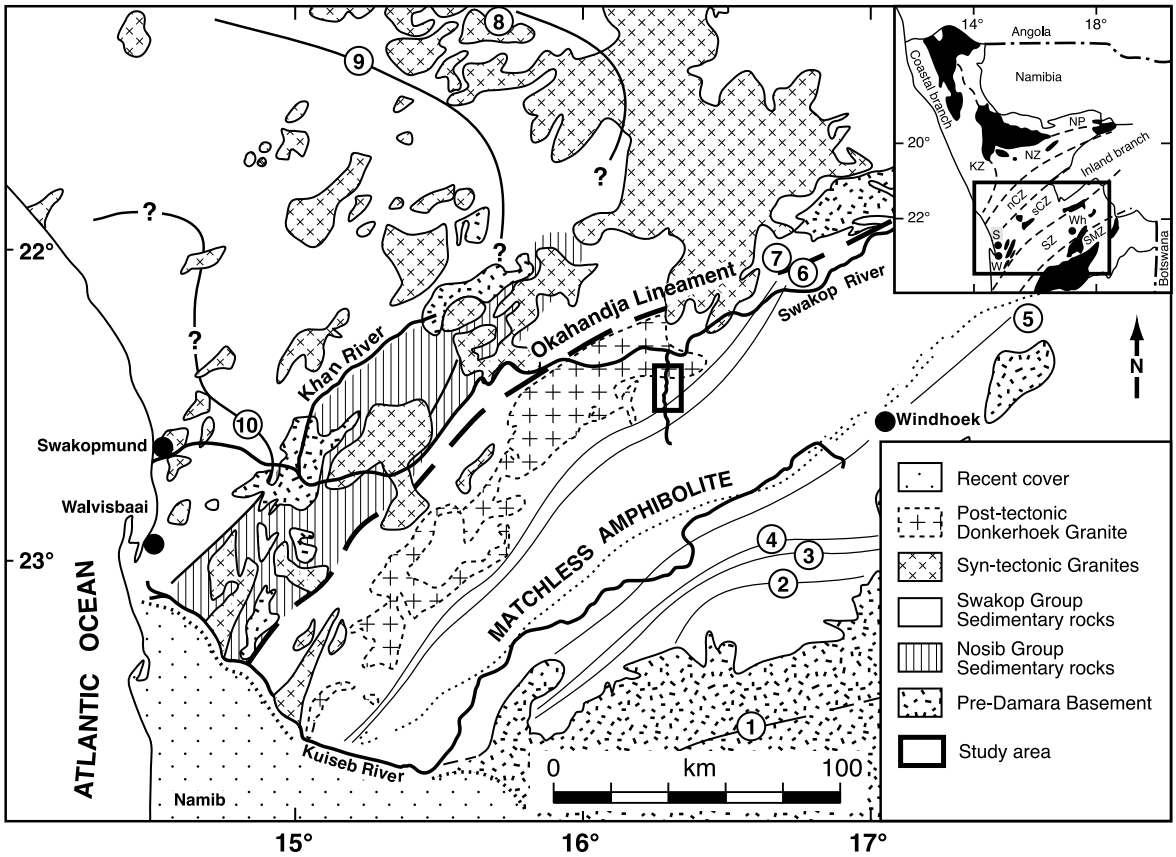

Figure 1 Generalised geological map showing the study area within the transition zone between the lower part of the southern Central Zone and Southern Zone of the Damara orogen, Namibia. Abbreviations in inset: KZ=Kaoko Zone; NP=Northern Platform; NZ=Northern Zone; nCZ=northern central Zone; sCZ=southern Central Zone; SZ=Southern Zone; SMZ=Southern Margin Zone. Isograd map (Hartmann *et al.* 1983) gives the distribution of pan-African regional metamorphic isograds within the southern and central Damara orogen. Isograds: (1) biotite-in; (2) garnet-in; (3) staurolite-in; (4) kyanite-in; (5) cordierite-in; (6) andalusite <--->sillimanite; (7) sillimanite-in according to staurolite-breakdown; (8) partial melting due to: muscovite+plagioclase+quartz+H_2O <--->melt+sillimanite; (9) K-feldspar+cordierite-in; (10) partial melting due to: biotite +K-feldspar+plagioclase+quartz+cordierite <--->melt+garnet.

1. Geological setting

The Damara orogen of Namibia comprises a deeply eroded section of a Pan-African mobile belt that can be divided into a N–S-trending coastal branch, the Kaoko belt, and a NE–SW-trending intracontinental branch (see inset to Fig. 1). This mobile belt has been divided into several zones based mainly on stratigraphy, metamorphic grade, structure and geochronology (Miller 1983). The intrusive rocks record ages between 750 Ma and 480 Ma and crop out over an area of approximately 75 000 km^2 (Fig.1). Granites are the most common igneous rock type (c. 94%) and the remaining intrusions are equally divided between diorite and tonalite/granodiorite (Miller 1983). Pre-Damara basement gneisses are overlain by various metasedimentary sequences containing quartzose sandstones, arkoses, schists and calc-silicate rocks, marble, conglomerate, metamorphosed glaciogenic diamictites, banded iron-stones, Al-rich metapelite and carbonates.

In the Central Zone (Fig. 1), the metamorphic grade increases from east to west, reaching high-grade conditions with local partial melting in the coastal area (Hartmann *et al.* 1983). Early maximum estimates for the peak metamorphic temperatures were ca. 645°C at 3 ± 1 kbar obtained on impure marbles (Puhan 1983) and ca. 650°C based on oxygen isotope fractionation in a variety of metasedimentary and metaigneous rocks (Hoernes & Hoffer 1979). More recently, pressure–temperature estimates were substantially revised indicating low-pressure high-temperature granulite facies conditions with temperatures between 700–750°C at 5–6 kbar (Masberg *et al.* 1992; Jung & Mezger 2003; Ward *et al.* 2008). These new p–t estimates are generally considered to be too low to cause widespread biotite dehydration melting, however, migmatisation is a local phenomenon and is not accompanied by large volumes of newly-formed melt. There is some disagreement as to whether the initial steps of melting were caused by muscovite-dehydration melting, since metamorphic K-feldspar is a common mineral in high-grade metapelites (Jung *et al.* 1999; Jung & Mezger 2003). On the other hand, initial partial melting under water-saturated conditions is a possibility; in this case the water may have come from some of the plutons associated with the migmatites. One major step forward in the interpretation of the metamorphic history of the Damara orogen is provided by Ward *et al.* (2008), who showed that fluid-assisted partial melting involving biotite breakdown is a possibility to explain some of the migmatites in the central Damara orogen. The large amount of sizeable plutons observed in the Central Damara orogen originated by partial melting processes in the deeper crust where temperatures in excess of 800–850°C are not unlikely.

To the south-east, there is a gradation into the Okahandja Lineament Zone that separates the Central Zone from the Southern Zone (Fig. 1). In the Southern Zone, regional metamorphism is characterised by a Barrovian-type sequence, with a general increase in the metamorphic grade from south to north. The metamorphic conditions range from low to medium pressures and reached up to 8 kbar at maximum temperatures of 600°C. There is evidence that suggests that

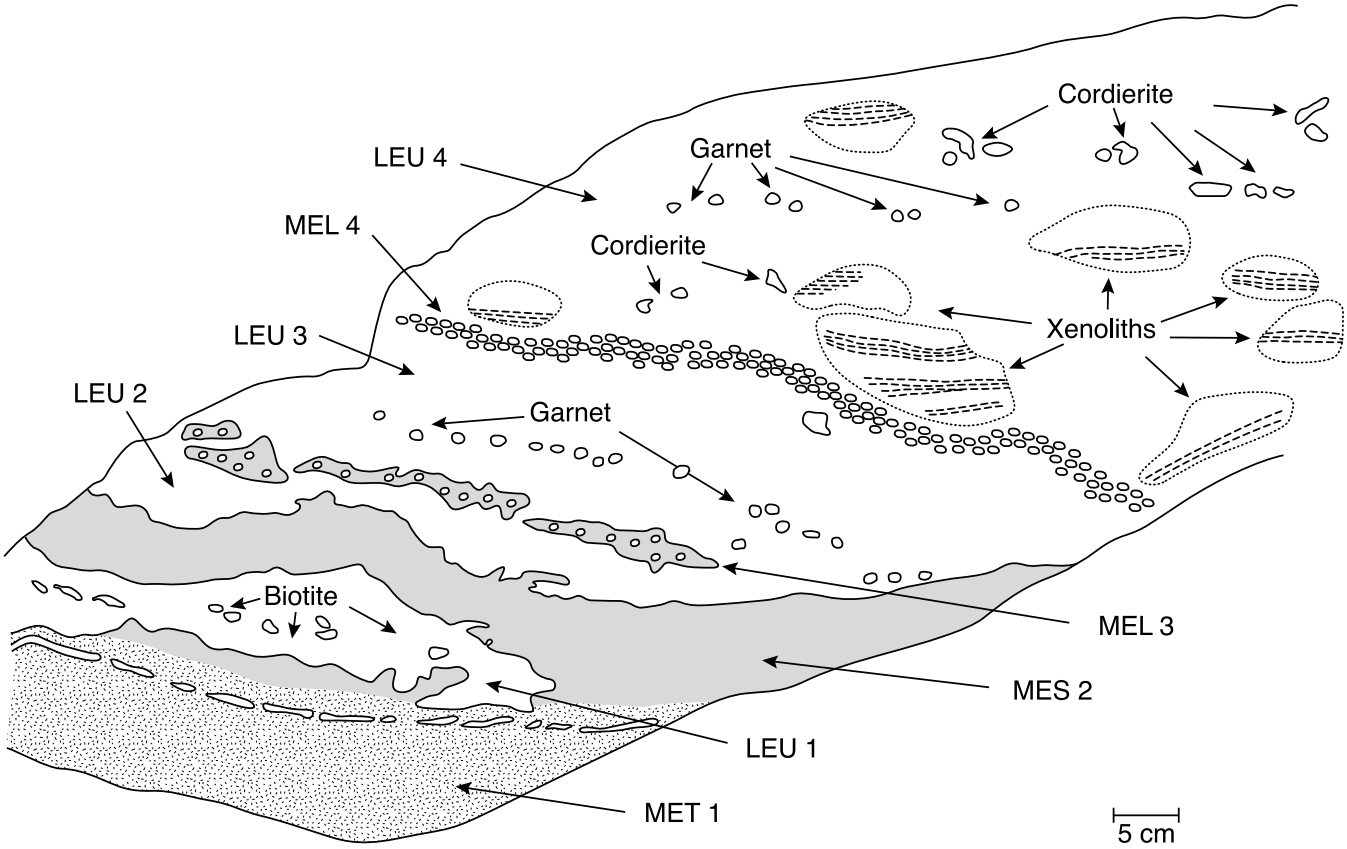

Figure 2 Sketch of the migmatite sample from the Davetsaub area showing the different lithological units.

regional metamorphism in the Southern Zone is more or less coeval with regional metamorphism in the Central Zone. This interpretation is based on U–Pb and Pb–Pb garnet and staurolite ages of 550 ± 10 Ma and 480 ± 20 Ma (Jung 2005), similar to the range of U–Pb monazite and Sm–Nd garnet ages obtained from metapelites and migmatites from the Central Zone. U–Pb garnet and staurolite ages must be interpreted with caution, since any incorporated high-U/Pb microinclusion may totally cover the initial radiogenic isotope composition of garnet and staurolite. However, in the present case, $^{206}Pb/^{204}Pb$ ratios of garnet and staurolite are <50, suggesting that high U/Pb inclusions do not play a major role here and the ages, although associated with a relatively large error, date the time of garnet and staurolite growth.

Rb–Sr and K–Ar biotite ages indicate cooling to 350–300°C between 480 Ma and 460 Ma (Miller 1983). More recently, Gray *et al*. (2006) obtained Ar–Ar isotope data on white mica and biotite, indicating cooling to 300–350°C between 495 Ma and 480 Ma. Intrusion of large volumes of granitic rocks are absent even in the highest grade zone of the Southern Damara orogen.

The formation of the migmatites of Davetsaub and Nomatsaus (22·4°S/16·3°E, Fig. 1) was originally thought to be related to the intrusion of the peak-metamorphic post-deformational Donkerhoek granodiorite (Nieberding 1976; Saywer 1981). Since the granodiorite has no extensive thermal aureole, the country rocks are assumed to have been still hot at the time of emplacement. Based on the geological map (Miller 1983), isotopic investigations by Kukla (1993), and detailed field investigations by the present authors, it is more likely that the Davetsaub area represents a portion of the Damaran metasedimentary rocks where intrusion of older granites produced various types of migmatites. Kukla (1993) presented structural evidence that the anatectic event that generated the migmatites occurred relatively late within the deformational history of the Damara orogen, but clearly predates the intrusion of the Donkerhoek granodiorite.

2. Description of the migmatite

Macroscopic and mesoscopic descriptions of the migmatites from the Davetsaub and Nomatsaus areas have been published by Kukla (1993), Kukla *et al*. (1991) and Jung *et al*. (1998). Additional information about the mineralogical composition of the different sub-domains of the migmatite (mesosome, melanosome, leucosome) is given in Jung *et al*. (1998). Metasedimentary and migmatitic rocks outcropping at the Davetsaub and Nomatsaus areas (Fig. 1) are fine to medium-grained dark-grey to dark-brown pelitic gneisses with a fabric defined by alternating biotite-bearing and biotite-poor domains. Most pelitic gneisses are impregnated by pegmatitic material, as well as concordant to discordant leucosomes. Banded migmatites are commonly folded, and most of the pegmatites cut the main foliation. Mesosomes (nomenclature according to Brown 1983) and leucosomes are well segregated and locally separated by biotite–garnet–cordierite-bearing melanosomes. Some leucocratic layers contain isolated xenoliths with the mineral assemblage quartz+plagioclase+sillimanite ± garnet ± K-feldspar ± biotite (Fig. 2). In some areas, the proportion of leucocratic material dominates, so that some melanosomes appear as rafts surrounded by leucosome material and the resulting rock is a diatexite. In the biotite-bearing domains of the mesosomes and melanosomes, the fabric is defined by aligned biotite flakes, biotite–sillimanite intergrowths, xenomorphic garnet porphyroblasts with inclusions of biotite, sillimanite, plagioclase and spinel and poikilitic, elongated, partly pinitised cordierite porphyroblasts with inclusions of sillimanite. Garnet has abundant (<30 μm) inclusions of zircon and monazite. In the biotite-poor domains of

some mesosomes, ribboned quartz aggregates and relict plagioclase porphyroblasts dominate the fabric.

Textural relations preserved within the pelitic migmatites suggest that the assemblage quartz+plagioclase+biotite+cordierite$_{(I)}$+sillimanite was developed at an early stage in the metamorphic history. Subsequently, the growth of garnet ± spinel at the expense of biotite and/or cordierite can be observed. Potential coexistence of spinel and quartz could be interpreted to be indicative of T>800°C during an earlier portion of the metamorphic path, although the significant gahnite component in the spinel suggests stability with quartz could have been possible at slightly lower temperatures (Vielzeuf 1983). There is no petrographic evidence for the coexistence of spinel and quartz, judging from the occurrence of spinel exclusively in garnet and, therefore, high grade metamorphism and partial melting must have occurred prior to the formation of the observed mineral assemblage, when aH_2O was higher. Melting could have been initiated at ca. 670°C at 3–5 kbar, producing small amounts of liquid while efficiently purging the remaining rock of H_2O (Thompson 1982). This initial melting step could have been water-saturated, in which the water needed for H_2O-saturated melting was derived from the nearby plutons. It is, however, difficult or even impossible to prove whether initial melting was water-saturated in rocks that have evolved to higher temperatures, and especially in those rocks that have lost melt. Unfortunately, no precise radiometric age determinations from all plutons in this area are available. In some layers, relict garnet porphyroblasts are often rimmed and partly replaced by coronas of cordierite$_{(II)}$ suggesting decompression later in the metamorphic history.

Garnet in the leucocratic layers of the migmatites is idioblastic and inclusion-free and remained apparently unreacted, or is only locally replaced by an aggregate consisting of green biotite and Ab-rich plagioclase. Fresh cordierite, sometimes twinned, occurs as large sub-idiomorphic grains, with rare inclusions of sillimanite. Minor amounts of late muscovite occur within the leucocratic layers, but not in the metapelitic domains. No prograde andalusite, staurolite or muscovite has been found in the pelitic migmatites and, interestingly no K-feldspar has been found in the residual portions of the migmatites. The high proportion of sillimanite and cordierite/garnet, the fact that metamorphic conditions probably exceed the stability of muscovite plus quartz, and the lack of K-feldspar in the most residual melanosomes suggests that a melt phase coexisted with the melanosomes. This melt phase was subsequently extracted and probably mixed with the leucosomes, since some of these leucosomes are clearly intrusive from the nearby plutons. The lack of K-feldspar and the decreasing abundance of plagioclase and quartz among the mesosomes and melanosomes (see table 1 in Jung *et al*. 1998) is also compatible with the view that a melt phase was extracted. Some of the plagioclase and K-feldspar may have formed cumulates in the leucosomes, since these leucosomes have small but discernable positive Eu anomalies. However, due to the absence of cumulate textures, the limited extraction distances of the leucosomes (some are only centimetres away from the melanosomes), the gradual nature of some leucosome-melanosome pairs and the evidence of progressive entrainment of xenoliths or wall rock material rather then fractional crystallisation, it is suggested that a cumulus nature of the leucosomes is, at least in part, unlikely. In addition, the amount of K-feldspar and plagioclase is way too large to be solely related to the inferred amount of these minerals in the melanosomes and consequently, most of the K-feldspar and plagioclase must be attributed to the original composition of the leucosomes. Note that a complex contamination–accumulation modelling was performed to explain the composition of some of the larger leucosomes associated with the most residual melanosomes (Jung *et al*. 1998) and up to 10 wt.% of K-feldspar/plagioclase may be regarded as accumulated minerals.

It is suggested that consumption of early muscovite+quartz+plagioclase+H_2O led to the formation of a first melt, but the appearance of spinel, garnet and cordierite indicates that also a biotite-dehydration melting reaction was operative. It is therefore reasonable to assume that melt production and extraction probably occurred episodically, both at the maximum P–T conditions and during decompression of the rocks. In summary, petrographic evidence, and thermobarometric constraints, indicate that the migmatites outcropping at the Davetsaub and Nomatsaus areas experienced upper amphibolite to lower granulite facies conditions with temperatures approaching 720–750°C at 4–6 kbars (Saywer 1981; Kukla *et al*. 1991; Jung *et al*. 1998). The major and trace element abundances as well as the Nd, Sr and oxygen isotope compositions suggest that mesosome MES 2, and the melanosomes MEL 3 and MEL 4 (Fig. 2) are strongly residual rocks. The chemical and isotopic composition of the leucosomes can be best explained by a complex partial melting–mixing–accumulation process (Jung *et al*. 1998).

3. Geochronology of the migmatite

Early age determinations on the migmatites from the Davetsaub area yielded a Rb–Sr whole-rock isochron age of 505 ± 5 Ma (Blaxland *et al*. 1979; Haack *et al*. 1982) consistent with a monazite age of 505 ± 4 Ma given by Kukla *et al*. (1991) for the intrusion of a late-tectonic granite in this area. Rb–Sr whole rock ages are 523 ± 8 Ma and 521 ± 15 Ma for the Donkerhoek granite in this area (Blaxland *et al*. 1979). U–Pb monazite ages from the migmatites give ages between 525 ± 2 Ma and 521 ± 2 Ma for composite migmatites and between 521 ± 2 Ma and 518 ± 2 Ma for monazite from neosomes (Kukla *et al*. 1991) providing a lower limit for the peak of metamorphism. More recently, the time of high-grade regional metamorphism and the duration of regional metamorphic events were constrained by Sm–Nd (garnet), U–Pb (monazite) and Rb–Sr (biotite) ages obtained from a composite migmatite sample (Jung & Mezger 2001). Sm–Nd garnet whole rock ages for a strongly restitic melanosome and an adjacent intrusive leucosome yield ages of 534 ± 5 Ma, 528 ± 11 Ma and 539 ± 8 Ma. These results provide substantial evidence for pre-500 Ma Pan-African regional metamorphism and melting for this segment of the orogen. Other parts of the migmatite yielded apparently younger Sm–Nd garnet whole rock ages of 488 ± 9 Ma for melanosome and 496 ± 10 Ma, 492 ± 5 Ma and 511 ± 16 Ma for the corresponding leucosomes. Garnet from one xenolith within the leucosomes yielded an age of 497 ± 2 Ma. Monazite from the leucosomes records $^{207}Pb/^{235}U$ ages of between 536 ± 1 Ma and 529 ± 1 Ma, indicating that this monazite represent incorporated residual material from the first melting event. Monazite from the mesosome and the melanosome gives $^{207}Pb/^{235}U$ ages of between 523 ± 1 Ma and 531 ± 1 Ma, broadly similar to the monazite ages from the leucosomes. The apparently unreacted metasedimentary rock MET 1 yielded a $^{207}Pb/^{235}U$ monazite age of 508 ± 2 Ma, which probably indicate another later thermal event. Taken together, these ages indicate that high-grade metamorphism started at c. 535 Ma (or earlier) and was followed by thermal events between c. 520 Ma and c. 490 Ma. Rb–Sr biotite ages from the different layers of the migmatite are c. 488 Ma, 469 Ma and 473 Ma.

These different ages indicate late-stage disturbance of the Rb–Sr isotopic system on the sub-sample scale. Nevertheless, these ages are close to the youngest Sm–Nd garnet ages indicating rapid cooling rates between 13–20°C/Ma and fast uplift of this segment of the crust (Jung & Mezger 2001).

4. Results

4.1. Garnet major element composition

Garnet is predominantly an almandine–pyrope–spessartine solid solution with a minor grossular component. Inclusion-rich garnet from melanosome MEL 3 has the composition $alm_{69}py_{16}sp_{12}gr_3$ and the inclusion-poor garnet from the same melanosome has the composition $alm_{71}py_{11}sp_{16}gr_2$. Inclusion-free garnet from the melanosome has the composition $alm_{70}py_{17}sp_{11}gr_2$. The garnets from the leucosome and the melanosome show rather similar zoning profiles, with flat element distributions over most of the crystal and increasing Fe/Mg at the outermost rim. There is no pronounced zoning with respect to the grossular component. Details are given in Jung *et al.* (1998).

4.2. Garnet trace element composition

Analytical details are summarised in the Appendix (see section 8). Three texturally distinct garnets can be distinguished, an inclusion-rich (Fig. 3a) and inclusion-poor garnet (Fig. 3b) within the melanosome and an apparently inclusion-free garnet within the leucosome (Fig. 3c). The garnets have a 10^{-3} –10^3 CI-normalised range in REE abundances and steep LREE-depleted and HREE-enriched element patterns (Fig. 4). A negative Eu anomaly of variable magnitude is developed in the garnets.

4.2.1. Inclusion-rich garnet (melanosome). This garnet (Fig. 3a) has a core composition enriched in HREE+Y and a rim composition that is depleted in HREE+Y (Fig. 4a and b). The core–rim variation is gradual, although Yb and Er display some more enriched domains in the garnet core. Furthermore, the zoning is significantly less pronounced for the middle REE (rim/core ~0·6–1·0 for Sm, Eu, Gd), compared to the more compatible heavy REE (rim/core ~0·2–0·5 for Dy–Yb) and Y (rim/core: 0·5). Furthermore, it shows an irregular or flat distribution of Ti, Cr, Zr and Sc over the crystal, but a tendency for enrichment in V (and to lesser extent Na) can be observed towards the rim of the crystal (Table 1). Asymmetric distribution of Zr of the crystal seems to indicate contamination with micro-inclusions of zircon. Sr seems to be slightly enriched in the core relative to the rim, although the concentrations appear to be similar within error. The distribution of Sm follows roughly that for HREE and Y, with a peak around the core region and depletion in Sm towards the rim. On the other hand, Nd shows a broad core region with low concentrations and a rim composition with elevated concentrations (Fig. 4c). Towards the outermost rim, Nd concentrations decrease again. However, fractionation of LREE ($(Sm/Nd)_N$ ratio, where N denotes normalisation to chondrite, according to Boynton 1984) seems to be more or less constant throughout the crystal (Table 1). On the other hand, fractionation of HREE (Yb/Dy and Yb/Er ratios) is more pronounced for the core than for the rim (Fig. 5). The magnitude of the negative Eu anomaly ranges from 0·03 to 0·09 with a tendency to decrease towards the rim.

4.2.2. Inclusion-poor garnet (melanosome). This garnet has also a core composition enriched in HREE+Y and a rim composition that is depleted in HREE+Y (Fig. 6a and b). Both types of garnet have roughly similar grain sizes and equally spaced ionprobe spots. Therefore, both analysed garnets are comparable and, in contrast to the inclusion-rich garnet, the HREE+Y-enriched core composition of the inclusion-poor garnet appears to be somewhat larger than the HREE+Y-depleted rim. Core–rim variation of HREE+Y is also gradual, but in contrast to the inclusion-rich garnet, the inclusion-poor garnet has a core composition that is slightly depleted in HREE+Y and also displays HREE enrichment at the outermost rim. Ignoring the HREE-enriched outermost rim, HREE concentrations are similar to both garnet types. In

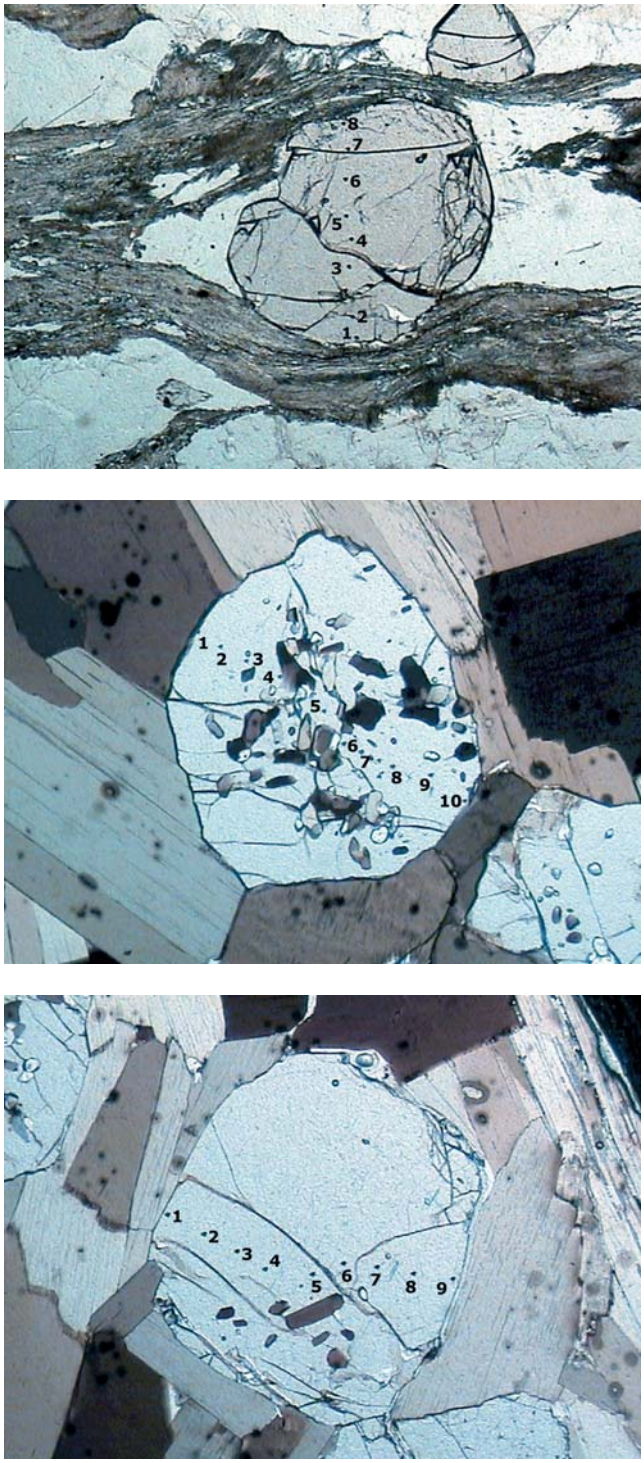

Figure 3 Photographs of garnet from the different samples with the approximate location of the spots analysed by ion microprobe: (top) inclusion-rich garnet from melanosome MEL 3; (middle) inclusion-poor garnet from melanosome MEL 3; (bottom) inclusion-free garnet from leucosome LEU 3. Lower side of each photograph is approximately 2 mm.

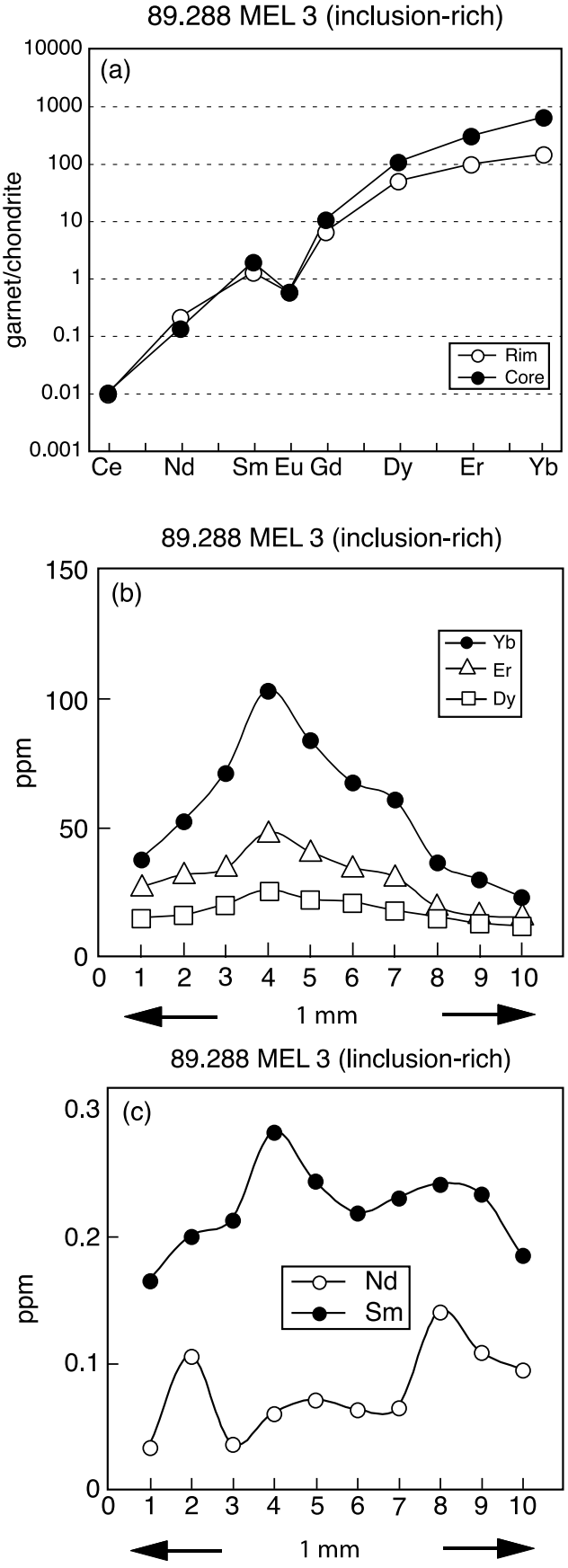

Figure 4 (a) Chondrite-normalised Rare Earth Element plot for core and rim for inclusion-rich garnet from melanosome MEL 3. (b) HREE variation along a rim-core–rim profile. (c) Sm and Nd variation along a rim-core–rim profile. Chondrite values are from Boynton (1984).

contrast to the inclusion-rich garnet from the melanosome, REE zoning is similar for the MREE (rim/core ~0·3–0·8 for Sm, Eu, Gd), and for the more compatible HREE (rim/core ~0·3–0·7 for Dy–Yb) and Y (rim/core: 0·3). Whereas in the inclusion-rich garnet, the core–rim distribution increases from Yb (core/rim: 0·22) and Er (core/rim: 0·32) to Dy (core/rim: 0·46), the core–rim variation in the inclusion-poor garnet decreases from Yb (core/rim: 0·68), Er (core/rim: 0·45) and Dy (core/rim: 0·28). Yttrium concentrations are similar at the outermost rim of both garnet types, but are enriched by a factor of two in the core of the inclusion-poor garnet. In contrast to the inclusion-rich garnet from the melanosome, concentration profiles for Ti, V, Cr, Zr and Sr show enriched core compositions and depleted rim compositions. Zr abundances are highly symmetric and cannot be explained by contamination with micro-inclusions of zircon. For Ti, there is a pronounced peak in the core region, whereas the concentration profiles for V, Cr, and Zr are rather flat. Sr displays re-enrichment at the outermost rim. Sc shows a rather flat concentration profile, with lower concentrations in the core than in the rim (Table 1). The distribution of Sm and Nd follows roughly that for HREE and Y, with low values in the core region followed by enrichment of Sm and Nd at the rim. At the outermost rim, Sm and Nd concentrations are significantly lower (Fig. 6c). Fractionation of LREE ($(Sm/Nd)_N$) shows a core with lower ratios and a rim with higher ratios. The outermost rim shows significantly lower ratios than both, core and rim. Fractionation of HREE (Yb/Dy and Yb/Er ratios) shows elevated ratios in the core and lower values in the rim. The outermost rim shows significantly higher ratios than in the core and rim (Fig. 7). The magnitude of the negative Eu anomaly ranges from 0·01 to 0·06 with a tendency to decrease towards the rim.

4.2.3. Inclusion-free garnet (leucosome). Like the other two garnet types from the melanosome, the garnet from the leucosome has a core composition enriched in HREE+Y and a rim composition that is depleted in HREE+Y (Fig. 8a, b). Compared to the other garnet, the trace element-enriched core region is only 1/3 that of the total garnet. Rare Earth Element zoning is similar or less pronounced for the middle REE (rim/core ~0·3–0·7 for Sm, Eu, Gd), compared to the more compatible heavy REE (rim/core ~0·3–0·2 for Dy–Yb) and Y (rim/core: 0·3). The core–rim variation in HREE and Y is gradual. In contrast to the other garnets, other trace elements exhibit either pronounced core–rim depletion (Sr, Zr, Sc) or core–rim enrichment (Ti, V, Cr, Na; Table 1). Again, the core is enriched in Zr. If contamination by micro-inclusions is responsible for this selective enrichment, it would be highly fortuitous that this occurred exactly in the core region. In some cases, elements may show enrichment (Sc) or depletion (Na) at the outermost rim. The distribution of Sm and Nd follows roughly that for HREE and Y, with high values in the core region followed by depletion of Sm and Nd at the rim. At the outermost rim, Sm and Nd concentrations are slightly enriched (Fig. 8c). Fractionation of LREE ($(Sm/Nd)_N$) shows a core with lower ratios and a rim with higher ratios. Fractionation of HREE (Yb/Dy and Yb/Er ratios) shows low ratios in the core followed by elevated values towards the rim. The outermost rim shows similar low ratios than in the core (Fig. 9). As in the inclusion-poor garnet from the melanosome, the magnitude of the negative Eu anomaly ranges from 0·01 to 0·06, with a tendency to decrease towards the rim.

5. Discussion

5.1. Garnet Gd/Dy geothermometry

Heavy Rare Earth Element variation, i.e. the Gd/Dy ratio, can be used to constrain the equilibration pressure that prevailed

Table 1 Trace element composition (in ppm) of garnet from melanosome MEL 3 and leucosome LEU 3. For sample reference see Jung *et al.* (1998).

Inclusion-rich garnet MEL 3	Rim			Core						Rim
Na	90·2	87·9	54·8	49·0	47·5	87·5	144	141	105	120
Sc	140	155	141	164	157	147	137	135	144	124
Ti	17·5	22·8	23·0	23·7	23·2	29·0	34·1	55·1	50·8	40·6
V	18·6	19·8	14·3	13·7	13·6	15·1	17·8	20·7	18·2	17·8
Cr	67·7	79·3	74·1	70·5	66·6	76·9	88·5	79·6	70·5	87·2
Sr	0·16	0·15	0·17	0·17	0·17	0·16	0·15	0·15	0·15	0·15
Y	161	187	209	287	241	227	199	168	133	139
Zr	12·2	14·2	3·8	3·80	2·12	24·3	41·0	82·9	55·1	50·2
La	0·01	0·11	0·00	0·00	0·00	0·00	0·00	0·00	0·00	0·00
Ce	0·01	0·18	0·01	0·01	0·00	0·00	0·00	0·01	0·00	0·01
Nd	0·03	0·11	0·04	0·06	0·07	0·06	0·07	0·14	0·11	0·09
Sm	0·17	0·20	0·21	0·28	0·24	0·22	0·23	0·24	0·23	0·19
Eu	0·027	0·014	0·024	0·032	0·025	0·029	0·016	0·026	0·045	0·032
Gd	1·28	1·32	1·60	2·06	1·94	1·78	1·34	1·54	1·45	1·26
Dy	15·0	16·2	20·2	25·7	22·3	21·1	17·9	15·4	12·9	11·9
Er	26·8	31·7	33·8	47·9	40·7	34·3	31·0	19·3	15·7	15·3
Yb	37·7	52·4	71·1	103·0	83·9	67·6	60·9	36·6	30·0	23·2
Sm/Nd(N)	4·9	1·9	5·9	4·7	3·4	3·5	3·5	1·7	2·1	2·0
Yb/Dy	2·5	3·2	3·5	4·0	3·8	3·2	3·4	2·4	2·3	1·9
Yb/Er	1·4	1·7	2·1	2·2	2·1	2·0	2·0	1·9	1·9	1·5

Inclusion-poor garnet MEL 3	Rim			Core					Rim
Na	89·9	95·6	83·6	90·2	96·4	94·9	87·4	80·9	71·9
Sc	124	88·0	91·5	98·6	97·8	104	107	122	149
Ti	41·9	161	202	164	613	123	101	217	40·8
V	15·9	19·2	21·3	24·3	23·4	23·2	25·2	23·3	16·7
Cr	81·5	104	105	124	113	114	101	91·2	83·6
Sr	0·19	0·16	0·18	0·20	0·23	0·24	0·18	0·18	0·23
Y	179	182	422	606	544	654	534	401	406
Zr	16·9	45·0	55·2	55·8	53·2	54·5	53·4	56·1	13·1
La	0·00	0·00	0·01	0·01	0·01	0·00	0·01	0·00	0·01
Ce	0·00	0·01	0·01	0·01	0·01	0·01	0·02	0·01	0·01
Nd	0·06	0·18	0·29	0·23	0·12	0·15	0·21	0·34	0·09
Sm	0·27	0·71	1·57	1·20	0·66	0·84	1·00	1·69	0·26
Eu	0·035	0·084	0·101	0·034	0·044	0·040	0·035	0·095	0·025
Gd	2·41	4·93	10·9	11·1	8·41	9·78	11·2	11·8	3·43
Dy	20·2	28·0	64·9	83·2	71·6	86·0	81·5	60·7	44·9
Er	33·7	21·6	44·4	83·0	73·7	90·3	55·8	39·4	102
Yb	69·7	22·7	43·0	107	102	124	50·5	36·7	220
Sm/Nd(N)	4·8	4·0	5·3	5·3	5·6	5·4	4·7	5·0	2·8
Yb/Dy	3·4	0·8	0·7	1·3	1·4	1·4	0·6	0·6	4·9
Yb/Er	2·1	1·0	1·0	1·3	1·4	1·4	0·9	0·9	2·2

during formation of the garnet (Bea *et al.* 1997). The studied garnets from the melanosome and leucosome show Gd and Dy zoning similar to the zoning observed for the more compatible HREE and, consequently, this type of zoning is interpreted to be the result of Rayleigh-type fractionation during growth of the garnet. It seems that Gd and Dy behave similarly and therefore Gd/Dy ratios are fairly constant over the crystal. Using the equation derived by Bea *et al.* (1997), average apparent equilibration pressures are $4{\cdot}1 \pm 0{\cdot}04$ kbar for the inclusion-rich garnet from the melanosome, $4{\cdot}4 \pm 0{\cdot}2$ kbar for the inclusion-poor garnet from the melanosome and $4{\cdot}2 \pm 0{\cdot}1$ kbar for the inclusion-free garnet from the leucosome. These pressures are slightly lower than the pressures of $5{\cdot}2 \pm 0{\cdot}4$ kbar and $5{\cdot}6 \pm 0{\cdot}2$ kbar obtained by conventional GASP and Grt–Crd cation exchange barometry (Jung *et al.* 1998).

5.2. Inclusion-rich garnet (melanosome)

The inclusion-rich garnet from the melanosome is part of a restitic mineral assemblage consisting of garnet, biotite, sillimanite, spinel and quartz (Jung *et al.* 1998). Based on distinct Sm–Nd garnet-whole rock ages and U–Pb monazite ages, the migmatite is considered to have undergone multiple high-grade episodes, including one or more metamorphic and/or anatectic events. With respect to the garnet, it is likely that the actual mineralogical composition of the melanosome records only the latter of these episodes. This suggestion is supported by a Sm–Nd garnet whole rock age of 488 ± 9 Ma, which is the youngest age among the different parts of the migmatite (Jung & Mezger 2001). Therefore, it is suggested that the garnet trace element composition can be used to place constraints on the garnet-forming process, namely growth of garnet in a closed system with no change in garnet growth reaction. In theory,

Table 1 *Continued.*

Inclusion-free garnet LEU 3	Rim			Core				Rim
Na	99·3	113	140	80·8	84·7	71·9	111	95·8
Sc	113	87·6	82·7	144	109	116	111	139
Ti	54·2	43·7	34·1	31·0	35·3	40·5	62·1	52·9
V	33·8	16·9	20·3	9·6	23·1	19·3	24·2	26·4
Cr	14·9	15·2	14·7	7·83	15·2	14·0	13·3	9·80
Sr	0·12	0·10	0·12	0·17	0·16	0·13	0·11	0·11
Y	163	103	130	553	274	149	99·5	167
Zr	7·41	7·50	8·60	63·5	8·58	3·65	10·5	13·7
La	0·00	0·00	0·00	0·00	0·00	0·00	0·00	0·00
Ce	0·01	0·00	0·00	0·00	0·01	0·01	0·01	0·00
Nd	0·07	0·03	0·04	0·13	0·05	0·09	0·07	0·06
Sm	0·21	0·14	0·14	0·52	0·30	0·16	0·16	0·28
Eu	0·02	0·02	0·01	0·02	0·02	0·03	0·03	0·03
Gd	1·71	1·23	1·28	6·37	2·33	1·49	1·47	2·50
Dy	18·5	11·9	13·0	63·8	20·4	10·3	11·2	22·3
Er	16·8	14·1	17·3	76·8	31·3	14·7	13·0	21·3
Yb	27·2	27·6	40·0	135·4	73·2	25·7	15·3	34·2
Sm/Nd(N)	3·0	4·5	3·6	4·0	6·3	1·8	2·4	4·7
Yb/Dy	1·5	2·3	3·1	2·1	3·6	2·5	1·4	1·5
Yb/Er	1·6	2·0	2·3	1·8	2·3	1·7	1·2	1·6

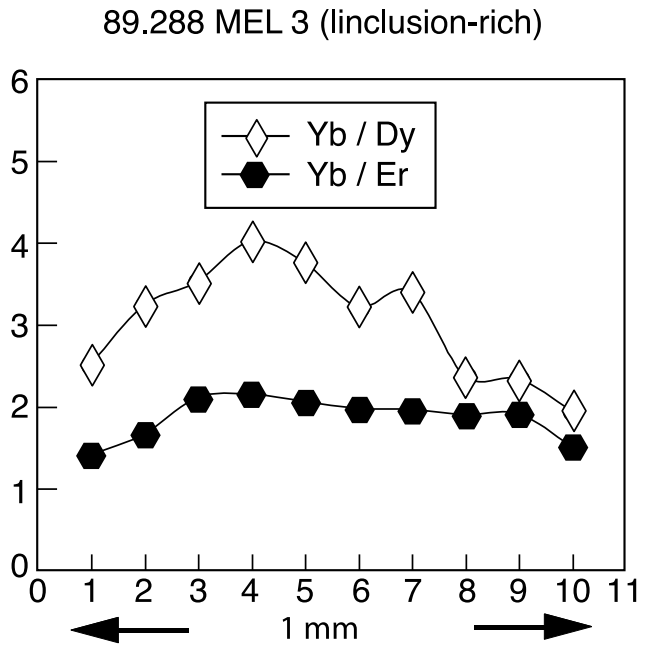

Figure 5 Yb/Dy and Yb/Er variation along the same profile for the inclusion-rich garnet from melanosome MEL 3.

the abundance of a trace element on the surface of a growing garnet in equilibrium with a surrounding metamorphic mineral assemblage is controlled by (i) the effective bulk composition and (ii) the bulk distribution coefficient (Kd) for partitioning of the element between the garnet and the matrix phases. Therefore, the zoning of elements that exhibit decreasing (Sr, Y, HREE, Sm) concentrations from core to rim can be explained in terms of equilibrium closed-system partitioning models (Hollister 1966; Cygan & Lasaga 1982; Otamendi *et al.* 2002). In this model, crystal diffusion-controlled partitioning is a Rayleigh fractionation process, whereby surface equilibrium is maintained and elemental diffusion is limited by the growing crystal. This process assumes mass balance in the reservoir (i.e., a closed system which in this case is the metamorphic host rock), constant Kd values and removal of a fractionating element by mineral growth.

One interesting feature is the distribution of Nd relative to Sm. Nd is more incompatible than Sm in garnet, and in the core region, at the point where Sm peaks, Nd concentrations are low followed by re-enrichment towards the rim (Fig. 4c). This feature may indicate limited volume diffusion of Nd during high-temperature metamorphism.

Heavy Rare Earth Element fractionation, monitored by Yb/Dy and Yb/Er ratios, is continuous from core to rim and more pronounced for Yb/Dy than for Yb/Er ratios which is consistent with the different partition coefficient, $D^{garnet/matrix}$ such that $D_{Yb}>D_{Er}>D_{Dy}>D_{Gd}$ (Fig. 5). Otamendi *et al.* (2002) described garnet from an anatectic terrane in which residual garnet cores, interpreted to have grown during high-grade regional metamorphism, have high Yb/Er and Yb/Dy ratios. Garnet rims, interpreted as peritectic garnet, show inverted ratios, i.e., lower Yb/Dy and higher Yb/Er ratios. The most prominent feature of the HREE systematics was an inflection of the HREE ratios at the core–rim interface. The continuous decrease of HREE ratios in the inclusion-rich garnet from the melanosome may arise from equilibrium partitioning during garnet growth, but the missing inflection indicates that partial melting processes are not monitored by the garnet composition.

5.3. Inclusion-poor garnet (melanosome)

In contrast to the other garnet from the melanosome, this garnet has much fewer inclusions (Fig. 3b). Elements such as Sr, Ti, V and Cr show core–rim depletion, whereas Sc shows core–rim enrichment (Table 1). The distribution of these elements may indicate equilibrium closed-system partitioning (Rayleigh fractionation). Generally, Heavy Rare Earth Element and Y abundances decrease from core to rim (Fig. 6a). However, in the core region, there is a slight depletion in HREE and Y relative to the adjacent rim. In addition, the outermost rim shows re-enrichment in HREE and Y (Fig. 6b). The slight depletion in the core, followed by higher values at the rim with subsequent depletion and re-enrichment at the outermost rim, suggests a multi-stage growth history. Taken

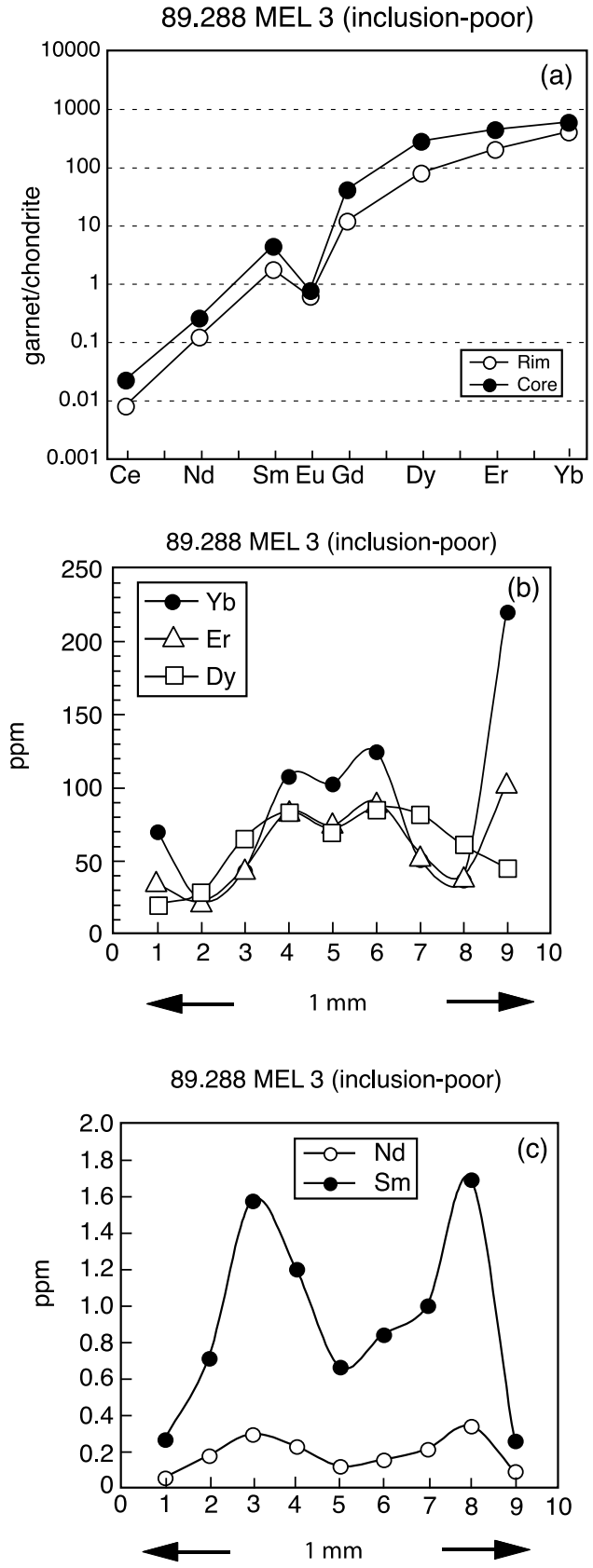

Figure 6 (a) Chondrite-normalised Rare Earth Element plot for core and rim for inclusion-poor garnet from melanosome MEL 3. (b) HREE variation along a rim-core–rim profile. (c) Sm and Nd variation along a rim-core–rim profile.

together, these features cannot reflect distribution of these elements following an equilibrium closed-system partitioning model.

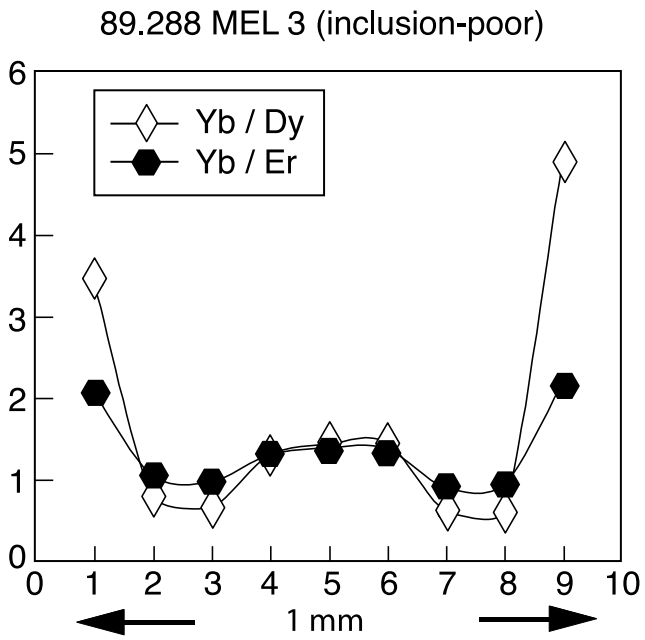

Figure 7 Yb/Dy and Yb/Er variation along the same profile for the inclusion-poor garnet from melanosome MEL 3.

It is possible that the core–rim distribution of HREE and Y can be attributed to variable garnet growth rates during high-grade metamorphism and melting. Variable garnet growth rates are possible because it is reasonable to assume that the garnet now preserved in the melanosome has, in part, started to grow within the melanosome matrix; but subsequently equilibrated with an *in-situ*-derived granitic melt where additional growth of this garnet took place. Such a process may explain the increase in HREE abundances towards the rim, because there is no sink for HREE in the inferred REE-depleted leucosome. If such a reaction indeed proceeded during migmatisation, changes in the phase assemblages are unavoidable because of the distinct mineralogical composition of the host melanosome and the *in situ*-derived melt. Such complex distributions patterns of enrichment/depletion of HREE and Y may indicate an episode of open system behaviour. In contrast to the inclusion-rich garnet from the melanosome, the inclusion-poor garnet shows a complex HREE fractionation pattern. In the core, Yb/Dy and Yb/Er ratios are high, with Yb/Dy>Yb/Er, which is consistent with partition coefficient $D_{garnet/matrix}$:D_{Yb}>D_{Er}>D_{Dy}. Subsequently, these ratios decrease towards the rim (Fig. 7). Towards the outermost rim, an inversion of these HREE ratios occur, with Yb/Dy<Yb/Er. Only the outermost rim shows Yb/Dy>Yb/Er. The inflection of these ratios between core and rim can be interpreted as a result of partial melting. Garnet cores with high Yb/Er and Yb/Dy>1 nucleated in the metamorphic environment without the presence of a melt, whereas the rims with lower Yb/Er and Yb/Dy<1 crystallised in the presence of a melt (Otamendi *et al.* 2002).

5.4. Inclusion-free garnet (leucosome)

Based on the apparent lack of inclusions, it can be suggested that this garnet is distinct to the other two garnets and probably equilibrated in the presence of a melt. The zoning of elements that exhibit either decreasing concentrations (LREE, HREE, Y, Sr, Zr, Sc) or increasing concentrations (Ti, V, Cr, Na) from core to rim can be explained in terms of a near-equilibrium closed-system partitioning model. Similar to the model that is suggested for the inclusion-rich garnet from the melanosome, crystal diffusion-controlled partitioning is a

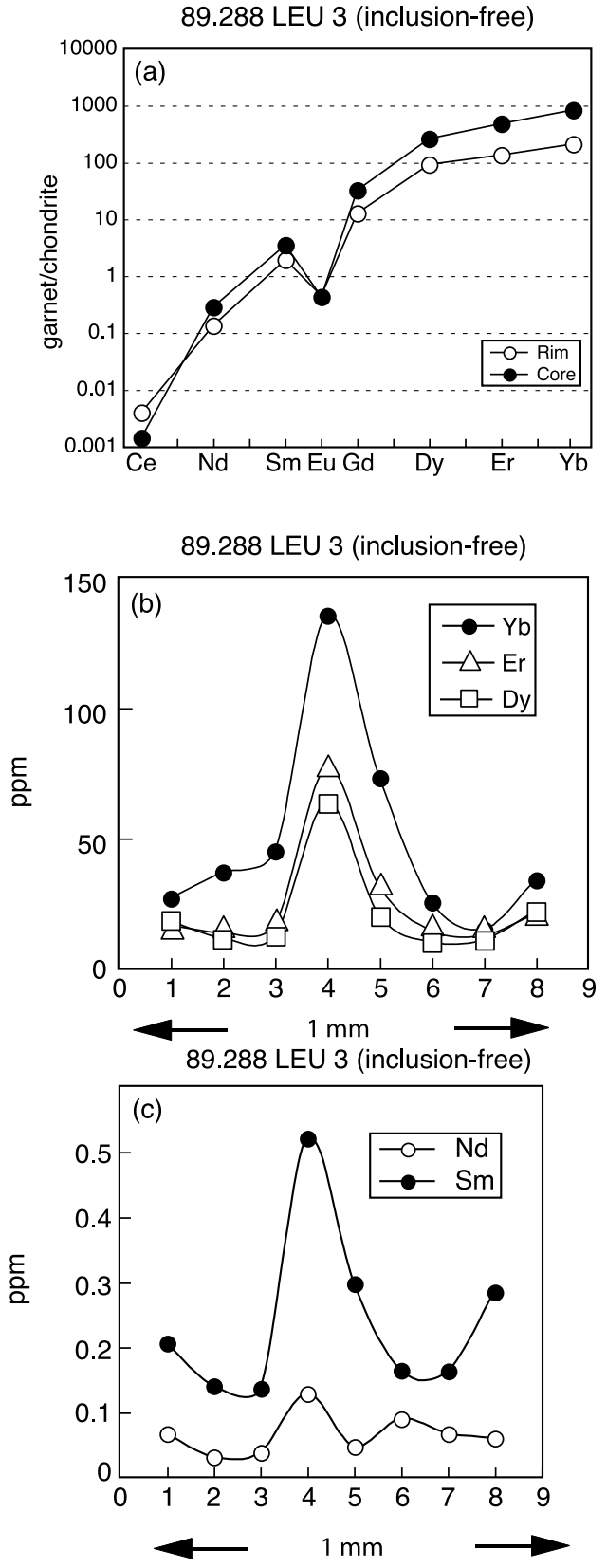

Figure 8 (a) Chondrite-normalised Rare Earth Element plot for core and rim for inclusion-free garnet from leucosome LEU 3. (b) HREE variation along a rim-core–rim profile. (c) Sm and Nd variation along a rim-core–rim profile.

Rayleigh fractionation process, whereby surface equilibrium is maintained and elemental diffusion is limited by the growing crystal. This process assumes mass balance in the reservoir (i.e., a closed system which in this case is the leucosome), constant Kd values and removal of a fractionating element by

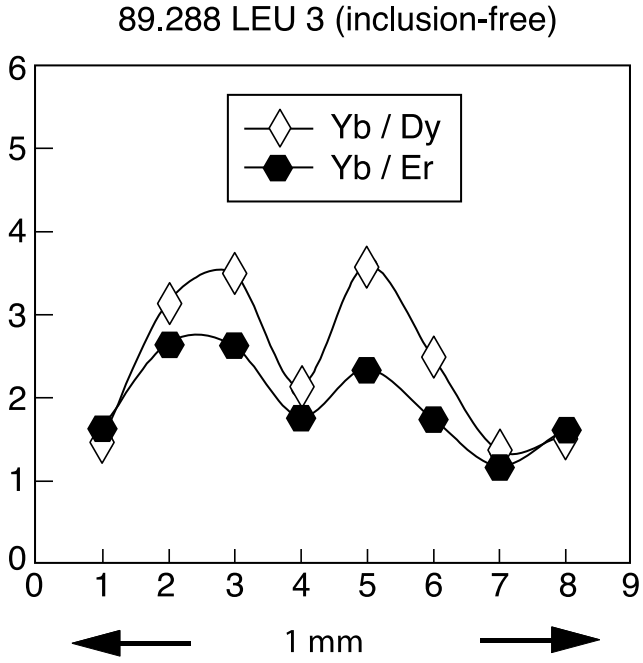

Figure 9 Yb/Dy and Yb/Er variation along the same profile for the inclusion-free garnet from leucosome LEU 3.

mineral growth. In the initial stages of garnet growth, the relatively small core of the garnet nucleated and acted as a sink for the most compatible trace elements (i.e., HREE, Y) that show decreasing concentrations from core to rim (Figs 8 & 9). Subsequently, the volumetrically much larger and trace element-depleted rim crystallised in equilibration with the LREE-depleted leucosome. The lower Yb/Dy and Yb/Er in the core are enigmatic; one possible explanation could be that the core region represents an entrained, restitic garnet from the melanosome. However, textural evidence does not support such a suggestion.

The accurate interpretation of trace element variation in garnet coexisting with a granitic liquid has important implications for trace element behaviour during partial melting processes. In general, garnet that crystallised in the presence of a melt is distinct to garnet from metamorphic environments. In contrast to garnet from strongly fractionated leucogranite (Sevigny 1993; Jung & Hellebrand 2006), the garnet from the leucosome shows a trace element distribution similar to those observed in garnet from high-grade metamorphic or migmatitic rocks. Due to the observation that the leucosome garnet is inclusion-free, incorporation of this garnet from the melanosome into the leucosome seems to be precluded. This implies that the process that formed the trace element pattern of the leucosome garnet was distinct from the liquid diffusion controlled process (i.e., Sevigny 1993) envisaged for leucogranitic garnets. One possible explanation could be that in hot, highly viscous, H_2O-poor leucosomes from high-grade terranes, the rate of diffusion of trace elements is similar to the rate envisaged for high-grade metamorphic rocks, but distinct to the rate suggested for fluid-dominated leucogranites.

5.5. Implications for the HREE composition of garnet-bearing leucosomes

It has been suggested that the HREE composition of metamorphic and peritectic garnet can be used to make assumptions about equilibration of garnet with *in situ*-derived melts (Otamendi *et al*. 2002). Here, the inflection of the Yb/Dy and Yb/Er ratios at the interface between garnet core and rim was interpreted as to result from partial melting processes in which

the garnet core with its characteristic high Yb/Dy ratios nucleated in the metamorphic environment and the rim with lower Yb/Dy ratios nucleated in an environment that is characterised by HREE depletion, i.e. representing an *in situ* partial melt. Therefore, calculated REE patterns of the inferred *in situ* melts can show a marked hump at Yb, using garnet core compositions and melts equilibrated with the rim that are depleted in Yb relative to Y and Er (see figure 3 of Otamendi *et al*. 2002 for reference). Since the inclusion-poor garnet from the melanosome and the inclusion-free garnet from the leucosome show some of these features (inverted Yb/Dy and Yb/Er ratios at the core–rim interface), it is pertinent to calculate corresponding leucosome compositions and to compare them with the leucosomes from the migmatite and with granitic melts from the Damara orogen.

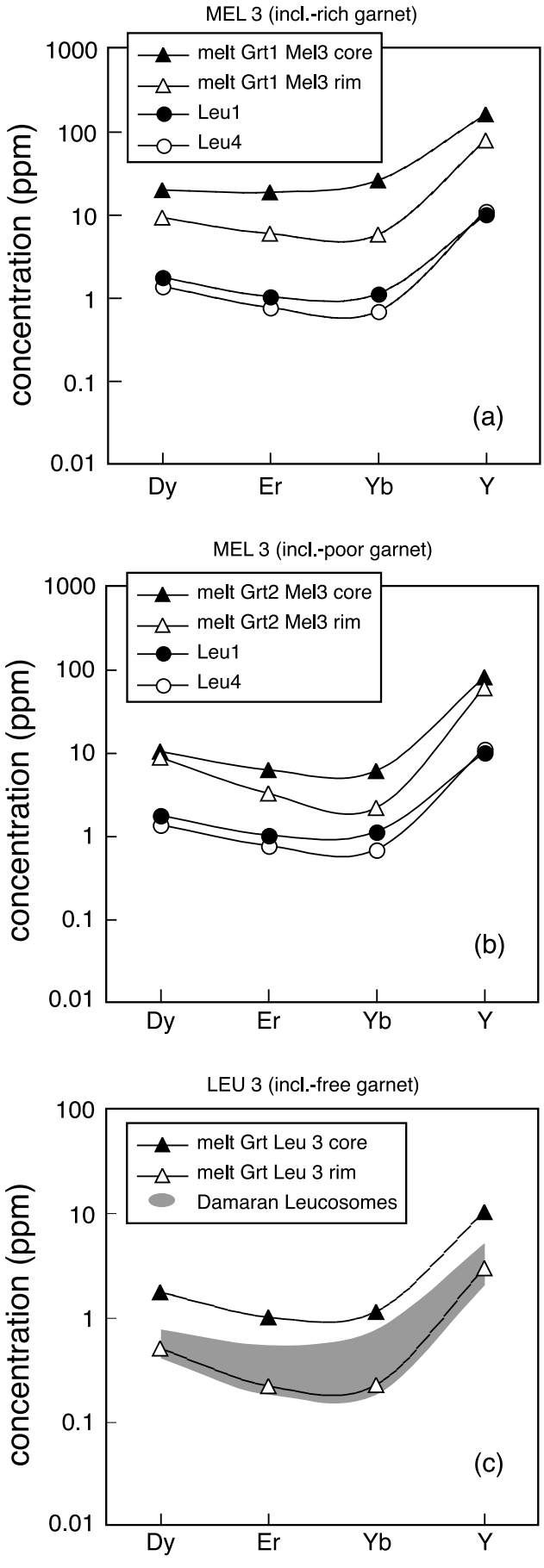

Figure 10a–c shows multi-element distribution pattern for equilibrium partial melts calculated from the garnet composition (core and rim) using calculated mineral-melt distribution coefficients according to the approach of Hollister (1966). From Figure 10a it is obvious that, for the inclusion-rich garnet from the melanosome, calculated compositions of corresponding felsic melts either in equilibrium with the garnet core or the rim are one order of magnitude higher in HREE and Y relative to unfractionated leucosomes from the migmatite. These features may indicate that this garnet was never in equilibrium with a felsic melt similar in composition to unfractionated leucosomes from the migmatite. In the case of the inclusion-poor garnet from the melanosome, the calculated melt compositions are also enriched in HREE and Y, but the rim composition tend to approach the composition of the leucosomes from the outcrop.

For the inclusion-free garnet from the leucosome, the melt composition calculated with the core composition of the garnet is markedly enriched in HREE and Y. On the other hand, the melt composition that is calculated using the garnet rim composition is depleted in HREE and Y, and is similar to other leucosome compositions from the Damara orogen. Based on the data of Otamendi *et al*. (2002), it was concluded that *in situ*-derived felsic melts were unable to equilibrate with garnet cores, but were able to equilibrate with garnet rims. Some of the features interpreted to be characteristic for peritectic garnet (i.e., inversion of Yb/Dy and Yb/Er ratios at the core–rim interface) are also observed in the migmatite garnets from the Davetsaub/Nomatsaus areas, and it seem also obvious that calculated melt compositions were in equilibrium with garnet rims but not the cores.

6. Conclusion

This study demonstrates that trace element zoning in garnet porphyroblasts from a polyphase migmatite from the high-grade part of the Damara orogen (Namibia) provide a powerful tool of investigating melting processes in the crust. Trace element zoning in garnet is more pronounced than major

Figure 10 Plots of calculated abundances of Dy, Er, Yb and Y in melts, assuming equilibration with either garnet cores or garnet rims. Assumptions for the calculation of the trace element abundances were (i) garnet is the only phase that govern these trace element abundances and (ii) bulk partition coefficients between garnet and matrix (melanosome or leucosome) are similar to partition coefficients between garnet and melt. The latter assumption is an oversimplification, but actual garnet/melt partition coefficients are likely to be similar to garnet/matrix partition coefficients and relative values of partition coefficients such as ($D_{Yb}>D_{Er}>D_{Y}>D_{Dy}$). Because of the large values for D, melt fraction has a minor effect on calculated trace element concentrations in the melt and, therefore, garnet/melt partitioning can be simplified to: $C(i)_{melt}/C(i)_{garnet}=1/D(i)$, where $C(i)_{melt}$ and $C(i)_{garnet}$ are concentrations of an element (i) in melt and garnet, respectively. Also shown in (c) are trace element abundances in leucosomes from the Damara orogen (Jung *et al*. 2000, 2003).

element zoning, and provides information on important metamorphic processes, i.e. *in situ* migmatisation and metamorphic growth; information that cannot be retrieved from major-element investigations alone. As anticipated, the garnet analysed in this study are important reservoirs for HREE and Y. The concentrations of HREE and Y in garnet cores are in most cases the result of simple Rayleigh fractionation between the growing garnet and the rock matrix. The signatures of this process are the bell-shaped element distribution patterns. However, inclusion-poor garnet from a melanosome shows a more complex trace element pattern with distinct distribution patterns, suggesting disequilibrium between garnet and an inferred *in situ*-derived melt. Such complex trace element distribution patterns probably mark the onset of open system processes. The preservation of such disequilibrium patterns may occur when mineral growth rates are rapid, particularly in migmatite environments where temperature overstepping may occur. Reacting metamorphic minerals and *in situ*-derived melts have distinct trace element compositions, and because trace element diffusivities in garnet are apparently slow at amphibolite facies to lower granulite facies conditions, variations in garnet trace element compositions can be used to track the metamorphic history of such rocks.

7. Acknowledgements

This study was supported by a grant from the Deutsche Forschungsgemeinschaft to E. Hoffer (Ho 1078/12-1) and the Max-Planck Gesellschaft. The authors would like to thank G. Lugmair and Al Hofmann (MPI Mainz) for access to the ionprobe hosted by the Max Planck Institut für Chemie in Mainz. Peter Hoppe and Elmar Gröner are warmly thanked for keeping the ionprobe in good shape. I. Bambach is warmly thanked for producing high quality figures. We would like to thank I. Buick and F. Bea for the instructive reviews and editor G. Stevens for smooth and patient editorial handling.

8. Appendix. Analytical techniques

Garnet was analysed for trace elements (selected REE and Na, Sc, Ti, V, Cr, Sr, Y, Zr) by secondary ion mass spectrometry (SIMS) on a recently upgraded Cameca IMS-3f in Mainz. Spots were selected for ion microprobe analysis after detailed petrographic and electron microprobe study. Only optically clear domains that showed no signs of alteration or opx exsolution were analysed. Negative oxygen ions were used as primary ions (accelerating potential of 12·5 kV and 20 nA beam current). The spot size for these operating conditions was 15–20 μm. For very small grains, the beam current was reduced to 10 nA, resulting in a smaller spot size (around 10 μm). Positive secondary ions were extracted using an accelerating potential of 4·5 kV with a 25 eV energy window, a high-energy offset of -80 V, and fully open entrance and exit slits. Each measurement consisted of a six-cycle routine, where in each cycle the species ^{16}O, ^{30}Si, ^{47}Ti, ^{51}V, ^{52}Cr, ^{88}Sr, ^{89}Y, ^{90}Zr, ^{138}Ba, ^{139}La, ^{140}Ce, ^{146}Nd, ^{147}Sm, ^{153}Eu, ^{157}Gd, ^{163}Dy, ^{167}Er and ^{174}Yb were analysed, in that order. In each cycle, the REE were measured for 30 s, Sr, Zr and Ba for 20 s, Ti, V and Y for 5 s, and the other elements for 1 s. At the beginning of each analysis, the energy distribution of ^{16}O was measured to determine the maximum intensity and the precise location of the 10% low-energy edge of the distribution. The location of this sharp edge can be determined more precisely than the location of relatively broad maximum intensity. Given that $U_{\text{max-edge}}$ is $+20$ V, the applied high-energy offset is about -100 V from the location of the 10% value of this steep flank. In this way, differences in ion energy as a result of charge build-up from one sample to the next do not affect the energy range of the ions being analysed (Zinner & Crozaz 1986). Subsequently, peak centres were determined for ^{30}Si, ^{47}Ti, ^{89}Y and ^{163}Dy by scanning the peak in 20 steps across a 1·5 wide B-field. The neighbouring masses (Cr and V on Ti, Sr and Zr on Y, and all REE on Dy) were then adjusted to these new peak centres. From one measurement to the next, however, the peak shift was rarely significant (<50 ppm). For all silicates, ^{30}Si (3·1% isotopic abundance) is used as a reference mass, as the SiO_2 concentration of standards and samples is known from electron microprobe analysis. For each cycle, mass to ^{30}Si ratios were determined after correction for time-dependence of count rates, detector deadtime (20 ms) and background [10^{-3} c.p.s. (counts per second)]. The average of these ratios was used to calculate the element concentration, multiplying the measured ratios by a constant factor. These so-called sensitivity factors were determined for each element on the well-studied standard glasses KL2–G, ML3B-G, StHs6/80–G, BM90/21–G and ATHO-G (Jochum *et al.* 2000). For this purpose, a different measurement routine that determines the mass spectrum between 133 and 191 was adopted (Zinner & Crozaz 1986), referred to below as the 'long routine'. This approach is necessary to obtain accurate sensitivity factors for the REE. Although the applied energy filtering technique (Shimizu *et al.* 1978) eliminates the effect of most molecular interferences, it is well known that element monoxides can produce significant interferences, particularly on REE (e.g. PrO on Gd). These have to be corrected. The intensity of an interfering oxide is a function of three parameters: the absolute concentration element of the interfering oxide (i.e. shape of the REE pattern), its isotopic abundance, and the oxide/element ratio of the interfering species. In contrast to the short routine described above, the long routine provides an internally consistent method to determine the corrected element/Si ratios and the oxide/element ratio. A detailed description of this iterative data reduction procedure was presented by Zinner & Crozaz (1986). Owing to the low LREE concentrations in garnet, the short measurement routine was preferred over the long routine, as the poor counting statistics at the extremely low counting rates caused an unacceptable propagating error and long duration time for a single analysis. Therefore, the short routine used the MO^+/M^+ values obtained by the long routine. Furthermore, six oxides were found to produce significant interferences: $^{137}BaO^+$ interferes with $^{153}Eu^+$, $^{141}PrO^+$ with $^{157}Gd^+$, $^{147}SmO^+$ with $^{163}Dy^+$, $^{151}EuO^+$ with $^{167}Er^+$, and both $^{158}GdO^+$ and $^{158}DyO^+$ with $^{174}Yb^+$, and their MO^+ to M^+ ratios used for the corrections are 0·046, 0·13, 0·06, 0·05, 0·08 and 0·07, respectively (with errors <10%). As all elements of these oxides are free of interferences, they were measured directly. For the concentrations of Eu, Gd, Dy and Er in a typical LREE-depleted garnet, these corrections were always <2% of the measured element/Si ratio. For Yb, the correction was 11%. The well-studied glass GOR132–G (Jochum *et al.* 2000) was used as an external standard, as its LREE-depleted pattern is broadly similar to that of the measured garnet (Table 1). The overall accuracy is between 7% and 19% for the REE and better than 11% for all other elements (95% confidence level). To distinguish 'real' counts from background noise at extremely low counting rates, separate background measurements with long counting times of between 10 and 30 min were carried out. All reported analyses are corrected for the background, which lies around 10^{-3} (c.p.s.) on average. The background concentration for each element that is based on such a count rate is controlled primarily by the intensity of ^{30}Si, which was $(1·0–1·3) \times 10^5$ c.p.s. Defining a conservative

detection limit at the six-fold background level, this corresponds to values for the REE that range from 0·6 ng/g (La) to 4 ng/g (Sm).

9. References

Bea, F., Montero, P., Garuti, G. & Zacharini, F. 1997. Pressure-dependence of rare-earth element distribution in amphibolite- and granulite-grade garnets. A LA-ICP-MS study. *Geostandards Newsletters* **21**, 253–70.

Blaxland, A., Gohn, E., Haack, U. & Hoffer, E. 1979. Rb/Sr ages of late-tectonic granites in the Damara orogen, Southwest Africa/Namibia. *Neues Jahrbuch für Mineralogie Monatshefte* **11**, 498–508.

Boynton, W. V. 1984. Geochemistry of rare earth elements: Meterorite studies. *In* Henderson, P. (ed.) *Rare earth element geochemistry*, 63–114. Amsterdam: Elsevier.

Brown, M. 1983. The petrogenesis of some migmatites from the Presqu'ile de Rhuys, Southern Brittany, France. *In* Atherton, M. P. & Gribble, C. D. (eds) *Migmatites, Melting and Metamorphism* 174–200. Nantwich: Shiva Press.

Chernoff, C. B. & Carlson, W. D. 1999. Trace element zoning as a record of chemical disequilibrium during garnet growth. *Geology* **27**, 555–8.

Cygan, R. & Lasaga, A. C. 1982. Crystal growth and the formation of chemical zoning in garnet. *Contributions to Mineralogy and Petrology* **79**, 187–200.

Essene, E. J. 1989. The current status of thermobarometry in metamorphic rocks. *In* Daly, J. S., Cliff, R. A. & Yardley, B. W. D. (eds) *Evolution of metamorphic belts. Geological Society, London, Special Publication* **43**, 1–44. Bath, UK: The Geological Society Publishing House.

Gray, D. R., Foster, D. A., Goscombe, B., Passchier, C. W. & Trouw, R. A. J. 2006. Ar^{40}/Ar^{39} thermochronology of the Pan-African Damara Orogen, Namibia, with implications for tectonothermal and geodynamic evolution. *Precambrian Research* **150**, 49–72.

Haack, U., Hoefs, J. & Gohn, E. 1982. Constraints on the origin of Damaran granites by Rb/Sr and $\delta^{18}O$ data. *Contributions to Mineralogy and Petrology* **79**, 279–89.

Hartmann, O., Hoffer, E. & Haack, U. 1983. Regional metamorphism in the Damara orogen: Interaction of crustal motion and heat transfer. *In* Miller, R. McG. (ed.) *Evolution of the Damara orogen. Special Publication of the Geological Society, South Africa* **11**, 233–41.

Hickmott, D. D., Shimizu, N., Spear, F. S. & Selverstone, J. 1987. Trace element zoning in a metamorphic garnet. *Geology* **15**, 573–6.

Hickmott, D. D. & Shimizu, N. 1990. Trace element zoning in garnet from the Kwoiek area, British Columbia: disequilibrium partitioning during garnet growth? *Contributions to Mineralogy and Petrology* **104**, 619–30.

Hickmott, D. D. & Spear, F. S. 1992. Major and trace element zoning in metamorphic garnets from western Massachusetts. *Journal of Petrology* **33**, 965–1005.

Hoernes, S. & Hoffer, E. 1979. Equilibrium relations of prograde metamorphic mineral assemblages – a stable isotope study of rocks of the Damara orogen. *Contributions to Mineralogy and Petrology* **68**, 377–89.

Hollister, L. S. 1966. Garnet zoning: an interpretation based on the Rayleigh fractionation model. *Science* **154**, 1647–51.

Jochum, K. P., Dingwell, D. B., Rocholl, A., Stoll, B., Hofmann, A. W., Becker, S., Besmehn, A., Dietze, H.-J., Dulski, P., Erzinger, J., Hellebrand, E., Hoppe, P., Horn, I., Janssens, K., Jenner, G. A., Klein, M., McDonough, W. F., Maetz, M., Mezger, K., Münker, C., Nikogosian, I. K., Pickhardt, C., Raczek, I., Rhede, D., Seufert, H. M., Simakin, S. G., Sobolev, A. V., Spettel, B., Straub, S., Vincze, L., Wallianos, A., Weckwerth, G., Weyer, S., Wolf, D. & Zimmer, D. 2000. The preparation and preliminary characterisation of eight geological MPI-DING standard reference glasses for in-situ microanalysis. *Geostandards Newsletter* **24**, 87–133.

Jung, S. 2005. Garnet and staurolite as potential geochronometers in low to medium grade metamorphic rocks – U/Pb and Pb/Pb garnet and staurolite ages from the Southern Damara orogen (Namibia). *Geophysical Research Abstracts* **7**, EGU05–A-06266.

Jung, S., Mezger, K., Masberg, P, Hoffer, E. & Hoernes, S. 1998. Petrology of an intrusion-related high-grade migmatite: implications for partial melting of metasedimentary rocks and leucosome-forming processes. *Journal of Metamorphic Geology* **16**, 425–45.

Jung, S., Hoernes, S., Masberg, P. & Hoffer, E. 1999. The petrogenesis of some migmatites and granites (Central Damara orogen, Namibia): Evidence for disequilibrium melting, wall-rock contamination and crystal fractionation. *Journal of Petrology* **40**, 1241–69.

Jung, S., Hoernes, S. & Mezger, K. 2000. Geochronology and petrology of stromatic and nebulitic migmatites from the Proterozoic Damara Belt – importance of episodic fluid-present disequilibrium melting and consequences for granite petrology. *Lithos* **51**, 153–79.

Jung, S., Hoernes, S. & Mezger, K. 2003. Petrology of basement-dominated terranes: II. Contrasting isotopic (Sr, Nd, Pb, and O) signatures of basement-derived granites and constraints on the source region of granite (Damara orogen, Namibia) *Chemical Geology* **199**, 1–28.

Jung, S. & Hellebrand, E. 2006. Trace element fractionation during high-grade metamorphism and crustal melting – constraints from ion microprobe data of metapelitic, migmatitic and igneous garnets and implications for Sm–Nd garnet geochronology. *Lithos* **87**, 193–213.

Jung, S. & Mezger, K. 2001. Geochronology in migmatites – An Sm–Nd, U–Pb and Rb–Sr study from the Proterozoic Damara belt (Namibia) and implications for polyphase development of migmatites in high-grade terranes. *Journal of Metamorphic Geology* **19**, 77–9.

Jung, S. & Mezger, K. 2003. Petrology of basement-dominated terranes: I. Regionalmetamorphic P–T–t path from U–Pb monazite and Sm–Nd garnet geochronology (Central Damara orogen, Namibia). *Chemical Geology* **198**, 223–47.

Kukla, C. 1993. Strontium isotope heterogeneities in amphibolite facies, banded metasediments – a case study from the late Proterozoic Kuiseb Formation of the Southern Damara orogen, Central Namibia. *Memoirs of the Geological Survey Namibia* **15**, 1–139.

Kukla, C., Kramm, U., Kukla, P. A. & Okrusch, M. 1991. U–Pb monazite data relating to metamorphism and granite intrusion in the northwestern Khomas Trough, Damara Orogen, central Namibia. *Communications of the Geological Survey of Namibia* **7**, 49–54.

Masberg, H. P., Hoffer, E. & Hoernes, S. 1992. Microfabrics indicating granulite-facies metamorphism in the low-pressure central Damara Orogen, Namibia. *Precambrian Research* **55**, 243–57.

Miller, R. McG. 1983. The Pan-African Damara Orogen of South West Africa/Namibia: *In* Miller, R. McG. (ed.) *Evolution of the Damara orogen. Special Publication of the Geological Society, South Africa* **11**, 431–515.

Nieberding, F. 1976. Die Grenze der zentralen Granitzone südwestlich Otjimbingwe (Karibib Distrikt, Südwestafrika): Intrusionsverband, Tektonik, Petrographie. *Göttinger Arbeiten zur Geologie und Paläontologie* **19**, 1–78.

Otamendi, J. E., de la Rosa, J. D., Patino Douce, A. E. & Castro, A. 2002. Rayleigh fractionation of heavy rare earths and yttrium during metamorphic garnet growth. *Geology* **30**, 159–62.

Puhan, D. 1983. Temperature and pressure of metamorphism in the Central Damara orogen. *In* Miller, R. McG. (ed.) *Evolution of the Damara orogen. Special Publication of the Geological Society, South Africa* **11**, 219–23.

Saywer, E. W. 1981. Damaran structural and metamorphic geology in an area southeast of Walvisbay, SWA/Namibia. *Memoirs of the Geological Survey, South West Africa/Namibia* **7**, 1–94.

Sevigny, J. H. 1993. Monazite controlled Sm/Nd fractionation in leucogranites: An ion microprobe study of garnet phenocrysts. *Geochimica et Cosmochimica Acta* **57**, 4095–102.

Shimizu, N., Semet, M. P. & Allègre, J. C. 1978. Geochemical applications of quantitative ion microprobe analysis. *Geochimica et Cosmochimica Acta* **42**, 1321–34.

Spear, F. S., Hickmott, D., Crowley, P. & Hodges, K. V. 1984. P–T paths from garnet zoning: a new technique for deciphering tectonic processes in crystalline terrains. *Geology* **12**, 87–90.

Spear, F. S. & Florence, F. P. 1992. Thermobarometry in granulites: Pitfalls and new approaches. *Precambrian Research* **55**, 209–41.

Spear, F. S. & Kohn, M. J. 1996. Trace element zoning in garnet as a monitor of crustal melting. *Geology* **24**, 1099–102.

Spear, F. S. & Selverstone, J. 1983. Quantitative P–T paths from zones minerals: theory and tectonic implications. *Contributions to Mineralogy and Petrology* **83**, 348–57.

Thompson, A. B. 1982. Dehydration melting of pelitic rocks and the generation of H_2O-undersaturated granitic liquids. *American Journal of Science* **282**, 1567–95.

Tracy, R. J. 1982. Compositional zoning and inclusions in metamorphic minerals. *In* Ferry, J. M. (ed.) *Characterization of metamorphism through mineral assemblages in metamorphic rocks. Mineralogical Society of America Reviews in Mineralogy* **10**, 355–97.

Vielzeuf, D. 1983. The spinel and quartz associations in high grade xenoliths from Tallante (S.E. Spain) and their potential use in geothermometry and barometry. *Contributions to Mineralogy and Petrology* **82**, 301–11.

Ward, R., Stevens, G. & Kisters, A. 2008. Fluid and deformation induced partial melting and melt volumes in low-temperature granulite-facies metasediments, Damara Belt, Namibia. *Lithos* **105,** 253–71.

Zinner, E. & Crozaz, C. 1986. A method for the quantitative measurement of rare earth elements in the ion probe. *International Journal of Mass Spectrometry and Ion Processes* **69**, 17–38.

MS received 5 December 2007. Accepted for publication 10 November 2008 (Stellenbosch); 15 January 2009 (RSE).

Crustal melt granites and migmatites along the Himalaya: melt source, segregation, transport and granite emplacement mechanisms

M. P. Searle, J. M. Cottle*, M. J. Streule and D. J. Waters

Department of Earth Sciences, Oxford University, Parks Road, Oxford OX1 3PR, UK

*Current address: Department of Earth Sciences, University of California, Santa Barbara, CA 93106, USA

ABSTRACT: India–Asia collision resulted in crustal thickening and shortening, metamorphism and partial melting along the 2200 km-long Himalayan range. In the core of the Greater Himalaya, widespread *in situ* partial melting in sillimanite+K-feldspar gneisses resulted in formation of migmatites and Ms+Bt+Grt+Tur ± Crd ± Sil leucogranites, mainly by muscovite dehydration melting. Melting occurred at shallow depths (4–6 kbar; 15–20 km depth) in the middle crust, but not in the lower crust. $^{87}Sr/^{86}Sr$ ratios of leucogranites are very high (0·74–0·79) and heterogeneous, indicating a 100% crustal protolith. Melts were sourced from fertile muscovite-bearing pelites and quartzo-feldspathic gneisses of the Neo-Proterozoic Haimanta–Cheka Formations. Melting was induced through a combination of thermal relaxation due to crustal thickening and from high internal heat production rates within the Proterozoic source rocks in the middle crust. Himalayan granites have highly radiogenic Pb isotopes and extremely high uranium concentrations. Little or no heat was derived either from the mantle or from shear heating along thrust faults. Mid-crustal melting triggered southward ductile extrusion (channel flow) of a mid-crustal layer bounded by a crustal-scale thrust fault and shear zone (Main Central Thrust; MCT) along the base, and a low-angle ductile shear zone and normal fault (South Tibetan Detachment; STD) along the top. Multi-system thermochronology (U–Pb, Sm–Nd, ^{40}Ar–^{39}Ar and fission track dating) show that partial melting spanned ~24–15 Ma and triggered mid-crustal flow between the simultaneously active shear zones of the MCT and STD. Granite melting was restricted in both time (Early Miocene) and space (middle crust) along the entire length of the Himalaya. Melts were channelled up via hydraulic fracturing into sheeted sill complexes from the underthrust Indian plate source beneath southern Tibet, and intruded for up to 100 km parallel to the foliation in the host sillimanite gneisses. Crystallisation of the leucogranites was immediately followed by rapid exhumation, cooling and enhanced erosion during the Early–Middle Miocene.

KEY WORDS: Channel flow, crustal melting, granite emplacement, Himalaya, leucogranite, migmatite, shear zones.

The collision of the Indian plate passive continental margin with the southern active continental margin of Asia (Karakoram in the west; Lhasa block in Tibet) is an ongoing process that started in the Palaeocene. Final marine sedimentation along the Indus–Yarlung Tsangpo suture zone was Early Eocene (49–50·5 Ma) and crustal thickening and shortening by folding and thrusting propagated southward across the north Indian plate margin (Searle *et al*. 1988, 1990, 1997; Rowley 1996; Zhu *et al*. 2005). Since the collision, India has continued to converge and penetrate north into Asia, resulting in double normal thickness continental crust both along the Indian plate margin (Himalaya) and along the south Asian margin (Karakoram–Lhasa Block).

The Himalayan upper crust (Tethyan Himalaya) is composed of folded and thrust Phanerozoic (Late Precambrian to Eocene) sedimentary rocks bounded along the north by the Indus–Tsangpo suture zone and along the south by the South Tibetan detachment (STD), a low-angle, north-dipping normal fault (Burg 1983; Hodges 2000; Cottle *et al*. 2007). South of this the Greater Himalayan Sequence (GHS) is composed of regional Barrovian facies metamorphic rocks, migmatites and leucogranites, bounded along the south by a 2–4 km-thick zone of inverted metamorphic isograds (from sillimanite–kyanite down to biotite–chlorite) with a brittle thrust fault along the base, the Main Central thrust (MCT) zone (Searle *et al*. 2008; Figs. 1, 2). The Lesser Himalaya to the south is composed of underthrust Indian plate rocks including Proterozoic basement and thin Palaeozoic cover sedimentary rocks. The deeper, unexposed lower crust beneath the Himalaya is thought to be underthrust granulite facies Indian shield rocks (Searle *et al*. 2006; Jackson *et al*. 2008). Since the Moho steepens northwards from ca. 40 km depth beneath the Himalayan foreland to ca. 80 km beneath southern Tibet (Schulte-Pelkum *et al*. 2005), or even 90 km beneath the Karakoram–west Tibet (Rai *et al*. 2006), these Precambrian granulites may have undergone a phase transition to eclogite facies rocks during the late Tertiary–present day (Searle *et al*. 2006).

Deep seismic profiling, combined with broadband earthquake and magnetotelluric data across southern Tibet suggest that a high-conductivity layer at 15–20 km-depth reflect partial melting in the middle crust of southern Tibet today (Nelson *et al*. 1996; Wei *et al*. 2001). 'Bright spots' of high electrical conductivity probably reflect pockets of leucogranite magmas forming today at similar P–T conditions and depth as the

© 2009 The Royal Society of Edinburgh. doi:10.1017/S175569100901617X

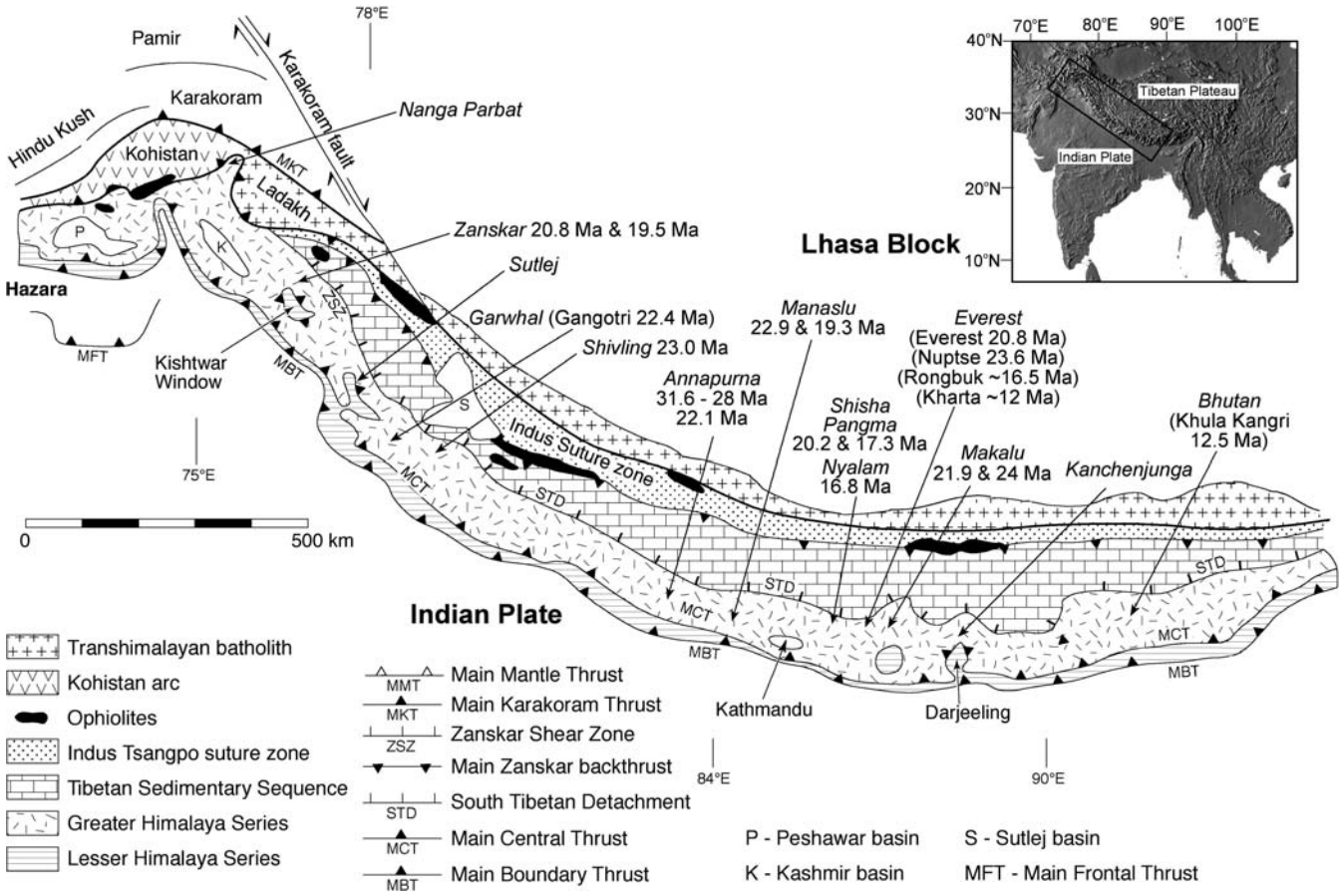

Figure 1 Geological map of the Himalaya showing U–(Th)–Pb ages along the orogen. See text and Godin *et al.* (2006) for sources of data.

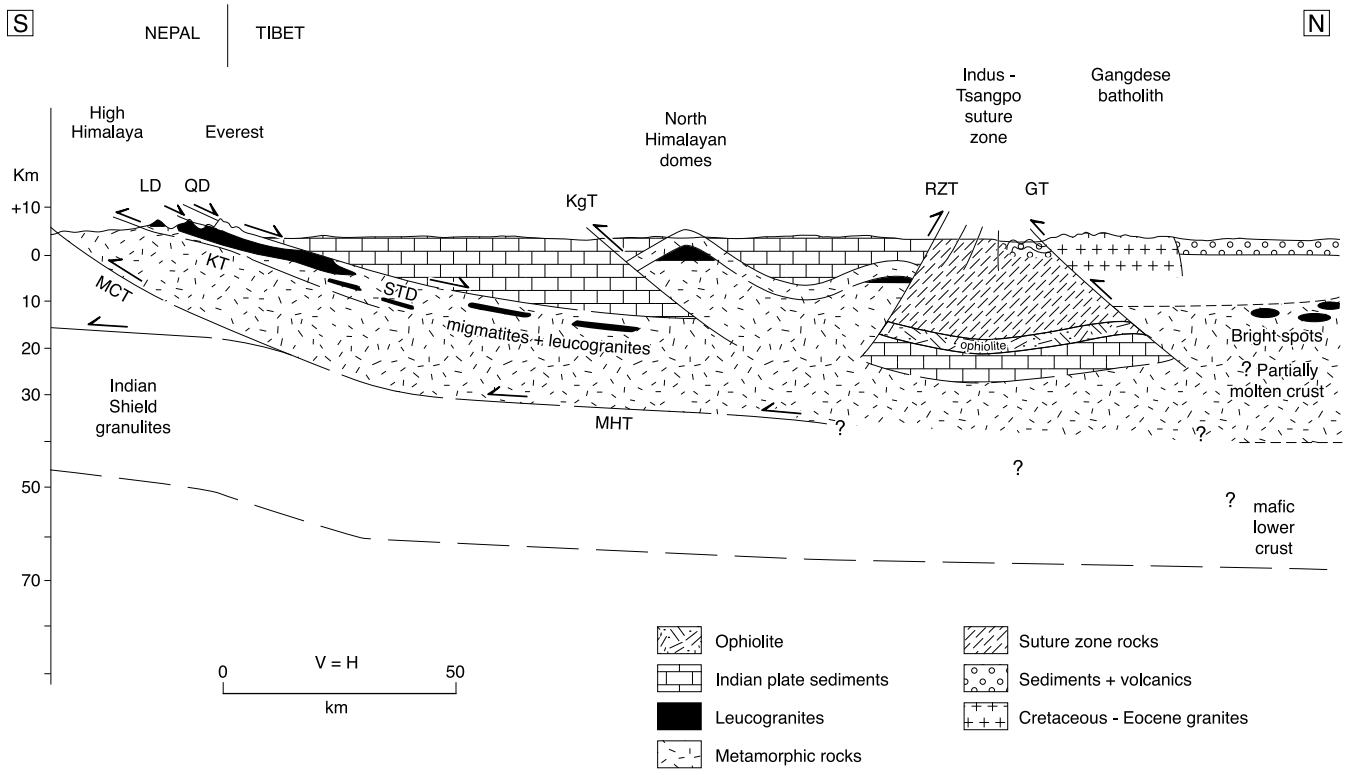

Figure 2 Cross-section across the Everest Himalaya, based on surface geological mapping combined with deep crust seismic constraints from INDEPTH (Nelson *et al.* 1996).

Miocene leucogranites along the Himalaya (Gaillard *et al.* 2004). Seismic reflectors bounding this mid-crustal zone of partial melting can be traced to the ca. 20–16 Ma MCT and STD shear zones along the Greater Himalaya (Hauck *et al.* 1998; Searle *et al.* 2006). Seismic tomographic studies suggest that southern Tibet and the Himalaya are underlain by cold,

strong upper mantle attached to the underthrusting Indian shield (Tilmann *et al.* 2003).

Following the India–Asia collision, crustal thickening and shortening (by folding and thrusting) along the northern margin of India resulted in increased pressure and temperatures. Progressive metamorphism evolved with time and in space from initial UHP coesite–eclogite-grade affecting only the leading margin of the Indian plate, to regional kyanite- and sillimanite-grade Barrovian metamorphism affecting most of the GHS and North Himalayan domes. During the Early Miocene increasing temperature and decreasing pressure resulted in decompression melting within the upper part of the middle crust of the Himalaya. One of the most spectacular results of the Himalayan collision was the formation of crustal melt leucogranites from a widespread migmatitic partial melt zone in the middle crust. Many of the highest peaks of the Greater Himalaya are composed of these anatectic granites (e.g. Shivling, Bhagirathi, Thalay Sagar, Manaslu, Makalu, Shisha Pangma, Kangchenjunga, the base of the Everest–Nuptse–Lhotse massif, Chomolhari and Masang Kang).

Since the major shear zones, faults and fabrics across the Himalaya dip to the north and many of the major river drainage access routes run north–south, it is possible to map out a three-dimensional view of the entire middle and upper crust. Thus the Himalaya is a unique orogen where it is possible to trace granitic melts from their mid-crustal source to their present high structural level. This paper reviews the field relationships, metamorphic history and chronology of metamorphism, melting and deformation along the Himalaya. The protolith source of leucogranite melts is discussed, and the partial melting process and melt reactions. These data are used to propose a model for the generation and emplacement of Himalayan leucogranites from source to high structural level, and discuss the role of partial melting and leucogranite formation in the Channel Flow model (Beaumont *et al.* 2001; Grujic *et al.* 2002; Searle *et al.* 2003, 2006; Searle & Szulc 2005; Jessup *et al.* 2006; Law *et al.* 2006).

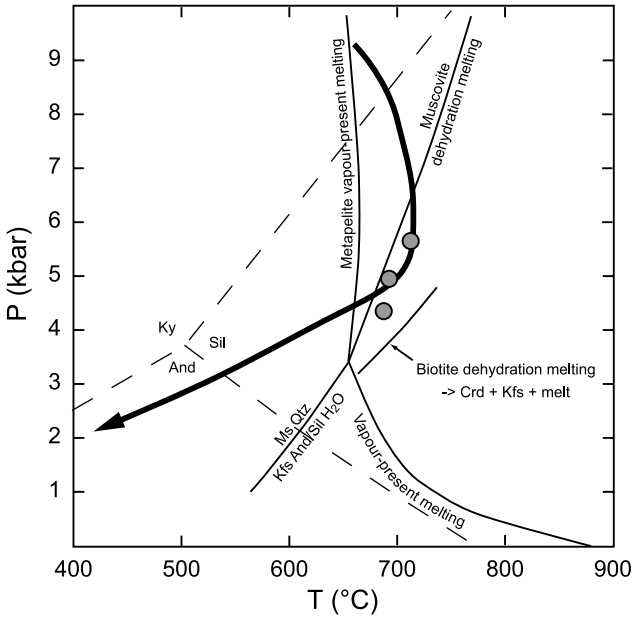

Figure 3 Pressure–temperature diagram showing key equilibria and P–T paths relevant to melting in the GHS. Filled circles are P–T conditions determined for migmatites in the Khumbu Valley, Everest region, from Searle *et al.* (2003). Bold arrowed curve is the P–T path determined for the migmatitic core of the GHS in the Zanskar Himalaya, from Searle *et al.* (1999a). Curves for significant metamorphic and melting reactions in muscovite- and biotite-bearing schists are based on the calculated phase diagram for 'average pelite' in White *et al.* (2001).

1. Review of metamorphic history of the Himalaya

The thermal history of the Himalaya involves four 'stages' during part of a 50 m.y. continuum: (1) eclogite metamorphism during initial crustal subduction of the leading edge of India to UHP depths (27·5 kbar; >100 km depth; 720–770 °C) at 46·4 Ma (U–Pb, zircon, allanite; Parrish *et al.* 2006); (2) crustal thickening resulted in peak kyanite grade metamorphism (550–680 °C; 9–11 kbar) at ca. 37–30 Ma (U–Pb, monazite and Sm–Nd garnet ages; Walker *et al.* 1999; Vance & Harris 1999); followed by (3) widespread sillimanite grade metamorphism (620–770 °C; 4·5–7 kbar) accompanied by partial melting and leucogranite formation at ca. 23–16 Ma (Noble & Searle 1995; Walker *et al.* 1999; Simpson *et al.* 2000; Viskupic & Hodges 2001). Burial and thickening, followed by heating, decompression, partial melting and rapid exhumation and cooling resulted in clockwise P–T–t paths (e.g. Hubbard 1989; Searle *et al.* 1999a, b; Hodges 2000; Walker *et al.* 2001; Jamieson *et al.* 2004; Fig. 3). Himalayan eclogite metamorphism is only known so far for certain from Kaghan, North Pakistan and Tso Morari, Ladakh, although it could have occurred elsewhere along the leading margin of the Indian plate and still remain unexposed. In North Pakistan the UHP metamorphism and the medium P–T metamorphic events were probably synchronous and juxtaposed by later thrusting (Treloar *et al.* 2003). The kyanite and sillimanite grade metamorphic events are common along the entire length of the GHS. A fourth Himalayan metamorphic event, characterised by low-P high-T metamorphism, metasomatism and generation of cordierite-bearing leucogranites, has only been recorded in the NW Himalayan syntaxis at Nanga Parbat (Whittington *et al.* 1998, 1999; Zeitler *et al.* 2001a, b; Crowley *et al.* 2009) and the NE Himalayan syntaxis at Namche Barwa (Booth *et al.* 2004).

Himalayan leucogranites were generated during the Early Miocene along the entire 2200 km length of the Greater Himalaya. Crustal melting occurred at relatively shallow depths of ca. 15–20 km depth, and granites were generated from a widespread partial melting migmatite zone in the middle crust. Many Himalayan leucogranites remain more-or-less *in situ* within the sillimanite–K-feldspar migmatite zone and have been exposed only because of underthrusting of successive thrust slices beneath, and subsequent hanging-wall uplift and erosion. Where melt migration has occurred, kilometre-scale, foliation-parallel sill complexes within the upper part of the GHS have transported magma horizontally or along very shallow north-dipping melt channels. No leucogranites cut up across the South Tibetan Detachment (e.g. Murphy & Harrison 1999; Searle & Godin 2003). U–(Th)–Pb ages of leucogranites have been used to constrain timing of motion along the ductile shear zone and the STD low-angle normal fault according to whether the leucogranites are pre-, syn- or post-kinematic with relation to the ductile fabric and brittle fault (e.g.: Searle *et al.* 1997, 2003, 2006).

In Nanga Parbat, Proterozoic granulite basement gneisses were rehydrated to amphibolite before undergoing Oligocene–Miocene metamorphism and at least four phases of melting. The youngest of these was Pleistocene and associated with a vigorous hydrothermal system (Zeitler *et al.* 2001a, b). Cordierite–K-feldspar–quartz pods and veins (Butler *et al.* 1997; Whittington *et al.* 1998, 1999; Whittington & Treloar 2002; Crowley *et al.* 2009) intrude along vertical extensional fractures in the core region of the Nanga Parbat massif. Cordierite occurs as coronas around Al and Fe–Mg rich

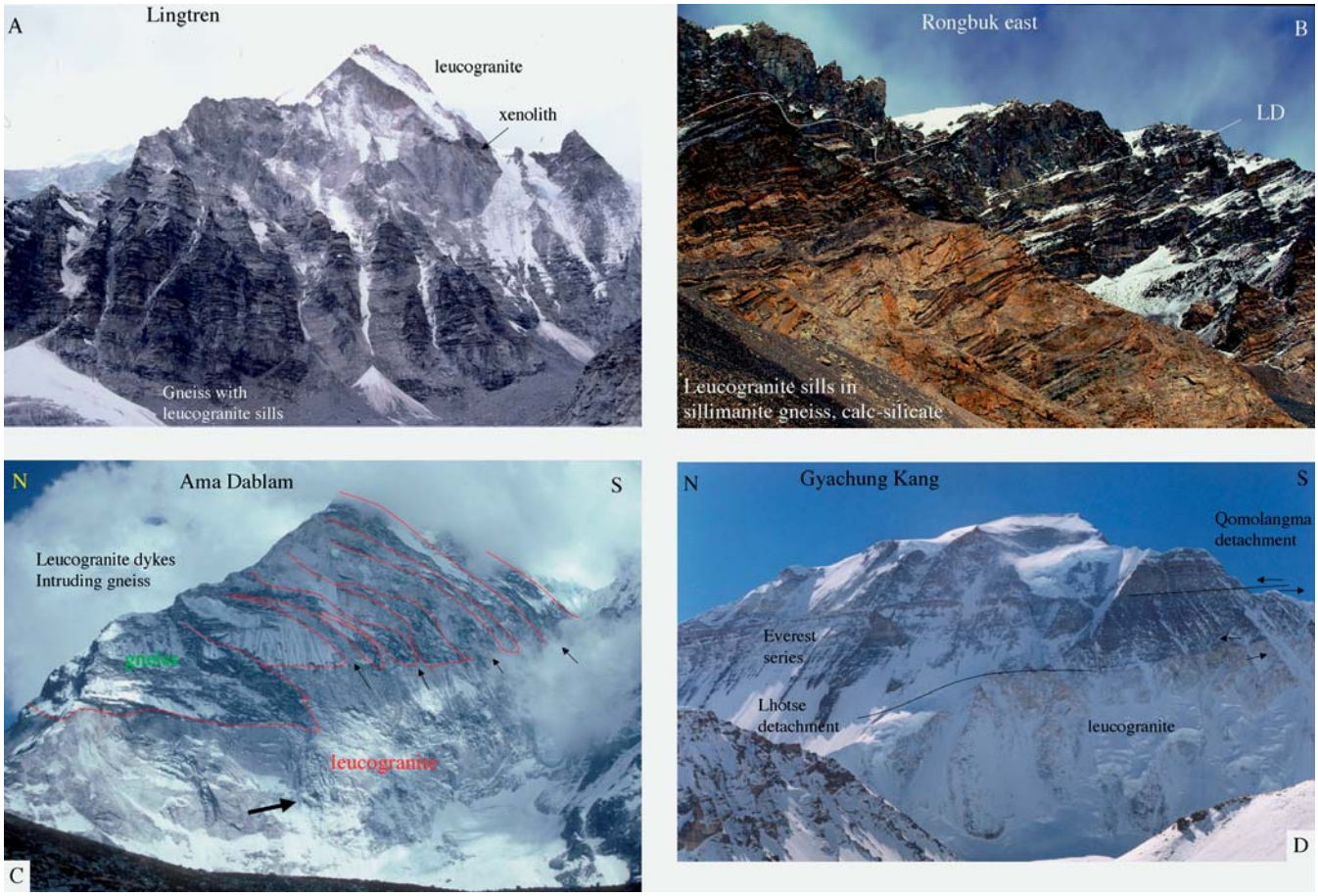

Figure 4 (a) South face of Lingtren (6749 m) showing a 3–4 km-thick sheeted sill complex of horizontally-layered leucogranite with a massive sill at the top enclosing rafts of sillimanite gneiss. (b) Layered leucogranites interlayered with GHS gneisses along footwall of the STD in the Rongbuk valley, north of Everest, south Tibet. (c) North face of Ama Dablam (6828 m) showing leucogranite sheets or thick sills with horizontal dykes bent to the north along the footwall of the STD. (d) Gyachung Kang (7922 m), west of Everest, showing the two low-angle normal faults, the upper Qomolangma detachment and the lower Lhotse detachment.

material which are probably small restitic enclaves. The coronas merge into coarse-grained cordierite in the presence of melt. The development of cordierite-bearing corona assemblages should reflect the final interaction between melt and solid at a time no earlier than that recorded by the crystallisation age of accessory phases in the leucosome. P–T conditions of cordierite coronas from the core of Nanga Parbat are 3·7–4·2 kbar at 700–720°C (Crowley *et al.* 2009). U–Th–Pb ages from monazites and xenotimes in leucogranites give ages as young as 0·76–0·71 Ma (Bowring *et al.* 2004; Crowley *et al.* 2005, 2009). Exhumation rates could be as high as 1·5–2 cm/yr, and 13–15 km of overburden has been eroded from the summit region of Nanga Parbat in less than one million years. In the Eastern Himalayan syntaxis at Namche Barwa, U–Pb SHRIMP zircon ages show the standard 25–18 Ma Himalayan melt events, but also a younger period of 10–3 Ma in the core of the massif (Booth *et al.* 2004), similar to the Nanga Parbat syntaxis.

2. Field relationships of Himalayan granites

Himalayan leucogranites are almost entirely found within the upper part of the Greater Himalayan mid-crustal slab, within the sillimanite+K-feldspar migmatite zone, or intruded along giant sill complexes beneath the STD. Similar field relationships are seen along the entire length of the Himalaya from Zanskar (e.g. Searle *et al.* 1999a; Walker *et al.* 1999; Dezes *et al.* 1999) through Garhwal (e.g. Scaillet *et al.* 1990, 1995; Searle *et al.* 1999b) to Nepal (e.g. Searle & Godin 2003), Sikkim (e.g. Searle & Szulc 2005) and Bhutan (e.g. Grujic *et al.* 2002). Although early studies suggested that the Manaslu leucogranite was an exception by intruding across the STD into the overlying base of the Tethyan sediments (e.g. LeFort 1975, 1981; Guillot *et al.* 1995; Harrison *et al.* 1999), Searle & Godin (2003) showed that the granite was emplaced into high-grade metamorphic rocks beneath the STD, and does not intrude across the STD. The metamorphism around the Manaslu granite is clearly continuous with the regional GHS metamorphism well away from the granite (Searle & Godin 2003), and not contact metamorphism around the granite (Guillot *et al.* 1995).

In the Everest area almost all leucogranites are layer-parallel sills of thicknesses varying from <1 m to 3–4 km (Searle 1999a, b, 2003, 2007; Searle *et al.* 2003, 2006; Jessup *et al.* 2006, 2008; Cottle *et al.* 2007, 2009). The sills can be traced in the field for up to 40 km horizontally across strike, within the upper part of the GHS from the upper Khumbu glacier in Nepal and along the Rongbuk glacier in Tibet (Searle *et al.* 2003, 2006; Jessup *et al.* 2006, 2008; Cottle *et al.* 2007, 2009). Massive horizontal sill complexes make up the upper part of the GHS, with the larger sills reaching 3–4 km thick. The massive granite sheet exposed around the base of the Everest massif is continuous west to Lingtren (Fig. 4a) Pumori, Gyachung Kang and Cho Oyu, east to the granites surrounding the upper Kangshung valley and the base of Makalu, and south to the ballooning Nuptse granite (Searle 1999a, b, 2003, 2007; Jessup *et al.* 2006, 2008). At Rongbuk, early folded and later foliation-parallel sills decrease in abundance up-section to the Lhotse

detachment (Fig. 4b), above which a prominent band of calc-silicate truncates the rocks beneath. The brittle Qomolangma detachment above the calc-silicate band and the Everest series pelites then dips north beneath the Tibetan plateau some 35–40 km north of Everest (Cottle *et al*. 2007). Vertical dykes feed magma up from lower sills to higher sills. The highest dykes have been bent around to the north along the footwall of the Lhotse detachment (e.g. on the north face of Ama Dablam; Fig. 4c). West of Mount Everest on Gyachung Kang (Fig. 4d) there are clearly two low-angle detachments, the first of which separates the Cambro-Ordovician sedimentary rocks on the summits from the Everest series greenschist–lower amphibolite facies metapelites and calcschists (Qomolangma detachment) and the second is the lower ductile Lhotse detachment which separates the Everest series above from sillimanite gneisses with abundant leucogranites beneath (Searle 1999a, b, 2003; Searle *et al*. 2003, 2006; Jessup *et al*. 2006, 2008). At deeper structural levels the melting zone, represented by the migmatites, shows layered or stromatic migmatites with *in situ* melts sweating out of quartzo-feldspathic or K-feldspar augen gneisses.

The Manaslu leucogranite in central Nepal is one of the larger Himalayan granites, being ca. 5 km thick (Fig. 5a). The upper margin of the granite is an abrupt fault-bounded contact that corresponds to the Phu detachment, the upper brittle STD normal fault (Searle and Godin 2003) that places Cambrian sedimentary rocks directly above the granite (Fig. 5b). The leucogranite contains rafts of the migmatitic gneiss from which it was apparently derived (Fig. 5c). Tourmaline is a common mafic phase within the Manaslu granite that also contains abundant muscovite, some biotite and garnet (Fig. 5d). Common textures include tourmaline + quartz 'ghosts' that form circular pods of metasomatic late mineral growth associated with boron-rich fluids (Fig. 5e). The stromatic migmatites and early leucogranite melts are cut by later dykes of leucogranite fed by later melting episodes deeper in the crust (Fig. 5f).

Most Himalayan leucogranite bodies are made up of a variety of two-mica ± tourmaline ± garnet leucogranite. Cordierite is uncommon in most Himalayan leucogranites, but it is widespread in the Makalu area, east of Everest, as well as in the younger Pliocene–Recent Nanga Parbat migmatitic leucosomes and very young leucogranite melts (Whittington *et al*. 1998; Bowring *et al*. 2004; Crowley *et al*. 2005, 2009). On Makalu the youngest intrusive phase is a 3 km-thick sill-like body of cordierite granite (Fig. 6a, b) that is fed by a 10 m-wide vertical dyke that cuts across earlier fabrics and older two mica tourmaline leucogranite sills (Fig. 6c). Cordierite occurs as large pale green crystals that are interpreted as a low-pressure (<5 kbar) peritectic phase formed as a product of the biotite dehydration reaction (Fig. 6d). In the Makalu area multiple dykes record at least six episodes of crustal melting in batches (Fig. 6e, f).

3. Review of the U–Th–Pb ages of Himalayan granites

The first attempts to date the crystallisation age of Himalayan leucogranites utilised the $^{87}Sr/^{86}Sr$ method (e.g. Deniel *et al*. 1987). However, the highly variable $^{87}Sr/^{86}Sr$ ratios made calculating ages by this method problematic. Most subsequent age determinations have therefore relied on the U(–Th)–Pb technique. This method is not without its problems however. Because anatexis occurred under low-T conditions, and the resulting melts are highly peraluminous, xenocrystic accessory phases are common. Most have inherited zircon; some have inherited monazite (Copeland *et al*. 1988); whilst inherited xenotime, although rare, is known (Viskupic & Hodges 2001). An additional problem is that monazite, the mineral of choice when dating Himalayan leucogranites, is usually reversely discordant in U–Pb space. This behaviour is interpreted to reflect an initial U–Th disequilibrium caused by the incorporation of excess ^{230}Th during crystallisation, leading to an excess of ^{206}Pb (Schärer 1984). The presence of excess ^{206}Pb results in the $^{206}Pb/^{238}U$ ages for monazite in this study being older than the $^{207}Pb/^{235}U$ and $^{208}Pb/^{232}Th$ ages by as much as 50% (Cottle *et al*. 2009). U–Pb dates can be corrected for the U–Th disequilibrium by estimating the degree of U–Th fractionation between mineral and melt (Schärer 1984; Parrish 1990), but given that the Th–Pb system and the $^{207}Pb/^{235}U$ ages are unaffected by this disequilibrium the $^{207}Pb/^{235}U$ or $^{208}Pb/^{232}Th$ dates are generally taken as the most reliable estimates of the ages of the grains measured.

Most U(–Th)–Pb ages for the melts in the central Himalaya (Fig. 1) are Early–Middle Miocene, ranging from 24–15 Ma (Harrison *et al*. 1995; Hodges *et al*. 1996; Coleman 1998; Searle *et al*. 1997, 1999a, b; Godin *et al*. 2001; Daniel *et al*. 2003; Harris *et al*. 2004; Cottle *et al*. 2009) to 13–12 Ma (Edwards & Harrison 1997; Wu *et al*. 1998; Zhang *et al*. 2004). However, evidence for leucosome melt production during the Oligocene (33–23 Ma) also exists (Coleman 1998; Thimm *et al*. 1999; Godin *et al*. 2001). In the Everest transect the oldest record of *in situ* partial melting occurs in the Namche orthogneiss at ~25–26 Ma (Viskupic & Hodges 2001). Immediately following initial melting, a major phase of pre- to syn-kinematic melt mobilisation occurred between ~22 and 21 Ma (Simpson *et al*. 2000; Viskupic & Hodges 2001; Searle *et al*. 2003; Viskupic *et al*. 2005). The timing of this earliest melt mobilisation is broadly synchronous with emplacement of many of the large granite sheets present at the highest structural level in the Everest region GHS, such as the Everest/Makalu granite (Schärer 1984; Simpson *et al*. 2000). Early foliation parallel granite sheets have U–Pb monazite ages spanning 24–18 Ma (Schärer 1984; Viskupic & Hodges 2001; Searle *et al*. 2003; Viskupic *et al*. 2005; Cottle *et al*. 2009), whereas later sets of undeformed dikes cross-cut ductile fabrics and have U(–Th)–Pb ages of ~18–16 Ma (Hodges *et al*. 1998; Murphy & Harrison 1999; Simpson *et al*. 2000; Viskupic & Hodges 2001; Searle *et al*. 2003; Viskupic *et al*. 2005).

4. Melt reactions

During progressive metamorphism, water-saturated melting may occur if a hydrous fluid phase is present when rocks cross the wet granite solidus. At mid-crustal pressure, appropriate simplified reactions might be:

$$Ms + Qtz + Pl + Kfs + H_2O = Melt$$
$$Ms + Qtz + Pl + H_2O = Sil + Melt$$

Unless there is an external supply of aqueous fluid, however, the amount of melt generated by these vapour- (or fluid-) present processes will be trivial, and significant melt generation will require access to the water locked up in hydrous minerals such as micas or amphiboles. These reactions are referred to as vapour-absent or dehydration melting reactions, and are incongruent melting reactions yielding solid peritectic products. Vapour-absent dehydration melting reactions generally have positive P–T slopes, with the two important consequences that, first, they can be intersected by rocks on a decompression path, and secondly, that in principle the melts generated are able to rise a considerable distance in the crust before reaching their solidus. The first such reaction encountered by a typical

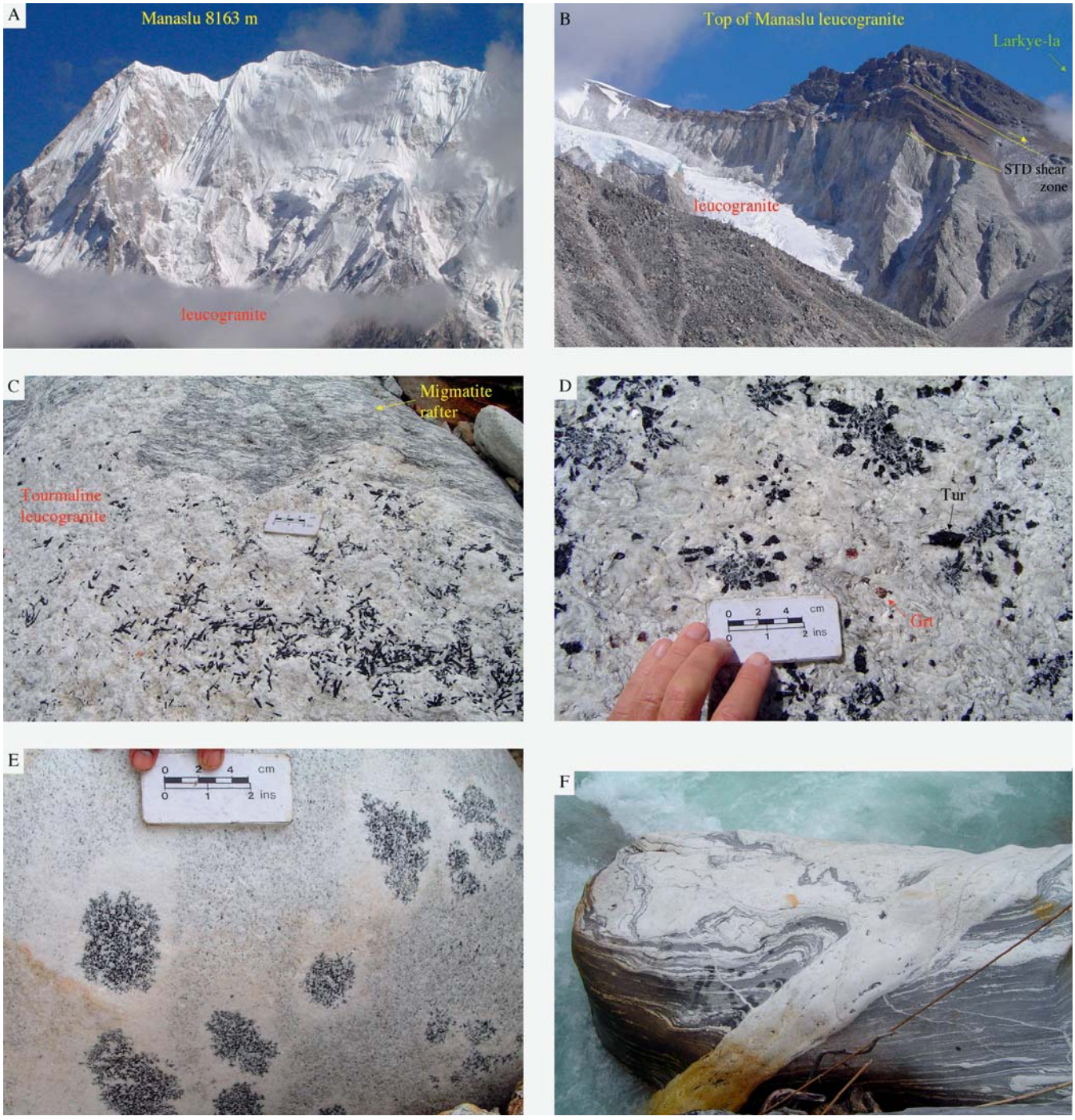

Figure 5 (a) Massive cliffs, approximately 3000 metres high, of pale leucogranite exposed on the south face of Manaslu (8163 m). (b) Upper contact of the Manaslu leucogranite truncated by the north-dipping STD low-angle normal fault; north of the Larkye-la, Nepal–Tibet border. (c) Toumaline leucogranite enclosing rafts of migmatitic gneiss, Bimthang, Manaslu west. (d) Tourmaline+garnet leucogranite, Bimthang, south of Manaslu. (e) Metasomatic 'ghosts' of tourmaline+quartz schorl within leucogranite, Manaslu west. (f) Leucogranite dyke cross-cutting gneissic fabrics, Jangle Karkar, south of Manaslu.

metapelite at mid-crustal depths is likely to be the muscovite dehydration melting reaction:

$$\text{Ms} + \text{Qtz} + \text{Pl} = \text{Kfs} + \text{Als (Sil)} + \text{Melt}$$

Experimental studies in the pressure range 6–10 kbar suggest that this curve is located between about 710°C and 790°C at 8 kbar (Petö 1976; Patiño-Douce & Harris 1998). Its calculated position, in the middle of this range, is shown in Figure 3. The amount of melt generated is typically of the order of ten volume percent, but depends primarily on the amount of muscovite present. Large migmatite terranes represent the *in situ* melt region. During muscovite melting, if the restite and liquid remain in equilibrium, melting will continue until the solid muscovite reactant phase is exhausted.

The biotite dehydration melting reaction:

$$\text{Bt} + \text{Pl} \pm \text{Als (Sil)} + \text{Qtz} = \text{Kfs} \pm \text{Crd} \pm \text{Grt} + \text{Melt}$$

occurs at higher temperature and lower pressure than muscovite melting. Le Breton & Thompson (1988) located the beginning of biotite dehydration melting between 760°C and 800°C at 10 kbar, although significant volumes of melt were not produced until temperatures reached 850°C. Pelitic source rocks will melt at lower temperatures (ca. 750°C; 5 kbar) whereas greywacke source rocks lacking sillimanite require

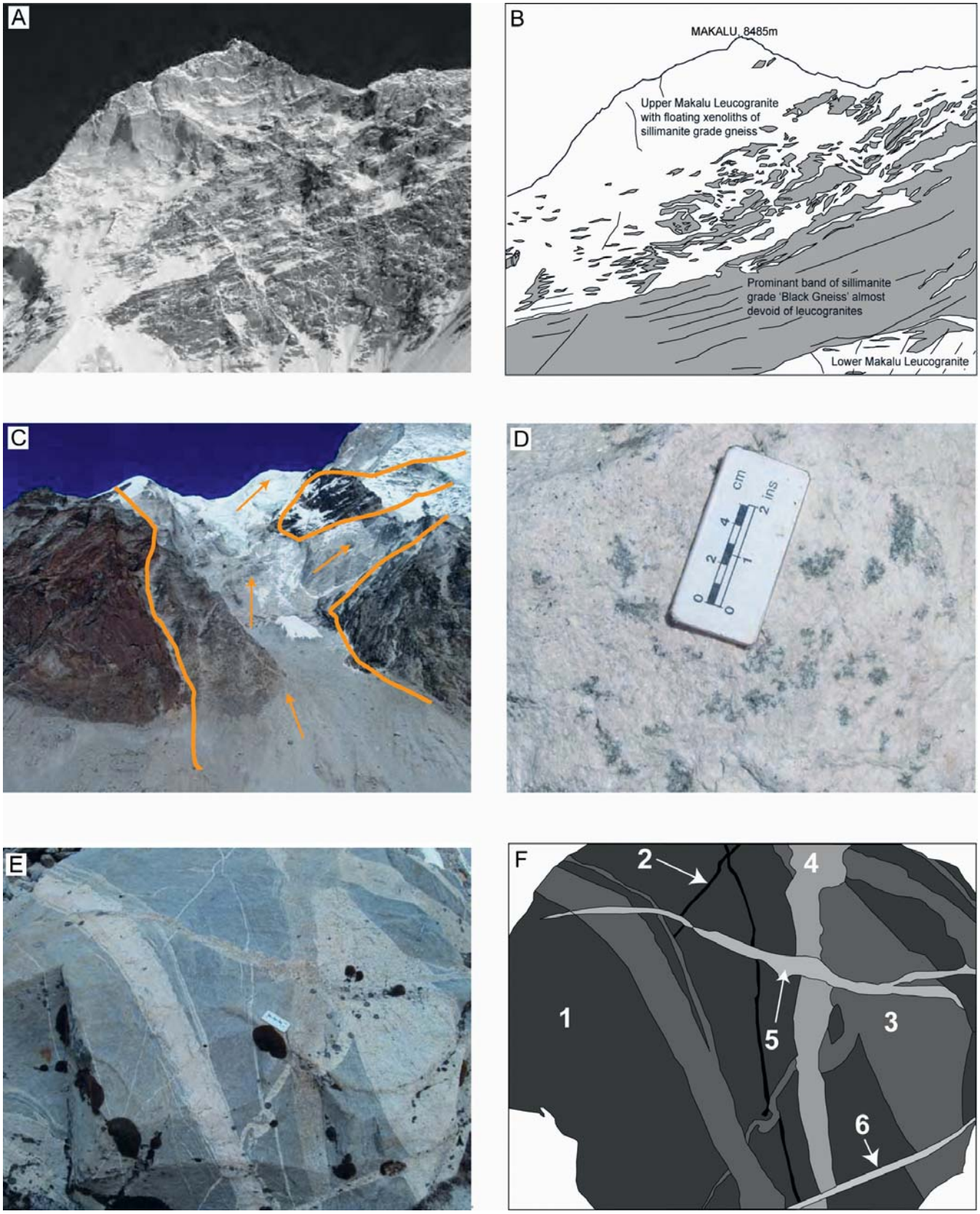

Figure 6 (a), (b) Massive cordierite-bearing leucogranite on the south face of Makalu (8485 m) showing abundant xenoliths along the base of the uppermost large sill. (c) Vertical feeder dyke to the uppermost cordierite leucogranite sill on the south face of Makalu. (d) Large green cordierite crystals enclosed in Makalu leucogranite, Barun glacier, Nepal. (e), (f) Six phases of cross-cutting leucogranite dykes, south face of Makalu, Barun glacier.

higher temperatures of about 825°C at 5 kbar (Vielzeuf & Holloway 1988; Stevens *et al.* 1997). Biotite dehydration melting results in formation of peritectic garnet and/or cordierite in metapelites and peritectic orthopyroxene in metagreywackes. For typical metapelite bulk compositions, cordierite is the stable phase at pressures less than about 5 kbar, whereas garnet is stable at higher pressure.

Himalayan metamorphism records clockwise P–T–t paths with sillimanite grade overprinting earlier kyanite grade conditions. Harris & Massey (1994) concluded that most

Himalayan granites were decompression melts formed on the exhumation part of the P–T path in the sillimanite field. However, the uncommon presence of kyanite-bearing migmatites, e.g. in the Marsyandi valley, Nepal (Coleman 1998), in Bhutan (Daniel *et al.* 2003) and in Sikkim, is evidence that melting probably started earlier (23–16 Ma from garnet Sm–Nd ages in Harris *et al.* 2004), and at higher pressure (8–12 kbar) in some parts of the Himalaya.

P–T phase relations and trace element modelling suggest that most Himalayan leucogranites formed by vapour-absent incongruent melting of muscovite in the temperature range 650–750°C at pressures between 9 and 4 kbar (Scaillet *et al.* 1990, 1996; Harris & Massey 1994; Searle *et al.* 1999b; Prince *et al.* 2001). A flux of aqueous fluid into the melting zone will augment the volume of granitic melt formed. There is geochemical evidence that melting was not typically an equilibrium process (Harris & Inger 1992), and that extracted melt entrained a proportion of restitic material. Incomplete mixing between different melt batches resulted in isotopic heterogeneity in crystallised leucogranite bodies (e.g. Deniel *et al.* 1987; Scaillet *et al.* 1996).

These crustal melt reactions require no heat or chemical input from the mantle. The achievement of high temperatures in the mid-crust would, however, be assisted by high internal heat production in the source region. In a ductile deforming channel such as the Early Miocene GHS, internal heat production could include both radiogenic and strain heating. In the following sections it is suggested that this is the case.

5. Source rocks

Himalayan leucogranites are strongly peraluminous, characterised by the presence of muscovite and tourmaline, with biotite and garnet also present in lesser amounts. Major element compositions are fairly homogeneous, but trace elements are highly variable and depend on the nature of the source. Sr, Nd and Pb isotopes are all indicative of a metasedimentary source (Deniel *et al.* 1987; Harris *et al.* 1995, Guillot & LeFort 1995). $^{87}Sr/^{86}Sr$ ratios of leucogranites are very high (0·74–0·79) and heterogeneous, suggesting a 100% crustal protolith. Harris & Massey (1994) made a detailed Sr isotope study of the Langtang leucogranites and concluded that the protolith was not the sillimanite migmatites into which the melts have been emplaced, but rather the kyanite-bearing meta-pelites structurally lower down the GHS section. They further implied that the granites were not *in situ* melts but had migrated some distance (>10 km) from their source. However, in most Himalayan profiles mapped by the present authors it is possible to physically trace the migmatite leucosomes coalescing into giant foliation-parallel sill networks, which feed larger plutons (e.g. Searle *et al.* 1997, 1999b). It is perfectly possible that the leucogranite bodies were tapping different migmatites at depth rather than ones immediately adjacent (Harris & Massey 1994) but the heterogeneous Sr isotopes probably reflect a wide range of protoliths with each batch of melt produced.

The leucogranite sill complexes are almost always within the sillimanite grade gneisses and melt migration was more horizontal, not vertical. The larger plutons are not actually intrusive into higher structural levels, but are more like subhorizontal ballooning sills (e.g. Nuptse leucogranite; Searle *et al.* 2003, Searle 2003, 2007). This is the case in Zanskar (e.g. Noble & Searle 1995), Shivling, Garhwal (Searle *et al.* 1993, 1999b), Manaslu (Searle & Godin 2003), Shisha Pangma (Searle *et al.* 1997), and the Everest region (Searle 1999a, b, 2003; Searle *et al.* 2003, 2006; Jessup *et al.* 2008).

Isotopic signatures can be used to determine the nature of granite protoliths, provided that the liquid is in isotopic equilibrium with the source. Trace element modelling of partial melting is only useful if equilibrium between the melt and the solid phases has been achieved (Harris & Inger 1992; Harris *et al.* 1995). Himalayan leucogranites are, however, rarely in isotopic equilibrium as a result of complex sedimentary protoliths and multiple batch melting (Deniel *et al.* 1987). Guillot & LeFort (1995) proposed a bimodal origin of Himalayan leucogranites with two-mica leucogranites ($^{87}Sr–^{86}Sr$ ratio <0·752) derived from a meta-greywacke source and tourmaline leucogranites ($^{87}Sr–^{86}Sr$ ratio >0·752) derived from a metapelitic source. However, in the field there is a complete range of granite composition with variable amounts of tourmaline, muscovite, biotite and garnet. It seems more likely that progressive batch melting tapped different source rocks ranging from black shales to meta-greywackes within the NeoProterozoic Haimanta Formation. Cambro-Ordovician augen gneisses (Formation 3; LeFort 1975, 1981) also commonly show *in situ* melt textures with tourmaline ± garnet bearing leucosomes.

6. Heat source for crustal melting

It has become increasingly clear that peak sillimanite grade metamorphism, crustal melting and ductile shear along the MCT along the base of the GHS and ductile shear along the STD at the top of the GHS were synchronous, and these metamorphic, magmatic and structural processes must be genetically linked. The greatest problem has been to explain why peak temperatures and granite melt generation in thickened Himalayan crust were at a relatively shallow depth (15–20 km depth; 4–6 kbar), and why melting does not occur at greater depths. P–T–t data across the GHS along the Everest profile show that high temperatures (>620°C) were maintained for ca. 15 million years (from 32 to 17 Ma) along the top of the GHS and that approximately 45–50 km width (20 km structural thickness) of the GHS was approximately isothermal in the sillimanite grade (Searle *et al.* 2003, 2006; Jessup *et al.* 2006, 2008). This shallow heating requires an unusually steep geothermal gradient, and crustal thickening alone cannot account for the thermal profile. Restoration of the GHS shows that the source for granite melts was the Neo-Proterozoic Haimanta–Cheka Formation. A combination of high internal radiogenic heat production from the melt source rocks and thermal relaxation after crustal thickening is proposed. Average heat production in the migmatites is a factor of two more than heat production in the schists (Harris & Massey 1994). Shear heating along the MCT (England *et al.* 1992; Harrison *et al.* 1998) cannot explain the heat distribution in the GHS because maximum temperatures are a long way up-section from the MCT. No granite melts are present along the exposed MCT anywhere along the Himalaya. No mantle heat input is present, so the only possible extra heat source for restricted shallow-level melting is internal heat production by highly radioactive sedimentary source rocks. Gariepy *et al.* (1985) noted that Himalayan granites have highly radiogenic Pb isotopic compositions which imply sources enriched in U and Th. Uranium concentrations from Himalayan granites are some of the highest found anywhere in granitic rocks (Pinet & Jaupart 1987).

7. Melt segregation – migmatites

The core of the GHS shows a vast migmatite terrane that stretches from the ductile shear zone along the STD at the top to the region above the zone of inverted metamorphic

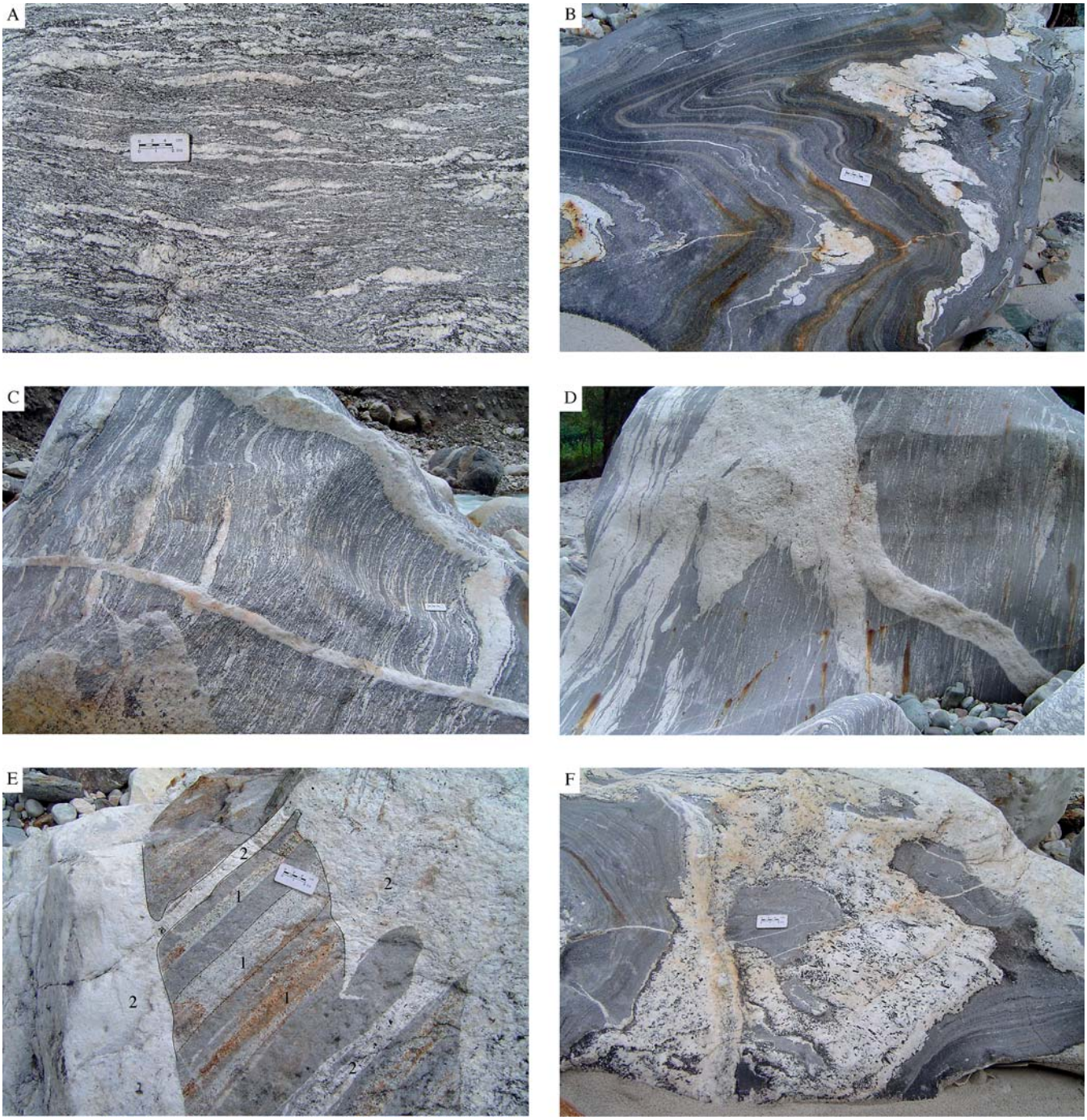

Figure 7 (a) Typical migmatite textures showing stromatic migmatite with melts generated along the foliation planes, south of Manaslu in the Marsyandi valley, Nepal. (b) Early leucogranites boudinaged in the foliation plane and subsequently folded, south of Manaslu, Nepal. (c) Melt extraction textures where melt is channelled out of leucosome into dykes that mobilise and cross-cut the migmatite fabric, south of Manaslu, Nepal. (d) Melt mobilisation from leucosome to channelled flow along dykes, south of Manaslu. (e) Early layered leucogranite sills (1) in gneisses, cut by late granite melts mobilised into sill-dyke networks (2), south of Manaslu, Nepal. (f) Late tourmaline leucogranite melts breaking up host gneisses into xenoliths, south of Manaslu, Marysandi valley, Nepal.

isograds along the MCT at the base. The zone of partial melting above the sillimanite–K-feldspar isograd can reach a maximum structural thickness of 15–20 km along the Zanskar profile in the western Himalaya (Searle & Rex 1989; Searle *et al*. 1992, 1999a, b), and 20 km along the Everest profile in Nepal (Searle *et al*. 2003, 2006; Jessup *et al*. 2006) and the Kangchenjunga profile in Sikkim (Searle & Szulc 2005). Although the protoliths differ (from Proterozoic in the south to Cambro-Ordovician in the north), metamorphic grade, P–T conditions and degrees of partial melting are similar across the GHS. *In situ* crustal melting forming migmatites is common in GHS quartzo-feldspathic gneisses, pelitic gneisses and K-feldspar augen gneisses. From field evidence it seems likely that all these lithologies constituted source rocks for granite melts.

Melt extraction pathways can be mapped out using leucosome networks. Layered stromatic migmatites are the most common textures, with melt segregations flattened in the foliation plane (Fig. 7a), similar to compaction bands (e.g. Brown 2007). K-feldspar augen gneisses commonly show *in situ* melting, for example in the Namche orthogneiss (Viskupic & Hodges 2001; Searle *et al*. 2003). Kinematic

indicators (rotated K-feldspar augen, C–S fabrics, etc.) and quantitative strain data from the Everest profile show that although south-directed simple shear is dominant across the GHS, a significant component of pure shear is apparent (Law *et al.* 2004; Jessup *et al.* 2006). This general shear is compatible with flow parallel to the extension direction in horizontal sheeted leucogranite sills. U–Pb dating of monazite shows that migmatite leucosomes have Early Miocene ages, similar to the higher level leucogranites (Noble & Searle 1995; Walker *et al.* 1999; Dezes *et al.* 1999), supporting a genetic relationship between migmatite and granite, despite the difference in Sr and O isotopes (Harris & Massey 1994).

Pervasive melt migration can initially occur by porous melt flow through hot, viscous crust (Weinberg & Searle 1999). This is like an intermediate stage between a migmatite terrane and a sheeted sill complex. Cross-cutting relationships show batch melting of leucogranite with early formed granites folded in with the schistosity (Fig. 7b). Early leucogranite sills commonly show boudinage fabrics, indicating extension at right angles to the flattening direction. Leucosomes are randomly distributed in the core of the GHS where exposed, but begin to coalesce into discrete veins and melt channels that tend to follow planes of anisotropy. As soon as leucosome *in situ* melts become interconnected, the melt extraction pathway is formed and the melt may start to flow (Fig. 7c, d). High-temperature igneous textures show that melt extracted from the migmatite feeds dykes may cross-cut the same migmatite fabric (Fig. 7e). Thus very short time intervals between melt extraction, dyking and crystallisation are involved in each batch of melt. Later foliation-parallel sheeted sill complexes feed magma, generated from the migmatite zone, horizontally along the foliation planes of anisotropy. Later dykes cross-cut the migmatite fabric and contain floating xenoliths of migmatitic gneiss within (Fig. 7f). Melt flows down pressure gradients by the easiest path, feeding magma to higher level sills. In the Himalaya these flow pathways gently up-dip from north to south along north-dipping foliation planes.

8. Melt transport; granite emplacement mechanisms

Several Himalayan leucogranites have been mapped out in 3-D and studied in detail. These include the Shivling–Bhagirathi granites in north India (Scaillet *et al.* 1990, 1995; Searle *et al.* 1993), the Manaslu leucogranite in west Nepal (Guillot *et al.* 1993, 1995; Searle & Godin 2003), the Shisha Pangma leucogranite in south Tibet (Searle *et al.* 1997) and the Everest–Makalu leucogranites in east Nepal–south Tibet (Searle 1999a, b, 2003; Searle *et al.* 2003, 2006; Jessup *et al.* 2006). Spectacular sheeted sill networks of leucogranite melts can be seen in many 3-D cliff sections along the Himalaya. Sills propagate by hydraulic fracturing, forcing cracks apart to accommodate magma injected from the migmatite zone. Composite intrusions show that multiple batches of magma are injected into the same zone. Occasional dykes connect sills, enabling magma to be channelled up structural section. Magma batches may be separated by short time intervals. Some outcrops show foliation-parallel sills concordant with the metamorphic fabric in the host sillimanite gneiss, which feed magma into a dyke that clearly crosscuts the same metamorphic fabric.

In the Himalaya there is almost no evidence of diapiric ascent of granite magma. Despite some earlier studies describing diapiric intrusions of the Manaslu leucogranite up across the STD into Tethyan sediments (LeFort 1975, 1981; Colchen *et al.* 1986; Harrison *et al.* 1999), subsequent work has shown that the granite was intrusive into high-grade marbles, augen gneiss and pelite of the GHS and that the STD wraps around the top of the leucogranite (Searle & Godin 2003). All Himalayan leucogranites are within the GHS, beneath the STD passive roof fault. In the deeper structural levels magma flow is almost entirely sub-horizontal along foliation-parallel sill complexes. At higher structural levels the sills amalgamate into larger sills and, as they approach the surface, they balloon up into inflated sills. This ballooning sill structure is typified by the Nuptse sill in the Everest region (Searle 1999a, b, 2003) and by the Shisha Pangma leucogranite in south Tibet (Searle *et al.* 1997). Even the largest Himalayan leucogranites such as the Manaslu (ca. 5 km thick) leucogranite are tabular sill-like bodies dipping gently north and truncated along the top by the STD ductile shear zone and low-angle normal fault (Searle & Godin 2003; Fig. 5b). Similarly, the Kangchenjunga leucogranite is a series of composite sills totalling approximately 12–14 km structural thickness (Searle & Szulc 2005), dipping gently north and truncated by the STD along the top.

In addition to field observations, the petrological and isotopic heterogeneity of leucogranites, and a thin upper thermal aureole, has been used as evidence for episodic emplacement of magmas to form larger leucogranite bodies. Thermal modelling of this emplacement (Annen *et al.* 2006) implies a 20–60 ka repeat time for the emplacement of 20–60 m-thick sills which form the larger 5 km-thick Himalayan leucogranite bodies (e.g. Manaslu, Fig. 5). To provide such a volume of melt, a highly fertile source must be heated for a prolonged time, producing low viscosity ($10^{4\cdot5}$PaS) magma that is emplaced via shear assisted melt extraction (Scaillet & Searle 2006).

9. Channel Flow model

The Himalayan Channel Flow model (Fig. 8) describes a protracted flow of a weak, viscous, partially molten layer of middle crust between relatively rigid, but still deformable bounding upper and lower crust slabs (e.g. Beaumont *et al.* 2001, 2004; Grujic *et al.* 2002; Godin *et al.* 2006; Grujic 2006). Ductile extrusion of high-grade metamorphic rocks, and leucogranite melts between a coeval normal sense shear zone above (STD) and a thrust-sense shear zone below (MCT) allowed southward extrusion of the GHS. The resultant geometry of the metamorphic isograds shows an inverted and condensed P–T profile above the Main Central Thrust along the base of the extruding slab (Searle & Rex 1989; Searle *et al.* 2008) and a right-way-up P–T profile beneath the South Tibetan Detachment along the top of the extruding slab (Searle *et al.* 2003, 2006; Jessup *et al.* 2006). Extrusion was driven ultimately by the crustal thickness and topographic variation between the Tibetan plateau hinterland (70–80 km thick crust; ca. 5 km elevation) and the Indian foreland (35–40 km thick crust, 0–1 km elevation).

Numerous geological studies across the GHS have shown that almost all the data supports the Channel Flow model for the GHS during the Early Miocene. These data include P–T profiles (e.g. Searle *et al.* 2003, 2006; Jessup *et al.* 2006), 3-D distribution of partial melts and granites in the middle crust (e.g. Searle 1999a, b; Searle *et al.* 1999a, b, 2006; Searle & Szulc 2005), and quantitative data on strain, deformation temperatures and vorticity of flow (e.g. Law *et al.* 2004; Jessup *et al.* 2006). Beaumont *et al.* (2001) used a thermal-mechanical numerical model to show that channel flow and ductile extrusion were dynamically linked to the effects of surface erosion focused along the Greater Himalaya at the extrusion front. As pointed out by Klemperer (2006) this model is consistent with

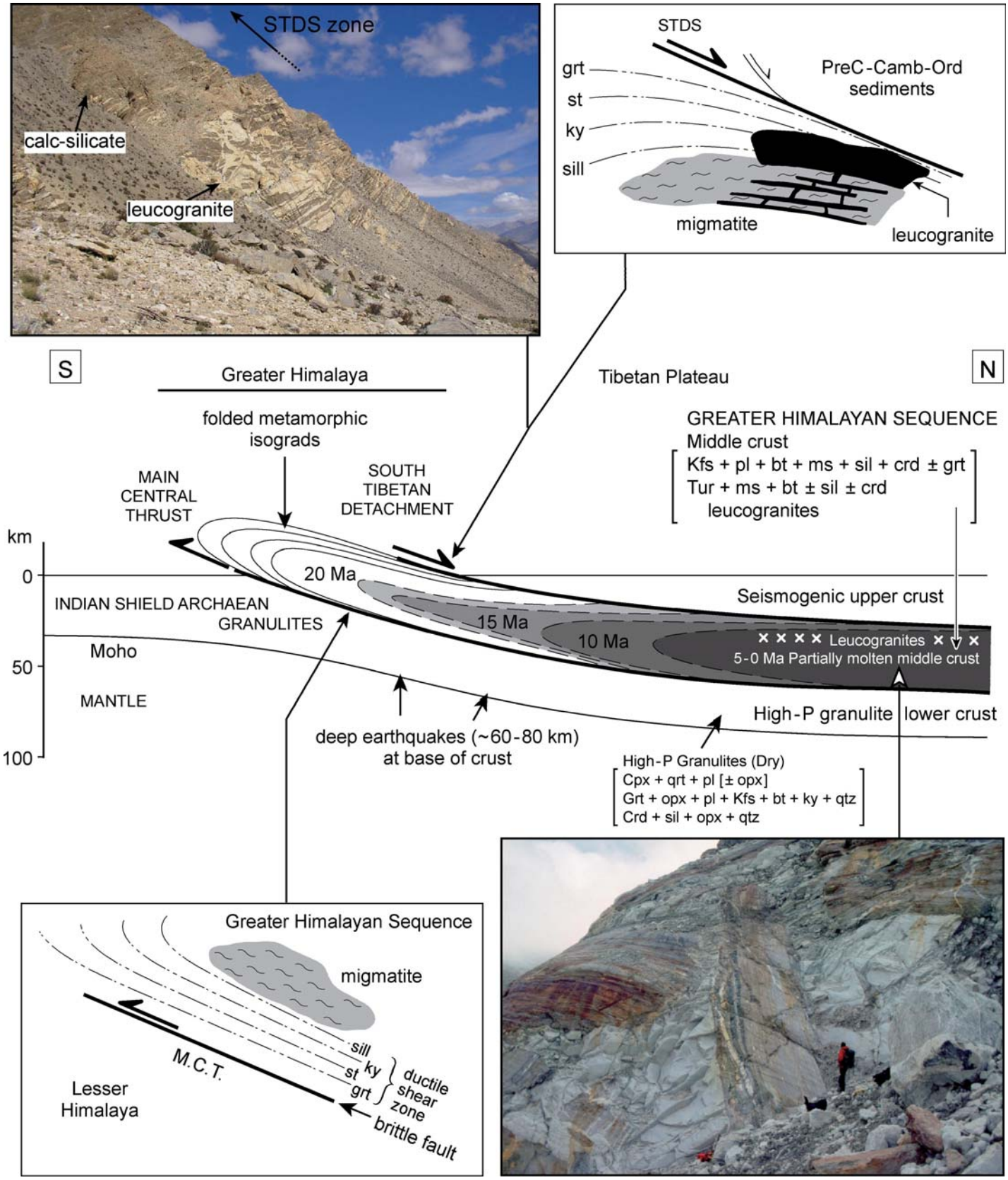

Figure 8 Himalayan channel flow model (after Searle *et al*. 2006; Cottle *et al*. 2009), a model that satisfies all geological and geophysical requirements in the Greater Himalaya. Inset top left shows the STD profile along Dzakaa chu, north of Everest, South Tibet. Inset bottom right shows the central part of the channel in the Kangshung valley east of Everest, south Tibet. Giant blocks or rafters of gneisses with early leucogranite sills are completely enclosed in Miocene leucogranite.

all the geological data . . . 'inevitably, since the model was designed *a posteriori* to fit the observations'.

Searle *et al*. (1988) and Searle & Rex (1989) first proposed that inverted, condensed metamorphic isograds from kyanite to biotite grade along the MCT ductile shear zone along the base of the GHS channel were linked to the right-way-up isograds along the footwall of the STD along the top of the GHS. Kinematic indicators and strain requires the GHS to be

extruding south relative to the stable seismogenic upper crust above (Tethyan Himalaya), and the subducting Indian shield and Lesser Himalayan cover rocks beneath. Later models based on the Bhutan Himalaya (Grujic *et al.* 1996, 2002) included the folded isograds in their wedge extrusion or layer extrusion models. Deep crustal seismic profiling now reveals that the partially molten mid-crustal layer imaged beneath southern Tibet can match the geologically constrained cross-sections across the GHS in Nepal (Nelson *et al.* 1996; Searle *et al.* 2003, 2006).

Extensive geophysical measurements in Tibet also imply that temperatures and rheologies require some form of crustal flow. Seismic velocities beneath southern Tibet are so low that the crust has to be fluid-rich, and predicted temperatures are so high that these fluids are likely to be partial melts. Low elastic thickness, low topographic relief and shallow cut-off of crustal seismicity all show that fluids weaken the middle crust (Klemperer 2006). The 'bright spots' as imaged by magneto-telluric studies beneath the Lhasa block (Wei *et al.* 2001; Unsworth *et al.* 2005), are at the same structural depth as the depth of formation of Himalayan leucogranites (Searle *et al.* 2003, 2006; Galliard *et al.* 2004) and in a similar down-dip structural position in the middle crust. Unlike the middle crust, the lower crust beneath the Himalaya and southern Tibet is relatively rigid and not melting, suggesting that it is composed of dry granulite facies metamorphic rocks of the underthrust lower Indian crust. Because crustal thickness reaches 75–80 km beneath southern Tibet (Nelson *et al.* 1996) or even up to 90 km beneath the Karakoram and western Tibet (Rai *et al.* 2006), the lower crust beneath these regions must be in high-pressure granulite (dry) or eclogite (wet) metamorphic facies today (Searle *et al.* 2003, 2006). Brown & Solar (1998) and Brown (2006, 2007) proposed that melt loss in the middle crust might leave a dry granulite residue behind in the lower crust. The lower crust in the Himalaya is inherited Precambrian granulite facies rocks, which are anhydrous and strong and can also explain the deep crustal seismicity beneath southern Tibet (Priestley *et al.* 2008).

10. Conclusions

The unique three-dimensional exposures around Himalayan leucogranites allow a comprehensive view of their internal and external structure to be mapped out. Extensive study of fabrics in the host gneisses, migmatites, leucogranite sills, dykes and larger bodies combined with detailed U–(Th)–Pb dating of peak metamorphic, migmatite leucosome and granite melting have allowed the fourth dimension, time, to be incorporated into models of melt generation and emplacement. Along the 2200 km length of the Himalaya, the larger leucogranite bodies always occur at similar structural horizons within the upper part of the GHS, beneath the STD low-angle normal fault. The STD forms a passive roof (stretching) fault (Searle *et al.* 2003; Law *et al.* 2004), beneath which channel flow and ductile extrusion of the GHS middle crust occurred.

Himalayan crustal melting occurred along the upper part of the middle crust (4–6 kbar; 15–20 km depth), but not in the lower crust. Sr, Nd and O isotopes indicate pure crustal melting with no input from the mantle. Melts were sourced from fertile muscovite-bearing pelites and quartzo-feldspathic gneisses of the Neo-Proterozoic Haimanta–Cheka Formations. The primary heat source was probably from high internal heat production rates within the Proterozoic source rocks in the middle crust. A vast *in situ* migmatite terrane generated melts from the melting of a heterogeneous variety of protolith rocks. Interconnected leucosome melts aggregated to force magma into layer-parallel sills and a few cross-cutting dykes. Early Miocene leucogranites (24–17 Ma) are largely concordant with the foliation, whereas later ones (16–12 Ma) may cross-cut the ductile fabrics. All leucogranites are cut by the uppermost brittle low-angle normal fault, the Qomolangma detachment.

Field observations, structural sections and geophysical evidence all provide support for the Channel Flow model, a description of the evolution of the Himalayan–south Tibetan crust during the Miocene. The Himalayan channel flow model is restricted both in time (Early–Middle Miocene) and space (Himalayan–south Tibet middle crust). It is not applicable to the earlier, Eocene subduction-related UHP coesite eclogite metamorphism, or to the Oligocene HP kyanite metamorphism. Whether channel flow is active today in the middle crust of southernmost Tibet–northernmost Himalaya is still open to debate (Nelson *et al.* 1996; Hodges 2000; Searle *et al.* 2006). The present model (Fig. 8) shows that the Greater Himalaya may represent the Miocene carapace of an actively extruding mid-crustal channel operating at depth beneath southern Tibet today.

11. Acknowledgements

This work was carried out using NERC grant NER/K/S/2000/00951 to MPS and PhD grants to JMC (New Zealand TEC scholarship) and MJS (NERC). We are grateful to Randall Parrish, Steve Noble, Bruno Scaillet, Laurent Godin, Rick Law, Micah Jessup and the late Doug Nelson for discussions. We also thank Peter Treloar and Alan Whittington for detailed and insightful reviews, and Alex Kisters for editorial and scientific comments.

12. References

Annen, C., Scaillet, B. & Sparks, R. S. J. 2006. Thermal constraints on the emplacement rate of a large intrusive complex: The Manaslu leucogranite, Nepal Himalaya. *Journal of Petrology* **47**, 71–95.

Beaumont, C., Jamieson, R. A., Nguyen, M. H. & Lee, B. 2001. Himalayan tectonics explained by extrusion of a low-viscosity crustal channel coupled to focused surface denudation. *Nature* **414**, 738–42.

Beaumont, C., Jamieson, R. A., Nguyen, M. H. & Medvedev, S. 2004. Crustal channel flows: 1. Numerical models with applications to the tectonics of the Himalayan–Tibetan orogen. *Journal of Geophysical Research – Solid Earth* **109**, B06406.

Booth, A. L., Zeitler, P. K., Kidd, W. S. F., Wooden, J., Liu, Y. P., Idleman, B., Hren, M. & Chamberlain, C. P. 2004. U–Pb zircon constraints on the tectonic evolution of southeastern Tibet, Namche Barwa area. *American Journal of Science* **304**, 889–929.

Bowring, S. A., Searle, M. P., Waters, D. J., Hodges, K. V., Schmitz, M. & Crowley, J. 2004. ID–TIMS geochronology of ca. 1 Ma leucogranites from the core of Nanga Parbat. *American Geophysical Union Fall Meeting San Francisco*, V22E-08.

Brown, M. 2006. Melt extraction from the lower continental crust of orogens: the field evidence. *In* Brown, M. & Rushmer, T. (eds) *Evolution and Differentiation of Continental Crust*, 332–84. Cambridge: Cambridge University Press.

Brown, M. 2007. Crustal melting and melt extraction, ascent and emplacement in orogens: mechanisms and consequences. *Journal of the Geological Society London* **164**, 709–30.

Brown, M. & Solar, G. S. 1998. Shear zone systems and melts: feedback relations and self-organization in orogenic belts. *Journal of Structural Geology* **20**, 211–27.

Burg, J. P. 1983. *Geological Map of South Tibet.* Beijing: Ministry of Geology.

Butler, R. W. H., Harris, N. B. W. & Whittington, A. G. 1997. Interactions between deformation, magmatism and hydrothermal activity during active crustal thickening: a field example from Nanga Parbat, Pakistan Himalayas. *Mineralogical Magazine* **61**, 37–51.

Colchen, M., LeFort, P. & Pecher, A. 1986. *Annapurna–Manaslu–Ganesh Himal. Carte geologique au 1:200 000 scale*. Paris: CNRS. 136 pp.

Coleman, M. E. 1998. U–Pb constraints on Oligocene–Miocene deformation and anatexis within the central Himalaya, Marsyandi Valley, Nepal. *American Journal of Science* **298**, 553–71.

Copeland, P., Parrish, R. R. & Harrison, T. M. 1988. Identification of inherited radiogenic Pb in monazite and its implications for U–Pb systematics. *Nature* **333**, 760–3.

Cottle, J. M., Jessup, M. J., Newell, D. L., Searle, M. P., Law, R. D. & Horstwood, M. S. A. 2007. Structural insight into the ductile evolution of an orogen-scale detachment: the South Tibetan Detachment System, Dzakaa Chu section, Eastern Himalaya. *Journal of Structural Geology* **29**, 1781–97. doi:10.1016/j.jsg.2007.08.007.

Cottle, J. M., Searle, M. P., Horstwood, M. S. A. & Waters, D. J. 2009. Timing of mid-crustal metamorphism, melting and deformation in the Mount Everest region of Southern Tibet revealed by U(–Th)–Pb geochronology. *Journal of Geology* **117**(6), 643–64. doi: 10.1086/605994

Crowley, J. L., Bowring, S. A. & Searle, M. P. 2005. U–Th–Pb systematics of monazite, xenotime, and zircon from Pleistocene leucogranites at Nanga Parbat (Pakistan Himalaya). *Geochimica et Cosmochimica Acta* **69**, 8.

Crowley, J. L., Waters, D. J., Searle, M. P. & Bowring, S. A. 2009. Pleistocene melting and rapid exhumation of the Nanga Parbat massif, Pakistan: Age and P–T conditions of accessory mineral growth in migmatite and leucosome. *Earth and Planetary Science Letters* **288**, 408–20. doi: 10.1016/j.epsl.2009.09.044

Daniel, C. G., Hollister, L. S., Parrish, R. R. & Grujic, D. 2003. Exhumation of the Main Central Thrust from lower crustal depths, Eastern Bhutan Himalaya. *Journal of Metamorphic Geology* **21**, 317–34.

Deniel, C., Vidal, P., Fernandez, A., Le Fort, P. & Peucat, J. J. 1987. Isotopic study of the Manaslu granite (Himalaya, Nepal); inference on the age and source of Himalayan leucogranites. *Contributions to Mineralogy and Petrology* **96**, 78–92.

Dezes, P., Vannay, J.-C., Steck, A., Bussy, F. & Cosca, M. 1999. Synorogenic extension: Quantitative constraints on the age and displacement of the Zanskar shear zone (northwest Himalaya). *Geological Society of America Bulletin* **111**, 364–74.

Edwards, M. A. & Harrison, T. M. 1997. When did the roof collapse? Late Miocene north–south extension in the high Himalaya revealed by Th–Pb monazite dating of the Khula Kangri Granite. *Geology* **25**, 543–6.

England, P., LeFort, P., Molnar, P. & Pêcher, A. 1992. Heat sources for Tertiary metamorphism and anatexis in the Annapurna–Manaslu region central Nepal. *Journal of Geophysical Research* **97**, 2107–28.

Gaillard, F., Scaillet, B. & Pichavant, M. 2004. Evidence for present-day leucogranite pluton growth in Tibet. *Geology* **32**, 801–4.

Gariepy, C., Allegre, C. & Xu, R. H. 1985. Pb-isotope geochemistry of granitoids from the Himalaya–Tibet collision zone: implications for crustal evolution. *Earth and Planetary Science Letters* **74**, 220–34.

Godin, L., Parrish, R. R., Brown, R. L. & Hodges, K. V. 2001. Crustal thickening leading to exhumation of the Himalayan metamorphic core of central Nepal; insight from U–Pb geochronology and $^{40}Ar/^{39}Ar$ thermochronology. *Tectonics* **20**, 729–47.

Godin, L., Grujic, D., Law R. D. & Searle, M. P. 2006. Channel flow, ductile extrusion and exhumation in continental collision zones: an introduction. *In* Law, R. D., Searle, M. P. & Godin, L. (eds) *Channel Flow, Ductile Extrusion and Exhumation in Continental Collision Zones. Geological Society, London, Special Publications* **268**, 1–23.

Grujic, D. 2006. Channel Flow and continental collision tectonics. *In* Law, R. D., Searle, M. P. & Godin, L. (eds) *Channel Flow, Ductile Extrusion and Exhumation in Continental Collision Zones. Geological Society, London, Special Publications* **268**, 25–37.

Grujic, D., Casey, M., Davidson, C., Hollister, L. S., Kundig, R., Pavlis, T. & Schmid, S. 1996. Ductile extrusion of the Higher Himalayan crystalline in Bhutan: Evidence from quartz microfabrics. *Tectonophysics* **260**, 21–43.

Grujic, D., Hollister, L. S. & Parrish, R. R. 2002. Himalayan metamorphic sequence as an orogenic channel: insight from Bhutan. *Earth and Planetary Science Letters* **198**, 177–91.

Guillot, S., Pêcher, A., Rochette, P. & LeFort, P. 1993. The emplacement of the Manaslu granite of Central Nepal: field and magnetic susceptibility constraints. *In* Treloar, P. J. & Searle, M. P. (eds) *Himalayan Tectonics. Geological Society, London, Special Publications* **74**, 413–28.

Guillot, S., LeFort, P., Pêcher, A., Barman, M. R. & Aprahamian, J. 1995. Contact metamorphism and depth of emplacement of the Manaslu granite (central Nepal): implications for Himalayan orogenesis. *Tectonophysics* **241**, 99–119.

Guillot, S. & LeFort, P. 1995. Geochemical constraints on the bimodal origin of High Himalayan leucogranites. *Lithos* **35**, 221–34.

Harris, N. B. W., Ayres, M. & Massey, J. 1994. Geochemistry of granitic melts produced during the incongruent melting of muscovite; implications for the extraction of Himalayan leucogranite magmas. *Journal of Geophysical Research B Solid Earth and Planets* **100**, 15767–77.

Harris, N. B. W., Ayres, M. W. & Massey, J. 1995. Geochemistry of granitic melts produced during the incongruent melting of muscovite: implications for the extraction of Himalayan leucogranite magmas. *Journal of Geophysical Research* **100**, 15767–77.

Harris, N. B. W., Caddick, M., Kosler, J., Goswami, S., Vance, D. & Tindle, A. G. 2004. The pressure–temperature–time path of migmatites from the Sikkim Himalaya. *Journal of Metamorphic Geology* **22**, 249–64.

Harris, N. B. W. & Inger, S. 1992. Trace-Element Modeling of Pelite-Derived Granites. *Contributions to Mineralogy and Petrology* **110**, 46–56.

Harris, N. B. W. & Massey, J. A. 1994. Decompression and anatexis of Himalayan metapelites. *Tectonics* **13**, 1537–46.

Harrison, T. M., McKeegan, K. D. & Le Fort, P. 1995. Detection of inherited monazite in the Manaslu leucogranite by $^{208}Pb/^{232}Th$ ion microprobe dating; crystallization age and tectonic implications. *Earth and Planetary Science Letters* **133**, 271–82.

Harrison, T. M., Grove, M., Lovera, O. M. & Catlos, E. J. 1998. A model for the origin of Himalayan anatexis and inverted metamorphism. *Journal of Geophysical Research* **103**, 27017–32.

Harrison, T. M., Grove, M., McKeegan, K. D., Coath, C. D., Lovera, O. M. & Le Fort, P. 1999. Origin and episodic emplacement of the Manaslu intrusive complex, central Himalaya. *Journal of Petrology* **40**, 3–19.

Hauck, M. L., Nelson, K. D., Brown, L. D., Zhao, W. J. & Ross, A. R. 1998. Crustal structure of the Himalayan orogen at similar to 90 degrees east longitude from Project INDEPTH deep reflection profiles. *Tectonics* **17**, 481–500.

Hodges, K. V. 2000. Tectonics of the Himalaya and southern Tibet from two perspectives. *Geological Society of America Bulletin* **112**, 324–50.

Hodges, K. V., Parrish, R. R. & Searle, M. P. 1996. Tectonic evolution of the central Annapurna Range, Nepalese Himalayas. *Tectonics* **15**, 1264–91.

Hodges, K. V., Bowring, S. A., Davidek, K. L., Hawkins, D. P. & Krol, M. A. 1998. Evidence for rapid displacement on Himalayan normal faults and the importance of tectonic denudation in the evolution of mountain ranges. *Geology* **26**, 483–6.

Hubbard, M. S. 1989. Thermobarometric constraints on the thermal history of the Main Central Thrust Zone and Tibetan Slab, eastern Nepal Himalaya. *Journal of Metamorphic Geology* **7**, 19–30.

Jackson, J., McKenzie, D., Priestley, K. & Emmerson, B. 2008. New views on the structure and rheology of the lithosphere. *Journal of the Geological Society, London* **165**, 453–65.

Jamieson, R. A., Beaumont, C., Medvedev, S. & Nguyen, M. H. 2004. Crustal channel flows: 2. Numerical models with implications for metamorphism in the Himalayan–Tibetan orogen. *Journal of Geophysical Research – Solid Earth* **109**, B06407.

Jessup, M. J., Law R. D., Searle, M. P. & Hubbard, M. S. 2006. Structural evolution and vorticity of flow during extrusion and exhumation of the Greater Himalayan Slab, Mount Everest Massif, Tibet/Nepal; implications for orogen-scale flow partitioning. *In* Law, R. D., Searle, M. P. & Godin, L. (eds) *Channel Flow, Ductile Extrusion and Exhumation in Continental Collision Zones. Geological Society, London, Special Publications* **268**, 379–413.

Jessup, M. J., Cottle, J. M., Searle, M. P., Law, R. D., Newell, D. L., Tracy, R. J. & Waters. D. J. 2008. P–T–t–D paths of Everest Series schist, Nepal. *Journal of Metamorphic Geology* **26**, 717–39. doi: 10.1111/j.1525-1314.2008.00784.x

Klemperer, S. L. 2006. Crustal flow in Tibet; geophysical evidence for the physical state of Tibetan lithosphere, and inferred patterns of active flow. *In* Law, R. D., Searle, M. P. & Godin, L. (eds) *Channel Flow, Ductile Extrusion and Exhumation in Continental Collision Zones. Geological Society, London, Special Publications* **268**, 39–70.

Law, R. D., Searle, M. P. & Simpson, R. L. 2004. Strain, deformation temperatures and vorticity of flow at the top of the Greater Himalayan Slab, Everest Massif, Tibet. *Journal of the Geological Society, London* **161**, 305–20.

Law, R. D., Searle, M. P. & Godin, L. (eds) 2006. *Channel flow, ductile extrusion and exhumation in continental collision zones. Geological Society, London, Special Publication* **268**. 620 pp.

Le Breton, N. & Thompson, A. B. 1988. Fluid-absent (dehydration) melting of biotite in metapelites in the early stages of crustal anatexis. *Contributions to Mineralogy and Petrology* **99**, 226–37.

LeFort, P. 1975. Himalayas the Collided Range – Present Knowledge of Continental Arc. *American Journal of Science* **A275**, 1–44.

LeFort, P. 1981. Manaslu Leucogranite – a Collision Signature of the Himalaya; a Model for its Genesis and Emplacement. *Journal of Geophysical Research* **86**, 545–68.

Murphy, M. A. & Harrison, T. M. 1999. Relationship between leucogranites and the Qomolangma detachment in the Rongbuk Valley, south Tibet. *Geology* **27**, 831–4.

Nelson, K. D., Zhao, W., Brown, L. D., Kuo, J., Che, J., Liu, X., Klemperer, S. L., Makovsky, Y., Meissner, R., Mechie, J., Kind, R., Wenzel, F., Ni, J., Nabelek, J., Chen, L., Tan, H., Wei, W., Jones, A. G., Booker, J., Unsworth, B., Kidd, W. S. F., Hauck, M., Alsdorf, D., Ross, A., Cogan, M., Wu, C., Sandvol, E. A. & Edwards, M. A. 1996. Partially molten middle crust beneath southern Tibet; synthesis of Project INDEPTH results. *Science* **274**, 1684–8.

Noble, S. R. & Searle, M. P. 1995. Age of Crustal Melting and Leucogranite Formation from U–Pb Zircon and Monazite Dating in the Western Himalaya, Zanskar, India. *Geology* **23**, 1135–8.

Parrish, R. R. 1990. U–Pb dating of monazite and its application to geological problems. *Canadian Journal of Earth Sciences* **27**, 1431–50.

Parrish, R. R., Gough, S. J., Searle, M. P. & Waters, D. J. 2006. Plate velocity exhumation of ultrahigh-pressure eclogites in the Pakistan Himalaya. *Geology* **34**, 989–92.

Patiño Douce, A. E. & Harris, N. B. W. 1998. Experimental constraints on Himalayan anatexis. *Journal of Petrology* **39**, 689–710.

Petö, P. 1976. An experimental investigation of melting relations involving muscovite and paragonite in the silica-saturated portion of the system K_2O–Na_2O–Al_2O_3–SiO_2–H_2O to 15 kb total pressure. *Progress in Experimental Petrology* **3**, 41–5.

Pinet, C. & Jaupart, C. 1987. A thermal model for the distribution in space and time of Himalayan granites. *Earth and Planetary Science Letters* **84**, 87–99.

Priestley, K., Jackson, J. & McKenzie, D. 2008. Lithospheric structure and deep earthquakes beneath India, the Himalaya and southern Tibet. *Geophysical Journal International* **172**, 345–62.

Prince, C., Harris, N. B. W. & Vance, D. 2001. Fluid-enhanced melting during prograde metamorphism. *Journal of the Geological Society, London* **158** (2), 233–41.

Rai, S. S., Priestley, K., Gaur, V. K., Mitra, S., Singh, M. P. & Searle, M. P. 2006. Configuration of the Indian Moho beneath the NW Himalaya and Ladakh. *Geophysical Research Letters* **33**, L15308.

Rowley, D. B. 1996. Age of initiation of collision between India and Asia: A review of stratigraphic data. *Earth and Planetary Science Letters* **145**, 1–13.

Scaillet, B., France-Lanord, C. & LeFort, P. 1990. Badrinath–Gangotri Plutons (Garhwal, India) – Petrological and Geochemical Evidence for Fractionation Processes in a High Himalayan Leucogranite. *Journal of Volcanology and Geothermal Research* **44**, 163–88.

Scaillet, B., Pecher, A., Rochette, P. & Champenois, M. 1995. The Gangotri Granite (Garhwal Himalaya) – Laccolithic Emplacement in an Extending Collisional Belt. *Journal of Geophysical Research – Solid Earth* **100**, 585–607.

Scaillet, B., Holtz, F., Pichavant, M. & Schmidt, M. 1996. Viscosity of Himalayan leucogranites: Implications for mechanisms of granitic magma ascent. *Journal of Geophysical Research – Solid Earth* **101**, 27691–9.

Scaillet, B. & Searle, M. P. 2006. Mechanisms and timescales of felsic magma segregation, ascent and emplacement in the Himalaya. *In* Law, R. D., Searle, M. P. & Godin, L. (eds) *Channel Flow, Ductile Extrusion and Exhumation in Continental Collision Zones. Geological Society, London, Special Publications* **268**, 293–308. Bath, UK: The Geological Society Publishing House.

Schärer, U. 1984. The effect of initial ^{230}Th disequilibrium on young U–Pb ages: the Makalu case, Himalaya. *Earth and Planetary Science Letters* **67**, 191–204.

Schulte-Pelkum, V., Monsalve, G., Sheehan, A., Pandey, M. R., Sapkota, S., Bilham, R. & Wu, F. 2005. Imaging the Indian subcontinent beneath the Himalaya. *Nature* **435**, 1222–5.

Searle, M. P. 1999a. Emplacement of Himalayan leucogranites by magma injection along giant sill complexes: examples from the Cho Oyu, Gyachung Kang and Everest leucogranites (Nepal Himalaya). *Journal of Asian Earth Sciences* **17**, 773–83.

Searle, M. P. 1999b. Extensional and compressional faults in the Everest–Lhotse massif, Khumbu Himalaya, Nepal. *Journal of the Geological Society, London* **156**, 227–40.

Searle, M. P. 2003. *Geological Map of the Mount Everest massif, Nepal – South Tibet Himalaya.* Scale 1:100,000. Oxford: Oxford University.

Searle, M. P. 2007. *Geological Map of the Mount Everest–Makalu region Nepal – South Tibet Himalaya.* Scale 1:100,000. Oxford: Oxford University.

Searle, M. P., Cooper, D. J. W. & Rex, A. J. 1988. Collision tectonics of the Ladakh–Zanskar Himalaya. *Philosophical Transactions of the Royal Society, London* **A326**, 117–50.

Searle, M. P., Pickering, K. T. & Cooper, D. J. W. 1990. Restoration and evolution of the intermontane Indus molasse basin, Ladakh Himalaya, India. *Tectonophysics* **174**, 301–14.

Searle, M. P., Crawford, M. B. & Rex, A. J. 1992. Field Relations, Geochemistry, Origin and Emplacement of the Baltoro Granite, Central Karakoram. *Transactions of the Royal Society of Edinburgh: Earth Sciences* **83**, 519–38.

Searle, M. P., Metcalfe, R. P., Rex, A. J. & Norry, M. J. 1993. Field relations, petrogenesis and emplacement of the Bhagirathi leucogranite, Garhwal Himalaya. *In* Treloar, P. J. & Searle, M. P. (eds) *Himalayan Tectonics. Geological Society, London, Special Publications* **74**, 429–44. Bath, UK: The Geological Society Publishing House.

Searle, M. P., Parrish, R. R., Hodges, K. V., Hurford, A. J., Ayres, M. W. & Whitehouse, M. J. 1997. Shisha Pangma leucogranite, south Tibetan Himalaya: Field relations, geochemistry, age, origin, and emplacement. *Journal of Geology* **105**, 295–317.

Searle, M. P., Waters, D. J., Dransfield, M. W., Stephenson, B. J., Walker, J. D., Walker, C. B. & Rex, D. C. 1999a. Thermal and mechanical models for the structural evolution of the Zanskar High Himalaya. *In* MacNiocall, C. & Ryan, P. D. (eds) *Continental Tectonics. Geological Society, London, Special Publications* **164**, 139–56. Bath, UK: The Geological Society Publishing House.

Searle, M. P., Noble, S. R., Hurford, A. J. & Rex, D. C. 1999b. Age of crustal melting, emplacement and exhumation history of the Shivling leucogranite, Garhwal Himalaya. *Geological Magazine* **136**, 513–25.

Searle, M. P., Simpson, R. L., Law, R. D., Parrish, R. R. & Waters, D. J. 2003. The structural geometry, metamorphic and magmatic evolution of the Everest massif, High Himalaya of Nepal – South Tibet. *Journal of the Geological Society, London* **160**, 345–66.

Searle, M. P., Law R. D. & Jessup, M. J. 2006. Crustal structure, restoration and evolution of the Greater Himalaya in Nepal-South Tibet; implications for channel flow and ductile extrusion of the middle crust. *In* Law, R. D., Searle, M. P. & Godin, L. (eds) *Channel Flow, Ductile Extrusion and Exhumation in Continental Collision Zones. Geological Society, London, Special Publications* **268**, 355–78. Bath, UK: The Geological Society Publishing House.

Searle, M. P., Law, R. D., Godin, L., Larson, K., Streule, M. J., Cottle, J. M. & Jessup, M. J. 2008. Defining the Himalayan Main Central Thrust in Nepal. *Journal of the Geological Society, London* **165**, 523–34.

Searle, M. P. & Godin, L. 2003. The South Tibetan detachment and the Manaslu Leucogranite; a structural reinterpretation and restoration of the Annapurna–Manaslu Himalaya, Nepal. *Journal of Geology* **111**, 505–23.

Searle, M. P. & Rex, A. J. 1989. Thermal-Model for the Zanskar Himalaya. *Journal of Metamorphic Geology* **7**, 127–34.

Searle, M. P. & Szulc, A. G. 2005. Channel flow and ductile extrusion of the high Himalayan slab – the Kangchenjunga–Darjeeling profile, Sikkim Himalaya. *Journal of Asian Earth Sciences* **25**, 173–85.

Simpson, R. L., Parrish, R. R., Searle, M. P. & Waters, D. J. 2000. Two episodes of monazite crystallization during metamorphism and crustal melting in the Everest region of the Nepalese Himalaya. *Geology* **28**, 403–6.

Stevens, G., Clemens, J. D. & Droop, G. T. R. 1997. Melt production during granulite facies anatexis: experimental data from 'primitive' metasedimentary protoliths. *Contributions to Mineralogy and Petrology* **128**, 352–70.

Thimm, K. A., Parrish, R. R., Hollister, L. S., Grujic, D., Klepeis, K. & Dorji, T. 1999. New U–Pb data from the Lesser and Greater Himalayan sequences in Bhutan. *Journal of Conference Abstracts* **4**, 57.

Tilmann, F., Ni, J., Hearn, T., Ma, Y. S., Rapine, R., Kind, R., Mechie, J., Saul, J., Haines, S., Klemperer, S., Brown, L., PanAnont, P., Ross, A., Nelson, K. D., Guo, J., Zhao, W. & INDEPTH III Seismic Team. 2003. Seismic imaging of the downwelling Indian lithosphere beneath central Tibet. *Science* **300**, 1424–7.

Treloar, P. J., O'Brien, P. J., Parrish, R. R. & Khan, M. a. 2003. Exhumation of Tertiary coesite-bearing eclogites from the

Pakistan Himalaya. *Journal of the Geological Society, London* **160**, 367–76.

Unsworth, M. J., Jones, A. G., Wei, W., Marquis, G., Gokarn, S. G., Spratt, J. E. & INDEPTH-MT Team. 2005. Crustal rheology of the Himalaya and Southern Tibet inferred from magnetotelluric data. *Nature* **438**, 78–81.

Vance, D. & Harris, N. 1999. Timing of prograde metamorphism in the Zanskar Himalaya. *Geology* **27**, 395–8.

Vielzeuf, D. & Holloway, J. R. 1988. Experimental determination of the fluid-absent melting relations in the pelitic system; consequences for crustal differentiation. *Contributions to Mineralogy and Petrology* **98**, 257–76.

Viskupic, K., Hodges, K. V. & Bowring, S. A. 2005. Timescales of melt generation and the thermal evolution of the Himalayan metamorphic core, Everest region, eastern Nepal. *Contributions to Mineralogy and Petrology* **149**, 1–21.

Viskupic, K. & Hodges, K. V. 2001. Monazite–xenotime thermochronometry: methodology and an example from the Nepalese Himalaya. *Contributions to Mineralogy and Petrology* **141**, 233–47.

Walker, J. D., Martin, M. W., Bowring, S. A., Searle, M. P., Waters, D. J. & Hodges, K. V. 1999. Metamorphism, melting, and extension: Age constraints from the High Himalayan Slab of southeast Zanskar and northwest Lahaul. *Journal of Geology* **107**, 473–95.

Walker, C. B., Searle, M. P. & Waters, D. J. 2001. An integrated tectonothermal model for the evolution of the High Himalaya in western Zanskar with constraints from thermobarometry and metamorphic modeling. *Tectonics* **20**, 810–33.

Wei, W., Unsworth, M., Jones, A., Booker, J., Tan, H., Nelson, D., Chen, L., Li, S., Solon, K., Bedrosian, P., Jin, S., Deng, M., Ledo, J., Kay, D. & Roberts, B. 2001. Detection of widespread fluids in the Tibetan crust by magnetotelluric studies. *Science* **292**, 716–18.

Weinberg, R. F. & Searle, M. P. 1999. Volatile-assisted intrusion and autometasomatism of leucogranites in the Khumbu Himalaya, Nepal. *Journal of Geology* **107**, 27–48.

White, R. W., Powell, R. & Holland, T. J. B. 2001. Calculation of partial melting equilibria in the system Na_2O–CaO–K_2O–FeO–MgO–Al_2O_3–SiO_2–H_2O (NCKFMASH). *Journal of Metamorphic Geology* **19** (2), 139–53.

Whittington, A. G., Harris, N. B. W. & Baker, J. 1998. Low-pressure crustal anatexis: the significance of spinel and cordierite from metapelitic assemblages at Nanga Parbat, northern Pakistan. *In* Treloar, P. J. & O'Brien, P. J. (eds) *What Drives Metamorphism and Metamorphic Reactions? Geological Society, London, Special Publications* **138**, 183–98. Bath, UK: The Geological Society Publishing House.

Whittington, A. G., Harris, N. B. W. & Butler, R. W. H. 1999. Contrasting anatectic styles at Nanga Parbat, northern Pakistan. *In* Macfarlane, A., Sorkhabi, R. B. & Quade, J. (eds) *Himalaya and Tibet: Mountain Roots to Mountain Tops. Geological Society of America, Special Paper* **328**, 129–44.

Whittington, A. G. & Treloar, P. J. 2002. Crustal anatexis and its relation to the exhumation of collisional orogenic belts, with particular reference to the Himalaya. *Mineralogical Magazine* **66**, 53–91.

Wu, C., Nelson, K. D, Wortman, G., Samson, S., Yue, Y., Li, J., Kidd, W. S. F. & Edwards, M. A. 1998. Yadong cross-structure and South Tibetan Detachment in the east central Himalaya. *Tectonics* **17**, 28–45.

Zeitler, P. K., Koons, P. O., Bishop, M. P., Chamberlain, C. P., Craw, D., Edwards, M. A., Hamidullah, S., Jan, M. Q., Khan, M. A., Khattak, M. U. K., Kidd, W. S. F., Mackie, R. L., Meltzer, A. S., Park, S. K., Pecher, A., Poage, M. A., Sarker, G., Schneider, D. A., Seeber, L. & Shroder, J. F. 2001a. Crustal reworking at Nanga Parbat, Pakistan: Metamorphic consequences of thermal-mechanical coupling facilitated by erosion. *Tectonics* **20**, 712–28.

Zeitler, P. K., Meltzer, A. S., Koons, P. O., Craw, D., Hallet, B., Chamberlain, C. P., Kidd, W. S. F., Park, S. K., Seeber, L., Bishop, M. & Shroder, J. 2001b. Erosion, Himalayan geodynamics and the Geomorphology of metamorphism. *GSA Today* **11** (January) 4–9.

Zhang, H. F., Harris, N. B. W., Parrish, R. R., Kelley, S., Zhang, L., Rogers, N., Argles, T. & King, J. 2004. Causes and consequences of protracted melting of the mid-crust exposed in the North Himalayan antiform. *Earth and Planetary Science Letters* **228**, 195–212.

Zhu, B., Kidd, W. S. F., Rowley, D. B., Currie, B. S. & Shafique, N. 2005. Age of initiation of the India–Asia collision in the east-central Himalaya. *Journal of Geology* **113**, 265–85.

MS received 11 December 2007. Accepted for publication 13 March 2008 (Stellenbosch); 15 January 2009 (RSE).

Zoning and resorption of plagioclase in a layered gabbro, as a petrographic indicator of magmatic differentiation

Takashi Hoshide and Masaaki Obata

Division of Earth and Planetary Sciences, Department of Geology and Mineralogy, Graduate School of Science, Kyoto University, Kyoto, Japan 606–8502
Email: hoshide@kueps.kyoto-u.ac.jp; obata@kueps.kyoto-u.ac.jp

ABSTRACT: The Murotomisaki Gabbroic Intrusion is a sill-like layered gabbro emplaced in sedimentary strata of Tertiary age in southwest Japan. The zoning (including resorption structures) and the compositional variations of plagioclase from throughout the intrusion were studied, and it was found that the zoning pattern may be classified into four types, which may well correlated with the hosting rock types, the mode of occurrences and their stratigraphic positions in the intrusion. The plagioclase zoning was successfully decoded, and the sequence of events that took place during the magmatic differentiation was deduced and further interpreted in the context of a stratified basal boundary layer slowly ascending in a solidifying magma body. It was shown that various layered structures – modal layering, podiform gabbroic pegmatites and anorthositic layers – observed in the Murotomisaki Gabbro were formed within the moving basal boundary layer by flushing of H_2O-rich fluid and fractionated silicate melts from below. By the fluxing of hydrous fluids, plagioclase crystals preferentially dissolved and then melt fraction increased in the basal boundary layer. Under these circumstances, plagioclase-rich fractionated melts diapirically segregated from the crystal pile. Calcic plagioclases, which are out of equilibrium in the central part of the intrusion, may have originated from the basal boundary layer in this manner.

KEY WORDS: Anorthosite, boundary layer, crystal mush, diapir, fluid fluxing, magma chamber

Magma reservoirs are subjected to crystallisation and associated fractionation that are driven by the various physico-chemical processes such as gravitational settling or flotation of crystals, compositional convection and compaction. As thermal gradient is created near the marginal zones of the magma reservoir (e.g. Brandeis & Jaupart 1986; Turner *et al*. 1986; Marsh 1988; Tait & Jaupart 1992), it is plausible that processes in the magmatic boundary layer play an important role in the magmatic differentiation after the settling of phenocrysts originally contained in the emplaced magma (Mangan & Marsh 1992). Recent studies of crystal size and crystal number density of olivine by Hoshide *et al*. (2006a, b) identified the zone of crystal accumulation (AC subzone) and the zone of crystal growth (GR subzone). On the basis of the vertical variation and the numerical balance of crystal number density, they thought that crystal settling hardly occurred and some sort of processes involved in *in situ* crystallisation (crystal growth) were important in the magmatic differentiation after the major phase of crystal settling of olivine originally contained in the magma at the time of its emplacement. Furthermore, they emphasised the occurrence of anorthosites in the GR subzone and proposed a hypothesis that segregation and diapiric ascent of anorthositic crystal-mush played an important role in the formation of the GR subzone and thereby affected the entire magmatic evolution. The argument is largely based on the observed whole-rock compositional trends and plume-like occurrence of the anorthosites. The present paper takes a different approach to studying the magmatic processes in more detail, by looking at rock microstructure, particularly, the zonal structure of plagioclase from the Murotomisaki Gabbro. In contrast to ferromagnesian minerals like olivine or augite, plagioclase has the advantage of slow diffusion kinetics, so that original zoning formed during crystal growth, i.e., growth zoning, is well preserved in the crystals, thereby providing useful information on the sequence of events and temporal change of physico-chemical environment in the magmatic system.

Following the geological outline and petrographic description, analytical data on plagioclase zoning are presented, and it is shown that the zoning pattern is well correlated to the hosting rock types and the mode of occurrence. The zoning data and rock systematics will be interpreted in the context of a moving and crystallising boundary layer. It is emphasised that the zoned plagioclase may be used as a useful tracer of mass movement within a magmatic system under differentiation.

1. Geological setting

The Murotomisaki Gabbroic Intrusion (abbr. 'MGI') is a wedge-shaped, sill-like layered gabbro (up to 220 m thickness) located near Cape Muroto, Shikoku, Japan. This intrusion is emplaced nearly concordantly to bedded sandstone and mudstone of the Tertiary sediments (Shimanto Group), giving rise to contact metamorphism on both sides of the sill. The intrusion has been dated at 14 Ma by the Rb–Sr whole-rock isochron method applied to anatexites in the contact aureole produced by the hot magma emplacement (Hamamoto & Sakai 1987). Regional geological and palaeomagnetic studies show that the intrusion was nearly horizontal when the magma was emplaced and solidified (Yajima 1972; Kodama *et al*. 1983; Kodama & Koyano 2003). The intrusion, together with

© 2009 The Royal Society of Edinburgh. doi:10.1017/S1755691009016090

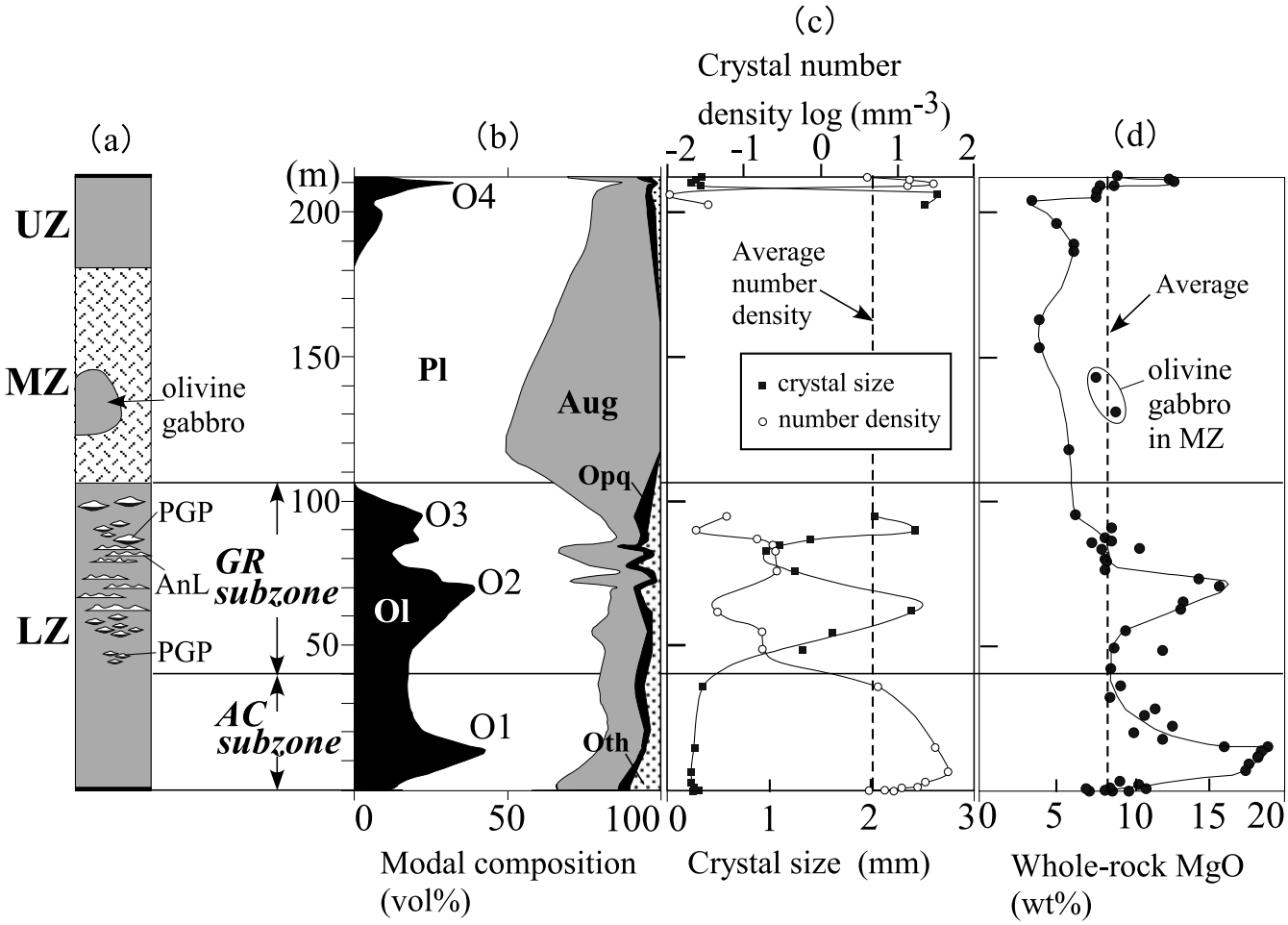

Figure 1 Lithological and compositional variations across the Murotomisaki Gabbroic Intrusion: (a) lithological variation; (b) modal variation; (c) crystal size and crystal number density of olivine; (d) whole-rock MgO content. Modified from Hoshide *et al.* (2006a). The crystal number density of olivine is shown in logarithmic scale. A broken line in (c) shows the level of average value of crystal number density of olivine of the intrusion. A broken line in (d) is the average value of the whole-rock MgO. Abbreviations: LZ=Lower Zone; MZ=Middle Zone; UZ=Upper Zone; PGP=podiform gabbroic pegmatite; AnL=anorthositic layer. Pl=plagioclase; Ol=olivine; Aug=augite; Opq=opaque minerals; Oth=other phases (hypersthene, biotite, hornblende and chlorite).

the surrounding sedimentary strata, was tilted by later tectonics by 60–70° towards northwest. A near-complete cross-section of the intrusion is exposed along the sea coast (Fig. 1a).

2. Petrographic subdivisions of the MGI

According to the rock types and the mesoscopic layered structures observable in the field, the intrusion is divided into the following three major stratigraphic zones: the Lower Zone (LZ: about 105 m thick); the Middle Zone (MZ: about 75 m thick); and the Upper Zone (UZ: about 30 m thick) (Fig. 1a). The Lower Zone and the Upper Zone contain thin chilled margins of a few metres thick. The Lower Zone consists of fine- to medium-grained olivine gabbro and contains, in places, subordinate amounts of anorthositic layers (Fig. 2a) and podiform gabbroic pegmatites (Fig. 3). The Middle Zone mainly consists of coarse gabbro that is composed of augite and plagioclase, and characteristically lacks olivine. The Upper Zone consists of medium-grained olivine gabbro, whose textures are different from those of Lower-Zone olivine gabbros. Important petrographic features are summarised in Figure 1 and described below.

2.1. The Lower Zone

Using the olivine crystal number density (i.e., total number of crystals of olivine per unit volume of rocks), the Lower Zone has been subdivided into two subzones, the AC subzone and the GR subzone above (Fig. 1). The AC subzone comprises the lower 40m and has crystal number density of olivine above the average of the whole intrusion, whereas the GR subzone (40–100 m) is less than the average. The crystal size of olivine and the presence or absence of the layered structures are clearly different between the AC and GR subzones. Therefore, the field occurrence and petrography are described separately for each subzone.

2.1.1. The AC subzone. The AC subzone appears uniform in the field; the grain size increases gradually upwards from the lower contact. The chilled margin, within a few cm from the contact, is very fine-grained, containing a few microphenocrysts of olivine (up to 8 vol%, average grain size 0·25 mm) and plagioclase (~1–3 vol%, average grain size 0·1 mm) in a dark-coloured matrix (probably a devitrified glass) that contains small skeletal or swallow-tailed crystals of plagioclase (average grain size 10 μm) (Fig. 4a).

Olivine increases rapidly in both mode and number density with distance from the lower contact, and the maximum is observed at ca. 15 metres (peak O1) before decreasing (Fig. 1b, c). Crystal size of olivine, on the other hand, remains nearly constant. Plagioclase monotonically increases in size, which results in an overall upward-coarsening of rocks.

The texture is typically poikilitic. Euhedral to subhedral plagioclase partially encloses euhedral olivine. Anhedral augite

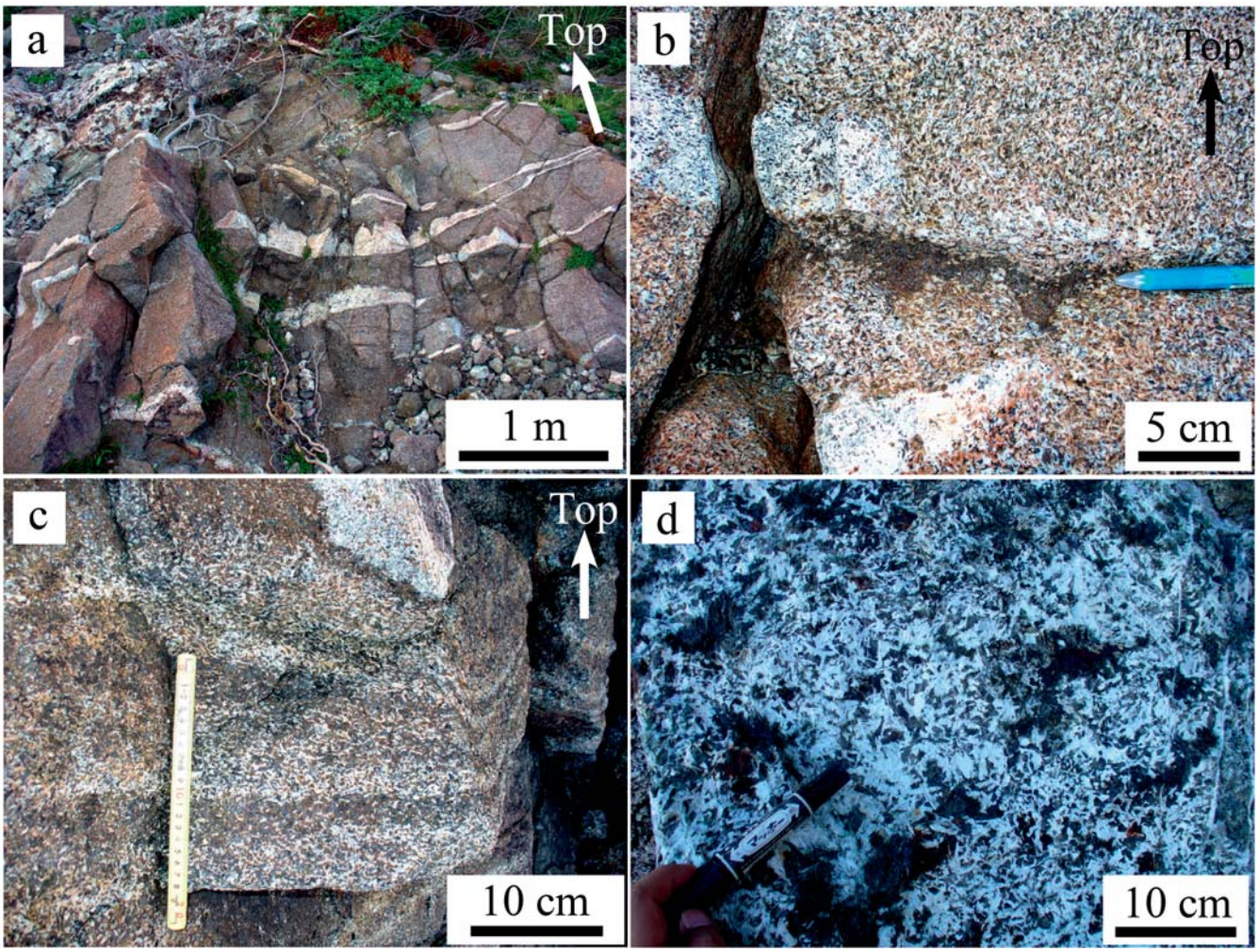

Figure 2 Field photographs of the Murotomisaki Gabbro: (a) Anorthositic layers (AnL, light coloured) in the olivine–gabbro matrix of the GR subzone (approximately 78 m from the bottom). Note a flat bottom and a wavy upper surface. Arrow indicates the top of the sill; (b) closeup of (a). Thin mafic selvage attached to the base of an anorthositic layer. The layer trails down in a wavy form; (c) Modally graded layering in the lowermost part of the GR subzone (approximately 40 m from the bottom); (d) Field photograph of a coarse gabbro in the Middle Zone (approximately 150 m from the bottom) showing a mesoscopic patchy structure, consisting of melanocratic patches rich in augite and opaque mineral and leucocratic plagioclase-rich matrix.

encloses olivine and plagioclase or occupies their interstices (Fig. 4b). Plagioclase usually has a euhedral calcic core nearly constant in An-content and this An-content decreases continuously towards the rim (Fig. 5a). The plagioclase cores often show oscillatory zoning and have thin edges of even more calcic composition than the core. More details of the zonal structures are given in the next section.

The olivine crystals often contain small polycrystalline clots (several tens μm in size) consisting of pargasitic amphibole, hypersthene and biotite that are hereafter called 'amphibole clots' (Fig. 5d). Many clots are nearly-round, but some have the form of a 'negative crystal' of the host olivine. The morphology and the occurrence suggest that these clots probably represent solidified hydrous silicate melt entrapped in growing olivine crystals at magmatic stages.

2.1.2. The GR subzone. The GR subzone is lithologically more variable. The observed modal range is 12–40% olivine, 5–30% augite and 52–65% plagioclase; olivine grain size varies from 1·0 mm to 2·5 mm. Compositional layering is more developed than in the AC subzone (Fig. 1). This zone contains abundant layers of anorthosite (Fig. 2a) and lenticular pods of gabbroic pegmatite (Fig. 3a, b). There are two modal peaks of olivine in the host gabbro (O2 and O3), where average grain size of olivine is maximum. These two peaks coincide in position with the minimum peaks of olivine number density. In addition, peak O2 coincides with the maximum whole-rock MgO content (Fig. 1).

In olivine gabbros of the GR subzone, euhedral to subhedral plagioclase partially encloses euhedral olivine in common with that of the AC subzone, but olivines are larger and have lower number density than in the AC subzone and thus the texture is not poikilitic. Around the peak O2, augite is less abundant (below 10 vol%) and fills interstices between cumulus olivine and plagioclase (Fig. 4c). Gabbros around the peak O2 have modal ratios of olivine/plagioclase universally higher than those around peak O3. Around peak O3, olivine crystals are large and irregularly shaped and typically enclose plagioclase. The amphibole clots in the olivine crystals (Fig. 5d) are more abundant and are larger in size (∼1 mm) than those of the AC subzone. The amphibole clots also occur at interstices of aggregates of olivine crystals.

A fine-scale rhythmic layering due to modal variation of plagioclase, olivine and augite (with typical wave length around 10 cm) locally develops in a lowermost part of the GR subzone (the 'compositional banding' of Yajima 1972) (Fig. 2c). The felsic layers show weak shape-preferred orientations of plagioclase parallel to the layering. The mode of the layering is vertically asymmetric, that is, a felsic layer gradually changes

into the overlying mafic layer, but sharply into the underlying one. The modally-layered portion is more coarse-grained than the surrounding massive and more homogeneous parts at the same level. Plagioclase varies in the modal amount by 15% to 60% in this layering. Plagioclase and olivine are cumulus phases, and augite occurs at interstitial positions. Plagioclase crystals have calcic cores, the shapes of which are slightly rounded or corroded compared to those in non-layered gabbros. In the felsic layers, their calcic cores are larger than those in the mafic layers.

2.1.3. Bimodal occurrence of anorthosites (in the 'GR subzone'). Two types of anorthosite occur in the GR subzone. One type forms a constituent part of podiform gabbroic pegmatites (Fig. 3a, b); the other forms individual medium-grained layers (Plagioclase grain size: 2 mm in length; ~50 cm thick) without a pegmatitic part (Fig. 2a). The anorthositic layer is abundant at the 70–80–m horizon, around the O2 peak, whereas the podiform gabbroic pegmatite is more abundant just below and above this horizon (Fig. 1a).

Podiform gabbroic pegmatite. The podiform gabbroic pegmatites are lenticular in shape, oriented sub-parallel to the layering and vary in thickness from a few cm to 2 m (Fig. 3). They form clusters of several metres to several tens of metres in size (Fig. 3c). Each pod typically has an internal layered structure consisting of an anorthositic roof, a pegmatitic filling, and a picritic floor (Fig. 3b).

The anorthositic roof is medium- to coarse-grained (plagioclase grain size, about 3–10 mm in length) and has strong shape fabrics of plagioclase; euhedral plagioclase crystals are aligned sub-horizontal, parallel to the lower and the upper boundaries. The upper boundary of the anorthositic roof against the host olivine gabbro is often wavy and the plagioclase crystals are aligned parallel to the wavy boundary. This wavy structure has locally developed into plume-like, 'diapiric structure', implying a gravitational fluid-dynamic instability being developed at magmatic stages (Fig. 3d). Globular small masses of anorthosite (about 10 cm in diameter) occur above these plumes (Fig. 3d, f). The anorthositic roof and the 'globular' anorthosite masses contain abundant clots of amphibole of a few mm in diameter (Fig. 3e). Near the margin of the globular anorthosite masses plagioclase crystals are also aligned roughly parallel to their boundaries.

Microscopically, the anorthosite in the roof has an ophitic texture, consisting of euhedral plagioclase crystals (60–80 vol%) enclosed in large augite crystals (20–35 vol%) (Fig. 4g). Some plagioclase crystals show undulose extinction, implying plastic deformation of crystals. They also contain small amounts of calcite, apatite, titanite and allanite that occur in the interstices of euhedral plagioclase. Other accessory phases are ilmenite, titaniferous magnetite and sulfides. Intergrowths of ilmenite with titanite or titaniferous magnetite are common in the anorthositic roofs, whereas these oxides occur as independent grains in the host olivine gabbro.

The pegmatitic filling is very coarse-grained and consists of euhedral plagioclase (about 1–4 cm in length; $\sim An_{30-50}$) and interstitial augite. Plagioclase crystals are aligned nearly perpendicular to the sharp boundary with the anorthositic roof (Fig. 3a).

The picritic floor is also medium-grained (olivine grain size: about 2–3 mm in length) and consists of euhedral olivine (40~70 vol%) and interstitial plagioclase and augite (Fig. 4h). Olivine in the picritic gabbro in the floor is identical in composition to that in the host olivine gabbro (Mg#=60–65).

An outstanding feature is the invariability of the sequence of the internal layering with the anorthositic roof always on the top and the picritic floor on the bottom. The volume proportion of these three parts varies; the anorthositic roof may be very thin in some podiform pegmatites (Fig. 3b), whereas the picritic floor is minor or even missing in others (Fig. 3a).

Anorthositic layers. Anorthositic layers vary in thickness between 10 cm and 1 m and are oriented parallel to the compositional layering. The upper boundary to the host gabbro is wavy, like that of the anorthositic roof of the podiform gabbroic pegmatite, and the lower boundary is flat (Fig. 2a). Anorthosite has strong crystal shape fabrics, with plagioclase crystals aligned parallel to the wavy contacts (see also fig. 3B in Hoshide *et al.* 2006b). Some anorthositic layers have thin discontinuous basal layers of medium-grained mafic rocks (olivine grain size: about 2–3 mm in length), like the picritic floor of the podiform gabbroic pegmatite, implying its genetic link with podiform gabbroic pegmatites (Fig. 2b). The texture and rock composition of the anorthositic layers are very similar to the roof anorthosite.

2.2. The Middle Zone

The Middle Zone lacks obvious layering, but characteristically contains patchy mafic domains of a few to tens of centimetres in size (Fig. 2d). Euhedral plagioclase crystals included in large augite grains (up to several centimetres in size) form an ophitic texture (Fig. 4d, e). Olivine is generally absent except in one sample (at the 152-m level). The olivine in this sample is very iron-rich and shows a reverse zoning from an Fe-rich core (~Fo37) to an Fe-poor rim (~Fo43). Hydrous minerals, such as hornblende, biotite and prehnite, occur as interstitial phases, as well as in the 'embayments' of the calcic cores of plagioclase. Some rocks from the lower part of the Middle Zone have large plagioclase crystals that fill interstices of euhedral to subhedral augite crystals. A large block (15 m across) of medium-grained olivine gabbro occurs within the Middle Zone. The boundary between the block and the surrounding coarse gabbro is not clear because of poor exposure.

2.3. The Upper Zone

Olivine gabbro, which consists of olivine, plagioclase and augite, is the main rock type in this zone. Starting from the upper contact, olivine rapidly increases downward in the modal abundance and in crystal number density, marking a sharp peak (O4) at about the 210-m level (2 m below the upper contact; Fig. 1). The olivine grain size near the contact is about the same as that of AC subzone in the Lower Zone, but increases rapidly below the modal peak O4 and reaches a maximum at about the 206-m level (Fig. 1c). Around peak O4 there is a horizon that contains abundant spherulitic clots of hornblende aggregate (about 0·2 mm to 3 cm in diameter).

Although the host rocks are mineralogically similar to the olivine gabbros in the Lower Zone, the texture is different. Whilst the plagioclase is euhedral to subhedral, olivine and augite are irregular in shape and fill the interstices of plagioclase crystals in the Upper Zone. Some plagioclase crystals contain subhedral to anhedral calcic cores nearly constant in An-content and the boundary between the calcic core and the sodic mantle is rather sharp, marking a compositional gap as described in next section. Other grains in the same sample do not contain such distinct calcic cores, but show more gradual normal zoning. Plagioclase crystals become aggregated and form cancellous plagioclase-rich networks at the centimetre-scale and are oriented in the same direction in the networks. In the networks or clusters (a few centimetres scale), plagioclase crystals show undulose extinction and deformation twins, implying that they have been plastically deformed (Fig. 4f).

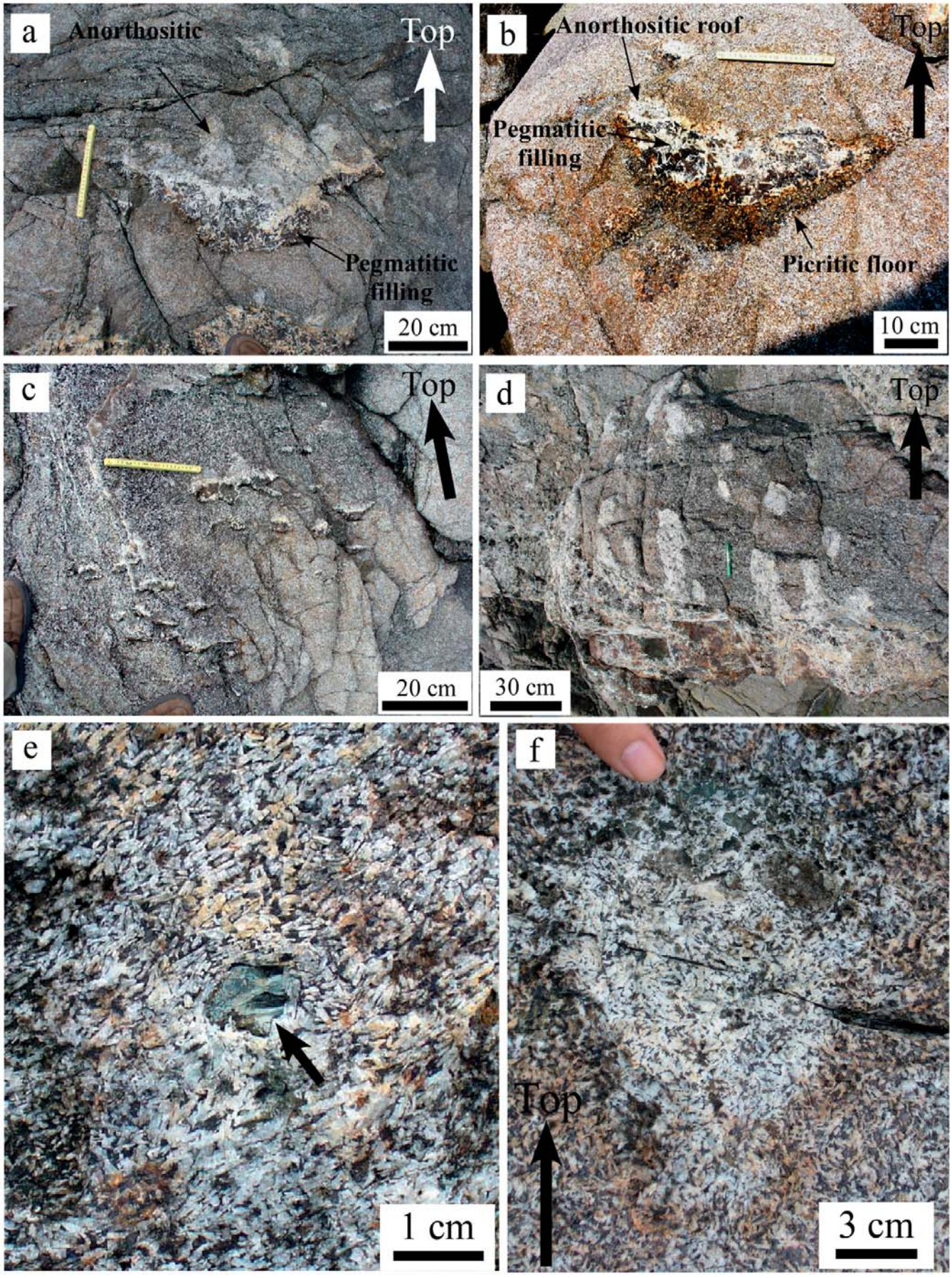

Figure 3 Photographs of podiform gabbroic pegmatites in the GR subzone. Arrow in each photograph indicates the top of the sill: (a) and (b) podiform gabbroic pegmatite (at approximately 40 m from the bottom); (c) Swarming podiform gabbroic pegmatites (at approximately 40 m from the bottom); (d) plume-like structure of anorthosite developed on the roof of podiform gabbroic pegmatite (approximately 50 m from the bottom); (e) An amphibole clot (arrow) in an anorthositic roof. Note plagioclase crystals aligned parallel to the outline of the amphibole clot; (f) A globular mass of anorthosite lying just above the anorthositic roof of the podiform gabbroic pegmatite. The anorthositic mass contains abundant hornblendes at the top of the mass (pointed by a finger).

Figure 4 Photomicrographs of the Murotomisaki gabbroic rocks: (a) the lower chilled margin, sample LCM32 (just contact with the country rocks); (b) Lower-Zone picritic gabbro, sample 91080503 (AC subzone, 15 m from the bottom, around O1 in Fig. 1); (c) Lower-Zone olivine gabbro, sample 91080706 (around O2 in Fig. 1, at 71 m); (d) Middle-Zone coarse gabbro, sample 91080906 (152 m from the bottom); (e) Middle-Zone coarse gabbro, sample 91081003 (162 m from the bottom); (f) Upper-Zone, sample 92081007 (203 m from the bottom). Plastically-deformed plagioclase crystals showing undulose extinction; (g) anorthositic roof of the podiform gabbroic pegmatite, sample 06050402 (53 m from the bottom); (h) picritic floor of the podiform gabbroic pegmatite, sample 06080603 (60 m from the bottom). Abbreviations for minerals are the same as in Figure 1.

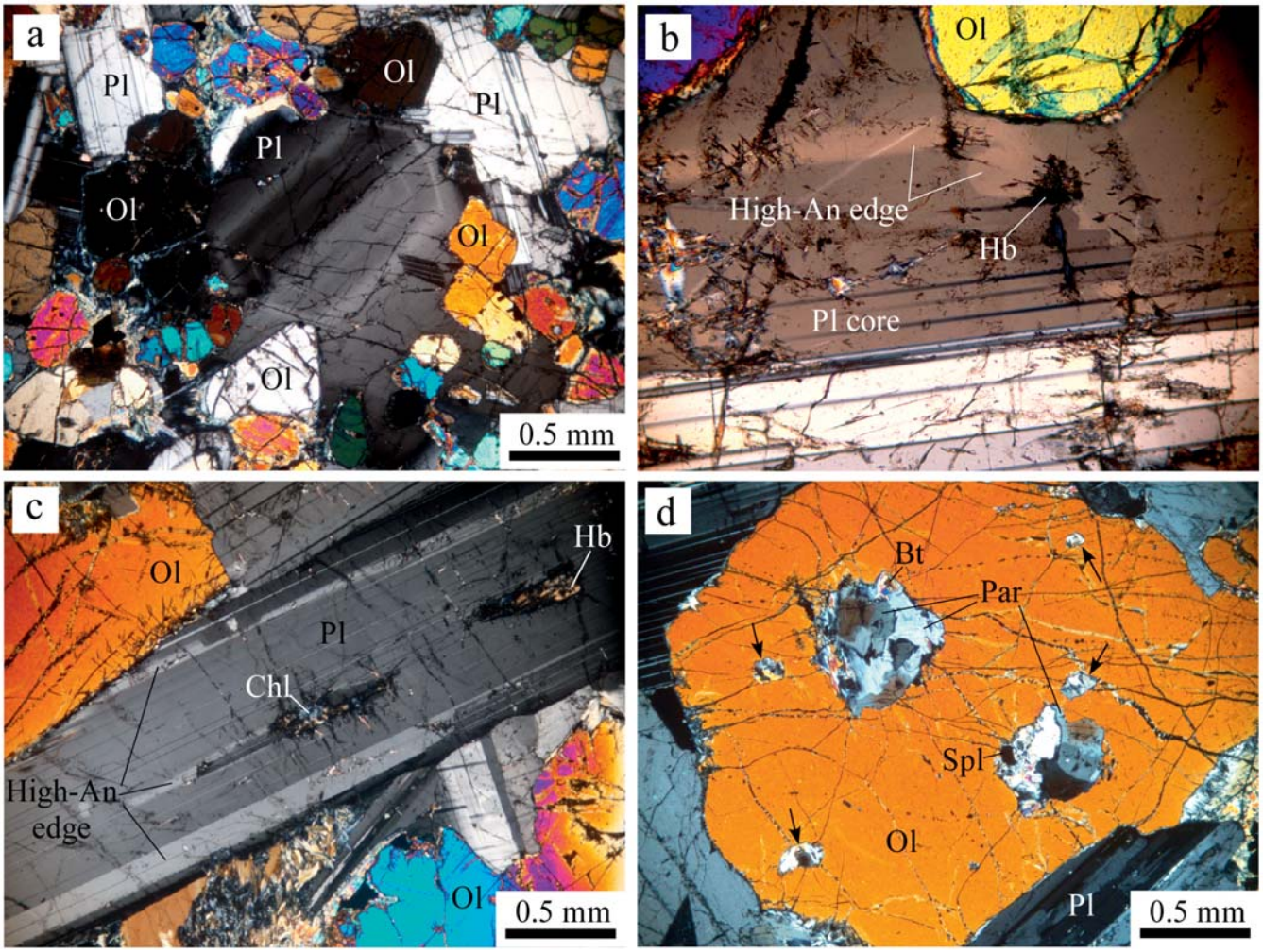

Figure 5 (a) Oscillatory zoned plagioclase of the Lower-Zone picritic gabbro (sample 91080503). (b) A high-An edge (bright part) occurring around the calcic core of plagioclase in the GR subzone. Note that boundary between the core and the edge is rough. (c) Embayments in the calcic cores that are filled with sodic plagioclase associated with small amount of hornblende, augite and chlorite. Thin small high-An edges are developed surrounding the embayment. (d) 'Amphibole clots' included in an olivine crystal of a Lower-Zone olivine gabbro. Abbreviations: Bt = biotite; Par = pargasite; Spl = spinel. Abbreviations for the other minerals are the same as in Figure 1.

3. Plagioclase zoning and its stratigraphic variations

3.1. Plagioclase zoning

The plagioclase-zoning pattern was studied in details using an EDS microprobe at Kyoto University (Hitachi S3500H scanning electron microscope equipped with an EDAX energy dispersive analytical system) and a WDS microprobe at Kobe University (JEOL JXA8900). The accelerating voltage and beam current were maintained at 20 kV and 500 pA at Kyoto, and at 15 kV and 12 nA at Kobe.

It was confirmed that the calcic core of plagioclases from the Lower Zone is nearly constant in An-content throughout the core (see below). Some plagioclase cores from the lower part of the Lower Zone (i.e. the AC subzone) show oscillatory zoning (Fig. 5a), but the oscillation tends to fade away in the upper parts. Olivine crystals are typically in contact with the outlines of the calcic cores of plagioclases (Figs 4c, 5a, 6a). The calcic core is typically surrounded by a narrow edge (of 20–100 μm width) of even more calcic composition (~An72–80). This narrow edge of high An-content is referred to as 'high-An edge' hereafter (Figs 4c, 5a–c, 6a). The outlines of the calcic cores (i.e. the boundaries between the core and the high-An edge) are nearly straight and smooth (Fig. 4c), but some of them are rough or wavy (Fig. 5b). Across the core to the high-An edge, the An-content abruptly increases and then rapidly decreases back to about the same An-content level as the core with a steep gradient (Fig. 7a). Furthermore, the gradient discontinuously changes and then the An-content continuously decreases outwards with a gentler gradient. This outer marginal zone of the gentle compositional gradient is referred to as 'mantle' hereafter. This zoning pattern, which is typically observed in the host olivine gabbros, is designated as Type A (Fig. 8). Locally, there are embayments or 'pools' in the calcic cores of the Type A plagioclases that are filled with distinctly sodic plagioclase (~An50) associated with small amount of augite and hornblende (Figs 5c, 6a). In some cases, narrow high-An edges surrounding the calcic cores are developed surrounding the embayment (Fig. 5c). Small grains of hydrous phases such as amphibole and chlorite occur in the embayments of the calcic cores (Fig. 5c) or along the boundaries between the calcic cores and the high-An edges (Fig. 5b). Such embayments or resorption structures are more pervasive and better developed in the anorthosites as described below.

The plagioclases in the anorthosites, both from the roofs of the podiform gabbroic pegmatites and the anorthositic layers, have similar zonal structure, but this differs from that of the host gabbros. They have the calcic cores nearly constant in

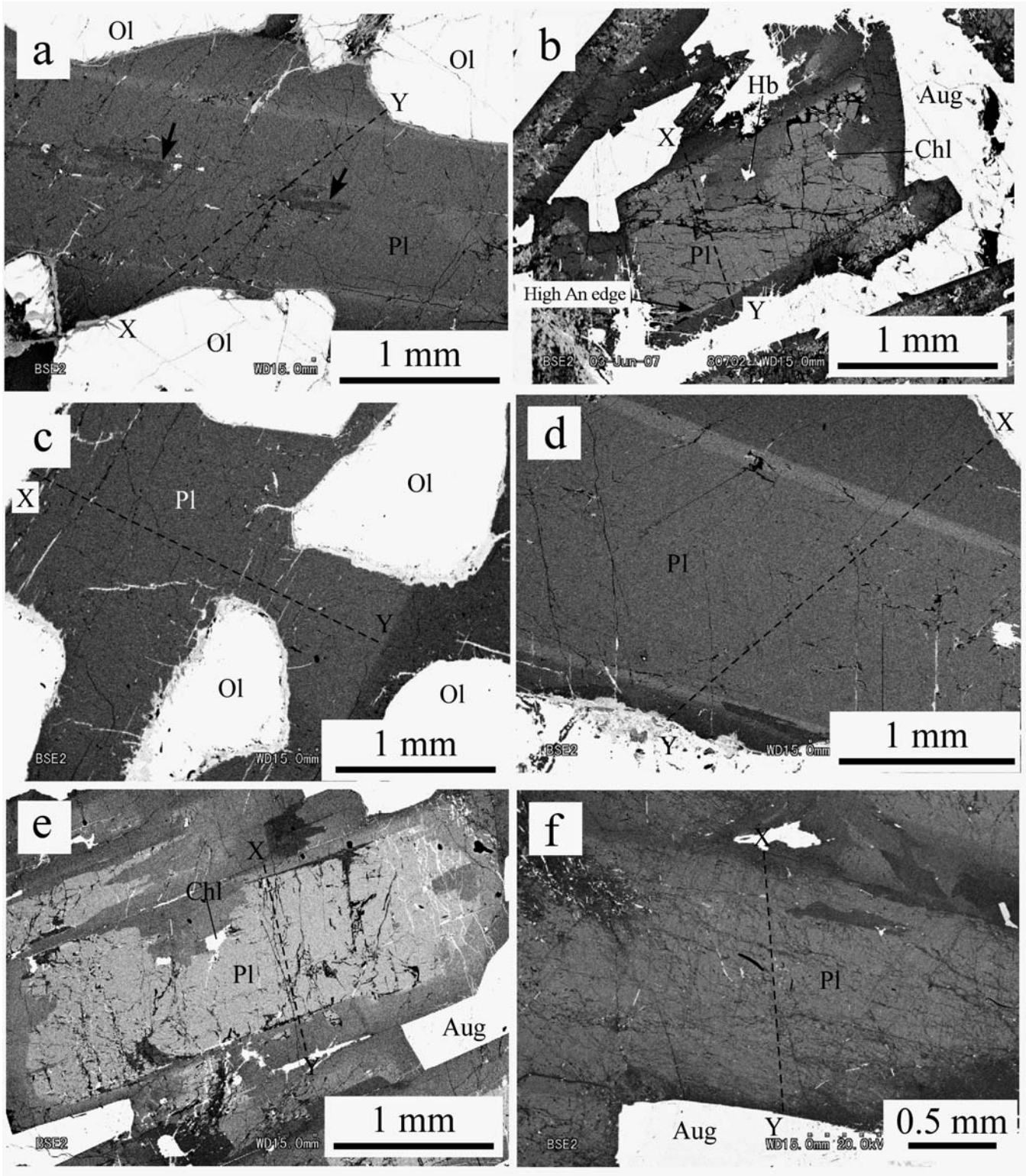

Figure 6 Back scatter electron images of plagioclase crystals from various rock types of the Murotomisaki Gabbro. Dashed lines in the BSE images indicate the zoning profile sections in Figure 7: (a) Plagioclase from the Lower Zone (GR subzone, 71 m from the bottom, sample 92080706); (b) Plagioclase from the anorthositic roof of the podiform gabbroic pegmatite (45 m from the bottom, sample 06080703). The narrow high-An edge (arrow) is partly retained where the calcic core is not embayed; (c) Plagioclase from the picritic floor of the podiform gabbroic pegmatite; (d) Plagioclase from the modal layering (about 40 m from the bottom, sample ML1); (e) Plagioclase from the coarse gabbro in the Middle Zone (152 m from the bottom, sample 91080906); (f) Plagioclase from coarse gabbro in the Middle Zone (162 m from the bottom, sample 91081003). Abbreviations: Hb=hornblende; Chl=chlorite. Abbreviations of the other minerals are the same as in Figure 1.

An-content, which are partly resorbed (Fig. 6b). The resorption structure is more conspicuous in the anorthosites than in the host gabbros. The high-An edges partly surround the outlines of the calcic cores. The An-content abruptly decreases from the core (or the high-An edge) to the mantle, marking a distinct compositional gap (typically by 15–20 An%) between the core and the mantle (Fig. 7b). Throughout the mantle, the An-content gently decreases outwards. This type of zoning is designated as 'Type B' (Fig. 8). The sodic plagioclase that fills the embayments of the calcic core often includes small grains

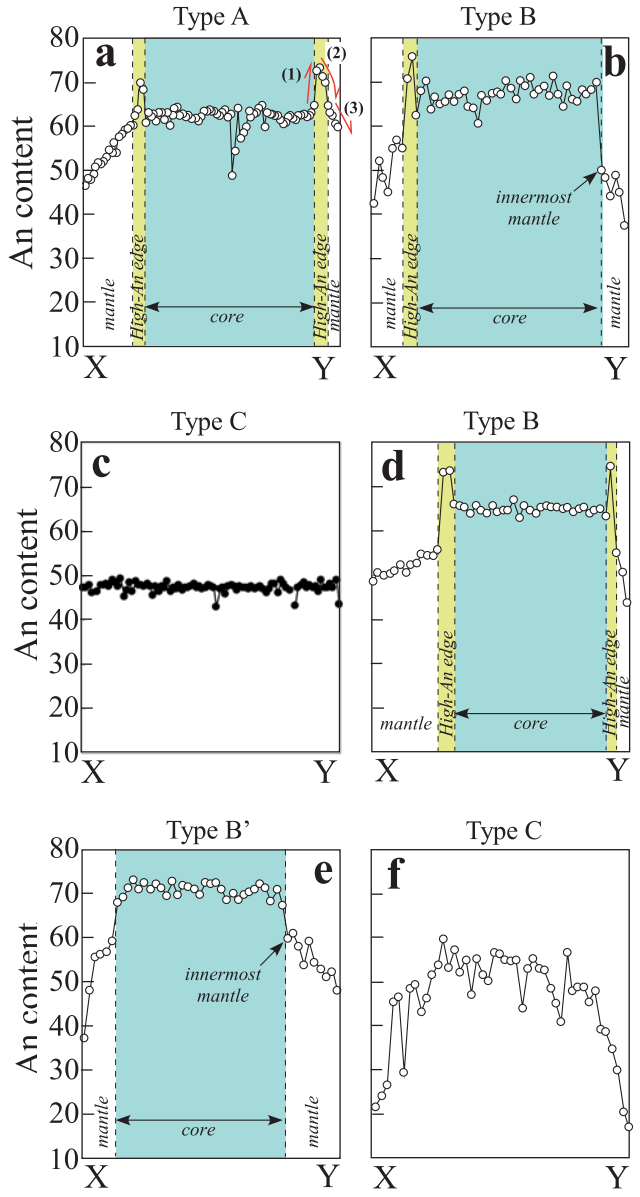

Figure 7 Zoning profiles of plagioclase crystals from various rock types of the Murotomisaki Gabbro: (a) Plagioclase from the Lower Zone (GR subzone, 71 m from the bottom, sample 92080706). Across the core to the high-An edge, (1) the An-content abruptly increases and then (2) rapidly decreases back to about the same An-content as the core with a steep gradient and then (3) continuously decreases outwards with gentler compositional gradients; (b) Plagioclase from the anorthositic roof of the podiform gabbroic pegmatite (45 m from the bottom, sample 06080703). The 'innermost mantle' shows the right outside of the calcic core; (c) Plagioclase from the picritic floor of the podiform gabbroic pegmatite; (d) Plagioclase from the modal layering (about 40 m from the bottom, sample ML1); (e) Plagioclase from the coarse gabbro in the Middle Zone (152 m from the bottom, sample 91080906); (f) Plagioclase from coarse gabbro in the Middle Zone (162 m from the bottom, sample 91081003).

of ferrohornblende, ferro-augite, Fe-chlorite, ilmenite and titaniferous magnetite (Fig. 6b).

Plagioclase in the picritic floors of the podiform gabbroic pegmatites is more sodic ($An_{43–55}$) than that in the host olivine gabbros and the anorthosites (Fig. 7c). They show nearly constant An-content throughout the crystal but locally have narrow sodic rims without calcic cores like those of Types A or B (Fig. 6c). This zoning type is designated as 'Type C' (Fig. 8). The An-content of the core is comparable to that of the innermost mantle (i.e., next to the high-An edge) of the Type B plagioclase from the anorthositic roof within the same podiform gabbroic pegmatites (Figs 7b, 9).

Plagioclases from the modal layering (in the lowermost part of the GR subzone) also have the resorbed calcic cores, like those from the anorthosites of the podiform gabbroic pegmatites and the anorthositic layers. The cores are partly surrounded by the high-An edge and have a compositional gap with a distinctly sodic mantle (therefore Type B) (Fig. 6d). However, the calcic cores are less resorbed and the compositional gap between the core and the mantle is smaller (10–15 An%) than those of the adjacent anorthosites (Figs 6d, 7d). The plagioclase from the modally layered gabbros is, therefore, regarded to be intermediate in terms of zoning and composition between those from the host gabbros and from the anorthosites.

Middle-Zone and Upper-Zone gabbros contain at least two types of plagioclase crystals with distinct zoning patterns. One type has irregular-shaped calcic core with nearly constant An-content surrounded by distinctly sodic mantles (Figs 6e, 7e). Some of them can be classified into Type B, but others lacks the high-An edges. Therefore, the latter zoning pattern is termed as Type B′ to distinguish it from Type B (Fig. 8). It is possible that the high-An edges have been lost by extensive resorption, in which case Type B′ is simply a derivative from Type B. The other type plagioclase is more sodic in composition and does not contain calcic cores with constant An-content (Figs 6f, 7f). It shows normal and gradual zoning and, therefore, is classified as Type C (Fig. 8). In summary there is a good correlation between the zoning type and host the rock type as illustrated in Figure 8 and Table 1. The Lower-Zone olivine gabbro is dominated by Type A, the anorthosites from the Lower Zone are characterised by Type B zoning, whilst both the picritic floor of the podiform gabbroic pegmatite and the mafic part of the modal layering show Type C. The Middle and Upper Zones contain two types, B and C mixed together, and never contain Type-A plagioclase.

3.2. Stratigraphic variation of plagioclase composition

Figure 9 shows a summary of the stratigraphic variation of the An-content of the plagioclase obtained by the microprobe analysis from the host gabbros and the anorthosites (both the anorthositic roofs of the podiform gabbroic pegmatites and the anorthositic layers).

In the AC subzone, the An-content of the core from the host gabbro is nearly constant (in the range of An 70–73), whereas in the upper half of the Lower Zone (i.e., the GR subzone), it gradually decreases with increasing stratigraphic height, from An 73 to about An 62. Note that the plagioclase core composition from the anorthosites is nearly the same as those from host olivine gabbro, except one sample at the 78-m level (No. 91040602). This exceptional anorthositic layer has about 5 An mole % higher cores than those from its host gabbro. The An contents of the high-An edges of the plagioclase core, which are constantly about 10 An % higher than the core values, also decrease with increasing stratigraphic height, again with the exception of the anorthosite layer mentioned above. The An content of the innermost parts of the plagioclase mantles (marked 'im' in Fig. 9), just outside the high-An edge, (Type B and B′ plagioclase) is about 15–20 mole % lower than those of the cores and it also roughly decreases upward.

In the Middle-Zone coarse gabbros, there is no clear correlation between the core composition and the stratigraphic height, although the data are sparse in this zone. Out of six samples analysed, four samples contain only plagioclase crystals of Type C zoning and their cores are all less calcic (An 50–69) than the Lower-Zone core compositions. The other two samples (at 152 and 153 m from the bottom) contain plagioclase of Type B or B′ zoning. These samples are very heterogeneous with respect to core composition, showing wide

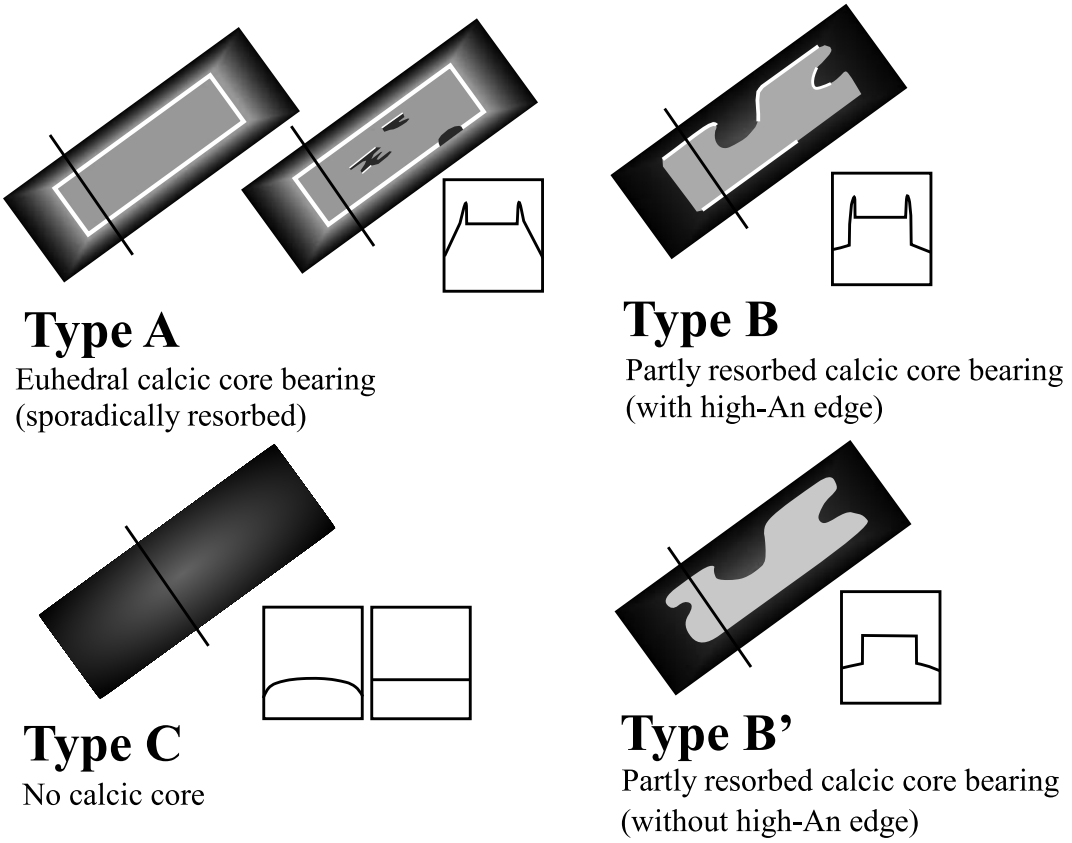

Figure 8 Schematic illustrations of plagioclase compositional zoning patterns observed from the Murotomisaki Gabbro. Each picture of zoned plagioclase is accompanied by a schematic drawing of the line profile.

Table 1 Four types of plagioclase compositional zoning patterns correlated with different rock types of the Murotomisaki Gabbro.

	LZ								
		Modal layering		Podiform gabbro pegmatite					
	Host gabbro	*felsic part*	*mafic part*	*roof*	*pegmatite*	*floor*	Anorthositic layer	MZ	UZ
Type A	○								
Type B	△	○	△	○		△	○	○	
Type B′				○			○	○	○
Type C			○		○	○		○	○

○=common △=present but rare.

compositional ranges of An 63–70 and An 53–68, respectively (Fig. 9). The high-An edges of these samples are about An 74, which is about An 8–10% higher than the core value.

In the Upper-Zone olivine gabbros, there is also no clear correlation between the core composition and the stratigraphic height. The maximum An value of the core composition (of Type B), however, seems to increase with stratigraphic height toward the upper chilled margin. Two samples from the middle of the Upper Zone (at 199 and 203 m levels) are particularly heterogeneous, containing plagioclases of Type B and Type C (Fig. 8).

4. Discussion on the origin of plagioclase zoning

4.1. Lower Zone

The sequence of events inferred from the zonal structure of plagioclase (Type A and Type B in particular) from the Lower Zone, is (1) the formation of homogeneous calcic plagioclase (though some exceptionally show oscillatory zoning); (2) partial resorption of the calcic plagioclase accompanied (or followed) by the formation of the high-An edges; and (3) the formation of sodic mantle by plagioclase overgrowth. This scheme applies to all the plagioclase throughout the lower zone, both in the host olivine gabbros and the anorthosites, but the extent of resorption is greater in the latter. The latter is also characterised by a distinct compositional gap between the calcic core and the mantle (i.e., Type B, or B′), which may bear important implications for the origin of these structures. The processes of these events will be discussed sequentially below.

4.1.1. Formation of calcic plagioclase and the origin of the stratigraphic variations. The compositional constancy of the plagioclase core observed in the AC-subzone gabbros, including the 'phenocryst' in the lower chilled margin (Fig. 9), indicates that the calcic-core parts represent the original

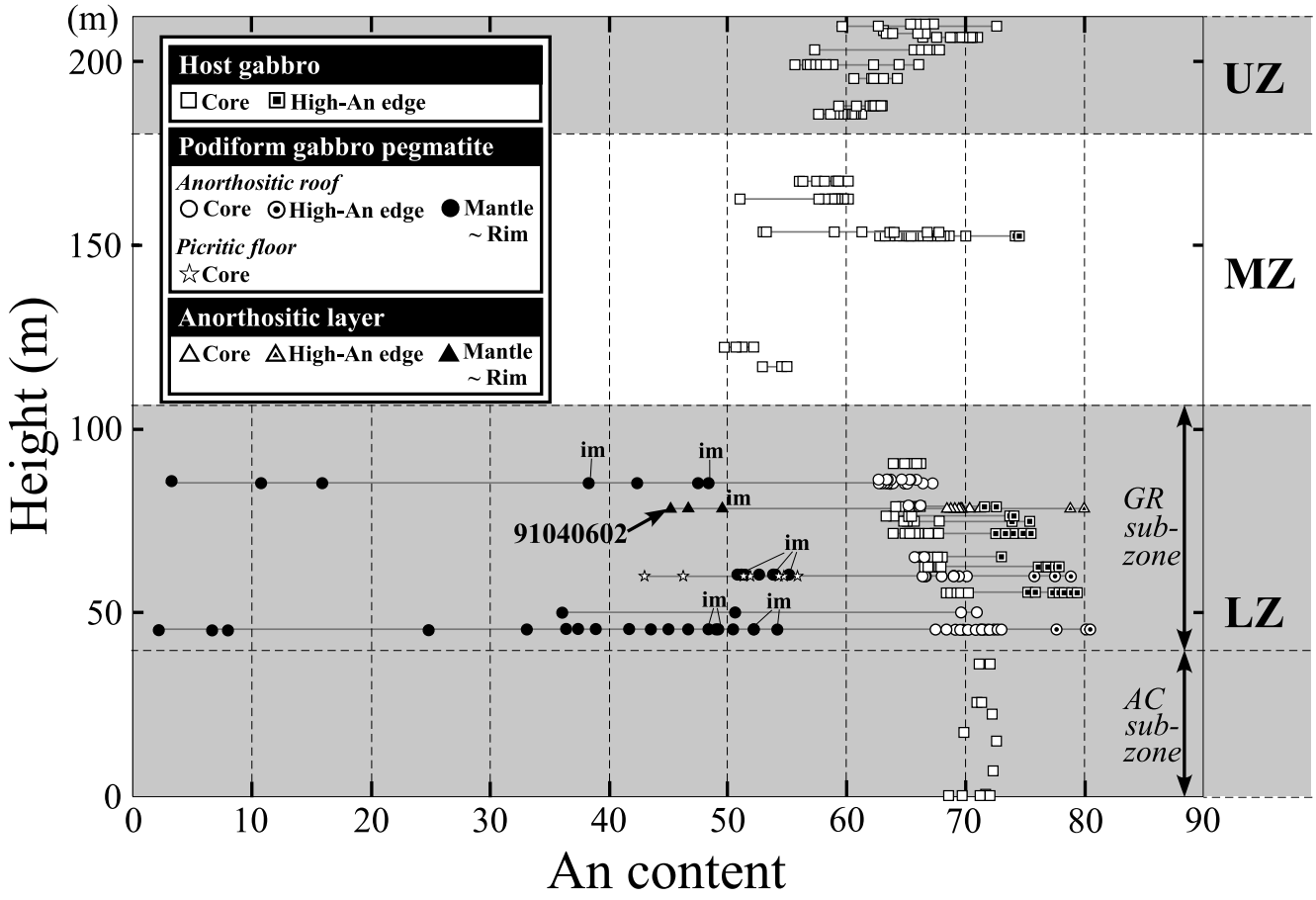

Figure 9 Stratigraphic variations of the plagioclase compositions throughout the Murotomisaki Gabbroic Intrusion. im=innermost mantle. The data of AC subzone are from Akatsuka *et al.* (1999). An exceptional sample, No. 91040602, is indicated by an arrow (see text).

plagioclase that was already present in the initial magma. It is remembered here that the size of the calcic core from the AC subzone is nearly the same as that of the phenocrysts in the chilled margin. The AC subzone was originally defined as the zone of crystal accumulation of olivine (Hoshide *et al.* 2006a), but the accumulation hypothesis may also apply to the plagioclase. The sodic mantle surrounding the calcic core, on the other hand, is considered to represent a postcumulus overgrowth as discussed below.

The vertical stratigraphic gradient of the plagioclase core composition in the GR subzone suggests that, in contrast to the AC subzone, some differentiation has taken place in the formation of this subzone (Fig. 9). Compositionally-uniform cores indicate that plagioclase crystallised without significant fractionation, which suggests that the effective size of the melt reservoir in equilibrium with the plagioclase was large enough and that the melt was thoroughly stirred. The vertical compositional gradient in the GR subzone, therefore, is interpreted to be a record of the melt composition evolved as the GR subzone grew (i.e., the upward migration of the boundary layer).

It is conceivable, therefore, that the GR subzone represents successively frozen magmatic boundary layers that have developed above the AC subzone. It was concluded from the observation of crystal grain size that olivine has grown significantly in the formation of the GR subzone (Hoshide *et al.* 2006a). Apparently, plagioclase has grown considerably as well. It was observed that, in the Lower Zone, olivine crystals are often partly included in the mantle of the plagioclase and are in contact with the outlines of the calcic cores (Figs 4c, 5a, 6a). It is plausible, therefore, that the calcic plagioclase and olivine came closer during the crystal settling and 'collided' with each other (i.e., crystal impingement) before the plagioclase overgrowth, forming a crystal-supported 'framework structure'.

4.1.2. Resorption of calcic plagioclase and the formation of the high-An edges. The presence of hydrous phases, such as amphibole and chlorite at the embayments of the calcic cores, indicates that the resorption and probably the formation of high-An edges may have occurred in a hydrous environment that was created by the introduction (or fluxing) of H_2O. The resorption may occur when melt becomes undersaturated with plagioclase, and such a disequilibrium situation may be realised if H_2O is introduced in the system as follows. An introduction of H_2O would depress the liquidi (and solidi) of anhydrous phases such as plagioclase, olivine and cpx. Because the extent of the depression is greater for plagioclase than for olivine and cpx (e.g., McBirney 1987), the plagioclase field shrinks, and therefore, the liquid originally coexisting with olivine and plagioclase becomes undersaturated with these silicates and, therefore, plagioclase (and olivine as well) simply starts to dissolve (Fig. 10, the 'simple dissolution' of Tsuchiyama 1985). The source of H_2O may be sought in the lower part of the boundary layer, because the H_2O content in the melt increases rapidly as fractionation advances. More advanced resorption observed in the anorthosite implies more pervasive and extensive introduction of H_2O there than in the host.

Following McBirney (1987), the present authors interpret the formation of high-An edges in the context of the hydrous crystallisation as follows. Suppose liquid L_1 and plagioclase S_1 once equilibrated (Fig. 10). When H_2O comes in, both liquidus and solidus are depressed according to the introduced H_2O

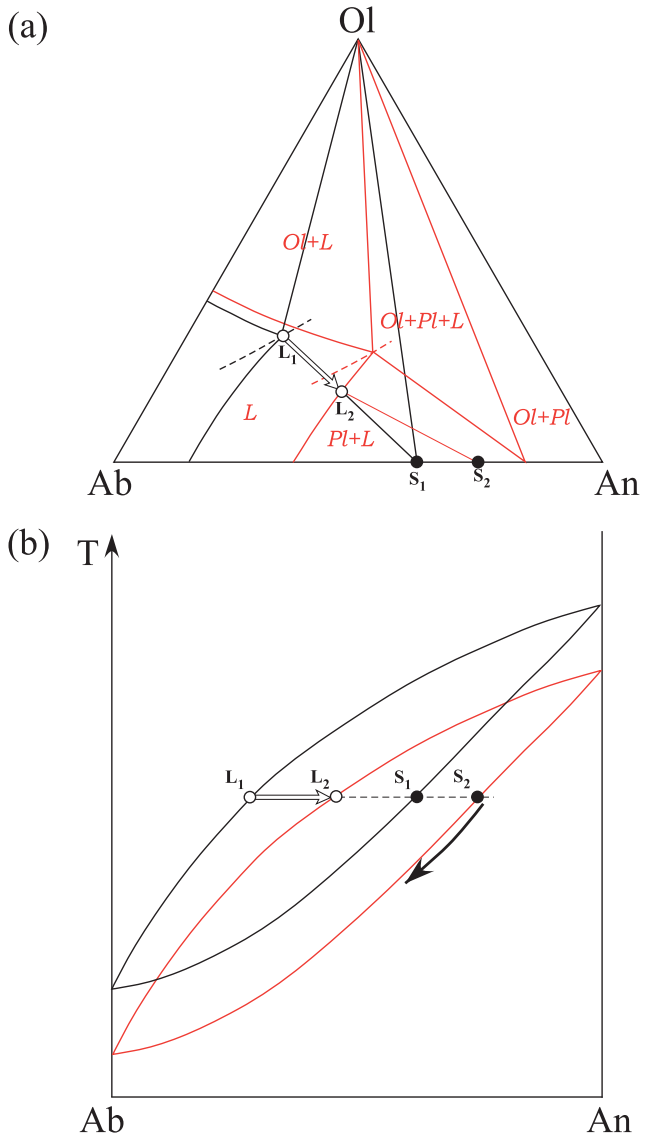

Figure 10 (a) Isothermal sections of a hypothetical liquidus diagram of an olivine–Ab–An-(+H_2O) system. Dry (black) and wet (red) isothermal sections at the same temperature and the same total pressure but of different activities of H_2O are drawn for comparison. Each field is labelled for wet condition for clarity only. Projections of Ol–Pl cotectic lines are partly drawn as dashed lines. When H_2O is introduced in the dry system in which liquid L_1 and plagioclase S_1 were equilibrated, the original liquid L_1 becomes undersaturated with plagioclase (and olivine) and the plagioclase (S_1) starts to dissolve, forming a thin film of hydrous liquid L_2 on the surface of the dissolving plagioclase crystals. L_2–S_2 is an equilibrium tie line between the hydrated liquid and plagioclase. (b) Schematic projections of the plagioclase liquidus and solidus from H_2O and olivine apexes onto the plagioclase-temperature plane. Dry (black) and wet (red) projections are compared. L_1, L_2, S_1, S_2 are projections of those in the isothermal sections in (a). See text for more explanation.

content, and then the original liquid becomes undersaturated and so the plagioclase (S_1) starts to dissolve, forming a thin film of hydrous liquid L_2 on the surface of the dissolving plagioclase crystals. The formation of liquid L_2 makes a steep compositional gradient from the original composition L_1, away from the plagioclase, toward L_2 on the plagioclase surface. If the ambient temperature decreases faster than the elimination of this compositional gradient by diffusion in the melt, the new plagioclase that is precipitated on the dissolved plagioclase surface will be strongly zoned, reflecting this compositional gradient as follows. The first plagioclase to precipitate will be very close to S_2, which is in equilibrium with L_2 and is more An-rich than the original composition S_1. Upon cooling, a sharp zoning will be formed from this S_2 toward composition S_1 which is in equilibrium with the original liquid L_1, thereby forming the high-An edge. After that, normal zoning due to ordinary fractional crystallisation follows, which should show a gentler compositional slope than that in the high-An edge.

Dissolution of olivine as well as of plagioclase should occur when H_2O comes in and, because of the shift of the olivine–plagioclase cotectic line toward plagioclase, the original liquid enters into the olivine field (Fig. 10a) and then, upon cooling, olivine starts to grow before the liquid gets saturated with plagioclase again. It is probable that hydrous melts, which are now represented by amphibole clots, were those entrapped in these growing olivines. Similar amphibole-bearing clots have been observed in olivine, apatite and chromite crystals in many plutonic rocks (Boudreau *et al.* 1986; Boudreau 1999; Jakobsen *et al.* 2005; Li *et al.* 2005). Jakobsen *et al.* (2005) interpreted those amphibole clots in olivine from the Skaergaard Intrusion to represent trapped immiscible liquids at some early stages of fractionation. The similar occurrences and mineralogies of these amphibole clots may suggest that similar hydrous processes as advocated above for the Murotomisaki Gabbroic Intrusion (MGI) were operative in many plutonic environments.

Pringle *et al.* (1974) observed similar calcic edges of plagioclase in a diabase sheet from Grand Manan Island (Canada) and ascribed it to a large pressure drop when host magma ascended from a deep magma reservoir. However, such a hypothesis cannot be applied to the MGI, because the calcic cores of plagioclase in the MGI are generally larger than the plagioclase phenocrysts from the chilled margin and, therefore, the formation of the high-An edges must be after the emplacement of the magma. Certain pressure drop may occur in a magma reservoir if eruption occurs in overpressurised circumstances (e.g., Williams & McBirney 1979). The observed compositional 'jump' of the high-An edge (about 10 An%) corresponds to as much as 5 kbar pressure drop (Takagi *et al.* 2005). This is too large to be accounted for by volcanic eruptions (Williams & McBirney 1979). Similar high-An edges of plagioclase have also been described from the Skaergaard Intrusion by Maaløe (1976), who ascribed the feature to a disequilibrium overgrowth of plagioclase from supercooled magma. The supersaturation hypothesis has been employed to explain the oscillatory zoning of plagioclase (e.g., Sibley *et al.* 1976), but will not fit the explanation for such a sharp and single An-edge as observed in the MGI. An alternative hypothesis has therefore been presented for the MGI for the formation of high-An edges, combining the resorption by means of an introduction of H_2O (H_2O fluxing) from the lower horizons of the boundary layer.

4.1.3. Origin of the sodic mantle. Overgrowth of the sodic mantle occurred after the resorption events described above. As emphasised above, the important difference between the host gabbro and the anorthosites in the GR subzone lies in the composition of the overgrown mantle of the plagioclase (Fig. 7a, b). Whilst the An-content gradually decreases from the core to the mantle of plagioclase in the host gabbro (Type A), it abruptly drops in the mantle in the anorthosites, marking a clear compositional gap at the edge–mantle boundary for the latter (Type B). The compositional gap in the plagioclase in the anorthosites may be ascribed to a discontinuous change in composition of the melt surrounding the plagioclase crystals. Such a change of melt composition cannot be explained by the introduction of H_2O alone, as advocated above, and an additional introduction of fractionated melt components would be required. The introduction of the hypothetical fractionated melt was probably restricted to the anorthosite and

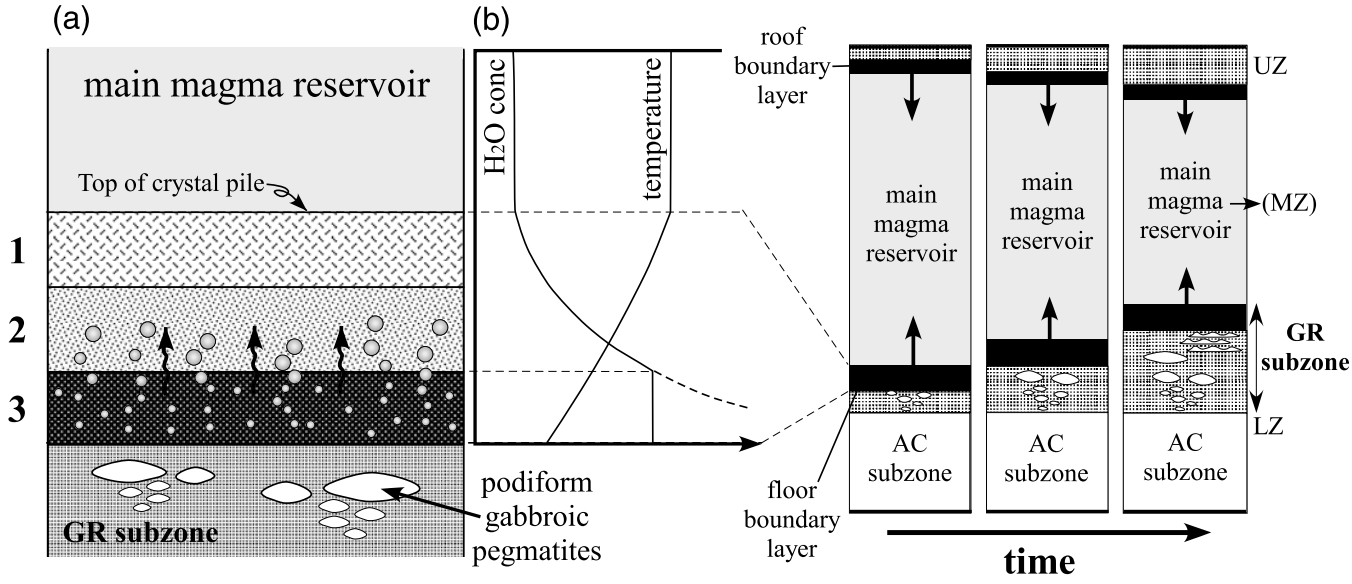

Figure 11 (a) Schematic picture of a stratified basal boundary layer. The boundary layer is divided into three zones: Zone 1, plagioclase and olivine precipitate; Zone 2, hydrous flux melting and melt segregation (podiform gabbroic pegmatites and anorthosite layers); Zone 3, source of H_2O and fractionated melts. See text for explanation. Thermal and H_2O concentration gradients are only schematic. Fractionated melt reaches H_2O saturation in Zone 3. (b) Advancing two boundary layers produce a stratified layered gabbro.

gabbro pegmatites. In other words, the anorthosite and the gabbro pegmatites are the very sites that were preferentially attacked by the flux of fractionated melts accompanied by H_2O. The gentle An-decrease zoning in the mantle reflects subsequent fractional crystallisation that took place in the interstitial melts.

The source of this hypothetical fractionated melt is also sought in the lower part of the boundary layer (Fig. 11). It is conceivable that both H_2O and fractionated melt come together from the same lower horizons. Fractionated melt will be enriched with H_2O, but considering the probable H_2O-saturated situation, it is likely that H_2O-rich fluids and the fractionated melt came together.

Plagioclase crystals from the picritic floor of the podiform gabbroic pegmatite hardly contain these calcic cores (Figs 6c, 7c). Their core composition is comparable to the mantle of the plagioclase from the anorthositic roof (Fig. 9). It is conceivable, therefore, that the crystallisation of plagioclase in the picritic floors took place concomitantly, maintaining chemical equilibrium with the mantle overgrowth of the plagioclase in the anorthositic roofs, i.e., after the invasion (or infiltration) of the fractionated melt. Similar to the plagioclase core in the anorthositic roofs, the olivine in the picritic floors has nearly the same composition as those in the adjacent host olivine gabbros. Therefore, it is conceivable that both the calcic plagioclase and the olivine formed together in the host gabbro and that they were separated and segregated when the fractionated melt came in.

4.2. Middle Zone

The Middle-Zone coarse gabbros contain three types of zoning, B, B′ and C (Fig. 8, Table 1). Many plagioclases from the Middle Zone are more sodic than those from the Upper and Lower Zones (Type-C), while those in some samples (at the 152- and 153-m levels) are strongly calcic and have a homogeneous calcic core (Types B and B′). The Type C plagioclase may represents *in-situ* crystallisation products from the ambient fractionated melt. Type B and B′ plagioclases on the other hand must be exotic in origin. Because plagioclase with the high-An edges (i.e. Types A or B) cannot be found in the Upper Zone, the source of these plagioclases must be sought in the Lower Zone. Occurrence of the Type-B and B′ plagioclase in the Middle Zone may be understood by considering the diapirism of anorthositic crystal mushes generated from the GR subzone below, as advocated by Hoshide *et al*. (2006b). In the samples containing Type-B and B′ plagioclase, the An-contents of plagioclase cores have a wide range amongst the different grains within one sample. This disequilibrium amongst the different grains suggests repeated supplies of diapiric anorthositic crystal mushes from the advancing basal boundary layer and incomplete magma mixing.

4.3. Upper Zone

The Upper Zone contains two types of zoning, B′ and C (Fig. 8 and Table 1). In the Upper Zone, the maximum value of An-content of the plagioclase core (Fig. 9) has an apparently vertical gradient. Some of the plagioclases forming the vertical compositional gradient have compositional gaps between the cores and the mantles (i.e., Type-B′). The compositional gaps may suggest mixing between the crystal and the fractionated melt, as inferred for the Lower Zone. It is possible that the Type B′ plagioclase has its origin in the Lower Zone as in the Middle Zone, but full understanding of the origin and the processes of the Upper Zone must await further, more detailed, investigations of this zone.

5. Segregation and diapirism of the anorthositic crystal mushes

Another important effect of H_2O is lowering the viscosity of silicate melt. The H_2O-charged flux-melting zone within the boundary layer may become fluid-dynamically unstable, because H_2O effectively reduces the viscosity of silicate melt and thus increases the readiness of segregation in crystal mushes (McBirney 1987), causing an effective separation of lighter plagioclase crystals from the heavier olivine forming a modally graded layering (Fig. 2c), as observed in the base of the GR subzone. The podiform gabbroic pegmatite and the anorthosite may represent evolved forms of such a modally-layered structure. If the H_2O-enriched magma is segregated, forming a pod or layer, it will gain more buoyancy because the

buoyancy is proportional to the volume of the masses, which would cause a gravitational instability. The wavy structure of the anorthosite roof and the upper surface of the anorthosite layer may be a manifestation of such instability. As crystallisation advances within the podiform gabbroic pegmatite, residual melt will become even more hydrous. This is consistent with the formation of pegmatitic filling between the anorthositic roof and the picritic floor, and also accounts for the observed coarsening of olivine crystals in the GR subzone. The occurrence of such buoyant hydrous melts in the anorthosite will enhance the buoyancy of the anorthositic magma and help the diapiric plume to develop. These plumes will eventually detach from their source, leaving the podiform gabbroic pegmatite with little anorthositic roof, as observed. The fact that the proportion of the anorthosite roof is very small in some podiform pegmatites (Fig. 3d) may indicate that substantial amounts of anorthositic magmas may have already escaped in the form of plumes from the site of their generation. The quantitative aspect of this process, i.e., the amount of the plume generated and the extent of its effect on the magmatic evolution, must be examined by studying mass balance using more extensive whole-rock data, which is a subject of future work.

6. Summary and synthesis

The processes deciphered from the analysis of the zonal structure of the MGI plagioclase may be summarised in the schematic picture in Figure 11. The whole process of the formation of the GR subzone (in the Lower Zone) may be understood in terms of a moving boundary layer in a crystallising magma body. The boundary layer, which contains steep thermal and chemical gradients, should be internally stratified in a steady state in three zones, 1, 2 and 3, as in Figure 11a. Zone 1, just beneath the crystallisation front, is that of crystal growth and crystal settling. Olivine and plagioclase steadily grow as the cooling advances and grown crystals will start to settle, probably leading to the 'crystal impingement'. Zone 2 is where H_2O-fluxed remelting and local crystal-melt segregation occurs, caused by the introduction of H_2O and fractionated melts ascending from Zone 3 below. The modal layering, podiform gabbroic pegmatites and anorthositic layers were probably formed in this zone. Microscopically high-An edges formed around the resorbed plagioclase crystals upon further cooling. Zone 3 is the source of the H_2O and hydrous fractionated melts which should be saturated with H_2O. Mixtures of H_2O-rich bubbles and fractionated melts probably rise together from this zone and get into Zone 2. Formation of the plagioclase sodic mantle and precipitation of augite occur in this zone. The compositional layering developed in the second layer will be frozen in this layer and, as the boundary layer migrates upward, accrete to the growing GR subzone just behind the moving boundary layer. Zone 2 is also a source of anorthositic crystal mush plumes, which may feed the main magma body above the boundary layer. The possibility that plagioclase crystals with high calcic cores (i.e., Type B and Type B′) found in the Middle Zones were derived from these anorthositic plumes was discussed previously.

This is a similar process to the 'constitutional zone refining' proposed by McBirney (1987) and Boudreau (1999), except for the diapiric ascent of anorthositic crystal mushes. H_2O accumulation in Zone 2 is responsible for the segregation and formation of the compositional layering as originally proposed by McBirney (1987). Quantitative aspects of the effects of the ascending plumes generated from Zone 2 remains to be examined with more geochemical data.

The Upper Zone may have been formed at the same time by another moving boundary layer descending from the top of the magma body (Fig. 11b). However, the detailed processes in this descending boundary layer have not been discussed. The Middle Zone may represent the last layer of freezing sandwiched by these two moving boundary layers.

More detailed analysis of the Middle and Upper zones is necessary for a full understanding of the whole process of magmatic differentiation.

7. Acknowledgements

We are grateful to Dirk Spengler and Tetsuo Kawakami of Kyoto University for their discussions and critical reading of the manuscript and to A. Toramaru (Kyushu University) for valuable discussions in the field. We also acknowledge T. Akatsuka for his permission for the use of unpublished data, and to H. Sato and U. Honma for arranging the electron microprobe facility at Venture Business Laboratory of Kobe University. The paper has benefited from critical and constructive criticisms of J. H. Bédard and R. A. Wiebe. This study was financially supported by a Grant-in-Aid for Research Fellow of the Japan Society for the Promotion of Science (No.19·4363) to TH.

8. References

Akatsuka, T., Obata, M. & Yokose, H. 1999. Formation of layered structure in the Murotomisaki gabbroic complex, especially picrite gabbro, Kochi Prefecture, Japan–Quantitative evaluation of crystal accumulation. *Journal of the Geological Society of Japan* **105** (11), 771–88. [In Japanese with English abstract.]

Boudreau, A. E. 1999. Fluid Fluxing of Cumulates: the J-M Reef and Associated Rocks of the Stillwater Complex, Montana. *Journal of Petrology* **40**, 755–72.

Boudreau, A. E., Mathez, E. A. & Mccallum, I. S. 1986. Halogen Geochemistry of the Stillwater and Bushveld Complexes: Evidence for Transport of the Platinum-Group Elements by Cl-Rich Fluids. *Journal of Petrology* **27**, 967–86.

Brandeis, G. & Jaupart, C. 1986. On the interaction between convection and crystallization in cooling magma chambers. *Earth and Planetary Science Letters* **77**, 345–61.

Costa, A., Blake, S & Self, S. 2006. Segregation processes in vesiculating crystallizing magmas. *Journal of Volcanology and Geothermal Research* **153**, 287–300.

Hamamoto, R. & Sakai, H. 1987. Rb–Sr age of granophyre associated with the Muroto-misaki gabbroic complex. *Science Reports of the Faculty of Science, Kyushu University, Geology* **15** (1), 131–5. [In Japanese with English abstract.]

Hoshide, T., Obata, M. & Akatsuka, T. 2006a. Crystal settling and crystal growth of olivine in the magmatic differentiation – the Murotomisaki Gabbroic Complex, Shikoku, Japan –. *Journal of Mineralogical and Petrological Sciences* **101**, 223–39.

Hoshide, T., Obata, M. & Akatsuka, T. 2006b. Magmatic differentiation by means of segregation and diapiric ascent of anorthositic crystal mush – the Murotomisaki Gabbroic Complex, Shikoku, Japan. *Journal of Mineralogical and Petrological Sciences* **101**, 334–9.

Jakobsen. J. K., Veksler, I. V., Tegner, C. & Brooks, C. K. 2005. Immiscible iron- and silica-rich melts in basalt petrogenesis documented in the Skaergaard intrusion. *Geology* **33**, 885–8.

Kodama, K., Taira, A., Okamura, M. & Saito, Y. 1983. Paleomagnetism of the Shimanto Belt in Shikoku, southwest Japan. *In* Hashimoto, M. & Uyeda, S. (eds) *Accretion Tectonics in the Circum-Pacific Regions,* 231–41. Tokyo: Terra Scientific Publishing Company.

Kodama, K. & Koyano, T. 2003. Paleomagnetism and magnetic fabric of a mafic intrusive body and surrounding sedimentary rocks in the shimanto belt, southwest Japan: structural evolution of an accretionary prism recorded in magnetization of fore-arc intrusive rocks. *IUGG 2003 Scientific Program Abstract*, GAI.06. Sapporo, Japan: International Union of Geodesy and Geophysics.

Li, C., Ripley, E. M., Sarkar, A., Shin, D. & Maier, W. D. 2005. Origin of phlogopite-orthopyroxene inclusions in chromites from

the Merensky Reef of the Bushveld Complex, South Africa. *Contributions to Mineralogy and Petrology* **150**, 119–30.

Maaløe, S. 1976. The zoned plagioclase of the Skaergaard Intrusion, East Greenland. *Journal of Petrology* **17**, 398–419.

Mangan, M. & Marsh, B. D. 1992. Solidification front fractionation in phenocryst-free sheet-like magma bodies. *Journal of Geology* **100**, 605–20.

Marsh, B. D. 1988. Crystal capture, sorting, and retention in convecting magma. *Geological Society of America Bulletin* **100**, 1720–37.

McBirney, A. R. 1987. Constitutional zone refining of layered mafic intrusions *In* Parsons, I. (ed) *Origins of Igneous Layering*, 437–52. Dordrecht, Holland: D. Reidel Publishing.

Pringle, G. J., Trembath, L. T. & Pajari, G. E. 1974. Crystallization history of a zoned plagioclase. *Mineralogical Magazine* **39**, 867–77.

Sibley, D. F., Vogel, T. A., Walker, B. M. & Byerly, G. R. 1976. The origin of oscillatory zoning in plagioclase; a diffusion and growth controlled model. *American Journal of Science* **276**, 275–84.

Tait, S. & Jaupart, C. 1992. Compositional convection in a reactive crystalline mush and melt differentiation. *Journal of Geophysical Research* **97**, 6735–56.

Takagi, D., Sato, H. & Nakagawa, M. 2005. Experimental study of a low-alkali tholeiite at 1–5 kbar: optimal condition for the crystallization or high-An plagioclase in hydrous arc tholeiite. *Contributions to Mineralogy and Petrology* **149**, 527–40.

Tsuchiyama, A. 1985. Dissolution kinetics of plagioclase in the melt of the system diopside-albite-anorthite, and origin of dusty plagioclase in andesites. *Contributions to Mineralogy and Petrology* **89**, 1–16.

Turner, J. S., Huppert, H. E. & Sparks, R. S. J. 1986. Komatiites II: Experimental and theoretical investigations of post-emplacement cooling and crystallization. *Journal of Petrology* **27**, 397–437.

Williams, H. & McBirney, A. R. 1979. *Vulcanology.* San Francisco, California: Freeman, Cooper. 397 pp.

Yajima, T. 1972. Petrology of the Murotomisaki gabbroic complex. *The Journal of the Japanese Association of Mineralogists, Petrologists and Economic Geologists* **67**, 218–41.

MS received 30 November 2007. Accepted for publication 16 May 2008 (Stellenbosch); 15 January 2009 (RSE).

CONTENTS

Preface
J.D. Clemens

Plutonism versus Neptunism at the southern tip of Africa: The debate on the origin of granites at the Cape, 1776–1844
S. Master

The sanukitoid series: Magmatism at the Archaean–Proterozoic transition
H. Martin, J.-F. Moyen, and R. Rapp

The geochemistry of Archaean plagioclase-rich granites as a marker of source enrichment and depth of melting
J.-F. Moyen, D. Champion, and R.H. Smithies

Similarities between mantle-derived A-type granites and voluminous rhyolites in continental flood basalt provinces
S. Turner and T. Rushmer

Structural controls on melt segregation and migration related to the formation of the diapiric Schwerin Fold in the contact aureole of the Bushveld Complex, South Africa
L. Longridge, R.L. Gibson, and P.A.M. Nex

Parental magmas of Grenville Province massif-type anorthosites, and conjectures about why massif anorthosites are restricted to the Proterozoic
J.H. Bédard

Granite formation: Stepwise accumulation of melt or connected networks?
P.D. Bons, J.K. Becker, M.A. Elburg, and K. Urtson

Emplacement and assembly of shallow intrusions from multiple magma pulses, Henry Mountains, Utah
E. Horsman, S. Morgan, M. de Saint-Blanquat, G. Habert, A. Nugent, R.A. Hunter, and B. Tikoff

Four-stage building of the Cambrian Carion pluton (Madagascar)
M.O.M. Razanatseheno, A. Nédélec, M. Rakotondrazafy, J.G. Meert, and B. Ralison

Anisotropy of magnetic susceptibility fabrics in syntectonic plutons as tectonic strain markers: The example of the Canso pluton, Meguma Terrane, Nova Scotia
K. Benn

Chemical structure in granitic magmas—A signal from the source?
J.D. Clemens, P.A. Helps, and G. Stevens

Causes of compositional diversity in a lobe of the Half Dome granodiorite, Tuolumne Batholith, Central Sierra Nevada, California
R.C. Economos, V. Memeti, S.R. Paterson, J.S. Miller, S. Erdmann, and J. Žák

The evolution of late-Hercynian granites and rhyolites documented by quartz—A review
A. Müller, A.M. van den Kerkhof, H.-J. Behr, A. Kronz, and M. Koch-Müller

Trace element constraints on mid-crustal partial melting processes—A garnet ionprobe study from polyphase migmatites (Damara orogen, Namibia)
C. Jung, S. Jung, E. Hellebrand, and E. Hoffer

Crustal melt granites and migmatites along the Himalaya: Melt source, segregation, transport and granite emplacement mechanisms
M.P. Searle, J.M. Cottle, M.J. Streule, and D.J. Waters

Zoning and resorption of plagioclase in a layered gabbro, as a petrographic indicator of magmatic differentiation
T. Hoshide and M. Obata

Author Index

THE GEOLOGICAL SOCIETY OF AMERICA®

3300 Penrose Place • P.O. Box 9140
Boulder, CO 80301-9140, USA

ISBN 978-0-8137-2472-0

9 780813 724720